THERMOMETRY AND COHERENCE PROPERTIES OF A ULTRACOLD QUANTUM GAS OF METASTABLE HELIUM

José Carlos Viana Gomes

▶ **To cite this version:**

José Carlos Viana Gomes. THERMOMETRY AND COHERENCE PROPERTIES OF A ULTRACOLD QUANTUM GAS OF METASTABLE HELIUM. Atomic Physics [physics.atom-ph]. Université Paris Sud - Paris XI, 2007. English. NNT : . tel-00142413

HAL Id: tel-00142413

https://pastel.hal.science/tel-00142413

Submitted on 18 Apr 2007

HAL is a multi-disciplinary open access archive for the deposit and dissemination of scientific research documents, whether they are published or not. The documents may come from teaching and research institutions in France or abroad, or from public or private research centers.

L'archive ouverte pluridisciplinaire **HAL**, est destinée au dépôt et à la diffusion de documents scientifiques de niveau recherche, publiés ou non, émanant des établissements d'enseignement et de recherche français ou étrangers, des laboratoires publics ou privés.

N° d'ordre : xxxx

INSTITUT D'OPTIQUE THÉORIQUE ET APPLIQUÉE
LABORATOIRE CHARLES FABRY

UNIVERSITÉ PARIS XI
U.F.R. SCIENTIFIQUE D'ORSAY

THÈSE

présentée pour obtenir

le GRADE de DOCTEUR EN SCIENCES

DE L'UNIVERSITÉ PARIS XI ORSAY

par

Jose Carlos VIANA GOMES

Sujet :

THERMOMÉTRIE ET PROPRIÉTÉS DE COHÉRENCE D'UN GAZ QUANTIQUE ULTRA-FROID D'HÉLIUM MÉTASTABLE

A soutenir le 9 fevrier devant la Commission d'examen :

M.	C. WESTBROOK	Directeur de thèse
M.	M. BELSLEY	Directeur de thèse
M.	V. LORENT	Rapporteur
M.	J. MENDONÇA	Rapporteur
M.	O. DULIEU	Examinateur
M.	J. FERREIRA	Examinateur
M.	D. BOIRON	Membre invité

Aos meus pais
e à memória da Nanda.

Remerciements

Ces travaux de thèse ont été réalisés au Laboratoire Charles Fabry de l'Institut d'Optique. Je remercie son directeur, Pierre CHAVEL, de m'y avoir accueilli.

Je remercie Alain ASPECT pour m'avoir accepté dans son équipe, et pour son amitié et sa disponibilité au cours de tout mon séjour à Orsay. C'était un privilège de pouvoir le connaître, entendre ses leçons de physique, toujours très riches et perspicaces.

Je remercie Chris WESTBROOK, mon directeur de thèse à Orsay, ses enseignements, son enthousiasme et l'énergie qu'il a toujours mis dans notre activité scientifique, ses mots d'incitation et d´encouragement ainsi que d'avoir été toujours disponible pour aider quand il y avait des problèmes, scientifiques ou autres.

Devo também um agradecimento muito especial ao Michael BELSLEY (Mike), o meu (desde sempre!) orientador em Braga. O Mike foi, sem dúvida, a pessoa que mais me influenciou em todo o meu percurso académico. Foi ele que, em grande medida, soube mostrar o prazer que há em "fazer" Física, o tornar simples e inteligível fenómenos que, à primeira vista, pareciam muito mais complicados. É sempre um prazer e um privilégio, poder discutir (e aprender) Física com o Mike, seja no "referencial do laboratório" ou no do "papel e lápis".Ele dizia-me, há dias, que a função de um professor de Física era ensinar os alunos a pensar: não conheço quem o faça melhor! Espero que guarde sempre a vontade e a motivação para continuar a ensinar Física.

O Mike é também o primeiro responsável pela minha ida para Orsay para doutoramento, pois sempre me incentivou a "sair de Braga" para conhecer outras realidades, porventura mais competitivas: foi ele que me levou a contactar o Alain para fazer o doutoramento em Orsay. Muito obrigado Mike!

Je remercie Vincent LORENT qui a bien voulu accepter de faire un rapport de ce manuscrit et pour le temps qu'il a consacré à sa relecture. Je le remercie aussi pour m'avoir aidé dans la compilation finale des petites erreurs qu'il contenait. *Agradeço igualmente a José TITO MENDONÇA por ter aceite amavelmente ser relator da minha tese.*

Je remercie également Olivier DULIEU pour avoir accepté de participer à mon jury. *Agradeço igualmente a João ALVES FERREIRA por ter aceite participar no júri da minha tese e pela sua consideração e amizade.*

Pendant tout le temps de ma thèse, le vrai 'gluon' qui liait toutes les personnes qui sont passées par la manip d'Hélium, qui était toujours prêt pour nous aider et auquel nous faisions appel chaque fois que le ciel semblait tomber sur nos têtes, a été Denis BOIRON. Il m'est difficile d'exprimer (surtout en Français !) le profond sentiment de gratitude que j'ai pour Denis (ça augmente chaque fois que je pense au nombre de fois qu'il a lu et corrigé le texte de ma thèse!). Il a été, certainement, la personne avec laquelle j'ai le plus appris de Physique (des condensats de Bose-Einstein, mais pas seulement) pendant ma thèse. Il a toujours essayé de répondre à toutes nos questions, même les plus 'stupides'. En plus, Denis a toujours été un très bon ami. Je le remercie aussi pour l'intérêt constant qu'il a toujours porté à mon travail. Merci beaucoup Denis!

Dans le groupe de pionniers dans la condensation de l'Hélium il y avait Antoine BROWAEYS, Alice ROBERT et aussi Olivier SIRJEAN (c'est lui qui a obtenu le premier condensat!). C'est Olivier qui m'a enseigné, avec patience, le fonctionnement de la manip et 'à comprendre' ses humeurs (de la manip, bien sûr!) pour mieux la contrôler. C'est aussi avec Olivier que j'ai passé beaucoup de ma période initiale de thèse, au laboratoire, à résoudre des problèmes quotidiens, à obtenir et à traiter les résultats. À lui, mon sincère merci pour tout.

Un mot de remerciement aussi à Antoine qui, après être revenu à Orsay, a toujours eu une énorme disponibilité pour nos questions sur l'expérience, toujours avec amitié.

Quelques mois avant moi, Signe SEIDELIN est aussi entrée dans le groupe Hélium. Signe a été ma collègue dans l'apprentissage des rudiments de la manip. En commun, nous avons fait plusieurs expériences et traité ces données. Plus tard sont venus Rodolphe HOPPELER (qui a même fini sa thèse avant moi, le malin!), Martijn SCHELLEKENS (le plus célèbre évangéliste de Root) et Aurélien PERRIN. De tous je garde une mémoire pleine de moments de camaraderie et, surtout, de grande amitié.

Finalement, déjà dans la période finale de ma thèse, nous avons été rejoints par Valentina KRACHMALNICOFF et Hong CHANG qui ont réussi très rapidement, avec l'aide de Denis, Martijn et Aurélien, à s'adapter aux caprices de la manip. Je suis très impressionné par les beaux résultats qu'ils ont aidé à obtenir dans l'expérience de corrélation des fermions: bravo Valentina et Hong!

Si les choses fonctionnaient aussi bien dans les manips, c'est grâce à nos électroniciens André VILLING et Frédéric MORON. Je les remercie chaleureusement pour leur compétence, leur disponibilité et tout leurs précieux enseignements d'électronique. *Tive também a sorte de poder contar com a ajuda do José CUNHA, o nosso "electrónico" em Braga. Para além da sua grande competência pude também usufruir da sua amizade.Espero poder aprender ainda muita electrónica com ele!*

Il est très difficile de parler de toutes les personnes que j'ai eu le plaisir de connaître à Orsay pendant ma thèse. Je garde le souvenir de l'ambiance très conviviale et amicale dans notre groupe. Les discussions (pas toujours de physique!!!) avec Isabelle, les 'coffee breaks' ('tee breaks'?) avec Rob ou les conversations à la rentrée chez nous à la *Cité Internationale Universitaire de Paris* (CIUP) avec Andrès me manquent déjà. Il faut encore rajouter des noms dans mes remerciements (j'espère n'oublier personne!): Guillaume, Christine, David S., Jérôme, Fabrice, Thorsten, Marie, Simon, Mathilde, Joseph, Jocelyn, David C., Yann, Jean-Felix, Jean-François, Jean-Baptiste, Gaël… et encore Philippe, Nathalie, Ronald, Carlos, Laurent, Sadiqali… merci à tous!

Paris & Casa de Portugal. *Muitas linhas seriam necessárias para citar todas as pessoas com quem travei amizade na Casa de Portugal na CIUP. Desde logo a Irina, mas também o meu grande amigo Nuno SILVA, que tantas vezes me aturou e ajudou durante todos estes anos em Paris. Muito obrigado Nunão! Mas houve mais quem me aturasse! Um grande obrigado aos meus amigos Inês, Alberto, Patrícia, Joana, Alexandro... Agradeço também, claro, à Casa de Portugal por me ter acolhido. Espero que tenha as suas portas sempre abertas para acolher jovens portugueses (e de outras nacionalidades!) que queiram prosseguir com os seus estudos em Paris.*

Braga. *Agradeço também aos meus colegas do Dep. Física o incentivo que me deram. Entre eles, um agradecimento especial aos meus amigos Teresa, Anabela, Luís Vieira, Nuno Peres e Eduardo. Também em Braga houve quem me aturasse: a Lau, o Chico, a Anabela, o Luís, a Clara, o Óscar, o Tozé... A todos o meu muito obrigado.*

Por fim, tenho que agradecer à minha família, os meus pais, o meu irmão, a Sofia, os meus sobrinhos, a Nanda, por todo o enorme apoio que sempre me deram e a paciência que sempre tiveram comigo e para com o meu trabalho. Depois de estar em Paris mais de três anos, longe de todos, quando voltei ainda tive muitas vezes que lhes dizer "não posso... tenho que ficar a trabalhar na tese..."!

Por fim, um agradecimento muito muito especial à Irina, a companheira com quem partilhei a minha vida, todas as pequenas vitórias mas também as grandes derrotas, em todos estes anos. Obrigado por teres estado sempre presente, mesmo quando estivemos separados por muitas centenas de quilómetros! Nunca desistas do sonho!

Contents

1 Bose-Einstein Condensation of Metastable Helium: the apparatus. 29

1.1 Road map to achieve *BEC* in He^*. 31

1.2 Producing a metastable helium *Bose Einstein condensate*. . . 33

1.2.1 The magnetic trap and evaporative cooling. 33

1.2.1.1 Trapping neutral atoms with a magnetic field. 34

1.2.1.2 Trap geometry and configurations. 36

1.2.1.3 Evaporative cooling. 40

1.2.2 The bias field fluctuation. Effort towards its stabilization. 43

1.2.3 From the helium bottle to a cloud of ultra-cold He^* atoms in the magnetic trap. 49

1.3 Experimental readout. 58

1.3.1 The *micro-channel plate*. 58

1.3.2 Saturation effects and the *counting* and *analog detection modes*. 59

1.3.3 The atoms' *time of flight* signal. 60

1.3.4 The ion signal. 62

1.3.4.1 The *two* and *three*-body *Penning* ionization processes. 62

1.3.5 The complete scheme of the detection system. 67

1.3.6 The calibration of the `MCP` detection system. 67

1.3.6.1 The difficult calibration of the number of atoms in a *TOF* signal. 67

1.3.6.2 The detection sensitivity for the *counting mode*. 70

2 The ultra-cold non-degenerate ideal gas. 71

2.1 An ideal gas cloud confined in a harmonic trap. 72

2.1.1 Atomic density in thermal equilibrium. 72

2.1.1.1 The *critical temperature*. 77

2.1.1.2 The finite size effect importance in the cloud density close to the critical transition point. . 79

2.1.2 The critical atomic peak density. 81

2.1.3 The *finite size SCA* for spatially integrated density expressions. 84

2.1.4 The momentum distribution. 85
2.2 Time of Flight: theoretical description. 87
2.2.1 Ballistic expansion of an ideal gas under the effect of a gravitational field. 87
2.2.1.1 Quantum mechanical flux. 88
2.2.1.2 Time evolution of a h.o. wave function in free fall 89
2.2.2 Ballistic expansion in the *far field* and *long fall* approximations. 92
2.2.2.1 The *far field approximation*. 92
2.2.2.2 The *long fall approximation*. 93
2.2.2.3 The *TOF* signal for the ideal gas. 93
2.2.2.4 Snap-shot measure of the cloud's density. . . 94

3 Hanbury Brown and Twiss effect in an expanding cold of non-interacting atoms. 97
3.1 The *Hanbury Brown and Twiss* experiment. 99
3.1.1 The transversal coherence length and time coherence of a wave field. 99
3.1.2 The *HBT* experiment. 104
3.1.2.1 Laser light. 104
3.2 Correlation functions in a non-interacting atomic gas. 106
3.2.1 Definitions 106
3.2.1.1 Correlation functions defined in coordinate space. 106
3.2.1.2 The influence of the ground state population. 109
3.2.1.3 Correlation functions in the momentum space. 110
3.3 Correlation functions in a harmonic trap. 111
3.3.1 At equilibrium in the trap 111
3.3.2 Integrated signals 116
3.4 Correlations in a harmonically trapped cloud after expansion . 119
3.4.1 Detection: *Snap-shot* and *flux* measurement. 119
3.4.2 Second order correlation function of a expanded cloud in a snap shot measurement. 120
3.4.3 Intensity-intensity correlation function of a expanded cloud. 121
3.4.3.1 Explicit calculation of the flux correlation function within the *far field* and *long fall* approximations. 122
3.4.4 Conclusion. 125
3.5 The *HBT* experiment with He^*. 126
3.5.1 State of the art on *HBT* measures with massive particles. 126

3.5.2 The *HBT* experiment with He^*. 127
3.5.2.1 The *delay line* detector. 127
3.5.2.2 The *bunching contrast* in function of the pixel size. 128
3.5.3 A simple derivation of the *signal-to-noise* ratio. 129
3.5.4 Exact results for the *SNR* in the high temperature limit. 131
3.5.5 The experimental results. 132
3.5.6 Conclusion. 133

4 Thermometry with ions and atoms: theoretical preliminaries. 135
4.1 Introduction 135
4.2 The ion signal. 137
4.2.1 Ion signal during the last evaporative ramp. 138
4.2.2 Simulation of the ion signal in the last evaporative ramp. 140
4.2.2.1 Ion signal in the non-degenerate cloud. 141
4.2.2.2 Ion flux in degenerate cloud. 141
4.2.3 The cloud's populations rate equations. 146
4.2.3.1 The atom losses due to inelastic collisions. . . 146
4.2.3.2 Atom losses due to the evaporative cooling. . 146
4.2.3.3 Numerical simulation: overview. 150
4.2.3.4 Presentation of some results. 151
4.2.4 Critical curve. 154
4.2.4.1 The critical curve in the simulated results. . . 154
4.2.4.2 Empirical determination of the critical transition point. 154
4.2.4.3 The *critical curve* for real data. 160
4.2.4.4 Further characterization of the ion signal. . . 162
4.2.5 Conclusion. 163
4.3 *TOF* based thermometry for non degenerate atomic clouds. . 165
4.3.1 Inclusion of interatomic interactions. 165
4.3.2 Atomic density matrix in the Hartree-Fock mean field approximation. 166
4.3.2.1 Redefinition of the chemical potential to account for the interaction energy at the cloud's center. 166
4.3.2.2 Further simplifications towards the derivation of $n(\mathbf{r})$. 167
4.3.2.3 The classical phase space distribution function $f(\mathbf{r}, \mathbf{p})$. 171
4.3.3 The *time of flight* of a thermal cloud. 172

4.3.4 The cloud's hydrodynamical expansion: thermometric correction. . . . 174
4.3.4.1 The Knudsen criterion . . . 175
4.3.4.2 Description using the Boltzmann-Vlasov kinetic equation. . . . 176
4.3.4.3 Hydrodynamical expansion and temperature correction. . . . 178
4.3.5 Conclusion. . . . 180

5 The cloud thermometry and the determination of the He^* scattering length. 181
5.1 Introduction. . . . 181
5.2 Determination of the scattering length. . . . 184
5.2.1 High order corrections for the ion flux signal in the non-degenerate case. . . . 185
5.2.1.1 Ion flux signal at $Z = 1$. . . . 186
5.2.2 The data analysis procedure. . . . 186
5.2.3 Variation of the fitted temperature with a. . . . 187
5.2.3.1 Experimental procedure. . . . 189
5.2.4 Sorting data at $Z = 1$. . . . 192
5.2.5 The found value for a. . . . 196
5.2.5.1 Obtained result. . . . 196
5.2.5.2 Error estimation. . . . 196
5.2.6 Final remarks on the determination of a. . . . 198
5.3 Revisiting the problem of the determination of the s-wave scattering length. . . . 200
5.3.1 The data dispersion and the bias fluctuation. . . . 200
5.3.1.1 Dispersion produced by the inclusion of thermal clouds. . . . 201
5.3.1.2 Dispersion due to the degenerate clouds. . . . 203
5.3.2 The problem of sorting data at $Z = 1$. Overview to the χ^2-*maps*. . . . 204
5.3.3 The problem of the initial guess for a. . . . 208
5.3.4 The results. . . . 209
5.3.4.1 The found a in function of the fugacities. . . . 209
5.3.4.2 The found a dependence on temperature for different fugacities. . . . 209
5.3.5 Final remarks. . . . 211
5.4 The systematic error on the measurement of the scattering length. . . . 215
5.4.1 The *slow* trap switch-off scenario for the thermal cloud release. . . . 217

5.4.2 The thermal cloud's trap relaxation time for obtaining $a = 7.5$ nm. 220
5.4.3 The influence on the measure of β and L of a *slow* release of the *BEC*. 220
5.4.3.1 The hydrodynamical *slow* expansion of the condensate. 222
5.4.3.2 Consequences on the determination of β and L. 224
5.4.3.3 Consequences on the measurement of a. . . . 226
5.4.4 Conclusion. The Raman transition outcoupling process. 228

A The condensate in the Thomas-Fermi approximation. 230
A.1 The condensed state: Gross-Pitaevskii equation. 230
A.2 Thomas-Fermi approximation. 231
A.3 The *TOF* of the *BEC*. 233
A.3.1 The time dependent *Gross-Pitaevskii* equation. The hydrodynamical equivalent. 233
A.3.2 The condensate detected atomic flux. 235
A.3.3 The ion flux from a condensate. 237

B The condensate and the determination of the ionizing rate constants. 239
B.1 The condensate. 239
B.1.1 The *pure BEC*. 239
B.1.2 Chemical potential and cloud's number of atoms. . . . 241
B.2 The measure of β and L experiment. 241
B.2.1 The experimental procedure. 241
B.2.2 Obtained results and their analysis. 243
B.2.2.1 Analysis and results with $a = 12nm$ 245
B.2.3 Dependence of the fitting result in the scattering length. 249

C Mean Field Approximation 251

D Fugacity determination with the χ^2 maps 255
D.1 Introduction 255
D.2 The $Z - T$ $\chi^2 - maps$. 256
D.3 Getting the fugacity from a $\chi^2 - map$. 261
D.3.1 χ^2-*map* strategy for finding Z_{map}. 262
D.3.2 Definition of the χ^2-*map* criteria for sorting data at $T = T_c$. 263
D.4 Using the *semi-ideal* model for testing the χ^2-*map* method. . . 265
D.4.1 The analysis of synthesized data at $Z = 1$. 265
D.4.2 Conclusion. 268

E Published Articles **271**

Résumé de la Thèse

Introduction.

En 1925, Albert Einstein a prédit que si un gaz idéal d'atomes bosoniques était refroidi en-dessous d'une certaine température, il subirait une transition de phase vers un nouvel état où une fraction macroscopique des atomes occuperait le même état fondamental du système. Cet effet remarquable est une conséquence de la statistique des particules identiques de spin entier, qui avait été récemment dérivée par lui et Satyendra Nath Bose. Malgré cette prédiction précoce, il n'est devenu possible de créer un condensat de Bose-Einstein (CBE) dans un échantillon atomique dilué que dans les années 90. Dans ces expériences le gaz est fortement localisé en position et en impulsion. Pour éviter la formation des états moléculaires (et réduire les pertes provoquées par les collisions non élastiques) l'échantillon est très dilué, des millions de fois moins dense qu'un gaz idéal à la pression atmosphérique et à la température ambiante. Les températures de transition de phase sont alors extrêmement petites, de l'ordre du microkelvin, ce qui a constitué pendant longtemps un défi considérable.

0.1 L'expérience d'hélium métastable.

L'hélium métastable (He^*) a rejoint, en 2001, le groupe des espèces atomiques diluées condensées. C'était également la première fois qu'un CBE a été réalisé dans un gaz atomique en dehors de l'état fondamental électronique. Pour He^*, il s'agit du premier état électronique excitée de l'hélium, 2^3S_1, un état métastable avec un temps de vie de 9000 secondes et une énergie interne de 20 eV. La manipulation optique de l'échantillon esot assurée par une transition fermée vers l'état excitée 2^3P_2 à la longueur d'onde de 1.083 μm. L'état métastable a également un moment dipolaire magnétique qui permet le piégeage magnétique et le refroidissement évaporatif par radiofréquence. La polarisation magnétique de l'échantillon supprime fortement les collisions non élastiques entre les atomes d'He^*, ce qui augmente la stabilité et la vie de l'échantillon, et a finalement permis d'atteindre la CBE. Les 20 eV d'énergie interne de l'He^* sont suffisants pour extraire un électron d'une surface métallique. Ce fait est employé dans la détection par temps-de-vol atomique (tdv),

en libérant les atomes du potentiel de piégeage et en les laissant tomber sur une galette de micro-canaux (GMC). Ce dispositif fonctionne comme un multiplicateur d'électrons et produit un signal proportionnel au flux atomique.

Le travail expérimental réalisé pendant la thèse.

Cette thèse rend compte du travail expérimental effectué sur deux sujets dans la manipulation expérimentale d'un nuage quantique d'He^* : i) nous avons mesuré les paramètres fondamentaux pour décrire les collisions élastiques entre atomes d'He^* (longueur de diffusion a) et les collisions non élastiques ionisantes entre deux et trois atomes d'He^* (constantes d'ionisation à deux et à trois corps β et L), ii) nous avons fait une mesure des corrélations entre He^* sur le flux atomique. Cette dernière expérience est conceptuellement équivalente à celle de Robert Hanbury Brown et Richard Twiss (HBT) avec des photons en 1956, et qui a été une expérience pionnière en Optique Quantique. Notre expérience a réalisé pour la première fois la mesure de la fonction de corrélation de densité de particules massives pour un échantillon atomique dégénéré et non dégénéré, confirmant le comportement prévu pour la cohérence du second ordre.

Le gaz dégénéré et le gaz à la température critique.

Pour ces expériences, il est très important de caractériser le gaz, c'est-à-dire faire sa thermométrie. Elles ont été effectuées avec des CBEs pur (presque à $T = 0$) ou avec des nuages thermiques à proximité de la température critique. Caractériser un nuage atomique condensé est plutôt simple, puisque le temps de vol atomique a une signature claire : c'est une parabole inversée, très bien décrite théoriquement dans l'approximation de Thomas-Fermi. Du point de vue expérimental, pour créer un CBE pur il suffit de refroidir le nuage atomique jusqu'à ce qu'aucune composante thermique (c.-à-d. non-dégénérée) ne reste piégée. Ce n'est évidemment possible que si le nombre initial d'atomes piégés au début du refroidissement est suffisant pour atteindre la dégénérescence avec un nombre raisonnable d'atomes. La production d'un nuage atomique au point critique présente une difficulté supplémentaire. Ici, le processus de refroidissement évaporatif doit être interrompu au moment précis où l'échantillon est au seuil de la CBE. C'est une tâche difficile puisqu'il faut connaître la fugacité (reliée au potentiel chimique) du nuage thermique en temps réel pendant l'évaporation. Dans une expérience standard de CBE où la détection du nuage est optique, ceci ne peut être fait qu'en mesurant

la variation de la densité optique d'un signal d'absorption. Une mesure en temps réel pour voir si le nuage est au point critique ou non est, dans ce cas, très difficile à réaliser. Avec l'He* nous avons une méthode additionnelle et très fructueuse, que nous décrivons ci-dessous.

Les outils de diagnostics spécifiques à l'He* - I : le flux d'ion.

La condensation d'He* est seulement possible dans un échantillon avec spin polarisé où les collisions non élastiques sont très faibles. Néanmoins, il y a toujours un petit taux d'ionisation encore discernable et proportionnel à la densité du nuage. Ce signal permet de suivre l'évolution de la densité du nuage vers la CBE, passant par la transition de phase, en temps réel et de manière non invasive. En particulier, le flux d'ions permet de déterminer le point critique de la transition de phase. Ce flux d'ions est également détecté

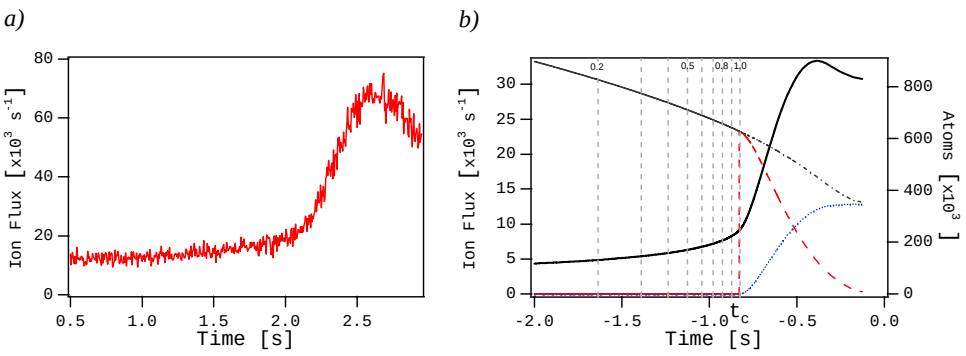

FIG. 1 – Le signal d'ion : a) signal real et b) signal simulé.

par la GMC. Contrairement aux atomes, les ions sont attirés vers la GMC par un champ électrique. Ceci a deux avantages : i) comme le temps de vol des ions est très faible, le signal détecté mesure en temps réel le taux d'ionisation dans le nuage, ii) le signal d'ions est une mesure absolue puisque, en principe, tous les ions peuvent être détectés. Ceci ne se produit pas par exemple avec le signal de tdv, où un calibration du nombre total d'atomes n'est pas possible. Un signal d'ions typique est présenté Fig.1$-a$. A un instant donné, sa pente change brutalement, ce qui est conforme à la présence d'une transition de phase. Pour mieux comprendre ce phénomène, nous avons fait une simulation (Fig.1$-b$), en utilisant un modèle semi-classique pour la densité du nuage atomique. Ce modèle inclut une composante thermique ainsi qu'un nuage condensé, traitant le premier comme un gaz idéal soumis à un potentiel de piégeage modifié par le champ moyen du CBE. L'analyse des résultats obtenus avec ce modèle permet d'interpréter l'évolution temporelle du flux

d'ions. Elle établit la correspondance entre l'évolution du signal d'ions et celle de la fugacité du nuage (ligne verticale sur Fig1.b) et indique la position du point critique. En comparant ces résultats aux données expérimentales, nous pouvons déterminer dans une expérience où se trouve la transition de phase. Ceci a été fait dans l'analyse de données ainsi qu'en temps réel pendant l'acquisition de données.

L'analyse du temps-de-vol atomique.

Même si elle est prometteuse, la thermométrie basée sur le flux d'ions n'est pas assez précise à cause des fluctuations du potentiel de piégeage. Ainsi, le diagnostic le plus important pour caractériser les nuages thermiques est le tdv atomique. Pour obtenir une bonne description de la densité du nuage, nous avons utilisé un modèle théorique qui inclut l'effet des interactions inter-atomiques. Nous avons développé une procédure d'ajustement fondé sur ce modèle pour déterminer la température ainsi que la fugacité du nuage. La valeur de ce dernier paramètre permet de décider si un nuage est au point critique.

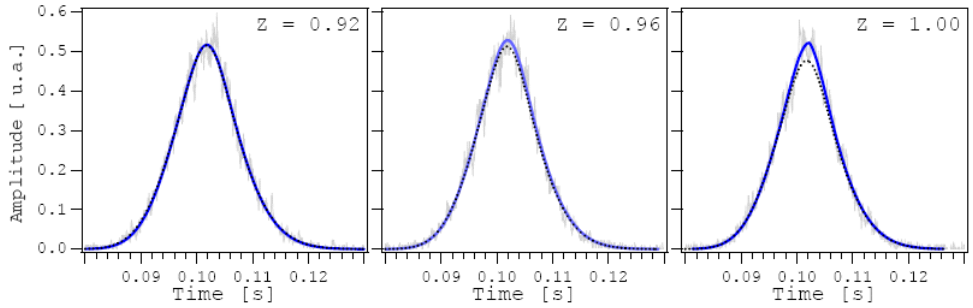

FIG. 2 – Trois exemples de tdv pour des nuages avec des fugacité assez différentes.

L'ajustement des tdv est très sensible à la bonne détermination du bruit dans ces signaux. Dans la Fig.2 nous traçons trois tdv de différentes fugacités. Les lignes pointillées représentent des courbes avec des fugacités beaucoup plus petites que 1 et les pleines l'ajustement à notre modèle. Nous notons que la différence entre les deux cas est tout à fait petite et comparable au bruit de tdv.

Les outils de diagnostics spécifiques à l'He^* - II : la détection d'atomes uniques.

La très bonne réponse temporelle et le fort gain de la GMC permet la détection d'atomes uniques, ce qui est très difficile à réaliser dans des ex-

périences plus conventionnelles de CBE utilisant l'imagerie optique. L'utilisation d'une GMC couplée avec un détecteur sensible de position (basé sur une ligne à retard) nous a permis de faire une expérience de corrélation HBT d'intensité. La cohérence de second ordre correspond à la fonction de corrélation du module carré du champ. D'un point de vue des particules, elle mesure des corrélations de densité et est liée à la probabilité conditionnelle de trouver une particule à un certain endroit étant donné qu'une autre particule est présente à un autre endroit. Les bosons ont tendance à être détectés ensemble, un effet habituellement appelé groupement ou bunching bosonique. La détection d'atomes uniques rend l'expérience de HBT particulièrement commode avec He*. Une part importante de la thèse est dévolue à la dérivation d'une expression analytique de la fonction de corrélation d'intensité du flux atomique. Cette analyse a permis d'obtenir des valeurs typiques pour les longueurs de corrélation, transverse et longitudinale, et de confirmer la possibilité de réaliser une expérience de type *HBT* sur notre montage expérimental. Ses conclusions principales sont : i) les fonctions de corrélation à l'intérieur du piège et dans le tdv atomique sont équivalents dans nos conditions expérimentales : elles peuvent être reliées simplement par une loi d'échelle sur les coordonnées, ii) le volume de cohérence augmente avec la taille de nuage, et vaut $\lambda_T \omega t$, avec λ_T la longueur d'onde thermique de de Broglie du nuage piégé et , la fréquence d'oscillation du potentiel de piégeage.

Les résultats sur la mesure de la longueur de diffusion.

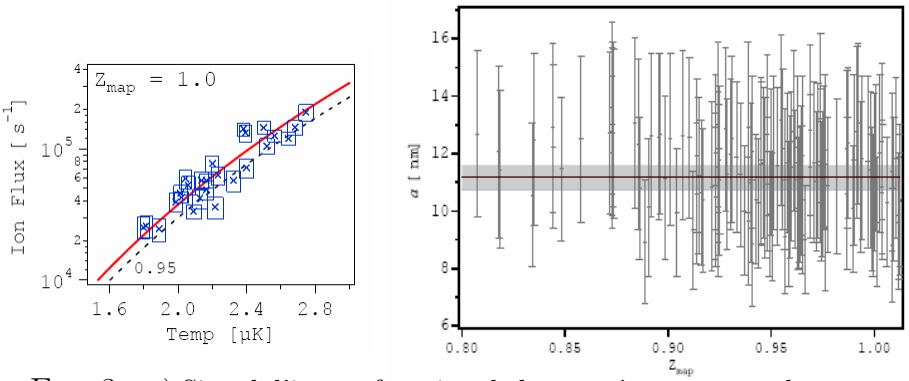

FIG. 3 – *a*) Signal d'ion en fonction de la température pour des nuages à $T = T_c$. *b*) les résultats finaux pour l'analyse des la détermination de la longueur de diffusion de l'He*.

Choisir des données à $T = T_c$ a joué un rôle très important dans l'analyse des expériences cherchant à mesurer la longueur de diffusion, a, de l'He*.

Cette longueur a été mesurée en comparant le flux d'ions, qui a une dépendance forte avec a, avec la densité atomique de nuages à la température critique (voir Fig.3-a). Ceci a été fait en utilisant les méthodes décrites ci-dessus pour l'analyse du *tdv* ainsi que du signal d'ions. Le résultat obtenu confirme une analyse précédente et donne $a = 11.2$ nm. L'analyse statistique des résultats a donné un écart type d'environ 0.3 nanomètre (voir le Fig.3-b).

Introduction to the thesis. Outline.

In 1925, Albert Einstein predicted that if an ideal gas of bosonic atoms were cooled below a certain transition temperature it would undergo a phase transition to a new state where a macroscopic fraction of the atoms would occupy the same fundamental state of the system[1] creating a highly coherent atomic ensemble. As Einstein pointed out, this remarkable statement is a consequence of the statistics of identical particles with integral spin, which had been recently derived by himself and Satyendra Nath Bose[2]. Despite this early prediction, it only became possible in the 1990's to create a *Bose-Einstein condensate* (*BEC*) in dilute atomic samples, as Einstein had originally imagined.

BEC in dilute gases.

In these experiments the gas is strongly localized in both coordinate and momentum spaces[3]. To avoid the formation of dimmers (and also to reduce losses due to inelastic collisions) the sample is very dilute, typically millions of times less dense than an ideal gas at atmospheric pressure and room temperature. This leads to extremely small phase transition critical temperatures, typically in the range of microkelvin[1], and has long constituted a considerable challenge for experimental physicists.

The first atomic *BEC*s were obtained in 1995. The impact was so great that only six years later E. A. Cornell, W. Ketterle and C. E. Wieman received the Nobel Prize in 2001 "for the achievement of Bose-Einstein condensation in dilute gases of alkali atoms, and for early fundamental studies of the properties of the condensates". One remarkable experiment reported by Wolfgang Ketterle's group at MIT demonstrated that when two independent *BEC*s were superimposed they interfere[5] in much the same way as coherent light. This was the first clear demonstration of first order coherence of the associated atomic quantum field, which could be characterized through the visibility of interference fringes. Other impressive experimental achievements were the realization of pulsed and CW atom lasers[6, 7, 8, 9] and the observation of the interference of two matter-wave beams emitted

[1] In condensed matter systems critical temperatures are much higher. For example, the superfluidity of liquid helium takes place at 2.18°K[4].

from two spatially separated regions of the same *BEC*[10]. These pioneering experiments have verified that in many senses, below the BEC condensation threshold, bosonic atoms become coherent in phase and degenerate in energy, much like the stimulated emission of a single mode laser beam. The similarities between coherent atoms and photons[11] allow many of the key ideas of quantum optics to be directly carried over to describe coherent atom optics. However there are several key differences between atoms and photons; atoms have both mass and internal states that have no counterparts in photons. An especially important difference is that atoms can also interact directly with each other, without requiring a nonlinear medium that mediates the interaction between photons. For example, it is possible to carry out an atomic four-wave mixing experiment in which three different coherent atomic beams interact in a vacuum to generate a fourth beam[12].

Bose-Einstein condensation in Metastable Helium.

To get to the point where it was possible to produce a *BEC* in a dilute sample, many important new experimental techniques have contributed. Among these, the demonstration of optical trapping of macroscopic objects dates from the beginning of the 70's[13] and of neutral atoms in the early 80's[14, 15]. Optical cooling techniques [16, 17, 18] were developed soon after and also those for magnetically trap the atoms[19]. Evaporative cooling was developed initially within the efforts to achieve *BEC* in hydrogen, also in the early 80's[20].

The first experiments achieving *BEC*were done in 1995 and counted three different alkalis: *rubidium* (^{87}Rb)[21], *sodium* (^{23}Na)[22] and *lithium* (^{7}Li)[23]. Still within the alkalis, there are today *BEC* experiments with potassium (^{41}K)[24], with another isotope of rubidium (^{85}Rb)[25] and also with cesium(^{133}Cs)[26], this one using an *optical dipole trap*[27]. Also using this type of trap, ytterbium (^{74}Yb)[28] and chromium (^{52}Cr) [29] have recently attained condensation. The pioneering atom, hydrogen, was condensed only in 1998[30].

In 2001, it was the time of metastable Helium (He^*) to join the group of condensed species in a dilute atomic sample[31, 32]. It was also the first time *BEC* was done in an atomic gas not in the electronic fundamental state[2]. Unlike the alkali, in the He^* experiment the atom is initially prepared into its first electronic excited state 2^3S_1, a *metastable* state with a life time of 9000 seconds and internal energy of 20 eV.

There are two main reasons for preparing the sample in the 2^3S_1 state. First, unlike the ground state, this metastable state has a closed optical transition to the excited triplet 2^3P_2 state[3], that can be addressed with available

[2]There is also one experiment aiming to achieve *BEC* with ^{20}Ne[33] and another where metastable xenon was optically trapped[34].

[3]The 2^3P_2 decays to the fundamental state 1^1S_0 in a few seconds[35] whereas it decays

laser sources (at the wavelength 1083 nm). This is essential to optically trap and cool the sample[36, 37] and also to use the most standard optical detection schemes as absorption, fluorescence and refractive measurements[38].

The sample is also prepared in the metastable state to have a permanent magnetic dipole moment, necessary for magnetic trapping. Moreover, the magnetic polarization of the sample strongly suppresses the inelastic collisions between He^* atoms, increasing the stability and the lifetime of the sample[39]. This has motivated the design of our experiment, where He^* was condensed for the first[31] and, also, in another experiment at the *École Normale Supérieure* (*ENS*)[32], that has achieved *BEC* almost simultaneously as in our group. He^* condensation was also be attained in Amsterdam[40] and, recently, also in Canberra[41]. The Amsterdam's group has also achieved degeneracy in the fermionic isotope ^3He using a two-color magneto-optical trap [42] and sympathetic cooling[43].

The He^* unique diagnostic tools: I-single atom detection.

The internal energy of the He* is sufficient to extract an electron from a metallic plate. This is used in our experiment, as well as in the one at Amsterdam, to detect the atomic cloud with micro-channel plate (`MCP`)[44]. This device works as an electron multiplier and outputs a signal proportional to the atomic flux that arrives at its sensitive surface. The extremely good MCP time response and high gain allows single atom detection, which is very difficult to achieve in more conventional BEC experiments based upon optical imaging.

The use of a MCP along with a position sensitive detector based on a delay line has allowed us to make an intensity correlation experiment with massive particles, an experiment that is conceptually very similar to the one carried out in 1956 by Robert Hanbury Brown and Richard Twiss with thermal light.

This experiment remains nowadays as one of the landmark experiments in quantum optics. It measured, for the first time, the second order temporal coherence (*i.e.*, the correlation function) of photons from a thermal field. We will refer to this experiment, form here on, as the *HBT* experiment. From a particle point of view it quantifies density correlations and is related to the conditional probability of finding one particle at a certain location given that another particle is present at some other location. Photons originating from a thermal source have the tendency to be detected close together, an effect usually referred as bosonic bunching. This behavior is common to any source of thermal bosons as is the case of a thermal cloud of He^* atoms. The single atom detection capability of our experiment is particularly convenient for carrying out a *HBT* type of experiment with massive particles.

---

to 2^3S_1 in only 98 ns.

The He* unique diagnostic tools: II - the ion signal.

BEC in spin polarized He* is possible because the inelastic collisions are highly suppressed. Even so, a small rate of ionizing processes remains giving rise to a small but still detectable flux of ions, proportional to the cloud's density. This is a very remarkable tool that allows following the evolution of the cloud's density toward BEC, passing through the phase transition, in real time and in a non invasive way. In particular, the ion signal can be used for determining when the critical phase transition happens. At this particular instant of time, the cloud's density and the ion flux increase abruptly, indicating the phase transition.

We have used the ion signal and its exceptional behavior close to the critical point to help producing clouds at the vicinity of the BEC threshold. This was used in one of the experiments we carried out, on the determination of the S-wave scattering length of the He*, a (which we will refer in the following). The determination of the critical point through the ion signal analysis could also be used in several other experimental situations. For instance, it could be used to sort data in a *HBT* experiment with clouds at the critical temperature. This would allow the investigation of quantum bosonic effects and of critical fluctuations through the analysis of the density correlation function.

The experimental work realized during the thesis.

In this manuscript we describe and present the results of three different experiments realized during my thesis.

The one we describe first is the already referred *HBT* experiment that has measured the intensity correlation function of a falling He* cloud. In this experiment, we realized for the first time a measurement of a massive particles' correlation function for a *BEC* and also for non-degenerate atomic samples at different temperatures close to the critical temperature. We have confirmed the expected behavior of the second order coherence function of bosons, with similar results as those already known for photons. This experiment is briefly described in Chapter 3, where we also show its main results.

The other two experiments realized during my thesis are quite different from the one just referred. They were carried out before the *HBT* experiment and had the goal of measuring collisional properties of the He*: i) the ionizing rates due to inelastic collisions between two and three atoms of He*, β and L respectively[45] and; ii) the He* S-wave scattering length a[46], the fundamental parameter that characterizes elastic collisions between atoms in a very cold gas. Conceptually, both experiments rely on a comparison between the ion flux produced within the cloud and its mean density, inferred from the analysis of the atomic time of flight (TOF) that is recorded when the cloud is released from the trap and falls over the `MCP`. In the first experiment (on the ionization constants), this comparison was done for condensed

clouds whereas in the second, we used thermal clouds close to the critical temperature.

We have summarized the description of the experiment on the measure of β and L to the Appendix B, where we also show its main results. The theoretical description of the BEC and of its time of flight is also postponed to the Appendix A.

The results obtained in this experiment for β and L were used subsequently in the data analysis of the experiment for measuring a. This latter one is described in detail in Chapter 5. As we referred above, it relies on the comparison of the ion flux of clouds at the critical temperature, which varies considerably with a, with the corresponding atomic densities, only weekly dependent on a. We use this experiment and its data analysis to describe, in Chapter 4, a few techniques we developed during the thesis to analyze both the ion flux and the atomic *TOF* of thermal clouds at the critical point. In Chapter 5, we discuss their use for improving the accuracy on the cloud's thermometry, mainly in the determination of the cloud's chemical potential. We show that the reduction of the uncertainty on the determination of this quantity leads to a reduction of the statistical uncertainty in the final result of a.

Thermometry in the critical phase transition I: the ion signal analysis.

Along with the theoretical description of the intensity correlation function, the development of techniques of analysis of the ion signal and of the atomic *TOF* has constituted the "tour de force" of the work I did outside the laboratory during my thesis.

To be able of carrying out any sort of experiments with atomic clouds at the critical phase transition, one needs first to have a very reproducible process to produce such clouds. In Chapter 4, we show that this is not possible due to the bias field fluctuations of the trapping potential: the shot-to-shot variation of the bias field makes that, even for similar conditions for the evaporative cooling and similar loads of the magnetic trap, the resulting clouds vary considerably in number of atoms and temperature.

A way around this is to take data as close as possible to the critical temperature and then use some process to sort from these data set those that better correspond to clouds at $T = T_c$. To get as close as possible to T_c may be achieved just by analyzing the ion signal which has the advantage of giving a real-time diagnostic of the cloud's evolution. The phase transition imposes an abrupt variation of the density, which produces a rather spectacular increase of the ion flux signal. Somewhere within this transient period of time lays the critical point and, to get clouds at T_c, the evaporative cooling should stop at that very especial *critical time*. The remaining question is how to determine accurately this critical time. If the scattering length and

the ionizing rate constants are known, the ion flux signal can be computed, taking some adequate model (with more or fewer approximations) for the theoretical description of the cloud's density. In any case, this latter one has only two parameters: the cloud's temperature and chemical potential μ (or, alternatively, the number of atoms). During evaporation, while the cloud cools down it also looses atoms due to the evaporation itself and also to the inelastic collisions. This leads to a continuous setting of the cloud's chemical potential that ends, hopefully, with $\mu \approx 0$ and a *BEC* growing within the cloud. The analytical description of this process is hard to workout due to the mutual interdependence of the various processes involved[4] making the theoretical prediction for the time evolution of the cloud's density and the ion flux a non trivial task.

In this thesis we have opted to carry out instead a simple numerical time-stepped simulation that computes the cloud's density and chemical potential evolution, admitting a certain variation of the temperature imposed by the evaporation process. In this routine we use a so called semi-ideal[47] model to describe the thermal cloud, which accounts to the *BEC* repulsion, with this latter described in the Thomas-Fermi approximation. Within the validity of this model, the routine is used to derive the location, on the ion signal, of the critical point.

The results of this simulation were used to characterize in a very generic way where the critical point should be found. This was used to deal with real data and to compute an empirical curve expressing the expected ion flux generated by a cloud at the critical point in function of the corresponding instant of time it happens, for all attainable critical temperatures in our experimental conditions (see §4.2.4). This critical curve was used to guide the procedure of taking data (it indicated where the evaporation should stop) and also in the posterior procedure to sort the data.

Thermometry in the critical phase transition II: The time of flight signal.

The determination of critical point through the analysis of ion signals can be made very accurate but only if the bias field fluctuations are small. Unfortunately, this is not the case in our setup and the precise moment at which the cloud is at T=Tc changes from one experimental run to the next. We show in Chapter 4 that this leads to an uncertainty in the determination of the cloud's chemical potential of about 10% of $k_B T$, which is not entirely adequate for sorting data at T_c.

This task should be carried out through the analysis of the cloud's time of flight (*TOF*) signal that is a direct inspection of the cloud's density (after

[4]This is true even for the simplest case where the thermal and the condensed clouds are treated as separate objects, using semi-classical formulae for describing their density profiles and mean field models for the interatomic interactions.

expansion). This is done fitting the *TOF*s to a theoretical model. Here, as before, the main problem is to obtain an accurate determination of the cloud's chemical potential. There is no simple fitting model that describes the cloud's density in both sides of the critical transition: the fitting expressions used for thermal clouds are not defined for positive chemical potentials. Therefore, for *TOF*s where this quantity is identically zero, a standard fitting procedure is unable to work properly since it cannot compute the chi-square in both sides of that minimum. In chapter 4 we propose a strategy (further detailed in Appendix D) to go around this problem. The idea, in brief, is to extrapolate the behavior of the chi-square for $\mu < 0$ into the critical region, where $\mu \approx 0$, and thus avoiding the computation of this quantity for $\mu > 0$. The resulting uncertainty in the value found for the chemical potential is estimated in Appendix D to be of about 2.5% of $k_B T$. We will denote this procedure in the following as the χ^2-map strategy.

The characterization of the noise in the experimental *TOF* and the use of an appropriate model for fitting these signals are essential ingredients to reduce the uncertainty on the determination of μ. One has two different issues: the description of the cloud's density at thermal equilibrium inside the trap and the description of its expansion under the influence of gravity.

The standard formulae for the description of density of harmonically trapped gases are derived in the semi-classical approximation and are expressed using infinite sum functions known as Bose functions (which are easily computable). These expressions may include a first order correction, on the trapping frequency, to account for the finite size of the cloud. This is however the only corrective term that can be considered, since all other higher order terms leads to diverging infinite sums. This leads us to further investigate the validity of the semi-classical approximation when used in the description of the cloud's density. We found that, when the contribution of the fundamental state is taken into account, the peak density critical value should be around $6.24/\lambda_T^3$ instead of the usual $\zeta(3/2)/\lambda_T^3$, with λ_T the thermal de Broglie wavelength. The discrepancy between an exact calculation and the semi-classical expressions is however only important close to the center of the cloud. We show that a single integration of the atomic flux over a spatial direction is enough to make the semi-classical approximation valid. We have verified in Chapter 2 that, for our data analysis, the semi-classical expression gives a good enough description of the atomic TOF signal. In Chapter 4 we complement this simple model for the ideal gas by including interatomic interactions. This is done within a mean field model[48] that relies upon some approximations of which the validity will be discussed.

The formalism for treating the expansion and fall of the cloud is given in Chapter 2, for the ideal gas case. We use a Green function to propagate the harmonic oscillator wave functions in the gravitational field and, using a

quantum mechanic definition of the matter flux, compute the atomic *TOF*. As for the cloud's density, the influence of the interaction between atoms is left to Chapter 4, where we discuss the hydrodynamical regime.

The second order coherence function in an atomic beam.

The formalism needed to derive the atomic *TOF* is extended in Chapter 3 to deal with the intensity correlation function of the particles flux when the cloud is released from the trap. This theoretical analysis has derived typical values for the transverse and longitudinal atomic coherence length that have confirmed the possibility of performing an *HBT* experiment with our apparatus. It has also helped in the study of the necessary upgrades of the detection system. We will briefly discuss these upgrades[49] and show the main results of this experiment[50].

The data treatment on the scattering length experiment. The systematic error on the determination of a.

Despite all our efforts to have a proper cloud's thermometry and an accurate determination of a, the value we have measured is affected by a large systematic error. Chapter 5 starts by describing our first data analysis on this experiment. It is based on a model that assumes from the beginning that $\mu = 0$, avoiding the determination of the actual value of the chemical potential for each cloud[51]. We develop then a second approach, using the χ^2-map strategy to determine the chemical potential of each individual cloud and use that value in the determination of a. This second analysis conduced to a smaller statistical uncertainty on the value we find for a, which however is not very different form the one that had been obtained previously: $a = 11.2 \pm 0.4$ nm.

A recent and very precise light-induced collision spectroscopy experiment, made in the group at the *ENS* has rather obtained $a = 7.512 \pm 0.005$ nm, a result that indicates we have committed an error of about 50% in our experiment. This manuscript ends with an attempt to explain this huge discrepancy. We will address the description of the process through which the cloud is released from the trap. We show that if the trapping potential switch-off is not fast enough, the initial moments of the cloud expansion may change dramatically the thermometric interpretation of the cloud's *TOF*, both for thermal and condensed clouds.

The plan of the manuscript.

In the following we present the outline of the thesis, highlighting for each Chapter, the more pertinent aspects regarding the structure of the manuscript.

- **Chapter 1** - In the first Chapter we present a detailed description of our experiment in what concerns the production and detection of an ultra-cold could of He^*. Most of the first and second Sections of this

Chapter describe very standard techniques widely used in the experimental field of cold quantum gases. We also introduce the working principle of the MCP (§ 1.3.1) and the process through which the cloud is released from the trapping potential. This Chapter discusses finally the two major experimental difficulties we have to deal with in our setup. The first of these, referred above, is bias field fluctuations. Section §1.2.2 describes in some detail this problem. The second major experimental problem we faced in this thesis had to do with the impossibility of getting an absolute calibration of the number of atoms in the atomic time-of-flight signals (see §1.3.6.1).

- **Chapter 2** - This Chapter introduces the theoretical models and definitions used throughout the manuscript. It is divided into two Sections: i) the theoretical description of an ideal gas in thermal equilibrium inside a harmonic potential (§2.1.1); ii) the description of the atomic time-of-flight in the ballistic approximation (§2.2). In i) we discuss the criteria for defining the critical phase transition (§2.1.1.1), in particular for the cloud's peak density and the validity of the semi-classical approximations (§2.1.1.2). In paragraph §2.2.2, we introduce the approximations we use in the analysis of the atomic time-of-flight signals.

- **Chapter 3** - This Chapter is based on Ref.[52] and details the calculation of the intensity correlation function in the atomic flux generated by the free fall of a cloud of atoms in the ideal gas approximation. The results reported here gave the first indication that our setup could be used in *HBT* experiment. The Chapter starts by reviewing the main ideas of first and second order coherence theory in optics and its generalization for a quantum field of massive particles. This is done explicitly for an ideal gas trapped in a harmonic trap (§3.3), stressing particularly the case of a cloud at the critical temperature. The case of an expanding cloud under the effect of gravity (§3.4) is then dealt with and expressions for the intensity correlation function are derived. The last Section of this Chapter reports briefly on the upgrade of the setup and on the main results of this experiment.

- **Chapter 4** - In this Chapter we describe the techniques we have developed during the thesis for the cloud's thermometry within the analysis of both the ion flux (§4.2) and the atomic *TOF* signals (§4.3). The first Section of this Chapter deals with the problem of how to interpret the ion signal. We start by presenting the simple model used in the simulation of the cloud's density and the ion signal temporal evolution. We discuss two possible procedures to determine the critical point in an ion signal and present the critical curve obtain for real data. We also derive

the relation between the experimentally observed bias field fluctuation and the uncertainty on the determination of the chemical potential. The second part of this chapter describes the mean field model used for fitting the *TOF* signals and the correction on the obtained temperature due to the hydrodynamical effect.

- **Chapter 5** - This manuscript last Chapter makes use of the cloud's thermometry to measure the scattering length. We start by describing this experiment in some details (§5.2) and the procedure we used, initially, to analyze the data. Then, and after discussing the data dispersion we observe on the result we explain how we can improve the accuracy, by improving the thermometry of the acquired TOFs. The proper determination of the temperature and fugacity of a thermal cloud at the vicinity of the critical point is the goal of the χ^2-map technique, a method we introduce in this Chapter. The last Section of this manuscript discusses the error committed on the determination of a.

CHAPTER 1

Bose-Einstein Condensation of Metastable Helium: the apparatus.

In this Chapter we will present our He* experiment. In the first part we will describe how we produce a cloud of cold atoms of He*and how we manage to achieve *BEC* with it; in the second part we describe how we detect the atomic cloud.

All the methods we describe here to trap and cool down the atoms are standard techniques in most of *BEC* experiments in dilute atomic samples. We will start the description of our experiment by presenting the magnetic trapping and the evaporative cooling techniques, explaining how they work and also describing their experimental implementation in our setup. The combination of these two techniques has constituted the final breakthrough in the achievement of *Bose-Einstein condensation* in dilute atomic samples.

The evaporative cooling is just the final part of all the processes involved in the production of a *BEC* and, in our experiment, it takes about thirty seconds to be completed. Most of the work presented in this thesis is related with the physics of non-degenerated clouds near the critical transition point. Since this transition is attained in the last few seconds of the evaporative cooling, this process takes an important role in many of the subjects presented throughout this manuscript.

To get a magnetically trapped atomic cloud, many other steps must be taken however. In the paragraph §1.2.3, we will come back a few steps back in the experimental track to explain how we manage to *produce* the He* atoms (the atomic source) and also to describe all the necessary laser based techniques we use to achieve loading an already cold atomic cloud into the magnetic trap.

Diversely to the techniques we use to trap and cool down the atoms, the detection system in our experiment can not be considered as a standard one when compared with most of the cold atoms experiments. Rather than using optical methods (like imaging the cloud's absorption of a laser beam), in our experiment the atoms' detection is made electronically using a *micro-channel plate* (`MCP`). The use of the `MCP` in this case is possible due to the He* internal

energy, sufficient to extract an electron from the metallic frontend surface of the MCP. We show how we use this device to detect our cloud. With it, it is even possible to make single atom detection. This is a very important ability of our setup and we will show in Chapter 3 how it was used to measure the density-density correlation function. Before entering into the experiment description, we will briefly present the *road map* we need to follow, in the experimental point of view, to achieve condensation.

1.1 Road map to achieve *BEC* in He*.

The critical phase transition.
Traditionally, the critical transition to *BEC* is presented for the homogeneous ideal gas case. In this case, *BEC* occurs when the spatial atomic density, n, and the gas temperature, T, is such that the following relation is respected[3],

$$n \times \lambda_T^3 = \zeta\,(3/2)\,, \tag{1.1}$$

where T enters in the definition of $\lambda_T = \sqrt{\frac{2\pi\hbar^2}{Mk_BT}}$, the *de Broglie* thermal wave length with M the atomic mass. In practice, the atomic cloud has to be trapped somehow and its density is, in general, inhomogeneous. This is the case of a harmonically trapped cloud, for which the above relation is still valid if one replaces the homogeneous density by the cloud's *peak density*, $n(\mathbf{0})$, the density at the center of the trap. The factor $n(\mathbf{0}) \times \lambda_T^3$ is, in fact, the phase space density and, its critical value $\zeta(3/2) \equiv 2.612$ is the objective one pursuit for achieving *BEC*.

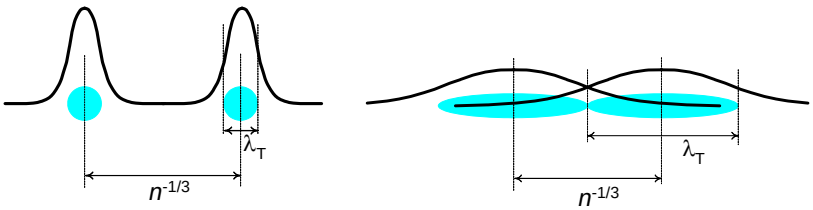

Figure 1.1: An intuitive interpretation of the critical phase transition relation for a dilute cloud of cold atoms. Here, λ_T is the *de Broglie* thermal wavelength of the atoms and n, the cloud's density. When $\lambda_T \sim n^{-1/3}$ the atoms start overlapping and the phase transition occurs.

A generally used interpretation of the expression in Eq.1.1 is the one sketched in Fig.1.1: for low enough temperatures, the atoms wave functions start to spread out and then to overlap with theirs neighbors, becoming indiscernible. In here, the critical transition happens when the spatial separation between two particles is comparable to the *de Broglie* thermal wavelength of their wave packets, a similar relation as that stated in Eq.1.1. We will revisit this relation in the Chapter 2, in more detail.

In cold atoms experiments, the typical value for the critical temperature is around 1μK, several orders of magnitude smaller than, for example, the critical temperature for the *lambda* transition point where the liquid helium becomes superfluid, around 2.2K[4]. Note that, for a critical temperature of 1μK, the relation of Eq.1.1 predicts a critical density for the He* gas around 10^{12}cm^{-3}, which is seven orders of magnitude smaller than the air density at normal conditions of pressure and temperature.

Brief comment in all-optical atom cooling methods.
Up to the moment this manuscript was finished, all *BEC* experiments have only attained condensation trough evaporative cooling methods, either in magnetic or dipole optical traps. As we will further explain in §1.2.1.3, one of the main disadvantages of the evaporative cooling is to be a depletive method: to cool down the cloud, some atoms (the hottest) has to be expelled out of the trap. In fact, due the finite life time of the sample, typically a few tens of seconds, evaporation must be completed in a time that must be short when compared to the trap losses rate. Speeding up the evaporation implies increasing the number of ejected atoms and, in the end of the cooling process, only a small percentage of the initial population remains trapped and cooled down to the *BEC* transition temperature.

There are also atom cooling techniques that work by laser cooling alone. There are especially two techniques that allow attaining temperatures below the *recoil limit*, $k_B T_r = (\hbar k)^2/2M$ [1]: the *velocity-selective coherent population trapping* (VSCPT) [53, 54] and the *Raman cooling* [55, 56]. These methods relies on the existence of single atom *dark states*, a Raman induced coherent superposition of two states with momentum $\pm\mathbf{k}$, insensitive to the cooling laser. These are stationary states, eigenvectors of the total Hamiltonian, being populated by atoms coming from the absorbing states through momentum redistribution due to spontaneous emission. The attained temperatures are in the nanoKelvin regime and, unlike the evaporative cooling, they preserve the initial number of atoms. Moreover, these all optical methods may complete an entire cooling cycle in a fraction of a second. This is an important advantage when compared to the tens of seconds needed by the evaporative cooling stage [2]. Additionally, laser cooling methods may be used to cool fermionic samples down to the superfluid *BCS* state[57], a regime where evaporative cooling techniques are unable to attain[58].

Unfortunately, laser cooling techniques present still serious limitations to achieve large atomic densities. In here, light reabsorption appears as the main obstacle for achieving low temperatures at the very dense optical media of the cold gases close to the critical transition. The above referred velocity dependent *dark states* are *dark* only for laser light involved in the cooling scheme. These atoms can interact with the light emitted spontaneously by other atoms in the sample, making them abandon the absorption-free state[59]. Several strategies have been proposed to overcome this difficulty as, for example, using very anisotropic potentials, where most of the spontaneously emitted

[1] This temperature corresponds to the kinetic energy that is transferred to the atom when it spontaneously emits a photon with momentum $\hbar k$.

[2] These times are reduced several times for experiments done in microchips devices, where the higher confinement of the atomic cloud enhances the elastic collisions rate (see also §1.2.1.3).

photons does not interact with the atomic sample, or very confining traps with linear sizes comparable to the wavelength of the emitted photon. The most promising however is a scheme known as the *festina lente* scenario[60]. Here, the time between two spontaneously emitted photons, Γ^{-1}, controlled by the Raman pumping rate, is made to be much larger than the inverse trapping frequency time. Theoretical predictions show that, within this condition, reabsorption processes are suppressed, avoiding the heating of the atomic sample. Even so, up to this date there is no experimental prove of the usefulness of any of these schemes for cooling atomic samples down to the degeneracy point.

Road map to the *BEC*.
Despite its depletive character, with evaporative cooling it is possible to increase the atom's phase space density up to the critical *BEC* transition. As we will describe in the following Sections, in our experiment, this technique is used on an atomic cloud trapped in a magnetic trap. The task of capturing and pre-cooling the atoms before loading them into the magnetic trap is taken by a *magneto-optical trap* (`MOT`). This apparatus uses both laser beams and magnetic fields to confined and cool down the atoms. The `MOT` is loaded by an atomic beam delivered by a *hot* atomic source. To achieve loading the `MOT`, a few other laser based techniques are used to first collimate transversely and then reduce the longitudinal velocity of the atomic beam (see §1.2.3).

In the Table1.1 we make a summary of the three intermediary stages needed to attain *BEC* in our experiment. There we present typical values for the phase space density, the number of trapped atoms and the cloud's temperature and density.

1.2 Producing a metastable helium *Bose Einstein condensate.*

Metastable helium has two fundamental characteristics that allow achieving *BEC*. First, the He^* atom can be optically manipulated by commercial lasers in the closed optical transition between the 2^3S_1 and 2^3P_2 states; second, it has a permanent dipole moment, μ, which allows using a magnetic trap. We will come to both of these characteristics in the following Sections. We start now with the latest and explain the magnetic trapping of neutral atoms.

1.2.1 The magnetic trap and evaporative cooling.

The magnetic trap and the evaporative cooling process rely in very simple but powerful ideas. Here, we revise briefly those ideas and emphasize the

	$n_0\lambda_T^3$	N	$T\ [\mu K]$	$n_0\ [cm^{-3}]$
Atomic beam	$10^{-30} - 10^{-20}$	–	–	–
Laser trapping and cooling	10^{-6}	10^8	$10^2 - 10^3$	10^9
Magnetic trap and evaporative cooling	≈ 1	$10^3 - 10^6$	$0.1 - 5$	10^{13}

Table 1.1: The cloud's degeneracy parameter, number of atoms, temperature and density at the end of each of the three main techniques involved in the *BEC* production: the production of a atomic source, the trapping and pre-cooling with laser based techniques and, finally, the evaporative cooling of the magnetically trapped cloud down to the *BEC* transition point.

most important details with respect to our experiment.

1.2.1.1 Trapping neutral atoms with a magnetic field.

Unlike the alkalis, the helium in its fundamental state is a singlet state without dipole moment. However, exciting one of its electrons to the first electronic excited state 2^3S_1, it stays in a metastable state (with a life time bigger than 2 hours [61, 62]) which has a permanent magnetic dipole moment, $\boldsymbol{\mu}$.

Immersed in a magnetic field, the He^* atom dipole has a position dependent interaction energy given by

$$U(\mathbf{r}) = -\boldsymbol{\mu} \cdot \mathbf{B}(\mathbf{r}).$$

In the classical picture, the magnetic dipole experiences a torque due to the interaction and processes around the magnetic field $\mathbf{B}$ at the *Larmor precession frequency*, $\nu_L = |\boldsymbol{\mu}\mathbf{B}|/\hbar$. If this frequency is much larger than the inverse of the typical variation time scale of the magnetic field, the dipole $\boldsymbol{\mu}$ will *adiabatically* follow the magnetic field $\mathbf{B}$. This *adiabatic condition*, if respected, predicts that the atom will preserve all the time its initial magnetic spin polarization. We will see further on in this Section that the magnetic field in our trap is never smaller than 0.3G. To this field corresponds a Larmor frequency of about 10^6Hz, which is about three orders of magnitude bigger than the maximum oscillation frequency of the trap. The adiabatic condition is then fulfilled and we may replace the scalar product of the above equation by $U(\mathbf{r}) = g_J\mu_B m_J|\mathbf{B}(\mathbf{r})|$ with m_J the projection of the total angular momentum $\mathbf{J}$, g_J the *Landé* factor and $\mu_B = e\hbar/2m_e$ the *Bohr magneton*.

Thus, to trap the atoms, the potential $U(\mathbf{r})$ must have a local minimum at some given location and deep enough when compared with the atom's thermal energy $k_B T$.

It is a well known result that the *Maxwell* equations predict the non existence of local maxima of *dc* magnetic fields in free space[63]. Thus, the only way to get a minimum in the potential energy is to create a minimum in the magnetic field with also $g_J m_J > 0$. This is the case of the magnetic sub-level $m_J = 1$ of the electronic state 2^3S_1. Since for this state $\mathbf{L} = 0$, $\mathbf{J} \equiv \mathbf{S}$ and $g_J = +2$. An atom polarized in this state is then a *low field seeker* in the sense that it tends to minimize the interaction energy moving into the field minimum. The electronic state 2^3S_1 has also other two magnetic sub-levels with projections $m_J = 0$ and $m_J = -1$. An atom polarized in this latter one simply fly away from the minimum of the magnetic field, escaping the trap. However, if it is polarized in the $m_J = 0$ sub-level, the atom is insensitive to the magnetic filed and will simply fall under the effect of gravity.

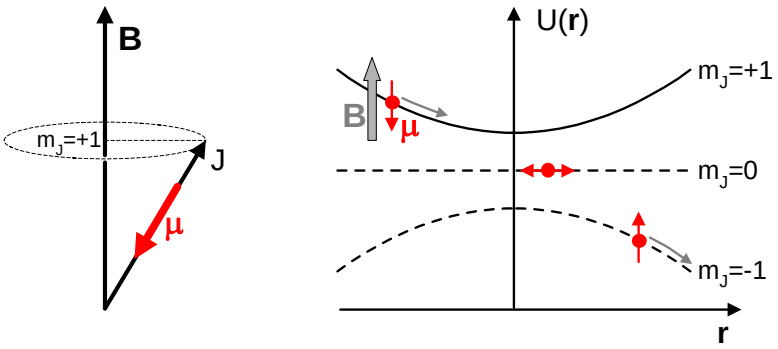

Figure 1.2: The left hand side image illustrates the precession of the *pure spin state* $m_J = 1$ around the magnetic field. The right hand side sketch represents the equipotential curves corresponding to the three magnetic sub-levels of the electronic state 2^3S_1 deformed by the *Zeeman* effect induced by a parabolically varying magnetic field. In here, the *low field seeker* state is the one with $m_J = +1$, corresponding to a magnetic moment $\mu = -g_J \frac{\mu_B}{\hbar}\mathbf{J}$, antiparallel to the direction of the field. The sub-level $m_J = 0$ is insensitive to the magnetic field and the one with $m_J = -1$ is an *anti-trapping* state. Atoms polarized in one of these two states escape from the trap.

In order to verify the previously referred adiabaticity condition and preserve the atom's spin polarization, the trapping potential needs to have a finite minimum. If an atom passes, momentarily, through a zero magnetic field it looses its magnetic quantization axis and may spin flip into any of the magnetic sub-levels. If it flips to a non-trapping state, it is lost from the trap. To avoid this effect, known as *Majorana* losses, it suffices then that the trapping potential is always non null. However undesirable when

trapping the atoms, the *Majorana* process become, in our experiment, very useful for detection proposes. It spin flips some of the atoms into the $m_J = 0$ state during the trap switch off allowing the detection of free falling cloud (cf. §1.3).

1.2.1.2 Trap geometry and configurations.

In our setup, the non-homogeneous magnetic field is produced by a set of several coils in a *clover leaf* configuration[64], schematized in Fig.1.3. It is an alternative configuration of the *Ioffe-Pritchard* quadrupolar trap [65, 66]: the axial trap confinement, in the Ox axis, is assured by a pair of coils, the *curvature coils*, in an off-Helmoltz configuration separated by a distance that is roughly twice their diameters; other eight coils, referred in the Figure as the *gradient coils*, creates a quadrupolar magnetic field that confines the atoms in the radial trap direction (the yOz plane). This configuration produces an on axis quadratic variation of the magnetic field with a non null minimum that verifies the adiabaticity condition. Up to second order in cartesian

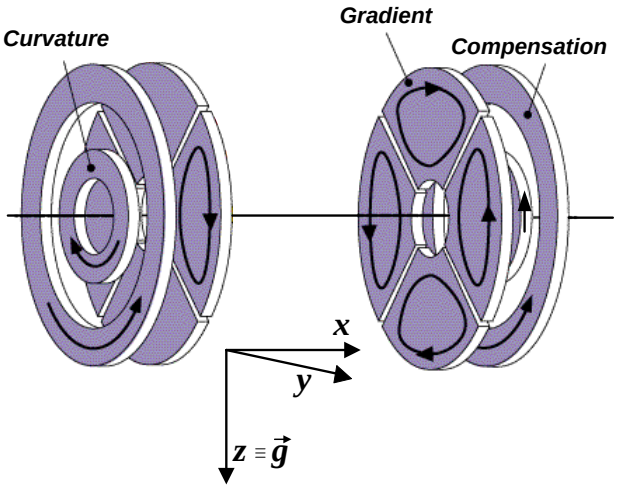

Figure 1.3: *Clover-leaf* magnetic trap schematic representation. The four inner coils, the *gradient coils*, create a gradient of the magnetic field in the transverse direction whereas the *curvature coils* are responsible for the axial confinement of the atoms. The *compensation coils* creates a magnetic field in the opposite direction of *dipole* field and are used to compress the trap (see also text). It is usual to refer to the axial direction as the *bias field* direction. The gravitational field direction coincides with the Oz direction. In our setup, the gradient coils are placed 44 mm apart (the shown Figure was taken from the Ketterle's group web site).

coordinates, the total magnetic field produced in such a *Clover-leaf* magnetic trap is

$$B(x,\rho) \simeq \sqrt{B'^2\rho^2 + \left[B_0 + B''(x^2 - \tfrac{1}{2}\rho^2)\right]^2}, \tag{1.2}$$

where $\rho^2 = y^2 + z^2$ is the radial variable and B_0, B' and B'' expansion coefficients for the constant, linear and quadratic terms respectively. The coefficient B_0, known as the *bias field*, is the magnetic field at the bottom of the trap. This one results from the compensation of the *curvature* field by the field produced by another additional pair of coils assembled, ideally, in the Helmoltz configuration. These *compensation coils* produce then a homogeneous field in the opposite direction of the curvature field and are used to decrease B_0 and consequently compressing the trap in the radial direction.

If the *compensation coils* are turned off, the bias field becomes much larger than the cloud thermal energy. With $\mu B_0 \gg k_B T$, one also gets $B_0 \gg B'\rho$ and $B_0 \gg B''x^2$[67], and then the expression in Eq.1.2 may be simplified to

$$B(x,\rho) \simeq B_0 + B''x^2 + \left(\frac{B'^2}{2B_0} - \frac{B''}{2}\right)\rho^2. \tag{1.3}$$

This expression represents a non-isotropic harmonic potential with radial and axial curvatures given by $\frac{1}{2}(B'^2/B_0 - B'')$ and B''. If the current in the compensation coils is increased, B_0 is reduced and, consequently, the radial trapping curvature is also reduced. B_0 has no influence in the axial curvature.

In the case where the bias field is small compared with $k_B T$, the expression in Eq.1.2 has not a simple quadratic expansion that decouples the axial and radial coordinates. The potential dependence in this latter coordinate gets dominated by a linear term and the trap is called a *semi-linear* trap. We will refer to this configuration as the *low-bias field* (*LBF*) trap, while that one with $B_0 \gg k_B T$ as the *high-bias field* one (*HBF*).

In Fig.1.4 we represent the equipotential curves, in temperature units and for a He^* atom in the $m_J = +1$ state, for the *LBF* and the *HBF* trap configurations. These curves are computed with the same parameters as those used in our experiment. In both graphs the *field gradient* is $B' = 85$ G/cm. The *field curvature* is $B'' = 25$ G/cm^2 for the *HBF* case and 20 G/cm^2 for the *LBF* one [3]. The *HBF* case is obtained by turning off the current in the compensation coils, a situation where $B_0 = 190$ G. In the *LBF* trap configuration, the compensation field almost cancels out the curvature field to obtain $B_0 = 360$ mG.

[3]The change in the curvature is involuntary and comes from the imperfect Helmoltz configuration of the compensation coils.

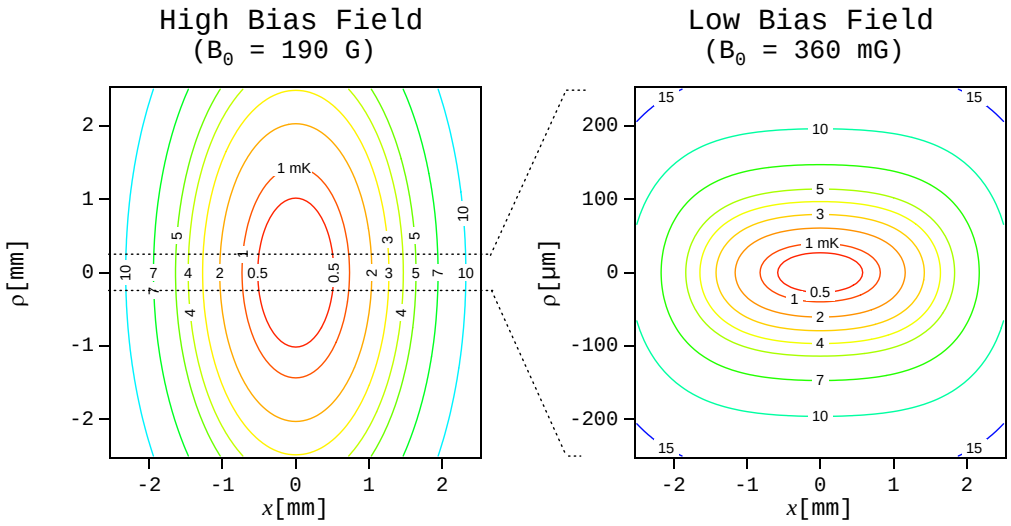

Figure 1.4: Equipotential lines for the magnetic sub-level $m_J = 1$, in temperature units (referenced to the bottom of the trap), of a *clover-leaf* type *Ioffe-Pritchard* trap. The graphs were computed for a magnetic filed gradient of $B' = 85\text{G/cm}$. The left hand side graph corresponds to an *high-bias field* of $B_0 = 190\text{G}$ and field curvature of $B'' = 25\text{G/cm}^2$, whereas the *low-bias field* case was computed for $B_0 = 360\text{mG}$ and a curvature of $B'' = 20\text{G/cm}^2$(note the different left axes scales). The different magnetic field curvatures in these two cases come from an imperfect compensation of the bias field due to a slight mismatch of the compensation coils from the Helmoltz configuration. The transverse and axial (*bias*) axes correspond to the ρ and x axes respectively. Temperature units are converted into magnetic field strength through the factor $k_B/g_J m_J \mu_B \sim 7.44\mu\text{K/G}$.

Correspondence between the trap curvatures and the harmonic potential oscillation frequencies.

As described in the following Section, during the evaporative cooling, we need to compress the trap in order to enhance the efficiency of the thermalization by increasing the rate of elastic collisions among the He^* atoms. However, to get a proper load of the large cloud trapped in the MOT into the magnetic trap, this one must be initially set in the uncompressed *HBF* configuration. After loading the cloud, the compression will transform the initially harmonic trap into a semi-linear one. Then, through the evaporative cooling the temperature of the gas decreases three orders of magnitude and once again $\mu B_0 \gg k_B T$. As in the *HBF* and *high temperature* case, in here, the trap is again well described by a three-dimensional harmonic potential. This one can be written as

$$U(\mathbf{r}) = \tfrac{1}{2} M \omega_{\parallel}^2 x^2 + \tfrac{1}{2} M \omega_{\perp} \rho^2,$$

where $\omega_{\parallel}$ and $\omega_{\perp}$ are the axial and transverse oscillation frequencies, parallel and perpendicular to the direction of the bias field, respectively (also in the expression, M is the helium mass). The correspondence between these trapping oscillation frequencies and the magnetic field parameters can be easily derived relating this last expression with Eq.1.3. One obtains,

$$\omega_{\perp} = \sqrt{\frac{4\mu_B}{M} B''} \quad \text{and} \quad \omega_{\parallel} = \sqrt{\frac{2\mu_B}{M}(B'^2/B_0 - B'')} \sim \sqrt{\frac{2\mu_B}{M}\frac{B'^2}{B_0}}. \quad (1.4)$$

where the simplification is justified in our case because $B'' \ll B'^2/B_0$. Within the *micro-Kelvin* regime, the oscillation frequencies in our *compressed* trap, with a bias field of $B_0 = 360$ mG, are finally $\omega_{\perp}/2\pi \simeq 1200$ Hz and $\omega_{\parallel}/2\pi = 50$ Hz.

Experimental determination of the trapping oscillation frequencies.

Knowing the exact geometry of every set of coils and the current passing through them we can calculate $\omega_{\perp}$ and $\omega_{\parallel}$. However, a much preferable method to determine these quantities is to measure them directly in a *parametric heating experiment*. We will briefly describe how it works.

Suppose we modulate the trap radial frequencies at a certain frequency ν_0 [4]. In this condition, the cloud will exhibit an excitation spectrum with narrow peaks at the modulation frequency $\nu = \nu_0$ and also at its second harmonic $\nu = 2\nu_0$[68, 69]. If one of these frequencies coincides with $\omega_{\perp}/2\pi$ the

[4] This can be achieved modulating the current in the compensation coils, for example. This results in a modulation of the bias field and consequently also of $\omega_{\perp}$.

cloud heats up quickly and, by observing the resulting clouds' temperature in function of the modulation frequency we could determine $\omega_\perp$.

Modulating the axial trapping oscillation frequency is more difficult since, as noted before, a change in the bias field has no effect in this axis. To overcome this, the experiment must be done with a *BEC* where the three spatial axes are *coupled* together. This *coupling* is induced by the *BEC* large mean field potential that makes the condensed cloud to behave as a classical fluid in a strong collisional regime. In here, due to the large number of collisions, a density modulation in one of the axis will produced a similar modulation in the other two. Thus, a modulation of the radial trapping frequency $\omega_\perp$ produces also a modulation in the the axial direction allowing the determination of $\omega_\parallel$. For this case the modulation frequency nu_0 is related with $\omega_\parallel$ according to $2\pi\nu_0 = \sqrt{\frac{5}{2}}\omega_\parallel$[68, 69] (for a more detailed description of the experimental procedure see Ref.[70].).

1.2.1.3 Evaporative cooling.

The atomic sample attains the critical phase transition after being *evaporativly cooled*. We have already anticipated the working principle of the evaporative cooling: remove some of the hottest atoms out of the cloud and wait for it to re-thermalize at a colder temperature. Repeating this process over and over again, the cloud's temperature decreases from a few millikelvin down to the phase transition critical temperature, around 1μK.

Despite this description of the evaporative cooling as an evolution through a *discrete* ensemble of intermediary stages at thermal equilibrium, in practice, it is an almost continuous process. The energy of the ejected atoms is *ramped* down continuously and, if it is done slowly enough, the cloud evolves between *quasi-equilibrium* states with an almost complete re-thermalization of the cloud.

The need of ultrahigh vacuum in the science chamber.

Thus, in respect to the cloud's thermalization, the evaporative cooling should be done as slow as possible. However, the unavoidable atom losses impose a finite *life time* to the trapped cloud and this is what ultimately establishes a restriction in the time evaporative cooling may last.

There are then two competitive processes that determine the duration of the evaporative cooling process in the He* experiment: the cloud's re-thermalization and its life time. The first of these is related with *elastic collisions* that promote the cloud's thermalization of the gas and should, because of this and as far as possible, be enhanced. The second one is related with *inelastic collisions* of He* atoms with other particles that may ionize

or simply spin-flip the internal magnetic state of the atoms leading, in both cases, to the losses.

An essential condition to a *BEC* experiment to work is to have very good vacuum conditions. Although losses due to inelastic collisions involving two or even three He^* atoms become very important for clouds close to the degeneracy (see §1.3.4), in most of the evaporative cooling process the cloud is still very dilute ($n \sim 10^9$ cm^{-3}) and the principal collisional processes are *Penning* ionizations involving only one He^* atom and a molecule from the vacuum background X. This process is described by

$$X + He^* \rightarrow X^+ + He + e^- \ , \tag{1.5}$$

where X^+ is a positive ion resulting from the reaction. These ions can be detect within our setup (see §1.3.4), what can be used to measure the cloud's life time, τ. In order to have a small number of background molecules and therefore a small rate of inelastic collisions, the vacuum conditions at the magnetic trap must be very good. To have a life time of about $\tau \sim 50$ seconds, we need to have a vacuum below the 10^{-10} mbar.

Enhancing the elastic collisions rate by compressing the trap.
To go faster with the evaporation and still keep the cloud at a *quasi-equilibrium* state, we need to increase the elastic collisions rate among He^* atoms, γ. This can be done by increasing the cloud's density, n. As we said earlier, this is achieved by compressing the trap before starting the evaporation.

The average value of γ can be estimated as

$$\gamma \simeq n_0 \ \sigma_0 \ v_T,$$

where n_0 is the cloud peak density and $v_T = \sqrt{k_B T/M}$ its thermal velocity. Also in this expression, σ_0 is the elastic collision cross section, which in the low-temperature limit is velocity independent. For $T = 1$ mK, a typical temperature of the cloud transferred into the magnetic trap, this cross section for the He^* is $\sigma_0 \sim 1.5 \times 10^{-11}$ cm^2. For this temperature, we may also estimate $n_0 \sim 5 \times 10^8$at/cm^3 and $v_T \sim 150$cm/s and, using the above formula, we obtain $\gamma \sim 1\text{s}^{-1}$, *i.e.* a collision per atom and per second. The role of the evaporative process is to truncate the cloud's thermal distribution at a certain high energy and wait the cloud to re-thermalize in a temperature colder than the initial one. Re-thermalization needs, at least, four collisions per atom [71] and, since the evaporation must be completed in a time smaller that the trap life time, it is necessary that $\gamma \geq 10s^{-1}$. This increase of γ by a factor of ten is obtained if the trap is compressed as it was described in §1.2.1.2.

Ejecting the atoms by $RF-$ induced spin flip.
The process through which the hottest atoms are ejected out of the trap is

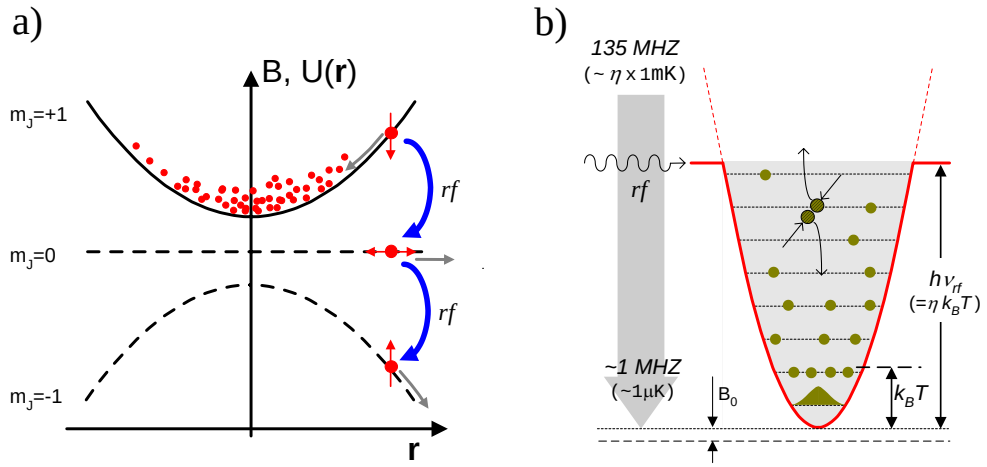

Figure 1.5: The $rf-$field induced evaporative cooling: a) energy levels of the 2^3S_1 electronic state in the presence of an inhomogeneous magnetic field. The trapped atoms, polarized in the $m_J = +1$ magnetic sub-level, are ejected from the trap whenever their kinetic energy is sufficient to reach regions of the trap where the $m_J = 1$ state is coupled through the rf-field to $m_J = 0$ (in a one-photon process) or to $m_J = -1$ (two-photon process); b) evaporative cooling in a binary elastic collision: two atoms exchange kinetic energy, with one of them ending with sufficient energy to escape the trap. To conserve energy one of the atoms remains trapped but with a smaller kinetic energy. Ramping down the $rf - knife$ from 130 MHz to about 1 MHz in half a minute, it is possible to cool the cloud down to the phase transition point. During all the process, the ratio between the $rf-$field energy and the cloud's thermal energy, $\eta = h\nu_{rf}/k_BT$ is kept constant around 6 (see text).

sketched in Fig.1.5a). The trapping inhomogeneous magnetic field induces a position dependent *Zeeman* shift in the magnetic sub-levels of the state 2^3S_1. The atoms with bigger kinetic energy explore regions where this shift is also bigger. A certain class of these hotter atoms can be removed from the trap by applying a *radio frequency* electromagnetic field (rf-field), resonant with the corresponding magnetic transition between the levels $m_J = +1$ and $m_J = 0$. All atoms with trajectories that go outside the shell defined by the rf-field see its magnetic spin flipped into the non-trapping state $m_J = 0$ or even, for intense rf-fields, into the anti-trapping state $m_J = -1$.

An illustration of the evaporative cooling in shown in Fig.1.5b). The ensemble of the trapping potential and the rf-field produce an *open trap*. The $rf-$field works here as a *knife*, cutting the trap at a certain height. If two atoms collide, it can happen that one of them gains an extra kinetic energy

at the expense of the other. This extra energy can be sufficient to the atom to escape the trap, decreasing the total thermal energy of the cloud [5]. The rf-field is spatially homogenous, radiated by an antenna made of two loops in the Helmoltz configuration, mounted close to the atomic cloud and with its polarization axis perpendicular to the bias field axis, the atoms' quantization axis. It is produced by a commercial *radio frequency* synthesizer (`ANRITSU MG3641A`), which was programmed to ramp down linearly the rf-frequency. The entire evaporation takes half a minute and is done in four different ramps (see Fig.1.6). The cloud, initially at 1mK and with about 5×10^8 atoms, is cooled down to the critical phase transition temperature, $\sim 1\mu$K, ending at the end of the process with only a few million atoms. To achieve the critical point, the phase space density increases by seven orders of magnitude.

The first linear ramp starts at an rf-frequency of 130MHz. This value corresponds to a temperature about six times bigger than the initial cloud's temperature $\sim$ 1 mK. The ratio between the thermal energy of the cloud and the energy of the rf-knife,

$$\eta = \frac{h\nu_{rf} - \mu B_0}{k_B T}, \tag{1.6}$$

is kept almost constant around 6 throughout all the rf-ramp and was determined as the optimum in order to maximize the number of atoms in the condensate. The ramp ends around 1 MHz, a frequency that corresponds to an energy slightly bigger than the bottom of the trap, μB_0 [6].

1.2.2 The bias field fluctuation. Effort towards its stabilization.

Among all the technical difficulties we have in our setup, there are two that we may consider as *the main problems*: the bias field fluctuation and the impossibly of calibrating our detection system. We explain now what is the first, letting the second for next Section.

The thermal energy scale of the cloud during the evaporative cooling has always as reference the bias field, B_0. Thus, a variation of B_0 in the end of the process produces also a variation of the final cloud's temperature. If B_0 had decreased (increased) from its initial value, the temperature attained by the cloud will be larger (smaller) than the one initially expected.

In practice, the bias field fluctuation over time cannot be avoided and the best we can do is to reduce them as much as possible. In the *low-bias field* configuration, we manage to reduce the bias fluctuation among different

[5] See Chapter 4 for a more detail description of this process.

[6] The ramp must stop before μB_0 in a quantity that is at least equal to the *BEC* size in energy, its chemical potential.

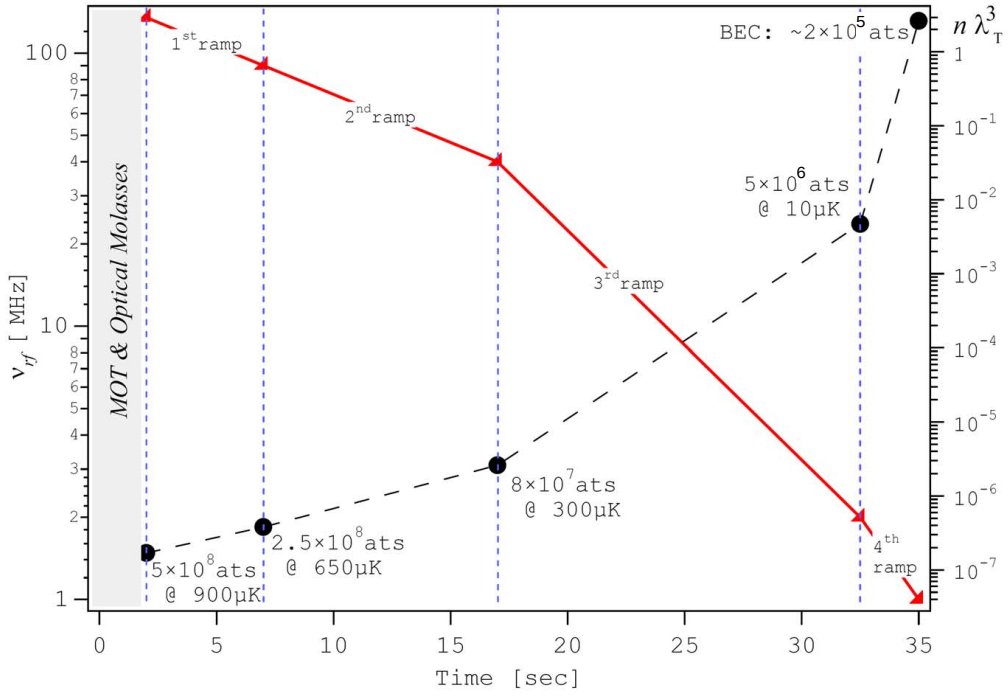

Figure 1.6: The solid line (left hand side axis) represents the variation of the *radio-frequency* field through four linear ramps starting at the frequency 130 MHz, and ending close to 1 MHz. The dashed line (right hand side axis) represents the correspondent variation of the phase space density, which is initially about $\sim 10^{-7}$ (the one of the MOT plus optical molasses) and ends at the critical one, ~ 1. At the end of each linear ramp are written the typical number of atoms in the cloud and its temperature.

experimental realizations to only about 10 mG (or 25 kHz in the rf-ramp units), less than 3% of its absolute value. This result may look reasonably good and, in fact, such a bias fluctuation would be completely harmless if the final cloud's temperature were much bigger than $\mu B_0/k_B$. However, this is obviously not the case when we ought to get a *BEC* or, even, a cloud at the critical transition phase. In here, all small perturbations of B_0 may affect the *purity* of the *BEC* or else stop the evaporation at a temperature slightly displaced from the critical one. As we will show in Chapter 4, this constitutes a major limitation in the cloud thermometry we could achieve.

Bias field stabilization scheme.
As we referred earlier the bias field is, mainly, the difference of two magnetic

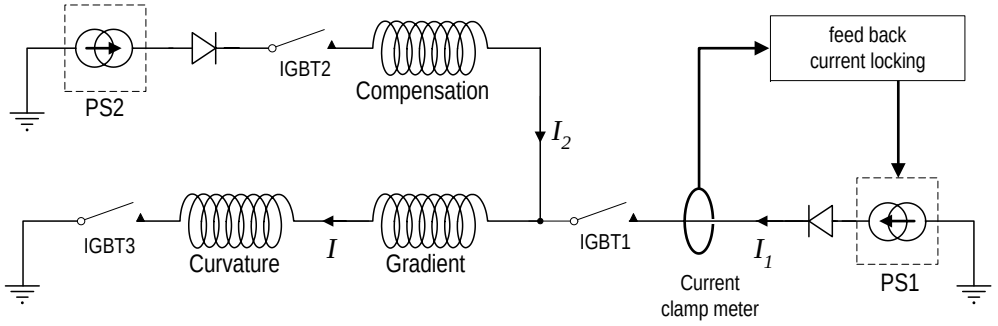

Figure 1.7: Electric circuit of the gradient, curvature and compensation coils, during the magnetic trap. Two power supplies, `PS1` and `PS2`, are use to drive a current I_2 into the compensation coils and $I = I_1 + I_2$ into the gradient and the curvature coils, assembled in series. The *high-bias field* configuration ($B_0 = 190$ G) is obtained closing the `IGBT`s 1 and 3, and adjusting `PS1` so that $I \equiv I_1 = 230$A. In the *low-bias field* case ($B_0 = 360$ mG), all `IGBT`s are closed and the power supplies are adjusted as to deliver the currents $I_1 = 10$ A and $I_2 = 220$ A, keeping $I = 230$ A. In here, `PS1` works in voltage control and a feed back locking circuit using a *current clamp meter* is used to stabilize I_1 (see also text). The bias field results from the difference between the fields produced by the compensation and gradient coils.

fields: the one produced by the *curvature coils* and that produced by the *compensation coils*. After compression, the current in these latter is around 220A, driven by a power supply working in current control. The current flowing through the curvature coils is the same as for the compensation plus a *small* current of 10A, which guarantees the bias field minimum around $360mG$.

The circuit that controls the current in the coils is shown in Fig.1.7. It has two power supplies (`PS1` and `PS2`) and three *insulated gate bipolar transistor*

(IGBT), a kind of *solid state relay* that switches on and off the currents.

Initially, after the MOT being switched off, all the IGBTs are open and no current flows in the circuit. Then, to switch on the *HBF* trap, all the IGBTs are closed with the power supplies PS1 and PS2 adjusted in a way to deliver respectively 230 A and 0 A. To obtain the *LBF* configuration, PS2 is then made to operate in current control and to ramp from 0A till 220A. Keeping PS1 always at the initial voltage the current in the gradient/curvature coils, I, is also kept constant at 230A. With I_2 ramping up, I_1 decreases down to $10A$. Since PS1 is always in voltage control, I_1 is stabilized using a *current clamp meter* that feeds back to a lock circuit that controls the power supply.

Bias fluctuations and the coils' current stability.

The bias field fluctuation matters only in the *LBF* case, where *BEC* is attained. In this trap configuration all the power supplies are made to function as current sources. Like this, any temperature induced instabilities of the coils' ohmic resistance do not affect, in principle, the stability of the magnetic field. Thus, the instabilities of the current flowing in the coils must be connected essentially with the degree of stability of the current sources. In the *LBF* configuration, the bias field is

$$B_0 = k_g(I_1 + I_2) - k_c I_2 = (k_g - k_c)I_2 + k_g I_1,$$

with k_c and k_g proportionality constants relying the current and the magnetic fields. The bias fluctuation is then

$$\delta B_0^2 = (k_g - k_c)^2 \delta I_2^2 + k_g^2 \delta I_1^2.$$

In the specifications given by the constructor for the power supplies, the output stability is about 0.1%. In the other hand, $k_c - k_g \simeq 0.045$ G/A. Thus, the first term in the left hand side of the previous expression may, alone, justify the *run-to-run* observed fluctuation of 10 mG. The second contribution in this expression depends only on the degree of stabilization we get for I_1. However, to justify 10 mG and using the fact that $k_b \sim 0.95$ G/A, we see that such a fluctuation corresponds to stability in the current look circuit also of 0.1%. In both cases, the current instabilities are reasonably small and seem hard to be further improved. Still, they may justify the bias instability we observe.

Bias fluctuations: other possible causes.

There are also other possible causes for the bias fluctuations, both in the small time scale between two consecutive experimental runs as well as in longer time scales.

Despite the rather small ohmic resistance of the coils ($\sim 0.5\Omega$), the large electric currents needed to create the trapping magnetic field produce huge heat dissipation: the average electric power consummation in the whole system of coils is about 5 kW. To avoid the coils' overheating, they are made of a hollow-core copper wire that allows the circulation of pressurized cooling water in its interior.

As noted before, as the power supplies function in current control, temperature drifts of the coils should not contribute to the bias instability. However, it is an empirical fact that the bias field could be influenced by the cooling water temperature. This could happen in a single day where we would observe (and correct) very slow drifts of the bias during the day or, even, between different seasons of the year, where for getting the same bias field, the current in the coils should be different. Discarding current instabilities, another possibility to explain these long term drifts is a change in the coils geometry induced by thermal dilation. For example, an increase of 20 μm in the distance between the two compensation coils makes B_0 to change by 30 mG[70].

These slow drifts in a long time scales (compared with the time of a single run) can always be corrected without undesired consequences. Harder to deal with, due to its unpredictability, are the *run-to-run* variations. Another possible cause for these, also of geometric nature, is the mechanical displacement (vibration) of the coils induced by magnetic forces when the magnetic field is turned on. To help reducing these effects, the coils are firmly fixed inside re-entrant flanges in the ultra-high vacuum stainless steel science chamber (see Fig.1.8) [7]. It is hard to evaluate how big this effect is and in what extend it influences the bias field.

[7] In order to preserve the vacuum conditions the coils are assembled outside the chamber. However, since we need large field gradients, they must place as close together as possible. This is why we have designed the UHV chamber with re-entrant flanges. They allow assembling the coils separated by only ~ 45 mm.

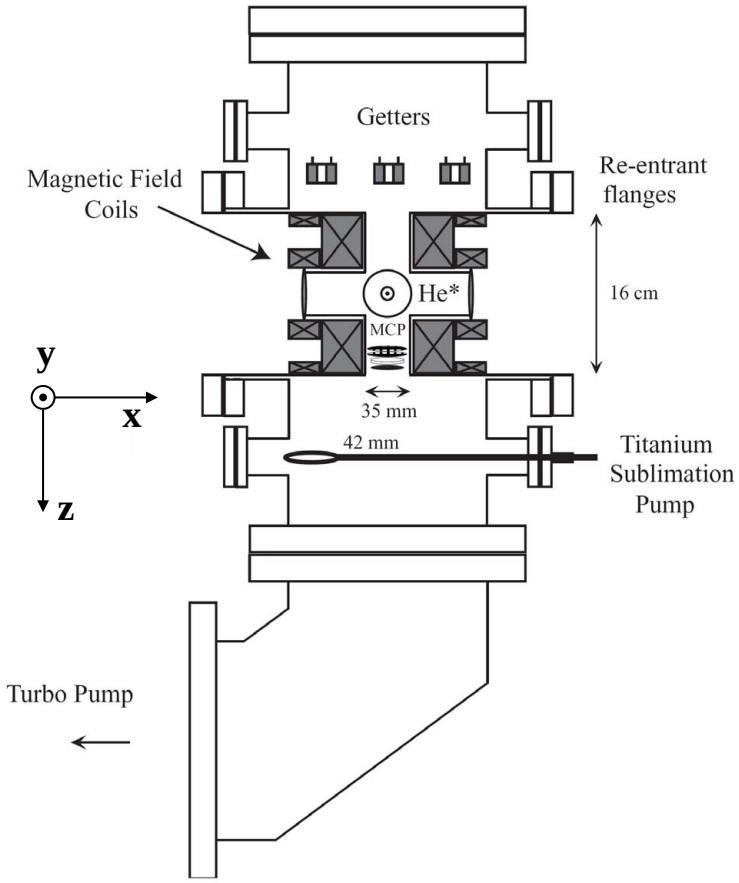

Figure 1.8: The ultra-high vacuum science chamber (`UHV-Ch`), where He* condensation takes place. To help preserving the vacuum conditions, the magnetic field coils (dark gray in the Figure) are assembled outside the chamber in re-entrant flanges, as shown in the Figure. This allows positioning the coils closer together, increasing the trapping field gradients. As before, gravity acts in the Oz direction. See further details in §1.2.3.

1.2.3 From the helium bottle to a cloud of ultra-cold He^* atoms in the magnetic trap.

We will describe in the following paragraphs all the experimental setup, detailing the most important characteristics of its components, the vacuum system and also explaining the laser cooling methods we use to obtain a cloud that can be properly loaded into the magnetic trap. In our experiment, to attain the millikelvin regime, we make use of four of these optical based methods: a transverse collimator, a *Zeeman* slower, a magneto-optical trap and, finally, a *3-D* optical molasses. The last two are already done in the science chamber `UHV-Ch`. The *Zeeman* slower and the transverse collimation have dedicated vacuum chambers.

The experimental setup: chambers and pumping stages.
The setup of our experiment is sketched in Fig.1.9. It is more than 4 m long, starting in the He^* source chamber (`S-Ch`) and ending at the science chamber. From one to the other chambers, a differential vacuum is established and maintained by two diffusion pumps (`DP1` and `DP2`, both with 3000 l/s pumping speed) and three turbo pumps (`TP1`,`TP2`,`TP3` with respectively 250 l/s, 50 l/s and 500 l/s). The vacuum varies from 2×10^{-4} mbar in `S-Ch` to less than 10^{-10} mbar in the `UHV-Ch`. Along the way from the source to the science chamber, the atoms pass also in the transverse collimation chamber (`TC-Ch`) and through the *Zeeman slower*. In the following we will explain the function of all these sub-systems and detail their working principles.

• The He^* source.
The production of the beam of metastable helium atoms is carried out in the *source chamber* (`S-Ch` in the scheme of Fig.1.9), through a high voltage discharge established in a gas of helium in its fundamental state and at 10^{-4} mbar. The working scheme of the *source* is sketched in Fig.1.10 and further explained in its caption. By cooling the source with liquid nitrogen (77 K) it is possible to obtain an atomic jet with a longitudinal velocity around 1200m/s. Its divergence is of about 40 mrad with a flux of 10^{12} atoms per second[72]. The initial pressure in the chamber, when the source is still off is 10^{-7} mbar rising to typically 2×10^{-4} mbar when the helium is admitted in and the discharge is switched on. These pressure conditions are assured by the 3000 l/s diffusion pump `DP1`. See further details in Ref.[72].

• Transverse collimation.
From the source chamber, the beam of He^* atoms enters in a chamber where it is subjected to a *transverse collimation* (`TC-Ch` in Fig.1.9). The working

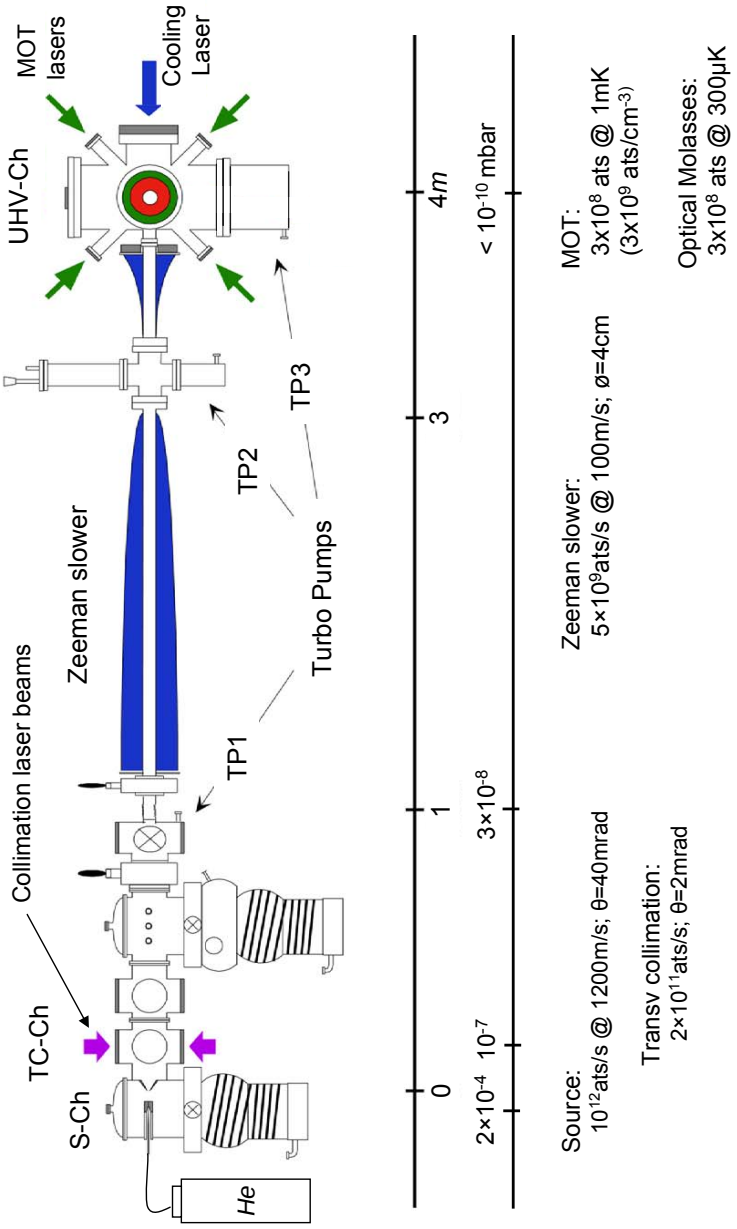

Figure 1.9: Sketch of our He* experiment. Legend: `S-Ch`-the He* source chamber; `TC-Ch`-transverse collimation chamber; `UHV-Ch`-science chamber; `DP1` and `DP1`-diffusion pumps ($3000l/s$ pumping speed); `TP1`,`TP2` and `TP3`-turbo pumps (respectively $250l/s$, $50l/s$ and $500l/s$); In the bottom of the Figure, we represent the variation of the vacuum along the setup and characteristic values of the atomic sample in each of its sub-units.

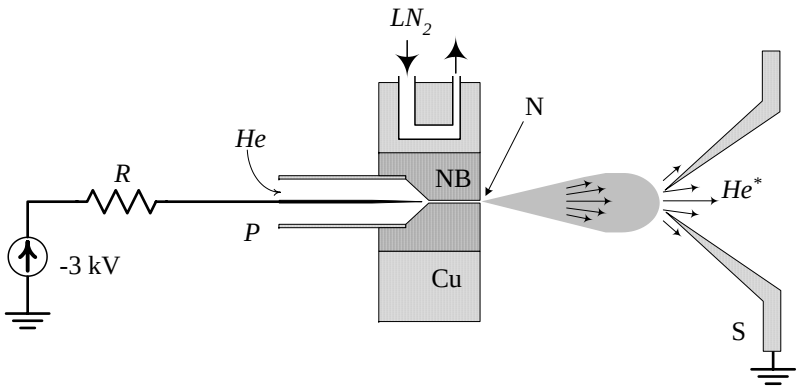

Figure 1.10: The He* source setup. Helium in its fundamental state and at a pressure of several *bars* undergoes a relaxation between a nozzle (N) with a tiny diameter of 0.25 mm and length of 1 cm and a skimmer (S) located approximately 2.5 cm further and with a diameter of 1 mm. An electric discharge of -3 kV, established between the pin P and the grounded skimmer, produces some metastable helium atoms (the resistance R stabilizes the discharge at an operating current of about 13 mA). The efficiency of the process in of only 10^{-4} and, starting from a total helium flow of 5×10^{15} at/s, the metastable jet flux is around 10^{12} at/s. The nozzle is manufactured out of boron nitride (electrical insulator but good thermal conductor), assembled inside a block of copper though which circulates liquid nitrogen at 77 K. The jet longitudinal velocity is of about 1200 m/s with a divergence around 40 mrad. At the level of the skimmer, the collisions between atoms become negligible and the atomic jet is supersonic[73].

pressure in this chamber, with the beam on, is maintained at 10^{-7} mbar by a similar diffusion pump as the one used in the source chamber with the differential vacuum between the source and transverse collimation chambers also assured by the low conductance of the skimmer at the source output.

The atomic beam transverse collimation is made by applying a two-dimensional molasses made of two pairs of almost contra-propagating laser beams resonant with the atomic transition $2^3S_1 - 2^3P_2$. Due to the radiation pressure, the beam of He^* atoms divergence is reduced from 40 mrad to only 2 mrad (see Fig.1.11). The helium atoms in the fundamental state are not affected by the molasses and by placing a 4 mm diaphragm further on in the path of the jet, the number of these atoms in the atomic beam is highly reduced. Even so, due to the low efficiency of the He^* production at the source, the flux of metastable atoms leaving the collimation region, around 2×10^{11} at/s, is still 70 times smaller than the one corresponding to atoms in the electronic ground state. These atoms, however, are not captured by the *magnetic-optical trap* (*TOF*) in the end of the path towards the science chamber (`UHV-Ch` in Fig.1.9) and are removed by the pumping system. To help preserving the very high vacuum in the science chamber and, therefore, the cloud's life time, after completed the *TOF* loading and during all the evaporative cooling, a mechanical shutter placed right before the 4 mm diaphragm is closed to block any particle to enter into the science chamber.

• Zeeman slowing.

In its path from the source to the science chamber, the atomic beam is slowed down by a *Zeeman slower* (`ZS`) [37]. Our `ZS` is made of two different coils, built over a double-wall metallic tube of internal diameter 43mm. To cool down the coils we make water circulate between the two walls of the tube. The radiation pressure of laser beam propagating in the opposite direction of the atoms makes the atoms decelerate. These are maintained in resonance with the laser, for any given velocity, by compensating its *Doppler* shift with a *Zeeman* shift induced by a space varying magnetic field, as explained in Fig.1.12. The `ZS` is made of two coils to allow reversing the magnetic field somewhere in its middle and thus, to have a global detuning of the cooling laser relatively to the atomic transition $2^3S_1 - 2^3P_2$, at its end. This *off-resonance* makes the trapped atoms in `MOT` to be insensitive to this laser.

The vacuum inside the `ZS` is maintained by two *turbo molecular* pumps (`TP1` and `TP2` in Fig.1.9) with pumping speeds of respectively 250 l/s and 50 l/s. Due to several diaphragms placed in the path of the beam and also because its low internal diameter, it is possible to attain a differential vacuum along the `ZS`, between the transverse collimation chamber and the final science chamber. It is of about 3×10^{-8} mbar in the beginning of `ZS` and drops

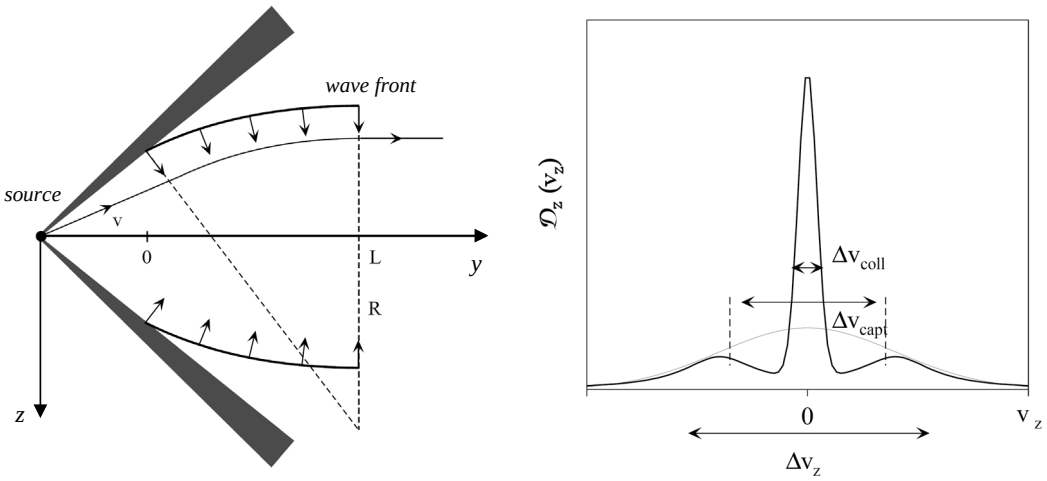

Figure 1.11: The left hand side image sketches the working principle of the transverse collimation in our experiment. For that, use a molasses made of two pairs of contra-propagating laser beams resonant with the atomic transition $2^3S_1 - 2^3P_2$ and disposed transversally to the atomic beam. The lasers are slightly un-collimated to get curved wave fronts, enhancing the momentum transfer to the atoms along these its focusing path. To maximize the interaction, the laser beams are also made highly astigmatic, elongated in the direction of the atomic beam.On the left hand side of the figure the graph shows the influence of the molasses on the transverse distribution of velocity of the jet: the curve in gray and width Δv_z, represents the transverse velocity distribution of the atomic beam in the absence of collimation, whereas the black one, characterized by the width Δv_{coll}, the attained distribution if the transverse collimation is turned on. Also in this graph, Δv_{capt} is the velocity capture range of the molasses, also represented in the right hand side drawing as the region inside the shadowed bars. The critical capture velocity is given by $v_{cap} = \overline{v_y}L/R$, with L the length of the collimation region, R the wave front radius and $\overline{v_y}$ the mean longitudinal beam velocity. Typical values are $R = 15$ m and $v_{cap} = 15$ m/s and a gain in intensity in the atomic flux of about 25[72]. The He* beam divergence is reduced from the initial40 mrad to only about 2 mrad. The effect of the transverse collimation in the efficiency of the *Zeeman slower* leads, in the end, to an increase of a factor of 70 in the atomic flux that is loaded into the *magnetic-optical trap* (images were taken from the Ref.[72]).

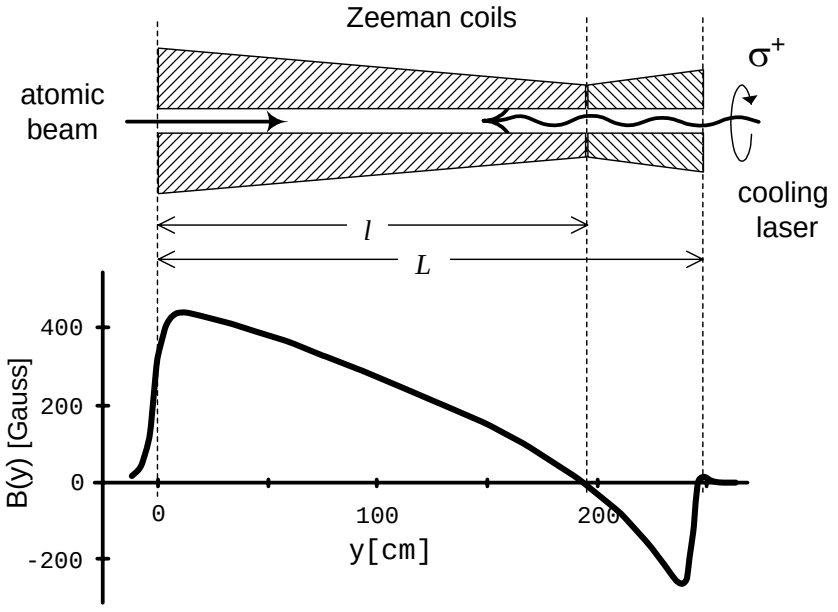

Figure 1.12: The top drawing is a schematic representation of our *Zeeman slower* (ZS). The atomic beam, coming from the left hand side in the scheme, is slowed down by a combination of the action of a contra-propagating laser beam with the spatial variation of a magnetic field. The laser is detuned from the atomic transition $2^3S_1 - 2^3P_2$ of $\Delta\omega_l$ and is *right hand polarized*, σ^+. The magnetic field along the deceleration axis is made to vary in a way to produce a *Zeeman* shift in the atomic transition, $\Delta\nu_Z$, that is, at any time, compensated by the *Doppler* shift, $\Delta\omega_D$, proportional to the atom's velocity[37]. Always at resonance with the laser, the atoms are decelerated by the radiation pressure (see also text).

down to less than 10^{-10} mbar at the entrance of the UHV science chamber.

The atom's final velocity after passing the ZS is of about 100 m/s for a flux of $\sim 5 \times 10^9$atoms/s. Due to the spontaneous emission over all optical cycles, the transverse section of the beam increases from few millimeters to around 4 cm.

• **The *magneto-optical trap.***

After being decelerated by the ZS, the atoms are captured by a *magneto-*

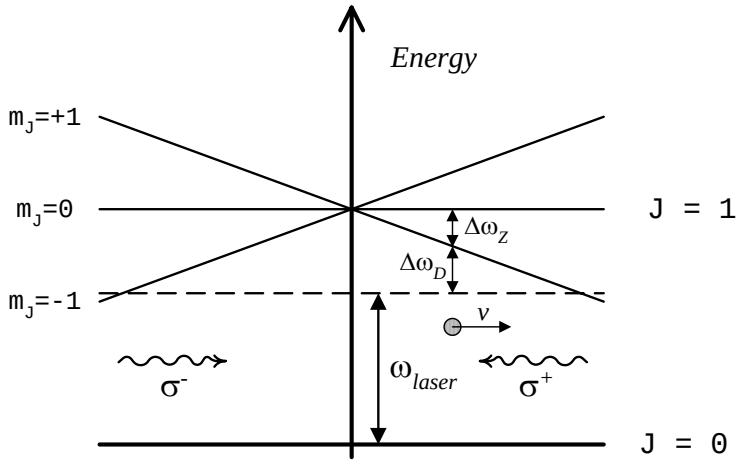

Figure 1.13: Working principle of a one dimensional *Magneto-Optical trap* (MOT) in a $J = 0$ to $J = 1$ atomic transition. Two contra-propagating laser beams, red detuned relatively to the atomic transition and polarizations σ^+ and σ^- are incident in a atomic cloud where a non-homogeneous magnetic field creates, from the center of the trap, a linear increase of the *Zeeman* shift of the atomic optic lines in that transition. The combination of the *Doppler* and of the *Zeeman* shifts makes fast out-coming atoms at the center of the trap to get in resonance with the laser and decelerate with the radiation pressure. This way, all the atoms with an initial velocity smaller than a critical capture velocity v_{cap} are confined at the center of the trap and cooled down. This critical velocity is proportional to the transverse size of region where the laser beams saturated the optical transition: the bigger this is, the bigger the number of optical cycles a given atom can make before escaping the trap

optical trap. This is made of three pairs of red-detuned, circular polarized and contra-propagating laser beams and a non-homogeneous anti-Helmoltz magnetic field that grows linearly from zero, at the center of the trap, in all outwards directions. This field gradient produces a *Zeeman* shift in the magnetic sub-levels of the atomic transition $2^3S_1 - 2^3P_2$, increasing also with

distance from the trap center. Again, the combination of this shift with the *Doppler* shift makes the laser to be tuned with the atomic transition, confining and cooling them down around the trap's center (see also the description of the working principle of a MOT in the simpler configuration of the $J = 0 \rightarrow J = 1$ atomic transition in Fig.1.13).

The laser detuning must be chosen to altogether maximize the number of trapped atoms and minimize their temperature and, in our case, there are two competitive processes. From the MOT efficiency point of view only, the minimal temperature is reached if [36]

$$\Delta_{opt} = -\tfrac{1}{2}\Gamma\sqrt{1 + 2I/I_{sat}}, \tag{1.7}$$

with Γ the atomic transition line width, I the laser intensity and I_{sat} the *saturation* intensity respectively. In our experimental conditions we have $I/I_{sat} \sim 25$ and therefore, at optimal MOT functioning conditions, the detuning should be $\Delta_{opt} = -3.6\Gamma$. In the other hand, quasi-resonant light enhances the two-body *Penning* collisions between different spin states, leading to atom losses within the cloud[74]. The reason for this relies on the fact that the interaction between two He^* atoms gets stronger if one of them is excited to the $P - state$[75]. To decrease the time an atom is in this excited state, we need to increase the detuning far above the prescription given before. Normally, what we want from the MOT is to trap as many atoms as possible even if this is done at the expense of a small augmentation of the temperature. We found empirically that this is achieved with an *optimal* laser detuning around $\Delta_{opt} = -25\Gamma$.

To compensate this large laser detuning, one needs a strong Zeeman splitting and, therefore, also a large magnetic field gradient in the axial direction. This one is equal to 50 G/cm and it is created by the same coils used for the compensation of the *magnetic trap* (but in an anti-Helmoltz configuration). At the end of the MOT phase, the trapped atomic cloud has typically an *rms* waist of 2 mm and a peak density of $n \sim 4 \times 10^8$ ats/cm^3, which corresponds to 5×10^8 atoms at a temperature around 1 mK. This is several times bigger than the *Doppler limit* temperature $\hbar\Gamma/2k_B \sim 40\mu$K.

• Optical molasses and the transfer to the magnetic trap.

To further decrease the cloud's temperature and get a favorable transfer into the *magnetic trap* (MT), we use a last laser-based method: a *3-D* optical molasses. It takes only 5 ms and is made with the same laser configuration as the one used in the MOT except that the laser detuning is only a few Γ and the beams intensity is reduced by a factor of 10. These three parameters, laser pulse duration, detuning and power, must be chosen as optimal to decrease as much as possible the cloud's temperature without loosing too

many atoms in *Penning* collisions. As in the MOT case, described before, these optimal conditions are found empirically. After the molasses phase the cloud's temperature drops to about 300μK.

Another *fine* adjustment needed to obtain a proper molasses phase is the compensation of residual stray magnetic fields, using three other external coils. Without the MOT strong magnetic field, the atom's magnetic quantization axis becomes very sensitive to any of these stray fields. A slight change in this quantization axis makes the cloud to walk away from the geometric center of magnetic trap, getting lost.

Adaptation of the cloud with the *magnetic trap.* Optical pumping into the $m_J = +1$ magnetic sub-level.

In order to transfer the atomic cloud into the magnetic trap without heating it up or loosing atoms, we need to adapt the curvature of the trap to the cloud size corresponding to this final temperature. If we admit that the cloud is isotropic, with its density described by a *Maxwell-Boltzmann* distribution in a harmonic potential of *rms* width r_0, the condition for optimal transfer is

$$2\mu_B B'' r_0^2 = \frac{1}{2} k_B T.$$

In our case $r_0 \sim 2$mm and the above formula gives for the MT field curvature, $B'' \simeq 30\text{G/cm}^2$. This is, in fact, the typical curvature of our uncompressed magnetic trap.

Before the MT, in both the MOT and molasses phases, the atoms are polarized in any of the possible magnetic sub-levels $m_J = \{+1, 0, 1\}$. Just before transferring the cloud into the MT (by just turning it on), it is still necessary to spin polarize the atomic cloud in the trapping magnetic sub-level $m_J = 1$. This is done simply by shining a retro-reflected laser beam, polarized σ^+, on the atoms for a period of 30μs.

1.3 Experimental readout.

After having described all the procedure used to *produce* a He^* condensate, we will now explain how we detect it. A major peculiarity of the He^* is its 20 eV of internal energy and the capability of being easily ionized (and also to ionize other particles). These are the key points that make our He^* experiment very different from almost all other *BEC* experiments.

We will start by presenting the detector we use in our setup readout apparatus, a *micro-channel plate*.

1.3.1 The *micro-channel plate*.

A *microchannel plate* (MCP) is a thin sheet, made of an array of millions of very small electron multipliers, the microchannels, oriented parallel to one another in a honey comb structure (Fig.1.14-a). These microchannels, of only a few microns of diameter and a fraction of a millimeter length, are glass made and their inner wall is treated to optimize the secondary electron emission characteristics and to have a semiconducting surface layer that allows the charge replenishment from an external voltage source[44]. Both faces of the MCP are metal coated. This puts all the microchannels in parallel electric contact, serving also as input and output electrodes. Each of these channels can be considered as continuous dynode structure, acting as its own dynode resistor chain, typically with a total resistance of 100 MΩ. This resistance limits the *strip current* that is established between the two faces of the MCP for a certain applied high voltage.

When an incident particle with sufficient energy to remove an electron from the inner semiconductor layer hits the MCP, the high voltage applied between the two faces of the MCP will promote an avalanche of secondary electrons and an amplified electronic current is outputted in the MCP back face (Fig.1.14-b). This one is then collected by the anode terminal. To further enhance the efficiency of the process, the microchannels are typically tilted at a small angle relatively to the MCP input surface. The electron multiplication factor can be as large as 10^5, with very good time resolutions, typically a few hundreds of picoseconds.

Specific characteristics of the MCP used in the experiment.
The MCP we used in out setup (HAMAMATSU; reference F 4655) is sketched in the Fig.1.14. It is a two-stage MCP assembled in a chevron configuration (Fig.1.14-*c*). Each of the MCPs is made of about 10^6 micro-channels with a typical diameter of 12 μm and around 0.5 mm long, covering 60% of the MCP total surface of 14.5 mm diameter. The gain of each single device, for a

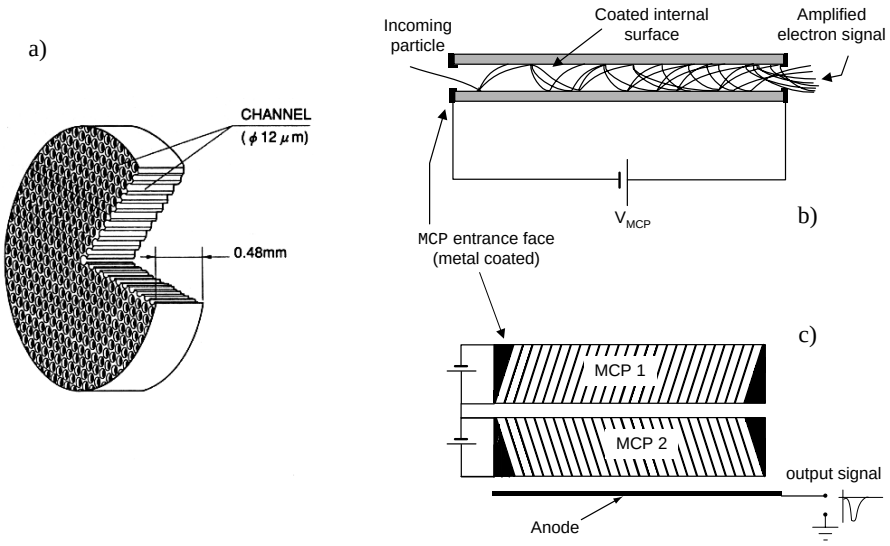

Figure 1.14: The MCP detector: *a*) sketch, with typical sizes, of the MCP we have used in our detection setup (the microchannels cover 60% of the total MCP surface); *b*) working principle of each microchannel (for $V_{MCP} = 1.75$ kV the gain is around 10^4); *c*) the two-stage chevron configuration (overall gain of $10^7 - 10^8$).

typical high voltage of 1.75 kV, is of about 10^4 with the two-stage ensemble overall gain equal to $10^7 - 10^8$ (refer to Ref.[70] for further details).

1.3.2 Saturation effects and the *counting* and *analog detection modes.*

Increasing the MCP high voltage to about 2.0 kV, the gain of the device saturates and the detection of single events become possible. In this regime, the total charge within an avalanche becomes important leading to the establishment of a *space charge* repulsive electric field that tends to decrease the electrons' kinetic energy. In some extend, this prevents further multiplication of the charge and results in a reduction of the fluctuation of the outputted pulses' amplitude. The small dispersion on the pulses' height allows the clear discrimination of an incoming particle from the signal noise.

We used a *fast* pulse amplifier followed by a level discriminator and a digital counter connected to a computer to record all individual events detected by the MCP. This detection method, which we will refer as the *counting mode* detection, was used in our experiment to detect the ion flux produced within the cloud (cf. §1.3.4) and also for the detection of the atomic flux of small clouds. Concerning this latter case, it was especially important making possible the realization of the intensity correlation measurement in a falling

atomic cloud (cf. Chapter 3).

The MCP saturation leads however to a reduction of the maximal events acquisition rate since the charge removed from the microchannels is not replaced as fast as it should. When the MCP current signal is no longer negligible when compared to the *strip current*, the remaining positive charge slow down the electrons and quenches the electron multiplication process.

In the *counting detection mode*, this makes that for some of the events there is no *saturated* pulse and, consequently, they are not detected. In our MCP, the maximum detection rate per channel was of about 1 particle/channel/s[70]. This corresponds, admitting a homogeneous flux, to a maximum detectable rate of 10^6 particles per second.

To detect particle's fluxes bigger than 10^6 s^{-1} we had to reduce the MCP high voltage to around 1.7 kV, where its gain did not saturate. At this operating voltage, the above referred saturation effects are less restrictive and the MCP saturates only for fluxes around $10^7 s^{-1}$. However, the distribution of the pulses' amplitude is larger and does not allow for an efficient counting; we rather measure the charge produced by the particles' flux integrated over the entire MCP surface. Amplifying the charge outputted from the MCP with a slow amplifier resulted in a continuous signal proportional to the flux envelope. This is our *analog detection mode*. Due to their large fluxes, atomic clouds were almost always detected using this method.

1.3.3 The atoms' *time of flight* signal.

After completed the evaporative cooling process, we get a cloud of He^* atoms trapped in the magnetic trap. It can be a *BEC* if the rf-field is ramped down to almost the level of the bias field or just an atomic cloud at some temperature above T_c, the critical temperature. This latter is usually known as a *thermal cloud*.

Either being a *BEC* or a thermal cloud close to T_c, the trapped cloud is too small [8] to be detected by conventional methods. Thus, before proceeding with the detection, it is necessary to release the cloud and let it expand for a while.

In conventional *BEC* experiments the cloud is then imaged in a video camera and in most experiments, this is done by shining a resonant laser beam on the cloud, expanded to a size that is large compared with the optical resolution of the detector. Typical cloud expansion times are of the order of tens of milliseconds. In our experiment, the detection system is quite different: we let the cloud fall and expand for a much longer time ($\sim$ 100 ms) and the measured signal is the atomic flux detected by the MCP, placed 5 cm below the center of the magnetic trap.

[8] Typical cloud sizes are 10μm in the radial direction by 200 μm in the axial one.

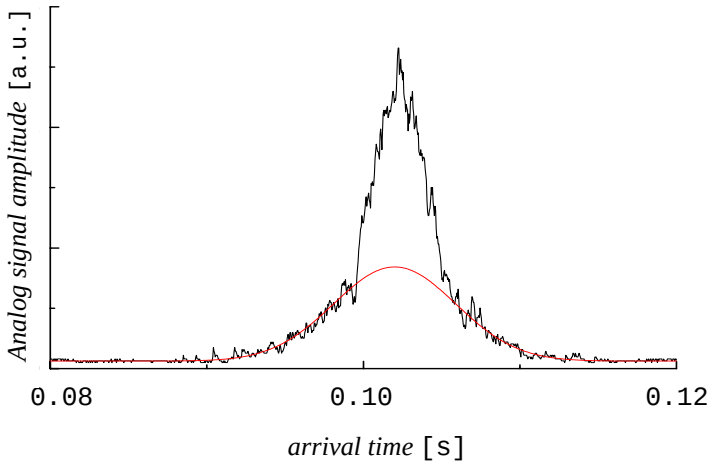

Figure 1.15: Example of a *TOF* signal of a cloud taken using the *analog mode*. This cloud has a temperature below the critical one since its *TOF* presents a double structure composed by a *thermal cloud*, the broader Gaussian curve in the wings of the curve, and a *BEC*, the *inverted parabola* structure in its center (cf. Appendix A).

Within the *analog detection mode*, as the atomic flux is integrated over the MCP surface the signal contains less information than a $2-D$ image obtained using a video camera. In the other hand, it can be easily acquired, after amplification, with a simple oscilloscope without any further signal processing.

The Fig.1.3.3 shows an example of such an *analog* signal for a *TOF* of a degenerate cloud, with both a *BEC* and a *thermal cloud*. This signal was amplified by a *slow* amplifier with a characteristic integration time of $RC = 0.45$ms, smaller than the time width of the smallest observed clouds, around 3ms [9].

Counting mode in the *TOF* acquisition.

The *counting* mode reproduces better the original signal and is always preferable to the *analog* mode whenever the events' rate were $\lesssim 10^5$ s^{-1}. As explained above, the use of the *analog detection mode* for acquiring atomic *TOF* signals is used due to the MCP saturation. Along with this, the maximal counting rate of our electronic chain was also limited to about 10^6 events per second (cf. §1.3.5). These two difficulties can be overcome however, using faster electronics and more performing MCP. This was done, in fact, in the

[9] This time of integration may seem very large, but for a *BEC*, which has the very simple profile of an inverted parabola, a few points are already sufficient to fit the *TOF*. For thermal clouds, the *TOF* is more complex but also larger in time. Typically, the *TOF* of a thermal cloud has a time width of 10ms, which is already twenty times larger than *RC*.

newest version of our detection apparatus described in §3.5.2.1. This new setup has also a *position sensitive* device, capable of measuring not only the arrival time of each atom but also its position.

1.3.4 The ion signal.

As we referred previously, in the Introduction of this thesis, the Bose-Einstein condensation of He^* is only possible in spin polarized samples where the *Penning* ionizing processes, induced by inelastic collisions, are highly suppressed. Even so, some of these processes persist and a measurable flux of ions is continuously produced within the cloud. The rate at which the ions are created within the cloud depends on its density. Therefore, the ion signal can be regarded as an indirect measure of that quantity. A major advantage of the ion flux signal is that it is a non destructive technique and may be used to follow in *real time* the cloud's density during the evaporative cooling.

In here, we will discuss some of the most important characteristics of this signal, describing also the experimental procedure we have used to detect it.

1.3.4.1 The *two* and *three*-body *Penning* ionization processes.

During a *Penning* ionizing collision, the total spin must be conserved[39]. For a two-body collision, the possible process are described by the reactions

$$He^*(2^3S_1) + He^*(2^3S_1) \rightarrow \begin{cases} He(1^1S_0) + He^+ + e^- \\ He_2^+ + e^- \end{cases} . \tag{1.8}$$

If the sample is prepared in the magnetic sub-level $m_J = +1$, the colliding atoms, represented in the left hand side of this expression, has each one a spin equal to $S = 1$. This amounts to a total spin of the incoming particles of $S = 2$. However, the total spin of the collision products, in any of the lines in the right hand side of the equation is never bigger than 1 and the spin conservation is not satisfied. The two-body ionization rate constant, about 10^9 cm^3/s for a non polarized sample[76] is reduced by, at least, 3 orders of magnitude for a cloud spin polarized in the $m_J = +1$ state.

The above reaction corresponds only to the lowest order electrostatic interaction. *Penning* collisions may also happen through a process known as *relaxation-induced Penning* ionization[39]. In here, the two colliding polarized He^* atoms may be considered as a quasimolecule where the total angular momentum has relaxed into a zero spin state due to a virtual dipole-spin interaction. The Hamiltonian governing this process is

$$\hat{H}_{int} = \frac{4\mu_B^2}{R^5}\left[(\hat{S}_1 \cdot \hat{S}_2)R^2 - 3(\hat{S}_1 \cdot \mathbf{R})(\hat{S}_2 \cdot \mathbf{R})\right],$$

where $\mathbf{R}$ is the internuclear distance and, $\hat{S}_1$ and $\hat{S}_2$ the spin operators of the colliding atoms. H_{int} may induce a transition from the initial quasimolecule state $|M_1 = 1\rangle|M_2 = 1\rangle$ into the zero spin state

$$\tfrac{1}{\sqrt{3}}\left(|M_1 = +1\rangle|M_2 = -1\rangle + |M_1 = -1\rangle|M_2 = +1\rangle - |M_1 = 0\rangle|M_2 = 0\rangle\right),$$

with M_1 and M_2 the spin projections of one and the other atoms. Once in this state, the quasimolecule ionizes *via* an ordinary *Penning* process [10].

Besides this two-body process, in a very dense polarized He^* cloud it may also exist collisions involving three atoms. In here, two of the atoms form a weakly bound molecule and the third one, with sufficient kinetic energy, carries away the binding energy[77],

$$\begin{array}{c} He^* + He^* + He^* \ \rightarrow He_2^* + He^*(\sim 1\text{mK}) \\ \downarrow \\ He^+ + He(1S) + e^-. \end{array} \tag{1.9}$$

The ion flux.

The *two* and the *three* body processes presented above as well as the reaction presented earlier in Eq.1.5, an inelastic collision involving a He^* atom and a molecule from the background, produces positive ions that may be detected and used as a monitoring tool. In the latter process, the ion rate production depends on the cloud's number of atoms. For the *two* and *three*-body processes, it depends on the average value of the square and of the cube of the cloud's density, respectively. For a thermal cloud, it is [11]

$$\Phi = \frac{N_{th}}{\tau_i} + \tfrac{1}{2}\beta \int_{R^3} d\mathbf{r}\, n_{th}^2(\mathbf{r}) + \tfrac{1}{3} L \int_{R^3} d\mathbf{r}\, n_{th}^3(\mathbf{r}). \tag{1.10}$$

In the first term on the right hand side of this expression $N_{th} = \int_{R^3} d\mathbf{r}\, n_{th}(\mathbf{r})$ is the cloud's number of atoms and τ_i is the rate constant for collisions with background gas. This latter is smaller than the above defined cloud life time τ, which also includes all other collisional processes that doesn't produce ions [12] but causes the heating and the depolarization of the cloud[78, 79]. In the two other terms, β and L are respectively the *two*- and *three-body*

[10] There are also two other processes that leads to spin relaxation (and to atom losses) but that preserves the total spin $S = 2$ and consequently can not relax through *Penning* ionizations. [39]

[11] For the *BEC* case it is necessary to include quantum reduction factors in the *two* and *three*-body processes (see Chapter 4, for details).

[12] Such collisions are possible with the very abundant molecules of water and hydrogen for example since theirs' energies of ionization are smaller than the internal energy of the He^* atom (energies of ionization of 12.5 eV and 15.5 eV respectively).

ionizing rate constants. These are defined according to their effect in the density of a thermal gas,

$$\left.\frac{dn_{th}}{dt}\right|_{ionization} = -\frac{n_{th}}{\tau_i} - \beta n_{th}^2 - L n_{th}^3. \tag{1.11}$$

Note that the factors $\frac{1}{2}$ and $\frac{1}{3}$ included in the *two* and *three* body terms of Eq.1.10 and not present in this latter expression simply reflects the fact that, to create a single ion in each of these processes, it is necessary to have two and three He^* atoms, respectively.

As in the case of the atoms' *TOF*, the ions can also detected by the MCP. Here, the MCP signal is obtained by accelerating the ions towards the MCP, applying an electric field through the polarization of a grid placed slightly above the MCP's input face. Typically, this grid is putted at -30V relatively to the ground, what is sufficient to capture all the ions produced within the cloud. The needed energy for triggering the detection in the MCP is obtained from the ion's kinetic energy after being accelerated towards the MCP entrance face at ~ -2 kV, which proves to be sufficient for efficient ion detection[80].

The measurement of the cloud's density *via* the ion signal.
The ion signal is in many aspects different from the atomic *TOF*. The main advantages are:

- It is a *non destructive* measurement. In fact, the ion signal is a measure of a flux of particles, products of an unavoidable reaction that exists even if we decide not to detect them. This is not the case of the atoms' *TOF*, where to make the detection one needs to release the cloud from the trap, destroying it.

- It is an *in-situ* measurement. Unlike the *TOF*, the ion signal is proportional to the density of the cloud when it is still trapped. We will show in the next Chapter that, for an ideal gas, the *TOF* signal is rather a signature of the momentum distribution of the cloud (in a non-ideal gas there is also the influence of the inter particle interactions). Here, there is no need to expand the cloud to allow its detection and, therefore, the ion signal may be seen as a measure of the cloud's density in the trap.

- It is an almost *real-time* measurement. As we explained before, the ions are attracted to the detector by an electric field, taking only a few microseconds to arrive at the detector. For practical proposes, in all that concerns the study of the dynamics of the cloud, the ion detection may be considered as instantaneous since the smallest time scales found in the experiment are in the milliseconds regime.

- Finally, it is possible to have an *absolute measurement*. Applying a large enough voltage at the grid below the `MCP`, it is possible to have a large capture solid angle, with the ion's trajectories all focused at the detector. In our case, we verified that voltages bigger than -30V did not produce an increase of the ion flux signal, an indication that all ions were, in fact, detected[70].

It also has some problems:

- Low *signal to noise* and the need of large integration times. The number of produced ions is small, typically smaller than 10^5 events per second and this limits the smallest time scale we may follow in a dynamic measurement of the density. For example, to get an $S/N = 10$ with 10^5 ev/sec, the shot noise limit for the signal integration time is already 1ms.

- It is a *non-local* measurement. In our setup, the ion signal is an overall cloud integrated signal and therefore contains information on the cloud's average density but not on its shape. This could be overcome if we used an ionic imaging system. However, such a system could be very difficult to implement due to the non-homogeneous magnetic field in the science chamber and also, the even lower S/N ratio we would obtain.

- It is difficult to interpret. The ion signal depends on different collisional processes and therefore on the contribution of different powers of the cloud's density. The knowledge of the two collision rate constants, β and L, would make possible to determine to one ion flux the equivalent cloud's density value. However, β and L are not, for the moment, very well known. Part of the work presented on this thesis (cf. Appendix §B) as well as on the thesis of references [70, 51] had the goal of helping solve this problem.

Despite the difficulties in the interpretation of the ion signal, it is nevertheless a unique diagnostic tool. A very good example of this, described in detail in Chapter 4, is its use for observe the *BEC* formation during the last ramp of the evaporative cooling. In here, the atomic cloud has a relatively large density and the ion signal gets stronger, allowing the observation in real time of the atomic cloud evolution through the phase transition. At the critical point, the ion signal shows a brusque variation of its amplitude what, in principle, can be used to determine the instant of time when the phase transition takes place.

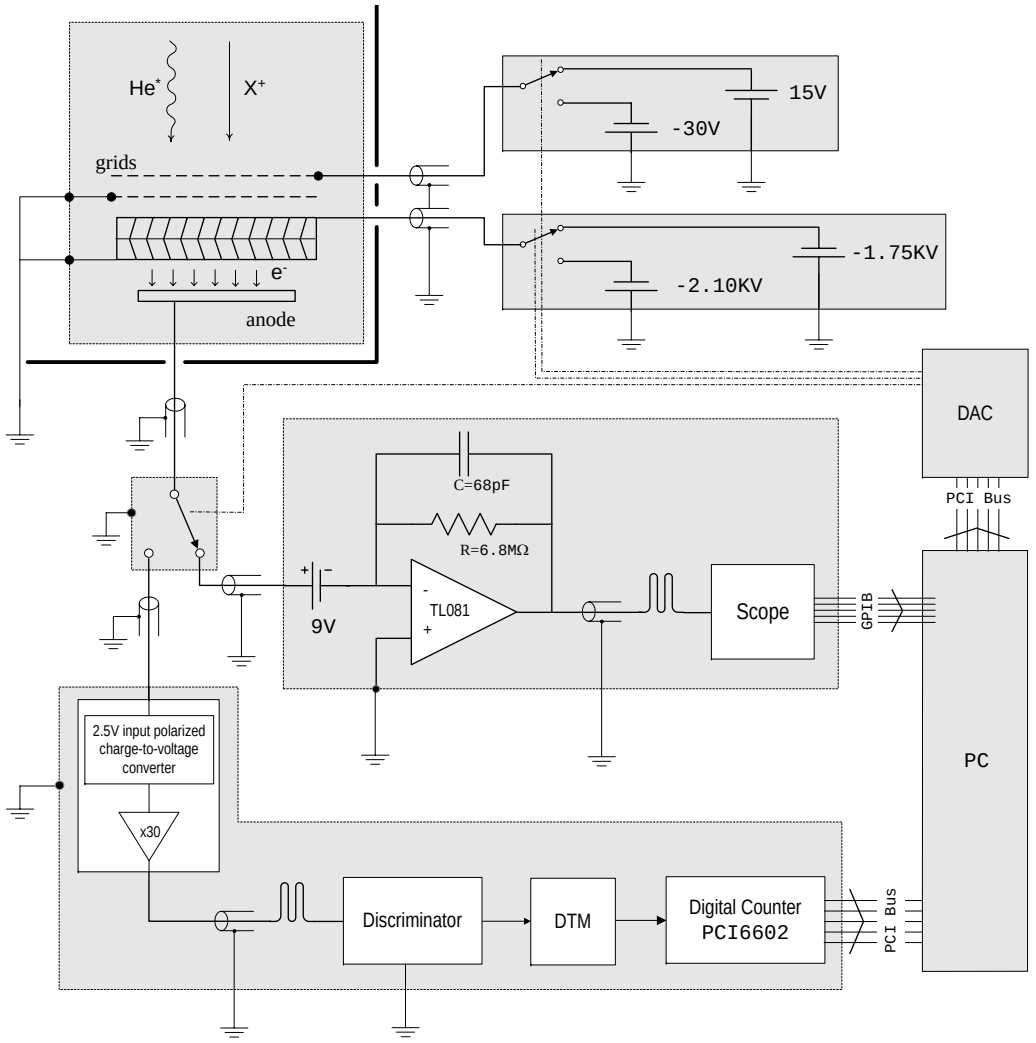

Figure 1.16: Scheme of the detection system. In the left upper corner of the image is represented the science chamber and the MCP mounted below a grid. The grid is polarized with $-30V$ for detecting He^* atoms alone or $+15V$ to detect both the atoms and ions. To switch between the *analog* and the *counting* modes the MCP high voltage is modified respectively to 1.75 kV or 2.1 V and a low noise relay (SR) redirects the MCP anode signal to either detection modes. The *analog mode* is made of just a slow amplifier with a time integration $RC \sim 0.45$ s, connected to a digital oscilloscope. The *counting mode* has a *charge-to-voltage* amplifier that feeds a chain with a discriminator, a *dead-time* module (600 ns) and, in the end, a digital counter (50 ns time resolution). Both amplifiers polarize the anode with a small positive voltage. All the signal transmission lines are *BNC* cables, made as short as possible (especially before amplification) to minimized the noise in the signal. A computer is used to record the data and also to control the experiment through a *digital to analog converter* card (DAC). For a more detailed description see Ref.[70]

1.3.5 The complete scheme of the detection system.

In the Fig.1.16 it is shown schematically the circuitry we have designed to switch between the *counting* and *analog* modes. Typically, we used the *analog* mode to record the atoms' *TOF* signal and the *counting* mode for the ion flux signal. In order to detect the atoms only, avoiding the ion flux, the grid mounted above the MCP input face (see Fig.1.16) could also be polarized with a positive electric potential (relative to ground), repulsing the ions from the detector. To discriminate the ion signal from that produced by the atoms (insensitive to the electric field) we switched the grid's potential between a positive and a negative value. This was done typically at a rate of a few times per second and the difference of the detected fluxes in one and the other cases gave the ion signal.

The commutation of the grid potential was controlled by a computer through a *digital to analog* card (*DAC*). This same computer could also switch the MCP's high voltage in order to operate in *counting* or *analog* detection modes and, also, control a low-noise (high-frequency signal) relay (*Teledyne Relays*) to redirect the MCP signal either to a charge-to-voltage fast amplifier (*counting mode*) or to an *OpAmp* based slow integrator (*analog mode*). Both of these amplifying circuits were designed to polarize the MCP anode with a positive voltage relatively to the grounded output face, in order to enhance the electron signal at the anode[70]. The *counting mode* system was based in a digital counter card (*National Instruments*) installed in a computer. For the *analog mode*, the measure of the *TOF* signal was performed with a digital oscilloscope connected by a *GPIB* card to the same computer (see Fig.1.16 and further details in Ref.[70]).

1.3.6 The calibration of the MCP detection system.

In §1.2.2 we made reference to the two main problems we have in our experiment. There we have reported one of them, the bias fluctuations; here we will present the second one: the impossibility of well calibrating the detection system for the measurement of the number of atoms in a cloud.

1.3.6.1 The difficult calibration of the number of atoms in a *TOF* signal.

In §1.2.1.1 we referred that the atoms *TOF* is produced by a spin flip of the trapped atoms from the magnetic sub-level $m_J = +1$ to the $m_J = 0$. In this latter state, the atoms become insensitive to the magnetic field and fall freely by the action of gravity. However, up to now, the process through which this happens in our experiment is almost uncontrolled and, in some extend, not well understood.

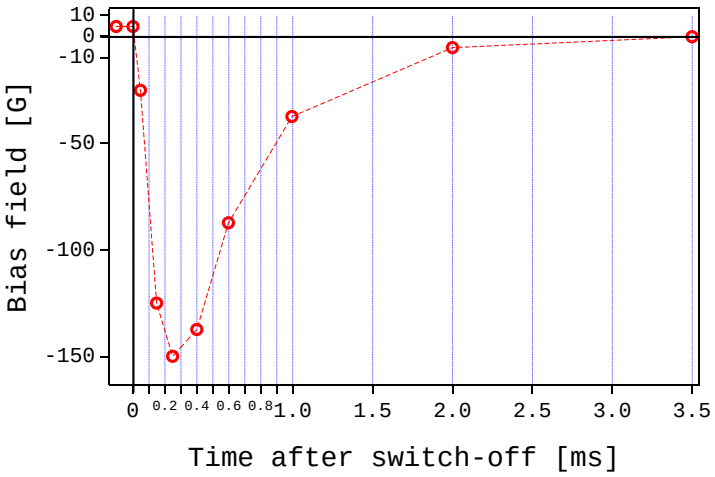

Figure 1.17: The evolution of the bias field after trap switch-off. The origin in the horizontal scale corresponds to the switch-off of the currents in the trap coils. The transient behavior lasts for more than 2 ms, before the field goes to zero. In the first tens of microseconds, the variation of the magnetic field is so fast that some of the atoms are incapable of following it adiabatically. Some of them spin flip to the magnetic sub-level $m_J = 0$ and fall freely.

To release the atoms from the *magnetic trap* we need to switch it off. At the moment this happens, in the compressed trap configuration (cf. §1.2.1.1), the current in the compensation, curvature and gradient coils is of around 200 A, with each of these coils producing a magnetic field of about 190 G. To get a ballistic expansion of the cloud, the trap has to be switched off much faster than the inverse oscillation frequency of the radial axis, ~ 1 ms, meaning that all the magnetic fields need to be switched off very rapidly. This induces very strong eddy currents in the stainless steel chamber and the magnetic field behaves in an uncontrolled way during a transient period of a few milliseconds before going to zero. In particular, the bias field at the center of the trap exhibits the behavior shown in Fig.1.17: it decreases very rapidly from $\sim$ 360mG to almost $-150G$, relaxing then to zero. The atoms at the center of the trap, during the passage at zero magnetic field, losses momentarily the magnetic quantization axis and, some of them, spin flip to the state $m_J = 0$ and fall under gravity. These are the atoms we see in the *TOF* signal.

This initially somehow unexpected behavior of the trap switch-off turned out to be very convenient since the atoms that spin flip to the $m_J = 0$ state are insensitive to stray magnetic fields, allowing the unperturbed expansion of the cloud. The only problem, however, is to know η_{tof}, the ratio between the total number of trapped atoms and those that contributes for the *TOF* signal. This ratio is not well known and the best we can do is to

estimate it approximatively.

Dependence with the temperature.
Moreover, we have empirical evidence that η_{tof} also varies with the temper-

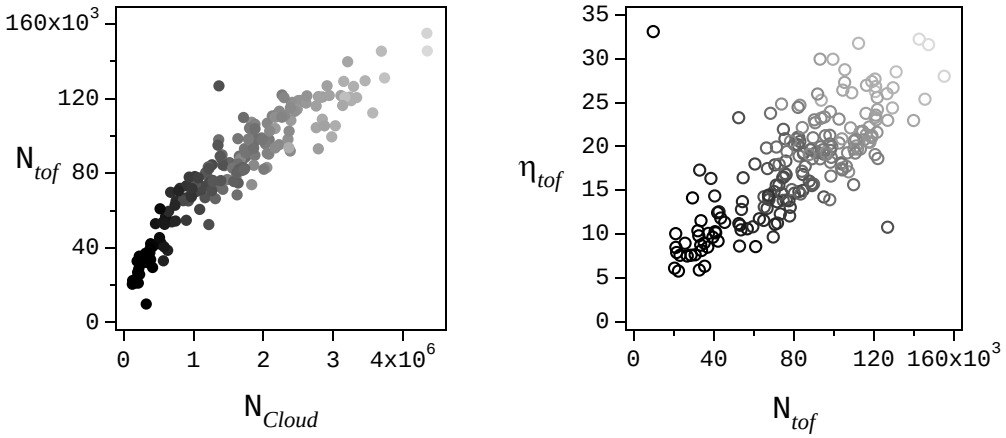

Figure 1.18: The left hand side graph plots the integrated flux of several *TOF*s, N_{tof}, in function of the theoretically expected number of atoms in the corresponding cloud, N_{cloud}. The computation of N_{tof} requires the knowledge of the temperature, fugacity and amplitude of each *TOF*, all these parameters found through a fitting procedure (cf. Chapter 4 and Appendix D) and also the overall detector efficiency (see text). N_{cloud} is computed using the thermodynamical expression that relates temperature, fugacity and number of atoms (cf. Eq.4.51). The right hand side graph, shows the corrective factor $\eta_{tof} = N_{cloud}/N_{tof}$ in function of the number of atoms in the *TOF*, N_{tof}. The data shown in both graphs covers a range of temperature from the 0.5μK, the darkest gray markers, to 3.2μK, the lightest ones.

ature of thermal clouds and with the size of condensates (*i.e.* their chemical potentials). The values we find for thermal clouds and condensates are very different, even for thermal clouds close to the degeneracy[51].

The Fig.1.18 shows an example of the variation of efficiency of detection for many different thermal clouds. Its left hand side graph plots N_{tof}, the number of atoms computed as the integral of the *TOF* signal acquired within the *analog mode* [13], in function of N_{cloud}, a theoretically computed number

[13] N_{tof} is derived from the *analog TOF* signals which is a voltage signal given by $V_{tof} = \eta_{atoms}\frac{dN_{tof}}{dt}$, with ϱ_{atoms} a *responsibility* constant that converts the atomic flux into Volt. This quantity is given by[70]

$$\varrho_{atoms} = e \cdot R \cdot QE\ \mathcal{G} \cdot T_{grid} \cdot S_{active} \sim 9.2 \times 10^{-8}\mathrm{V} \cdot \mathrm{sec},$$

where $R = 6.8 \times 10^6$ is the charging resistor, $QE\ \mathcal{G} = 2 \times 10^5$ is the product of the quantum efficiency and the gain of the MCP, $S_{active} \sim 0.6$ is the ratio of its active surface

of atoms obtained from a fit analysis of the *TOF*. This graph shows that these two quantities are quite different. The right hand side graphs of this Figure plots the ratio $\eta = N_{cloud}/N_{tof}$ in function of N_{tof}. In these graphs, N_{cloud} is computed for known values of the cloud's temperature and fugacity (cf. Eq.4.51), which are obtained from a fit of the *TOF* to the theoretical model we will present latter in Chapter 4. Thus, the values we plot here for η_{tof} cannot be considered as an absolute calibration of the detection system.

1.3.6.2 The detection sensitivity for the *counting mode*.

The effective atomic flux acquired with the *counting* mode is given by

$$\Phi_{atoms} = T_{grid} \cdot S_{active} \cdot QE \cdot \frac{dN_{tof}}{dt}. \tag{1.12}$$

This expression is independent of the MCP gain. Comparing the *analog* and the *counting mode* signals we could determine $\mathcal{G} \sim 5.2 \times 10^5$ and then, that QE for a He^* atom is of about $\sim 40\%$.

Ion signal calibration.

The ion flux expression differs from the expression given in Eq.1.12 for the atomic flux only in the quantum efficiency, which is different for ions (we admitting, as before, that all the ions are detected by the MCP). For a MCP high voltage of about 2 kV, this quantity approaches unity[80] and then, the overall efficiency for the ion detection is only

$$\eta_{ions} = T_{grid} \cdot S_{active} \sim 0.42.$$

and $T_{grid} = (0.84)^2$ the grid transmission.

CHAPTER 2

The ultra-cold non-degenerate ideal gas.

In this Chapter we present an introduction to simple and standard results of the physics involved in an ultra-cold, non-interactive atomic gas confined in a harmonic trap[3]. It also introduces the formalism we use to describe theoretically the atomic *time of flight* (*TOF*).

The Chapter is divided into two Sections. In Section 2.1, we will describe the atomic cloud inside the trap, using a formalism based in the density matrix operator in thermal equilibrium. We will derive standard results for the cloud's spatial density as well as for its momentum distribution. Along with the theoretical formalism, this Section will also introduce some of the definitions we will use further on in this manuscript.

In Section 2.1, we also introduce the *semi-classical approximation* (*SCA*) and the critical temperature. We show that the *SCA* formalism is not sufficient to properly define the cloud's peak density at the critical transition point and we need to take into account the contribution of the harmonic oscillator fundamental state[81]. The validity of the *SCA* is further investigated for the spatially integrated density cases, as those found in experimental detection schemes or, more generally, for the number of particles in the cloud. For these cases, we show that the *SCA* works well.

In the second part of this Chapter, Section 2.2, we will model the ballistic fall of a cloud after being released from the trap. As before, the used formalism is very standard[82, 83]: we use a *Green function* for computing the propagation of the atoms' wave functions in a gravitational field. This is done considering the ideal gas case only. Even so, the derived result proves to be a rather good description even for the case where we consider a weakly interactive gas. It is used in Chapter 4, along with a correction for hydrodynamical effects, in the derivation of the *TOF* expressions we use to fit our data.

We have also used this ballistic expansion model to interpret the results of a recent experiment, where we have measured the density-density correlation function of a falling cloud[84]. The results obtain in Section 2.2, for the atomic flux, will then be generalized to deal with this correlation experiment.

2.1 An ideal gas cloud confined in a harmonic trap.

In following paragraphs we will derive simple expressions describing a cloud of an ideal bosonic gas trapped in a harmonic potential at the thermal equilibrium. We start by introducing the harmonic oscillator Hamiltonian and its eigenfunctions. These are then used to define a thermal equilibrium density matrix operator at non null temperature, using the *Bose-Einstein* distribution as the statistical weighting function. The *Green* function for this problem is well known and, generalized to *imaginary time*, describes the density matrix at finite temperature. Within this framework, we derive the cloud's atomic density in the coordinate space and also in the momentum space.

In this Section we will also discuss the usually denoted *semi-classical approximation* (*SCA*) which is widely used to simplify the analytical density expressions, that involves infinite sums, to approximated expressions written through the use of polylogarithmic (*Bose*) functions. Expressed in this way, the density functions has simpler analytical derivations and, since the polylogarithmic function are easily computed numerically, simplifies the analysis of experimental results as, for example, fitting *TOF* data. However, the type of approximations used in this *SCA* can, in some cases, be very inaccurate. We check their validity for our experimental situation.

A relevant aspect of the validity or not of the *SCA*, is the problem of the determination of a harmonically trapped cloud's peak density at the critical transition. An exact calculation of this quantity, for the *ideal gas* case, gives an unexpected result, quite different from the standard one found in the literature.

2.1.1 Atomic density in thermal equilibrium.

Our magnetic trap potential can be well approximated by a harmonic oscillator (h.o.) potential [1]:

$$V(\mathbf{r}) = \sum_{\alpha} \tfrac{1}{2} M \omega_\alpha^2 r_\alpha^2 \tag{2.1}$$

where ω_α are the frequencies of oscillation in each of the Cartesian directions and M is the He*mass. For the ideal gas, the total Hamiltonian is simply

$$\hat{H} = \frac{\hat{\mathbf{p}}^2}{2M} + V(\hat{\mathbf{r}}). \tag{2.2}$$

[1] Throughout all this manuscript the Greek letter α will always denote an index running over all the spatial coordinates.

This Hamiltonian is known to have a discrete set of eigenfunctions that can be written in terms of the Hermite polynomials, $H_m(x)$. The eigenfunction of order $\mathbf{m}$ is given by

$$\psi_{\mathbf{m}}(\mathbf{r}) = \prod_{\alpha} A_{m_\alpha}\ e^{-r_\alpha^2/2\sigma_\alpha^2}\ H_{m_\alpha}(r_\alpha/\sigma_\alpha). \tag{2.3}$$

with $A_{m_\alpha} = (\sqrt{\pi}\sigma_\alpha\ 2^{m_\alpha}\ m_\alpha!)^{-1/2}$ being the normalization factor. The spatial dimensions of the trap are characterized, in each direction of space, by the characteristic length scale $\sigma_\alpha = (\hbar/M\omega_\alpha)^{1/2}$.

The trapped cloud density, in thermal equilibrium can be written as

$$n(\mathbf{r}) = \langle \mathbf{r}|\hat{\rho}_{eq}|\mathbf{r}\rangle = \sum_{\mathbf{m=0}}^{\infty} \psi_{\mathbf{m}}(\mathbf{r})\psi^*_{\mathbf{m}}(\mathbf{r})\ \langle n_{\mathbf{m}}\rangle \tag{2.4}$$

where

$$\hat{\rho} = \sum_{\mathbf{m}=0}^{\infty} |\psi_{\mathbf{m}}\rangle\langle\psi_{\mathbf{m}}|\ \langle n_{\mathbf{m}}\rangle$$

is the density matrix operator. $\langle n_{\mathbf{m}}\rangle$ is the thermal occupation of state $\mathbf{m}$, which is given by Bose-Einstein statistics

$$\langle n_{\mathbf{m}}\rangle = \frac{\mathcal{Z}}{\exp(\beta\varepsilon_{\mathbf{m}}) - \mathcal{Z}} \tag{2.5}$$

with $\varepsilon_{\mathbf{m}} = \hbar\sum_\alpha \left[\left(m_\alpha + \frac{1}{2}\right)\omega_\alpha\right]$ and $\beta = 1/k_BT$, where T is the temperature and k_B is the Boltzmann constant. In this expression we also have $\mathcal{Z}$ which is the fugacity. $\mathcal{Z}$ is an alternative way of representing the chemical potential μ, $\mathcal{Z} = \exp(\mu/k_BT)$. Using the fugacity rather than the chemical potential if often preferable since the fugacity is bound on a finite interval while the chemical potential can range to $-\infty$. The two limiting values for $\mathcal{Z}$ are attained for the classical high temperature limit and for the zero temperature *BEC* gas. In the classical limit since many levels of the harmonic oscillator are occupied the sum in Eq.2.4 is extended to large values of $\mathbf{m}$. However, the total number of particles N, given by

$$N = \int_{R^3} d\mathbf{r}\ n(\mathbf{r}),$$

is fixed and therefore the fugacity should be small enough to fulfill the last Equation. For a fixed number of particles, the fugacity decreases when the temperature grows and, in the limit of very high temperature, tends to zero.

In the limit where the temperature decreases to zero, only the lowest energy level is occupied and

$$N = N_0 = \frac{\mathcal{Z}}{\exp(\beta\varepsilon_0) - \mathcal{Z}}$$

where $\varepsilon_{\mathbf{0}} = \frac{3}{2}\hbar\widetilde{\omega}$ is the *zero point energy*, with $\widetilde{\omega} = (\omega_x + \omega_y + \omega_z)/3$ the arithmetic mean of the trap frequencies. As N_0 must be positive, this equation defines the maximum value for the fugacity

$$\mathcal{Z}_{max} = \exp(-\beta\varepsilon_0)\ \frac{N_0}{N_0 + 1} \approx \exp(-\beta\varepsilon_0). \tag{2.6}$$

In the last equation we have assumed a very large number of particles. Consequently, the maximum value the chemical potential can obtain is $\mu = \varepsilon_0$.

There are several alternative strategies to evaluate the expression in Eq.2.4 [85, 86]. Here we will make use of the single particle h.o. Green function, $\mathcal{G}^{ho}(\mathbf{r}, \mathbf{r}', t) = \langle \mathbf{r}' | \exp(-i\hat{H}t/\hbar) | \mathbf{r} \rangle$. This Green function propagates a wave function from position $\mathbf{r}$ to $\mathbf{r}'$ during the time interval t,

$$\begin{aligned} \mathcal{G}^{ho}(\mathbf{r}, \mathbf{r}'; t) &= \langle \mathbf{r}' | \exp(-i\hat{H}t/\hbar) | \mathbf{r} \rangle = \\ &= \sum_{\mathbf{m},\mathbf{m}'} \langle \mathbf{r}' | \psi_{\mathbf{m}'} \rangle \langle \psi_{\mathbf{m}'} |\ \exp(-i\hat{H}t/\hbar) | \psi_{\mathbf{m}} \rangle \langle \psi_{\mathbf{m}} | \mathbf{r} \rangle. \\ &= \sum_{\mathbf{m}} \psi^*_{\mathbf{m}}(\mathbf{r}') \exp\left(-i\frac{\epsilon_{\mathbf{m}}}{\hbar}t\right) \psi_{\mathbf{m}}(\mathbf{r}) \end{aligned} \tag{2.7}$$

Our interest here is not in the particles' motion but rather in their distribution of thermal equilibrium. Substituting the (real) time in this propagator by $t = -i\hbar\beta$, a purely imaginary quantity, inversely proportional to the temperature, we obtain

$$\mathcal{G}^{ho}(\mathbf{r}, \mathbf{r}'; \beta) = \sum_{\mathbf{m}} \psi^*_{\mathbf{m}}(\mathbf{r}') \exp(-\beta\epsilon_{\mathbf{m}}) \psi_{\mathbf{m}}(\mathbf{r}). \tag{2.8}$$

We will refer to this expression as the *temperature Green function*[86]. This expression is similar to the one in Eq.2.4 if the occupation factor is taken as the Boltzmann factor $\exp(-\beta\epsilon_{\mathbf{m}})$. Note however that we can express the Bose-Einstein formula of Eq.2.5 as a sum of Boltzmann factors multiplied by the fugacity,

$$\frac{\mathcal{Z}}{\exp(\beta\varepsilon_{\mathbf{m}}) - \mathcal{Z}} = \sum_{l=1}^{\infty} \mathcal{Z}^l \exp(l\beta\varepsilon_{\mathbf{m}}),$$

and therefore

$$n(\mathbf{r}, \mathbf{r}') = \langle \mathbf{r} | \hat{\rho} | \mathbf{r}' \rangle = \sum_{l=1}^{\infty} \mathcal{Z}^l \mathcal{G}^{ho}(\mathbf{r}, \mathbf{r}'; l\beta). \tag{2.9}$$

which is the first order correlation function evaluated at the spatial locations $\mathbf{r}$ and $\mathbf{r}'$. The actual expression for the h.o. Green function proves to be equal to[87]

$$\mathcal{G}^{ho}(\mathbf{r},\mathbf{r}';t) = \\ = \frac{(2\pi)^{-3/2}}{\overline{\sigma}^{\,3}} \prod_{\alpha} \sqrt{\frac{-i}{\sin(\omega_{\alpha} t)}} \times \exp\left[i \frac{(r_{\alpha}^2 + r_{\alpha}'^2)\cos(\omega_{\alpha} t) - 2 r_{\alpha} r_{\alpha}'}{2\sigma_{\alpha}^2 \sin(\omega_{\alpha} t)} \right] \quad (2.10)$$

where $\overline{\sigma} = (\prod_{\alpha} \sigma_{\alpha})^{1/3}$ is the geometric mean trap size. The *temperature Green function* becomes [2]

$$\mathcal{G}^{ho}(\mathbf{r},\mathbf{r}';\tau) = \\ = \frac{(2\pi)^{-3/2}}{\overline{\sigma}^{\,3}} \prod_{\alpha} \sqrt{\frac{1}{\mathrm{sh}(\tau_{\alpha})}} \; \exp\left[-\left(\tfrac{r_{\alpha}+r_{\alpha}'}{2\sigma_{\alpha}}\right)^2 \mathrm{th}\left(\frac{\tau_{\alpha}}{2}\right) - \left(\tfrac{r_{\alpha}-r_{\alpha}'}{2\sigma_{\alpha}}\right)^2 \mathrm{cth}\left(\frac{\tau_{\alpha}}{2}\right) \right], \quad (2.11)$$

where we have introduced the temperature dependence through the parameter

$$\tau_{\alpha} = \beta \hbar \omega_{\alpha}. \quad (2.12)$$

This expression will be used in the following Chapter for computing correlation functions of the atomic cloud. For now we are only interested in its particles' density function which, at location $\mathbf{r}$, is obtained from Eq.2.9 with $\mathbf{r}' = \mathbf{r}$,

$$n(\mathbf{r}) = \sum_{l=1}^{\infty} \mathcal{Z}^l \mathcal{G}^{ho}(\mathbf{r},\mathbf{r};l\tau).$$

In the high temperature limit, $\beta\hbar\omega_{\alpha} = \tau_{\alpha} \ll 1$ and only the first term of the sum will contribute significatively to the expression. If we take only this term we get

$$n^{\infty}(\mathbf{r}) = \frac{\mathcal{Z}}{\lambda_T^3} \prod_{\alpha} \sqrt{\frac{\tau_{\alpha}}{\mathrm{sh}(\tau_{\alpha})}} \exp\left[-\frac{r_{\alpha}^2}{\sigma_{\alpha}^2} \mathrm{th}\left(\frac{\tau_{\alpha}}{2}\right) \right],$$

with

$$\lambda_T = \hbar \sqrt{2\pi / M k_B T}, \quad (2.13)$$

the thermal *de Broglie* wavelength. Since $\tau_{\alpha} \ll 1$ we can also replace the hyperbolic functions by corresponding series expansions in τ_{α}, truncated at the lowest order term, to obtain

$$n^{\infty}(\mathbf{r}) = \frac{\mathcal{Z}}{\lambda_T^3} \prod_{\alpha} \exp\left[-\frac{\tau_{\alpha}}{2} \frac{r_{\alpha}^2}{\sigma_{\alpha}^2} \right] = \frac{\mathcal{Z}}{\lambda_T^3} \exp\left[-\beta V(\mathbf{r}) \right], \quad (2.14)$$

[2] The symbols th(), cth() and sh() will be used for the hyperbolic tangent, cotangent and sine functions, respectively.

which can be recognized as the usual Boltzmann distribution function derived in the framework of classical statistical mechanics. Here, the fugacity plays the role of phase space degenerecency parameter and is related with the number of atoms N through $\mathcal{Z} = N\overline{\tau}$ with

$$\overline{\tau} = \left(\prod_{\alpha} \tau_{\alpha}\right)^{1/3} \tag{2.15}$$

the geometric mean value of τ.

The maximum density occurs at the center of the trap for $\mathbf{r} = 0$ and is equal to $\mathcal{Z}\lambda_T^{-3}$. The thermal cloud size s_α, in each spatial dimension α, is given by

$$s_\alpha = \frac{v_T}{\omega_\alpha} \tag{2.16}$$

where $v_T = \sqrt{k_B T/M}$ is a convenient measure of the thermal velocity.

It is useful to redefine the fugacity so that its maximum value is always bounded by one. This can be accomplished by redefining the fugacity to include the zero point energy for the harmonic motion in the trap,

$$\mathrm{Z} = \mathcal{Z}\exp\left(-\tfrac{3}{2}\tilde{\tau}\right), \tag{2.17}$$

with $\tilde{\tau} \equiv \beta\hbar\widetilde{\omega} = \frac{1}{3}\sum_\alpha \tau_\alpha$ the arithmetic mean value of τ. With this fugacity definition, the density matrix operator is now given by

$$\hat{\rho}_{eq} \;=\; \sum_{\mathbf{m}} |\psi_{\mathbf{m}}\rangle\langle\psi_{\mathbf{m}}| \sum_{l=1}^{\infty} \mathrm{Z}^l \exp\left(\tfrac{3}{2} l\tilde{\tau}\right) \exp\left(-l\beta\epsilon_{\mathbf{m}}\right).$$

The temperature Green function with the zero point energy removed becomes

$$G^{ho}(\mathbf{r},\mathbf{r}';\tau) = \prod_{\alpha} \exp\left(\tau_\alpha/2\right) \sum_{m_\alpha} \psi^*_{m_\alpha}(r'_\alpha)\psi_{m_\alpha}(r_\alpha) \exp\left(-\beta\epsilon_{m_\alpha}\right) =$$

$$= \frac{1}{\left(\sqrt{\pi}\overline{\sigma}\right)^3} \prod_{\alpha} \sqrt{\frac{1}{1-e^{-2\tau_\alpha}}}\; \exp\left[-\left(\frac{r_\alpha + r'_\alpha}{2\sigma_\alpha}\right)^2 \mathrm{th}\left(\frac{\tau_\alpha}{2}\right) - \left(\frac{r_\alpha - r'_\alpha}{2\sigma_\alpha}\right)^2 \mathrm{cth}\left(\frac{\tau_\alpha}{2}\right)\right] \tag{2.18}$$

and the particle density becomes

$$n(\mathbf{r}) = \sum_{l=1}^{\infty} Z^l G^{ho}(\mathbf{r},\mathbf{r};l\tau). \tag{2.19}$$

Note that in the limit when $T \to 0$, or $\tau \to \infty$, last expression reduces to

$$n_0(\mathbf{r}) = \frac{Z}{1-Z}|\psi_0(\mathbf{r})|^2, \tag{2.20}$$

i.e., the ground state density.

Rearranging terms in Eq.2.19 to put in evidence λ_T^{-3}, we get for the particles density,

$$n(\mathbf{r}) = \frac{1}{\lambda_T^3} \sum_{l=1}^{\infty} \mathrm{Z}^l \prod_{\alpha} \mathrm{F}_l(\tau_\alpha) \exp\left[-\frac{r_\alpha^2}{2s_\alpha^2} \frac{\mathrm{th}(l\tau_\alpha/2)}{\tau_\alpha/2} \right], \tag{2.21}$$

where we have defined

$$\mathrm{F}_l(\tau_\alpha) = \sqrt{\frac{2\tau_\alpha}{1 - e^{-2l\tau_\alpha}}}. \tag{2.22}$$

The expression in Eq.2.21 can be significatively simplified in the limit of high temperature for which $\tau_\alpha \ll 1$. As before, we can expand the expression in series on τ_α. If we keep only the first order terms, $\mathrm{F}_l(\tau_\alpha)$ simplifies to $l^{-1/2}$ and, the argument in the exponential, to $-\frac{1}{2} l\alpha^2/s_\alpha^2 = -l\beta V(r_\alpha)$. Making these simplification we arrive at the expression

$$\begin{aligned} n(\mathbf{r}) &= \frac{1}{\lambda_T^3} g_{3/2} \left(Z \prod_{\alpha} \exp\left[-\frac{r_\alpha^2}{2s_\alpha^2} \right] \right) \\ &= \frac{1}{\lambda_T^3} g_{3/2}\big(Z \exp\left[-\beta V(\mathbf{r}) \right] \big) \end{aligned} \tag{2.23}$$

where $g_{3/2}(x)$ is the polylogarithmic function [3] of order 3/2, defined for an arbitrary order u as

$$g_u(x) = \sum_{l=1}^{\infty} \frac{x^l}{l^u}. \tag{2.24}$$

The approximation that leads to the expression in Eq.2.23 for the density is known as the *semi-classical approximation* (*SCA*) and is widely used for getting simple analytical expressions for the density. This approximation is very good in the *thermodynamical limit*, where the number of particles $N \to \infty$ while $N\omega^3$ tends to a given constant. This also fulfills the condition $\tau \to \infty$. We emphasize, however, that the expression on Eq.2.23, contrarily to the one in Eq.2.19, does not include the ground state contribution, since now, in the limit when $T \to 0$, the thermal cloud density is $n(\mathbf{r}) = 0$. We will discuss the validity of the *SCA* in the following paragraphs.

2.1.1.1 The *critical temperature.*

We calculate now the total number of atoms, N. It is obtained integrating Eq.2.21,

$$N = \int_{R^3} d^3\mathbf{r}\; n(\mathbf{r}) = \sum_{l=1}^{\infty} Z^l \frac{1}{\prod_\alpha \left(1 - e^{-l\tau_\alpha}\right)}. \tag{2.25}$$

[3] These type of functions are also known, among physicists, as the *Bose functions*.

Using now the *SCA*, replacing the exponential and the hyperbolic sine by the respective arguments, we get

$$N \simeq \frac{1}{\overline{\tau}^3}\, g_3(Z), \tag{2.26}$$

with $\overline{\tau}$ defined above in Eq.2.15. We could also get this result, integrating Eq.2.23.

The usual criteria for defining the critical temperature, T_c, at which the phase transition takes place and the BEC starts to grow, is when the saturated excited states population is equal to the total number of atoms[3], *i.e.*

$$\sum_{\mathbf{m}\neq\mathbf{0}} N_{\mathbf{m}}(Z=1,T_c) = N. \tag{2.27}$$

Within the *SCA*, the ground state population is neglected, $N_{\mathbf{0}} \approx 0$, and the critical temperature is

$$T_c^0 = \frac{\hbar\overline{\omega}}{k_B}\left(\frac{N}{\zeta(3)}\right)^{1/3}. \tag{2.28}$$

If the temperature decreases from T_c^0, the total excited state population will also decrease according to $N_{th} = \zeta(3)/\overline{\tau}^3$. If the total number of atoms N, is fixed, a condensed population of $N_0 = N - N_{th}$ atoms will accumulate in the ground state. The fraction of these condensed atoms is then given by

$$\frac{N_0}{N} = 1 - \left(\frac{T}{T_c^0}\right)^3. \tag{2.29}$$

Finite Size Effect.

The previous expressions for the critical temperature and the fraction of condensed atoms were obtained in the semi-classical approximation, which considers only the lowest order terms τ in the series expansion of the right hand side of Eq.2.25. A better approximation can be obtained if higher orders terms are included. Since the lowest order in the denominator is already proportional to l^3 we can simply expand the exponential in the numerator of that expression up to terms linear in $\tilde{\tau}$, $\exp\left(\frac{3}{2}l\tilde{\tau}\right) \simeq 1 + \frac{3}{2}l\tilde{\tau}$, to get the lowest order correction to Eq.2.26,

$$N \simeq \frac{1}{\overline{\tau}^3}\left[g_3(Z) + \tfrac{3}{2}\tilde{\tau}\, g_2(Z)\right]. \tag{2.30}$$

The correction for the number of atoms in the thermal cloud included in Eq.2.30 has a counterpart in the critical temperature: it will also change in

relation to the lowest order approximation of Eq.2.28. Taking $\delta T_c = T_c - T_c^0$ as the small temperature correction, with T_c^0 given by Eq.2.28 and keeping only the lowest order term in N we get

$$\frac{\delta T_c}{T_c^0} = -\frac{\widetilde{\omega}\zeta(2)}{2\overline{\omega}\zeta(3)^{2/3}} N^{-1/3}. \tag{2.31}$$

The fraction of condensed atoms will also change. The propagation of a small variation δT in the temperature of the condensed fraction of Eq.2.29 is given by $\delta\left\{\frac{N_0}{N}\right\} = 3\left(\frac{T}{T_c^0}\right)^2 \frac{1}{T_c^0}\,\delta T$. With δT given by Eq.2.31, we get

$$\frac{N_0}{N} = 1 - \left(\frac{T}{T_c^0}\right)^3 - \frac{3}{2}\frac{\widetilde{\omega}}{\overline{\omega}}\frac{\zeta(2)}{\zeta(3)^{2/3}} N^{-1/3}\left(\frac{T}{T_c^0}\right)^2. \tag{2.32}$$

The above expressions for the first order correction to the fraction of condensed atoms and to the critical temperature are generally refereed as *finite size effect*. It is negligible for large clouds where the factor $N^{-1/3}$ goes to zero. It also depends on the anisotropy of the trap through the factor $\widetilde{\omega}/\overline{\omega} = (2+\lambda)/3\lambda^{1/3}$, with $\lambda = \omega_z/\omega_\perp$. For $\lambda > 1$ the trap is disk-shaped while for $\lambda < 1$, like the one in our experiment, it is cigar-shaped. In both cases, $\widetilde{\omega}/\overline{\omega}$ always increases for values of $\lambda \neq 1$, since its minimum is at $\lambda = 1$. The limiting cases are for $\lambda \gg 1$, $\widetilde{\omega}/\overline{\omega} \simeq \lambda^{2/3}/3$ and for $\lambda \ll 1$, $\widetilde{\omega}/\overline{\omega} \simeq \frac{2}{3}\lambda^{-1/3}$. This finite size effect correction for our experimental setup is small: for a cloud with $N = 10^6$ atoms, the correction in the critical temperature will be of the order of 1%.

2.1.1.2 The finite size effect importance in the cloud density close to the critical transition point.

Despite being a good approximation when dealing with the total number of atoms, the *SCA* fails seriously to describe the density at the center of the trap and when the fugacity is near one. In fact, in the sum of Eq.2.21, if both the fugacity and the Gaussian terms are near or equal to one, those terms will decrease slowly with l and the terms contributing to the sum are not limited to the small values of l. In this case, the first order expansion of $\mathrm{F}_l(\tau_\alpha)$ is very poor since, even for very small values of τ_α, l can grow to very large values making large as well the argument of the exponential in the denominator of $\mathrm{F}_l(\tau_\alpha)$. It is convenient to emphasize, however, that the *SCA* presents no problem for the case of the hyperbolic tangent in the argument of the Gaussian. This is so because in this term only small l's will contribute significatively to the decaying exponential. Likewise, if we define

$$[W(\mathbf{r})]^l = \mathrm{Z}^l \prod_\alpha \exp\left[-\frac{r_\alpha^2}{2s_\alpha^2}\frac{\mathrm{th}\left(\frac{1}{2}l\tau_\alpha\right)}{\frac{1}{2}\tau_\alpha}\right], \tag{2.33}$$

it is reasonable to approximate this factor to

$$W(\mathbf{r}) \approx W_\infty = Z \prod_\alpha \exp\left(-\frac{r_\alpha^2}{2s_\alpha^2}\right). \tag{2.34}$$

The density becomes

$$n(\mathbf{r}) = \lambda_T^{-3} \sum_{l=1}^{\infty} W_\infty^l \prod_\alpha \mathrm{F}_l(\tau_\alpha). \tag{2.35}$$

If we expand $\mathrm{F}_l(\tau_\alpha)$ in a power series in l but now retaining a few more terms beyond the first one

$$\mathrm{F}_l(\tau_\alpha) = l^{-1/2} + \tfrac{1}{2} l^{1/2} \tau_\alpha + \tfrac{1}{24} l^{3/2} {\tau_\alpha}^2 + O\left(l^{7/2} {\tau_\alpha}^3\right) \tag{2.36}$$

we get

$$\prod_\alpha \mathrm{F}_l(\tau_\alpha) = l^{-3/2} + \tfrac{3}{2} l^{-1/2} \tilde{\tau} + \mathcal{R}_l \tag{2.37}$$

where $\mathcal{R}_l \equiv O(l^{1/2})$ stands for the remainder of the series. The sum over l of this remainder term, as well as the one for the $\mathrm{F}_l(\tau_\alpha)$ term itself, converges only if multiplied by W_∞^l. For the moment we continue by neglecting $\mathcal{R}_l$. We will discuss later the question of how appropriate this approximation is, depending on the physical situation. If we keep only the two first terms of Eq.(2.37) we account for the finite size effects. The density is then approximately given by

$$\begin{aligned} n(\mathbf{r}) &\simeq \lambda_T^{-3} \sum_{l=1}^{\infty} W_\infty^l \left(l^{-3/2} + \tfrac{3}{2} l^{-1/2} \tilde{\tau}\right) = \lambda_T^{-3} \left[g_{3/2}(W_\infty) + \tfrac{3}{2} \tilde{\tau} g_{1/2}(W_\infty)\right] \\ &= \lambda_T^{-3} \left\{ g_{3/2}\Big(Z \exp\left[-\beta V(\mathbf{r})\right]\Big) + \tfrac{3}{2} \tilde{\tau}\ g_{1/2}\Big(Z \exp\left[-\beta V(\mathbf{r})\right]\Big) \right\}. \end{aligned} \tag{2.38}$$

Note that, as expected, if we integrate this expression over real space, we recover the expression in Eq.2.30 for the total number of atoms. Remember now, that in Eq.2.30 we had to truncated the expansion to the term $g_2(Z)$ to avoid the divergence at $Z = 1$. In the above expression we have limited the series expansion in a similar way. Nonetheless, if we used it for calculating the density peak, *i.e.* the density at the center of the cloud, we get again a divergence. The peak density is

$$n(\mathbf{0}) \simeq \lambda_T^{-3} \left[g_{3/2}(Z) + \tfrac{3}{2} \tilde{\tau}\ g_{1/2}(Z)\right],$$

and for $Z = 1$, we find that the phase space density at the center of the trap, $\lambda_T^3 n(\mathbf{0})$, is infinite, since $g_{1/2}(1) = \infty$. The *SCA* model with the *finite size*

effects correction, thus leads to an incorrect description of the cloud's particle density. The fact it works well when used for computing the cloud's number of atoms N, is explained because the spatial integration were done before performing the approximations and evaluating the sum in l (cf. Eq.2.25). This procedure avoided the anomalous *peak density divergence*.

The ground state contribution.
The approximation that leads to Eq.2.34, *i.e.* making $\mathrm{th}\left(\frac{1}{2}l\tau_\alpha\right) \approx \frac{1}{2}l\tau_\alpha$, neglects the ground state contribution. Note that as $l \gg {\tau_\alpha}^{-1}$, the hyperbolic tangent has only a weak dependence in l and *saturates* at one. In this limiting case, the exponential in Eq.2.33 tends thus to $\exp\left(-\frac{r_\alpha^2}{2S_\alpha^2}\right)$ whereas within the referred approximation it goes to zero. Replacing also $\mathrm{F}_l(\tau_\alpha)$ by its asymptotic limit $\sqrt{2\tau_\alpha}$, the neglected quantity amounts to [4]

$$n_0(\mathbf{r}) = \frac{Z}{1-Z}\frac{\prod_\alpha e^{-r_\alpha^2/\sigma_\alpha^2}}{(\sqrt{\pi}\overline{\sigma})^3}, \tag{2.39}$$

which is the ground state contribution, written before in Eq.2.20.

2.1.2 The critical atomic peak density.

The problem found on the previous paragraph could be avoided if we limit the fugacity to values strictly smaller than one. This is moreover always the case. As referred before, the *SCA* doesn't take into account the ground state contribution. We can cure this defect by including explicitly the ground state density in Eq.2.38,

$$n(\mathbf{r}) \simeq \lambda_T^{-3}\left\{g_{3/2}[W_T(\mathbf{r})] + \tfrac{3}{2}\tilde{\tau}\, g_{1/2}[W_T(\mathbf{r})]\right\} + n_0(\mathbf{r}) \tag{2.40}$$

and, for the corresponding total number of atoms

$$N = \overline{\tau}^{\,-3}\left[g_3(Z) + \tfrac{3}{2}\tilde{\tau}\, g_2(Z)\right] + \frac{Z}{1-Z}. \tag{2.41}$$

Because N is finite, we must necessarily have $Z < 1$. Here we should keep the *standard* criteria for the critical temperature T_c given in Eq.2.27, *i.e.* the temperature at which the saturated excited states population equals the total number of atoms. However, the inclusion of the ground state population forces the critical fugacity Z_c to be slightly smaller than one. We can estimate this *new* critical fugacity.

We will first examine the situation where $\tau_\alpha \ll 1$. This corresponds to a large number of atoms (the *high-N* limit) and we may disregard the finite

[4] To be strict, the factor $Z/(1-Z)$ in this expression should rather be $\sum_{l=L}^{\infty} Z^l = Z^L/(1-Z)$ with $L \approx 2\tau_{\|}^{-1}$ where $\tau_{\|}$ is the smallest of the τ's.

size term proportional to $\tilde{\tau}$ [5]. Since Z_c is very close to one, if we express it as $Z = e^{-x_c}$, the Bose function can be expanded around $x_c = 0$ like

$$g_3(Z_c) \simeq \zeta(3) - \zeta(2)x_c. \tag{2.42}$$

Similarly, the critical ground state population is approximated to[88]

$$\frac{Z_c}{1-Z_c} \simeq \frac{1}{x_c} = \overline{\tau}^{\,-3/2}\sqrt{\zeta(2)}, \tag{2.43}$$

where we used the approximation $N \simeq \overline{\tau}^{\,-3}\zeta(3)$. The critical fugacity is then modified to

$$Z_c \simeq 1 - \overline{\tau}^{\,3/2}\zeta(2)^{-1/2}. \tag{2.44}$$

This correction, from an experimental point of view is negligible since it is very small, far below the accuracy of the experimental measurements. In our experiment $\overline{\tau}^{\,3/2}\zeta(2)^{-1/2} \sim 2 \times 10^{-4}$ and, as we will show in Chapter 4, the uncertainty in the measure of the fugacity is 5%.

Despite its negligible experimental impact, this correction does change the degeneracy parameter at the critical transition. In the *high-N* limit for a harmonic trap the criteria for the critical transition is

$$\lambda_T^3 n(0)\Big|_{T=T_c} = \zeta(3/2) \approx 2.61 \ .$$

If we substitute Eq.2.43 in Eq.2.40 we find that this criteria should be modified to

$$\lambda_T^3 n(0)\Big|_{T=T_c} = \zeta(3/2) + 2\sqrt{2\zeta(2)} \approx 6.24 \ .$$

This result means that the ground state density at the center of the cloud, neglected in the *standard* criteria, is even larger than the density of the excited states. Again, the experimental verification of this local value for the density peak in a non degenerate cloud is very hard to achieve. The *TOF* signals involves always, at least, one spatial integration over the cloud's density profile. As we will see in the following Section, this spatial integration washes out this contribution of the ground state density. This is further accentuated in our experiment where, for the moment, the experimentally accessible *TOF* results from a two-dimensional spatial integration over the `MCP` surface (cf. §1.3).

Finite size effects will change the previous expressions somehow. The actual derivation of these expression is more cumbersome as it involves the

[5] Note that in the thermodynamical limit, *i.e.* when $N \to \infty$ with $N\overline{\omega}^3 \to$ *constant*, the condensate density is infinite, since as $\sigma_\alpha = \sqrt{\frac{\hbar}{M\omega_{0\alpha}}}$, $n_0 \sim N\overline{\omega}^{3/2} \to \infty$. Therefore, it is preferable to take a limit where N is kept finite.

derivative of the $g_2(Z)$ function at $Z = exp(-x_c)$ and we have opted for a numerical study of its influence[81]. Figure2.1 presents two examples for clouds with 10^6 and 10^3 atoms, confined in an isotropic harmonic oscillator. The graphs in this Figure represents the evolution of the condensate fraction N_0/N and condensate peak density fraction in function of the temperature. What prevails in those graphs is the sharp increase of the condensate peak density compared to the condensate population. In this respect, the peak density is a much better marker of the Bose-Einstein condensation than the atom number. This feature is in fact used experimentally: the appearance of a small peak over a broad distribution is the usual criterion to distinguish clouds above or below the transition temperature. We have compared the

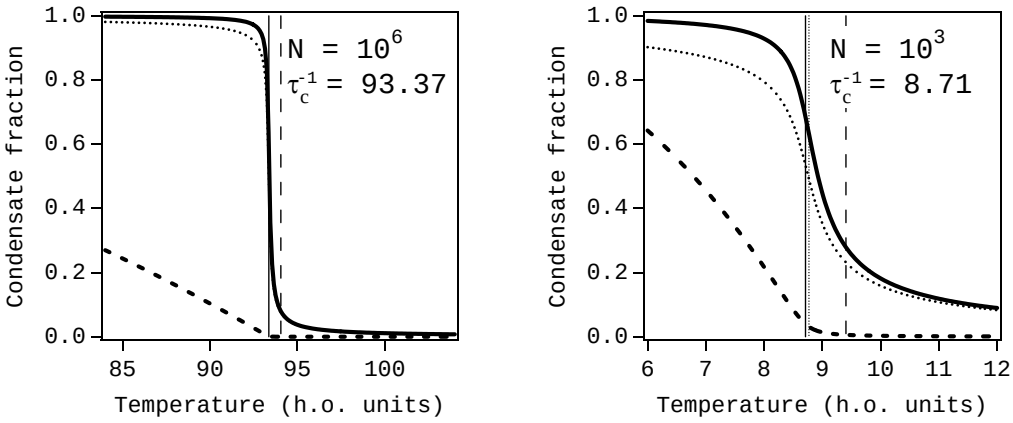

Figure 2.1: Condensate atom number fraction N_0/N (dash line) and peak density fraction $n_0(0)/n(0)$ (solid line) in function of the temperature in harmonic oscillator unit $\hbar\omega/k_B$ for clouds with 10^6 and 10^3 atoms confined in an isotropic potential. The corresponding transition temperatures are $T_c = 93.37\hbar\omega/k_B$ and $T_c = 8.71\hbar\omega/k_B$ respectively and are marked in the graph by a solid vertical lines. T_c^0, given by the *SCA* expression of Eq.2.28 gives critical values of respectively $T_c^0 = 94.04\hbar\omega/k_B$ and $T_c = 9.40\hbar\omega/k_B$, represented in the graphs by the vertical dashed lines. Also, the doted vertical line in the right hand side graph represents the critical temperature if *finite size effects* are taken into account ($T_c^{fs} = 8.77\hbar\omega/k_B$). For the $N = 10^6$ case, this value is almost indistinguishable from T_c, but is slightly different for $n_0(0)/n(0)$ (dotted lines in both graphs). The corresponding effect in N_0/N is very small for both cases. In both graphs, the ground-state peak density increases much more sharply than the ground-state population around the transition temperature. The peak density has also a significant value above T_c.

degenerecency parameter computed with the approximated density expressions in Eq.2.38 and Eq.2.40, and with the exact one in Eq.2.21, for different number of atoms. These results are compiled in the Ref.[81], which is also

presented in AppendixE.

2.1.3 The *finite size SCA* for spatially integrated density expressions.

The discussion above has shown that the expression for the density in Eq.2.38 should be corrected by including the ground state contribution. As we have referred, this correction is experimentally important only if one has access to *local* density measurements, what is not the case in any of the existing experiments. We hope, however, to achieve performing such a three-dimensional density measurement in the near future using the position sensitive detector (see §3.5.2.1 for details) we have recently installed in our setup.

For the calculation of the number of atoms, the integration over the three dimensions is done without mathematical difficulties for the simple *SCA* model. We emphasized that the ground state volume, $\propto \overline{\sigma}^3$, is very small when compared with the cloud's volume, $\propto \overline{s}^3 = (v_T/\overline{\omega})^3$: they scale as $(\overline{\sigma}/\overline{s})^3 = \overline{\tau}^3 \ll 1$. We can expect then that even a single integration will wash out the effects of neglecting the ground state contribution. Finally, another reason that makes us not consider this correction is because, for the moment, we don't know how to deal simultaneously with both this effect and the interatomic interactions. In a density integrated detection these latter leads, in fact, to a measurable correction.

We will proceed now by estimating an upper bound of the error for the expression obtained for the density in Eq.2.38. To reach the *SCA* density expression we have expanded $\prod_\alpha \mathrm{F}_l(\tau_\alpha)$ in series [cf. Eq.2.37]) and neglected the remainder

$$\mathcal{R}_l = \prod_\alpha \left(\frac{2\tau_\alpha}{1-e^{-2l\tau_\alpha}} \right)^{1/2} - \frac{1}{l^{3/2}} - \frac{3\tilde{\tau}}{2}\frac{1}{l^{1/2}}.$$

This quantity, when l goes to infinity, will asymptotically approach the value

$$\mathcal{R}_\infty = \lim_{l\to\infty} \mathcal{R}_l = (2\overline{\tau})^{3/2}.$$

Furthermore it can be shown that for all finite values of $l \geq 1$, $\mathcal{R}_l < \mathcal{R}_\infty$. Now, defining

$$G^{\mathcal{R}_\infty}(\mathbf{r},\mathbf{r};l\beta) = \lambda_T^3 \mathcal{R}_\infty \prod_\alpha \exp\left[-\tfrac{1}{2}\left(\tfrac{\alpha}{2S_\alpha}\right)^2 \tfrac{\mathrm{th}(l\tau_\alpha/2)}{\tau_\alpha/2} \right],$$

which is $G^{ho}(\mathbf{r},\mathbf{r};l\beta)$ with the replacement of $\mathrm{F}_l(\tau_\alpha)$ by $\mathcal{R}_\infty$, one can obtain un upper bound on the possible error of the estimated density,

$$\delta n(\mathbf{r}) < \lambda_T^3 \sum_{l=1}^{\infty} Z^l G^{ho}_{\mathcal{R}_\infty}(\mathbf{r},\mathbf{r};l\beta) = (\pi\overline{\sigma})^{-3/2} \sum_{l=1}^{\infty} W_T^l, \tag{2.45}$$

The relative error for the density is

$$\frac{\delta n(\mathbf{r})}{n(\mathbf{r})} < \pi^{-3/2}\left(\frac{\lambda_T}{\pi\sigma_0}\right)^3 \frac{W_\infty(1-W_\infty)^{-1}}{g_{3/2}(W_\infty)+\frac{3}{2}\tilde{\tau}g_{1/2}(W_\infty)}. \tag{2.46}$$

Again we see that the approximation fails if $W_\infty \to 1$ (in the peak density at the critical transition) [6].

The approximation works much better for the volume integrated expression. Here, one obtains for the relative error on the number of atoms N,

$$\frac{\delta N}{N} < \left(\frac{\overline{\tau}}{\pi}\right)^{3/2} \frac{g_{3/2}(Z)}{g_3(Z)+\frac{3}{2}\tilde{\tau}g_2(Z)},$$

where, as before, δN is the difference in number of atoms induced by the *improved SCA*. The relative error is as small as $\overline{\tau}^{3/2}$. In our experiment this is equal to 0.3%. It is interesting to derive as well the expressions integrated in one- and two-dimensions, since these are actually the experimentally measured quantities: the first in typical *CCD*-based detection systems and, the second, our case with the *MCP*. It is simple to show that they are proportional to $\tau_x^{1/2}$ and $(\tau_x\tau_y)^{1/2}$, respectively, with the subscripts denoting the integrated dimensions. Our experiment has $(\tau_x\tau_y)^{1/2} \simeq 1\%$.

An important conclusion of the preceding paragraph is that for experimental proposes, as fitting data, the *SCA* is sufficient. The density or correlation functions expressions derived within this approximation can be expressed through the use of polylogarithmic(*Bose*) functions. The use of these functions simplifies the writing of the expressions and, frequently, their analytical manipulation.

2.1.4 The momentum distribution.

We can also compute the momentum distribution function of the cloud. This result will be important for interpreting the expansion of the cloud when it is released from the trap in §2.2.2. It is given by

$$\tilde{n}(\mathbf{p}) = \langle \mathbf{p}|\hat{\rho}|\mathbf{p}\rangle.$$

which can be evaluated at the thermal equilibrium in terms of the *temperature Green function*

$$\begin{aligned}\tilde{n}(\mathbf{p}) &= \int_{R^3} d\mathbf{r}\int_{R^3} d\mathbf{r}'\langle \mathbf{p}|\mathbf{r}\rangle\langle \mathbf{r}|\hat{\rho}|\mathbf{r}'\rangle\langle \mathbf{r}'|\mathbf{p}\rangle \\ &= \sum_{l=1}^{\infty} Z^l \int_{R^3} d\mathbf{r}\int_{R^3} d\mathbf{r}' \frac{e^{-i\mathbf{p}(\mathbf{r}-\mathbf{r}')/\hbar}}{(2\pi\hbar)^3} G^{ho}(\mathbf{r},\mathbf{r}';l\tau).\end{aligned} \tag{2.47}$$

[6] Note that when $W_\infty \to 1$, $(1-W_\infty)^{-1} \to \infty$ but also $g_{1/2}(W_\infty) \to \infty$. However, the divergence of the $g_{1/2}(x)$ at $x=1$ behaves like $(-\sqrt{-\ln(x)}) \sim (1-x)^{-1/2}$, which is a weaker divergence than $(1-x)^{-1}$.

Using Eq.2.18 we arrive at

$$\tilde{n}(\mathbf{p}) = (2\pi)^{-3/2} \frac{1}{\overline{\tau}^3} \frac{1}{p_T^3} \sum_{l=1}^{\infty} Z^l \prod_{\alpha} \mathrm{F}_l(\tau_\alpha) \ \exp\left[-\frac{1}{2} \frac{p_\alpha^2}{p_T^2} \frac{\mathrm{th}\left(\frac{1}{2} l \tau_\alpha\right)}{\frac{1}{2}\tau_\alpha} \right], \qquad (2.48)$$

where p_T is the momentum distribution width $p_T = M v_T = \sqrt{M k_B T}$. This is an isotropic quantity related to the thermal *de Broglie* wave length through

$$p_T \lambda_T = \sqrt{2\pi}\hbar. \qquad (2.49)$$

From Eq.2.48 we see that the momentum distribution is not, in general, isotropic. In the *SCA* however, with $\tau_\alpha \ll 1$, the expression simplifies to

$$\tilde{n}(\mathbf{p}) = (2\pi)^{-3/2} \frac{1}{\overline{\tau}^3} \frac{1}{p_T^3} g_{3/2}\left(Z \exp\left[-\frac{p_\alpha^2}{2p_T^2} \right] \right), \qquad (2.50)$$

which is, now, an isotropic distribution. The Boltzmann limit is given simply by

$$\tilde{n}^{\infty}(\mathbf{p}) = (2\pi)^{-3/2} \frac{1}{\overline{\tau}^3} \frac{Z}{p_T^3} \exp\left[-\frac{p_\alpha^2}{2p_T^2} \right]. \qquad (2.51)$$

It is important to emphasize that $\tilde{n}(\mathbf{p})$ *is not* the Fourier transform of the particles density $n(\mathbf{r})$, as it should be if we were dealing with a pure state instead of a thermal ensemble. Actually, Eq.2.49 (a kind of *generalized thermal Heisenberg relation*), relates the width of the momentum distribution, not with the cloud size s_α, but rather with λ_T. This latter one is, as we will see in next Chapter, the appropriate *measure* of the particles correlation function within the cloud[84]. This dependence on the correlation of the particles location is already present on Eq.2.47, where the momentum density distribution is calculated through a *double Fourier transform* of the temperature Green function, which characterizes the particle correlation function at locations $\mathbf{r}$ and $\mathbf{r}'$.

2.2 Time of Flight: theoretical description.

In the previous section we have described the density of a cloud of non-interacting atoms in thermal equilibrium within a harmonic trap. Here we derive the expressions describing the atoms' *Time of Flight* signal (*TOF*), *i.e.* the atomic flux that results when the cloud is released from the trap and falls under the influence of the gravitational field.

As before, we will restrict the model to the case of the ideal non-interacting gas. This leads to the ballistic expansion of the cloud, a physical situation where it is possible to deduced exact and very intuitive expressions for the atomic flux. The formalism presented here will then be extended, in the next Chapter, for interpreting the results of an experiment where we measure the *intensity-intensity correlation* function of the falling cloud[84]. The *signal to noise* ratio of this experience makes this simple ballistic description good enough to deal with its data.

However, when analyzing *cloud density* through our two-dimensional integrated *TOF* signals, especially for thermometric proposes, the ideal gas approximation can be insufficient. At the early stages of the cloud expansion, it behaves more like a hydrodynamic fluid, what changes slightly the results predicted by the simple ballistic expansion. For the moment, we will disregard this effect, leaving for Chapter 4 the derivation of a hydrodynamical correcting factor.

2.2.1 Ballistic expansion of an ideal gas under the effect of a gravitational field.

We are interested in deriving analytical expressions for the experimentally observed signal of the atoms when they fall on the detector. This signal is in practice the number of atoms that hit the detector per second or, else, the atomic flux crossing the plane of the detector.

This atomic flux, in the ideal gas case, can be derived by computing the time evolution of the wave functions of each harmonic oscillator state separately and then by evaluating, after the fall, the overall contribution in the thermodynamical equilibrium. The time evolution of each wave function can be described through the use of the free fall Green function. We start with the definition of the quantum mechanical atomic flux.

2.2.1.1 Quantum mechanical flux.

In thermal equilibrium, the atomic cloud can be represented in second quantization through the atomic field operators

$$\left\{ \begin{array}{rcl} \hat{\Psi}^{\dagger}(\mathbf{r}) & = & \sum_{\mathbf{m}} \psi^{*}_{\mathbf{m}}(\mathbf{r}) \hat{a}^{\dagger}_{\mathbf{m}} \\ \hat{\Psi}(\mathbf{r}) & = & \sum_{\mathbf{m}} \psi_{\mathbf{m}}(\mathbf{r}) \hat{a}_{\mathbf{m}} \end{array} \right. \tag{2.52}$$

where the sum runs over all harmonic oscillator wave functions $\psi_{\mathbf{m}}(\mathbf{r})$ and the operators $\hat{a}^{\dagger}$ and $\hat{a}$ are the usual bosonic creation and annihilation operators, obeying the commutation relations $[\hat{a}^{\dagger}_{\mathbf{m}}, \hat{a}_{\mathbf{m}'}] = \delta_{\mathbf{m},\mathbf{m}'}$ and $[\hat{a}^{\dagger}_{\mathbf{m}}, \hat{a}^{\dagger}_{\mathbf{m}'}] = [\hat{a}_{\mathbf{m}}, \hat{a}_{\mathbf{m}'}] = 0$. The thermal occupation of the state $\mathbf{m}$ is given by (cf. Eq.2.5)

$$n_{\mathbf{m}} = \langle \hat{n}_{\mathbf{m}} \rangle = \langle \hat{a}^{\dagger}_{\mathbf{m}} \hat{a}_{\mathbf{m}} \rangle.$$

These expressions can be generalized for the time varying wave functions,

$$\left\{ \begin{array}{rcl} \hat{\Psi}^{\dagger}(\mathbf{r},t) & = & \sum_{\mathbf{m}} \psi^{*}_{\mathbf{m}}(\mathbf{r},t)\ \hat{a}^{\dagger}_{\mathbf{m}} \\ \hat{\Psi}(\mathbf{r},t) & = & \sum_{\mathbf{m}} \psi_{\mathbf{m}}(\mathbf{r},t)\ \hat{a}_{\mathbf{m}} \end{array} \right. , \tag{2.53}$$

In these latter expressions, the field operator $\hat{\Psi}(\mathbf{r},t)$ carries the spatiotemporal information of the evolution of the cloud after being released from the trap. The wave functions vary now with time but the statistical occupation of their corresponding h.o. levels is constant. In here, we assume that there is no scattering of particles between different quantum states, what is only true in the case treated here of non-interacting particles. The matter flux associated with the field operators given in Eqs.2.53, is

$$\begin{array}{rcl} \hat{I}(\mathbf{r},t) & = & \frac{\hbar}{M} \mathbf{Im} \left[\hat{\Psi}^{\dagger}(\mathbf{r},t) \partial_z \hat{\Psi}(\mathbf{r},t) \right] \\ & = & \frac{i\hbar}{2M} \left\{ [\partial_z \hat{\Psi}^{\dagger}(\mathbf{r},t)] \hat{\Psi}(\mathbf{r},t) - \hat{\Psi}^{\dagger}(\mathbf{r},t) \partial_z \hat{\Psi}(\mathbf{r},t) \right\}, \end{array} \tag{2.54}$$

where $\mathbf{Im}[x]$ gives the imaginary part of x and $\partial_z \hat{\Psi}$ the partial derivative of the field in respect to the spatial falling direction oz. The measured atomic flux is the thermal average of this operator, given by

$$\begin{array}{rcl} \left\langle \hat{I}(\mathbf{r},t) \right\rangle & = & \frac{i\hbar}{2M} \sum_{\mathbf{m},\mathbf{m}'} \left\{ [\partial_z \psi^{*}_{\mathbf{m}}(\mathbf{r},t)] \psi_{\mathbf{m}'}(\mathbf{r},t) - \psi^{*}_{\mathbf{m}}(\mathbf{r},t) \partial_z \psi_{\mathbf{m}'}(\mathbf{r},t) \right\} \langle \hat{a}^{\dagger}_{\mathbf{m}} \hat{a}_{\mathbf{m}'} \rangle \\ & = & \frac{i\hbar}{2M} \sum_{\mathbf{m}} \left\{ [\partial_z \psi_{\mathbf{m}}(\mathbf{r},t)]^{*} \psi_{\mathbf{m}}(\mathbf{r},t) - c.c. \right\} \langle \hat{n}_{\mathbf{m}} \rangle. \end{array} \tag{2.55}$$

To proceed with the calculation of the last expression we need first to derive explicitly the wave functions $\psi_{\mathbf{m}}(\mathbf{r},t)$ and theirs partial derivative $\partial_z \psi_{\mathbf{m}}(\mathbf{r},t)$.

2.2.1.2 Time evolution of a h.o. wave function in free fall

The free fall Green function

The free fall of a particle of mass M is described by the time independent Schrödinger equation,

$$\left[-\frac{\hbar^2}{2M}\frac{d^2}{dz^2} - Mgz\right]\varphi(z) = E\varphi(z) \tag{2.56}$$

where, as before, the fall is the $z-$ axis and the gravitational energy is $-Mgz$, with g the gravity's acceleration. Eq.2.56 is, formally, the Airy's equation

$$\frac{d^2}{d\zeta^2}\varphi_E(\zeta) + \zeta_E\varphi_E(\zeta) = 0 \quad \text{with} \quad \zeta_E = \left[z + \frac{E}{Mg}\right]\left(\frac{2M^2g}{\hbar^2}\right)^{1/3}. \tag{2.57}$$

The physically relevant solution[89] of this equation is the normalized Airy function of the first kind $Ai(-\zeta)$ [7], which has the integral representation

$$Ai(-\zeta) = \frac{1}{\sqrt{\pi}}\int_{-\infty}^{+\infty}\exp\left[i\frac{u^3}{3} - i\zeta u\right]du. \tag{2.58}$$

Knowing the solution of Eq.2.56, it is now possible to write down the corresponding Green function

$$K(z,t;z_0) = \int_{-\infty}^{+\infty}\varphi_E^*(z_0)\varphi_E(z)\exp(-iEt/\hbar)\,dE. \tag{2.59}$$

which propagates an initially steady state wave function $\varphi(z)$ in time according to the time dependent Schrödinger equation for the Hamiltonian in the left hand side of Eq.2.56. This Green function is

$$K(\mathbf{r},t;\mathbf{r}_0) = \left(\frac{M}{2\pi i\hbar t}\right)^{3/2}\exp\left\{\frac{iM}{2\hbar t}\left[(\mathbf{r}-\mathbf{r}_0)^2 + 2(z+z_0)\eta(t) - \tfrac{1}{3}\eta^2(t)\right]\right\} \tag{2.60}$$

where $\eta(t) = \frac{1}{2}gt^2$ is the distance covered in a fall of an atom, initially at rest, during the time interval t. The detector is placed at a fixed height, H, from the center of the trap and $\eta(t_0) = H$ defines the *classical* time of flight $t_0 = \sqrt{2H/g}$.

The expanding h.o. wave functions.

Here, we are interested in the time evolution of the particles that are initially confined inside the harmonic trap, described by the steady state h.o. wave

[7] There is one other solution for this equation, the Airy function $Bi(-\zeta)$. This solution, however, has no physical meaning since it diverges in the non-classical region.

functions $\psi^{ho}_{\mathbf{m}}(\mathbf{r}_0)$. The z dependence for the time evolving wave function $\psi(\mathbf{r},t)$ is given by

$$\psi_{\mathbf{m}}(z,t) = \int_{-\infty}^{+\infty} d\mathbf{r}_0 \; K(z,t;z_0) \; \psi_{\mathbf{m}}(\mathbf{r}_0). \tag{2.61}$$

The generalization for the three-dimensional wave function is straightforward since this latter one is space separable, $\psi_{\mathbf{m}}(\mathbf{r},t) = \prod_\alpha \psi_{\mathbf{m}}(\alpha,t)$. The transversal components of the $\psi_{\mathbf{m}}(\mathbf{r},t)$ are those of a free particle. The Green function in this case is found through Eq.2.59 with $\varphi_E(x) \propto \exp(ikx)$, plane waves with momentum $k = \sqrt{2ME}/\hbar$.

Substituting Eqs.2.3 and 2.60 into Eq.2.61, we find [8]

$$\begin{aligned} \psi_{\mathbf{m}}(\mathbf{r},t) &= \int_{R^3} d\mathbf{r}_0 \; K(\mathbf{r},t;\mathbf{r}_0) \; \psi_{\mathbf{m}}(\mathbf{r}_0) \\ &= \prod_\alpha i^{m_\alpha} \frac{\exp\left[i(m_\alpha \delta_\alpha + \phi_\alpha)\right]}{\sqrt{\omega_\alpha t - i}} \; \psi_{m_\alpha}(\tilde{r}_\alpha) \end{aligned} \tag{2.62}$$

with $\delta_\alpha = \tan^{-1}(1/\omega_\alpha t)$, $\tilde{r}_\alpha$ re-scaled coordinates defined as

$$\tilde{x} = \frac{x}{\sqrt{1+\omega_x^2 t^2}} \;, \quad \tilde{y} = \frac{y}{\sqrt{1+\omega_y^2 t^2}} \quad \text{and} \quad \tilde{z} = \frac{H-\eta(t)}{\sqrt{1+\omega_z^2 t^2}} \tag{2.63}$$

and $\phi_\alpha \equiv \phi_\alpha(t)$ a global phase that depends on α and t but not in the index m_α. In the falling direction (Oz axis), it is given by

$$\phi_z(t) = \frac{M}{2\hbar t}\left\{[H^2 - \tilde{z}^2] + \eta(t)\left[2H - \tfrac{1}{3}\eta(t)\right]\right\} - \pi/4. \tag{2.64}$$

In the other directions of space, last expression is still valid with $\eta(t) = 0$ and replacing H by either x or y and respectively $\tilde{z}$ by $\tilde{x}$ or $\tilde{y}$. We will see in the following of this section and in Chapter 3, that this phase will disappear if we are interested in the calculation of the atomic flux or in the intensity-intensity correlation function. However, it gives rise to fringes in the first order correlation function.

The atomic flux.

Using the identity $\partial_z H_n(z) = 2nH_{n-1}$, the partial spatial derivative of the

[8] In here, a useful integral result can be found in Ref.[90](7.374-8),

$$\int_{-\infty}^{+\infty} e^{-(x-y)^2} H_n(\alpha x) dx = \sqrt{\pi}(1-\alpha^2)^{n/2} H_n\left[\frac{\alpha y}{\sqrt{1-\alpha^2}}\right]$$

wave function can now be carried out

$$\begin{aligned}\partial_z\psi_{\mathbf{m}}(\mathbf{r},t) &= \\ &= \frac{M}{\hbar}\left\{[-v_1+iv_2]\psi_{m_z}(z,t) - i\,v_3\,e^{i\delta_z}\sqrt{m_z}\,\psi_{m_z-1}(z,t)\right\}\psi_{m_x}(x,t)\psi_{m_y}(y,t),\end{aligned} \tag{2.65}$$

where the *velocities* v_1, v_2 and v_3 are given by

$$\begin{aligned} v_1 = \omega_z\frac{H-\eta(t)}{1+\omega_z^2t^2}\ , \quad v_2 = \frac{1}{t}\left[H+\eta(t)-\frac{H-\eta(t)}{1+\omega_z^2t^2}\right] \\ \text{and } v_3 = \frac{\sqrt{2}\omega_z\sigma_z}{\sqrt{1+\omega_z^2t^2}}.\end{aligned} \tag{2.66}$$

Substituting this expression in Eq.2.55, we see that the term depending on v_1 disappears when subtracted to its complex conjugate. We have then, for the atom's flux,

$$\begin{aligned}\langle\hat{I}(\mathbf{r},t)\rangle &= \\ &= \sum_{\mathbf{m}}\left[v_2|\psi_{\mathbf{m}}|^2 - \frac{\sqrt{m_z}}{2}(\overline{v_3}\psi^*_{m_z}\psi_{m_z-1} + \overline{v_3}^*\psi^*_{m_z-1}\psi_{m_z})|\psi_{m_x}\psi_{m_y}|^2\right]\langle\hat{n}_{\mathbf{m}}\rangle,\end{aligned} \tag{2.67}$$

where, we have used the short hand $\psi_{m_\alpha} \equiv \psi_{m_\alpha}(\mathbf{r},t)$. Also for simplicity, and latter convenience, we have defined the *complex velocity*

$$\overline{v_3} = v_3 e^{i\delta_z}.$$

Note however that (cf.Eq.2.62),

$$\overline{v_3}\psi^*_{m_z}\psi_{m_z-1} = -\overline{v_3}^*\psi^*_{m_z-1}\psi_{m_z} = i\frac{v_3}{\sqrt{1+\omega_z^2t^2}}\psi^{ho}_{\mathbf{m}}(\tilde{z})\psi^{ho}_{\mathbf{m}}(\tilde{z})$$

where $\psi^{ho}_{\mathbf{m}}$, the h.o. wave functions, are real functions. Thus, the second term in the sum of the right hand side in Eq.2.67 cancels out. This expression is finally given by

$$\begin{aligned}\langle\hat{I}(\mathbf{r},t)\rangle &= v_2\sum_{\mathbf{m}}|\psi_{\mathbf{m}}|^2\langle\hat{n}_{\mathbf{m}}\rangle \\ &= \frac{v_2}{\prod_\alpha(1+\omega_\alpha^2t^2)^{1/2}}\sum_{\mathbf{m}}|\psi_{\mathbf{m}}(\tilde{\mathbf{r}})|^2\langle\hat{n}_{\mathbf{m}}\rangle\end{aligned}$$

or, simply

$$\langle\hat{I}(\mathbf{r},t)\rangle = \frac{v_2}{\prod_\alpha(1+\omega_\alpha^2t^2)^{1/2}}\ n(\tilde{\mathbf{r}}), \tag{2.68}$$

with $n(\tilde{\mathbf{r}})$ the cloud's density in thermal equilibrium, but with the re-scaled coordinates given by Eqs.2.63.

The above derivation of the atomic flux used no approximations. It has conduced to the very simple result of Eq.2.68. This expression has a very simple interpretation: during the expansion and fall, the atomic cloud maintains its original density distribution with just a re-scale of its coordinates. The atomic flux is proportional to a certain velocity v_2 and, due to the expansion, to the pre-factor $\prod_\alpha (1+\omega_\alpha^2 t^2)^{-1/2}$ that accounts fir the decrease in the cloud's density consistently with the coordinates' re-scaling. v_2 can be identifies, as we will show in the following, with the classical center of mass of the falling cloud.

2.2.2 Ballistic expansion in the *far field* and *long fall* approximations.

To simplify the previous expression for the atom flux, we will use two approximations that are valid under our experimental conditions. These approximations will also be used on Chapter 3, when we deal with the intensity correlation function.

2.2.2.1 The *far field approximation.*

The first of these approximations, which we will refer to as *far field*, valid for $\omega_\alpha t \gg 1$, replaces $1+\omega_\alpha^2 t^2$ by simply $\omega_\alpha^2 t^2$ in all the previous expressions that includes that factor. The term *far field* is motivated by an analogy we can establish of the atomic flux with a *hermite-gaussian laser beam*. In this, the *far field condition* is fulfilled when the beam propagates a distance from its waist, z, much bigger than a characteristic length z_R, the *Rayleigh length* [91]. It can be proved that the integral equation for the propagation of the atomic beam, in Eq.2.61, is formally equal to the *Huygens-Fresnel* integral for the propagation of a *hermite-gaussian laser beam*. Thus, analogously to the *Rayleigh length*, we can define a *Rayleigh propagation time*, which is given by $t_R = \omega^{-1}$. The *far field condition* accomplished when $t \gg t_R$ which states that, in every axis, we should have $\omega_\alpha t \gg 1$. Our experimental conditions are in good agreement with this condition: in the worst case, taking the frequency of the *slowest* axis and putting $t = t_0$ we have $\omega t \sim 30$. For the other two axis, $\omega t > 750$.

As in the case of the propagation of a *hermite-gaussian* beam, this approximation amounts to neglect the cloud's initial extension in the calculation of its spread for $t \gg t_R$. The *RMS* value of the size of the cloud at any time is $\sqrt{\langle x^2(t)\rangle} = \sqrt{\langle x_0^2\rangle + \langle v_0^2\rangle t^2}$. If we neglect $\langle x_0^2\rangle$, then $\sqrt{\langle x^2(t)\rangle} = v_T t$ with v_T the *RMS* value of the initial thermal velocities of the trapped atoms. This

approximation is equivalent to the above simplification $\sqrt{1+\omega^2 t^2} \sim \omega t$. To see this, note first that the density in the trap is described through the exponential factor $e^{-\alpha^2/2S_\alpha^2}$ with $s_\alpha = v_T/\omega_\alpha$ the characteristic cloud size in the α direction. After released from the trap, the cloud expands freely and this expansion is given by the coordinate re-scaling presented before. If we use the *far field* approximation, this re-scaling is given simply by $\alpha/\omega_\alpha t$. Substituting this expression in the argument of the exponential, we obtain the time varying cloud size

$$s_\alpha(t) = s_\alpha(t=0)\omega_\alpha t = v_T t. \tag{2.69}$$

As before, this expression takes into account only the *RMS* value of the trapped atoms' momentum distribution, p_T, an isotropic quantity. Thus, within this approximation, the cloud expansion is said to be *ballistic*, *i.e.* isotropic and proportional to the atoms's thermal velocity, a result that was anticipated earlier in §2.1.4.

2.2.2.2 The *long fall approximation.*

We will use a second approximation that we will call the *long fall approximation*. Here, the necessary condition to fulfill is that the *time observation window*, Δt, must be much smaller than $t_0 = \sqrt{2H/g}$, the *time of flight* of the cloud's *classical* center of mass. In the case of interest here, Δt is just the *time spread* of the cloud, t_{cl}. As the cloud is accelerated by gravity, this quantity is given by $t_{cl} = s_z(t_0)/gt_0$. In the *far field*, $s_z(t_0) = v_T t_0$ and we get then

$$t_{cl} = \frac{v_T}{g}. \tag{2.70}$$

Note that this quantity doesn't vary in time since the *gravitational compression* $1/gt$, compensates the thermal expansion $v_T t$.

The *long fall* condition $\Delta t \sim t_{cl} \ll t_0$, can now be re-casted as

$$v_T \ll g t_0 \equiv v_G,$$

with v_G the final velocity of the cloud due to the gravitational acceleration. In our experiment $v_G \sim 1$m/s, whereas for a cloud with a temperature around $T \sim 3$ μK, the thermal velocity is $v_T \sim 0.08$ m/s.

2.2.2.3 The *TOF* signal for the ideal gas.

For $T \lesssim 3$ μK, we can rewrite $t = t_0 + \delta t$, with $\delta t \ll t_0$. It follows that

$$H - \eta(t) = \tfrac{1}{2} g(t_0^2 - t^2) \approx g t_0 \delta t \quad \text{and} \quad H + \eta(t) \approx 2H.$$

Since $\omega_z t_0 \gg 1$, the velocity v_2 given in Eq.2.66 can be simplified to

$$v_2 \approx \frac{2H}{t_0} = v_G,$$

and, the atomic flux of Eq.2.68 can be re-written in a very simple form

$$I(x,y,t) \sim \frac{v_G}{(\overline{\omega}t)^3}\; n\!\left(\frac{x}{\omega_x t}, \frac{y}{\omega_y t}, \frac{g}{\omega_z}\delta t\right).$$

with, as before, $\delta t = t - t_0 \ll t_0$. For the ideal gas case within the *SCA*, this expression can be written as

$$I(x,y,t) \sim \frac{v_G}{(\overline{\omega}t)^3}\;\frac{1}{\lambda_T^3}\; g_{3/2}\!\left[Z\;\exp\left(-\frac{x^2+y^2}{2(v_T t)^2}\right)\exp\left(-\frac{g^2}{2v_T^2}\delta t^2\right)\right].$$

If we assume an infinite detector, the integration of the previous expression over all the xOy plane, gives the *TOF* signal,

$$I(t) \sim \frac{\overline{\tau}^{-2}}{\overline{\omega}t_0}\frac{v_G}{\lambda_T}\; g_{5/2}\!\left[Z\exp\left(-\frac{\delta t^2}{t_{cl}^2}\right)\right]. \tag{2.71}$$

A further integration in δt gives, as expected, $\overline{\tau}^{-3} g_3(Z) \equiv N$.

2.2.2.4 Snap-shot measure of the cloud's density.

The most usual technic to measure the cloud's atomic density is to let it expand for a while and then take a two-dimensional absorbing image. This results in a single integration of $n(\mathbf{r}, t_0)$, the density after the cloud had expanded for a time t_0. This latter quantity can be straightforwardly written down using the Eq.2.62, the expanded harmonic oscillator wave functions and noting that

$$n(\mathbf{r},t) = \sum_{\mathbf{m}=\mathbf{0}}^{\infty} \psi_{\mathbf{m}}(\mathbf{r},t)\psi^*_{\mathbf{m}}(\mathbf{r},t)\;\langle n_{\mathbf{m}}\rangle.$$

All the phases terms in Eq.2.62 appears in here multiplied by the corresponding complex conjugates, canceling out. The latter expression resumes simply to

$$n(\mathbf{r},t_0) = \frac{n(\tilde{\mathbf{r}})}{\prod_\alpha \sqrt{1+\omega_\alpha^2 t_0^2}}, \tag{2.72}$$

with, as before, $\tilde{\mathbf{r}}$ given by Eqs.2.63 but for a constant time $t = t_0$. This expression is equivalent to the one in Eq.2.68 and except for factor v_2, which

converts density units into flux units, and as expected, they contains the same physical information.

The integration over one spatial dimension of Eq.2.72 is straightforward. In the *SCA* it is simply

$$n(x,z) = \frac{1}{\sqrt{1+\omega_x^2 t_0^2}\sqrt{1+\omega_z^2 t_0^2}} \frac{\tau_y^{-1}}{\lambda_T^2}\; g_2\left[Z \exp\left(-\frac{\tilde{x}^2}{2\sigma_x^2} - \frac{\tilde{z}^2}{2\sigma_z^2} \right) \right],$$

where the integration was done over the $0y$ direction.

Closing remarks

The expression in Eq.2.71 is valid only for the ideal gas case. To use in real *TOF* data analysis and make proper measurements of the cloud's temperature and fugacity, this simple result is however insufficient since it doesn't take into account interatomic interactions. These will slightly change the atoms density distribution in the trap as well as induce a *non-ballistic* behavior at the initial few milliseconds of the cloud's expansion. Both these effects will be addressed in Chapter 4, where we deal with the cloud's thermometry. There we include interactions in the thermal equilibrium density matrix and also correct the simple ballistic model for the cloud expansion for accounting to the initial hydrodynamical regime.

In the next Chapter we will still be considering the cloud as an ideal atomic gas. We will introduced the theoretical model we used to interpret the experimental measure of the intensity-intensity correlation function we have done and present some results.

CHAPTER 3

Hanbury Brown and Twiss effect in an expanding cold of non-interacting atoms.

In this Chapter we will discuss the coherence properties of an atomic sample as probed by the measurement of the intensity correlation function of the particle's flux after releasing the atoms from the magnetic trap. Using bosonic atoms, we expect to observe a bunching of particles at small separation as the photonic bunching of a chaotic light source[92].

We will use the formalism we have introduced in the previous Chapter to describe the cloud's ballistic expansion. As before, we will consider a cloud of non-interacting bosonic atoms at thermal equilibrium. The calculation is generalized to the second order correlation function of the atomic flux, a quantity that can be measured, on the time domain, with our experimental apparatus. Particular emphasis is given to the physical situation where the cloud is in the vicinity of the phase transition's critical temperature.

A large part of the contents of this Chapter is based upon Ref.[52] where we present our calculations that predicted that our experiment could be used to carry out a *Hanbury Brown* and *Twiss*[93] type of experiment (*HBT*) with He^* atoms. This work derives the characteristic temporal coherence and the transverse coherence length for the particles' flux generated by a falling atomic cloud, under the influence of the gravity. We show that, for a pulsed atomic beam, the temporal coherence may be obtained from the same kind of expressions used to derive the coherence lengths in the propagation transversal directions. Moreover, due to the *gravitational compression* and similarly to what happens with the temporal extension of the cloud, the temporal coherence is independent of the time of propagations.

Using the specific characteristics of our experiment and those of a new detector (recently installed to up-grade our apparatus), we have estimated the attainable *signal-to-noise* ratio (*SNR*) of the correlation signal. Here, it was of particular importance to compare the *SNR* with the expected *bunching* of the signal at short delay times with non-degenerate samples. We predicted a *SNR* of about 10, a result that would allow improving on the quality of the former result obtained in the pioneering work of 1996 by Yasuda *et al.*[94] on

a thermal beam of metastable Neon.

Unlike Yasuda's experiment, using our experience we could also setup the measurement of the atomic correlation function for a degenerate cloud. In this case, the bosonic bunching is expected to disappear as for laser light[95]. Our experiment could also be suited to measure, for the first time, the correlation function of atoms at the *BEC* phase transition (also observed in the optics field[96]). Possible extensions of this experiment would allow obtaining information about the process of *BEC* formation, probing the development of a long range phase over the atomic cloud and the symmetry breaking when the *BEC* starts to growth.

Recently, the theoretical predictions we present here were confirmed in a successful realization of a *HBT* experiment carry out on both degenerate and non-degenerate clouds[84]. We will briefly report the main results we have obtained in this experiment and, also briefly, on the necessary upgrade we had to operate on our setup. A more detailed discussion on the experiment's upgrade is given in R. Hoppeler's Ph.D. thesis[49] and on the results, in M. Schellekens' Ph.D. manuscript still in preparation.

We will start by a general introduction to the *HBT* experiment with photons before considering the experiments with massive particles.

3.1 The *Hanbury Brown and Twiss* experiment.

We begin this Chapter by considering, briefly, the original idea of Robert Hanbury Brown and Richard Twiss to measure the angular diameter of a star. This will also introduce the notions of transverse coherence and temporal coherence of a wave source.

3.1.1 The transversal coherence length and time coherence of a wave field.

Transversal coherence length.
Consider the scheme of Fig.3.1, where we represent an incoherent wave source and two detectors D_1 and D_2. For simplicity, we consider the source as only one-dimensional and monochromatic, with a characteristic length $2s_\perp$. The two independent detectors are separated from each other by a distance l, both placed very far away from the wave source at a distance $R \gg s_\perp, l$.

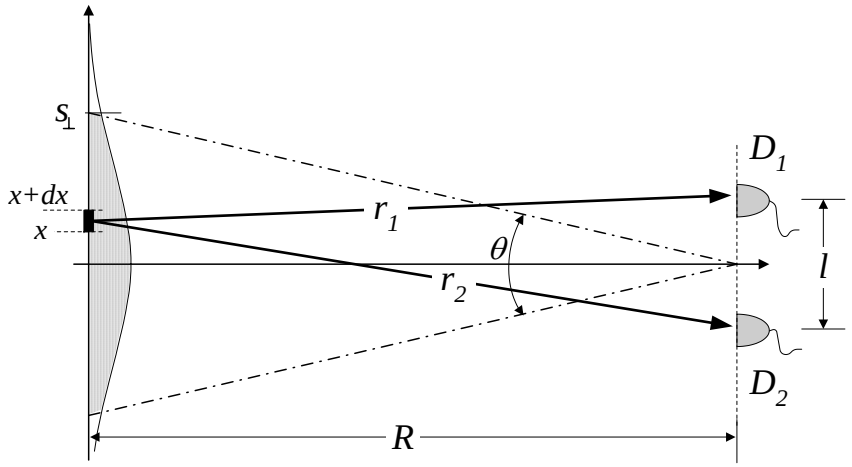

Figure 3.1: An extense wave source emits radiation detected by two detectors, D_1 and D_2, located at a long distance R from the source. The correlation between the photocurrents generated by the two detectors is related with the angular size θ of the source by the van Cittert-Zernike theorem. This was first used by R. Hanbury Brown and R. Twiss to measure the angular diameter of a star (see also text).

The amplitude of the field emitted by a small segment dx of the source, at the location x, is equal to $A(x)dx$, with $A(x)$ the spatial profile of source's wave amplitude. The corresponding scalar wave field produced at the space

location $\mathbf{r} \gg s_\perp, 2\pi/k$ may be written as

$$du(\mathbf{r}) = A(x)dx\,\frac{e^{i\mathbf{k}(\mathbf{r}-\mathbf{x})+i\phi(x)}}{|\mathbf{r}-\mathbf{x}|}$$

with $\phi(x)$ the random phase of the wavefront at x on the plane of the source and $\mathbf{x}$ a vector pointing at that location. The instantaneous intensity detected by D_1 is proportional to

$$\begin{aligned} I_1 = \left|\int du(\mathbf{r}_1)\right|^2 &\simeq \frac{1}{R^2}\left|\int dx A(x) e^{ikr_1(x)-i\phi(x)}\right|^2 \\ &= \frac{1}{R^2}\left|\int dx A(x) e^{i\frac{k}{2R}\left(x-\frac{1}{2}l\right)^2-i\phi(x)}\right|^2, \end{aligned} \tag{3.1}$$

where we have used the approximation $r_1 \simeq R+(x-\frac{1}{2}l)^2/2R$ (see Fig.3.1). A similar expression holds for the intensity detected by D_2 with the substitution $r_2 \simeq R+(x+\frac{1}{2}l)^2/2R$. If we assume that the phases $\phi(x)$ are random and uncorrelated, averaging the above expression over the statistics of the field effectively converts the above integral into an incoherent sum over the individual contributions from each separate source element. In this case the above expression simplifies to

$$\langle I_1\rangle = S\int dx\ |A(x)|^2 = \langle I_2\rangle,$$

where S is a constant that incorporates the detector sensitivity and geometric factors such as $1/R^2$.

Since each source element is assumed to be independent and incoherent the detected intensity is independent of the detector position provided $l \ll R$. However, if we compute instead the *correlation* in the intensities registered by the two detectors $\langle I_1\, I_2\rangle$, again assuming that the phases of the waves emitted at each spatial location on the source are independent so that

$$\langle e^{i\phi(x_1)-i\phi(x_1')+i\phi(x_2)-i\phi(x_2')}\rangle = \delta(x_1-x_1')\delta(x_2-x_2') + \delta(x_1-x_2')\delta(x_1-x_2') \tag{3.2}$$

we obtain

$$\langle I_1\, I_2\rangle = \langle I_1\rangle\langle I_2\rangle + S^2\left|\int dx\,|A(x)|^2\, e^{i\frac{k}{R}xl}\right|^2, \tag{3.3}$$

a result that depends on both R and l. This result is just the (one-dimensional) *van Cittert-Zernike* theorem[97]. It could also be derived, in a more formal

and general manner, by invoking the fact that $u(\mathbf{r})$ is a Gaussian distributed zero mean random variable. The mean value of the m^{th} moment of such a random variable $E(\mathbf{r},t)$ is[98]

$$\begin{aligned} G^{(m)}(\mathbf{r}t,\mathbf{r}'t') &= \langle E_1^* E_2^* \dots E_m^* E_{1'} E_{2'} \dots E_{m'} \rangle \\ &= {\sum}' \langle E_{j_1}^* E_{j_1'} \rangle \langle E_{j_2}^* E_{j_2'} \rangle \dots \langle E_{j_m}^* E_{j_m'} \rangle, \end{aligned} \tag{3.4}$$

with the summation running over all the possible combinations of conjugated pairs $E_j^* E_{j'}$.

To work out an explicit result we continue by assuming that $A(x)$ has a gaussian profile [1], given by

$$A(x) = \frac{1}{\sqrt{2\pi}\, s_\perp} \exp\left(-\frac{x^2}{2s_\perp^2}\right).$$

Replacing this expression in Eq.3.3 and normalizing the result by the square of the total detected intensity of the source we obtain

$$g^{(2)}(l) = \frac{\langle I_1, I_2 \rangle}{\langle I_1 \rangle \langle I_2 \rangle} = 1 + \exp\left[-\left(\frac{l}{l_\perp}\right)^2\right], \tag{3.5}$$

with

$$l_\perp = \frac{1}{\pi}\frac{\lambda}{\theta}, \tag{3.6}$$

the *transversal coherence length* of the source, with λ its wavelength and $\theta = 2s_\perp/R$ its *angular length*, as seen by the detector. The expression on Eq.3.5 is equal to one for $l \gg l_\perp$ and is $g^{(2)} = 2$, for $l = 0$. This result expresses the *bunching* for small ls: the photons have a tendency to be detected in pairs, after traveling the same length from the source.

Using the result of Eq.3.5 it is possible to measure θ in an experiment where the correlation of the intensity signals of the two detectors is registered, varying their relative distance l. This was first used by R. Hanbury Brown and R. Twiss to measure the angular diameter of a star[99].

We may try to apply this formula to a wave field of massive particles. Consider a thermal cloud with a size $s = v_T/\omega$ and temperature $T = Mv_T^2/k_B$, trapped within a harmonic trap of oscillation frequency ω (cf. §2.1.1). If it is released from the trap it spreads ballistically at the characteristic velocity v_T (cf. Eq.2.69), and after a time $t \gg 1/\omega$ the *angle* θ may be identified with

$$\theta \equiv \frac{s}{v_T t} = \frac{1}{\omega t}. \tag{3.7}$$

[1] This has the advantage of simplifying the calculation and also mimics the result we will obtain latter for a thermal cloud with a gaussian velocity distribution.

Identifying the wavelength λ of Eq.3.6 with the thermal de Broglie wavelength λ_T (cf. Eq. 2.13) we get

$$l(t) \sim \lambda_T \omega t, \tag{3.8}$$

showing that the coherence length increases linearly with time. This result will be derive in a proper manner latter in this Chapter.

The coherence time.
In the above calculation we have assumed, implicitly, that the phase information $\phi(x)$ of the wavefront emitted by the small segment dx is kept unaltered over time when the wave propagates a distance which is large if compared to $r_1(x) - r_2(x)$. For a velocity of propagation c, this is equivalent to say that the source's coherence time is $t^{coh} \gg (r_1 - r_2)/c$. This quantity grows with the inverse of the source's frequency bandwidth, $t^{coh} \sim 1/\delta\omega$, and thus, to arrive at a proper expression for the intensity correlation function we need to also take into account the spectral properties of the source.

For simplicity, we admit now the source is almost a point source and, thus, that $l_\perp$ is very large when compared with l, the separation between the detectors in Fig.3.1. Then, the wave field can be expressed as a superposition of spherical waves with amplitudes given by a spectral weight function $S(\omega)$,

$$u(t) = A_0 \int d\omega S(\omega) \frac{e^{-i\omega(t-R/c)}}{R},$$

with A_0 a certain normalization constant. The averaged intensity registered in either of the detectors is independent of time for stationary sources and equal to the integral of the power spectrum,

$$\langle I(t) \rangle = \frac{|A_0|^2}{R^2} \left| \int d\omega S(\omega) \right|^2,$$

On the other hand, the correlation in the intensity detected at different time instants t and $t + \delta t$ is

$$\langle I(t)\, I(t+\delta t) \rangle = \iint d\omega_1 d\omega_1' \iint d\omega_2 d\omega_2' S(\omega_1) S^*(\omega_1') S(\omega_2) S^*(\omega_2') e^{-i(\omega_2 - \omega_2')\delta t} \times \\ \times \langle e^{-i(\omega_1 - \omega_1' + \omega_2 - \omega_2')t} \rangle.$$

As before, this expression is only nonzero for certain choices of the frequencies. In this case, we have

$$\langle e^{-i(\omega_1 - \omega_1' + \omega_2 - \omega_2')t} \rangle = \delta(\omega_1 - \omega_1')\delta(\omega_2 - \omega_2') + \delta(\omega_1 - \omega_2')\delta(\omega_2 - \omega_1') \tag{3.9}$$

and then

$$\langle I(t)\, I(t+\delta t)\rangle = \langle I(t)\rangle\langle I(t+\delta t)\rangle + \left| \int d\omega \, |S(\omega)|^2 \; e^{-i\omega\delta t} \right|^2 ,$$

a result that can also be obtained if we consider each frequency component of the field as to be an independent random gaussian variable. The integral in the second term of the right hand side is just the Fourier transform of the power spectrum and in this case, according to the Wiener-Khintchine theorem[92], it is just the amplitude correlation function $G^{(1)}(t, t+\delta t) = \langle u(t)u(t+\delta t)\rangle$ and then

$$\langle I(t)\, I(t+\delta t)\rangle = \langle I(t)\, I(t+\delta t)\rangle + \left| G^{(1)}(t, t+\delta t) \right|^2 .$$

Note also that, for this case, a single detector would be sufficient to obtain the temporal correlation. However, this would only work in practice if the detector's dead time is much smaller than the coherence time.

We assume again that the spectral weight distribution function $S(\omega)$ has a gaussian shape (*i.e.* that the source has a inhomogeneous broadening) around a certain central frequency ω_0 and with a waist $\Delta\omega$,

$$S(\omega) = \frac{1}{\sqrt{2\pi}\,\Delta\omega} \exp\left(-\frac{(\omega-\omega_0)^2}{2\Delta\omega^2} \right).$$

This is the distribution of Doppler broadened light emitted from an atomic gas at a certain temperature T. In this case, $\Delta\omega = k_0 v_T$, with $k_0 = \omega_0/c$ and, as usual, $v_T = \sqrt{k_B T/M}$.

It is straightforward to compute the normalized correlation function, as defined previously,

$$g^{(2)}(\delta t) = \frac{\langle I_1(t) I_2(t+\delta t)\rangle}{\langle I_1(t)\rangle\langle I_2(t+\delta t)\rangle} = 1 + \exp\left[-\left(\frac{\delta t}{t^{coh}} \right)^2 \right]. \tag{3.10}$$

This expression is, of course, the expression equivalent to Eq.3.5 for a time correlation experiment with

$$t^{coh} = \frac{1}{\sqrt{2}\pi} \frac{\lambda}{v_T},$$

the source's coherence time.

Replacing again the wavelength in this expression by the massive particles's thermal de Broglie wavelength λ_T, we obtain the continuous flux temporal coherence

$$t^{coh} \sim \frac{1}{\sqrt{\pi}} \frac{\hbar}{k_B T},$$

which is inversely proportional to the temperature.

For an expanding cloud under the effect of gravity, we will show that this quantity is given by

$$t^{coh}(t) = \frac{\lambda_T \omega}{g}. \tag{3.11}$$

3.1.2 The *HBT* experiment.

Such an experiment to measure the time of coherence in an intensity correlation measurement was also done, for the first time, by R. Hanbury Brown and R. Twiss[93]. A simplified version of this experiment is sketched in the upper part of Fig.3.2. Light from the 435.8 nm line (Doppler broadened) of a mercury lamp is focused onto a pinhole to produce a transversely coherent source. Two photomultipliers are used to measure the coincidences of photon arrivals for different propagation times of the waves traveling in both arms after the beam-splitter.

The bottom graph of Fig.3.2 shows the results obtained in this experiment.

These showed that for large values of τ, the time difference in the travel of the two detected waves, no intensity correlations existed. This were observed only for small time mismatches, with $g^{(2)}(\tau)$ increasing for decreasing values of τ. This was the first observation of what is known as *photon bunching*, the characteristic tendency of the bosons particles to be detected in pairs. This is also illustrated by the simple models used above (cf. Eqs3.5 and 3.10): when $\tau \to 0$, $g^{(2)} \to 2$ while, if $\tau \to \infty$, $g^{(2)} \to 1$.

3.1.2.1 Laser light.

For a perfectly coherent field, as is the case of am ideal monochromatic infinite plane wave with $l_\perp, t^{coh} \to \infty$, both of the correlation functions in Eqs. 3.5 and 3.10 are always equal to one. In fact, the expression in Eqs.3.2 and 3.9 do not decompose into two terms but are simply given by

$$\langle e^{i\phi(x_1)-i\phi(x_1')+i\phi(x_2)-i\phi(x_2')} \rangle = 1 \quad \text{and} \quad \langle e^{-i(\omega_1-\omega_1'+\omega_2-\omega_2')t} \rangle = 1,$$

a result that follows from the fact that the wavefront phase being always constant and, also, from the *monochromaticity* of the field. In optics, such a source is well approximated by a mono-mode laser field. The Hanbury Brown and Twiss type of experiments using laser light[95] showed a absence of any correlation on the arrival of the photons with a normalized correlation function equal to

$$g^{(2)}(\tau) = 1.$$

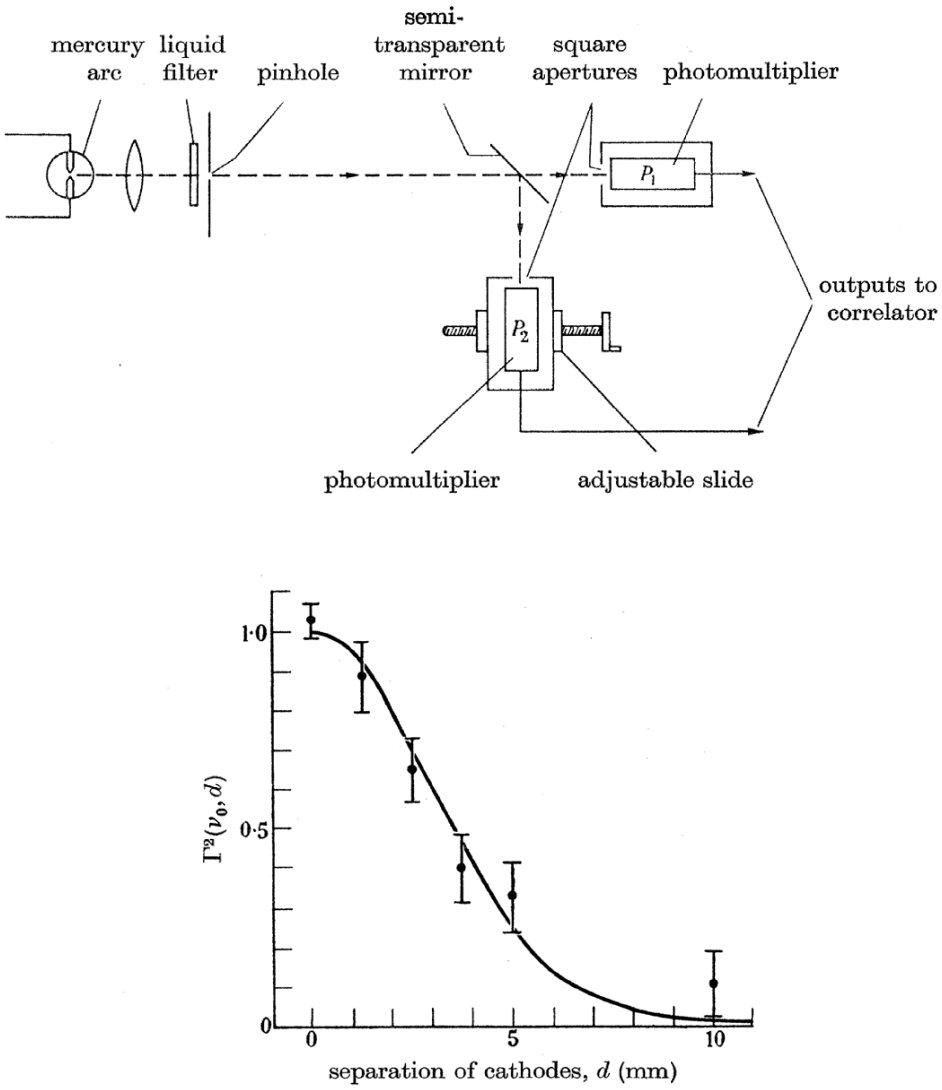

Figure 3.2: The top graph sketches a simplified outline of the optical setup used by *Robert Hanbury Brown* and *Richard Twiss* in their pioneering experiment to measure the second order correlation function of photons from a thermal source. The source was a mercury lamp, filtered to the 435.8 nm line of its spectrum. The source was made spatially coherent by the inclusion of a pinhole. The photon-photon correlation function was measured by correlating the intensities of two beams split in a semi-transparent mirror and using two photomultiplier tubes as detection devices. To vary the difference in propagation time of one and the other beams, one of the photomultipliers was mounted on a translation stage and displaced transversely to the incoming beam. Supposing a perfect spatially coherent source (point like) and small enough detectors, this allow them to measure of the temporal coherence of the light. The bottom graph plots the observed results for *bunching* $g^{(2)}(d) - 1$ in function of the separation of the photomultiplier cathodes.

3.2 Correlation functions in a non-interacting atomic gas.

We turn now to a more formal derivation of the correlation functions of a quantum field defined within the many-body second quantization formalism. Our main objective is the computation of the first and second correlation functions of a cloud of non-interacting bosonic atoms at thermal equilibrium[100].

3.2.1 Definitions

3.2.1.1 Correlation functions defined in coordinate space.

In the framework of second quantization, particles are described by a field operator $\hat{\Psi}(\mathbf{r})$ (cf. Eq.2.52) and correlation functions are expressed by an statistical average of hermite conjugated pairs of these operators, such as $\hat{\Psi}(\mathbf{r})\hat{\Psi}^\dagger(\mathbf{r}')$. A functions of k^{th} order is defined as average of k of these pairs.

Since we are dealing with a bosonic field, this statistical average must follow the Bose-Einstein distribution (cf. Eq.2.5)

$$\langle \hat{a}^\dagger_{\mathbf{m}} \hat{a}_{\mathbf{n}} \rangle = \delta_{\mathbf{mn}} \langle n_{\mathbf{m}} \rangle,$$

with, as before, $\langle n_{\mathbf{m}} \rangle$ representing statistical occupation of the level $\mathbf{m}$. The simplest expression is the first order correlation function, obtained for $k = 1$,

$$G^{(1)}(\mathbf{r}, \mathbf{r}') = \langle \hat{\Psi}^\dagger(\mathbf{r}) \hat{\Psi}(\mathbf{r}') \rangle. \tag{3.12}$$

With $\mathbf{r} = \mathbf{r}'$, this expression is just the cloud density at the location $\mathbf{r}$,

$$n(\mathbf{r}) = \langle \hat{\Psi}^\dagger(\mathbf{r}) \hat{\Psi}(\mathbf{r}) \rangle = G^{(1)}(\mathbf{r}, \mathbf{r}),$$

which is the same as Eq.2.4. Evaluated at different points of the space, this function gives rise to the interference term describing the fringe pattern observed in Michelson's or Young's type of experiments.

In the scope of this manuscript, we are mostly interested in the second order correlation function,

$$G^{(2)}(\mathbf{r}, \mathbf{r}') = \langle \hat{\Psi}^\dagger(\mathbf{r}) \hat{\Psi}^\dagger(\mathbf{r}') \hat{\Psi}(\mathbf{r}) \hat{\Psi}(\mathbf{r}') \rangle. \tag{3.13}$$

For a non-degenerate ideal gas atomic cloud, this latter expression can be factorized in simpler first order correlation functions, in just the same way as it occurs for a thermal optical field. In fact, the statistical average in the above expression reduces to the computation of a *four point* correlation of the type $\langle \hat{a}^\dagger_{\mathbf{j}} \hat{a}^\dagger_{\mathbf{k}} \hat{a}_{\mathbf{l}} \hat{a}_{\mathbf{n}} \rangle$, which is, for a thermal field, equal to

$$\langle \hat{a}^\dagger_{\mathbf{j}} \hat{a}^\dagger_{\mathbf{k}} \hat{a}_{\mathbf{l}} \hat{a}_{\mathbf{m}} \rangle = \langle \hat{a}^\dagger_{\mathbf{j}} \hat{a}_{\mathbf{j}} \rangle \langle \hat{a}^\dagger_{\mathbf{k}} \hat{a}_{\mathbf{k}} \rangle \times (\delta_{\mathbf{jl}} \delta_{\mathbf{km}} + \delta_{\mathbf{jm}} \delta_{\mathbf{kl}}). \tag{3.14}$$

This factorization rule is just the same as the one used above to work out the averages over the wave's *Gaussian distributed* random phases. This same result may also be derived using the Wick's theorem [101, 102] which is, in fact, the most common way of computing mean values of field operator expressions in atomic and condensed matter physics, as it is easily adapted to carry out perturbative expansions and Bogoliubov type of transformations for systems of interacting particles.

• The *density-density* correlation function.

In the definition of the second order correlation function, given in Eq.3.13, the field operators are written in the *normal order*, with all the annihilating operators at its left hand side. However, the correlation function that is inspected directly in our experiment is rather the *density-density correlation function*, given by

$$\langle n(\mathbf{r})n(\mathbf{r}')\rangle = \langle \hat{\Psi}^\dagger\hat{\Psi}\hat{\Psi}^\dagger\hat{\Psi}\rangle. \tag{3.15}$$

The expression in Eq.3.13 expresses the (conditional) probability of detecting a particle at the location $\mathbf{r}$ after having been detected another one at $\mathbf{r}'$. The one in Eq.3.15 is the statistical average over the ensemble of particles of the density at locations $\mathbf{r}$ and $\mathbf{r}'$. Using the bosonic commutation relations, the expression in Eq.3.15 can be re-expressed using $G^{(2)}(\mathbf{r},\mathbf{r}')$ as

$$\langle n(\mathbf{r})n(\mathbf{r}')\rangle = G^{(2)}(\mathbf{r},\mathbf{r}') + n(\mathbf{r})\delta(\mathbf{r}-\mathbf{r}').$$

The last term in the right hand side of this equation is proportional the cloud's number of atoms N and usually referred as the *shot-noise term*, since $G^{(2)}(\mathbf{r},\mathbf{r}')$ is proportional to $N(N-1)$. Note that, for an ensemble with only one particle, $G^{(2)}(\mathbf{r},\mathbf{r})$ is zero but $\langle n(\mathbf{r})n(\mathbf{r})\rangle = n(\mathbf{r})$.

For a large N, the shot noise term becomes negligible and the two possible definitions for the second order correlation function yields the same result,

$$\langle n(\mathbf{r})n(\mathbf{r}')\rangle \cong G^{(2)}(\mathbf{r},\mathbf{r}') = n(\mathbf{r})n(\mathbf{r}') + |G^{(1)}(\mathbf{r},\mathbf{r}')|^2. \tag{3.16}$$

• The normalized correlation function.

Eq.3.16 shows that $G^{(2)}(\mathbf{r},\mathbf{r}')$ depends not only on the modulus square of the first order *correlation term*, $|G^{(1)}(\mathbf{r},\mathbf{r}')|^2$, but also on the product of the densities at $\mathbf{r}$ and $\mathbf{r}'$. A more convenient way to define the second order correlation function, that avoids this dependence on the density, is

$$g^{(2)}(\mathbf{r},\mathbf{r}') = \frac{G^{(2)}(\mathbf{r},\mathbf{r}')}{n(\mathbf{r})n(\mathbf{r}')},$$

which is the same type of *normalized* correlation function definition as that which we have used above in Eq.3.5. Neglecting the *shot-noise* term, this function reduces to the simple expression

$$g^{(2)}(\mathbf{r},\mathbf{r}') = 1 + |g^{(1)}(\mathbf{r},\mathbf{r}')|^2, \tag{3.17}$$

where we also used the definition of the first order *normalized correlation function*,

$$g^{(1)}(\mathbf{r},\mathbf{r}') = \frac{G^{(1)}(\mathbf{r},\mathbf{r}')}{\sqrt{n(\mathbf{r})\ n(\mathbf{r}')}}. \tag{3.18}$$

This function, in optics, gives the *visibility* of the fringes in a interferometric pattern made of two beams of equal intensity[103]. A field is said to exhibit *first order coherence* or to be *fully coherent* if $|g^{(1)}(\mathbf{r},\mathbf{r}')| = 1$ irrespectively to the locations $\mathbf{r}$ and $\mathbf{r}'$.

Actual fields are not fully coherent and the visibility generally decreases as $|\mathbf{r}-\mathbf{r}'|$ increases. The coherence length, l, is defined as the distance for which the interference fringes are still visible or, similarly, as the length scale where the first-order correlation function is still non vanishing. The expression in Eq.3.17 then has the same behavior as the one derived earlier in Eqs.3.5 and 3.10 for a classical field,

$$g^{(2)}(\mathbf{r},\mathbf{r}) = 2 \quad \text{and} \quad g^{(2)}(\mathbf{r},\mathbf{r}') \sim 1 \text{ for } |\mathbf{r}-\mathbf{r}'| \gg l.$$

We may generalize the above definition of *full coherence* to any correlation function of arbitrary order k. A sufficient condition for a field to be k^{th}-order coherent is that the corresponding correlation function can be factorized as[103],

$$G^{(k)}(\mathbf{r}_1,\ldots,\mathbf{r}_k,\mathbf{r}'_1,\ldots,\mathbf{r}'_k) = \phi^*(\mathbf{r}_1)\phi^*(\mathbf{r}_2)\ldots\phi^*(\mathbf{r}_k)\phi(\mathbf{r}'_1)\ldots\phi(\mathbf{r}'_2)\phi(\mathbf{r}'_k).$$

This condition is equivalent to have $|g^{(r)}| = 1$ and implies that

$$\langle \hat{a}^\dagger_{\mathbf{m}_1}\hat{a}^\dagger_{\mathbf{m}_2}\ldots\hat{a}^\dagger_{\mathbf{m}_k}\hat{a}_{\mathbf{m}'_k}\ldots\hat{a}_{\mathbf{m}'_2}\hat{a}_{\mathbf{m}'_1}\rangle = 1,$$

which is only true for a pure quantum state of the field[92], as for example a *BEC* at zero temperature. For this particular case, we have

$$\langle\Psi^\dagger_0(\mathbf{r})\Psi_0(\mathbf{r})\Psi^\dagger_0(\mathbf{r}')\Psi_0(\mathbf{r}')\rangle = \langle\Psi^\dagger_0(\mathbf{r})\Psi_0(\mathbf{r})\rangle\langle\Psi^\dagger_0(\mathbf{r}')\Psi_0(\mathbf{r}')\rangle = n_0(\mathbf{r})n_0(\mathbf{r}'),$$

and thus

$$g^{(2)}(\mathbf{r},\mathbf{r}') = 1.$$

This is the result we obtain in the example given in §3.1.2.1 for a classical full coherent monochromatic wave, where the phase is constant over the wavefront and the spectral distribution is proportional to a *delta function* in frequency, as occurs for an ideal laser source.

3.2.1.2 The influence of the ground state population.

For a degenerate atomic cloud, the factorization we used to derive the expression of Eq.3.16 is no longer valid. The calculation of $\langle \hat{a}^\dagger_{\mathbf{j}} \hat{a}_{\mathbf{k}} \hat{a}^\dagger_{\mathbf{l}} \hat{a}_{\mathbf{n}} \rangle$ was done, in the spirit of Wick's theorem, assuming that the system is properly described within the grand canonical ensemble [2]. This ensemble assumes the existence of a particle reservoir leading to unphysically large fluctuations of the condensate at low enough temperature[85]. However, at the thermodynamic limit this pathology disappears in the more realistic case where interatomic interactions are present[85] [3] The fluctuation of the *BEC* number of atoms is also eliminated for a finite number of non-interacting particles if we describe the system using the canonical ensemble[105].

To keep using the grand canonical ensemble description, taking into account this effect, we can correct the *grand canonical* result of Eq.3.14 by subtracting the *canonical result* found for the ground-state $\langle \hat{a}^\dagger_{\mathbf{0}} \hat{a}_{\mathbf{0}} \rangle^2 \delta_{\mathbf{k0}} \delta_{\mathbf{l0}} \delta_{\mathbf{m0}}$. This strategy, which we will make use in the following, is proposed in Ref.[100] and is validated by the results in Ref.[105] [4]. Then denoting as before the ground-state density by $n_0(\mathbf{r})$, it follows that,

$$G^{(2)}(\mathbf{r}, \mathbf{r}') = n(\mathbf{r}) n(\mathbf{r}') + |G^{(1)}(\mathbf{r}, \mathbf{r}')|^2 - n_0(\mathbf{r}) n_0(\mathbf{r}'). \tag{3.19}$$

For a non-degenerate cloud, the ground state density is still negligible and the normalized correlation function $g^{(2)}(\mathbf{r}, \mathbf{r}')$ still follows Eq.3.17, decreasing from 2 to 1 as $|\mathbf{r} - \mathbf{r}'|$ increases to infinity. The opposite situation happens for a *BEC* at $T = 0$ where only the ground-state is occupied. Thus, we have

$$|G^{(1)}(\mathbf{r}, \mathbf{r}')|^2 \Big|_{T=0} = n_0(\mathbf{r}) n_0(\mathbf{r}') = n_0(\mathbf{r}) n_0(\mathbf{r}')$$

and, as before,

$$g^{(2)}(\mathbf{r}, \mathbf{r}') = 1,$$

for every $\mathbf{r}$ and $\mathbf{r}'$, corresponding to an infinite *BEC* correlation length.

Such a system, with a correlation function given by Eq.3.19, is said to exhibit bunching at high temperature for separations smaller than the correlation length and no bunching in the condensed phase.

[2] This is also implicitly assumed in the *optical equivalence theorem*, where the number of photons in the field is not conserved.

[3] The same happens with the amplitude of a laser, due to its gain saturation[104].

[4] In this reference it is also shown that the largest deviation between a description employing the grand canonical ensemble and that using the canonical ensemble is expected to occur near the transition temperature. This is the physical situation where the cure proposed for the grand canonical ensemble may become less accurate. A yet to be done detailed experimental investigation of atomic clouds at $T = T_c$ could help characterize the size of this unveil how large this inaccuracy.

3.2.1.3 Correlation functions in the momentum space.

In most experiments, and particularly in ours, the correlation signal is not measured directly in the atomic cloud. As described in the previous Chapter, the cloud is only detected after being released from a trap and allowed to expand during a certain *time of flight*. As already noted in §2.2.2, for a sufficiently long time of flight and neglecting interatomic interactions, the atomic flux measured at the detector reflects the initial momentum distribution of the atoms.

The results we derived in Section §3.2.1, concerning the correlation functions in position space, all have analogs in momentum space. In fact the correlation functions in the two reciprocal spaces are closely related. For a trapped cloud at thermal equilibrium, the following relationships can be easily derived:

$$\int d\mathbf{p}\; G^{(1)}(\mathbf{p},\mathbf{p}) e^{-i\mathbf{p}.\mathbf{r}/\hbar} = \int d\mathbf{R}\; G^{(1)}(\mathbf{R}-\mathbf{r}/\mathbf{2},\mathbf{R}+\mathbf{r}/\mathbf{2})$$

$$\int d\mathbf{r}\; G^{(1)}(\mathbf{r},\mathbf{r}) e^{i\mathbf{q}.\mathbf{r}/\hbar} = \int d\mathbf{P}\; G^{(1)}(\mathbf{P}-\mathbf{q}/\mathbf{2},\mathbf{P}+\mathbf{q}/\mathbf{2})$$

These two expressions express the fact that *i*) the spatial correlation length is related to the width of the momentum distribution and, *ii*) the momentum correlation length is related to the width of the spatial distribution, *i.e.* the size of the cloud.

No simple and equally general relationship holds for the second order correlation functions. This is because, close to the *BEC* transition temperature, and at points where the ground state wave function is not negligible, the special contribution of the ground state, the last term in Eq.3.19 must be included, and this contribution depends on the details of the confining potential. On the other hand, for an ideal gas far from the transition temperature one can neglect the ground state density, make the approximation that the correlation length is very short, neglect commutators such as $[\hat{\mathbf{r}},\hat{\mathbf{p}}]$, and then write the thermal density operator as $\hat{\rho} = \exp\left(-\beta\frac{\hat{\mathbf{P}}^{\mathbf{2}}}{2M}\right)\,\exp\left[-\beta V(\hat{\mathbf{r}})\right]$, with $V(\mathbf{r})$ the trapping potential. These approximations lead to:

$$G^{(2)}(\mathbf{p},\mathbf{p}') = \rho_{eq}(\mathbf{p})\rho_{eq}(\mathbf{p}') + |G^{(1)}(\mathbf{p},\mathbf{p}')|^2$$

and,

$$G^{(1)}(\mathbf{P}-\mathbf{q}/\mathbf{2},\mathbf{P}+\mathbf{q}/\mathbf{2}) \sim e^{-\beta\frac{\mathbf{P}^{\mathbf{2}}}{2m}} \int d\mathbf{r}\; e^{-\beta V(\mathbf{r})} e^{i\frac{\mathbf{q}.\mathbf{r}}{\hbar}}$$

One sees that in this limit, the interesting part of $G^{(2)}$ in momentum space is proportional to the square of the Fourier transform of the density distribution and independent of the mean momentum $\mathbf{P}$. This result is entirely equivalent

to its optical analog, the *van Cittert-Zernike* theorem[97]. For a harmonically trapped cloud of size s_α in the α direction, $V(\mathbf{r})$ is given by Eq.2.1 and the above expression leads to a definition of the *momentum correlation length* as

$$p_\alpha^{coh} s_\alpha = \hbar. \tag{3.20}$$

If the cloud expands freely during a time period t, the coherence length l_α at the α spatial direction may be written as [5]

$$l_\alpha(t) = \frac{p_\alpha^{coh}}{M} t = \frac{\lambda_T}{\sqrt{2\pi}} \omega_\alpha t. \tag{3.21}$$

Comparing this expression with the one in Eq.3.8 we see that, in this case,

$$l = \frac{\lambda_T}{\sqrt{2\pi}}, \tag{3.22}$$

a result we will derive formally latter in this Chapter.

The above relations between the extension of a trapped cloud and its coherence length were confirmed experimentally[84] for thermal clouds for temperatures large compared to T_c. They suffice to interpret the available experimental data.

It is however interesting to investigate further in more detail how the the correlation functions behaves for clouds near the transition temperature where effects due to the Bose nature of the atoms are expected to be important. To do this we need to concretize the calculation for the proper second order correlation function of a harmonically trapped atomic gas and also understand, with some care, how to describe the time evolution during the free fall under the effect of the gravitational field.

3.3 Correlation functions in a harmonic trap.

3.3.1 At equilibrium in the trap

The first order correlation function can be obtained from the density matrix at thermal equilibrium,

$$G^{(1)}(\mathbf{r}, \mathbf{r}') \equiv n(\mathbf{r}, \mathbf{r}') = \langle \mathbf{r} | \hat{\rho}_{eq} | \mathbf{r}' \rangle.$$

[5] This expression may give the wrong idea that l_α goes to zero for $t = 0$. In fact, the above formula for θ in Eq.3.7 is only valid in the *far field approximation*. Its exact value is rather $\theta = \left[1 + (\omega t)^2\right]^{-1/2}$ and, as expected, for $t = 0$, $l_\alpha = l_\alpha(0)$.

Using Eq.2.18, this expression is given by

$$\begin{aligned} G^{(1)}(\mathbf{r},\mathbf{r}') &= \sum_{l=1}^{\infty} Z^l G^{ho}(\mathbf{r},\mathbf{r}';l\tau) \\ &= \frac{1}{\lambda_T^3}\sum_{l}\; Z^l \prod_{\alpha} \mathrm{F}_l(\tau_\alpha)\; e^{-\left(\frac{r_\alpha+r'_\alpha}{2\sigma_\alpha}\right)^2 \mathrm{th}\left(\frac{1}{2}l\tau_\alpha\right)-\left(\frac{r_\alpha-r'_\alpha}{2\sigma_\alpha}\right)^2 \mathrm{cth}\left(\frac{1}{2}l\tau_\alpha\right)}. \end{aligned} \tag{3.23}$$

Replacing this expression in Eq.3.19 results in a explicit expression for the second order correlation function $G^{(2)}(\mathbf{r},\mathbf{r}')$. As for the case of the cloud's density, this quantity has different behaviors depending on the cloud's temperature and whether it is *i*) far above, *ii*) at the vicinity but still above or, else, *iii*) below the phase transition critical temperature. We start by considering the simplest case, for which we have $T \gg T_c$.

• The high-temperature limit.
In the high temperature limit, $Z \to 0$ and one recovers the Maxwell-Boltzmann distribution by taking only the $l = 1$ term in the sum and, also, after expanding all the factors in τ_α, keeping only the leading terms (cf. Eq.2.22),

$$\mathrm{F}_l(\tau_\alpha) \sim 1, \quad \mathrm{th}\left(\tfrac{1}{2}l\tau_\alpha\right) \sim \frac{\tau_\alpha}{2} \quad \text{and} \quad \mathrm{cth}\left(\tfrac{1}{2}l\tau_\alpha\right) \sim \frac{2}{\tau_\alpha}.$$

In this case, the expression in Eq.3.23 simplifies to

$$G^{(1)}(\mathbf{r},\mathbf{r}') = \frac{N\overline{\tau}}{\lambda^3} e^{-\sum_\alpha \frac{\tau_\alpha}{2}\left(\frac{r_\alpha+r'_\alpha}{2\sigma_\alpha}\right)^2} e^{-\pi\left(\frac{\mathbf{r}-\mathbf{r}'}{\lambda_T}\right)^2}, \tag{3.24}$$

with N given by Eq.2.26.

The first exponential factor in the right hand side of Eq.3.24 depends on $\frac{1}{2}(\mathbf{r}+\mathbf{r}')$ and clearly accounts for the cloud's density dependence at the mid location between $\mathbf{r}$ and $\mathbf{r}'$ (compare with Eq.2.23). This factor makes $G^{(1)}(\mathbf{r},\mathbf{r}')$ tends to vanish as either $\mathbf{r}_\alpha$ or $\mathbf{r}'_\alpha$ become much larger than the cloud's size, $s_\alpha = \sigma_\alpha/\sqrt{\tau_\alpha}$. The second exponential is the *coherence term* as it depends on $|\mathbf{r}-\mathbf{r}'|$. The characteristic length here is the one suggested before in Eq.3.22, proportional to the thermal *de Broglie* wavelength, λ_T. It is an isotropic quantity because the momentum distribution is, in this approximation, also isotropic. It is interesting to re-write the expression given before in Eq.2.49 of Chapter 2, and the one of Eq.3.20,

$$p_T\; l \;=\; p_\alpha^{coh} s_\alpha \;=\; \hbar.$$

These relations states that for a thermal sample the product of *momentum distribution width* of the sample with its *correlation length* is equal to the

product of the *momentum correlation length* times the size of the cloud, both equal to $\hbar$.

With $|\mathbf{r} - \mathbf{r}'| = 0$ one recovers the cloud's density (cf. Eq.2.23), that enters in the normalized correlation function definition. Unlike the *coherence term* in Eq.3.24, the normalized second order correlation function is, strictly speaking, *not* isotropic. With $\delta r_\alpha = |r_\alpha - r'_\alpha|$, one has

$$g^{(2)}(\delta\mathbf{r}) = 1 + \exp\left[-\frac{\delta r_\alpha^2}{l^2} - \frac{\delta r_\alpha^2}{4s_\alpha^2}\right],$$

which defines the anisotropic coherence length as $[l]_\alpha \to l \times (1 - \frac{1}{4}{\tau_\alpha}^2)^{-1}$. However, since usually $\tau_\alpha \ll 1$ [6] the anisotropic correction may be disregarded. Doing so, we obtain the simple formula

$$g^{(2)}(\delta\mathbf{r}) = 1 + \exp\left[-\left(\frac{\delta\mathbf{r}}{l}\right)^2\right]. \tag{3.25}$$

This is just the expression we have found before in Eq.3.5, for a inhomogeneous broadened thermal source of light. The same interpretation given there also applies in here: the correlation function presents a bunching at $\delta\mathbf{r} = 0$ where $g^{(2)} = 2$ and then falls to $g^{(2)} = 1$ when $\delta\mathbf{r} \gg l$. Within the example given for the thermal light, the gaussian dependence of this function resulted from the source's line shape. Here, it is just a consequence of the momentum distribution of the atoms.

• Quasi-degenerated case.

For temperature close to but above the Bose-Einstein transition temperature, one has to keep the summation over the index l, in Eq.3.23. In this case, the terms with increasing values of l contribute more and more as the temperature decreases. It becomes clear from the expression of $G^{(1)}$ in Eq.3.23 that the correlation length near the center of the trap ($r_\alpha, r'_\alpha \ll s_\alpha$) will increase and that the normalized correlation function is no longer Gaussian. Far from the center, only the terms with small values of l are important and the correlation function remains almost Gaussian. Thus, in general, close to degeneracy the correlation length is no longer a constant and becomes position-dependent

In the Fig.3.3 we trace some examples of the function $|g^{(1)}(\mathbf{r}, \mathbf{0})|$ for cloud fugacities from $Z = 0.8$, which is far from degeneracy, to $Z = 0.995$, where the temperature is close to the critical one. The graphs in this Figure also show, in the shadowed region, the corresponding function for the high temperature

[6] For our trapping potential, this correction amounts to 5% for the more confined axes with $T = 1\mu K$.

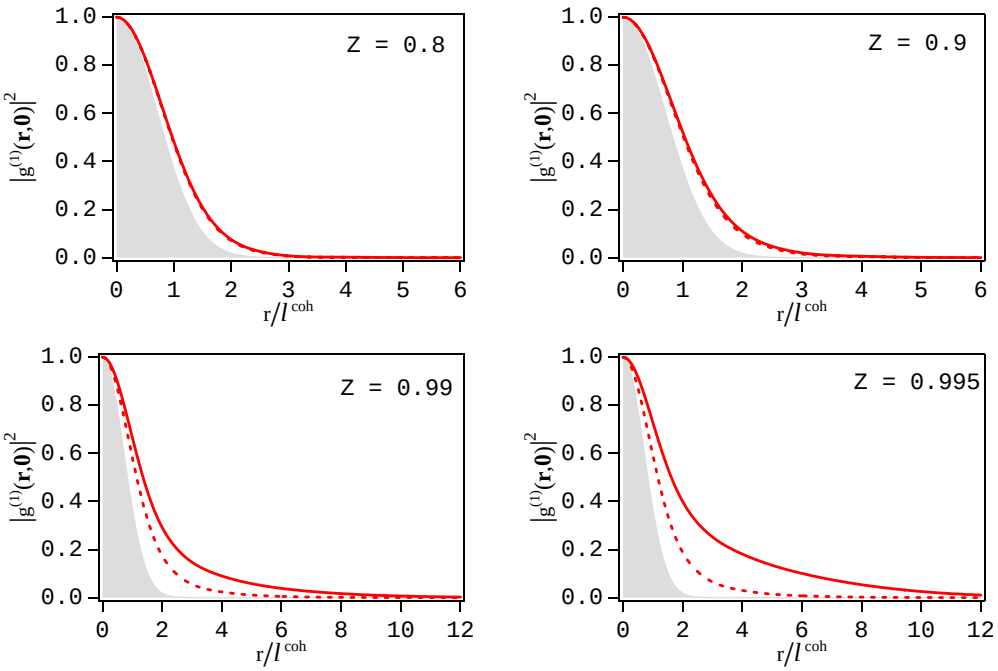

Figure 3.3: Two-body normalized correlation function $g^{(1)}(\mathbf{r},\mathbf{0})$ for a cloud at $T = 1\ \mu$K and four different fugacities. The solid line represents the exact calculation using Eqs.3.23 and 3.18. Shadowed regions correspond to the high temperature limit curve (cf. Eq.3.25). $l = \lambda_T/\sqrt{2\pi} = \hbar/p_T$ corresponds to the high temperature limit correlation length. The number of atoms in the examples shown ranges from $\approx 125 \times 10^3$ for $Z = 0.8$ to $\approx 170 \times 10^3$ if $Z = 0.995$.

limit. The departure of $|g^{(1)}(\mathbf{r},\mathbf{0})|$ from the gaussian shape is already obvious for $Z = 0.9$ and, for fugacities closer to one, it presents a long tail denoting the build up of a long range correlation among the atoms within the cloud.

• Degenerate case.
Increasing further the fugacity to $Z = 1$ leads to a saturation of the excited

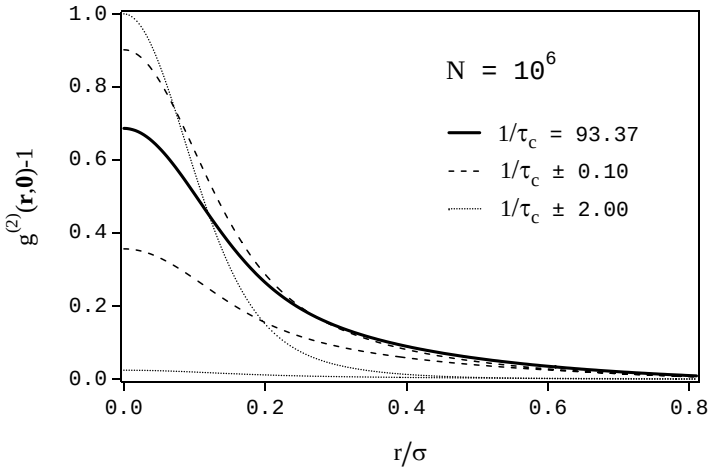

Figure 3.4: Two-body normalized correlation function at the trap center, $g^{(2)}(\mathbf{r},0)$ for 10^6 atoms confined in a isotropic harmonic trap as function of the position $\mathbf{r}$ and for various temperatures around transition temperature. The horizontal axis is labelled in units of the size of the harmonic oscillator wave function σ. The thick solid line corresponds to defined in Ref.[81] and is 93.37 $\hbar\omega/k_B$ for 10^6 atoms. The top dashed and dotted lines correspond to temperatures higher than T_c. The thermal de Broglie wavelength is $\sim 0.26\ \sigma$. The effect of the ground state population is clearly visible in the reduction of $g^{(2)}(0,0)$, and in the rapid flattening out of the correlation function slightly below T_c.

states and a proper calculation of the second order correlation function must take into account the presence of a macroscopic population in the ground state. The density correlation function is now given by Eq.3.19 with the corresponding normalized function equal to

$$g^{(2)}(\mathbf{r},\mathbf{r}') = 1 + \frac{|G^{(1)}(\mathbf{r},\mathbf{r}')|^2 - n_0(\mathbf{r})n_0(\mathbf{r}')}{G^{(1)}(\mathbf{r},\mathbf{r})G^{(1}(\mathbf{r}',\mathbf{r}')}. \tag{3.26}$$

where $n_0(\mathbf{r})$ is given by Eq.2.39. With $Z \sim 1$ and $T \sim 0$, τ_α goes to infinity and, in the expression of Eq.3.23, the hyperbolic functions tends to one and $\mathrm{F}_l(\tau_\alpha)/\lambda_T \sim 1/\sigma_\alpha$. In this case, $G^{(1)(\mathbf{r},\mathbf{r}')}$ factorizes as

$$G^{(1)}(\mathbf{r},\mathbf{r}') \sim n_0(\mathbf{r})n_0(\mathbf{r}'),$$

the expression in Eq.3.26 is always $g^{(2)}(\mathbf{r},\mathbf{r}') = 1$ for any $\mathbf{r}$ and $\mathbf{r}'$ and the correlation length becomes infinite.

The behavior of $g^{(2)}(\mathbf{r},\mathbf{r}')$ for cloud temperatures around $T = T_c$ is traced in Fig.3.4, following the criteria we have used in §2.1.2 for defining the critical temperature[81]. The graph in this Figure shows that, close to the *BEC* transition, the bunching is already significantly different from 2 near the center of the trap.

3.3.2 Integrated signals

From the experimental point of view, since the number of atoms in a cloud is finite, it is very difficult to measure the function $G^{(2)}(\mathbf{r},\mathbf{r}')$ explicitly for arbitrary values of $\mathbf{r}$ and $\mathbf{r}'$. This measurement could be achieved averaging over many clouds with similar thermodynamical characteristics. Even so, as we will see later, to get a good *signal-to-noise* ratio, we would need an unpracticable number of clouds. This difficulty is overcome if we average the correlation function also within each cloud. This results in *one-parameter* correlation function whose argument is the relative distance $\delta\mathbf{r} = |\mathbf{r}-\mathbf{r}'|$. We define the averaged value of the second order correlation function as

$$g_m^{(2)}(\delta\mathbf{r}) = \frac{\int d\mathbf{R}\; G^{(2)}(\mathbf{R}-\frac{1}{2}\delta\mathbf{r},\mathbf{R}+\frac{1}{2}\delta\mathbf{r})}{\int d\mathbf{R}\; n(\mathbf{R}-\frac{1}{2}\delta\mathbf{r})n(\mathbf{R}+\frac{1}{2}\delta\mathbf{r})}. \tag{3.27}$$

Although it is more easily obtained, this function washes out the non-classical behavior of $g^{(2)}(\mathbf{r},\mathbf{r}')$ for clouds close to the degeneracy (as shown in Fig.3.3) as well as the effects coming from the ground state contribution, manifested mainly at the center of the cloud. These effects are also illustrated in Fig.3.5. In the top graph, *a*), we represent the *bunching amplitude* $g^{(2)}(\mathbf{r},\mathbf{r}) - 1$ as a function of $\mathbf{r}$ at different fugacities, around the critical transition point for a cloud with 10^6 atoms. The bottom graph, *b*) represents similar curves as the ones in Fig.3.4, but always with $T = T_c$ and centered at different locations $\mathbf{r}_0$, $g^{(2)}(\mathbf{r}_0,\mathbf{r}) - 1$ rather than at the center of the cloud. This function is plotted normalized by the corresponding *bunching amplitude*.

It is clear form the Graph *a*) of Fig.3.5 that the decrease from one of the bunching observed for degenerated clouds in Fig3.4 is no longer observed at locations in the cloud far off the region of influence of the ground state. Thus, we should expect that an integration over all the cloud, as the one proposed in Eq.3.27, will make $g_m^{(2)}(\mathbf{r}=0)$ decrease slowly to one for smaller and smaller temperatures, if compared to the curves shown in Fig.3.4. This can be observed in the graph of Fig.3.6 where we plot $g_m^{(2)}(\mathbf{r}) - 1$ for the same temperatures as those plotted before in Fig.3.4. For the critical temperature, for example, the non-integrated bunching at the cloud's center is around 0.7

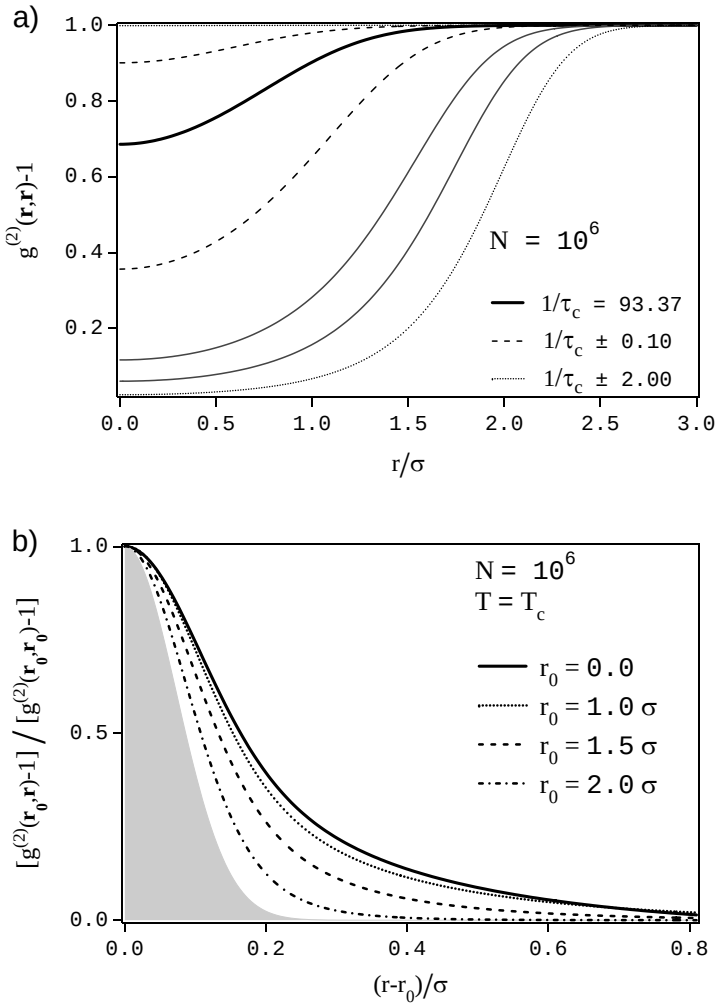

Figure 3.5: Two-body normalized correlation function $g^{(2)}(\mathbf{r},\mathbf{r})$ for 10^6 atoms confined in a isotropic harmonic trap for several different temperatures. The conditions are the same as for Fig3.4. Even for $T < T_c$ the correlation goes to 2 far from the center. This is due to the finite spatial extent of the condensate. It can also be understood in terms of the chemical potential $\mu(\tilde{r})$ which, in a local density approximation, decreases as $\tilde{r}$ increases and thus the correlation is equivalent to that of a hotter cloud.

while the integrated bunching given by $g_m^{(2)}(\mathbf{r})$ is still almost equal to one (see Fig.3.6).

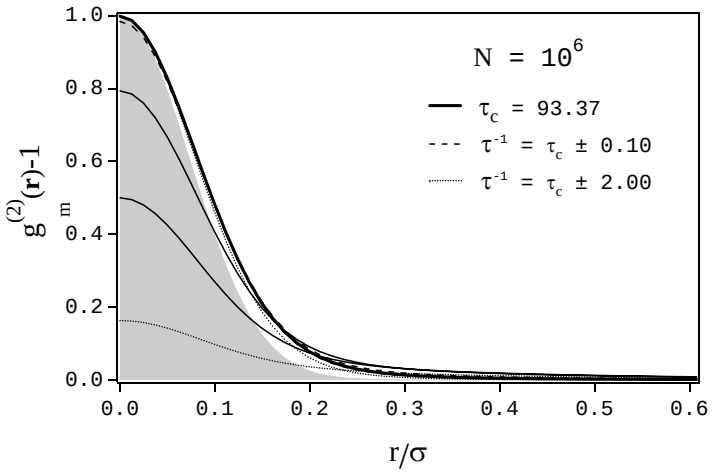

Figure 3.6: Two-body normalized correlation function $g_m^{(2)}(\mathbf{r})$ for 10^6 atoms confined in a isotropic harmonic trap for several different temperatures. The conditions are the same as for Fig3.4. $g_m^{(2)}(\mathbf{r})$ is an average of the two-body correlation function over the cloud. Unlike Fig.3.4, the shape is always almost Gaussian and converges more slowly to a flat correlation for low temperatures. See also text.

Another striking difference, between the curves in Figs.3.4 and 3.6 is the shape of their tails: $g_m^{(2)}(\mathbf{r})$ resembles a gaussian function even at the critical temperature, whereas $g^{(2)}(\mathbf{r}, \mathbf{0})$ has already a larger tail. The Graph *b*) of Fig.3.5 shows where this difference comes from. The more we displace the *center of measurement*, $\mathbf{r}_0$, away from the center of the cloud, the more the correlation function takes the on shape of a gaussian, even if the cloud is at the critical transition point. We can simply interpret this effect by observing that, locally at $\mathbf{r}_0$, the *effective chemical potential* is $\mu - V(\mathbf{r}_0)$. Thus, even if the cloud has a fugacity close to one, the *local density approximation effective fugacity* is smaller and, locally, the cloud behaves as a thermal cloud.

Although containing less information than a simple non-integrated correlation function, the bunching and *RMS* waist of $g_m^{(2)}(\mathbf{r})$ shows an interesting dependence on the temperature, across the critical transition point. This can be seen in the graphs of Fig.3.7. In particular, the *coherence length* of the curve (identified here as the $1/e^2$ waist of the correlation function) increases much more rapidly with the decreasing of the temperature, when this latter is below T_c.

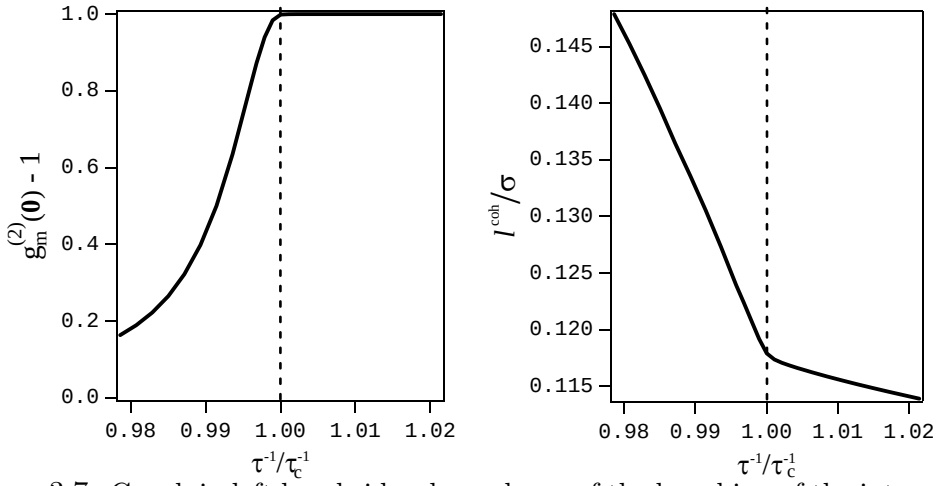

Figure 3.7: Graph in left hand side: dependence of the bunching of the integrated two-body correlation function on the temperature for an isotropic harmonically trapped cloud with 10^6 atoms; right hand side graph: variation of the *RMS* waist of the same function when the temperature crosses the critical point. This graph shows that there is a clear change in the dependence of this l on temperature in each side of its critical value.

3.4 Correlations in a harmonically trapped cloud after expansion

The previous Section has considered correlation functions within the trap. Here we consider them after the cloud's expansion. We first distinguish two different ways to measure the correlation function.

3.4.1 Detection: *Snap-shot* and *flux* measurement.

As in §2.2.1.1, where we have computed the atomic flux in a *time of flight* measurement, here we will also assume that the trap is switched off at $t = 0$ with the cloud expanding freely afterward and falling due to gravity. As before, we can consider two types of detection: a *snap shot* or *flux* measurement.

• Snap shot

Here, an image is taken after a expansion time t_0. Most commonly the imaging technique is based on an acquired absorption image and so one has access to the above correlation functions integrated along the imaging beam axis. This is the case of, for example, the experiments of Refs.[106, 107]. In this case, the relevant quantity is

$$G^{(2)}_{im.}(\mathbf{r}, t_0; \mathbf{r}, t_0) = \langle \hat{\Psi}^\dagger(\mathbf{r}, t_0)\hat{\Psi}(\mathbf{r}, t_0)\hat{\Psi}^\dagger(\mathbf{r}, t_0)\hat{\Psi}(\mathbf{r}', t_0)\rangle.$$

• **Flux measurement**

The atoms are detected when they cross a given plane. As for the *TOF*, we will only consider the situation in which this plane is horizontal at $z = H$. Here the measurable second order correlation function takes the form of a intensity-intensity correlation function,

$$G^{(2)}_{fl.}(\mathbf{r} = \{x, y, z = H\}, t; \mathbf{r} = \{x', y', z' = H\}, t') = \langle \hat{I}(\mathbf{r}, t)\hat{I}(\mathbf{r}', t')\rangle$$

where $\hat{I}$ is the flux operator defined in Eq.2.54. This type of measurement corresponds more closely to the experiment of Ref.[94] and, also, the one we have realized, both using a MCP. In Yasuda's experiment only the arrival times of the atoms were recorded; in ours, we also record their locations when they arrive at the detector (see §3.5.2.1). Intensity-intensity correlation measurements were also performed in the experiment of Ref.[108], in which the transmission of a high finesse optical cavity records atoms as they cross the beam and it also corresponds closely to imaging a cloud that crosses a thin sheet of light, an experiment reported in Ref.[109]. The two correlation functions are different, but if the detection is performed after a long time of flight, they are in fact nearly equivalent. We will discuss this equivalence in the following.

3.4.2 Second order correlation function of a expanded cloud in a snap shot measurement.

The calculation of the second order correlation function of a expanded cloud in both the snap shot case and the flux measurement are described in detail in Ref.[52]. In here we will briefly present these calculations.

The snap-shot correlation function is

$$G^{(2)}_{im.}(\mathbf{r}, t; \mathbf{r}', t) = \sum_{\mathbf{j},\mathbf{k},\mathbf{l},\mathbf{m}} \psi^*_{\mathbf{j}}\psi_{\mathbf{k}} \times \psi'^*_{\mathbf{l}}\psi'_{\mathbf{m}}\ \langle \hat{a}^\dagger_{\mathbf{j}}\hat{a}_{\mathbf{k}}\hat{a}^\dagger_{\mathbf{l}}\hat{a}_{\mathbf{m}}\rangle,$$

where, in order to simplify our notation, we used $\psi_{\mathbf{m}} \equiv \psi_{\mathbf{m}}(\mathbf{r}, t)$ and $\psi'_{\mathbf{m}} \equiv \psi_{\mathbf{m}}(\mathbf{r}', t')$ and similarly for the complex conjugated expressions. Using Eq.(2.62), we find, without any approximation (except the neglect of the shot-noise term) the expression[52]

$$G^{(2)}_{im}(\mathbf{r}, t; \mathbf{r}', t) = \frac{1}{\prod_\alpha (1 + \omega^2_\alpha t^2)} \left[n(\tilde{\mathbf{r}})n(\tilde{\mathbf{r}}) + |G^{(1)}(\tilde{\mathbf{r}}, \tilde{\mathbf{r}}')|^2 - n_0(\tilde{\mathbf{r}})n(\tilde{\mathbf{r}}')\right],$$

where $\tilde{\mathbf{r}}$ are the re-scaled coordinates defined before in Eqs.2.63. As in the case of the expression for the cloud's density after ballistic expansion, the snap-shot second order correlation function is equal to the one found for a trapped cloud if we re-scale the coordinates and include also the scaling factor $\left[\prod_\alpha (1 + \omega^2_\alpha t^2)\right]^{-1}$.

3.4.3 Intensity-intensity correlation function of a expanded cloud.

The calculation of $G^{(2)}_{fl.}$ is just a generalization of the expression in Eq.2.55, the atomic flux to second order,

$$\langle \hat{I}(\mathbf{r},t)\hat{I}(\mathbf{r},t')\rangle = -\left(\tfrac{\hbar}{2M}\right)^2 \sum_{\mathbf{j,k,l,m}} [\psi^*_{\mathbf{j}}(\partial_z\psi_{\mathbf{k}}) - (\partial_z\psi^*_{\mathbf{j}})\psi_{\mathbf{k}}] \times [\psi'^*_{\mathbf{l}}(\partial_z\psi'_{\mathbf{m}}) - (\partial_z\psi'^*_{\mathbf{l}})\psi'_{\mathbf{m}}]\ \langle \hat{a}^\dagger_{\mathbf{j}}\hat{a}_{\mathbf{k}}\hat{a}^\dagger_{\mathbf{l}}\hat{a}_{\mathbf{m}}\rangle \quad (3.28)$$

To obtain a more explicit expression for this quantity, we will start by rewriting the flux operator (cf. Eq.2.54),

$$\hat{I}(\mathbf{r},t) = \sum_{\mathbf{j,k}} \left[v_2\psi^*_{\mathbf{j}}\psi_{\mathbf{k}} - \frac{1}{2}\left(v_3\sqrt{k}\psi^*_{\mathbf{j}}\psi_{\mathbf{k-1_z}} + v^*_3\sqrt{j}\psi^*_{\mathbf{j-1_z}}\psi_{\mathbf{k}}\right)\right]\ \hat{a}^\dagger_{\mathbf{j}}\hat{a}_{\mathbf{k}}$$

with the velocities v_2 and v_3 defined as in Eq.2.66 and where we have also used the definition $\mathbf{j}-\mathbf{1_z}$ for the vector $(j_x, j_y, j_z - 1)$. The second order correlation function of the flux is then,

$$\begin{aligned}\langle \hat{I}(\mathbf{r},t)\hat{I}(\mathbf{r}',t')\rangle \ &= \\ \sum_{\mathbf{j,k,l,m}} &\left[v_2\psi^*_{\mathbf{j}}\psi_{\mathbf{k}} - \tfrac{1}{2}\left(v_3\sqrt{k_z}\psi^*_{\mathbf{j}}\psi_{\mathbf{k-1_z}} + v^*_3\sqrt{j_z}\psi^*_{\mathbf{j-1_z}}\psi_{\mathbf{k}}\right)\right] \times \\ &\left[v'_2\psi'^*_{\mathbf{l}}\psi'_{\mathbf{m}} - \tfrac{1}{2}\left(v'_3\sqrt{m_z}\psi'^*_{\mathbf{l}}\psi'_{\mathbf{m-1_z}} + v'^*_3\sqrt{l_z}\psi'^*_{\mathbf{l-1_z}}\psi'_{\mathbf{m}}\right)\right] \times \langle \hat{a}^\dagger_{\mathbf{j}}\hat{a}_{\mathbf{k}}\hat{a}^\dagger_{\mathbf{l}}\hat{a}_{\mathbf{m}}\rangle.\end{aligned}$$

Neglecting shot-noise and ground-state contribution, this leads to

$$\langle \hat{I}(\mathbf{r},t)\hat{I}(\mathbf{r}',t')\rangle = \langle \hat{I}(\mathbf{r},t)\rangle\langle \hat{I}(\mathbf{r}',t')\rangle + Re(A) \quad (3.29)$$

where

$$A \equiv \sum_{\mathbf{j,l}} \left\{ \begin{array}{c} v_2v'_2\,\psi^*_{\mathbf{j}}\psi'_{\mathbf{j}}\psi_{\mathbf{l}}\psi'^*_{\mathbf{l}} \\ +\frac{1}{2}v_3v'_3\,\sqrt{j_zl_z}\,\psi^*_{\mathbf{j}}\psi'_{\mathbf{j-1_z}}\psi_{\mathbf{l-1_z}}\psi'^*_{\mathbf{l}} \\ +\frac{1}{2}v_3v'^*_3\,l_z\,\psi^*_{\mathbf{j}}\psi'_{\mathbf{j}}\psi_{\mathbf{l-1_z}}\psi'^*_{\mathbf{l-1_z}} \\ -v_2v'_3\,\sqrt{j_z}\,\psi^*_{\mathbf{j}}\psi'_{\mathbf{j-1_z}}\psi_{\mathbf{l}}\psi'^*_{\mathbf{l}} \\ -v'_2v_3\,\sqrt{l_z}\,\psi^*_{\mathbf{j}}\psi'_{\mathbf{j}}\psi_{\mathbf{l-1_z}}\psi'^*_{\mathbf{l}} \end{array} \right\} \times \langle \hat{a}^\dagger_{\mathbf{j}}\hat{a}_{\mathbf{j}}\rangle\langle \hat{a}^\dagger_{\mathbf{l}}\hat{a}_{\mathbf{l}}\rangle. \quad (3.30)$$

Two major differences appear compared to the mean flux calculation: in this latter expression, the terms in v_3, which comes from the derivative of Eq.2.65 and the phase factor [7] $\delta_\alpha + 3\pi/2$ in Eq.(2.62) does not cancel. This makes the exact calculation of the the intensity correlation function cumbersome.

[7] Recall that $\delta_\alpha = \tan^{-1}(1/\omega_\alpha t)$ (cf.2.2.1.2).

On the other hand, if the *far field* (*f.f.*) and *long fall* (*l.f.*) approximations hold (cf.2.2.2), we see from the expression on the Eq.2.66 that

$$\frac{v_3}{v_2} = \frac{1}{\sqrt{2}}\frac{\sigma_z}{H} \ll 1, \tag{3.31}$$

and only the the first term of Eq.3.30 has a non neglectable contribution for the intensity correlation function. It can be proved[52], that keeping only this term leads to an expression for $\langle \hat{I}(\mathbf{r},t)\hat{I}(\mathbf{r}',t')\rangle$ which is sufficiently accurate to interpret all experimental data we may obtain with our experimental apparatus.

3.4.3.1 Explicit calculation of the flux correlation function within the *far field* and *long fall* approximations.

In the following we will evaluate Eq.3.29 considering only the first term of Eq.3.30. This latter is given by

$$\begin{aligned} T_1 &= v_2 v_2' \sum_{\mathbf{j},\mathbf{l}} \prod_{\alpha} \frac{e^{i(j_\alpha - l_\alpha)(\delta_\alpha' - \delta_\alpha)}}{\sqrt{(1+\omega_\alpha^2 t^2)(1+\omega_\alpha^2 t'^2)}}\ \tilde{\psi}_{\mathbf{j}}\tilde{\psi}_{\mathbf{j}}'\tilde{\psi}_{\mathbf{l}}\tilde{\psi}_{\mathbf{l}}'\ \langle \hat{a}_{\mathbf{j}}^\dagger \hat{a}_{\mathbf{j}}\rangle\langle \hat{a}_{\mathbf{l}}^\dagger \hat{a}_{\mathbf{l}}\rangle \\ &= \frac{v_2 v_2'}{\prod_\alpha \sqrt{(1+\omega_\alpha^2 t^2)(1+\omega_\alpha^2 t'^2)}} \left| \sum_{\mathbf{j}} \tilde{\psi}_{\mathbf{j}}\tilde{\psi}_{\mathbf{j}}'\, e^{i\mathbf{j}.\mathbf{\Delta}} \langle \hat{a}_{\mathbf{j}}^\dagger \hat{a}_{\mathbf{j}}\rangle \right|^2, \end{aligned} \tag{3.32}$$

where $\tilde{\psi}_{\mathbf{m}} \equiv \psi_{\mathbf{m}}(\tilde{\mathbf{r}})$ is the harmonic oscillator wave function with re-scaled coordinates and the following definitions have been used in the last line,

$$\Delta_\alpha = \delta_\alpha' - \delta_\alpha \quad \text{and} \quad \sum_\alpha j_\alpha(\delta_\alpha' - \delta_\alpha) = \mathbf{j}.\mathbf{\Delta}. \tag{3.33}$$

The modulus squared term in the last line may be seen as the first order correlation function with an additional phase term. Using the temperature Green function, in Eq.2.18, this term can be written as

$$\sum_{\mathbf{j}} \psi_{\mathbf{j}}\psi_{\mathbf{j}}'\, e^{i\mathbf{j}.\mathbf{\Delta}} \langle \hat{a}_{\mathbf{j}}^\dagger \hat{a}_{\mathbf{j}}\rangle = \sum_l Z^l\ G^{ho}(\tilde{\mathbf{r}}, \tilde{\mathbf{r}}', \{l\tau_\alpha - i\Delta_\alpha\}). \tag{3.34}$$

• Further simplification within the *far field* and *long fall* approximations.

The exact evaluation of this expression may be obtained numerically in a case to case analysis but with no trivial analytical and general result. However, again within the validity of the *f.f.* and the *l.f.* approximations, this expression can be further simplified.

Using the *f.f.* followed by the *l.f.* approximations, the first expression in the Eq.3.33 can be written as

$$\Delta_\alpha \simeq \frac{1}{\omega t'} - \frac{1}{\omega t} \simeq \frac{1}{\omega_\alpha t_0}\frac{\delta t}{t_0},$$

where, in the first identity, we used the approximations $\delta_\alpha \approx 1/\omega_\alpha t$ and $\delta'_\alpha \approx 1/\omega_\alpha t'$ and in the second $\delta t = t - t' \ll t_0$, with the usual definition for the time of fall $t_0 = \sqrt{2H/g}$.

The evaluation of Δ_α involves the estimation of δt, whose maximum value is of the order of what we may call the *time observation window*, in analogy with what was written before in §2.2.2.2 within the derivation of the atomic flux formulae. There, δt was compared with the time spread of the cloud, t_{cl}. Here, this time window scales rather with the expanding cloud's *coherence time*, $t^{coh}(t)$. We will show in the next paragraph that its expression is

$$t^{coh} = \frac{\lambda_T \omega_z}{g} \tag{3.35}$$

where $\omega_z \equiv \omega_\perp$ is the trap oscillation frequency in the Oz fall direction. We can now compare the two quantities in the Green's function argument in Eq.3.34, which also scales as the ratio in the above Eq.3.31

$$\frac{\Delta_\alpha}{\tau_\alpha} \lesssim \frac{\sigma_\alpha}{H} \ll 1.$$

For most experiments this ratio is vanishingly small (in our experiment, it is smaller than 10^{-5}) and the phase term proportional to Δ_α in Eq.3.34 may be neglected.

Within the above approximations, the intensity correlation function takes the simple form of

$$\langle I(\mathbf{r},t;\mathbf{r}',t')\rangle = \frac{v_2 v'_2}{\prod_\alpha \sqrt{(1+\omega_\alpha^2 t^2)(1+\omega_\alpha^2 t'^2)}} \left[n(\tilde{\mathbf{r}})n(\tilde{\mathbf{r}}') + |G^{(1)}(\tilde{\mathbf{r}},\tilde{\mathbf{r}}')|^2 - n_0(\tilde{\mathbf{r}})n_0(\tilde{\mathbf{r}}')\right] \tag{3.36}$$

Again, we find the same correlation function as in the trap, here with the rescaling pre-factor slightly different from the one of $G^{(2)}_{im.}$, reflecting also the expansion of the cloud between the times t and t'. The corresponding normalized correlation function obtained using Eq.2.68 is

$$\begin{aligned} g^{(2)}(\mathbf{r},t;\mathbf{r}',t') &= \frac{\langle I(\mathbf{r},t;\mathbf{r}',t')\rangle}{\langle I(\mathbf{r},t)\rangle\langle I(\mathbf{r}',t')\rangle} \\ &= 1 + \frac{|G^{(1)}(\tilde{\mathbf{r}},\tilde{\mathbf{r}}')|^2 - n_0(\tilde{\mathbf{r}})n_0(\tilde{\mathbf{r}}')}{n(\tilde{\mathbf{r}})n(\tilde{\mathbf{r}}')}. \end{aligned} \tag{3.37}$$

This expression is the equivalent of Eq.3.26 for an intensity correlation measurement. Except for the coordinate re-scaling of Eq.3.37, this expression is equal to Eq.3.26 and can be interpreted in the same manner (cf. §3.3).

Coherence lengths at the detector.
The transverse coherence length and the temporal coherence can be easily derived from Eq.3.37, taken at the high temperature limit. This results in the flux equivalent of Eq.3.25,

$$g^{(2)}(\delta x, \delta y, \delta t) = 1 + \exp\left[-\left(\frac{\delta\tilde{\mathbf{r}}}{l}\right)^2\right], \tag{3.38}$$

with $\delta x = x - x'$, $\delta y = y - y'$ and $\delta t = t - t'$. Using the definitions of the coordinate rescaling we obtain, straightforwardly the relation

$$l_\alpha(t) = l \times \sqrt{1 + (\omega_\alpha t)^2} \sim \frac{\lambda_T}{\sqrt{2\pi}}\,\omega_\alpha t, \tag{3.39}$$

confirming the scaling laws obtained previously by simple considerations in Eqs.3.8.

The time dependent argument of Eq.3.38 is

$$\frac{\tilde{z} - \tilde{z}'}{l_z} = \frac{\frac{1}{2}g(t^2 - t'^2)}{\sqrt{1 + (\omega_z t)^2 l}} \simeq \frac{g\delta t}{l\omega_z},$$

where in the last step we have used the *f.f.* and *l.f.* approximations. Note that in absence of gravity this expression modifies to

$$\frac{g\delta t}{l\omega_z}\frac{v_T}{v_G} = \frac{v_T\delta t}{l\omega_z t} = \frac{\delta z}{l\omega_z t}$$

which corresponds to have the same coherence length as the one of Eq.3.39. Thus, the temporal coherence is just the equivalent, in time, of the coherence length in the other two spatial directions modified by the *gravitational compression*. It is given by

$$t^{coh}(t) = l\frac{\omega_z}{g}. \tag{3.40}$$

This expression states that the *coherence time* remains independent of the propagation time as long as the *far field* and the *long fall* approximations are valid.

3.4.4 Conclusion.

One of the main results of former analysis is that the *volume of coherence* expands linearly in time at the same rate as the cloud itself. So, even at $T = T_c$, the time varying correlation lengths are well approximated by:

$$l_\alpha(t) = l_\alpha(0) \times \omega_\alpha t.$$

This may be interpreted in many different and simple ways.

We may consider the analogy with optical speckle. Increasing the time of flight corresponds to increasing the propagation distance to the observation plane in the optical analog. The speckle size, *i.e.* the correlation length, obviously increases linearly with the propagation distance.

Another way to understand the time dependence is to remark that after release, the atomic cloud is free and the phase space density should be constant. Since the density decreases with time as $\prod_\alpha(\omega_\alpha t)$ and the spread of the velocity distribution is constant, the correlation volume must increase by the same factor [110].

Yet another way to look at the correlation length is to observe that, far from degeneracy, the correlation length inside the trap is the thermal de Broglie wavelength, that is,

$$l = \frac{\lambda}{\sqrt{2\pi}} = \hbar/\Delta p$$

where $\Delta p = m\Delta v$ is the momentum width of the cloud. By analogy, after expansion, the correlation length is

$$l(t) = \hbar/(\Delta p)_{loc},$$

where $(\Delta p)_{loc}$ is the *local* width of the momentum distribution. As the pulse of atoms propagates, fast and slow atoms separate, so that at a given point in space the width in momentum is reduced by a factor $\frac{s_\alpha}{\Delta v t}$.

3.5 The *HBT* experiment with He^*.

In this Section we describe briefly our *HBT* experiment made with a cloud of cold metastable helium atoms. As already emphasized in Chapter 1, our setup is very suited for this type of measure since it is possible to detected single He^* atoms. However, to make it possible, we had to upgrade our apparatus with a new `MCP` based detector, different from the one described in Chapter 1, capable of resolving the clouds' atomic flux not only in time but also capable of imaging it in the fall's transversal direction. This detector was used only in this experiment. A detailed description of it and all of its electronic circuitry can be found in the Ph.D. thesis of M. Schellekens[50]. The Ph.D. thesis of R. Hoppeler[49] also reports on this and, also, on all the modifications we have done in the experiment to house this detector. In this Section we will describe some preliminary calculations, based on the results derived in the previous Section, showing that the correlations measurements can be carried out in our experiment (also included in Ref.[49]). Most of the discussion is centered on the estimation of the visibility of the bunching and on its *signal-to-noise* ratio (*SNR*).

Before starting with our experiment, we will briefly refer others realization of *HBT* type of experiments done with massive particles. Among these we will highlight recent achievements done with cold atoms, both bosons and fermions.

3.5.1 State of the art on *HBT* measures with massive particles.

If we compare with the standard optics experiments, *HBT* measurements done for massive particles are richer because these can be either Bosons or Fermions, they often have a more complex internal structure and a large range of possible interactions with each other. Some correlation measurements carried out in the field of nuclear physics are reported in Refs.[111, 112] (see also review texts of Ref.[113, 114, 115]) and for low energy electrons in Refs.[116, 117].

These type of experiments were first realized with neutral atomic species by Yasuda *et al.*[94], soon after the first realization of a *BEC* in a cold atomic gas. It was done, however, only with a non-degenerated gas.

More recently a wide variety of different situations have been studied with degenerated bosonic gases [118, 107, 106, 108, 119] and also ours[84] which, for he first time, evidenciate in the same experiment the different behavior of the correlation function on degenerated and non-degenerated atomic clouds. Two very recent experiments demonstrated anti-bunching with fermionic atomic species[120, 121].

3.5.2 The *HBT* experiment with He*.

3.5.2.1 The *delay line* detector.

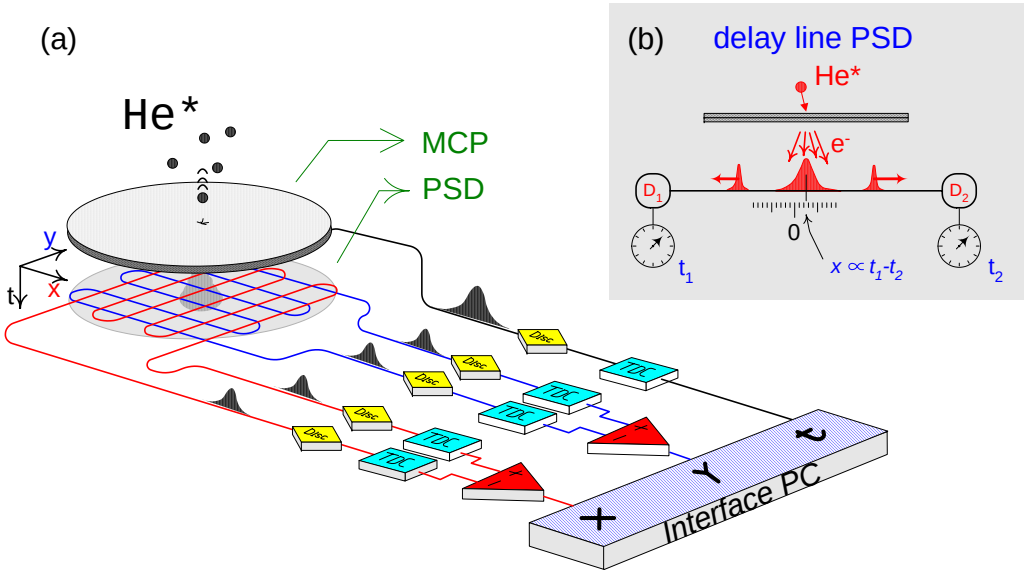

Figure 3.8: The detection system used in *HBT* experiment. It is made of two main parts: a `MCP` and a *delay line position sensitive detector* (`PSD`). The `MCP` used in this setup is larger than the one describe in Chapter 1 and placed further down from the trap's center ($H \approx 470$ mm). The `PSD` is placed bellow the `MCP` and is used to record the atoms' location hitting the `MCP`. It is made of two long wires displaced as shown in the main image. Its working principle is summarized in the inset Figure. The amplified charge generated by the `MCP` when it detects an atom is collected by two wires (the *delay lines*) placed below the `MCP`. This charge propagates to both ends of these wires and, depending on the location of the incident atom, the resulting signals arrives at the *time-to-digital converters* (`TDC`), at different times. By computing this time difference it is possible to infer the location where the charge was generated. The system with two delay lines use four discriminators(`Disc`) and `TDC`s. This is equivalent to have a discrete anode detector with 10^5 *pixels* with a spatial resolution of about 250 μm. Another chain with a `Disc` and a `TDC` is used to get the absolute time arrival of the atoms, with a resolution of less than 1 ns.

As referred above, our *HBT* experiment was implemented in our original setup (described in Chapter 1) with a new detector sensitive to both the time of arrival but also to their location in the transversal plane. The determination of the atoms' locations is of particular importance since the transversal coherence length (cf. Eq.3.39) is much smaller than the size of the detector. Thus, the simultaneous detection of several *volumes of coherence* in just one

detector washes out the bunching.

To see this, consider the calculation of the bunching contrast (with $\delta t = 0$) of the a density normalized correlation signal on the high-temperature limit and integrated over a detector's surface S_D. This is given by

$$g^{(2)}(\delta t = 0) - 1 = \frac{\int_{S_D} \left| G^{(1)}(d\tilde{\mathbf{r}}, d\tilde{\mathbf{r}}') \right|^2 d\tilde{\mathbf{r}}\, d\tilde{\mathbf{r}}'}{\int_{S_D} n(d\tilde{\mathbf{r}}) d\tilde{\mathbf{r}} \times \int_{S_D} n(d\tilde{\mathbf{r}}') d\tilde{\mathbf{r}}'}$$

where we used $\tilde{\mathbf{r}} = \{\tilde{x}, \tilde{y}\}$, with also Eqs.3.24 and 2.23 for $G^{(1)}(x, x')$ and $n(x)$ respectively. Note that, in this expression, we have not considered the time resolution of the detector because this one is much smaller than the cloud's time of coherence. For a very large detector (when compared with the atomic cloud), this expression simplifies to

$$g^{(2)}(\delta t = 0) - 1 = \frac{l_x(t)}{s_x \omega_x t} \frac{l_y(t)}{s_y \omega_y t} = \frac{l^2}{s_x\ s_y}, \tag{3.41}$$

which states that the bunching contrast is proportional to the ratio between an area of coherence l^2 and the transversal section of the atomic cloud $s_x \times s_y$ [8]. This ratio is also given by $\tau_x \tau_y$ which is, in our experiment, about 10^{-4}. To measure this signal, we would need a comparable *signal-to-noise* (*SNR*) which is, in practice, very difficult to achieve.

The working principle of the detector we used is sketched in Fig.3.8 (more detailed information may be found in Refs.[122, 123]). A `MCP` [9] is used to generate an amplified signal charge that is collected by the *delay line*, two long wires wrapped up in orthogonal directions in squared structure assembled below the `MCP`. By measuring the time of arrival of the charge at the ends of these two wires we can compute where the charge was collected. The spatial resolution of this device is of about 250 μm. The measure of the time of arrival of the atoms is done directly on the `MCP` signal with a time resolution that can be smaller than one nanosecond. As referred earlier, this value is several orders of magnitude smaller than the cloud's temporal coherence, a few hundreds of microseconds.

3.5.2.2 The *bunching contrast* in function of the pixel size.

A similar result to the one of Eq.3.41 can be also derived for a finite detector[52]. If this one is much smaller than the cloud, as in the case of our experiment, the

[8] If we had integrated also the the longitudinal direction, we would find a generalization of this as the ratio of the cloud and the coherence volumes. Note also that this expression is valid for both the expanding and the trapped cloud, since its size and the volume of coherence grow in time at the same rate.

[9] We use a `MCP` manufactured by `Burle`, model 33845.

bunching contrast depends rather on the ratio between the coherence lengths and the pixel size. In our experiment $l_x(t) \ll d \approx l_z(t)/4$ and, to simplify the derivation, we approximate the observed contrast to (cf. Ref.[52])

$$g^{(2)}(\delta t = 0) - 1 \simeq \frac{l_x(t_0)}{2d}, \tag{3.42}$$

which corresponds to the limit of $l_x(t) \ll d \ll l_z(t)$. This expression shows that we may increase the bunching contrast by using a small enough detector. However, if we used a detector with a size comparable to $l_x(t_0) < 1$ μm, only a very small portion of the atoms would be detected (the expanded cloud has a few millimeters) decreasing drastically the *SNR*, as we show in the following Section.

The PSD device, described above, allows detecting most of the atoms without compromising the bunching contrast. Each PSD's *pixel* may be considered as a single detector and the entire PSD as an ensemble of about 10^5 independent detectors, juxtaposed side by side. Using the approximate expression of Eq.3.42 for computing the bunching contrast of a cloud at $T = 1$ μK we obtain $g^{(2)}(\delta t = 0) \approx 5\%$.

3.5.3 A simple derivation of the *signal-to-noise* ratio.

The experimental procedure of the experiment we describe in here is, conceptually, very simple: after producing an atomic cloud at a given temperature, we release it over the detector and record all time instants and correspondent locations at the detector for each detected atom.

The intensity correlation function is obtained then, making the histogram of all the *time delays* between two different events. To get a better idea of this, suppose that the atomic flux may be represented as a sum of N time dependent delta functions,

$$I(t) = \sum_{i=1}^{N} \delta(t - t_i),$$

each one corresponding to the arrival of an atom. The auto-correlation function of this quantity is, by definition, equal to

$$\begin{aligned} h(\delta t) &= \int_{-\infty}^{+\infty} I(t)I(t+\delta t)\, dt \\ &= \int_{-\infty}^{+\infty} \sum_{i,j} \delta(t - t_i)\delta(t - \delta t - t_j)\, dt \\ &= 2\sum_{i>j} \delta(|t_i - t_j| - \delta t), \end{aligned}$$

where, in the last line, it is written a count of the pairs of atoms arriving with a *time-delay* equal to a certain δt. This is just the value of an histogram of these *time-delays*, a function of δt.

In practice, we need to consider a finite time binning t_{bin} for the histogram and the last expression modifies to

$$h(\delta t) \to h_k = 2\sum_{i>j} \Theta\left[kt_{bin} < |t_i - t_j| < (k+1)t_{bin}\right],$$

with $\Theta(x)$ equal to one x is true and zero otherwise. t_{bin} determines the number of points of the histogram *inside* the bunching and, also, the *SNR* of the observed signal. To derive this latter quantity we will use some approximations that rends its computation rather simple. First, we will simplify the analysis by calculating the noise for fictitious uncorrelated cloud (we neglect the bunching to calculate the noise) and at temperatures much larger than the transition temperature. Second, we will assume that the uncertainty in the counting of the histogram follows a Poissonian law and, then, for N_k counts an estimated *error* of $\sqrt{N_k}$. Finally, we will assume that the atomic cloud has a homogenous density distribution with a time extension $t_{cl} = \frac{v_T}{g}$ (cf. Eq.2.70) and transversal section equal to $s(t_0) = v_T t_0$ (cf. Eq.2.69).

On average, each one of PSD's pixels will detected, during the whole *TOF*, a number of atoms that is, approximatively, given by $N_p = \eta N \left(d/s(t_0)\right)^2$ where ηN is the number of detected atoms and d, the pixel size, which we will also assume to be equal to the separation between contiguous pixels. Then the mean number of pairs of events per detector is $n_p = \frac{1}{2}N_p(N_p - 1)$ and the number of pairs for the whole detector is then

$$n_{all} = \left[\frac{s(t_0)}{d}\right]^2 n_p = \eta^2 N^2 \left[\frac{d}{s(t_0)}\right]^2.$$

The histogram contains this amount of pairs.

The calculation of the *SNR* is now straightforward. In the few first bins of the histogram, where the bunching manifests, its amplitude is of about

$$h_0 = n_{all}\frac{t_{bin}}{t_{cl}} = \frac{\eta^2 N^2}{n_b}\frac{d^2}{s(t_0)^2}\tau_z \tag{3.43}$$

where, as usually, $\tau_\alpha = \hbar\omega_\alpha/k_B T$ [10] and $n_b = t^{coh}/t_{bin}$ is the number of histogram bins inside the bunching region. The signal *noise* is given by $\sqrt{h_0}$. Our goal is to detect the bunching which is, in number of counts, equal to $\left[g^{(2)}(0) - 1\right] \times h_0$. If we assume that the uncertainty of this counting is similar

[10] Note that $\tau_\alpha = t_{coh}/t_{cl} = (2\pi)^{-1/2}\lambda_T/s_\alpha$.

to those corresponding to the uncorrelated pairs and using Eq.3.42 for the bunching contrast, we obtain for the *SNR* the expression

$$\begin{aligned} SNR_1 &= \left[g^{(2)}(0)-1\right] \times \frac{h_0}{\sqrt{h_0}} \\ &= \frac{1}{2}\frac{\eta N}{\sqrt{n_b}}\tau_x\sqrt{\tau_z} \end{aligned} \tag{3.44}$$

This expression shows that the *signal-to-noise* decreases with the temperature and the number of bins used to *resolve* in time the bunching. It increases with increasing number of detected atoms.

3.5.4 Exact results for the *SNR* in the high temperature limit.

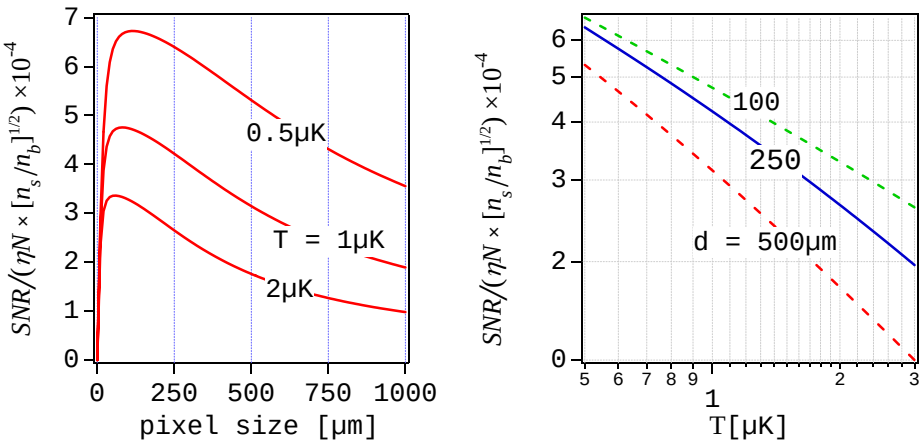

Figure 3.9: These graphs plots $SNR/\eta N\sqrt{n_s/n_b}$, in function of temperature and pixel size. The *SNR* decreases for larger temperatures and pixel sizes. However, if the pixel size becomes too small, the number of pairs of atoms detected by each pixel becomes very small and, despite the larger bunching contrast, the *SNR* shoots down. For $T = 0.5\ \mu$K, the optimal value is $d \sim 100\ \mu$m.

The simple derivation of the *SNR* presented before gives a result that is overestimated by a factor of $4\pi^{3/4} \approx 10$ because we have not considered the cloud's density distribution. Moreover, the use of Eq.3.42 for the bunching contrast results in an expression for the *SNR* that is independent of the pixel size d which is in general not true. The exact expression for *SNR* in the high temperature limit case can be found replacing in Eq.3.44, for the bunching

contrast, the expression

$$g^{(2)}(\delta t = 0) - 1 = \prod_{\alpha} \sqrt{\frac{1 + d_\alpha^2/s_\alpha(t)^2}{1 + 4d_\alpha^2/l_\alpha(t)^2}},$$

and then dividing the obtained result by $4\pi^{3/4}$. In the Fig.3.9 we plot the resulting expressions for different temperatures and pixel sizes. These are computed for the case where the histogram is built using data form n_s different experimental realizations. This increases the *SNR* by a factor of $\sqrt{n_s}$ and should be done using data of clouds with similar temperature and fugacity, therefore with similar correlation functions. The left hand side graph shows that if the pixel size decreases too much, the *SNR* also decreases. Despite the bunching contrast increases for smaller values of d (see Fig.3.10), the number of delay times between pairs of atoms used in construction of the histogram decreases to zero and, then, also the *SNR*. Using our experiment's

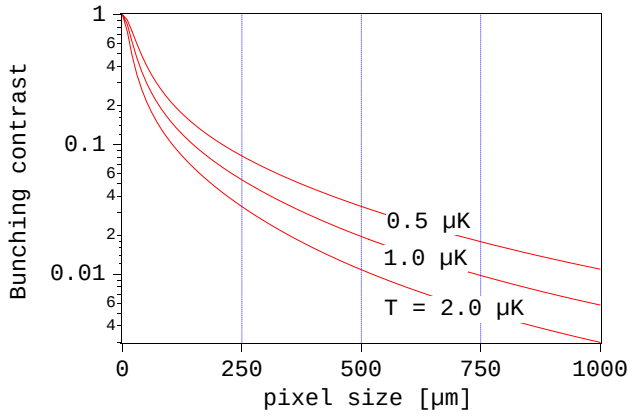

Figure 3.10: The bunching contrast in function of the pixel size, for three different temperatures.

parameters and for a typical number of detected atoms equal to $\eta N \lesssim 10^4$, 1000 different runs results in a *SNR* ≈ 2.5 with the bunching resolved within 10 histogram bins. This *SNR* should be enough to *see* the bunching.

3.5.5 The experimental results.

The derivation of the above result for the *SNR* showed that, if upgraded with the referred PSD detector, it should be possible to carry out a *HBT* experiment in our setup. This result was of great importance in the design of the new apparatus and proved to be correct. This can be seen in the graphs of Fig.3.11, reprinted from Ref.[84], where we plot the final results we have obtained in this experiment. The curves corresponds to four different cloud's

temperatures: three above the critical temperature (the three top graphs) and another for a degenerate cloud (bottom graph).

The temperature determination of the non-degenerate clouds was obtained form a fit to the corresponding *TOF* signals. The correlation signals were built with typically 1000 different shots with clouds of similar temperatures but paying no attention to their fugacities, all below $Z = 1$. The observed bunching contrast and *SNR* are approximatively equal to our estimative.

Finally, in the correlation curve of the degenerate case we observe, as expected, no bunching.

3.5.6 Conclusion.

In this Chapter initial Sections we try to show why measuring the density correlation at the vicinity of the critical temperature may become interesting. The results we have obtained so far doesn't explore this possibility as no sorting procedure was used for choosing clouds at the $T = T_c$. The task of sorting data regarding its fugacity and temperature is not trivial as we will try to demonstrate in the two following Chapters. We will present some data analysis technics that may help, in the future, observe how the particles correlation behaves at the *BEC* formation.

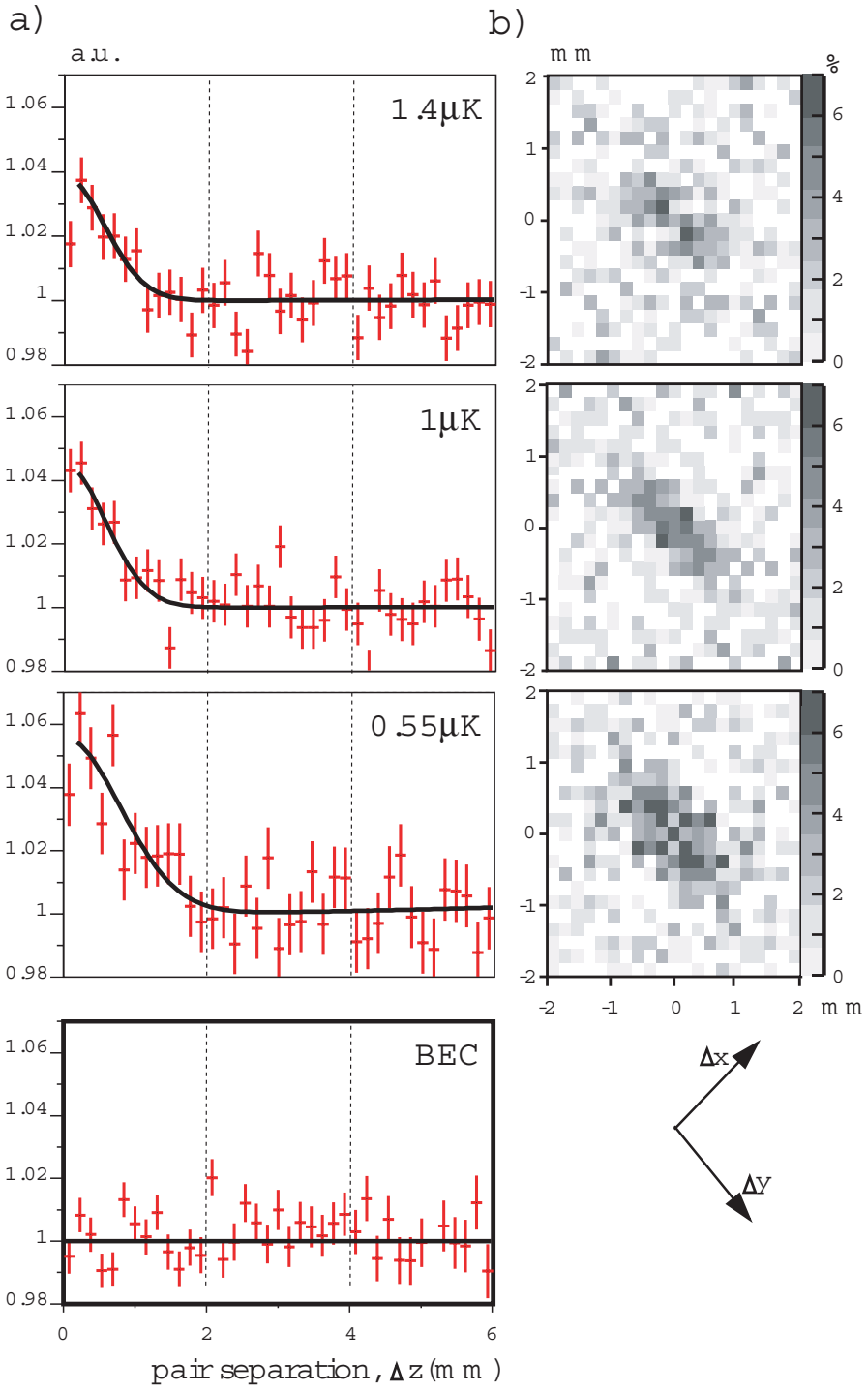

Figure 3.11: a) normalized correlation functions along the vertical (z) axis for thermal gases at three different temperatures and for a *BEC*. For the thermal clouds, each plot corresponds to the average of a large number of clouds at the same temperature. Error bars correspond to the square root of the number of pairs; b) Normalized correlation functions in the $\Delta x - \Delta y$ plane for the three thermal cloud cases. The arrows at the lower right show the 45° rotation of our coordinate system with respect to the axes of the detector. The inverted ellipticity of the correlation function relative to the trapped cloud is clearly visible. Figure from Ref.[84].

CHAPTER 4

Thermometry with ions and atoms: theoretical preliminaries.

4.1 Introduction

The propose of this Chapter is to go further in the theoretical description of both the ions flux generated inside the cloud, due to inelastic collisions involving He^* atoms, and also of the atomic *time of flight* signal. This is done with the goal of improving the thermometry of the cloud using these two signals.

The ion signal was briefly presented in Chapter 1. There, we were mostly concerned with the description of its detection. In here we will make a more detailed description of this signal and present the results of a simple model simulating the time evolution of the ion signal during the last ramp of the evaporative cooling. This period of time is of great importance since it includes the instant where the cloud undergoes the phase transition and also the growth of the *BEC*.

The analysis of the numerical results of this simulation allows a better understanding of the ion signal and helps to better interpret it in a real experimental realization. A major outcome of this model is the determination of the instant of time where the critical transition takes place. This information helped us to get a better control of the experimental procedure, in particular in experimental realizations where we needed to obtain clouds at the critical temperature. Another important result of this simulation establishes a relation between the bias fluctuation and the uncertainty in the determination of the cloud's fugacity.

Although very interesting and useful to visualize the evolution in *real time* of the cloud's density, the ion signal is not as suitable as the atomic *TOF* for determining its temperature and fugacity, due to the unavoidable run to run bias fluctuations. These have no influence in the *TOF*'s analysis which is for this reason a more reliable diagnostic technique to achieve an accurate thermometric characterization of the cloud.

In Chapter 2 we have presented a simple model for describing this signal for the ideal gas case. To get a more accurate determination of the cloud's temperature and fugacity we need to correct this model by including the effect of the interatomic interactions. In §4.3 of this Chapter, we will workout a model that describes a cloud of interactive atoms at thermal equilibrium in the mean field approximation. This will lead to the inclusion of corrective terms proportional to the He^* *s-wave* scattering length a.

The effect of interatomic interactions also affects the cloud's expansion after the trap switch-off, making the simple ballistic model derived in Chapter 2 slightly inaccurate. The initial moments of the cloud's expansion are very similar to the behavior of a classical fluid in a hydrodynamical regime. This behavior lasts only for a short period but is sufficient to impose a non negligible correction on the determination of cloud's temperature.

4.2 The ion signal.

In the first Chapter of this manuscript (cf. §1.3.4) we have shortly described the ion production mechanisms through Penning collisions. Ions may be produced in collisions between two or three He^* atoms or, most simply, in a collision involving only one He^* atom and a molecule from the background gas inside the science chamber. The *two-* and *three-body* processes are cloud density dependent and can therefore constitute a good diagnostic tool for measuring this quantity and its evolution during the evaporative cooling process. This is, as we pointed out in §1.3.4, a *real time*, *non destructive* and *absolute* measurement of the cloud's density: the spontaneously produced ions inside the cloud are detected at every time with a known efficiency.

The unique characteristics of the ion signal makes possible the observation of the *BEC* growth and provided the means for a direct measurement of collisional properties of the He^*. This was used in an experiment, discussed in the following Chapter, in which we have attempted to measure a, the He^* scattering length[46]. One other experiment was realized with the aim of determining β and L, the inelastic ionizing constants for the *two-* and the *three*-body processes[45]. The knowledge of these constants, along with the one for the simple Penning ionizations in collisions with the background gas, would allow us to fully characterize the ion signal. Unfortunately, the results we have obtained within these experiment are certainly affected by an experimental systematic error and are, for this reason, not very conclusive (this will also be further discussed in the following Chapter).

Along with the problem of a good determination of the ionizing rate constants, the ion signal analysis presents other difficulties if it is intended to be used in the cloud's thermometry. Since it is an overall cloud integrated signal, it doesn't contain information on the shape of the cloud but only on its average density. Thus, it is not possible to observe local variations of the cloud's density which are very important, especially at the cloud's center, for properly determine the cloud's temperature and fugacity [1].

As we have already referred, the ion signal is made of contributions of different collisional processes that depends on different powers of the density and thus, with different weights for denser or diluter clouds. We may question then if the *inverse problem* of finding the cloud's density from a given measured ion signal is feasible. The flux generated by a thermal cloud at its location $\mathbf{r}$ is

$$\Phi(\mathbf{r}_0) \propto \frac{1}{\tau_i} n_{th}(\mathbf{r}) + \frac{\beta}{2} n_{th}(\mathbf{r})^2 + \frac{L}{3} n_{th}(\mathbf{r})^3.$$

This expression shows that the *local* ion flux grows monotonically with the

[1] Note however that this could be overcome by using adequate ion optics and a spatially resolved ion detector as the `PSD` described in the previous Chapter.

density. This is a sufficient condition to allow obtaining a unique result for the cloud's density at the location $\mathbf{r}$, knowing the ion flux Φ.

If the rate constants β and L does not depend on the density (which is an *a priori* assumption), the above conclusion does also apply to the cloud integrated ion flux

$$\Phi = \frac{N_{th}}{\tau_i} + \tfrac{1}{2}\beta \int_{R^3} d\mathbf{r}\; n_{th}^2(\mathbf{r}) + \tfrac{1}{3} L \int_{R^3} d\mathbf{r}\; n_{th}^3(\mathbf{r}), \tag{4.1}$$

if the analytical form of $n_{th}(\mathbf{r})$ is known.

4.2.1 Ion signal during the last evaporative ramp.

As explained earlier in §1.2.1.3, in our experiment's evaporative cooling, the frequency of the *rf*-field is ramped down from 130 MHz to around 1 MHz, where the condensation takes place. This is done throughout four linear ramps as represented in the Fig.1.6. The physics involved in the last ramp is by far the more interesting of all since it involves the crossing over the critical phase transition and also the *BEC* growth[124]. These phenomena can be followed in real time through the observation of the ion signal.

In Fig. 4.1 we show the evolution of the ion rate starting 2 seconds before the end of the *rf-ramp*, where the *pure BEC* is formed [2]. We also show the corresponding *TOF* signals in five different instants of time before $t = 0$. In the first part of the curve (the darker curve), between $t = -2s$ to $t = 0$, the ramp frequency was varied linearly from $1.4MHz$ to $1MHz$.

The interpretation of these graphs suggests two remarks:

- The comparison of the *TOF* and ion signals shows that the appearance of a narrow structure in the *TOF* signal corresponds to an abrupt change in the slope of the ion signal, indicating then the critical instant of the *BEC* threshold. This is the typical behavior observed in a phase transition.

- The *pure BEC* (last inset graph) occurs only after the ion signal has passed through its maximum value. Since the ion signal is proportional to the cloud's density, it could give the impression that the *pure BEC* does not correspond to the densest cloud possible. For a fixed number of atoms this is indeed the case: the evaporation ejects continuously atoms out of the trap and, despite the relative increase of cloud's density towards the *BEC*, at the end the number of trapped atoms is largely reduced leading also to a decrease of the ion flux.

[2] The term *pure BEC* here is, some how, not well defined since it is difficult to say when a *TOF* corresponds effectively to the situation where $T = 0$ (see details in §B.1.1 of Appendix B). In the following we will refer as *pure BEC* a cloud where the thermal cloud is not visible in the *TOF*.

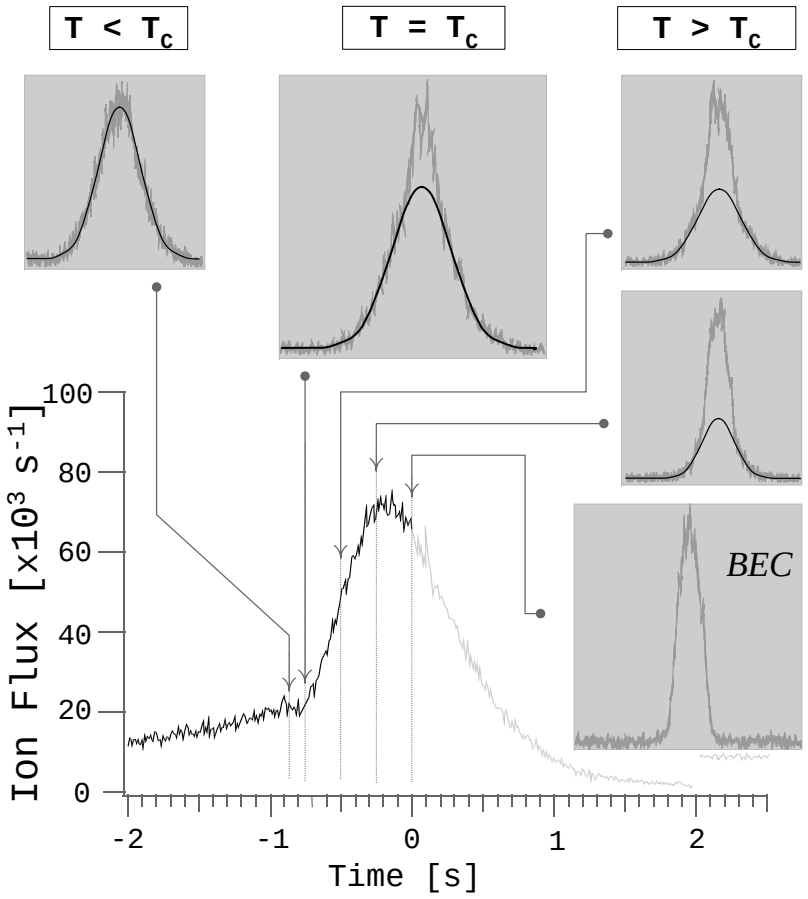

Figure 4.1: A single-shot measurement of the ions flux. The black part of the curve correspond to the last rf-ramp, where the *rf*-frequency ramps down from $1400kHz$ at $t = -2s$ to $1000kHz$ when, at $t = 0$, a *pure BEC* is formed. The five insets on this figure, represents typical *TOF* signals for some given time instants. Although these *TOF* curves does not correspond to the same experimental realization as the one shown in the main graph (recall that the *TOF* acquisition implies releasing the cloud and, consequently, interrupting the evaporative process) they were chosen among similar ions signal curves. In the column $T \ll T_c$, the presented *TOF* signal is well fitted by a Gaussian since its temperature is much higher than T_c. In the mid column a Gaussian is not sufficient to interpret the experimental curve, which starts to have a cusp shape at its center. The right hand side column represents different stages of the cloud in its evolution towards a *BEC*. The last frame corresponds to the *pure* BEC, characterized by an inverted parabolic shape (cf. A). The light gray curve in the ion signal, for $t > 0$, corresponds to the evolution of the cloud after achieving *BEC*: the cloud start to heat with the decrease of its density and a consequent reduction of the ion flux signal.

Experimental location of the critical transition point.
The determination of the *critical transition point* or, as we usually call it, the *critical time*, constitutes an important tool to help *producing* clouds at the vicinity of the phase transition. The ion signal is a remarkable tool for this. As we saw in the last Chapter, this is a quite remarkable physical situation with interesting properties [3]. However, the ion signal is only an indirect measure of the cloud density and is this latter quantity (or, to be correct, its peak value) that really determines the critical temperature and, therefore, the location of the *critical time* (cf. §2.1.2).

Moreover, since the observed ion signal results from an overall cloud integration of different collisional processes that depends on different powers of the density, the critical transition may appear as a smooth variation of the ion flux at the *critical time* even if there is a brusque variation of the cloud's peak density, as the one plotted in Fig.2.1 of §2.1.2. This smooth variation of the ion signal helps *hiding* the exact location of the *critical time*.

To get a better understanding of how the density evolves and also to get a proper determination of the *critical time* location within the ion signal we will simulate the ion flux produced within the cloud during that period.

4.2.2 Simulation of the ion signal in the last evaporative ramp.

As shown in Fig.4.1, in the last *rf*-ramp of the evaporative cooling the cloud evolves from a non-degenerate to a degenerate gas. These two cases corresponds to very different physical situations and must also be modeled quite differently. The initial non-degenerate cloud is described by a simple ideal gas model within the *semi-classical* approximation as derived in the expression of Eq.2.23. The degenerate gas will be described by a model that uses the *Thomas-Fermi* approximation (see Appendix A) to describe the *BEC* and the *semi-ideal* model to describe the thermal cloud. This model includes the influence of the *BEC* mean field.

The results of these two models coincides in the critical transition point what allows the continuous simulation of the time evolution of the cloud's density evolution. Finally, we remark that this model doesn't include neither finite size effects nor interatomic interactions in the thermal cloud. Despite that, we will see that the obtained results are similar to the experimental ones.

[3] We have also used clouds at $T = T_c$ in the experiment we made for measuring a(see §5.2)

4.2.2.1 Ion signal in the non-degenerate cloud.

The ion flux produced in a thermal cloud is given by Eq.4.1. The integrals in this expression can be evaluated substituting Eq.2.23 for the cloud's density. The general form for moment of order p of the average value of the cloud's density is

$$\overline{n_{th}^{p}} \equiv \int_{R^3} d\mathbf{r}\; n_{th}^{p}(\mathbf{r}) = \frac{\overline{\tau}^{-3/2}}{\lambda_T^{3(p-1)}}\; f_{\underbrace{33\ldots3}_{p}}(Z), \tag{4.2}$$

where the symbol $f_{33\ldots3}(x)$ stands for a class of function we use throughout this manuscript and defined as

$$f_{jk\ldots p}(x) = \sum_{l_j,l_k,\ldots,l_p} \frac{x^{l_j+l_k+\ldots+l_p}}{l_j^{j/2} l_k^{k/2} \ldots l_p^{p/2} (l_j + l_k + \ldots + l_p)^{3/2}}. \tag{4.3}$$

Note that the simplest form of this function is just $f_3(Z) = g_3(Z)$. In Fig.4.2*a*) we plot three examples of these functions. With the above definitions, the ions flux signal produced within a thermal cloud is

$$\Phi = \overline{\tau}^{-3/2} \times \left[\frac{1}{\tau_i} g_3(Z) + \frac{\beta}{2}\; \frac{1}{\lambda_T^3}\; f_{33}(Z) + \frac{L}{3}\; \frac{1}{\lambda_T^6}\; f_{333}(Z) \right]. \tag{4.4}$$

4.2.2.2 Ion flux in degenerate cloud.

Below the critical temperature we need to take into account the influence of the *BEC* for the ion flux. This will involve the computation of, for instance, the q^{th} moment of the mean of the *BEC* density $\overline{n_0^q}$ similar to those expressed in Eq.4.2 for the thermal cloud. Moreover, since now we may have collisions involving atoms from both the condensate and the thermal cloud, we will also need to derive *mixed mean terms* such as $\overline{n_{th}^{p}\, n_0^q}$. In both cases, we will describe n_0, the *BEC* density, in the *Thomas-Fermi* approximation (see Appendix A).

The calculation of the ion flux of a degenerate cloud involves also:

- The inclusion of weighing coefficients accounting for the different possible combinations on the number of involved thermal and condensed atoms and, also, of the *reduction quantum factor* included to account for the lack of the symmetrization term in collisions involving condensed atoms;

- Taking into account the influence of the repulsive mean field of the *BEC* on the thermal cloud (mainly in its center where the *BEC* is):

we will need to consider a *degenerate thermal cloud density* $n'_{th}(\mathbf{r})$ that accounts for this effect and recompute all the above moments of the mean cloud's density. This will be done within the *semi-ideal* model described latter on.

• **the *quantum reduction factor***

The ionizing rate constant for collisions involving atoms from the condensate are smaller from those defined in Eq.1.11. They are reduced to respectively β' and L', respectively for the *two-* and *three*-body processes according to[125, 70]

$$\beta' = \frac{1}{2!}\beta \quad \text{and} \quad L' = \frac{1}{3!}L.$$

In these expressions, the factors $\frac{1}{2}$ and $\frac{1}{3}$ are known as *quantum reduction factors*. They are included because in a collision between condensed atoms the bosonic exchange term needed to symmetrize the collisional process does not exist. This term, responsible for the Hanbury-Brown bunching effect, increases the probability for two or more thermal atoms to come close and to participate in a collision (cf. §3.2.1.2).

For terms involving mixed collisions, these factors are not so trivial since we need to account for all the allowed permutations of the bosonic operators involved in the description of the collisional process. If we have p thermal atoms colliding with q from the *BEC* we need to consider a multiplicity factor given by for details and Ref.[70])

$$M_{pq} = \left(\frac{(p+q)!}{p!q!}\right)^2.$$

In the other hand, the symmetrization of the processes involving thermal atoms adds the factor $p!$ and then, the total probability of a collision of p thermal with q condensed atoms is equal to

$$\mathcal{P}^{p+q} = p! \times M_{pq}.$$

If we want to keep the definition for the ionizing rate constants of Eq.1.11, which reports to processes involving thermal atoms only, we finally obtain

$$\beta' = \kappa_2 \times \beta \quad \text{and} \quad L' = \kappa_3 \times L, \tag{4.5}$$

with

$$\kappa_2 = \frac{p! \times M_{pq}}{2!} \quad \text{and} \quad \kappa_3 = \frac{p! \times M_{pq}}{3!}.$$

All the values of these two factors are compiled in Table 4.2.2.2 for all the collisional processes involving two and three atoms.

	two-body			*three-body*			
	n_{th}^2	$n_{th}n_0$	n_0^2	n_{th}^3	$n_{th}^2 n_0$	$n_{th}n_0^2$	n_0^3
$p!$	2	1	1	6	2	1	1
M_{pq}	1	1	4	1	9	9	1
$\mathcal{P}^{p+q}$	2	1	4	6	18	9	1
κ_2, κ_3	2	1/2	2	1	3	3/2	1/6

Table 4.1: The *quantum reduction* factors for all collisional processes involving two (κ_2) and three atoms (κ_3).

• **The *semi-ideal* model.**

The density of the thermal cloud of a degenerate gas is modified by the presence of the *BEC* that pushes the thermal atoms away from the center of the trap. This leads to a local decrease of the thermal cloud's density. A easy way to describe the density of such a thermal cloud is to take the *semi-classical* expression within a effective trapping potential modified by the *BEC* mean field repulsive energy. It becomes

$$n'_{th}(\mathbf{r}) = \frac{1}{\lambda_T^3} g_{3/2}\left(e^{-\beta[V(\mathbf{r})+2gn_0(\mathbf{r})-\mu]}\right),$$

with μ the *BEC* chemical potential. The interactive term is then $2gn_0(\mathbf{r})$, where the factor two comes also from the the symmetrization of the interaction process that occurs between atoms of different wave functions. The *BEC* density $n_0(\mathbf{r})$ is only slightly influenced by the thermal cloud and here this small influence will be neglected. In the *Thomas-Fermi* approximation the *BEC* density is given by (see Appendix A)

$$n_0(\mathbf{r}) = \left\| \frac{\mu - V(\mathbf{r})}{g} \right\|,$$

with g the coupling constant (cf. Eq.4.24) and $\|x\| = x$ for nonnegative x or zero otherwise. Inserting this last expression in the previous one we get the surprisingly simple result

$$n'_{th}(\mathbf{r}) = \frac{1}{\lambda_T^3} g_{3/2}\left(e^{-\beta|\mu-V(\mathbf{r})|}\right), \tag{4.6}$$

an expression independent, explicitly, of the actual number of condensed atoms. This dependence, that physically must exist, is passed into the expression through the chemical potential which is, in the degenerate gas case, a *positive* quantity. Note also that in the non-degenerate case, $\mu < 0$ and this expression reduces to the one in Eq.2.23. The model used in the derivation of the above expression in Eq.4.6 is referred in Ref.[47] as the *semi-ideal* model.

• **Average moments of the cloud's density.**
Within the above definitions, the ion flux for a degenerate cloud is given by

$$\begin{aligned}\Phi = \quad & \frac{1}{\tau_i}(N_0 + N_{th}) + \tfrac{1}{2}\beta\left(\overline{{n'_{th}}^{\,2}} + 2\overline{n'_{th}n_0} + \tfrac{1}{2}\overline{n_0^2}\right) + \\ & \tfrac{1}{3}L\left(\overline{{n'_{th}}^{\,3}} + 3\overline{{n'_{th}}^{\,2}n_0} + \tfrac{3}{2}\overline{n'_{th}n_0^2} + \tfrac{1}{6}\overline{n_0^3}\right),\end{aligned} \tag{4.7}$$

with $N_0 = \int d\mathbf{r} n_0(\mathbf{r})$ and $N_{th} = \int d\mathbf{r} n'_{th}(\mathbf{r})$ the number of atoms in the condensate and thermal cloud respectively. This two quantities and all other mean moments $\overline{{n'_{th}}^{\,p} n_0^q}$ in this expression need to be computed.

The terms involving only powers of the density of the condensate are easy to compute. In the *Thomas-Fermi* approximation they are given by

$$\begin{aligned}\overline{n_0^q} \equiv \int_{R^3} d\mathbf{r}\; n_0^q(\mathbf{r}) &= \left(\frac{\mu}{g}\right)^q \int_{T.F.} \left(1 - \frac{V(\mathbf{r})}{\mu}\right)^q, \\ &= \left(\frac{\mu}{g}\right)^q \frac{4\pi}{3} {R_{BEC}}^3\; I_q,\end{aligned} \tag{4.8}$$

where the integration is restricted to the volume inside the *Thomas-Fermi* ellipsoid, with $\frac{4}{3}\pi {R_{BEC}}^3$ the *BEC* volume (cf. §A.2 of Appendix A) and

$$I_q = \frac{3\sqrt{\pi}}{4}\frac{\Gamma(1+q)}{\Gamma(5/2+q)}. \tag{4.9}$$

This latter expression is equal to 2/5, 8/35 and 16/105, for q equal to respectively one, two and three. With $q = 1$ the expression in Eq.4.8 gives the *BEC* number of atoms, N_0 (cf. Eq.A.8).

The terms involving powers of n'_{th} lead to less trivial expressions. These can be written in terms of functions of the type

$$\underbrace{f'_{33\ldots3}}_{p}(x) = \frac{4}{\sqrt{\pi}} x^{3/2} \int_0^\infty d\rho\, \rho^2 \left[g_{3/2}\left(e^{-x|1-\rho^2|}\right)\right]^p$$

which is a modified version of the $f_{33\ldots3}(x)$ (cf. Eq.4.3) that takes into account the hole in the thermal cloud density caused by the presence of the *BEC* and also

$$F_{lm}(x) = \frac{4}{\sqrt{\pi}} x^{3/2} \int_0^1 d\rho\, \rho^{2l} \left[g_{3/2}\left(e^{-x(1-\rho^2)}\right)\right]^m. \tag{4.10}$$

Some of these functions, used in the derivation of the ion flux, are plotted in the Fig.4.2.

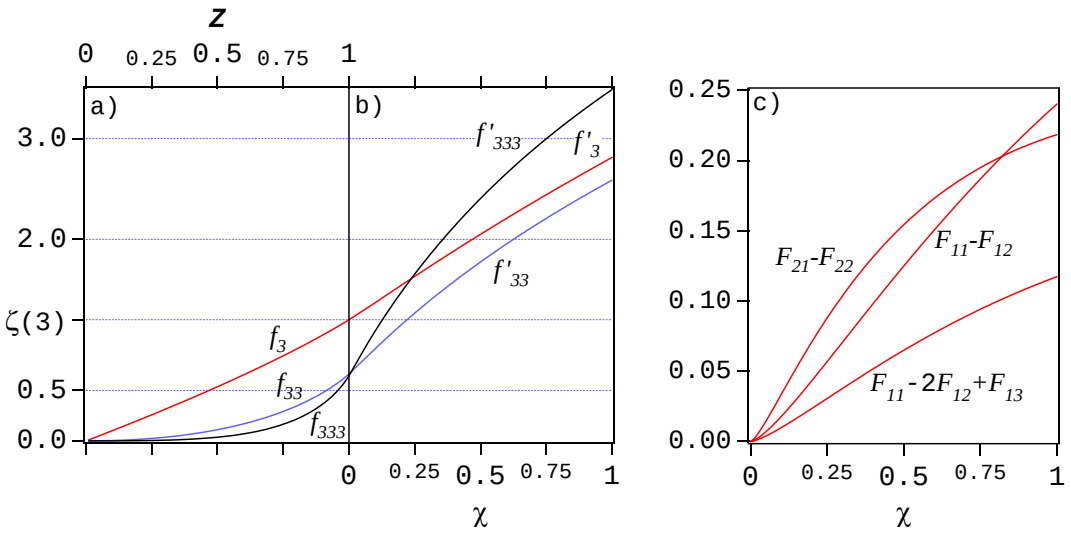

Figure 4.2: Graphical representation of the functions used in computation of the various average moments of the density of the cloud. These curves are plotted in function of the fugacity Z for non-degenerate clouds and for $\chi = \beta\mu$ for clouds where a condensate of chemical potential μ is already present (see also text).

The p^{th} order moment of the mean value of the density of the thermal part of the degenerate cloud is, within the *semi-ideal* model, given by

$$\overline{n'^{p}_{th}} \equiv \int_{R^3} d\mathbf{r}\; n'^{p}_{th}(\mathbf{r}) = \frac{\overline{\tau}^{-3/2}}{\lambda_T^{3(p-1)}}\; \underbrace{f'_{33\ldots3}}_{p}(\chi), \tag{4.11}$$

where the chemical potential is written as $\chi = \mu/k_BT$.

Finally, for collisions involving p thermal and q condensed atoms, the required density mean moment is

$$\overline{n'^{p}_{th}\, n_0^{q}} \equiv \int_{R^3} d\mathbf{r}\; n'^{p}_{th}(\mathbf{r}) n_0^{q}(\mathbf{r}) = \int_{T.F.} d\mathbf{r}\; n'^{p}_{th}(\mathbf{r}) n_0^{q}(\mathbf{r})$$

where the integration is limited to the *BEC* volume. Using the definition of Eq.4.10, this latter expression is re-casted in the particular cases of interest,

$$\begin{cases} \overline{n'_{th} n_0} = \dfrac{1}{\overline{\tau}^3}\dfrac{\mu}{g}\;[F_{11}(\chi) - F_{12}(\chi)] \\ \overline{n'^2_{th} n_0} = \dfrac{1}{\overline{\tau}^3}\dfrac{1}{\lambda_T^3}\dfrac{\mu}{g}\;[F_{21}(\chi) - F_{22}(\chi)] \\ \overline{n'_{th} n_0^2} = \dfrac{1}{\overline{\tau}^3}\left(\dfrac{\mu}{g}\right)^2\;[F_{11}(\chi) - 2F_{12}(\chi) + F_{13}(\chi)] \end{cases},$$

using again the definition $\chi = \mu/k_BT$.

4.2.3 The cloud's populations rate equations.

Up to now we have derived expressions for the ion rate production. To be applicable however, one needs to know the cloud's temperature and chemical potential at a specific instant of time. In the simulation we present here, we assume explicitly that the temperature varies linearly with time. This is the same as saying that η of Eq.1.6 is constant what is not far from the truth (see right hand side graph of Fig.4.4).

The cloud's chemical potential can be deduced from the temperature and number of atoms. To carry on with the simulation we need then to compute for every instant of time the number of atoms in the cloud. Since its initial value is a given parameter, this amounts to compute the atom losses during the process. We must consider two major mechanisms: *i*) the losses due to the inelastic collisions itself and, *ii*) the atoms losses imposed by the evaporative process.

4.2.3.1 The atom losses due to inelastic collisions.

The rate at which the atoms are lost in the inelastic collisions, in the thermal and condensed clouds are readily derivable from the above analysis. For the thermal cloud, this rate is given by

$$\begin{aligned} \dot{N}_{th} = \quad & -\frac{1}{\tau}N_{th} \\ & -\beta\left[\overline{n_{th}^2} + \overline{n_{th}n_0}\right] \\ & -L\left[\overline{n_{th}^3} + 2\overline{n_{th}^2 n_0} + \tfrac{1}{3}\overline{n_{th}n_0^2}\right], \end{aligned} \tag{4.12}$$

with τ the inverse of the cloud life time, which is, necessarily, smaller than τ_i, the ionization rate constant in collisions with the background gas (cf. §1.3.4.1).

The rate of atom losses in the condensate due to inelastic collisions is

$$\begin{aligned} \dot{N}_0 = \quad & -\frac{1}{\tau}N_0 \\ & -\beta\left[\overline{n_0^2} + \overline{n_{th}n_0}\right] \\ & -L\left[\tfrac{1}{6}\overline{n_0^3} + \overline{n_{th}n_0^2} + \overline{n_0 n_{th}^2}\right]. \end{aligned} \tag{4.13}$$

4.2.3.2 Atom losses due to the evaporative cooling.

We present now a simple model[126] that gives an approximate result for the atom losses dN in the evaporative cooling when the temperature decreases by dT. This model is derived using only very general arguments based on

the conservation of the system's mean thermal energy. Even so, its results agree qualitatively with a more rigorous treatment developed by Luiten *et al.* within the framework of a kinetic theory model[127]. In the end of this paragraph we correct the results of the simple model presented here with those obtained in the kinetic model.

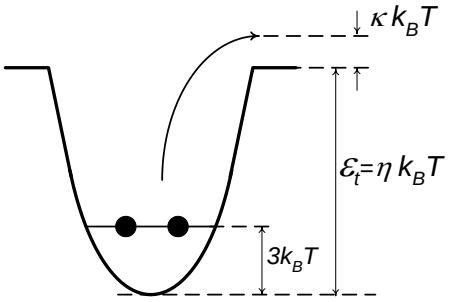

Figure 4.3: Schematic representation of the evaporation process. There are two energy scales involved: the mean particle energy equal to $3k_BT$, which obeys the energy equipartition theorem with $\frac{1}{2}k_BT$ for each quadratic term in the Hamiltonian and the energy depth of the trap $\epsilon_t = \eta k_BT$, established by the rf-knife and defined here through η, the ratio between this energy and the thermal energy k_BT.

• A simple model for describing the evaporative cooling.

At a determined instant of time during the evaporative cooling, the magnetic trap has the configuration depicted in Fig.4.3, with a finite depth determined by the *rf*-field frequency $\epsilon_t/\hbar$. The cloud, standing on the bottom of the trap, has a per particle energy of $3k_BT$, which accounts for the kinetic and potential energies. If there are N atoms in the trapped cloud, the total cloud energy is then $3Nk_BT$.

To escape the trap, the particles must possess an energy bigger than ϵ_t: we assume that the energy of those particles that escapes the trap is given by $(\eta + \kappa)k_bT$, with $\kappa \ll \eta$. Thus, if dN atoms escapes the trap, the total cloud energy decreases by

$$dE = dN\ (\eta + \kappa)k_BT.$$

After re-thermalization the energy is conserved and we must have

$$3Nk_BT - dE = 3(N - dN)k_B(T - dT).$$

Substituting the former expression on this one and neglecting the $2nd$ order term $dN\ dT$ we get

$$\frac{dN}{dT} = \alpha_\eta^{-1}\frac{N}{T}, \tag{4.14}$$

with $\alpha_\eta = \left[\frac{\eta+\kappa}{3} - 1\right] \simeq \frac{1}{3}\eta - 1$. If we know, at a certain instant, the number of atoms on the cloud and its temperature, we can then compute dN knowing that the cloud cooled down by dT.

• Correcting α_η with the result of the kinetic model.

The simple model presented above doesn't consider the cloud's thermal statistical distribution. The cloud is characterized only by its mean thermal average, $3k_BT$, without any details about the statistical occupation of the different harmonic oscillator energy levels or its density of states. This is a huge simplification since we know that the *Maxwell-Boltzmann* distribution predicts smaller occupation probability for atoms with larger energies and these are, in fact, those that are ejected out of the trap.

A better model for describing the evaporative cooling is proposed in Ref.[127]. This model is derived in the approximation where the cloud is described by the *Boltzmann* distribution and that the phase-space particles distribution corresponds always to a thermal equilibrium distribution. This latter condition is referred by the authors as a *sufficient ergodicity* condition and justified as being a consequence of the large rate of interatomic elastic collisions. Here, if η doesn't change during the evaporation, the Eq.4.14 is still valid if α_η is modified according to

$$\alpha_\eta = \frac{\eta + \kappa}{3\mathrm{R}(3,\eta)} - 1, \tag{4.15}$$

where $\mathbf{R}(a,\eta)$ and κ are given by

$$\mathbf{R}(a,\eta) = \frac{P(a+1,\eta)}{P(a,\eta)} \quad \text{and} \quad \kappa(\eta) = 1 - \frac{P(5,\eta)}{P(3,\eta)}\left[\eta - 5\mathrm{R}(3,\eta)\right],$$

with $P(a,\eta)$ the incomplete Gamma functions[128].In the left hand side graph of Fig.4.4 we plot the expression of Eq.4.15 for α_η in function of η (solid line) and also the result of the above present simpler model (dashed curve). For large values of η, the expression in Eq.4.15 is very well approximated by its asymptote (dotted line in the graph) which is given by

$$\alpha = \frac{\eta}{3} - 2/3. \tag{4.16}$$

As we referred, Eq.4.14 is only valid if $\eta = \epsilon_t/k_BT$ is kept constant during the evaporative cooling process. Experimentally, this is a hard task to accomplish since we have no information about the cloud's temperature on the course of the evaporation. An estimation of η can however be obtained by interrupting the evaporation at a given time and measuring the correspondent cloud's temperature through a fit to its *TOF*. We observe the dependence

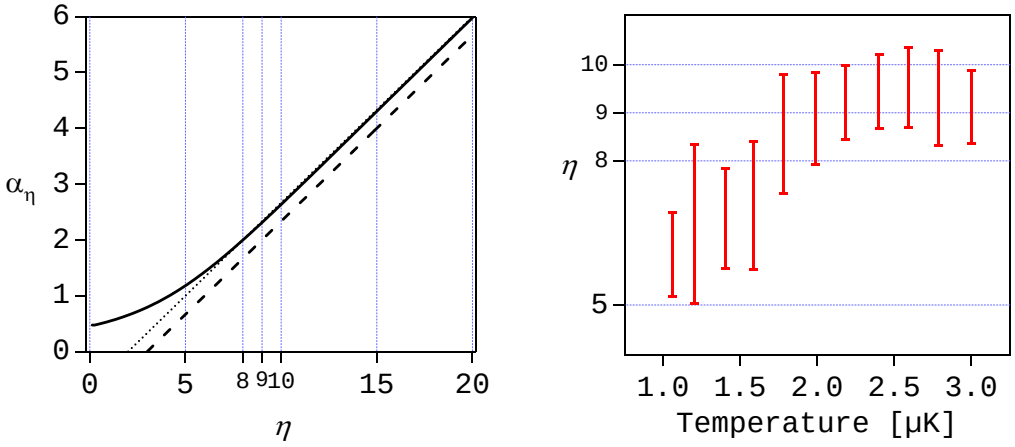

Figure 4.4: In the left hand side graph it is represented the dependence of α_η in η. The dashed line corresponds to the value of α_η obtained with the simple model presented in the beginning of this Section. The solid and dotted lines corresponds to the value of α_η found with the model of Luiten *et al.* and an asymptotic approximation for this model respectively. In the right hand side graph, we plot experimental results obtained for η for different temperatures (see also the text). The error bars correspond to the standard deviations for many experimental runs.

of η on the temperature shown in the right hand side of Figure4.4. In this graph η varies less than 30% for temperatures ranging from 1 μK to 1.75 μK. Above this temperature, η is almost constant.

• Discussion.

Taking η as constant can eventually conduce to an erroneous estimation of the losses induced by the evaporation, especially in very small clouds where the final value of ϵ_t corresponds to very small temperatures. This should also be true for larger clouds whenever they are close to the critical temperatures or below. The variation of η over time is also misleading since it changes the *velocity* at which the cloud attends the critical density and, then, the instant of time at which we expect to observe the phase transition.

To get an estimate of how this could modify the results of the simulation we present further in this Section, we accounted for the temperature dependence of η as shown in the graph of Fig.4.4 (this assumes a *local* constant value of η in each step of the simulation). However, the results obtained with this procedure shown to be not significatively different from those obtained with a constant value of $\eta = 9$.

Another approximation used in here is the description of the atomic cloud with a classical Maxwell-Boltzmann instead of a *Bose-Einstein* distribution function. However, since $\eta \gg 1$, the evaporation removes atoms mainly from the tails of the distribution, where both functions are very similar. Note

that the number of ejected atoms and the corresponding loss in energy also depends in the density of states that is only determined by the shape of trap.

4.2.3.3 Numerical simulation: overview.

As we have referred, our major goal in simulating the ion flux signal is to understand where is located the instant of time for which $T = T_c$. Reasonably, we may expect it to be nearby the knee of the curve but, the exact location, is not known.

In the numerical simulation we present here, the cloud's temperature is ramped down linearly in time, in a scenario that resembles closely with what happens in the evaporative cooling of our experiment. For each instant of time we compute the value of the cloud's fugacity and thus determine the *critical time* for which $Z = 1$. The routine is divided in two different parts for the non-degenerate and the degenerate case.

The non-degenerate cloud.

Initially, in the non-degenerate case, we impose a certain variation of the temperature in time, starting well above the critical transition. Knowing the initial number of atoms N_{th} in the thermal cloud we compute the cloud's density and fugacity and, for these values the expected atom losses ΔN_{th}. For the new number of atoms in the cloud, $N_{th} - \Delta N_{th}$, on a further instant of time and smaller temperature, we recompute the new density and fugacity. Doing this repeatedly, we get to the critical temperature at the instant of time where $Z = 1$.

In any instant of time, this procedure relies on the knowledge of the

$$\Delta N_{th} \simeq \dot{N}_{th} \Delta t$$

with Δt the time step and

$$\dot{N} = -\Gamma_{ev}(T) N(t) - \dot{N}\big|_{coll}, \tag{4.17}$$

where $\dot{N}\big|_{coll}$ is the atom losses due to inelastic collisions of Eq.4.12 and

$$\Gamma_{ev}(T) = \frac{1}{T}\frac{dT}{dt}\tilde{\alpha}, \tag{4.18}$$

with $\tilde{\alpha}$ given by Eq.4.16. Also, the temperature variation is given by $\Delta T = \dot{T}\Delta t$ where $\dot{T} = \hbar v_{rf}/k_B$ is the *velocity* at which the temperature decreases in time with $v_{rf} = 2\pi \times 400$ kHz $\cdot\, \mathrm{s}^{-1}$, our ramp velocity.

At each instant of time the ion flux is given by

$$\Phi = \frac{1}{\tau_i} N + \tfrac{1}{2}\frac{\Delta N}{\Delta t}\Big|_{2Body} + \tfrac{1}{3}\frac{\Delta N}{\Delta t}\Big|_{3Body}. \tag{4.19}$$

where, for the *two-* and *three-body* ionizing rate constants we use the theoretically predicted values [129, 130, 131], $\beta = 5 \times 10^{-21}$ m^3/s and $L = 4 \times 10^{-39}$ m^6/s. For the rate of ionizations with the background gas we use $\tau_i = 1000$ s and a cloud's life time of $\tau = 100$ s, two values measured experimentally.

After having attained $T = T_c$, the simulation runs with a second routine based on the *semi-ideal* model and instead of keeping constant steps of time (and temperature decrease) we have opted to vary the *BEC* chemical potential μ of equal amounts in successive steps of the simulation. Knowing μ we can derive N_0, the condensate number of atoms and, using $\chi = \mu/k_BT$ in the *semi-ideal* model, we can derive N'_{th}, the number of atoms in the thermal cloud. Taking η constant, with also a constant *ramp velocity*, we compute the time and the thermal cloud's temperature for each step of the simulation.

The *BEC* chemical potential is always much smaller than $\varepsilon = \eta k_B T$ and thus we may neglect the atom losses due to the evaporative cooling in the condensate. These losses are however considered in the thermal cloud. We also have includes all atom losses due to the inelastic collisions, for both clouds and also those that depend on *cross-collisions*.

4.2.3.4 Presentation of some results.

In Fig.4.5 we present the results, for three different clouds, of the ion signal variation obtained in our numerical simulation. The time axis, in all graphs, corresponds to the last two seconds of the last evaporative ramp, coinciding with zero at the time where the number of thermal atoms is zero and only a pure *BEC* remains trapped.

Discussion of the results.

The curves presented in Fig.4.5 compares qualitatively well with the one presented before in Fig.4.1 for real ion signal curves.

We also remarks that:

- At first look, the curves of Fig.4.5 confirm that the *critical point*, at $Z = 1$, is close to the *knee* of the curve.
- As noted before in §4.2.1, the ion flux maximum value happens before the $T = 0$ where *BEC* is almost *pure*.
- For cloud with smaller initial densities, the critical point appears latter, the initial slope of the curve is smaller and curvature of the *knee* is also smaller.

Pushing further the comparison between real ion ion signals and those simulated in here leads to erroneous conclusions since the model we have used

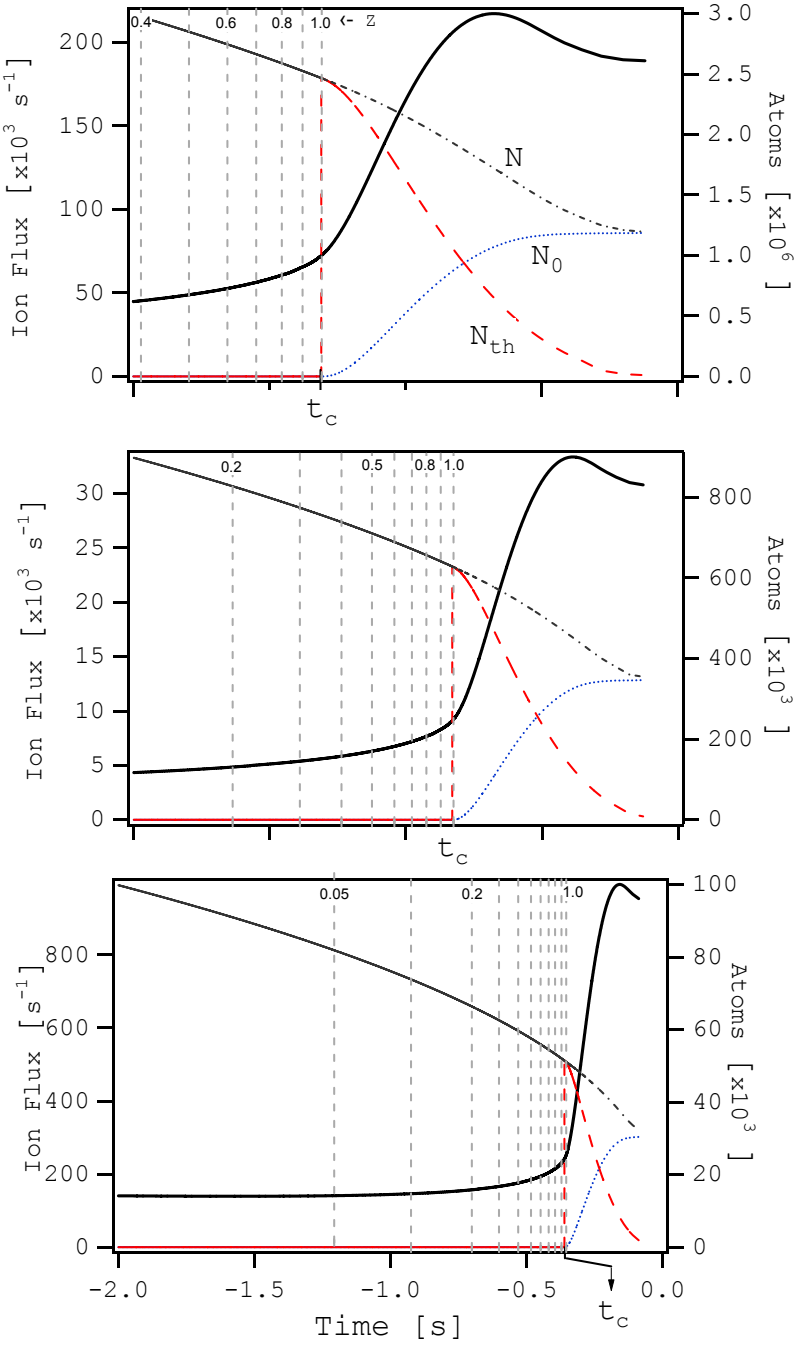

Figure 4.5: In these Figure are represented three graphs corresponding to simulation of the evolution of clouds with different initial densities in the last *rf*-ramp. The full line with circles represent the ion signal evolution (left axis) and the dotted, dashed and dot-dashed lines (right axis) represent the number of atoms in the condensate, in the thermal cloud and the total number of atoms, respectively. Fugacities are different values are signalized by vertical lines The time $t = 0$ corresponds to the situation where no more atoms persists in the thermal cloud. The model used for computing the evolution below T_c is based in the *semi-ideal* model and *Thomas-Fermi* approximation. See text for details.

in here doesn't take into account the influence of the interatomic interactions in the production of ions (nor the finite size effect). We will see further in §5.2.1 that, at least for the thermal cloud, the interactions does increase significatively the ion signal.

4.2.4 Critical curve.

In this Section we describe the construction of an important tool made possible by the ion signal, the *critical curve*. We will start by describing it in the framework of the numerical results obtained in the last paragraph and then for real ion signal data.

4.2.4.1 The critical curve in the simulated results.

Within this model, we can derive the value of the ion flux at the time where $T = T_c$. We name *critical curve* the plot of the critical ion flux in function of the *critical time*. The obtained result is shown in Fig.4.6, which resumes the most important results we obtain with the simulation. These results will prove to be very useful in the next Chapter, for helping analyzing real data.

The ion curves in this Figure were simulated for clouds with different initial number of atoms but all with the same initial temperature. The dashed lines marks the locations where the curves have a given fugacity in the *non degenerate region*, for values between $Z = 0.9$ and $Z = 0.4$. The critical curve, the solid line marked with $Z = 1$, divides this non-degenerate region from the degenerate one. On the left hand side of this curve and represented by dotted lines, we show how the chemical potential (in temperature units) varies with the $rf-$ramp. This is done for fixed chemical potential ranging from 0.04 μK to 0.20 μK.

We have also plotted a shadowed region around the critical curve with a width, in each side, of 25 kHz in $rf-$field units. This corresponds to the uncertainty imposed by the fluctuations of the bias field in the final rf frequency (cf. §1.2.2). This fluctuation of the bias field relatively to the ending frequency of the ramp induces an undesired shift in the fugacity that can be greater than 10%. This result is of great importance for understanding the data dispersion we see in the experiment described in the following Chapter.

4.2.4.2 Empirical determination of the critical transition point.

In the following we present two empirical methods that propose a location of the critical point in the ion curve: *i*) looking for a discontinuity on the derivative of the curve and, *ii*) fitting a hyperbola to the region where the transition takes place, identifying the critical point with the center of the hyperbola. The first of these methods, which we shall call the *slope-break* method, is just the usual definition found for a first order phase transitions[132] [4] and was

[4]The ion curves we present here presents a typical behavior of a phase transition although they are not a spontaneous process but rather forced by the evaporative cooling. Thus, the time scale as well as the shape of the ion signal is determined by the rf-ramp velocity and not by a *stand alone* bosonic stimulated process. Such a spontaneous transition

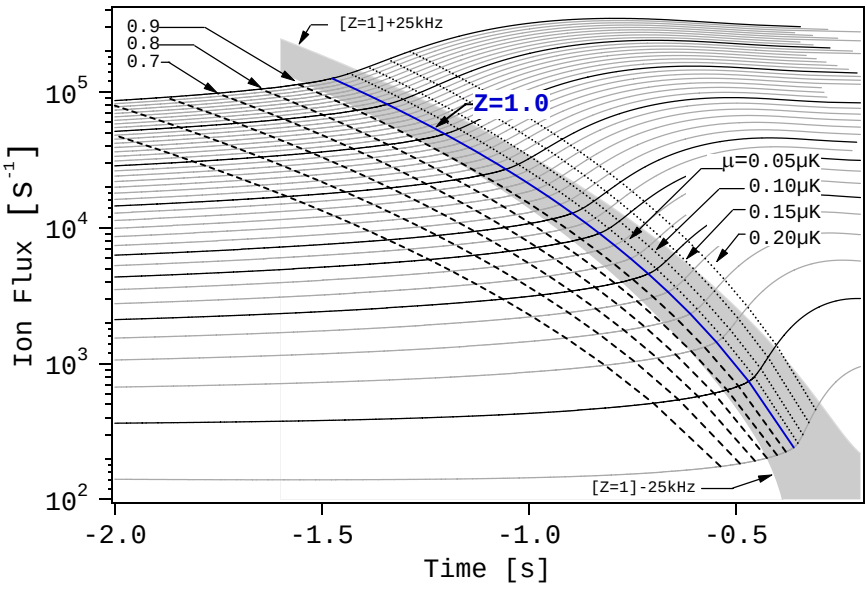

Figure 4.6: Ion signal curves obtained by numerical simulation and presented in a logarithmic graph. The values used in the simulation for the ionizing rate constants values were $\beta = 5 \times 10^{-21}$ m^3/s, $L = 4 \times 10^{-39}$ m^6/s and $\tau_i = 1000$ s (see also text). The solid line marked with $Z = 1$ is the *critical curve*, made of the points where the curves are passing through the *BEC* threshold. Similarly, the dashed lines correspond to different values of the fugacity, between $Z = 0.9$ and $Z = 0.4$. The dotted lines correspond to points already in the degenerate part of the curves with (positive) chemical potentials ranging from 0.04 μK to 0.20 μK in temperature units. The shadowed region represents the region of bias fluctuation that corresponds in $rf-$ramp units to ± 25 kHz around the critical curve. This graph shows that, if one tries to stop the evaporation at $T = T_c$ (*i.e.* at the critical curve), the bias fluctuation may impose a shift on the fugacity of more than 10%.

the method used originally in the data analysis of Ref.[46] (see also Ref.[51]).

The second method is the *hyperbola-based* method. This was developed only after the publication of Ref.[46] and constitutes, we believe, a more convenient method for characterizing the ion signal, being also more easily implemented.

• **The *slope-break* method.**

The idea underneath this method, rather simple, is sketched in Fig.4.7. If at a certain instant of time the ion curve changes its slope abruptly, its derivative is discontinuous and thus, its third derivative is zero (see inset on the right of Fig.4.7). This condition defines the location of the *critical time*.

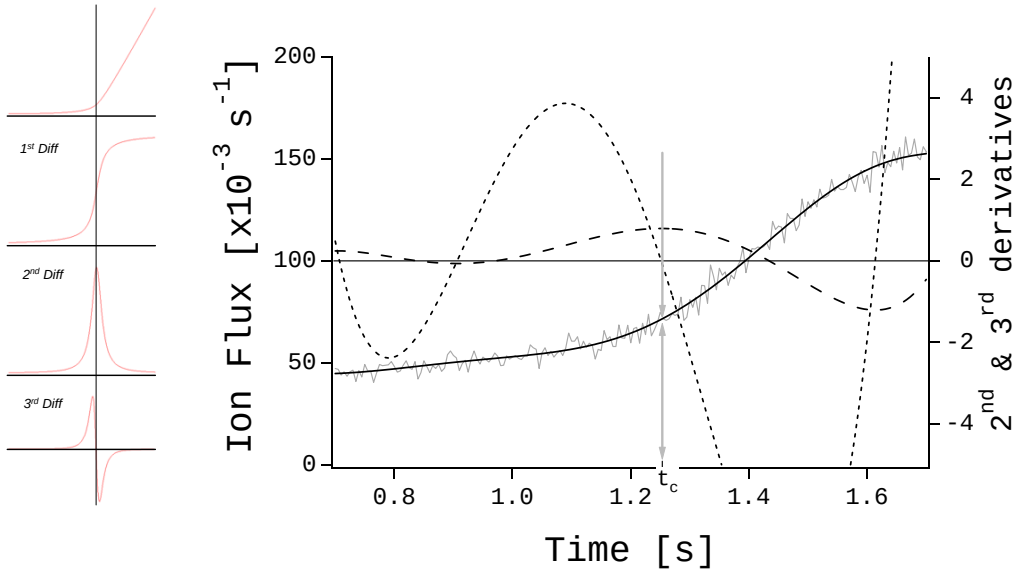

Figure 4.7: In the upper part of the Figure we schematize the idea of the *slope-break* method. Starting from a curve in which the slope changes bruskly at a certain instant, we see that, differentiating it three times and then searching for its zero, we recover the location of the that brusk change. In the lower part of the Figure, we present a graph with real data. In it, we also represent the 2^{nd} (dashed line) and 3^{rd} derivatives (dotted line). The critical point is found when the 3^{rd} derivative is null.

To implement this method in real data, we need first to produce a smoother version of the ion signal to avoid all the null third derivatives induced by the

was however observed for uncondensed cloud put out of thermal equilibrium[133].

noise in the signal. To do this we first fit the ion signal to a polynomial function and use the fitted curve for the analysis. However, to guaranty that the fit follows correctly the ion signal, especially at the vicinity of the critical time, we have used polynomials of high order, typically between 8 and 10. The third derivative of such function has several different zeros and, therefore, to determine the critical time it was still necessary to choose the *good* zero that would correspond to the phase transition location. This should correspond to the nearest zero to the curve knee with its location being determined by the one with the largest positive maximum of the second derivative of the curve. This corresponds taking the *brusquest* change in slope of the fitted polynomial.

There are some disadvantages in this method. First of all, the value found for the *critical time* may be some times very dependent on the degree we choose for the polynomial. It cannot be too small, otherwise the zero of the third derivative is shifted from its actual location in the ion signal. It cannot be too large to avoid including erroneous answers due to the noise of the ion signal.

A second disadvantage of this method compared with the *hyperbola-based* one is that its only result is the determination of the location of the critical point without characterizing any further the signal. It is not obvious to interpret physically (or else, geometrically) the fitted polynomial coefficients. This can be done if, instead of a polynomial, we use as fitting function another analytical function with parameters we may interpret.

• The *hyperbola*-based method.

At the vicinity of the critical transition the shape of the ion signal is very similar to a hyperbola. The graph in Fig.4.8 shows an example of this. To define the hyperbola we need to consider three main parameters: an *angle of attack* of the curve, represented in the figure by its tangent n, a radius of curvature, R, and finally, the *aperture angle* (with tangent m) that determines if the hyperbola is more or less open. Along with these three parameters we still need other two to locate the hyperbola's center at a given location C (see graph) at coordinates x_0 and y_0. These two latter parameter will be related with the *critical time* and the *critical ion flux*, respectively.

With the above defined parameters, the hyperbola is a function defined as

$$\begin{aligned} y = y_0 \quad &+ \quad \tfrac{(m+n)(1-mn)}{1-2mn-m^2}(x-x_0) + \\ &+ \quad \tfrac{m(1+n^2)}{1-2mn-m^2}\sqrt{(x-x_0)^2 + \tfrac{m^2}{1+n^2}(1-2mn-m^2)R^2}, \end{aligned} \tag{4.20}$$

We note that the third derivative of this expression has only one zero located at $x = x_0$, the abscise of the center of the hyperbola. This is the *critical time*

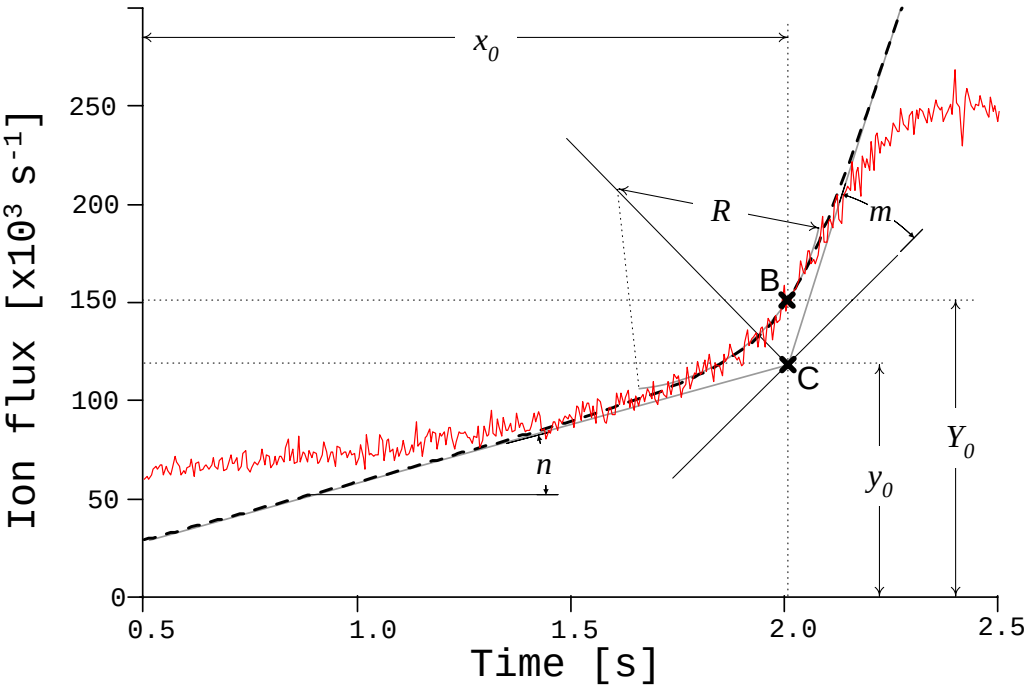

Figure 4.8: The *fit to hyperbola* method. In here, we fit the ion signal by a rotated hyperbola. The fitted function has five parameters: x_0 and y_0 for the location of the center of the hyperbola (C); m, related with the angle of aperture; R and n for the radius of curvature and the initial *attack angle* of the curve. This function third derivative is null also at x_0. Therefore, the *slope-break* method give the same result for the abscise of the *critical-point* and Y_0 for its ordinate (B).

location we may also find with the *slope-break* method. However, the critical ion flux is different (B in the Figure 4.8), given by

$$Y_0 = y_0 + m^2 R\sqrt{\tfrac{1+n^2}{1-2mn-m^2}}. \tag{4.21}$$

• Comparison of both methods within the analysis of simulated data.

We may ask now which location, y_0 or Y_0, should be identified with the

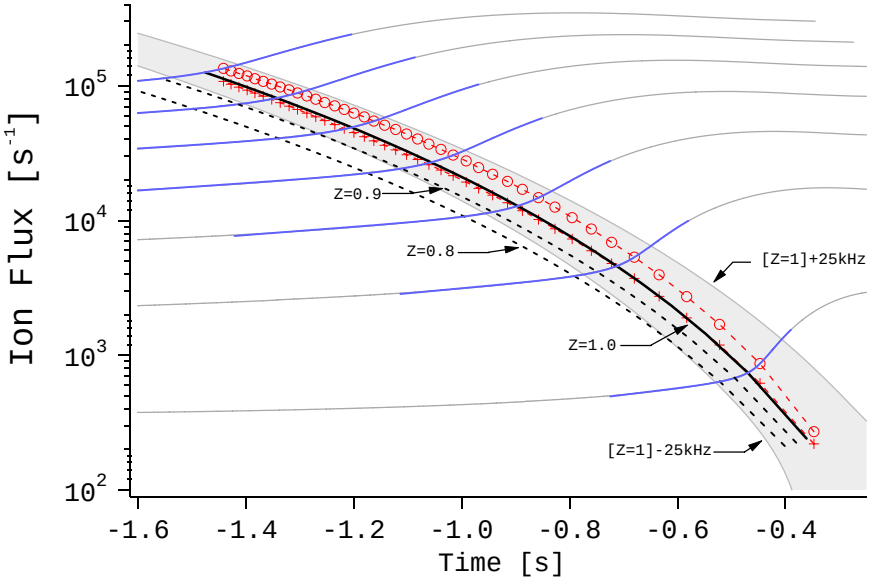

Figure 4.9: Similar graphical representation as the one presented above in Fig.4.6. In this graph we also add the *critical curves* we find using the *slope-break* (circles) and *hyperbola-based* (crosses) methods in the numerical simulated curves (see also text). In the *slope-break* (*hyperbola-based*) method the location of the critical point corresponds to the point B (C) in Fig.4.8. The *hyperbola-based* results almost coincide with the curve $Z = 1$.

critical ion flux. This question can be answered by comparing the results of these two methods with the curve $Z = 1$ obtained with the simulated data. The result of such a procedure is shown in Fig.4.9, where we also compare the obtained critical curves with the bias fluctuation. The graph in this figure clearly shows that the best choice for defining the *critical locations* is to take the hyperbola's centers x_0 and y_0. Based on this analysis, the *slope-break* method gives critical locations slightly displaced into the degenerate region but still inside the region of bias field fluctuation.

4.2.4.3 The *critical curve* for real data.

We come now to the *critical curve* made of real data. In Fig.4.10 we present an ensemble of ion curves taken in several experimental realizations. As before, this data corresponds only to the interval of time at the last *rf-ramp*. To get *critical points* spanning over all possible *critical times*, we needed to use several clouds with very different initial densities. This can be done by inducing controlled losses in the evaporative cooling process such as stoping the ramp at a given frequency for some time. This leads, in the end of the evaporative cooling, to less dense clouds.

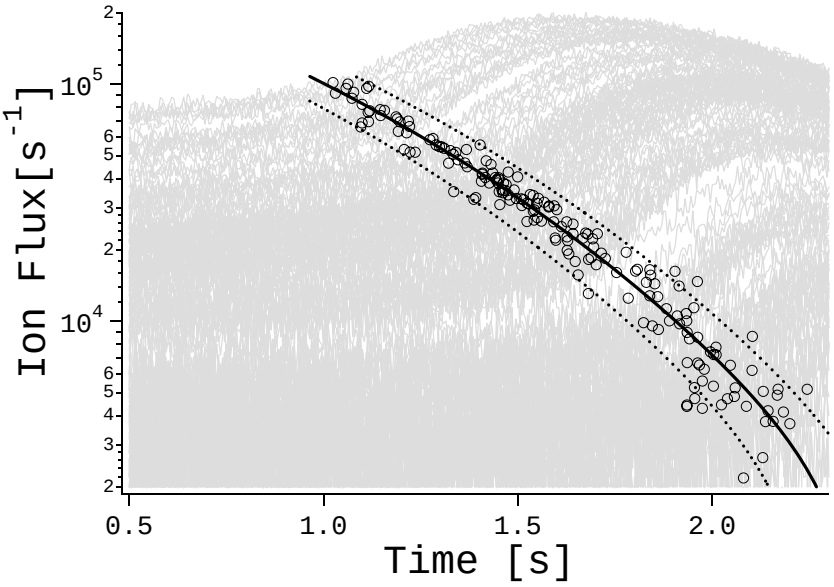

Figure 4.10: Ion curves corresponding to several different experimental runs. The initial number of atoms was varied to get as many as possible different critical times. The circles marks the *critical points* found through the *slope-break* method. The region between the two dashed lines corresponds to a ±25 kHz region around the *critical curve*. This one (solid line) is an exponential fit to all the *critical points*. Note that experimentally observed bias fluctuation of ±25 kHz agrees very well with the dispersion observed in this graph.

In Fig.4.10, the *critical points*, represented for each ion curve by circles, were computed through the *slope-break* method. Although probably not the best suited method for build the critical curve, the *slope-break* was, as already referred, the method we used originally in Ref.[46]. For practical proposes and due to the bias fluctuations, we will see that the differences between the results of both presented methods are almost irrelevant.

The solid line in this graph is the *critical curve* obtained in a exponential fit to the critical points. This is the major result of this analysis. Another remark about this graph is that the dispersion of the critical points confirms

our experimental estimative for the bias fluctuation since almost all critical points fall inside the region of the *bias fluctuation*, delimited by the dashed lines placed 25 kHz in each side of the critical curve.

The definition of this *bias fluctuation region* is of great importance in the data acquisition and its analysis: any ion signal that has stop inside this region may correspond to a cloud at the *BEC* threshold. This constitutes then a criteria for determining if a given experimental realization was successful in the goal of producing a cloud at $T = T_c$.

• ***Slope-break* versus *hyperbola-based* method.**
The comparison we presented earlier in Fig.4.9 shows that the *slope-break* method we used may include a systematic shift for the obtained critical curve. This can in fact be observed for real data comparing the critical points we obtain using both methods. The graph in Fig.4.11 shows some examples of this. The *critical ion flux* is always bigger if we use the *slope-break* method resulting in a shift of the critical curve for the *degenerate region*.

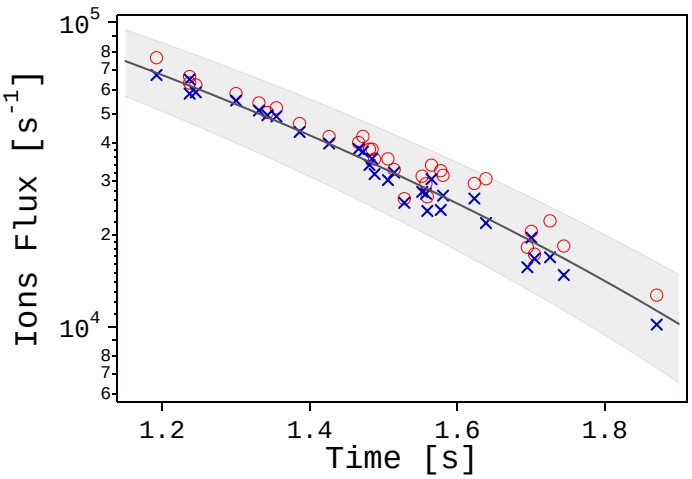

Figure 4.11: Same as in the preceding Figure but for fewer *critical points*, represented for both *hyperbola-based* (crosses) and the *slope-break* (circles) methods. The shadowed region corresponds, as before, to the ±25 kHz region around the *critical curve*.

However, the difference we get between the results in the two methods is small if compared with the bias fluctuation and this latter is, in fact, what ultimately limits the efficiency of any of these methods for thermometric proposes. Of course, since the bias fluctuations are of random nature and the shift in the definition of the critical curve induces a systematic error, it would be preferable to use, from the beginning, the *hyperbola-based* method for defining the critical curve.

4.2.4.4 Further characterization of the ion signal.

As explained above, the cloud's thermometry using the ion signal analysis is limited by the bias fluctuations. This limitation is however of technical nature and, if solved, would make the ion signal analysis well suited for precise and real-time thermometry of cloud at the vicinity of the critical transition point. This would require however a good theoretical characterization of the ion signal around $T = T_c$ and it is likely that this would only be possible through a numerical simulation similar to the one we have presented, preferably with a more robust theoretical model (with the inclusion of finite size effects and interactions in the thermal cloud). Despite the general interest on the output of such a simulation, for data analysis it would be preferable to rely on a simple analytical expression that can be easily fitted to the data such as the presented hyperbolic function. In the following we present how this function could be used in the comparative analysis of real and simulated data.

• The additional information obtained from the *hyperbola-based* method.

The hyperbola has only five parameters: x_0 is the location of the *critical time*; n, m and R define the shape of the curve and the fifth, y_0, accounts for the critical ion flux. In Fig.4.12 we plot the parameters n, m and R in function of y_0 using simulated curves (lines) and real ion signals (symbols).

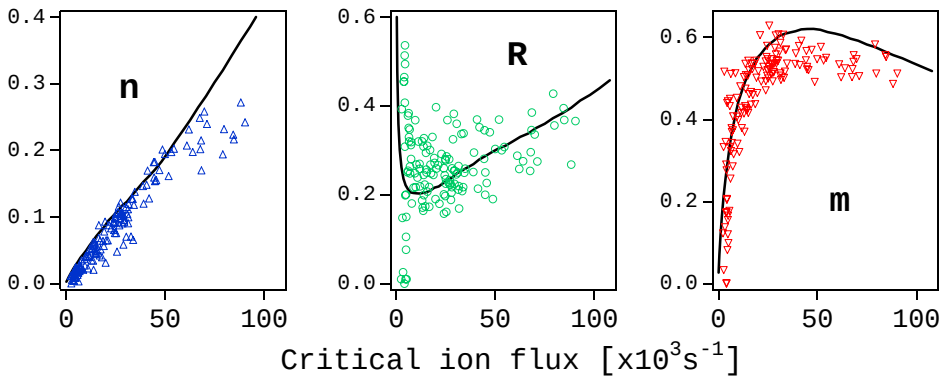

Figure 4.12: Representation of the hyperbola fitted parameters m, n and R in function of the corresponding critical ion flux for all the simulated curves presented before in Fig.4.6 (lines) and also for similar fits to real data (symbols). The good accordance between the data sets seems to validate the simple semi-ideal model we used in the simulation and also the values used for the ionizing rate constants (see also text).

In these graphs we made no effort to fit the data to the curves obtained

in the numerical simulation. Even so, they are in good agreement suggesting that:

- Despite its simplicity, the semi-ideal model reproduces the general behavior of the critical phase transition;
- At the vicinity of the phase transition, the ion flux seems to be well approximated by a hyperbola.

• Thermometry with the ion signal. Insensibility to the bias fluctuations.

If we admit that the model we used in the simulation (or another more sophisticated) produces a good description of the ion curve, comparing the set of values m, n and R found for a real ion signal to those found on a simulation can give the information of the cloud's temperature and fugacity. However, this is only applicable to degenerate clouds since the fit to the hyperbola requires the ion signal to pass through the *knee* characteristic of the critical transition [5].

An obvious advantage of this thermometric technique, or any other relying on the analysis of the shape of the ion signal, is that it is insensitive to the bias fluctuation since the origin of the time referential is unimportant. This makes this latter type of analysis immune to the bias fluctuations, what may be seen as a great advantage of this method for the data analysis [6]

4.2.5 Conclusion.

Although not completely suitable for accurate thermometry, the ion signal is an extremely important tool both in the laboratory and when analyzing the data. It is a unique diagnostic tool for *real-time* observation and may be used to determine, during an experimental run, the approximate location of the phase transition. This allows a much better control of the experiment, especially when the goal is to create clouds at $T = T_c$.

[5] A solution for this case would probably imply the use of another analytical expression for describing the ion signal behavior long before the critical transition, with probably fewer parameters. For instance, it could take the ion flux at a given instant of time and an angle similar to n, related with the rate of increase of the signal at that same location.

[6] We note that a fluctuation in the bias field will also change the confining potential, inducing a change in the ions curve. This effect is however very small and has no major effect in the behavior of the ion signal. We see from Eq.4.4 that (disregarding the contribution of the *one-body* term) $\frac{\delta\Phi}{\Phi} \sim -\frac{2}{3}\frac{\delta\overline{\tau}}{\overline{\tau}}$, and from Eq.1.4 that $\frac{\delta\overline{\tau}}{\overline{\tau}} = -\frac{1}{3}\frac{\delta B_0}{B_0}$. In our experiment we know that, close to the critical transition, $\frac{\delta B_0}{B_0} \simeq \pm 2.5\%$ (cf. §1.2.2) and then the critical ion flux changes with bias fluctuation of about $\frac{\delta\Phi_c}{\Phi_c} \sim \pm 1\%$, which is comparable to the ion signal shot noise.

We have also considered a simple model to simulate the ion signal that allowed us to obtain an approximated idea of how the temperature and the fugacity vary over time in the last ramp of the evaporative cooling. The results obtained in this Section, specially those shown in Fig.4.6, will be very useful for understanding the experimental data we present in the following Chapter.

The above method enables to determine the critical ion rate and is largely insensitive to the bias field fluctuations. The actual value of the critical temperature through the critical time is sensitive to the bias fluctuation, however. To get a better thermometry of the cloud we will need to make use of the analysis of the atomic *TOF* signals. This will be the subject of the following Section of this Chapter.

4.3 *TOF* based thermometry for non degenerate atomic clouds.

In the previous Sections of this Chapter we analyzed up to what point we could go with the study of the ion flux signal to determine the cloud's temperature and, most specially, its fugacity. In here, we will discuss the cloud's thermometry using instead its *TOF*. We have already presented in Chapter 2 expressions for describing the atomic flux for a ideal gas expanding ballistically (cf. §2.2.2.3). In this Section we will present similar expressions, also for a ballistic expansion, but including interatomic interactions.

4.3.1 Inclusion of interatomic interactions.

In the following paragraphs we will include the interatomic interactions, in the mean field approximation. An interaction between two atoms in the cloud includes an extra term to the ideal gas harmonic oscillator Hamiltonian(2.2). The corresponding *multi-body* Hamiltonian is

$$\hat{H} = \sum_{i=1}^{N} \left[\frac{\hat{\mathbf{p}}_i^{\,2}}{2M} + U(\hat{\mathbf{r}}_i) \right] + \tfrac{1}{2} \sum_{i \neq j} V_{int}(\hat{\mathbf{r}}_i - \hat{\mathbf{r}}_j), \tag{4.22}$$

with $V_{int}(|\hat{\mathbf{r}}_i - \hat{\mathbf{r}}_j|) \equiv V_{int}(\hat{\mathbf{r}}_{ij})$ the interaction potential, which depends only on the distance between pairs of particles. At low temperatures, the thermal de Broglie wavelength λ_T is much larger than the characteristic range of $V_{int}(\hat{\mathbf{r}}_{ij})$ and this latter one can be approximated by a *contact potential*

$$V(\mathbf{r}_1, \mathbf{r}_2) = g\delta(\mathbf{r}_1 - \mathbf{r}_2) \tag{4.23}$$

with g a coupling constant that measures the strength of the interaction. This coupling constant is related to the *s-wave scattering length*, a, through the expression

$$g = \frac{4\pi\hbar^2 a}{M}, \tag{4.24}$$

with, as before, M the Helium mass. Essentially, at these low energies only s-waves are able to penetrate the centrifugal barrier. In this approximation the elastic collision cross section does not depends on the velocity of the particles neither on their relative angular momentum [134] [7].

[7] The p-wave contribution in only important for temperatures bigger than 1 mK where the elastic collision cross section becomes proportional to $1/T$[72].

4.3.2 Atomic density matrix in the Hartree-Fock mean field approximation.

As a result of including interactions, the Hamiltonian in Eq.4.22 is no longer an *one-body* Hamiltonian, and a second quantization formalism is preferable. The correspondent second quantized Hamiltonian in the grand canonical ensemble is

$$\hat{H} = \int d^3\mathbf{r}\ \hat{\Psi}^\dagger(\mathbf{r}) \left[\hat{H}_0 - \mu + \frac{g}{2}\hat{\Psi}^\dagger(\mathbf{r})\hat{\Psi}(\mathbf{r})\right] \hat{\Psi}(\mathbf{r}). \tag{4.25}$$

with $\hat{H}_0 = \frac{\hat{\mathbf{p}}^2}{2M} + U(\hat{\mathbf{r}})$ the ideal trapped gas Hamiltonian and $\hat{\Psi}(\mathbf{r})$ and $\hat{\Psi}^\dagger(\mathbf{r})$ the atomic field operators defined previously in Eq.2.52. The interactions term depends on the fourth power in these operators and, because of that, the derivation of the energy spectrum of this Hamiltonian is non trivial and must be done perturbatively. Another way around the problem is to simplify the Hamiltonian to a quadratic form that can be written in a diagonal basis and, therefore, reduced to a one body problem. We show in the Appendix C that this can be done self consistently through the following approximation

$$\hat{\Psi}^\dagger(\mathbf{r})\hat{\Psi}^\dagger(\mathbf{r})\hat{\Psi}(\mathbf{r})\hat{\Psi}(\mathbf{r}) \simeq 4n(\mathbf{r})\hat{\Psi}^\dagger(\mathbf{r})\hat{\Psi}(\mathbf{r}). \tag{4.26}$$

Here, $n(\mathbf{r})$ is the usual atomic density of the cloud at the location $\mathbf{r}$. The underlying physical picture expressed in this approximation is the one of a single atom system subject to an effective potential created by the *mean field* of the ensemble of all the other atoms in the cloud. Within this approximation, the density matrix of the atomic system may be written as (see Appendix C)

$$\hat{\rho} = \sum_{l=1}^{\infty} \exp\left\{-\beta l \left[\hat{H}_0 + 2gn(\hat{\mathbf{r}}) - \mu\right]\right\}. \tag{4.27}$$

4.3.2.1 Redefinition of the chemical potential to account for the interaction energy at the cloud's center.

This expression shows that, if we include interactions between atoms trapped in a harmonic potential, the upper bound for the chemical potential will increase in order to take into account the interaction energy at the center of the cloud,

$$\mu \leqslant \tfrac{3}{2}\hbar\widetilde{\omega} + 2gn(\mathbf{0}),$$

where $n(\mathbf{0})$ is the cloud's peak density. This motivates a further redefinition of the fugacity [cf. Eq.2.17] to include also this interaction energy

$$\mathrm{Z} = \mathcal{Z}\exp\left(-\tfrac{3}{2}\tilde{\tau} - 2g\beta n(\mathbf{0})\right). \tag{4.28}$$

With this definition for the fugacity, Eq.4.27 is $\hat{\rho} = \sum_{l=1}^{\infty} \mathrm{Z}^l \ \hat{\rho}_l$, with

$$\hat{\rho}_l = \exp\left\{-l\beta \sum_{\alpha} \left(\frac{\hat{p}_\alpha^2}{2M} + \tfrac{1}{2} M\omega_\alpha^2 \hat{r}_\alpha^2 + 2g\left[n(\hat{\mathbf{r}}) - n(\mathbf{0})\right] \right) \right\}. \tag{4.29}$$

4.3.2.2 Further simplifications towards the derivation of $n(\mathbf{r})$.

Our goal is to evaluate the atom density $n(\mathbf{r})$ by calculating $\langle r|\hat{\rho}|r\rangle$. However, this is not easily done since $\hat{r}_\alpha$ and $\hat{p}_\alpha$ do not commute and the exponential of Eq.4.27 cannot be factorized. On the other hand Eq.4.27 reduces to the solvable problem of the harmonic oscillator if $V_{int} \sim 0$. Thus, if this interaction term is small compared to the ideal gas Hamiltonian $\hat{H}_0$ one can develop a valid perturbation solution.

Is the interaction term a small perturbation?
To use perturbation theory, the interaction energy $V_{int}(\hat{\mathbf{r}}) = 2gn(\hat{\mathbf{r}})$ must be small when compared with the other energies found in the problem.

We consider first the thermal mean energy of the cloud. This one, for the ideal gas case, is given by

$$\begin{aligned} \langle \hat{H}_0 \rangle = \frac{Tr(\hat{\rho}\ \hat{H}_0)}{Tr(\hat{\rho})} &= \frac{1}{Tr(\hat{\rho})} \sum_{\alpha} \left(\tfrac{1}{2} m\omega_\alpha^2 \langle r_\alpha^2 \rangle + \frac{\langle p_\alpha^2 \rangle}{2M} \right) \\ &= 3\frac{g_4(\mathrm{Z})}{g_3(\mathrm{Z})}\ k_B T. \end{aligned} \tag{4.30}$$

This expression attains the classical limit for $\mathrm{Z} \to 0$, where it just expresses the *energy equipartition theorem* average energy of the system [4]. An estimation of the *mean interaction energy* may be derived as

$$\langle V_{int} \rangle = 2g\frac{Tr(\hat{\rho}\ \hat{V}_{int})}{Tr(\hat{\rho})} = 2g\frac{\int_{R^3} d\mathbf{r}\ n^2(\mathbf{r})}{\int_{R^3} d\mathbf{r}\ n(\mathbf{r})} = \frac{4a}{\lambda_T} k_B T \frac{f_{33}(Z)}{g_3(Z)} \tag{4.31}$$

with $f_{33}(Z)$ as defined in Eq.4.3.

We can also compute the cloud's maximum *interaction energy*, at the center of the cloud, which is

$$V_{int}(\mathbf{0}) = 2gn(\mathbf{0}) = \frac{4a}{\lambda_T} g_{3/2}(Z) k_B T. \tag{4.32}$$

We can now compare the two interaction energies derived above with Eq.4.30 for the mean thermal energy. We obtain

$$\frac{\langle V_{int} \rangle}{\langle H_0 \rangle} = \frac{4a}{3\lambda_T} \frac{f_{33}(Z)}{g_4(Z)}\bigg|_{Z=1} \simeq 0.013 \ \text{ and } \ \frac{V_{int}(\mathbf{0})}{\langle H_0 \rangle} = \frac{4a}{3\lambda_T} \frac{g_{3/2}(Z) g_3(Z)}{g_4(Z)}\bigg|_{Z=1} \simeq 0.063,$$

where the numerical quantities are for a thermal cloud at *BEC* threshold at the critical temperature of $T_C \sim 2\ \mu$K (which in our experiment corresponds to $N_{th} \sim 10^6$ atoms) and assuming a scattering length of $a \sim 10$ nm.

The last expression shows that, compared with the thermal energy, the interaction energy is indeed small enough to be dealt with as a perturbation. We note also that the strength of the interactions at the center of the cloud can be several times larger than its *mean* value. In fact, the above example where $Z = 1$, the ratio $V_{int}(\mathbf{0})/\langle V_{int}\rangle \approx 5$.

How the interactions change the harmonic oscillator energy levels.

In the last paragraph, we have compared the interaction energy only with the mean thermal energy of the particles. But, how does the interactions change the energy spectrum? Here, $\overline{V_{int}}$ can be of the order of the energy of the lowest level of the harmonic trap, $\varepsilon_0 = \frac{3}{2}\hbar\widetilde{\omega}$, suggesting that a perturbative analysis would fail.

Things get worse if the comparison is made for the interaction energy at the center of the cloud where the importance of the fundamental level is bigger. In this case, the local interaction energy can be twice as big as ε_0 what certainly affects significatively the energy spectrum (and the respective eigen-functions) in the low lying trapping levels.

Note that this problem is not present if $T \ll T_c$, where the cloud's many-body wave function is dominated by the fundamental ground state and where the system is rather *perturbed* by the population of the excited states. In this case a Bogoliubov transformation diagonalizes the Hamiltonian and it is possible to compute properly the spectrum of energy of the system[102].

For $T \sim T_c$ almost all atoms are in the excited states with k_BT several times larger than $\varepsilon_0 = \frac{1}{2}\hbar\omega_0$ [8]. The interactions will shift the quantum levels' energy $\varepsilon_i = \hbar\omega_i$ by $\sim (4a/\lambda_T)k_BT$ which, for the higher occupied levels, is a small quantity when compared with their energies ε_i. Moreover, since the harmonic oscillator density of states grows with ϵ_i^2, despite their small statistical occupation, the population of these higher levels is still dominant (see Figure 4.13). Thus, since most of the atoms interact only weakly the perturbative solution should apply, despite failing at the center of the trap.

We may argue however that since the critical temperature is defined through a critical value of the density at the center of the cloud the perturbative result should not give an accurate answer for δT_c, the shift in the critical temperature due to the interactions. However, there is experimental evidence[135] that the simple mean field result, first order in a/λ_T[48], is correct. This result was also confirmed theoretically in a high order perturbative

[8] In our experiment, taking $T = 2\ \mu$ K, $k_BT \sim 30 \times \varepsilon_0$.

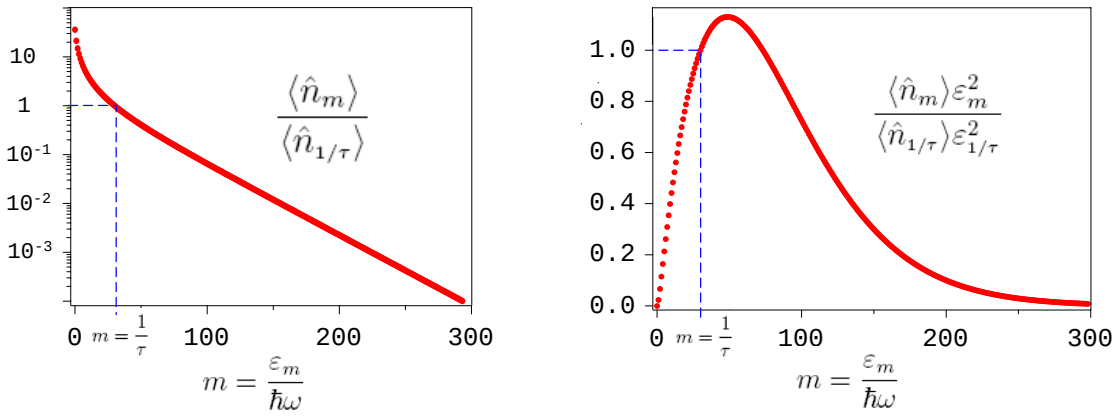

Figure 4.13: The Bose-Einstein distribution $\langle \hat{n}_m \rangle$ (left) and density of states times $\langle \hat{n}_m \rangle$ (right). Both curves are normalized by the respective value for $m = 1/\tau = k_B T/\hbar\omega = 30$ and correspond to an isotropic trap.

treatment with the same result in its lower order correction[136].

• Density matrix factorization

To proceed with the calculation one needs to derive the representation of the density matrix operator in the real space $n(\mathbf{r}) = \langle \mathbf{r}|\hat{\rho}|\mathbf{r}\rangle$. This is not a easy task since the exponential in the density operator cannot be factorized. Due to the non commutativity of the momentum and position operators, for any position and momentum functions $\hat{A} \equiv f(\hat{\mathbf{r}})$ and $\hat{B} \equiv g(\hat{\mathbf{p}})$, $e^{\lambda(\hat{A}+\hat{B})} \neq e^{\lambda\hat{A}} \times e^{\lambda\hat{B}}$. Note that if the expression *could be* factorized, it would easily be evaluated in the coordinate space through

$$\langle \mathbf{r}|e^{\lambda\hat{A}} \times e^{\lambda\hat{B}}|\mathbf{r}\rangle = \int d\mathbf{p} \langle \mathbf{r}|e^{\lambda\hat{A}}|\mathbf{p}\rangle\langle \mathbf{p}|e^{\lambda\hat{B}}|\mathbf{r}\rangle.$$

One way of overcoming this problem is by using the Trotter formula[137]

$$e^{\lambda(\hat{A}+\hat{B})} = \lim_{m\to\infty} (e^{\lambda\hat{A}/m} e^{\lambda\hat{B}/m})^m \tag{4.33}$$

which allows the exact factorization of the expression. Although very useful for numerical computation this formula is, for analytical calculation proposes very cumbersome, involving a product with an infinite number of terms. Approximate expressions can be derived then by just limiting m to small integers in the last equation. The simplest one is to take just $m = 1$. This is in fact the usual approximation used to include, analytically, the mean field interactions effect in the expression for the atomic density[48] and is often referred

as the *semi-classical* approximation as it neglects the commutation relation $[A, B]$. A slightly better approximation that does not yet involve excessive analytical complexity is to take $m = 2$[138]. In this case the approximate expression reads [9]

$$e^{\lambda(\hat{A}+\hat{B})} = e^{\lambda\hat{A}/2}e^{\lambda\hat{B}}e^{\lambda\hat{A}/2} + O(\lambda^3). \tag{4.34}$$

Making use of the approximation proposed in Eq.(4.34), one obtains the factorized expression for the matrix operator,

$$\begin{aligned}\hat{\rho}_l \simeq \exp\left\{-\tfrac{1}{2}l\beta 2g\left[n(\hat{\mathbf{r}}) - n(\mathbf{0})\right]\right\} \times \\ \times \exp\left[-l\beta\hat{H}_0\right] \times \\ \times \exp\left\{-\tfrac{1}{2}l\beta 2g\left[n(\hat{\mathbf{r}}) - n(\mathbf{0})\right]\right\}.\end{aligned} \tag{4.35}$$

Actually, this expression, when used to evaluate the atoms' density reduces to the simplest case with $m = 1$ in Eq.4.33. This is so because in the density case, the projection in the coordinate space is made on both sides of the expression in the same position,

$$\begin{aligned}n(\mathbf{r}) \equiv \langle\mathbf{r}|\hat{\rho}|\mathbf{r}\rangle &= \sum_l Z^l e^{-2l\beta g\left[n^{(0)}(\mathbf{r}) - n^{(0)}(\mathbf{0})\right]}\langle\mathbf{r}|e^{-l\beta\hat{H}_0}|\mathbf{r}\rangle \\ &= \sum_l Z^l G^{ho}(\mathbf{r},\mathbf{r};l\beta)e^{-2l\beta g\left[n^{(0)}(\mathbf{r}) - n^{(0)}(\mathbf{0})\right]}\end{aligned} \tag{4.36}$$

where, in the right hand side, $n(\mathbf{r})$ is replaced by $n^{(0)}(\mathbf{r})$, the non-interacting density given by Eq.2.19, in order to keep only the perturbation's smallest order.

To further simplify Eq.4.36, we can make use of the fact that

$$\beta g\left[n^{(0)}(\mathbf{r}) - n^{(0)}(\mathbf{0})\right] \ll 1$$

and expand the exponential in series. If we keep only the first order term, linear in $n^{(0)}(\mathbf{r})$, we get

$$n(\mathbf{r}) \simeq \sum_l Z^l G^{ho}(\mathbf{r},\mathbf{r};l\beta)\left\{1 - 2l\beta g\left[n^{(0)}(\mathbf{r}) - n^{(0)}(\mathbf{0})\right]\right\}.$$

Substituting Eq.2.19 we obtain,

$$\begin{aligned}n(\mathbf{r}) \simeq \sum_l Z^l G^{ho}(\mathbf{r},\mathbf{r};l\beta) - \\ -2\beta g\sum_{l,l'} Z^{l+l'} l G^{ho}(\mathbf{r},\mathbf{r};l\beta)\left[G^{ho}(\mathbf{r},\mathbf{r};l'\beta) - G^{ho}(\mathbf{0},\mathbf{0};l'\beta)\right].\end{aligned} \tag{4.37}$$

[9] For $m = 4$, Ref.[139] gives the formula

$$e^{\lambda(\hat{A}+\hat{B})} = e^{\lambda\hat{A}/2}e^{\lambda\hat{B}/2}\, e^{\lambda^3\left[[\hat{B},\hat{A}],\hat{A}+2\hat{B}\right]/24}\, e^{\lambda\hat{B}/2}e^{\lambda\hat{A}/2} + O(\lambda^5),$$

which calculates the contribution up to λ^4.

For the *SCA* case, we use the simplification

$$G^{ho}(\mathbf{r},\mathbf{r};l\beta) \approx \frac{1}{\lambda_T^3} e^{-l\beta U(\mathbf{r})} \left[\frac{1}{l^{3/2}} + \tfrac{3}{2}\frac{\tilde{\tau}}{l^{1/2}} \right] \tag{4.38}$$

where the *finite size effects* were also included. Keeping only the first order terms in g and $\tilde{\tau}$, the expression in Eq.4.37 reduces to

$$n(\mathbf{r}) = \tag{4.39}$$

$$= \frac{1}{\lambda_T^3} \left\{ g_{3/2}(W_T) + \tfrac{3}{2}\tilde{\tau} g_{1/2}(W_T) - \frac{4a}{\lambda_T} \left[g_{3/2}(W_T) - g_{3/2}(Z) \right] g_{1/2}(W_T) \right\} \tag{4.40}$$

where, as before, $W_T \equiv W_T(\mathbf{r}) = Z \exp\left(-\beta U(\mathbf{r})\right)$ with Z given by Eq.4.28. Finally, we note that, within the choice we made for the re-normalization of the fugacity, Eq.4.28, the peak density doesn't depend on the interaction parameter, being still expressed through Eq. 2.39. The total number of atoms is

$$N = \frac{1}{\overline{\tau}^3} \left\{ g_3(Z) - \tfrac{3}{2}\tilde{\tau} g_2(Z) + \frac{4a}{\lambda_T} \left[g_{3/2}(Z) g_2(Z) - f_{13}(Z) \right] \right\}, \tag{4.41}$$

with, again, $f_{13}(Z)$ given by Eq.4.3 . Note that the term in square brackets is always positive. For a fixed number of atoms in the cloud, the inclusion of the interactions are compensated by a reduction of the fugacity. This has a simple physical interpretation: interactions pushes atoms apart, reducing the cloud's peak density. For recovering the non interactive peak density, we need to pack more atoms into the cloud.

4.3.2.3 The classical phase space distribution function $f(\mathbf{r},\mathbf{p})$.

If we had replaced Eq.4.38 directly in Eq.4.36, but neglecting the *finite size effect* term, we would get the expression

$$n(\mathbf{r}) = \int \frac{d\mathbf{p}}{(2\pi\hbar)^3} f(\mathbf{r},\mathbf{p}) \tag{4.42}$$

with $f(\mathbf{r},\mathbf{p})$ given by

$$f(\mathbf{r},\mathbf{p}) = \sum_{l=1}^{\infty} Z^l e^{-l\beta\left(U(\mathbf{r}) + \frac{\mathbf{p}^2}{2M} + 2g\left[n^{(0)}(\mathbf{r}) - n^{(0)}(\mathbf{0}) \right] \right)}. \tag{4.43}$$

This last expression is just the classical phase space distribution function,

$$f(\mathbf{r},\mathbf{p}) = \frac{Z}{\exp\left[\beta\varepsilon(\mathbf{r},\mathbf{p})\right] - Z},$$

where $\varepsilon(\mathbf{r},\mathbf{p}) = U(\mathbf{r}) + \frac{\mathbf{p}^2}{2M} + 2g\left[n^{(0)}(\mathbf{r}) - n^{(0)}(\mathbf{0})\right]$ is the *classical energy* of an atom located at $\mathbf{r}$ with momentum $\mathbf{p}$. In the framework of the *semi-classical* approximation the distribution function $f(\mathbf{r},\mathbf{p})$ is more intuitive and can replace the exact quantum mechanical density matrix operator in calculation of the density of particles $n(\mathbf{r})$ or related quantities. Note, however, that this is *not* the case if one wants to compute quantities that depend on the two-body density matrix operator (or higher) as is the case of, for instance, the density-density correlation function derived in the previous Chapter.

The function in Eq.4.43 does not take into account corrections due to the *finite size effects* [10]. We can go around this problem, adding to $f(\mathbf{r},\mathbf{p})$ the extra term $\frac{3}{2}l\tilde{\tau}\sum Z^l e^{-l\beta\left[U(\mathbf{r})+\mathbf{p}^2/2M\right]}$. Adding this term and expanding, as before, the exponential in the interaction term, we finally get

$$f(\mathbf{r},\mathbf{p}) \approx \sum_{l=1}^{\infty} Z^l e^{-l\beta\left[U(\mathbf{r})+\frac{\mathbf{p}^2}{2M}\right]} \times \left\{1 - 2lg\beta[n^{(0)}(\mathbf{r}) - n^{(0)}(\mathbf{0})] + \tfrac{3}{2}l\tilde{\tau}\right\}. \quad (4.44)$$

In the following we will use this expression for deriving the *TOF* signal. It will also be used in the following Chapter to compute different average moments of the cloud density that enters in the calculation of the ion signal produced by a cloud of interactive atoms (see §5.2.1).

4.3.3 The *time of flight* of a thermal cloud.

The goal here is to derive an expression that depends only on the time, equal to the atomic flux integrated over a detector surface on an xOy plane perpendicular to the fall direction and at a certain distance below the trap center. The simplest way of doing this, within the *semi-classical* approximation, is starting with cloud's classical distribution function $f(\mathbf{r},\mathbf{p})$ of Eq.4.44. The expression in Eq.4.44 can be written as

$$\begin{aligned} f(\mathbf{r},\mathbf{p}) &= \sum_l Z^l \exp\left[-l\beta\left(U(\mathbf{r}) + \frac{\mathbf{p}^2}{2M}\right)\right]\{1 + l\mu_0(Z)\} \\ &\quad -\frac{4a}{\lambda_T}\sum_{l,l'} Z^{l+l'}\,\frac{l}{l'^{3/2}}\exp\left[-(l+l')\beta U(\mathbf{r}) - l\beta\frac{\mathbf{p}^2}{2M}\right] \quad (4.45) \end{aligned}$$

with

$$\mu_0(Z) = \tfrac{3}{2}\tilde{\tau} + \frac{4a}{\lambda_T}g_{3/2}(Z). \quad (4.46)$$

[10] To explicitly include the *finite size* term in Eq.4.43 we must include a non trivial term proportional to l^3, $e^{-l^3\beta\tilde{\tau}\mathbf{p}^2/2M}$, with which the expression is no longer a Bose-Einstein distribution function.

The Eq.4.45 gives the probability for a trapped atom to have a momentum $\mathbf{p}$ and to be at the location $\mathbf{r}$. When released from the trap, this atom undergoes a parabolic trajectory depending on its initial location and momentum and also in the effect of the gravity, according to

$$\mathbf{r} = \mathbf{r}_0 + \frac{\mathbf{p}_0}{M}t + \tfrac{1}{2}gt^2\hat{z} \quad \text{and} \quad \mathbf{p} = \mathbf{p}_0 + gt\hat{z}.$$

Neglecting the transversal dimension of the cloud in the $\hat{z}$ direction, we can identify in the first expression $z_0 = H$, with H the distance of fall. This change of variables has a Jacobian given by $|p_{0_z}|$ and the integral

$$I(t) = \iint dx_0 dy_0 \iint dp_{x0} dp_{y_0} \int |p_{0_z}| f(x_0, y_0, p_{x0}, p_{y_0}, p_{z0}) \tag{4.47}$$

gives the atomic flux passing over the infinite plane xOy. Explicitly, this expression is given by

$$I\left[\mathcal{W}(\delta t)\right] = \frac{1}{\sqrt{2\pi}}\frac{1}{\overline{\tau}^3}\frac{v_2}{v_T}\frac{1}{t_0} \times \\ \times \left\{ g_{5/2}\left[Z \cdot \mathcal{W}(\delta t)\right] + \mu_0(Z) g_{3/2}\left[Z \cdot \mathcal{W}(\delta t)\right] - \frac{4a}{\lambda_T} f_B[Z, \mathcal{W}(\delta t)] \right\}, \tag{4.48}$$

where $\mathcal{W}(\delta t) = \exp\left[-\frac{1}{2}\left(\delta t / t_{cl}\right)^2\right]$ and the function $f_B(z, w)$ is the sum expression

$$f_B(z, w) = \sum_{l,l'} \frac{z^{l+l'} w^l}{l'^{3/2}(l + l')^{3/2}}. \tag{4.49}$$

The expression in Eq.4.48 is presented after being simplified with the *far field* and the *long fall* approximations and using the definition $\delta t = t - t_0$, with $t_0 = \sqrt{H/2g}$. However, these approximations are not essential in the derivation to achieve to this result. This is not the case if we want to achieve this same result but in a more rigorous calculation, starting from the quantum density matrix of Eq.4.35.

Since the `MCP` has a finite size, the integration in Eq.4.47 should not be extended over all the xOy plane but only to the detector surface. For this case, the atomic flux becomes

$$I_D(\delta t) = I[\mathcal{W}(\delta t)] - I[\mathcal{W}(\delta t) \cdot \mathcal{W}_D] \tag{4.50}$$

with $I[\mathcal{W}(\delta t)]$ the expression in Eq.4.48 for the infinite detector case and

$$\mathcal{W}_D = \exp\left[-\tfrac{1}{2}R_D^2/(v_T t_0)^2\right],$$

where we considered a circular shaped `MCP` of radius R_D.

Integrating Eq.4.50 over time, we obtain the total number of detected atoms N_D. In general, this number can be smaller than the cloud's total number of atoms N since the transversal size of this latter one, at the level of the detector, can be larger than $2R_D$. The explicit expression for the number of detected atoms is now

$$N_D = \frac{1}{\overline{\tau}^3}\Big\{ [g_3(Z) - g_3(Z\cdot\mathcal{W}_{\mathcal{D}})] + \mu_0(Z)\,[g_2(Z) - g_2(Z\cdot\mathcal{W}_D)] - \frac{4a}{\lambda_T}\,[f_{13}(Z) - f'_B(Z,\mathcal{W}_D)]\Big\}, \tag{4.51}$$

with yet another two-parameter function $f'_B(z,w)$ defined as

$$f'_B(z,w) = \sum_{l,l'} \frac{z^{l+l'}w^l}{l^{1/2}l'^{3/2}(l+l')^{3/2}}. \tag{4.52}$$

The *TOF* fitting expression.
We have now all the ingredients to write down the expression we used for fitting our *TOF*s. It is

$$f_{tof}(\delta t; Amp, t_0, v_t, Z) = Amp\,\left(1 + \frac{\delta t^2}{2t_0^2}\right)\,\left[h(Z,\mathcal{W}) - h(Z,\mathcal{W}\mathcal{W}_D)\right], \tag{4.53}$$

with

$$h(z,w) = g_{5/2}(z.w) + \mu_0(z)g_{3/2}(z.w) - \tfrac{4a}{\lambda_T}f_B(z.w)$$

and Amp the *TOF* amplitude (*i.e.* its maximum value) given by

$$Amp = \eta \times \frac{N}{N_D} \tag{4.54}$$

where N_D is given by Eq.4.51 and η is an auxiliary factor that accounts for the detection efficiency and geometry [11].

4.3.4 The cloud's hydrodynamical expansion: thermometric correction.

In the previous paragraph, we have considered the expansion and fall of a atomic cloud that, when trapped within thermal equilibrium, is affected by interatomic interactions. However, during the expansion and fall period, the atoms are treated as ideal, falling freely without interacting with the others.

[11] In our experiment, for obtaining Amp in Volt this parameter is equal to $\eta = 2.3 \times 10^{-8}V^{-1}$ (see §1.3.6.1).

We will show that this ideal gas ballistic expansion is, indeed, a good approximation since the gas fast expansion leads to a decrease of the cloud's density and therefore of the rate of collisions among atoms. Nevertheless, to achieve a proper measure of the cloud's temperature we need to account for the breve anisotropic expansion the cloud undergoes in the first initial moments after being released from the trap. During this period, the cloud's expansion is *hydrodynamical*, a strong collisional regime similar to the one of a dense classical fluid.

4.3.4.1 The Knudsen criterion

The strong collisional regime is characterized by a mean free path of an atom between two consecutive collisions much smaller than the cloud's extension. In here the gas behaves as a hydrodynamical fluid. The mean free path at the trap center, where the atomic density is $n(\mathbf{0})$, is given by the uniform gas expression[140]

$$\lambda_0 = \frac{1}{\sqrt{2}\; n(\mathbf{0})\sigma_S},$$

where $\sigma_S = 8\pi a^2$ is the collision cross-section in the low temperature limit with a, as before, the *s-wave* scattering length. For the sample size we can simply take the thermal size $s_\alpha = v_T/\omega_\alpha$. The above criterion establishing the hydrodynamical behavior can be written, in each spatial trap axis, as

$$\frac{\lambda_0}{s_\alpha} \ll 1.$$

This is known as the Knudsen criterion. Taking the densest case, at the center of a cloud in the transition temperature, this criterion can be re-written as

$$\left(\frac{\lambda_T}{a}\right)^2 \ll \frac{8\sqrt{\pi}}{\tau_\alpha}\zeta(3/2),$$

with the usual definition $\tau_\alpha = \hbar\omega_\alpha/k_BT$. Differently from the mean field approach, where the relevant parameter to measure the interaction strength is a/λ_T (cf. Eq.4.39), here the collisional regime is characterized by $(a/\lambda_T)^2$. For a typical temperature in our samples of 2 μK and taking $a \sim 10$ nm, $\lambda_T/a \sim 60$. In these conditions, for our trap with axial and radial frequencies $\omega_\parallel/2\pi \sim 50$ Hz and $\omega_\perp/2\pi \sim 1250$ Hz, we get

$$\lambda_0/\sigma_\perp \sim 5 \quad \text{and} \quad \lambda_0/\sigma_\parallel \sim 0.2,$$

showing that, within the Knudsen criterion, in the two fastest axes the gas is almost in the ideal collisionless regime. In the slowest one, things are different: the collisional regime is already of hydrodynamical character. In

this axis, during a round trip oscillation in the cloud, an atom can experience a few collisions. After a collision, an atom that travels in the less confined trapping axis will be scattered into a different momentum state that will preferably help inflate the cloud in the transverse direction. This process will ultimately produce a anisotropic expansion very similar to what is observed in the geometry inversion of the *BEC* expansion (see Appendix A).

For a trapped gas in thermal equilibrium the hydrodynamical regime may be seen as a higher order correction to the mean field effect. The classical distribution function of Eq.4.44 may be corrected if derived within the framework of a *Boltzmann-Vlasov* kinetic equation that accounts for both mean field and hydrodynamical effects.

4.3.4.2 Description using the Boltzmann-Vlasov kinetic equation.

The ideal gas ballistic expansion derived with in §2.2.1 was entirely derived using quantum mechanics, in a rigorous way. Here, to allow the inclusion of the mean-field and dissipative effects we rather need to use a classical equation, the Boltzmann-Vlasov equation (BVE), which is capable of describing the time evolution of $f(\mathbf{r},\mathbf{v},t)$, a generalization of the time independent classical distribution function of Eq.4.44. The Vlasov part of the BVE just adds to the common Boltzmann kinetic equation the mean field term $2gn^{(0)}(\mathbf{r})$, with the dissipative processes being considered, as usual, in the collision integral term $I_{coll}[f]$,

$$\frac{\partial f}{\partial t}+\mathbf{v}\frac{\partial f}{\partial \mathbf{r}}-\frac{1}{M}\frac{\partial}{\partial \mathbf{r}}\left[U(\mathbf{r})+2gn^{(0)}(\mathbf{r})\right]\frac{\partial f}{\partial \mathbf{v}}=I_{coll}[f]. \tag{4.55}$$

For solving this equation we follow Ref.[141]. First, the collision integral will be simplified, within the *relaxation time approximation*, to

$$I_{coll}[f]\approx\frac{f-f_{le}}{\tau_{coll}}$$

with f_{le} the *local equilibrium* distribution function and the relation time τ_{coll}, the average time between collisions.

In a second approximation, we assume that the solution of Eq.4.55 $f(\mathbf{r},\mathbf{v},t)$ may be found simply by recasting the equilibrium distribution function $f_0(\mathbf{r},\mathbf{v})$, being the scaling ansatz given by

$$f(\mathbf{r},\mathbf{v},t)=\Gamma\ f_0(\mathbf{R}(t),\mathbf{V}(t)), \tag{4.56}$$

with

$$\begin{cases} R_\alpha=\dfrac{r_\alpha}{b_\alpha}, \quad V_\alpha=\dfrac{1}{\theta_\alpha^{1/2}}\left(v_\alpha-\dfrac{\dot{b}_\alpha}{b_\alpha}r_\alpha\right) \\ \Gamma=\left[\displaystyle\prod_\alpha b_\alpha\theta_\alpha^{1/2}\right]^{-1} \end{cases} \tag{4.57}$$

and where $b_\alpha \equiv b_\alpha(t)$ and $\theta_\alpha \equiv \theta_\alpha(t)$ are dimensionless parameters, that describes, respectively, the cloud dilatation and the effective temperature in the $\alpha-$ axis.

The equations of motion for $b_\alpha(t)$ and $\theta_\alpha(t)$ can be derived by computing the average moments of $R_\alpha V_\alpha$ and V_α^2 of the re-scaled Boltzmann-Vlasov equation [12]. Finally, using $U(\mathbf{r}) = \frac{1}{2}M{\omega_{0\alpha}}^2\mathbf{r}^2$, with $\omega_{0\alpha}$ the steady state trapping oscillation frequencies, one gets

$$\begin{cases} \ddot{b_\alpha} + \omega_\alpha^2 b_\alpha - \theta_\alpha b_\alpha^{-1}{\omega_{0\alpha}}^2 + \zeta b_\alpha^{-1}{\omega_{0\alpha}}^2\left(\theta_\alpha - \prod_\alpha b_\alpha^{-1}\right) = 0 \\ \dot{\theta}_\alpha + 2\dot{b}_\alpha b_\alpha^{-1}\theta_\alpha = -\frac{1}{\tau_{coll}}(\theta_\alpha - \bar{\theta}) \end{cases} \tag{4.58}$$

with $\bar{\theta} = \frac{1}{3}\sum_\alpha \theta_\alpha$, $\omega_\alpha \equiv \omega_\alpha(t)$ the transient trap frequencies and

$$\zeta = \frac{2g\langle n(\mathbf{r})\rangle_0}{2g\langle n(\mathbf{r})\rangle_0 + \frac{2}{3}M\langle v^2\rangle_0}$$

a dimensionless parameter that accounts for the mean field interaction where the mean values $\langle\chi\rangle_0$ are defined as the average in position and velocity space of the function $\chi(\mathbf{r},\mathbf{v})$ weighted by the equilibrium distribution function, *i.e.*

$$\langle\chi\rangle_0 = \frac{\iint d\mathbf{r}\, d\mathbf{v}\, f_0(\mathbf{r},\mathbf{v})\chi(\mathbf{r},\mathbf{v})}{\iint d\mathbf{r}\, d\mathbf{v}\, f_0(\mathbf{r},\mathbf{v})}.$$

During the trap switch off, the trapping frequencies will decrease, in some way, from $\omega_{0\alpha}$ to $\omega_\alpha = 0$. The simplest case we may have is when this happens instantaneously. Admitting that this is the case, the equation in the first line of Eqs.4.58 simplifies to

$$\ddot{b_\alpha} - \theta_\alpha b_\alpha^{-1}{\omega_{0\alpha}}^2 + \zeta b_\alpha^{-1}{\omega_{0\alpha}}^2\left(\theta_\alpha - \prod_\alpha b_\alpha^{-1}\right) = 0.$$

Recovering the perfect gas behavior.

The last expression in Eq.4.59 may as well describe the ballistic expansion in the limit where we *switch off* the interactions. The *non interactive* version of the expressions in Eq.4.58 is obtained simply by replacing $\tau_{coll} = \infty$ and $\zeta = 0$. This reduces the equation in the second line of Eq.4.58 to the simple relation $\theta_\alpha = b_\alpha^{-2}$. Furthermore, if we replace this identity in the first equation and solve the differential equation, we get $b_\alpha = \sqrt{1+\omega_\alpha^2 t^2}$, which is the same coordinate re-scaling found on §2.2.1 [13]. Also, the *normalization* parameter

[12] The first of these expressions doesn't depend on the collisional integral since the quantity $R_\alpha V_\alpha$ is conserved in the collisions. For computing the average moment $\langle V_\alpha^2\rangle$, the *relaxation time approximation* is used along with the condition of isotropic temperature within the local equilibrium.

[13] We do not consider here the effect of gravity, which is not included in the ansatz of Eqs.4.57

Γ in Eqs.4.57 reduces to $\Gamma = \prod_\alpha (1+\omega_\alpha^2 t^2)^{-1/2}$, the same factor that appears in the flux expression in Eq.2.68.

Note that the above analysis is independent of the equilibrium distribution function $f_0(\mathbf{r},\mathbf{v})$ that can be any generic distribution function within the *semi-classical distribution*. It can be chosen as the one describing a thermal cloud at the critical temperature or above it. Integrating the expression of Eq.4.56 over momentum space we obtain, as before in Eq.2.72,

$$M\int \frac{d\mathbf{v}}{(2\pi\hbar)^3} f(\mathbf{r},\mathbf{v},t) \rightarrow n(\mathbf{r},t) = \frac{n(\tilde{\mathbf{r}})}{\prod_\alpha \sqrt{1+\omega_\alpha^2 t^2}},$$

irrespectively to the initial shape of the cloud.

4.3.4.3 Hydrodynamical expansion and temperature correction.

In Fig.4.14 we present a numerical solution for the rescaling parameters b_α of Eqs.4.58. We assume that the trap is abruptly switched off and the cloud is at the critical temperature $T = 3\ \mu$K. We have also used for the scattering length $a = 7.5$ nm. In this Figure the solid lines represent the interaction free ballistic expansion of the cloud, whereas the dotted line the numerical solution. The left hand side graph shows the evolution of the cloud's size in its axial (bias) direction which is slower than the ballistic expansion. Conversely, in the perpendicular direction the cloud inflates slightly faster than an non-interacting gas. This leads also to a bigger *TOF* waist and, thus, to an apparent bigger cloud's temperature.

The hydrodynamical and ballistic curves in both graphs of Fig.4.14 seems to differ only in its slopes. To get a better idea of this we define the relative hydrodynamical expansion factors as

$$\varepsilon_\perp(t) = \frac{b_\perp(t)}{b_\perp^0(t)} \quad \text{and} \quad \varepsilon_\parallel(t) = \frac{b_\parallel(t)}{b_\parallel^0(t)}, \tag{4.59}$$

where $b_\alpha^0(t)$ stands for the ballistic expansion. These two quantities are plotted in the left hand side graph of Fig.4.15. This Figure shows that except for an initial transient period the two regimes tends to have a similar behavior but with different expansion velocities (ε_α tends asymptotically to a constant). If we disregard the initial transient behavior, the hydrodynamical regime may be incorporated into the analysis by simply redefining the *effective* trapping oscillation frequencies in each axis. This procedure *saves* the validity of the ballistic expansion analysis of the *TOF*. Nevertheless, the temperature we may find in a fit to a given *TOF* must be corrected to account to this effect. As the *TOF* signal results from a spatial integration over the bias axis, the temperature correction is determined only by the cloud's

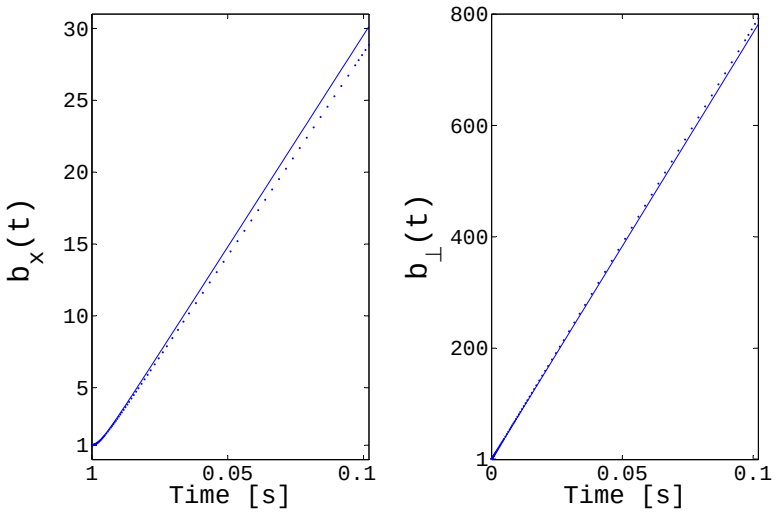

Figure 4.14: The time evolution of the dimensionless cloud dilation parameters $b_x(t)$ and $b_\perp(t)$, in the bias (slow axis) and perpendicular directions respectively. The solid line represents the simple law of the ballistic expansion $b_\alpha = \sqrt{1+\omega_\alpha^2 t^2}$ and the dotted one the solution of Eqs.4.58 when ω_α goes instantaneously to zero when the trap is switch off. Other parameters used in the computation of these curves are $T = 3$ μK, $Z = 1$ and $a = 7.5$ nm. The graphs shows that, due to the hydrodynamical effect, the cloud expands slightly more in the transverse axes than what happens in the ballistic expansion. This happens at the expense of a smaller expansion in the bias axis direction.

expansion correction of the perpendicular axis and

$$T \to T \times \varepsilon_{\perp}^2(t = t_0), \tag{4.60}$$

with t_0 the time of fall. This relative correction is shown, in percentage, in the right hand side graph of Fig.4.15 for four different cases and reflecting its dependence in the value of the scattering length and fugacity.

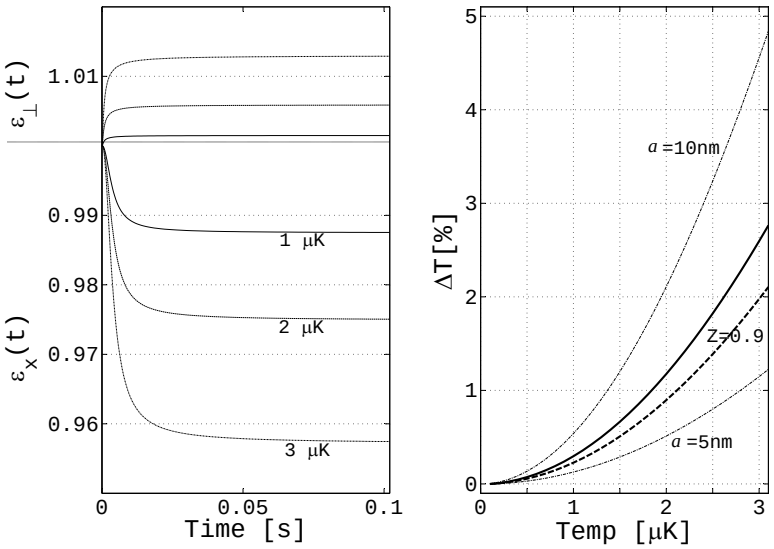

Figure 4.15: Left hand side graph: relative hydrodynamical expansion in the bias and perpendicular axis for clouds at three different temperatures; right hand side graph: the hydrodynamical induced variation of the temperature of a cloud at the critical temperature for $a = 7.5$ nm (central solid line) and also for $a = 5$ nm and $a = 10$ nm. This graph also plots a similar curve with $a = 7.5$ nm and $Z = 0.9$ (dashed line)

4.3.5 Conclusion.

The expressions derived in this Section, as well as the results of the ion signal analysis done before will be used in the following Chapter in the analysis of data obtained in an experiment realized to measure the scattering length a. As we will see, in the data analysis of this experiment, the cloud's thermometry plays a major role. This will allow us to test the theoretical formalism and the expressions developed in this Chapter.

CHAPTER 5

The cloud thermometry and the determination of the He^*scattering length.

In the previous Chapter, we show that the atomic cloud is characterized by the temperature, fugacity and by the scattering length. For the ion rate we must add the rate constant β and L. A combination of measurements at $T = 0$ and $T = T_c$ should allow us to extract a, whose value was not well known at the beginning of my Ph.D. thesis. In this Chapter we will describe, Section 5.2, the experiment and the data analysis to perform this measurement[51, 46]. In 2005, an independent and very precise measurement of a was performed and the result is in disagreement with ours by 50%. We have decided then to reanalyze our data more carefully, what is done in Section 5.3. In this new analysis we achieved to reduce the statistical uncertainty on the determination of a, but we have obtained the same result as in the former analysis. Section 5.4 is devoted to a possible explanation of the observed discrepancy.

5.1 Introduction.

At the moment we write this manuscript, there is a very reliable measurement of the *s-wave* scattering length a obtained through *light-induced collision spectroscopy* experiments[142, 143] and conduced in the group of M. Leduc at the *École Normale Supérieure de Paris* (*ENS*). The measured value has a high level of accuracy: $a = 7.512 \pm 0.005$ nm. The result we have obtained in the experiment of Ref.[46] and also reported in here is rather $a = 11.2 \pm 0.4$ nm, which denotes a serious problem in our experimental procedure or in the interpretation of the obtained data.

At the time this experiment was done, a was not yet well known and the existent experimental results relied on studies of the condensate expansion[31, 32] or in studies of the evaporative cooling of a thermal cloud[40]. All these experiments were however not very conclusive due to their large uncertainties on the final results.

The idea of our experiment for measuring a relies on the comparison of the ion flux generated by a cloud at the critical transition temperature, which depends on a, and its average atomic density, which also depends on a but in a smaller extend. To analyze the results of this experiment it was necessary to know *a priori* the values of the ionization rate constants β and L. These constants were measured by us in a previous experiment[45, 70] whose outcome was the value of β and L parameterized by a.

The idea of this earlier experiment, described in some detail in Appendix B, was very similar to the one we present here for measuring a: we ought to derive β and L by comparing the ion flux originated by a *pure BEC* with its peak density. This latter quantity, proportional to μ/a (cf. §A), can be well determined from the *BEC*'s *TOF*, but only if a is accurately known, which is not the case. To overcome this difficulty we have opted to present the results for β and L parameterized by a, to allow determining them when a was known accurately.

The fact that the measurement of a depended on the knowledge of the ionizing rate constants that, in their turn, were computable only for a given value of a presented no problem in our analysis on the determination of a: we simply had to use the information from one and the other experiments iteratively to find the proper value of a. Note that these two experiments analyzed data acquired in two different physical realities: one of them used condensates, the other thermal clouds at the critical phase transition.

In this Chapter we will push forward the data analysis we have done initially for this experiment to measure a. This will be used as a *good excuse* for describing some techniques we have developed for improving the accuracy in the determination of the temperature and fugacity of thermal clouds.

This somehow more *robust* data analysis has achieved producing a result with a smaller statistical uncertainty and also explaining a relatively large data dispersion we have observed in the first analysis we have done. Nevertheless, the final result we get for a confirms the value obtained initially, around $a \sim 11$ nm.

It seams less probable that the large discrepancy between this result and the one found by the *ENS* group results from the fitting analysis of the *TOF*s. Another possibility, we consider here, is that the hydrodynamical correction we use is incorrect. This may happen if the trap switch-off is not an instantaneous process as it was assumed in §4.3.4 (thermal cloud case) and also in the Appendix A (*BEC* case). We will show that if the atomic cloud is slowly released from the trap (compared with the oscillation trap frequencies), its expansion is smaller and the hydrodynamical correction should be larger than the one predicted by the sudden switch-off case. This correction results in bigger values of the *BEC* chemical potential and of the thermal cloud's temperature. Within the data analysis on the determination

of the ionization rate constants (Appendix B), this leads to smaller values of β and L. A value of $a = 7.5$ nm may be achieved for certain switch-off *velocities* which, in general, might be different for *BEC*s and the thermal clouds.

Chapter outline.

This Chapter is divided in three Sections. In the first one we present the experiment we have done. We will describe the experimental procedure, some technical details and also our initial data analysis, published in Ref.[46] and further detailed in the Ph.D. thesis of S. Seidelin. The data analysis here relies on a description of the cloud's density by a theoretical model at the critical phase transition. Both the atomic *TOF* and the ion flux signals are derived for $Z = 1$ and the main difficulty we face is how to properly choose experimental data at the critical point.

The second Section revisits this experiment and its data analysis. Instead of assuming from the beginning a theoretical description with $Z = 1$, in here we will propose that the analysis relies on the determination of the fugacity of all the available data of non-degenerate clouds. To discard all data with $Z > 1$ we will use a strategy developed expressly for this problem, the χ^2-*map* method. This is briefly presented in this Section and further explained in Appendix D.

Finally, in the third Section we detail our hypothesis for explaining our huge systematic error on the determination of a. We will use a model where the trapping potential relaxes exponentially when is switched-off. We find what should be the trap relaxation time for obtaining $a = 7.5$ nm in our experiment. We end discussing the obtained result of this analysis.

5.2 Determination of the scattering length.

The easiest way to determine the *s-wave* scattering length a of an atomic species, in a cold atoms' experiment, is by relating the size of a condensed cloud with its number of atoms (see Eq.A.8 of Appendix A, §A.2). This is not, unfortunately, an option in our experiment since we are unable to measure with enough accuracy the number of atoms on the condensate.(cf. 1.3.6.1).

In the other hand, our experiment gives us an extra diagnostic signal on the atomic cloud: the ion flux signal. This is proportional to the cloud's density and, also, to the magnitude of the interatomic interactions. Comparing the information obtained from the cloud's *TOF* and the one from the ion signal we may determine some of the characteristics of the collisional processes involved in the production of the ions.

This idea was used twice by us. Initially we have used it with condensates to determine the ionizing rate constants β and L (see Appendix B). In a second experiment, we used thermal clouds *produced* at the critical phase transition to determine the value of a. In this Section we will present in some detail this experiment and also its data analysis.

General ideas

To get a good interpretation of the ion signal, we need to know the collisional rate constants and also make a proper determination of the cloud's density from its *TOF* signal. The collisional rate constants may be derived from the expressions on Eq.B.3 of Appendix B. These are parameterized by a and, as we have referred earlier, we will determine this quantity in a self consistent iterative way.

In general, an proper characterization of the atomic clouds density through their *TOF* signal is not trivial. For simplifying the task of determining the cloud's temperature, we have decided in this first analysis to use only clouds at the critical point. To chose the data to be analyzed we started by using the criteria we have developed in §4.2.4.3, based on the ion flux signal. This criteria is complemented in here with another one based on the clouds' *TOF* analysis.

The *TOF* of a thermal cloud of interactive atoms can be fully determined with only three parameters: the cloud's temperature T, its fugacity Z and a, the scattering length. This latter appears in the density model in a perturbative correction term and, thus, it influences only weakly the *TOF* signal. Fixing the fugacity to be $Z = 1$, we see that the only parameter we need to measure for determining the cloud's density is its temperature.

The ion flux signal has a stronger dependence on the value of a, making it suitable for its measurement. We will start by stressing this idea, deriving

the full expression for this signal in the case of an sample with interatomic interactions.

5.2.1 High order corrections for the ion flux signal in the non-degenerate case.

In the §4.2.2.1 we have derived a simple expression for the ion flux signal for a non-degenerate cloud within the ideal gas model. In here we correct this expression to account to interatomic interactions and the finite size effect.

For the non-degenerated case, the ion flux signal is given by Eq.4.1, rewritten here as

$$\Phi = \frac{1}{\tau_i}\overline{n(\mathbf{r})} + \tfrac{1}{2}\beta\overline{n^2(\mathbf{r})} + \tfrac{1}{3}L\overline{n^3(\mathbf{r})}. \tag{5.1}$$

The average moments of the cloud density, $\overline{n(\mathbf{r})}$ will be computed within the *semi-classical* approximation. Starting from the *classical phase space distribution function* $f(\mathbf{r},\mathbf{p})$, presented before in Eq.4.44 (cf. §4.3.2.3), the cloud's density $n(\mathbf{r})$ is

$$f(\mathbf{r}) \equiv n(\mathbf{r}) = \frac{1}{\lambda_T^3}\sum_l \frac{Z^l}{l^{3/2}} e^{-l\beta U(\mathbf{r})}\left\{1 - 2l\beta g[n^{(0)}(\mathbf{r}) - n^{(0)}(\mathbf{0})] + \tfrac{3}{2}l\tilde{\tau}\right\}, \tag{5.2}$$

Using the notation of §4.2.2.1, the first average moment, *i.e.* the number of atoms, is

$$\begin{aligned}\overline{n(\mathbf{r})} \equiv N &= \int d\mathbf{r}\, n(\mathbf{r}) \\ &= \frac{1}{\overline{\tau}^3}\left\{g_3(Z) + \tfrac{3}{2}\tilde{\tau}g_2(Z) + \frac{4a}{\lambda_T}[g_{3/2}(Z)g_2(Z) - f_{31}(Z)]\right\}\end{aligned} \tag{5.3}$$

which is the same expression as in Eq.4.41. Keeping only first order terms in a/λ_T and $\tilde{\tau}$ [1], the second and third order average moments of the density are given by

$$\overline{n^2(\mathbf{r})} = \frac{1}{\overline{\tau}^3\lambda_T^3}\left\{f_{33}(Z) + 3\tilde{\tau}f_{31}(Z) + \frac{8a}{\lambda_T}[g_{3/2}(Z)f_{31}(Z) - f_{331}(Z)]\right\} \tag{5.4}$$

and

$$\overline{n^3(\mathbf{r})} = \frac{1}{\overline{\tau}^3\lambda_T^6}\left\{f_{333}(Z) + \tfrac{9}{2}\tilde{\tau}f_{331}(Z) - \frac{12a}{\lambda_T}[g_{3/2}(Z)f_{331}(Z) - f_{3331}(Z)]\right\} \tag{5.5}$$

[1] High order terms are very small and we can neglect them [51].

In these expressions we have used the usual definition for $f_{jk...p}(x)$ given in Eq.4.3.

Substituting the above expressions in Eq.5.1, we get the total ion flux produced within the cloud,

$$\Phi \equiv \Phi(Z, T, a; \beta[a], L[a]). \tag{5.6}$$

an expression that depends on the temperature, fugacity, scattering length a and on the ionization rate constants. These latter are obtained from Ref.[45], parameterized by a (see also Appendix B).

5.2.1.1 Ion flux signal at $Z = 1$.

In the Section §5.3 we will make use of the expression indicated on Eq.5.6 with free parameters for the temperature and fugacity. For the analysis we present in here, this expression is simplified to the very special case of a cloud at the critical phase transition. Putting $Z = 1$ we obtain

$$\begin{aligned}\Phi_c(T_c; a) = \overline{\tau}_c^{-3} \times \Big[& \frac{1}{\tau_i}(1.20 + 2.48\tilde{\tau}_c + 12.35 a/\lambda_c) \\ & + \frac{\beta[a]}{\lambda_c^3}(0.33 + 1.81\tilde{\tau}_c + 6.75 a/\lambda_c) \\ & + \frac{L[a]}{\lambda_c^6}(0.22 + 2.21\tilde{\tau}_c + 6.50 a/\lambda_c)\Big],\end{aligned} \tag{5.7}$$

where T_c and λ_c are *critical* values of the temperature and of the thermal de Broglie wavelength. This expression depends only on cloud's critical temperature and of the scattering length a. As referred before, the ionization rate constants β and L are evaluated using the empirical relations of Eq.B.3 of Appendix B.

The expression on Eq.5.7 shows that the ion signal depends significatively on the value of a. For instance, for a cloud at the critical phase transition with $T_c = 2$ μK, the ratio a/λ_T is only of the order of 0.5% but it is sufficient to increase the ion flux by 5%, 10% and 15% for the *one-*, *two-* and *three-*body processes, respectively.

5.2.2 The data analysis procedure.

The data analysis of this experiment may be summarized in the following iterative procedure:

1. Choose a first trial guess for the value of a and, fitting the *TOF* signals, derive the corresponding peak densities, $n_{th}(\mathbf{0})$;

2. Keep the same value for a and derive the *rate constants*, β and L, from Eqs.B.3;

3. With the obtained values for the *ionizing rate constants* [2] and the cloud's peak density, derive algebraically the expected ion signal.

4. Compare the value computed for the ion signal with the real one and, if different, choose an other trial value for a and repeat the entire procedure again.

5. Stop when the ion signal is well fitted by the theoretical model.

In practical terms, this iterative procedure may be implemented very easily through a fit of the ion flux in function of the temperature and expressing all the involved parameters in the fitting expression in function of a. However, this procedure is simple only if the cloud's peak density, found through a fit to the respective *TOF*, doesn't depend much on a. Otherwise, each time we have a new a we had to refit all the *TOF* data. We show next that, fortunately, this is not the case: taking a reasonable value for a, we can skip the first step in the above list and implement the remanning three with a simple fitting routine.

5.2.3 Variation of the fitted temperature with a.

The small perturbation parameter a/λ_T has a much smaller influence on the mean field expression for the atomic *TOF* (cf. Eq.4.48) than on the ion flux. This is shown in Fig.5.1 where we see that the temperature we find fitting a given *TOF* curve for different values of a doesn't change very much. This allow us to chose a *reasonable* value for a and fit all the *TOF* data only once.

The *reasonable* value we used for a in our data analysis was $a = 12\ nm$. This was long before the measurement made by the *ENS* group (equal $a \sim$ 7.5 nm) and, at that time, it was the most reasonable value regarding both available theoretical predictions and also some preliminary results we had obtained in our experiment.

The two upper graphs in the Fig.5.1 shows how the fitted temperature and amplitude is modified by the initial trial value we use for the value of a. In these graphs, we have fitted curves computed numerically with $a = 7.5$ nm to a model where a was kept fixed for several value between 5 nm and 15 nm. This was done for numerical curves with a fixed amplitude of $Amp = 1$ and for several different temperatures from 0.5 μK to 3 μK with, also, two different fugacities ($Z = 1.0$ and $Z = 0.9$). The obtained curves shows that

[2] This also includes τ_i, measured independently.

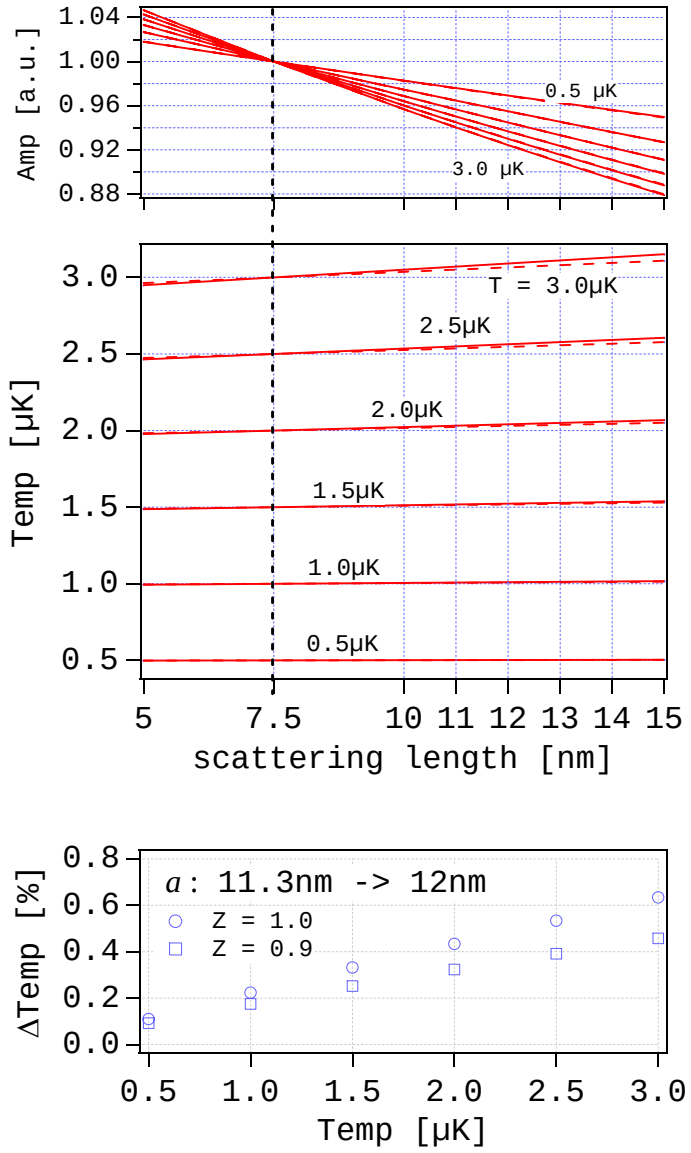

Figure 5.1: This set of graphs shows the dependence the *TOF*'s amplitude and temperature on a(top graphs). The dependence in derived by fitting a *theoretical* *TOF* curve with $a = 7.5$ nm (the value found by the *ENS* group) to a model where a is varied from 5 nm to 15 nm but hold constant during the fit. This is done for two different fugacities, $Z = 0.9$ and $Z = 1.0$ (dashed and solid lines respectively), also hold constant in the fit and equal to the original values of the *theoretical* curves. Since Z is fixed, the variation of a is mainly compensated by a change in the *TOF*'s amplitude. The temperature is only weakly affected. More specifically we plot in the lower graph the variation of a fitted temperature when a is changed from 12 nm (the value we have used to fit our curves) to $a = 11.3$ nm, which is the final result of our analysis. The bottom graph represents the relative variation of the temperature (in percentage) in this case for temperatures ranging from 0.5 μK to 3.0 μK. This variation is smaller than the incertitude on the determination of T in a *TOF* fit, typically $\sim 2 - 3\%$.

the amplitude may be quite modified by an erroneous choice of a, but not the temperature which is only slightly modified.

The bottom graph in the Fig.5.1 shows the relative variation of the temperature found in a fit to clouds with fugacities of $Z = 1.0$ and $Z = 0.9$ when we use $a = 12$ nm instead of $a = 11.3$ nm. This latter value is the value of a found in the data analysis presented here (see Figure 5.5) and this graph shows that the error we could have committed in the evaluation of a, due to the initial choice of a for fitting proposes, is in the worst case equal to 0.6%. This is a small error, comparable, for instance, to the one involved in the *semi-classical* approximation (cf. §2.1.3).

5.2.3.1 Experimental procedure.

From the point of view of the experimental procedure, this experiment is almost identical to the one described in Appendix B for measuring β and L. Unlike this latter one where we had to stop the evaporative cooling at the time the *BEC* is formed, in here we stop it at the vicinity of the critical transition point. This was done with the help of a critical curve (cf. §4.2.4.3) obtained before the data acquisition.

As the experiment relies in comparison of the ion flux produced within a cloud and its density, we had to span as much as possible the cloud's critical densities. As in the *construction* of the critical curve (cf.4.2.4.3), this could be done by varying the number of atoms in the clouds at the beginning of the last evaporative ramp by stopping the ramp for a short period or by changing its velocity. However, this could only be done before the last ramp in order to keep the experiment synchronous with the *critical curve*.

• Bias Field correction.

The *critical curve* is obtained for a given fixed bias field and it is only valid if this quantity is kept constant during the data acquisition. However, as we have remarked in §1.2.2 this is not entirely the case since there is always a slow drift of this bias field over time. Unlike the fast *run-to-run* bias fluctuations of about 25 KHz, this slow drift can be corrected. For that, we need to let the evaporative cooling continue down to the $rf-$frequency where we expect to have a *pure BEC*. Here, and if the bias field has not changed much, the observed *TOF* should follow the typical Thomas-Fermi inverted parabola profile with non observable thermal cloud (see §B.1.1 of Appendix B).

When the bias does change, two outcomes are possible in this procedure: no cloud remained trapped (bias field was too high) or, else, the observed cloud presents a significant thermal component (too low bias field). In either cases, we could smoothly change the current in the compensation coils in

order to correct the bias field and achieve the situation where a *pure BEC* is formed. This same procedure was used also in the $\beta - L$ experiment (see §B.2.1 of Appendix B), where the bias field could be checked permanently for all experimental runs as the final objective was to produce *pure BEC*s. In the experiment we describe here, this was not the case and, we had to interrupt the data acquisition, typically once every three runs, to check the value of the bias field.

• **Tuning to the *critical curve*.**
After getting sure that the bias field was correct, we could take data at the critical phase transition. To achieve doing that we had to *guess* the optimal final ramp frequency, in each experimental realization, in a way that the evaporation would stop at the critical curve. When the experiment was stable, looking at the ion flux signal in the beginning of the evaporative cooling (30 seconds before its end) and observing the evolution of the number of atoms loaded into the magnetic trap give enough information to help determining approximatively the desired value for the ramp final frequency.

• ***In the run* change of the final ramp frequency.**
For stability reasons, the tuning of the final ramp frequency must be done *during* the run.

As we have briefly referred in Chapter 1, the timing of the sequences in our experiment was done with a digital analog card controlled by a computer program. The *rf-ramp* was delivered by a *ramp generator* which was also computer programmed, through a `GPIB` card, and triggered. To get a very good synchronization the computer used a simple `DOS` operative system which has non system-forced interruptions as the most recent windows based multitasking operative systems. The disadvantage of this was that we could not change any experimental parameter, as the final ramp frequency, without stopping the program. This disturbed the normal functioning of the experiment (a run every minute) and, with it, its more or less predictable behavior.

To avoid stopping the experience, we have modified the control setup to the one showed in Fig.5.2. Now, the *rf-ramp* was obtained using two *rf-ramp generators*: an *Anritsu* synthesized signal generator to work over almost all the ramp from 130 MHz down to 2 MHz and, a *Stanford Research Systems (SRS)* function generator to complete the *rf*-ramp from the 2 MHz to the *pure BEC* frequency of ~ 1 MHz [3]. The `SRS` outputted a `TTL` signal synchronous

[3]We were forced to use a second ramp generator because the *Anritsu* had a *scale frequency commutation* in the *frequency region* from 2 MHz to 1 MHz. This was a technical unavoidable problem that induced a large burst of noise in our ion signal, right at the region

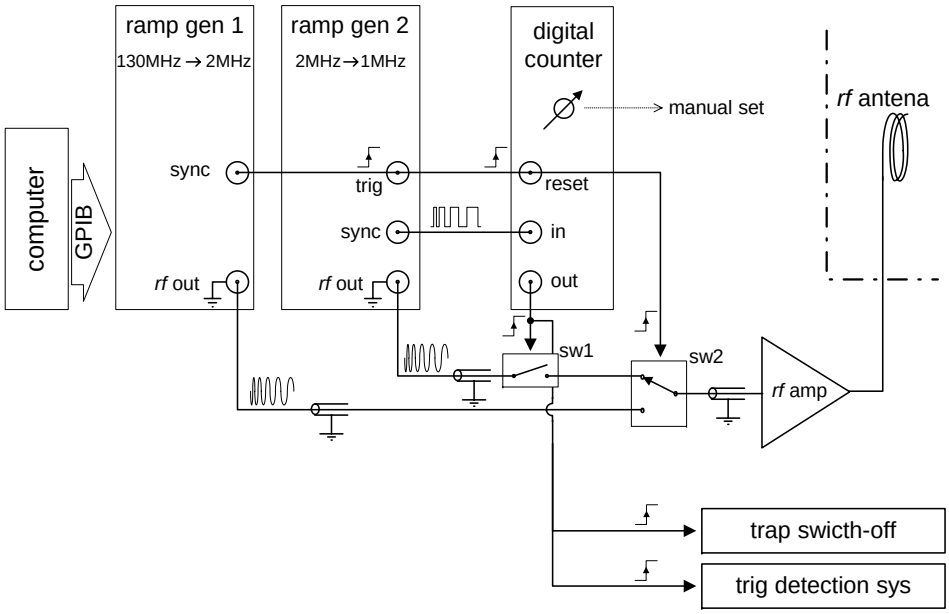

Figure 5.2: The Figure shows the adaptation we made on the experiment to be able to modify, at any time, the final ramp frequency. Here, the *rf-field* is delivered by two ramp generators, an *Anritsu* (*ramp gen 1* in the Figure) which ramps the frequency from 130 MHz down to 2 MHz within different ramp velocity sequences (defined by `GPIB` commands) and a *Stanford Research Systems* (`SRS`) *function generator (ramp gen 2)*, that completes the ramp down to 1 MHz. The beginning of this ramp is triggered by the *Anritsu* at the end of its sequences, triggering as well the *rf-switch (sw2)*. This synchronism signal was also used to reset a digital counter which controls the duration of the last ramp by *sw1*. This counter outputs a `TTL` signal after counting a certain number of pulses from the `SRS` ramp generator, synchronous with the *rf*-ramp: longer ramps would correspond to bigger pulse counts. The digital counter could be reprogrammed at any time, by hand set and independently from the computer generated experimental sequence.

with its rf frequency output. Imputing this synchronism signal into a digital counter, we could measure the instantaneous ramp frequency from the output of the counter.

5.2.4 Sorting data at $Z = 1$.

• The ion signal criteria.

As referred above, the success of this experiment relied on the good choice of clouds at $Z = 1$. The graph in the Fig.5.3 shows typical ion signals (it also shows some technical details about the data analysis we will refer further on). In this graph, the shadowed region corresponds to the ± 25 kHz *critical region* and, in principle, all the ion curves that stops inside this region could correspond to clouds at T_c. This is our first criteria to sort data as *good* and to include them in the data analysis. This *ion signal* sorting criteria is used already during the data acquisition where, for every given experimental run, we decided if the ion signal did stopped inside the ± 25 kHz region around the *critical curve*, discarding from further analysis all data that clearly did not.

• The *TOF* signal criteria.

In the proceeding Chapter we have come to the conclusion that the thermometric analysis based on the ion signal would only be capable of sorting data at the critical transition point within an error of 10% in the fugacity. To do better we need to use the information given by the analyzes the *TOF* signals. The approach we will describe first for this analysis is based on the study of how well the *TOF* signals fit to a model describing the atomic flux of a cloud at the critical transition point, with $Z = 1$[51]. Later, in §5.3, we will generalized this analysis to a fitting model where we leave the fugacity as a free parameter.

To fit the *TOF* signals we used a commercial version[144] of a *Levenberg-Marquardt* (LM) routine. This routine computes a *chi square* value, weighting the fit by the *TOF* characteristic noise. This one is of *shot noise* nature, growing with the square-root of the amplitude of the signal[51]. The good characterization of the noise revealed to be crucial for obtaining proper values of the fitted parameters and also for computing a meaningful value of the *chi-square*. As we will show next, this quantity is the one that will ultimately inform about the quality of the fit. The *TOF*s are fitted to the expression in Eq.4.50, evaluated for $Z = 1$. The resulting *fitting function* is rather complex to be used within a fitting routine, involving functions with

where the critical transition takes place (see [70]). The solution was thus to make this last part of the *rf-ramp* with another ramp generator which had no functioning problems in that frequency range.

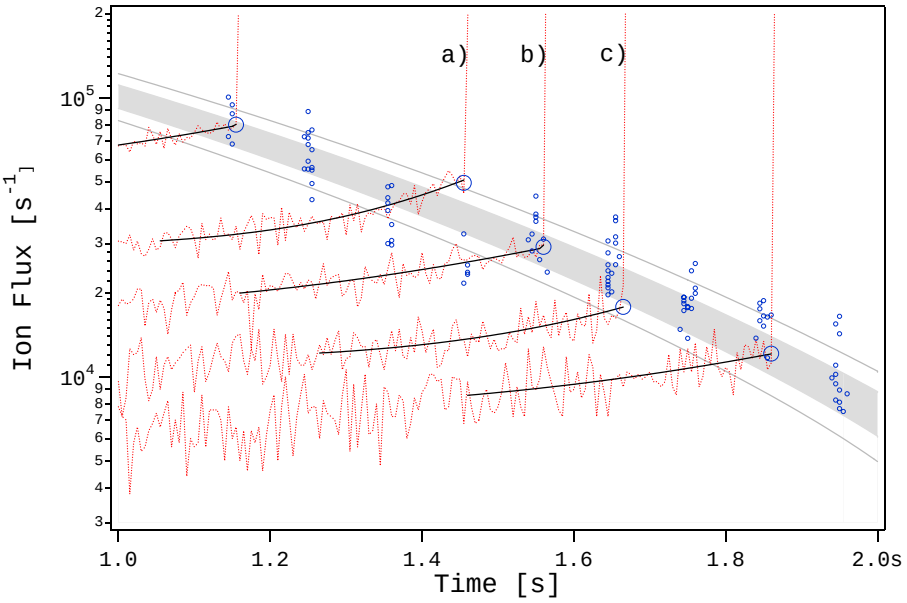

Figure 5.3: Example of some ion flux signals that stop in the vicinity of the critical curve. This later one is represented by a gray region corresponding to the *critical region* defined as the critical curve plus and minus 25 kHz, the estimated bias field fluctuation. The adjacent lines to the *critical region* are distanced from the *critical curve* by 40 kHz. Among the shown ion curves, some does fall inside the *critical region* as the one labeled as *b*). Others don't stop either before, *c*), and after, *a*), the *critical region*. The end of the ion curves is signaled by the superposition in the ion signal of a external large frequency signal that producing a kind of *wall* in the detected signal (vertical lines). This *wall* makes the determination of the trap switch-off instantaneous ion flux very easy to determine. We need only to *find the wall*, searching for an abrupt change of the signal (for that we looked for both the signal's derivative and amplitude). This instant of time, which we call the *wall time*, corresponds to an instantaneous ion flux, the wanted *wall ion flux* value. To get a better estimate of this quantity and also of its uncertainty we proceed as follows: we fit the final half second of the ion signal by the power law expression $y_0 + at^b$ (which fits well this signal); the *wall ion flux* is then defined as the value of this fitted curve at *wall time* abscise; finally, the error estimation of this quantity was identified with the standard deviation of the fit *residuals* distribution. The small circles marks the data obtained in one afternoon and considered during acquisition *at the wall*. Some of these points were ulteriorly sorted out as described in §5.2.4.

infinite sums. To allow the fitting routine to call efficiently this function, all the infinite sum expressions are rather computed as a weighted sum of exponentials or through a polynomial expansion.

Variation of the quality of the fit with the width of the fitting domain.

The original *TOF criteria* idea is presented in Fig.5.4. To sort a cloud at $T = T_c$, we observed how the cloud's fitted temperature changed with the width of an excluding window around the TOF center.

For a *TOF* signal of a cloud at the critical transition point, the fit should work well for any choice of the fitting region and give, always, the same temperature. In the case of a thermal cloud far above the critical temperature, the fit to the $Z = 1$ curve should only work properly in its tails. In this case, the more one considers the central part of the *TOF* the worst the fit becomes.

The graphs in Fig.5.4 shows two limiting situations. In the left hand side graphs, *a*), we represent a *TOF* of a cloud close to the critical transition point. The graph in the bottom shows that the found temperature doesn't change much even when the sharp central part of the curve is included in the fit.

The *TOF* represented in the right hand side of the Fig.5.4 has a quite different behavior. It corresponds to a thermal cloud and when we fit only its tails, we find a temperature that is smaller than the one found on a fit to the entire curve. This happens because the fit tries to match the fitting function, which has a cusp at the center, to a signal that is, essentially, a *gaussian*. The fitting routine achieves the best *chi-square* by increasing the width of the fit and, then, the found temperature.

The *chi-square* compact criteria.

The above analysis of the variation of the fitted temperature in function of the width of the fitting region can be further complemented studying the obtained value of *reduced chi-square*. In the case presented in the graph *b*) of Fig.5.4, due to the mismatch of the fit at the center of the *TOF*, the value of the *reduced chi-square* [4] is much larger that one. On the contrary, the fit presented in *a*) has a χ^2/N of almost one.

We have always found that the two methods were consistent sorting data at $T = T_c$. Due to its greater simplicity we opted to used as *figure of merit* the *chi-square* value alone, sorting data as being at the critical temperature

[4] The *reduced chi-square* is simply χ^2/ν, with ν the fitting degrees of freedom. The number of fitting degrees of freedom is, by definition, the number of data points in the *TOF*, $N = 1500$, minus the number of fitting parameters.

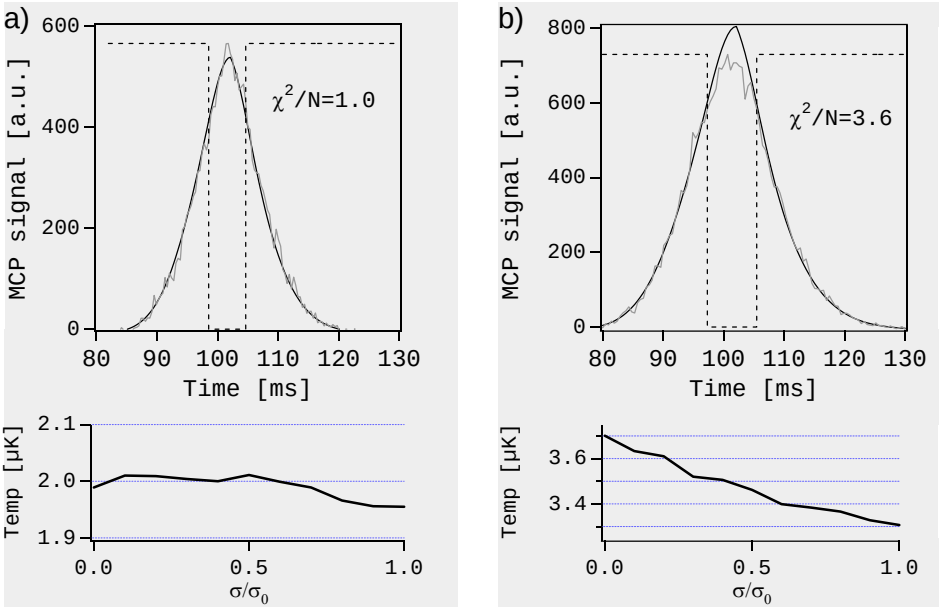

Figure 5.4: The left hand side graph corresponds to a cloud with a fugacity very close to $Z = 1$. The *TOF* signal fits very well to the theoretical curve (top graph) with a *reduced chi square* close to one (N is the number of points in the graph). The temperature doesn't change much if we fit all the signal or only its tails (bottom graph). The parameter σ/σ_0 is the size (divided by the FWHM waist of the curve) of the central region that is excluded from the fit. In this *TOF*, the found temperature doesn't depend much on this parameter. The top graph on the right hand side plots a *TOF* of a cloud with a temperature $T > T_c$. The overall curve *reduced chi square* is much bigger than one, denoting a bad fit to the theoretical curve. This is corroborated by the bottom graph where we see that the fitted temperature depends much on the size of the excluded region (see also text).

if the corresponding *chi-square* were $\chi^2/N \leqslant 2$ [5]. This established then the final *TOF sorting criteria*.

5.2.5 The found value for a.

We present now the sorted experimental results and the result obtained for a within this data analysis.

The data we have considered into the analysis is plotted in the graph of Fig.5.5, represented by black circles and was sorted using both the *ion signal* and *TOF* criteria. In the same graph, the open circles correspond to data that, despite verifying the *ion signal criteria*, failed with the one for the *TOF*. These points are only a few and, in the graph, look to be displaced out of the ensemble of the plotted data.

This graph plots the measured ion flux divided the η_{ion}, the ion detection efficiency (cf. §1.3.6.2), in function of the corresponding temperature. This latter quantity is found fitting each *TOF* and is corrected for the initial non ballistic hydrodynamical expansion of the cloud using Eq.4.60 and the results of §4.3.4.3.

The dispersion of the plotted data is large, large enough that some of the non sorted data appears among those that were considered as *good* data. We will show later that this dispersion of the data is consistent with a *run to run* bias fluctuation of ± 25 kHz or less.

5.2.5.1 Obtained result.

The final value for a is obtained fitting the data to Eq.5.7. This fit is represented in the graph of the Fig.5.5 by the solid line and corresponds to a *scattering length* of $a = 11.3$ nm. The other lines, in the same graph, are used to estimative the error of a, which was done as explained in the following.

5.2.5.2 Error estimation.

The data in Fig.5.5 fits differently for temperatures below and above 2 μK. This is emphasized in the Figure with the dotted and dashed lines that result from fits to the set of data with temperatures smaller and bigger than $2\mu K$, respectively. Admitting that the data is not affected by systematic errors, the discrepancy of the two values obtained in these fits may be interpreted as an uncertainty in the determination of a.

[5] We have also tried other alternative definitions for this *figure of merit*, as for example, the magnitude of the slope in the temperature variation with the fit mask width (see Figure5.4). However, none of them added much significative information to the standard *reduce chi square* definition.

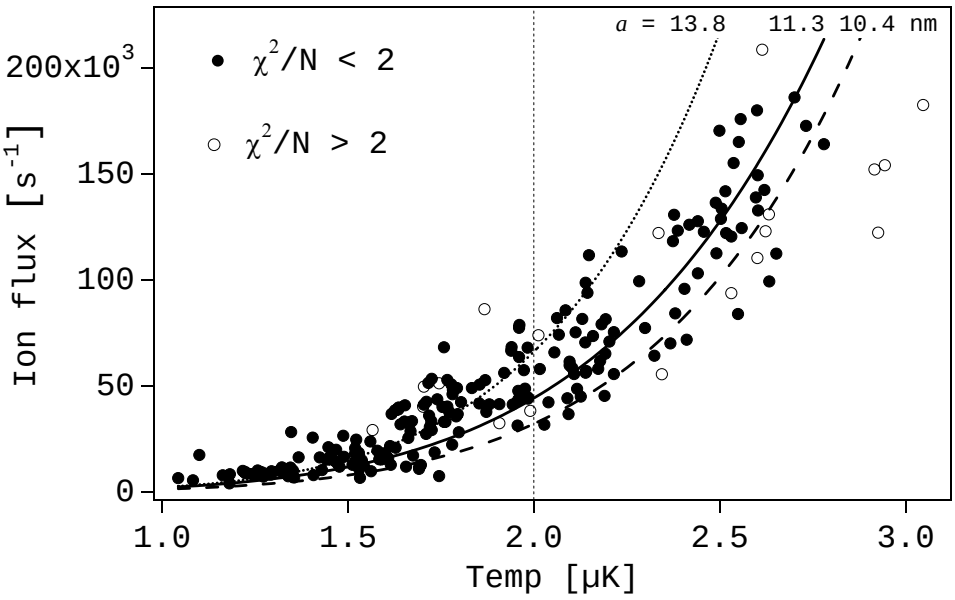

Figure 5.5: This graph resumes our final results in this experiment. In the bottom axis is represented the temperatures of the chosen data (value found in the fit and corrected for hydrodynamical effects). In the left axis, the corresponding ion flux points are corrected for the ion detection efficiency of our system, dividing the measured *ion wall flux* values by η_{ion}, . All the data points were sorted by the *ion flux criteria, i.e.* by comparing where the ion signal stopped relatively to the *critical curve*. The filled circles were further sorted to have a *reduced chi square* smaller than 2. The curves in the graph were obtained by fitting the data to Eq.5.7 (along with the expressions for β and L of the proceeding Section). The solid line was obtained in a fit to all the temperature range, while the dotted and dashed lines corresponds respectively to fits where only data with temperatures below and above $T = 2\mu K$ were used. This is done to estimate the error we are doing in the determination of a (see also text). The found values for a, in each case, are shown in the top edge of the graph.

This error estimation is based uniquely on the dispersion of the data and doesn't take into account the uncertainty in the determination of the ionizing rate constants (see §B.2.2.1 of Appendix B), the error propagated from the bad choice of the value of a in the fitting procedure, the use of an incorrect detection efficiency for the ions or, even, a bad estimation of the hydrodynamical corrective factor. We have estimate all these sources of systematic errors small enough and unimportant in the final obtained result [6].

We only take into account the errors of β and L. Using the confidence regions for β and L obtained in Ref.[45] (cf. §B.2.3 of Appendix B) we can infer a correspondent confidence region for a.

This was done by refitting the data in the graph of Fig.5.5 using algebraic expression for β and L that describes the extremes of the confidence regions on these two constants [7]. The obtained values for a differ from the central value of about 0.5 nm[51], which is smaller but still comparable to the above estimated uncertainty due to the data dispersion. As these two errors are statistically independent, the overall error of a is obtained summing the two contributions in quadrature. We get, finally

$$a = 11.3^{+2.5}_{-1.0} \text{ nm}. \tag{5.8}$$

When compared with the result of the *ENS* group, this value is 50% incorrect! The obvious conclusion is that we have certainly disregarded some very important systematic effect in our experiment. We will come to this issue latter in §5.4.

5.2.6 Final remarks on the determination of a.

In the following Section we will revisit the data analysis of this experiment. This new analysis was also done before the *ENS* result being known and its objective was to verify the value found here and to reduce its experimental uncertainty. We will also have the objective of understanding the data dispersion which, as we will see, is due to a bad determination of the cloud's fugacity.

We have also decided to revisit this analysis with the objective of developing better methods on the cloud's thermometry, based on the analysis of *TOF* signals. We will try to answer the question of how precise can we be on

[6] The ion detection efficiency may actually induce no error at all, since we have used the same value for this quantity when we have determined β and L. An hypothetical error in the calibration of the ion detection system would induce an error in the determination of the ionizing rate constants but not in the determination of a[51].

[7] Here, we only need to consider two cases, the extremes for large and small β which are highly correlated with the corresponding extremes of small and large L.

the measure of the cloud's chemical potential. The answer to this question is very important, for example, if we want to carry out an experiment to measure the density correlation function at $T = T_c$.

5.3 Revisiting the problem of the determination of the s-wave scattering length.

Introduction

In the last Section we describe the experiment we have done to measure a. The idea there was to compare the ion flux produced by clouds at the critical phase transition with the corresponding critical density (or rather, the critical temperature), finding a in a fit of the former to the later quantities. For convenience, we have used clouds at $T = T_c$, since for this case the analytical characterization of both the atomic *TOF* and the ion flux simplifies to expressions that are easily computed. Furthermore, we were convinced that the information obtained with the ion signal would gives us a precise procedure to sort the data at exactly at $Z = 1$. However, the bias fluctuations prevent an accurate determination of $T = T_c$ from the ion signal analysis and we had to also rely on the *TOF* signals, used on the determination of the clouds' temperature, to sort the data at the critical phase transition.

This sorting criteria based in the *TOF* analysis was based on the *quality* of the fit of a given *TOF* signal to our theoretical model for $Z = 1$. This procedure sorts data with fugacities almost, but not necessarily, equal to one. In fact, we will see latter in this Section that only a few clouds were in this condition. To have a reasonable number of clouds in the final analysis we had to use a less constraining criteria. Only a few clouds were excluded by the *TOF* criteria alone, indicating that this one is also consistent with a mismatch in the fugacity and temperature equivalent to 25 kHz in $rf-$ramp units. According to the results plotted in the graph of Fig.4.6, this produces an error in the fugacity of about 10% which produces, as we will show further, an error in the cloud's temperature also around 10%. This error in the determination of the cloud's temperature explains the somehow large data dispersion we see in the graph of Fig.5.5.

5.3.1 The data dispersion and the bias fluctuation.

We could have two different and independent causes for the dispersion of data plotted on the graph of Fig.5.5: an erroneous determination of the *critical ion flux* or, else, of the clouds' critical temperature. The first of these causes is very unlikely to be determinant on the observed data dispersion. The determination of the critical ionizing rate is an almost direct measure and its incertitude, shot noise limited, is in the worse case of about 5%.

If we admit that fugacity is equal to one, the determination of the temperature can be made very rigorous: within the validity of the theoretical model we use, we estimate that the error on its determination is smaller than

$0.1\mu K$, for a confidence interval of 68.3% (see also AppendixD). This error is also not sufficiently large enough to justify, alone, the data dispersion. It should be justified then by the *imperfect* choice of data at $Z = 1$.

Relation between the bias fluctuation and the final fugacity variation.

The Fig.4.6 of §4.2.4 shows that, for an ideal gas, 25 kHz of fluctuation in the bias field corresponds to a variation of the cloud's final fugacity of about 10% (it can be as much as 20% for very small clouds). Thus, the evaporation ramp may stop either too early or too late for getting a $Z = 1$ cloud. As we saw this has consequences in the determination of the temperature and, also, in the determination of the critical ion flux. This latter will be larger if the cloud is already degenerate or smaller if it still above the critical temperature.

We will describe the dispersion caused by the inclusion of thermal and degenerate clouds separately.

5.3.1.1 Dispersion produced by the inclusion of thermal clouds.

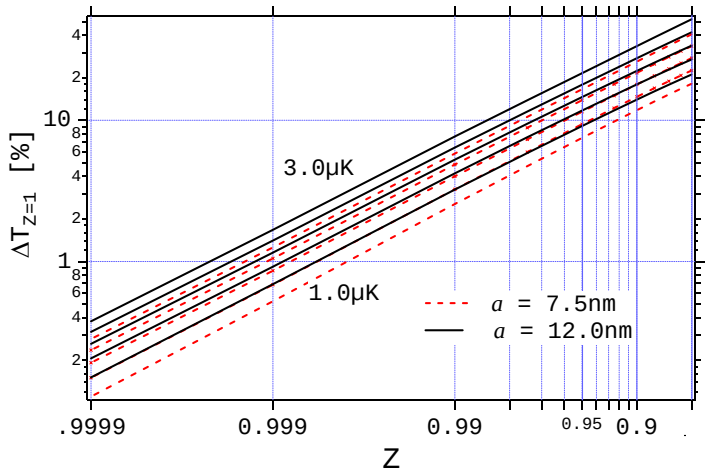

Figure 5.6: Mismatch of the value found for the temperature when clouds with $Z < 1$ are fitted with a model that assumes $Z = 1$. Each curve in the graph is computed synthesizing *TOF* signals with different fugacities but equal amplitude, temperature and scattering length. These synthesized data are then fitted taking as free parameters the temperature and amplitude, with $Z = 1$ and a, equal to $a = 7.5$ nm (dashed line with marks) and 12.0 nm (solid line). The graphs shows results for different cloud temperatures ranging from $T = 1.0\mu K$ to $T = 3.0\mu K$. We note that an error of 10% in the determination of the fugacity (that corresponds approximatively to the observed bias fluctuations) propagates into the determination of the temperature of a cloud with $T = 2\mu K$ as 20% or greater.

The Fig.5.6 shows how the error committed on the temperature determination if one assume that $Z = 1$ in function of proper cloud's fugacity Z. If a cloud with a typical temperature of $T = 2$ μK is produced within a ramp that stops 25 kHz before the critical point, its fugacity will be, according to the results of Fig.5.6, close to $Z \sim 0.9$. In this case, the mismatch in the found value for the temperature would be as large as 20%. This value is quite high and does explain the data dispersion we observe in Fig.5.5.

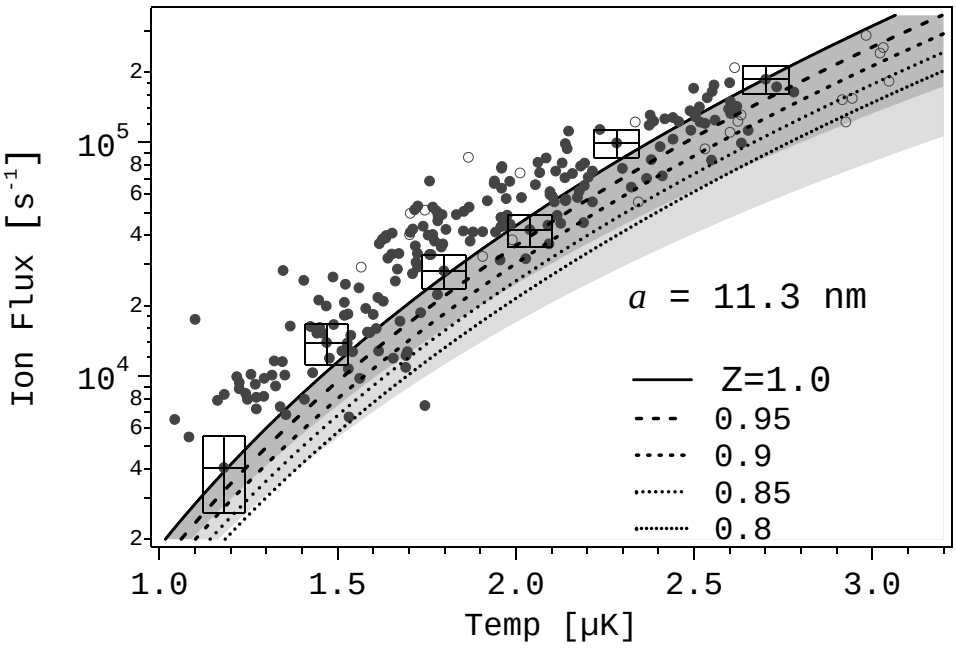

Figure 5.7: Similar graph as in Fig.5.5 with the ion flux in a *log* scale. The solid line is a theoretical curve for $Z = 1$ and $a = 11.3$ nm. Boxes indicate typical error for the temperature (from the fit) and the critical ion flux. Dispersed points plotted in the right hand side of the $Z = 1$ line correspond to thermal cloud with $Z < 1$. Shadowed regions are computed using the results on Fig.4.6 and indicates *dispersion regions* for the entire bias fluctuation (lighter) or only half of it (darker). This latter seems to be sufficient to explain the data dispersion. The dashed and dotted lines correspond to theoretical curves for different Z. Those with $Z = 0.95$ and $Z = 0.9$ would limit the above dispersion regions if, disregarding the ion flux error, a proper value of the *TOF*'s fugacity is included in the determination of the temperature (see also text).

In Fig.5.7 we plot the same graph of Fig.5.5 but with the ion flux in a *log* scale. This graph also represents, by shadowed regions, the *dispersion region* corresponding to a bias fluctuation of 25 kHz (lighter shadowed region) and to only half of this value (darker region). These regions are computed using the information of Fig.4.6 that relates a shift of 25 kHz of the bias field to a shift of the fugacity to $Z \sim 0.9$ and, of Fig.5.6 that gives the corresponding

shift on the temperature.

The solid line in the graph of Fig.5.7 corresponds to a theoretical prediction of the ion flux for $Z = 1$ and $a = 11.3$ nm, this latter the value found in our analysis. All scattered data points plotted below this line should correspond to thermal clouds, since their temperatures are shifted for higher values and, after the results of Fig.5.6, this should be justified by a decrease of the fugacity.

The observed data dispersion is justified by just *half* of the bias fluctuation, what suggests that the process of sorting data at $T = T_c$ is slightly better than expected: note that even the points sorted out by the *TOF* criteria falls inside the 12.5 kHz region.

Also in the graph of Fig.5.7 we represent theoretical curves for the ion flux for several fugacities smaller than $Z = 1$ (always for $a = 11.3$ nm). If we compare the curve corresponding to $Z = 0.95$ with the 12.5 kHz *dispersion region*, which also reports to a fugacity of $Z = 0.95$, we may conclude that the data dispersion could be largely reduced if the actual values of the fugacity of each *TOF* is derived and included in the data analysis. In other words, the fact of admitting from the beginning that the fugacity is exactly $Z = 1$ for every *TOF* sorted into the analysis, lead to the large observed data dispersion and, consequently, to larger uncertainty in the determination of a. To reduce them, we need to determine each cloud's fugacity and, thus, to consider a fitting model where the fugacity is a free parameter (cf. §5.3.2)

5.3.1.2 Dispersion due to the degenerate clouds.

Up to now we have explained the data dispersion observed in Fig.5.7, below the critical ion curve. The data dispersion we observe above it comes from the inclusion of slightly degenerate clouds. To estimate how much this data dispersion is, we need first to estimate how much the temperature of a degenerate cloud is modified when it is fitted with a model that takes $Z = 1$. Again, since we don't have a *good* description of the density of a degenerate cloud, this estimation is non trivial. It is also hard to quantify the *BEC* chemical potential when the evaporation stops 25 kHz after the threshold.

Again, we may do something if we assume that the simplified *semi-ideal* model makes a fair enough description of the degenerate cloud density. The procedure we used is the following. Using the *semi-ideal* model we have synthesize several *TOF* curves with given temperatures and (positive) chemical potentials. Then, we find the mismatch in the temperature as the difference between the value used initially in the *TOF* synthesization and the one found in a fit of the synthesized data to a model also based in the *semi-ideal* approximation but with $\mu = 0$ ($Z = 1$). The results we obtained are displayed in Fig.5.8.

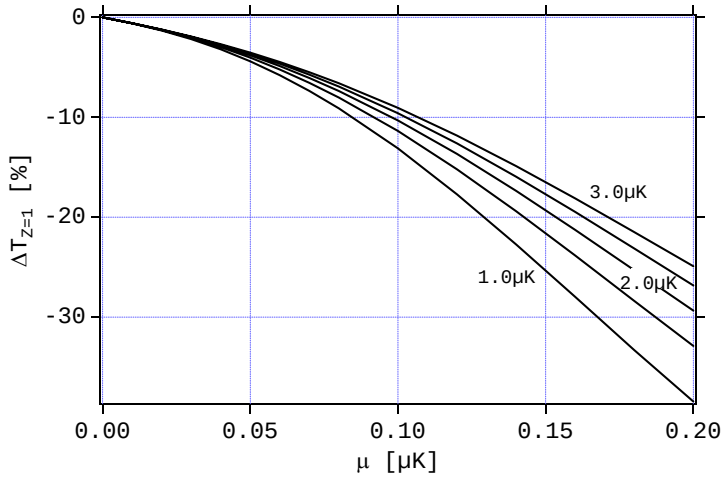

Figure 5.8: The graph plotted in this Figure is similar to the one in Figure 5.6 except that, in here, we present what would be the error in the temperature determination if a small condensate with a (positive) chemical potential μ is present. The curves are computed synthesizing data with the *semi-ideal* model (cf.4.2.2.2) and then fitted with a *ideal gas* model. It is interesting to note that, in contrary to the *thermal case*, the error committed in the temperature estimation is negative (*real* temperatures are bigger) and its relative absolute value grows for smaller temperatures.

In Fig.5.9 we present an analysis similar to the one in Fig.5.7 but now for the degenerate case. Using the results of Fig.5.8 we estimate the dispersion region represented by the shadowed region This dispersion region corresponds to a maximum chemical potentials of $\mu = 0.1\mu K$ which, according to the *semi-ideal* model corresponds to the habitual 25 kHz shift in frequency (cf. Fig.4.6). This is enough to justify the data dispersion.

5.3.2 The problem of sorting data at $Z = 1$. Overview to the χ^2-*map*s.

As noted before in §5.3.1.1, the data dispersion we observe in the graph of Fig.5.5 could be greatly reduced if we determine, for each non-degenerate cloud, its actual fugacity. This would also reduced the statistical uncertainty on the determination of a. In here we will briefly address the problem of deriving the cloud's fugacity from its *TOF* and the method we have used. A detailed description of this method is postponed for the Appendix D.

The major problem we find for fitting *TOF*s of clouds close to critical transition point is that the fitting function is not defined for $Z \geq 1$. This makes the fitting routine to malfunction whenever it needs to calculate the variation of the *chi-square* at $Z = 1$, since it cannot compute this quantity

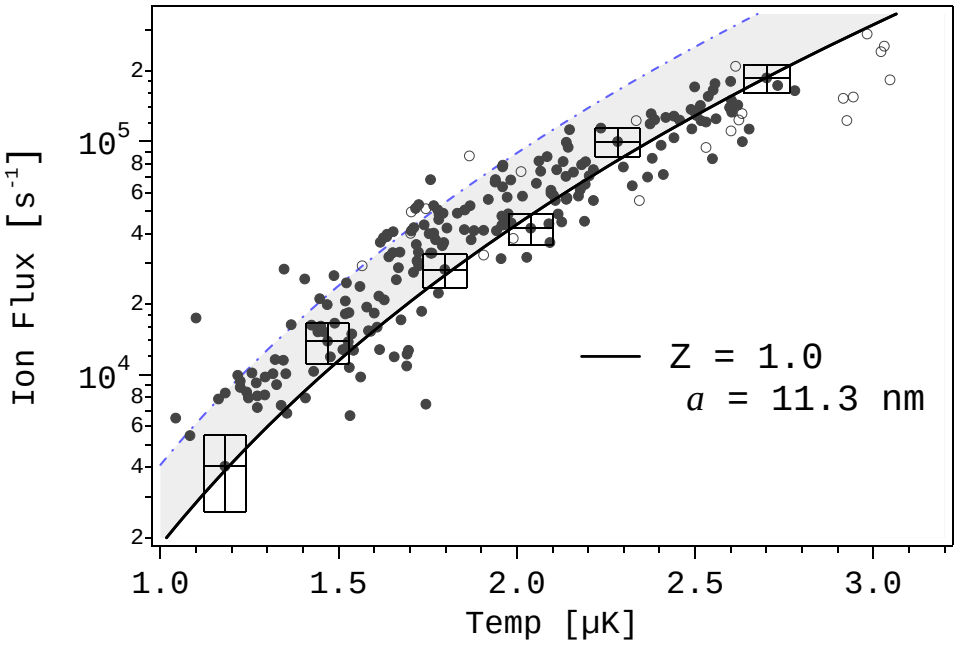

Figure 5.9: Similar as the graph of Fig.5.7 but describing the dispersion above the curve $Z = 1$. All the data in left hand side of the $Z = 1$ curve corresponds to degenerate clouds that are shifted leftward due to fact that their temperatures are smaller than the critical one (the $Z = 1$ model under estimates the temperature of slightly degenerate clouds, as shown in Fig.5.8). In here, the shadowed region represents the maximum data dispersion we may expect if a small *BEC* with a chemical potential of $\mu = 0.1\mu K$ is present. The curve that delimits this region was obtained by estimating the shift in the fitted temperature due to the presence of the *BEC* and also taking into account the variation of the ion flux signal in the upper border of the critical region. As for the thermal case, this latter contribution is much smaller than the one of the error in the temperature determination. See text for details.

for larger fugacities. This prevents the determination of the fugacity of a cloud that is, exactly, at $T = T_c$, making hard to sort the clouds at $Z = 1$.

This problem doesn't exist for fitting *TOF* of clouds with $T > T_c$. However, when the fugacity is close to one, its determination by a simple fit can lead to an erroneous result, due to a deformation of the *chi-square* variation close to $Z = 1$ (see also Appendix D).

The χ^2-*map* strategy.

To help solving the problem of fitting *TOF*s at the critical transition point, we have developed a strategy based on the *extrapolation* of the behavior of the *chi-square* obtained where the fitting function is well defined (*i.e.* for $Z \leqslant 1$) into the *degenerate region*, where it is not.

The idea is simple: around the location where the *chi-square* has its minimum value, it can be approximated by a paraboloid, with a quadratic dependence on each parameter [8]. Now, in the case we deal with here, we are able to compute this paraboloid only partially, since it is truncated for $Z > 1$. If we admit however that the *chi-square* still varies quadratically with Z and with the same curvature as for $Z \leqslant 1$, we can make an estimation on how bigger than one can the fugacity be.

The fitting function we use (cf. Eq.4.50) has four parameters: the *TOF* amplitude *Amp*, the time of fall t_0 and the cloud's thermal velocity v_T and fugacity Z. If we project the full four-dimensional *chi-square* into the two-dimensional one of the thermal velocity and fugacity we find a structure similar to that shown in the plot of Fig.5.10. We refer to this structure as a χ^2-*map* and is just a contour plot of

$$\Delta\chi^2(v_T, Z) = \chi^2(v_T, Z) - \chi_0^2$$

where χ_0^2 is the minimum *chi-square* found inside the χ^2-*map* at some location $\{v_{T0}, Z_0\}$. Every value of $\chi^2(v_T, Z)$ is found fitting the *TOF* for fixed v_T and Z, but letting free *Amp* and t_0, using a standard *LM* routine. This results in the $v_T - Z$ plane in the elliptical curves of constant *chi-square* shown in the graph of Fig.5.10, which may be seen as projections on that plane of the four-dimensional *chi-square* paraboloid. This graph shows that these lines of equal *chi-square* are continuously deformed approaching $Z = 1$, a consequence of the fast variation of the fitting function (especially at its center) for fugacities close to one.

The particular example given in Fig.5.10, the location of χ_0^2 tell us that this cloud is not degenerate and that its fugacity should be around $Z = 0.94$. In here and similar cases, v_{T0} and Z_0 are then the actual values of the cloud's

[8] This paraboloid defines the *curvature matrix* used in a standard *Levenberg-Marquardt* routine[145].

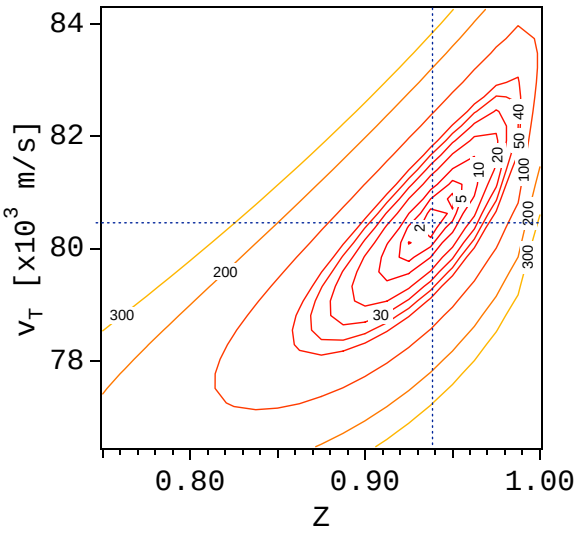

Figure 5.10: A χ^2-*map* computed for a *TOF* of a cloud with a fugacity of $Z \sim 0.94$ and a thermal velocity of $v_T \sim 8.05$ cm/s, corresponding to the location of χ^2_0, the minimum value of the *chi-square*. The tags in the contour lines correspond to values of $\Delta\chi^2 = \chi^2 - \chi^2_0$ and the one with 5 incloses the one standard deviation confidence region on the values found for the parameters. The contour lines are continuously deformed towards $Z = 1$ due to the fast variation of the fitting function for those values of fugacity. The particular case presented in this graph could be analyzed with a standard *LM* routine avoiding the task of computing the χ^2-*map*. The χ^2-*map* method can become very useful however for analyzing *TOF*s of clouds very close to the critical phase transition (see text and also Appendix D).

thermal velocity and fugacity. However, if $Z_0 > 1$, this is not anymore necessarily true and we need to estimate how far on the right of $Z = 1$ is the *true* location of the *chi-square* minima.

A detailed description of how we proceed to get an estimative of the cloud's chemical potential within the χ^2-*map*'s method and on the criteria we have used to sort data at $T = T_c$ is postponed for the Appendix D. In here we will only present the results we obtain using it on the analysis of the data of the experiment on the determination of a. It could also be used in any other experiment where it is necessary to sort data at the critical phase transition. Its most interesting application would be to help in the analysis of an experiment made to measure the second order coherence function of clouds at the *BEC* threshold, such as those numerically computed in the Chapter 3.

The increase of the complexity of the fitting expressions.
The implementation of the above analysis presents the additional technical difficulty of having to compute in a very efficient way all the functions involved in the description of the *TOF* and ion signal. As we have remarked earlier, the *TOF* is described by non trivial expressions that requires some intensive computational work. This may become a problem if these functions are to be used within a fitting routine that works iteratively calling them many times over a fitting cycle until convergence is attained. This difficulty, already present in the above analysis for $Z = 1$, gets more complex in here since now all the function will include Z as a free parameter.

This is particulary true for the function $f_B(Z, W)$, in the Eq.4.50, that has now two independent parameters and requires a more elaborated numerical implementation [9].

5.3.3 The problem of the initial guess for a.

As in §5.2.3, for the former analysis on the derivation of a, in here we also need to make an initial guess for a in the *TOF* fitting procedure. As before, the data analysis is significatively simplified if we could fit all the *TOF* curves only once. This is only possible if the results obtained for the temperature and, now, also for the fugacity depend little on the initial guess of a.

In the graph of Fig.5.11 we present similar results to those of Fig.5.1 but now for the mismatch of the found fugacity in a fit due to a bad choice of a.

[9] Note that $f_B(Z, W)$ involves two infinite sums with Z and W depending in different powers of the summing indices. This prevents to reduce the number of parameters of this function to only one as in all the other defined *Bose functions*. The numerical implementation of this functions requires then a two-dimensional interpolation or other equivalent procedure.

As in Fig.5.1 we synthesize data for $a = 7.5$ nm and study the variation of the fitted parameters when a is modified.

The error we commit on the fugacity determination when the fit is made with $a = 11$ nm instead of $a = 7.5$ nm is, for $Z > 0.9$ always smaller that 1.5%. Another interesting result in the bottom graph of Fig.5.11 is that for clouds almost degenerate, the influence of the initial choice of a in the fitted fugacity is small. For $Z \leqslant 0.99$ the change in the fugacity is very small even if we consider the non-interacting case (at $a = 0$ nm). The reduction of the interactions is compensated by an increase of the overall *TOF* amplitude and a reduction of the temperature. This means that, for almost degenerated clouds, the shape of a thermal cloud is mostly affected by the amplitude (number of atoms) and waist (temperature) but not by interactions.

5.3.4 The results.

5.3.4.1 The found a in function of the fugacities.

In Fig.5.12 we summarize the results we have obtained for all clouds we have considered. In this graph we plot the value of a for each cloud in function of the found value for its fugacity. The shown error bars were computed by propagating the uncertainties in all the quantities involved in the calculation of a. These include the confidence intervals of the fits for the temperature and the fugacity and the standard deviation of the fluctuation of the ion signal at the *wall*.

The statistical analysis of the data presented in the graph of Fig.5.12 gives a final result for the scattering length in the interval defined by

$$a = 11.2 \pm 0.4 \text{ nm} \tag{5.9}$$

and represented in this graph by a shadowed band. This result must be compared with the one obtained earlier in Eq.5.8.

5.3.4.2 The found a dependence on temperature for different fugacities.

Rather than presenting the obtained values of a in function of the fugacity, we can plot the *wall ion flux* of every sorted cloud in function of its temperature, as we have done in the previous section in Fig.5.5. Since in here we also know the fugacity, this representation can be made for each set of fugacities used in the previous Figure. In the graphs of Fig.5.13 we show the cases where $Z = 0.975 \pm 0.0125$ and $Z = 1 \pm 0.0125$. As well in the graph are represented the theoretical curves for the ion flux at the corresponding fugacity and, also, for a fugacity 5% smaller. The data dispersion in these graphs is comparatively

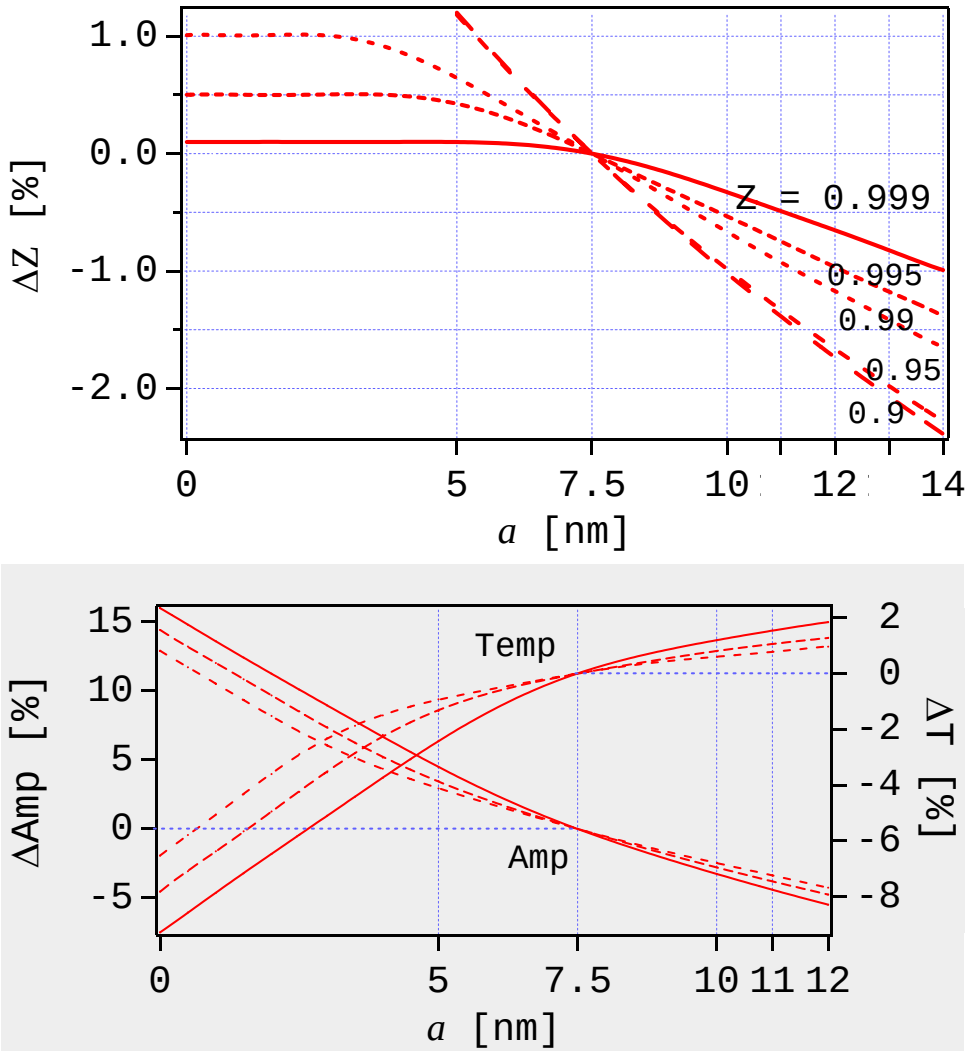

Figure 5.11: Top graph: dependence of the fugacity on the initial guess in the fit for a. The curves presented in this Figure were built finding the better Z that fits a *theoretical TOF* curve synthesized with $a = 7.5$ nm, $T = 2$ μK and five different values of Z ranging from 0.9 to 0.999 to others where a was varied from zero to 15 nm and for a several initial values of Z. If this initial guess is $a = 11$ nm the error is smaller than 1.5% for any fugacity grater than 0.9. For all guesses larger than $a = 7.5$ nm, the predicted values for Z are always smaller than the initial one. When Z approaches 1, the predicted fugacity becomes unsensitive to a and *saturates*. Bottom graph: this graph shows that the decrease of a is compensated by a proportional increase of the *TOF* global amplitude and a decrease of its temperature.

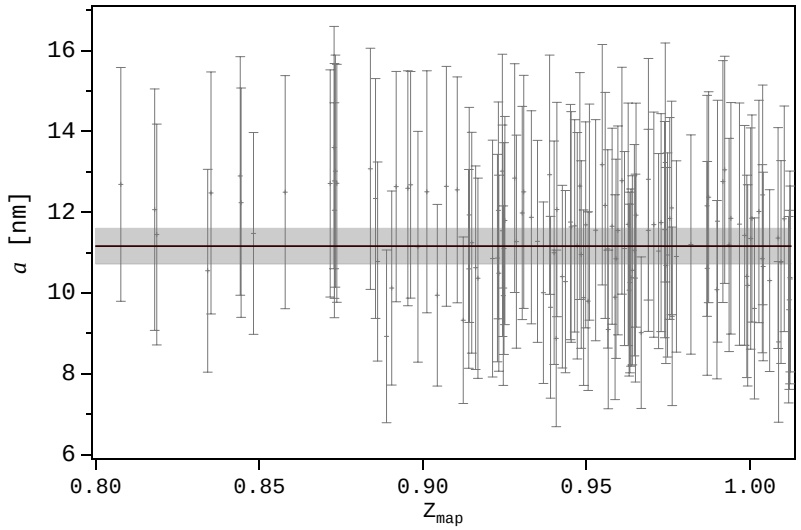

Figure 5.12: Values of the scattering length, a, found for each *TOF* in function of the corresponding value for the fugacity, Z_{map}, derived with the χ^2-*map* method (cf. Appendix D). The procedure that computes the a values invokes the empirical expressions for the ionizing rate constants β and L found in Ref.[45] (cf. Appendix B). The uncertainty in the determination of Z is 0.0125 making that the points with $1 > Z_{map} > 1.0125$ could correspond to data at the critical phase transition. The shadowed band marks the *standard error of the mean* of all the ensemble, equal to $a = 11.2$.

much smaller than that of Fig.5.7, where the data were sorted with a fugacity uncertainty of about $\Delta Z = 0.05$. In these two graphs we still have some data dispersion that, in some cases, is not justified by the error in the ion flux and temperature. We must remember, however, that these points still suffers from a incertitude in their fugacity of about $\Delta Z = 0.0125$. For example, taking a cloud at $Z = 1$ with $T = 2\mu K$, this ΔZ could justify a temperature variation, according to Fig.5.6, of about 5%. If this indirect error in the temperature were included in the analysis, the error boxes in Fig.5.13 would be sufficient to justify the data fluctuation.

In Fig.5.14 we also present the *ion flux versus temperature* graphs for the fugacities $Z = 0.95$ and $Z = 0.925$. Again, we have joined theoretical ion flux curves at the corresponding fugacity and for those at $\pm 5\%$ of this one.

5.3.5 Final remarks.

The first remark is that this new analysis gives the same result as the *old* analysis presented in the previous section. We are able to reduce the data dispersion on the relation ion flux/cloud's temperature and, with this, the statistical uncertainty of the final result for a. This is accomplished by discarding many data points that are sorted out, in our analysis, as correspond-

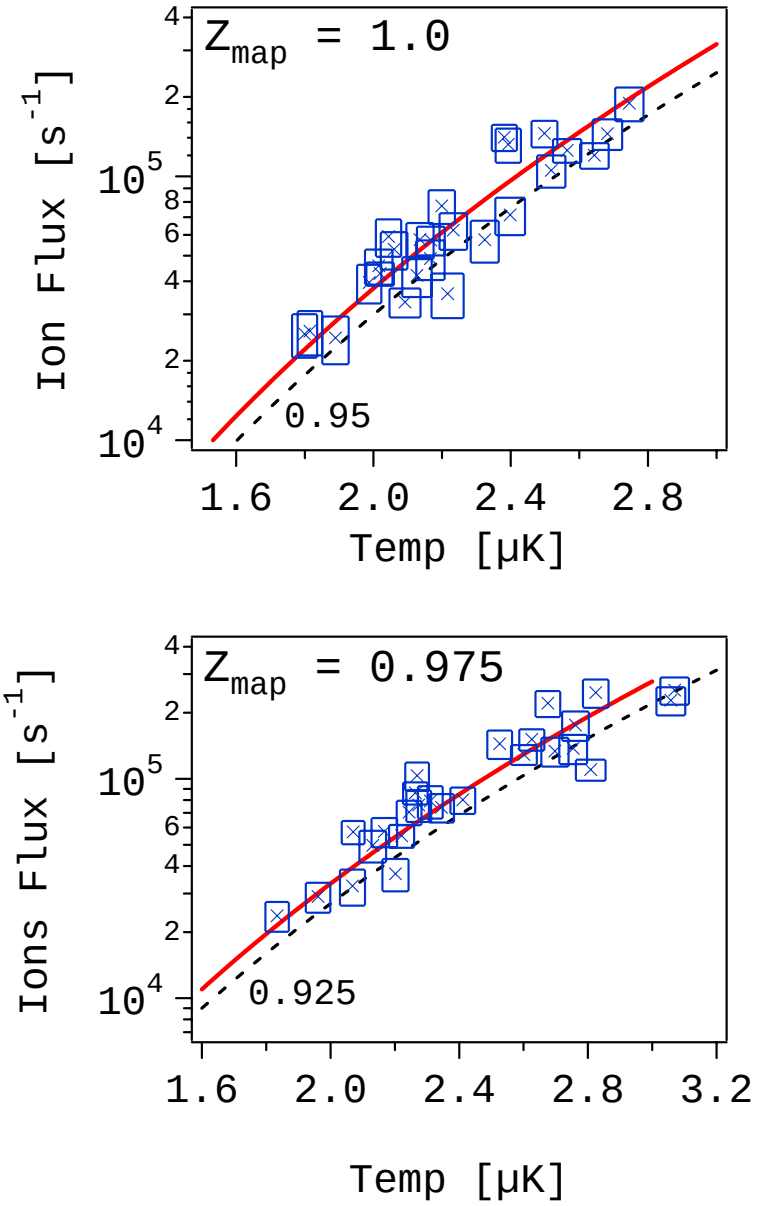

Figure 5.13: The top and bottom semi-logarithmical graphs represents the *wall ion flux* in function of the temperature for clouds with fugacities $Z = 1.000 \pm 0.0125$ and $Z = 0.9750 \pm 0.0125$, respectively. These fugacity intervals are the same as the one used in the bottom graph of Fig5.12 and corresponds to one standard deviation in the determination of Z_{map}. The boxes represent the error regions for the ion flux and temperature, this latter one taken as $2\sigma_T$ of the fit, corresponding to 95% confidence interval. The solid lines, in each graph, represents the theoretical variation of the ion flux with the temperature, when we take $a = 11.3$ nm and the each graph proper fugacity. The dashed lines correspond to the same theoretical curves but for a fugacity 0.05 smaller. This graph should be compared with the one in Fig.5.7.

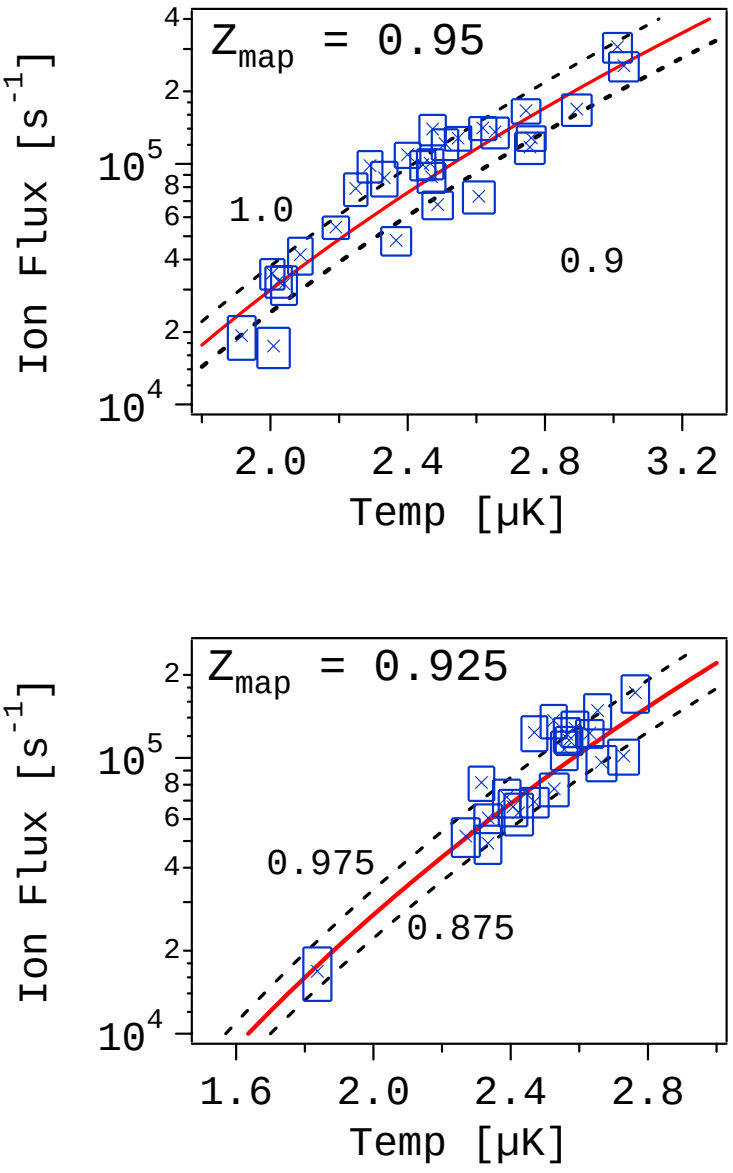

Figure 5.14: Same as in the previous Figure but for fugacities spanned over $Z = 0.9500 \pm 0.0125$ and $Z = 0.9250 \pm 0.0125$, respectively in the top and bottom graphs.

ing to degenerate data (most of them considered before as corresponding to small critical temperatures) and, also, by the proper determination of the temperature of clouds that were not exactly at $Z = 1$.

We are now quite confident in the analysis of the data. The discrepancy of its final result with the one obtained by the *ENS* group should be found elsewhere.

5.4 The systematic error on the measurement of the scattering length.

We will finish this manuscript discussing the error we made on the determination of a.

In the previous Sections of this Chapter we have explained how we can derive a from the comparative study of the cloud ion rate production and its average mean density. The accuracy of the result we may obtain within this idea depends only on two things: a good knowledge of the ionizing rate constants, β and L and the good determination of the cloud's peak density, which is to say, its temperature. This latter one depends on how good is our cloud thermometry: the good choice of the data at $Z = 1$ (or else an accurate determination of the fugacity) and the proper determination of their temperatures (corrected for the hydrodynamical effect). It is not conceivable that the error we made evaluating a, around 50%, can be addressed to an inaccurate thermometry of the cloud, regarding the *TOF* fitting procedure. Within the validity of the semi-classical mean field model we used in the *TOF* analysis, we may say that the maximum error we may have done determining a due to a bad determination of the cloud's temperature is the one given in Eq.5.9, *i.e.* on the order of 5%.

Thus, we must find the solution for this problem elsewhere. We turn our attention to the process of the cloud release from the trap. Throughout all the manuscript, we have always assumed that the trap switch-off is *instantaneous* and that the atomic cloud is released abruptly. We investigate how our results would change if this is not true and the trapping potential fades out slowly to zero.

The trap switch off and the atomic *time of flight*.

In §1.3.6.1 of Chapter 1 we have explained how we believe the atoms are coupled out from the trap when this one is switched off. They undergo a process of spin flip driven by very fast variations of the trapping potential when it switches off, as shown in the Fig.1.17. As shown in this Figure, which plots the behavior of the magnetic field in the bias field direction at the center of the trap, in this axis, the field decreases from a *steady state* trapping bias level of some hundreds of milligauss, down to $-170G$, passing very rapidly through a zero field condition. This fast passage by the zero magnetic field makes that the atomic spins fail to follow adiabatically the field, with some of them spin flipping to the field insensitive magnetic state $m_J = 0$.

These are the atoms we detect in the *TOF* and correspond to only about 10% of the total number of atoms in the cloud. We have experimental evidence[70] that most of the other 90% are polarized in the state

$m_J = +1$ [10]. It is not trivial to understand how these atoms respond to the fast variation of the trapping field. However, regarding the graph of the Fig.1.17, the most probable is that all of them fly rapidly away from the trap center due to the large and negative bias field. According to this graph and admitting that the detected atoms spin-flip to the $m_J = 0$ state at the first passage of the field through zero, the effective trap switch-off is in fact almost instantaneous, certainly much smaller than the time for one oscillation in the fastest axis of the trap. This has motivated our interpretation for the cloud released as instantaneous.

Mean field effects on the cloud release.

We don't know, however, how looks like the transient behavior of the trapping field over all the volume of the trap. The behavior of the gradient and of the curvature of the fields may induce an effective trapping potential during the transient period to the atoms spin polarized in the $m_J = +1$ state [11]. If these atoms do stay trapped for even a short period, their mean field potential may influence the expansion of the free falling atoms with $m_J = 0$. This corresponds to a picture where a $m_J = 0$ cloud expands inside a larger cloud of $m_J = +1$ atoms, which is also expanding but at a slower rate. This would modify the switch-off of the *effective* trapping potential of the cloud observed in the *TOF*. Because of the very different atomic densities, this effect may be different for thermal clouds and for *BEC*s. In fact, we should expect a bigger effect for condensed clouds. We will further comment this latter in this Section.

To understand how a slower switch-off of the trap would influence the atomic cloud's expansion, we will admit a phenomenological overall behavior for the *effective* trapping potential. The simplest one is the one where the trapping potential decreases exponentially to zero with some characteristic time. This is equivalent to admit that the trapping oscillation frequencies relax toward zero according to

$$\omega_\alpha(t) = \omega_{0\alpha} \times e^{-t/\tau_T}, \tag{5.10}$$

where τ_T is the trap *relaxation time*.

[10] This atoms can be detected in the MCP applying a inhomogeneous magnetic field with a negative gradient towards the detector. This further accelerate the atoms *low field seekers* of the $m_J = +1$ state, producing a large *TOF* signal a few tens of milliseconds before the standard one for the $m_J = 0$ atoms. A similar procedure was also done for detecting the $m_J = -1$ atoms, but no signal was detected.

[11] Indeed, for a negative bias field, keeping the same values for the field's gradient and curvature, and assuming that the atoms follows adiabatically the field potential, we find that the trapping potential is almost plane. This would predict a free fall of the $m_J = +1$ atoms, what is not observed.

5.4.1 The *slow* trap switch-off scenario for the thermal cloud release.

We will consider first the influence of a *slow* trap relaxation in the released of a thermal cloud.

As in the *BEC* expansion (cf. §A.3 of Appendix A), but in a much smaller extend, at the initial moments of expansion of the thermal cloud happens in the strong collisional hydrodynamical regime and the total energy in each of the three cartesian axes is not conserved, since the cloud's interaction energy is partially redistributed among them. This effect modify slightly the result of the simple ideal gas *ballistic model* for the cloud's expansion. This was taken into account in §4.3.4 to correct the value found for the temperature from the *TOF*'s fits. Now, if the *effective* trap switch-off for the thermal cloud is a non-instantaneous process, this hydrodynamical behavior will become more important since the cloud remains for a longer time in the strong collisional regime.

As before, for the *simple* hydrodynamical regime, we need to find how much this effect will change the temperature, with respect to the abrupt switch-off case. For that, we need to solve again the set of differential equations of Eqs.4.58, for a trapping potential that will somehow relax to zero after being switched-off. We will use the phenomenological behavior expressed by Eq.5.10. It is also convenient to define

$$\gamma_{th} = \frac{2\pi}{\tau_T \omega_\perp},$$

a quantity normalized by the trapping oscillation frequency in the fall direction axis $\omega_\perp$ [12], which we will refer to as the *effective relaxation constant* of the trapping potential.

The dynamics of the expansion of the cloud can be addressed to the scaling relations of Eq.4.57. These defines two dimensionless parameters $b_\alpha(t)$ and $\theta_\alpha(t)$ to re-scale, respectively, the cloud expansion and the effective temperature in each the $\alpha-$axis. In particular we have

$$b_\alpha(t) = \frac{s_\alpha(t)}{s_\alpha(t=0)}.$$

Solving numerically the Eqs.4.58 we find the time evolution of this parameter in the three directions of space. This results in the curves in the graphs of Fig.5.15 which are plotted for several different values of γ_{th}. The curves marked with $\gamma_{th} = \infty$ corresponds to the instantaneous cloud release and almost coincides to the ballistic behavior (cf. Fig.4.14). In these graphs we

[12]Remember that the fall direction Oz coincides with one of the trap fast axes, perpendicular to the bias field. Thus, we have $\omega_z \equiv \omega_\perp$; this latter notation is used here.

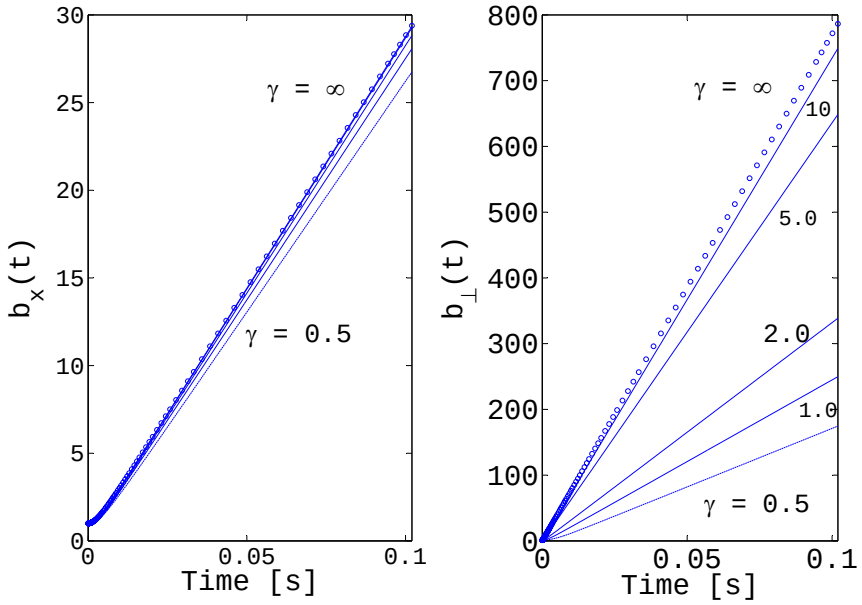

Figure 5.15: Numerically computed values for $b_{\parallel}(t)$ and $b_{\perp}(t)$, for different values of γ_{th}, defined as previously, and for a cloud with $T = 2\mu K$ and $Z = 1$. The model assumes a exponential relaxation of the trapping potential, with each axis frequency varying according to $\omega_{\alpha}(t) = \omega_{\alpha}(0)e^{-t/\tau_T}$ with $\tau_T = 2\pi/(\gamma_{th}\omega_{\perp})$. Circles correspond to the sudden trap switch-off case.

see that, for smaller values of γ_{th} (*i.e.* slower trap relaxation with larger τ_T) the expansion velocity of the cloud is reduced in all the axes. This effect is much stronger in the more confined axes ($b_{\perp}(t)$ in the right hand side graph), one of which influences directly the detected *TOF* signal.

The kind of *inversion of geometry* exhibited in the graphs of Fig.4.14, with the expansion velocity in the less (more) confined axis being bigger (smaller) that the ballistic expansion, is, in here, somehow washout by the *damping* effect of the slow trap relaxation. In the initial transient period (about the inverse trap relaxation time), the cloud's size is continuously adapting to the trap volume, which increases in time at the same velocity in all axes. After the cloud attaining the collisionless regime, the expansion proceeds ballistically but with a velocity that is given by the trap oscillation frequencies at that time. These are smaller than the initial frequencies $\omega_{0\alpha}$ and then the expansion proceeds also at a smaller velocity.

• The constant expanding velocity approximation.

To better compare the cloud dynamics between the sudden trap switch-off and the case where it relaxes slowly, we use a similar definition as the one of

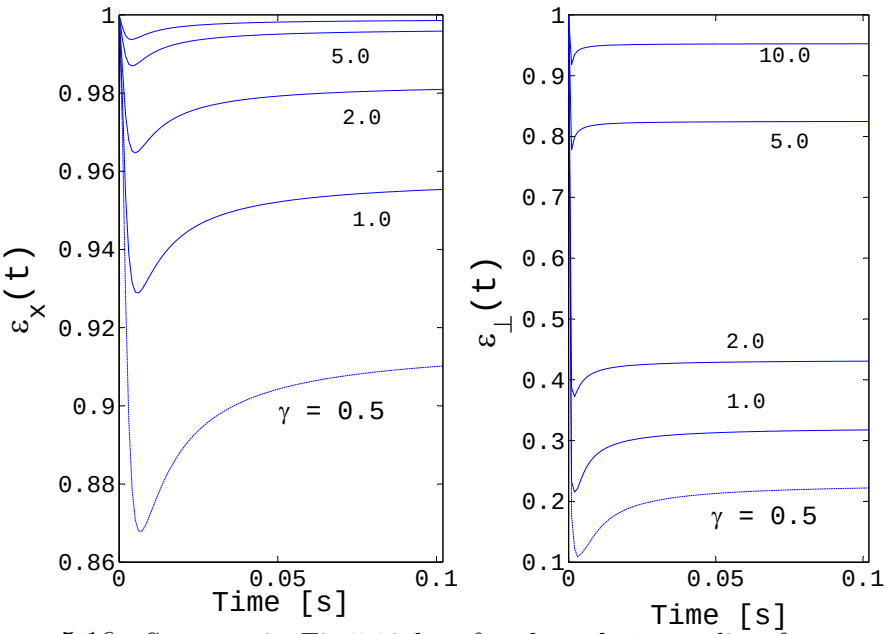

Figure 5.16: Same as in Fig.5.18 but for the *relative* scaling factors. What is represented is $b_\parallel(t)$ and $b_\perp(t)$ divided by the correspondent expressions for the abrupt switch off case (see also caption of Fig.5.18).

Eqs.4.59 for the parameters

$$\varepsilon_\perp(t) = \frac{b_\perp(t)}{b_\perp^\infty(t)} \quad \text{and} \quad \varepsilon_\parallel(t) = \frac{b_\parallel(t)}{b_\parallel^\infty(t)}. \tag{5.11}$$

where $b_\perp^\infty(t)$ and $b_\parallel^\infty(t)$ are the scaling parameters when $\gamma = \infty$ (*i.e.* for the sudden switch-off). These *normalized* scaling parameters are plotted in Fig.5.16, for $T = 2\mu K$ and $Z = 1$. If we disregard the initial transient period, we see that the scaling factors grow linearly in time with a certain velocity, smaller than those for the sudden switch-off. Thus, the factors $\varepsilon_\alpha(t)$ are smaller than one and almost constant. This is particularly true for $\varepsilon_\perp(t)$ and large values of γ_{th}, where the asymptotic behavior is attained very rapidly. Making the approximation where the velocity is considered constant over time, the cloud expansion in the fast axes may be expressed through the simple relation

$$b_\perp(t) = b_\perp^\infty(t) \times \varepsilon_\perp^\gamma(\infty), \tag{5.12}$$

where $\varepsilon_\perp^\gamma(\infty)$ is the value that $\varepsilon_\perp$ attains at $t = \infty$ for a given value of γ_{th}.

In the slow axis, the relative change of the cloud expansion for different values of γ_{th} is not as large as on the transverse axes. Moreover, the expansion in this axis is, for $\gamma_{th} = \infty$, much smaller than in the other two

(see Fig.5.15). To simplify the analysis, in the following we will neglect completely the expansion in this axis [13], and use $b_{\parallel}(t) = 1$. As in §4.3.4, the relation in Eq.5.12 leads to a correction on the cloud's temperature. Calling $\widetilde{T}$ the temperature found in the *TOF* fit, the cloud's actual temperature T is obtained according to

$$T = \widetilde{T} \times \varepsilon_{th}^{-2}. \tag{5.13}$$

where, to simplify the notation, we used $\varepsilon_{th} = \varepsilon_{\perp}^{\gamma}(\infty)$.

5.4.2 The thermal cloud's trap relaxation time for obtaining $a = 7.5$ nm.

Taking $\gamma_{th} \neq \infty$ will change the data analysis we presented in the preceding Section. We may ask what should be the value for ε_{th} that makes this analysis return $a = 7.5$ nm. This may be answered just by repeating the analysis using now Eq.5.13 to renormalize the temperature, given a certain value for ε_{th}. The results of such a procedure are shown in the left hand side graph of Fig.5.17, where we plot ε_{th} in function of the correspondent value found for a. This graph shows that, for obtaining $a = 7.5$ nm, we would need to have $\varepsilon_{th} \simeq 0.905$. Using the information obtained from the curves of the graph of Fig.5.16, we can also compute the corresponding values for γ_{th} [14]. This is plotted in the right hand side graph of Fig.5.17 and to get $a = 7.5$ nm the *good* value is $\gamma_{th} \simeq 6.8$, which corresponds to about one seventh of the time of a round trip on the trap fastest axis, ~ 0.1 ms. This latter value is comparable with the time scale of the variation of the bias field in Fig.1.17.

5.4.3 The influence on the measure of β and L of a *slow* release of the *BEC*.

In the former analysis, as in the §5.3, we have used values for the ionization rate constants β and L according to Ref.[45] (*i.e.* Eqs.B.3 of Appendix B). These were computed assuming that when the *BEC* is released the trapping potential goes instantaneously to zero. However, if we admit that the trapping potential relaxes slowly also at the *BEC* release, the values of these constants will also be affected since the *measured* condensate's peak density changes with the expansion velocity of the cloud.

[13] We could keep an equivalent corrective factor for the slow axis through all the calculation. However, since in the end, in the detection process, we will integrate the density profile in this axis, this correction would only affect the *TOF* amplitude but not its profile.

[14] The results shown in Fig.5.16 where computed for $T = 2$ μK and $Z = 1$. Nevertheless, they can be used for any thermal cloud since they doesn't vary much with temperature and fugacity.

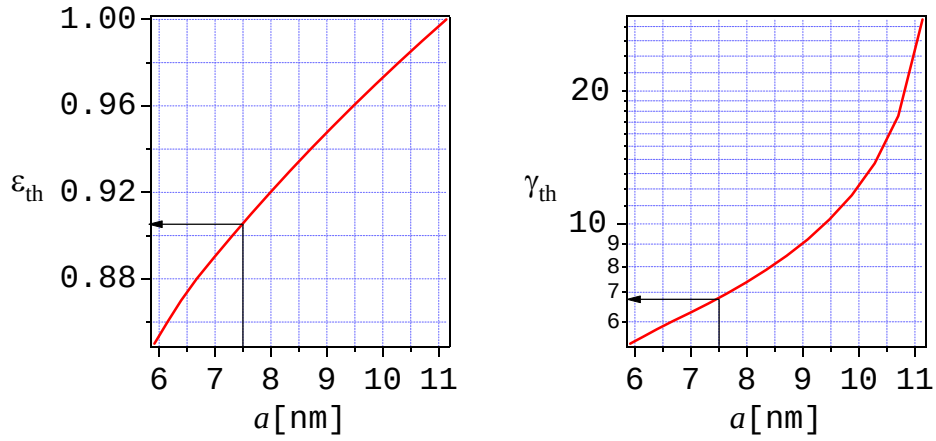

Figure 5.17: Left hand side graph: in the left axis are represented the values of ε_{th} with which the analysis of the data of the *scattering length* experiment returns the values for a represented in the bottom axis; right hand side graph: similar as previous but for γ_{th}. For getting $a = 7.5$ nm one needs $\varepsilon_{th} \simeq 0.905$, which corresponds to $\gamma_{th} \simeq 6.8$, *i.e.* about one seventh of the time of a round trip on the trap fastest axis.

The general formulation for dealing with the *BEC* expansion[68, 146] simplifies a time dependent Gross-Pitaevskii equation to a set of equations similar to those that describe a non-viscous classical fluid in the hydrodynamical regime. Within this model, the *BEC* expansion is determined by a non-isotropic scaling law, maintaining the cloud's general profile of an ellipsoid with an atomic density that decreases parabolically from the center. The cloud expands faster along directions where the atoms are more confined and slower in the other direction. This is leads to what is known as the *BEC* geometry inversion. In Appendix A.3 we present a more detailed description of this phenomena and we derive the exact equation of motion of the referred scaling law within the approximation of an abrupt switched-off of the trapping potential. This approximation leads to a great simplification of the calculation and allows deriving analytical solutions. It is, also, a very good approximation for most of the experiments.

In here, we will describe the *BEC* expansion with the same equations of Appendix A.3, but admitting that the trap switches-off according Eq.5.10. As in the case of the thermal cloud, no simple algebraic solution exists and we will have to deal with the equations numerically.

5.4.3.1 The hydrodynamical *slow* expansion of the condensate.

We recall here the Eqs.A.16 of Appendix A for the time evolution of the scaling parameters b_α,

$$\ddot{b_\alpha}(t) + \omega_\alpha^2(t)b(t) = \frac{{\omega_{0\alpha}}^2}{b_\alpha(t)\mathcal{V}(t)}, \tag{5.14}$$

with $\mathcal{V}(t) = \prod_\alpha b_\alpha(t)$, $\omega_{0\alpha}$ the initial trapping oscillation frequencies and $\omega_\alpha(t)$, their evolution over time after the switch-off, given by Eq.5.10. As before, using $\gamma = 2\pi/(\tau_T\omega_\perp)$ and, also, $\theta = \omega_\perp t$, the Eqs.5.14 become

$$\frac{d^2}{d\theta^2}b_\perp + e^{-2\gamma\theta}b_\perp = \frac{1}{b_\perp^3 b_\parallel} \quad \text{and} \quad \frac{d^2}{d\theta^2}b_\parallel + e^{-2\gamma\theta}b_\parallel = \frac{\lambda^2}{b_\perp^2 b_\parallel^2}. \tag{5.15}$$

Numerical solutions of this set of equations are represented in Fig.5.18 for different values of γ. The curves for $\gamma = \infty$ (dotted lines) evidenciate the typical geometry inversion during the condensate's expansion with the scaling parameter for the more confined axis, $b_\perp(t)$, increasing much faster than the one for the other axis, $b_x(t)$. A slow relaxation of the trapping potential results in a decrease of this anisotropic effect. During the period of the trap relaxation, the *BEC* remains always in the strong collisional regime with the *damped* interaction energy of the cloud on the directions of bigger confinement being transferred to the one where the *BEC* is less confined.

• The constant expanding velocity approximation.

We may define for the *BEC* case similar parameters as those of Eq.5.11 for the thermal cloud:

$$\varepsilon_\alpha^{BEC}(t) = b_\alpha(t)/b_\alpha^\infty(t)$$

with $b_\alpha^\infty(t)$ given by Eqs.A.21 of Appendix A. These time evolution of these parameters is plotted in the graphs of Fig.A.1. As for the case of the thermal cloud, in the following we will only consider the parameter $\varepsilon_\perp^{BEC}(t)$, assuming as negligible the cloud's expansion in the less confined axis. We will also consider that the expansion velocity in the fast axes is constant, which is, according to the right hand side graphs of Figs.5.18 and A.1, a good approximation. Thus, we use

$$b_\perp(t) = b_\perp^\infty(t) \times \varepsilon_{BEC}, \tag{5.16}$$

with now, $\varepsilon_{BEC} = \varepsilon_\perp^\gamma(\infty)$ the value of $\varepsilon_\perp^{BEC}(t)$ for a certain value of γ and when $t \to \infty$.

In the Fig.5.20 we plot ε_{BEC} and also ε_{th} defined above, in function of γ. These graphs are computed after the results of the curves of Figs.5.16

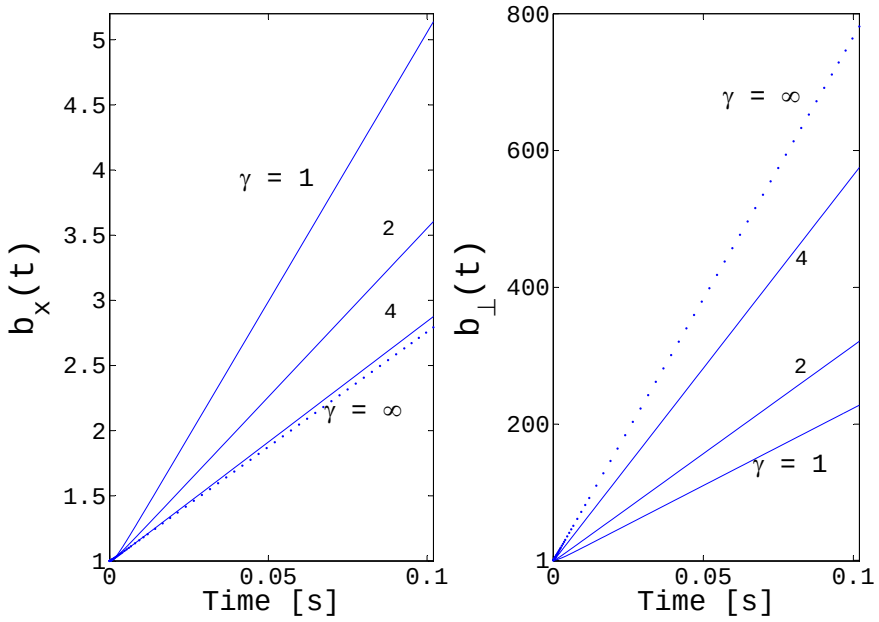

Figure 5.18: Numerical computed values for $b_{\parallel}(t)$ and $b_{\perp}(t)$, for different *effective* relaxation constants γ of the trapping potential. The model assumes that this potential fades out exponentially with each axis frequency varying according to $\omega_{\xi}(t) = \omega_{\xi}(0)e^{-t/\tau_T}$ with $\tau_T = 2\pi/(\omega_{\perp}\gamma)$. Dashed lines correspond to the evolution in a sudden switch-off of the trap that corresponds to the approximation used in Appendix A.

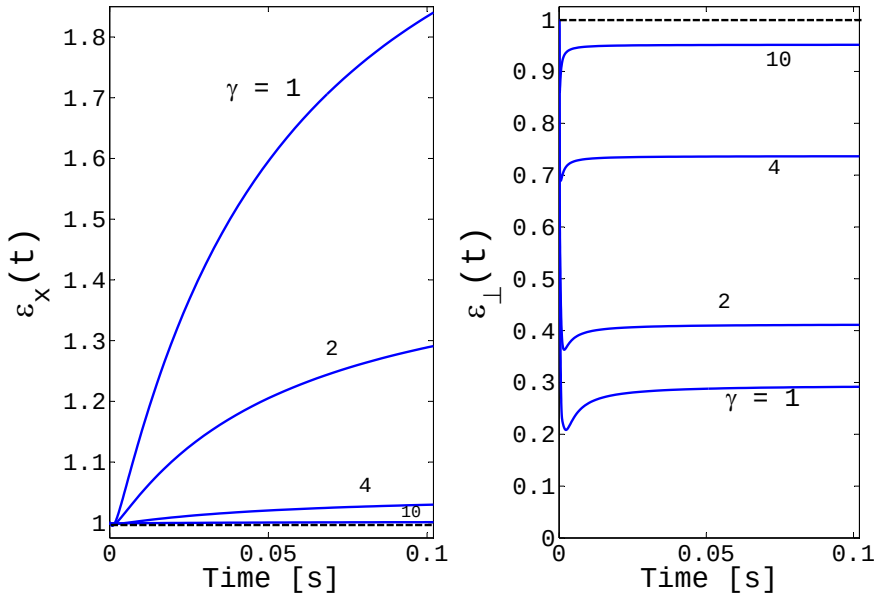

Figure 5.19: Graphical representations of the same quantities of Fig.5.18 but *normalized* by $b_{\alpha}^{\infty}(t)$, the scaling factor for $\gamma = \infty$: $\varepsilon_{\alpha}(t) = b_{\alpha}(t)/b_{\alpha}^{\infty}(t)$.

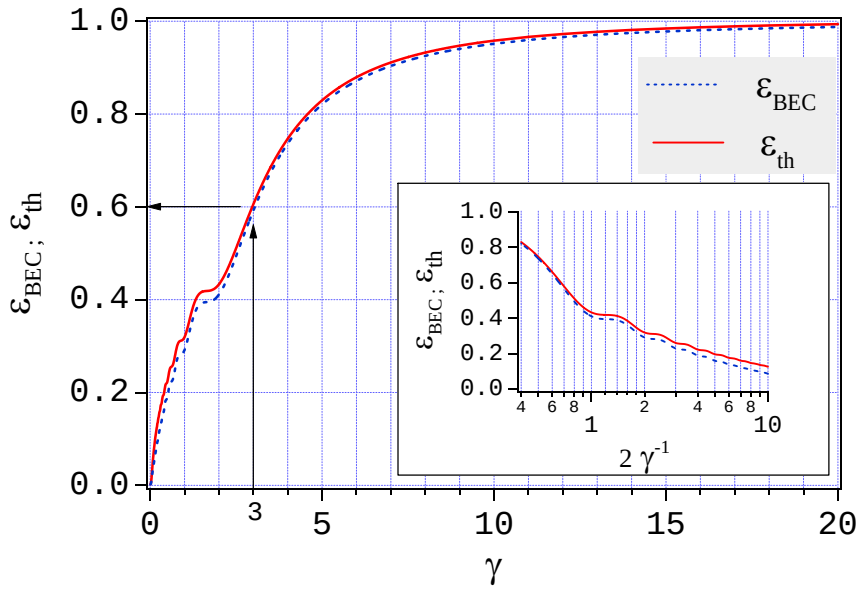

Figure 5.20: Dependence of ε_{BEC} and ε_{th} on the trapping potential relaxation constant γ. The inset graph shows the resonances that appears when the trapping relaxation time equals a semi-integer multiple of the time of an oscillation in the fast trapping axis.

and A.1 and allows reporting the final results obtained for the ε parameters to the equivalent relaxation constants γ. In the graphs of the Fig.5.20 it is interesting to note the *resonances* for certain relaxation times τ_T equal to semi-integers of $2\pi/\omega_\perp$, the period of one oscillation in the fast trapping axis: the cloud's interaction energy is better transfer to the trap in these cases and the cloud expansion is reduced.

5.4.3.2 Consequences on the determination of β and L.

We workout now how the above results would modify the measurement of β and L. In the Appendix B we describe with some details the experiment we realized for determining these two constants: it relies on the comparison of the *BEC* peak density with the instantaneous ion flux at the time when it is released from the trap. The condensate *TOF* signal, integrated over the MCP plane, is derived in Appendix A (cf. Eq.A.24). Within the *long fall* and *far field* approximations it is given by

$$I_{BEC}(\delta t) \propto \left\| 1 - \frac{M\omega_\perp^2}{2\mu} \frac{(gt_0\delta t)^2}{b_\perp^2(t)} \right\|^2 ,$$

with, as usually, $\delta t = t - t_0$ and $t_0 = \sqrt{2H/g}$. Substituting Eq.5.16 in this last expression we obtain

$$I_{BEC}(\delta t) \propto \left\| 1 - \frac{M}{2\mu}\frac{g^2\delta t^2}{\varepsilon_{BEC}^2} \right\|^2 ,$$

This expression defines the *Thomas-Fermi time radius* as (cf. Eq.A.25)

$$t_{TF} = \sqrt{\frac{2\mu}{M}}\frac{\varepsilon_\perp}{g} = \sqrt{\frac{2\widetilde{\mu}}{M}}\frac{1}{g}$$

where

$$\mu = \frac{\widetilde{\mu}}{\varepsilon_{BEC}^2}. \tag{5.17}$$

This expression relates the actual *BEC* chemical potential, μ, with the one measured directly from the *TOF* signal, $\widetilde{\mu}$, and the parameter ε_{BEC}. This latter is obtained, for any given relaxation trap constant γ, from the graph of Fig.5.20.

In the experiment we did for deriving β and L, we measured the quantities Φ and $\tilde{\mu}$. For this latter quantity we inferred the *BEC* atom number and peak density. This means that the measurement we did, $\Gamma = \phi/N_0$ in function of n_0 (cf. Eq.B.1 and Fig.B.4), would be $\widetilde{\Gamma} = \Phi/\widetilde{N}_0$ in function of $\widetilde{n}_0$ where

$$\widetilde{N}_0 = N_0 \times \varepsilon_{BEC}^5 \quad \text{and} \quad \widetilde{n}_0 = n_0 \times \varepsilon_{BEC}^2 \tag{5.18}$$

We obtain then,

$$\begin{aligned}
\widetilde{\Gamma} &= \frac{1}{\tau_i}\frac{N_0}{\widetilde{N}_0} + \frac{2}{7}\kappa_2\beta\frac{N_0}{\widetilde{N}_0}n_0 + \frac{8}{63}\kappa_3 L\frac{N_0}{\widetilde{N}_0}n_0^2 \\
&= \frac{1}{\tau_i\varepsilon_{BEC}^5} + \frac{2}{7}\kappa_2\beta\frac{\widetilde{n}_0}{\varepsilon_{BEC}^7} + \frac{8}{63}\kappa_3 L\frac{\widetilde{n}_0^2}{\varepsilon_{BEC}^9} \\
&= \frac{1}{\widetilde{\tau}_i} + \frac{2}{7}\kappa_2\widetilde{\beta}\,\widetilde{n}_0 + \frac{8}{63}\kappa_3\widetilde{L}\,\widetilde{n}_0^2.
\end{aligned}$$

Comparing the two last lines in this Equation we finally derive

$$\beta = \widetilde{\beta} \times \varepsilon_{BEC}^7 \quad \text{and} \quad L = \widetilde{L} \times \varepsilon_{BEC}^9, \tag{5.19}$$

where, as before, $\widetilde{\beta}$ and $\widetilde{L}$ are the measured quantities. For a *slow* exponential relaxation of the trapping potential and within the *constant expansion velocity* approximation used above, the values obtained in Ref.[45] for β and L (cf. Appendix B) should then be corrected according to the Eqs.5.19.

In the former analysis we have disregarded the corrections concerning the quantum and thermal depletions on the parameters κ_2 and κ_3. As we point out in Appendix B, these parameters depends on $\sqrt{n_0}$ (cf. §B.2.2.1) and should also be corrected according to the second expression in Eq.5.18. These corrections are however small and, for simplicity, we don't consider them in here.

5.4.3.3 Consequences on the measurement of a.

We investigate now how the value derived in §5.3 for a varies when the ionization rate constants are re-scaled according to Eqs.5.19. These expressions predict smaller values for β and L if the trap opens slowly. If we take this effect alone, *i.e.* admitting that the trap opens abruptly for the thermal cloud case, Eq.5.7 shows that it would lead to a even bigger value for a. In this case, to obtain $a = 7.5$ nm, the cloud should expand even faster than what happens in the abrupt switch-off case. It is hard to imagine how this may happen and then, the effect due to a *slow released* of the *BEC* is only meaningful if compensated by the effect of the *slow released* of the thermal cloud.

• Slow trapping potential relaxation for both *BEC* and thermal cloud.

We may now ask what are the set of values $\{\varepsilon_{BEC}, \varepsilon_{th}\}$ with which our data analysis returns $a = 7.5$ nm. As noted before, these two parameters correspond to *effective* relaxation constants, γ_{BEC} and γ_{th}, that need not to be equal. The physics involved in one and in the other cases are very different and then, these two phenomenological constants may also be very different.

The answer to the above question is compiled in the graphs of Fig.5.21. In this Figure left hand side graph, we plot all the sets of values $\{\varepsilon_{BEC}, \varepsilon_{th}\}$ that *produce* the desired result $a = 7.5$ nm. In the right hand side graph, we use the results of Fig.5.20 to plot the corresponding sets of values $\{\gamma_{BEC}, \gamma_{th}\}$.

• Interpretation.

If we impose similar trap relaxations for the thermal cloud and the *BEC*, we obtain $\gamma_{BEC} = \gamma_{th} = 3.15$. Bigger values for the relaxation times are possible if the effective trapping potential opens faster for condensates than to thermal clouds. As we have referred previously, this is not very likely to happen since the mean field of the $m_J = +1$ atoms of the condensate is bigger than those of a thermal cloud. Taking $\gamma_{BEC} < \gamma_{th}$, many different possibilities exists for values below 3.15, which is impossible to determine in the analysis presented here.

• The ionization rate constants for $\gamma_{BEC} = \gamma_{th} \simeq 3$.

A better understanding of the physics involved on the trap switch-off is needed to draw definitive conclusions about our bad determination of a. Without having a way of releasing the clouds in a more controllable way, no proper interpretation can be made of our *TOF* signals. All the analysis we have presented in this Chapter for the cloud's thermometry, based on the

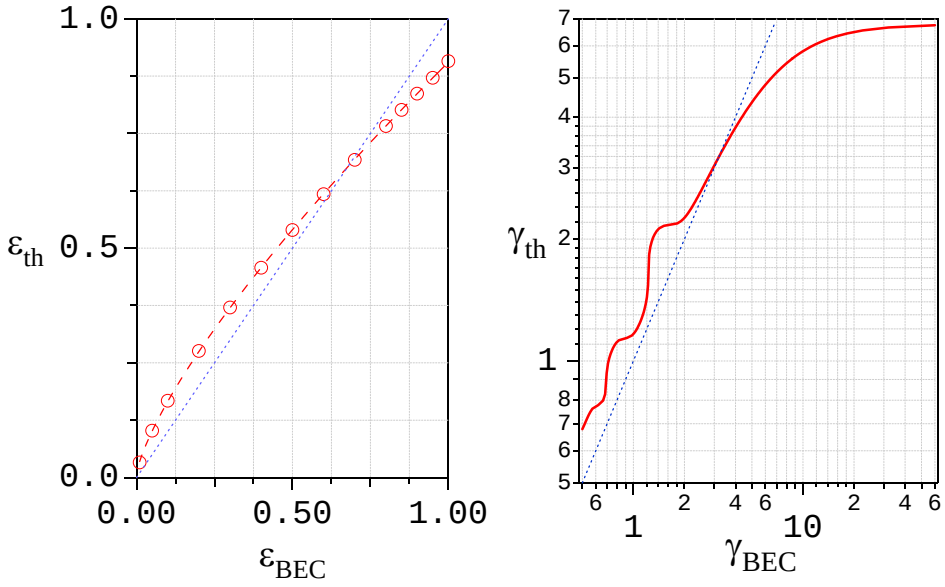

Figure 5.21: Left hand side graph: plot of the values of ε_{th} in function of those of ε_{BEC} that results in $a = 7.5$ nm in the data analysis of the *scattering length* experiment; right hand side graph: similar representation as the previous but for the trapping relaxation constants γ_{BEC} and $\gamma_{th} = 3.15$. The oblique dashed lines in both graphs correspond to equal constants for thermal cloud and condensate: the curves cross these line for $\varepsilon_{BEC} = \varepsilon_{th} = 0.67$ and $\gamma_{BEC} = \gamma_{th} = 3.15$.

TOF analysis, may be affected by somehow large errors. Using Eqs.5.17 and 5.13 we see that

$$\left|\frac{\delta\mu}{\mu}\right| = \tfrac{1}{2}\frac{\delta\varepsilon_{BEC}}{\varepsilon_{BEC}} \quad \text{and} \quad \left|\frac{\delta T}{T}\right| = \tfrac{1}{2}\frac{\delta\varepsilon_{th}}{\varepsilon_{th}}.$$

In particular, if we admit that the relaxation times are equal for thermal and condensed clouds, *i.e.* $\varepsilon_{BEC} \simeq \varepsilon_{th} = 0.67$, the use of $\varepsilon_{BEC} \simeq \varepsilon_{th} = 1$ in the previous Sections may have induced an error on the determination of the chemical potential and temperature as large as 15%. In this case, the ionization rate constants become

$$\beta\Big|_{\varepsilon=0.67} = 1.26 \times 10^{-16}\text{cm}^3\text{s}^{-1} \quad \text{and} \quad L\Big|_{\varepsilon=0.67} = 6.98 \times 10^{-30}\text{cm}^6\text{s}^{-1}, \quad (5.20)$$

where we used, as usually, the parametric relations of Ref.[45] evaluated for $a = 7.5$ nm.

Wondering about a good interpretation for the trap switch-off.
The values indicated in Eq.5.20 for the ionization rate constants are rather small if compared with theoretical predictions (see dashed lines in the graphs of Fig.B.5). To get them bigger, we need to consider parameters ε closer to one and, then, to admit that the *BEC* release is faster. In the interpretation we proposed above for the trap switch-off, we made the assumption that the $m_J = +1$ atomic cloud remains trapped for a longer time and that its mean field would somehow slow down the expansion of the smaller cloud with atoms polarized in the $m_J = 0$ state. This assumption is also based on the hypothesis that, when the magnetic fields are turned off, most of the atoms at the trap's center spin flips to the $m_J = 0$ state, admitting that the Majorana effect is bigger there. This leads to the picture, after the transient period, of a $m_J = 0$ cloud enclosed in a hollow-core cloud of $m_J = +1$ atoms.

However, if we admit that the atoms spin flip to the $m_J = 0$ state homogeneously over all the cloud, then the $m_J = +1$ atoms will remain trapped at the center of the cloud producing a strong repulsive mean field for the free expanding $m_J = 0$ cloud. This scenario would be consistent with a faster expansion of this cloud than if it was released abruptly and with no other external influences. It would also slightly deform the *TOF* signal because those atoms close to the center of the cloud would have a bigger initial velocity and arrive sooner at he `MCP`.

5.4.4 Conclusion. The Raman transition outcoupling process.

To achieve a proper conclusion on this problem we still need to obtain more empirical knowledge about the trap switch-off process. This will be done in

the near future in an experiment were the *BEC* is released from the trap by a Raman outcoupling process. In here, a combination of laser pulses transfers, almost instantaneously, the atoms form the trapping spin state $m_J = +1$ to $m_J = 0$, insensitive to the field. The comparison of the *TOF* in this case with the one we observe in the usual trap switch-off would allow the measurement of $\varepsilon_\perp$ and, then, the calibration of the detection system. However, this procedure would work properly only if all the atoms are released from the trap to avoid mean field effects. Such procedure would also allow an accurate calibration of our detection system for the total number of atoms in the *BEC*, which is still not possible and constitutes one of the major problems we have in our experimental setup.

A similar calibration for thermal clouds, based in a Raman process is, unfortunately, more difficult to achieve. The thermal cloud as a much larger velocity distribution and it is harder to *tune* the Raman transition to all the atoms in the cloud [15]. However, for a very short Raman pulse, its frequency bandwidth may become large enough and address all the atoms in the thermal cloud. For a cloud at $T = 1$ μK, the cloud's spread in frequency units is of about $\eta \times (k_B T/2\pi\hbar) \sim 120$ kHz, where we took $\eta = h\nu_{rf}/k_B T \sim 6$. This imposes a maximum width of 10 μs. We are currently setting up a device that would allow producing a Raman π pulse with a sufficient intensity to transfer a thermal cloud at this temperature. Clouds with bigger temperatures would require a more accurate calculation of the transfer ratio. This issue will be addressed by A. Perrin in his Ph.D. thesis[147].

[15] The results of Fig.5.21 may be used to determine ε_{th}, knowing ε_{BEC}, which is easier to measure.

APPENDIX A

The condensate in the Thomas-Fermi approximation.

In this Appendix we derive the expressions that describe the density of the condensate in the Thomas-Fermi approximation and its time evolution during the expansion of the cloud after being released from the trap. We start by presenting the Gross-Pitaevskii equation.

A.1 The condensed state: Gross-Pitaevskii equation.

In the ideal gas, at $T = 0$, all the atoms are in the ground state and the system's wave function is

$$\Psi_0(\mathbf{r}_1, \mathbf{r}_2, \ldots, \mathbf{r}_N) = \prod_{i=1}^{N} \psi_0(\mathbf{r}_i),$$

where $\psi_0(\mathbf{r})$ is the single-particle wave function, the fundamental state of the harmonic oscillator, *i.e.* a gaussian function. Since all the atoms are in the same quantum state, the N-particles wave function in the last Equation is a symmetric state with the respect to the exchange of particles.

If interatomic interactions are present, due to the trapping confinement and even for a very small number of atoms, the ideal gas model is very inaccurate for treating the ground state wave function. To give a good description of the condensate density we use the many-body Hamiltonian of Eq.4.22 introduced in §4.3.1. Using again a contact potential to describe the interactions, the second quantized Hamiltonian describing the *BEC* field operator is given by

$$\hat{H} = \int d^3\mathbf{r}\ \hat{\Psi}_0^\dagger(\mathbf{r}) \left[\hat{H}_0 - \mu + \frac{g}{2}\hat{\Psi}_0^\dagger(\mathbf{r})\hat{\Psi}_0(\mathbf{r})\right] \hat{\Psi}_0(\mathbf{r}). \tag{A.1}$$

Here, as usual the field operators $\hat{\Psi}_0^\dagger(\mathbf{r})$ and $\hat{\Psi}_0(\mathbf{r})$ create and annihilate a particle in the condensate. The thermal mean value of the interaction

potential for this case can be calculated in the canonical ensemble, assuming that the fluctuations of the condensate atom number are very small [105]. It is given by

$$\begin{aligned}\langle \hat{V}_{int}(\mathbf{r})\rangle &= \frac{g}{2}\langle \hat{\Psi}_0^\dagger(\mathbf{r})\hat{\Psi}_0^\dagger(\mathbf{r})\hat{\Psi}_0(\mathbf{r})\hat{\Psi}_0(\mathbf{r})\rangle \\ &= \frac{g}{2}\left[\langle \hat{\Psi}_0^\dagger(\mathbf{r})\hat{\Psi}_0(\mathbf{r})\rangle\right]^2 \\ &= \frac{g}{2}N_0^2|\psi_0(\mathbf{r})|^2 = \frac{g}{2}n_0^2(\mathbf{r}), \end{aligned} \tag{A.2}$$

where $n_0(\mathbf{r}) = N_0\psi_0(\mathbf{r})$ is the *BEC* density, with N_0 the number of condensed atoms and $\Psi_0(\mathbf{r})$ the BEC single-particle wave function. To reduce the Hamiltonian of Eq.A.1 to a quadratic form, in the spirit of a self-consistent mean-field theory (see §C), we approximate the interaction terms to

$$\hat{V}_{int}(\mathbf{r}) \sim \frac{g}{2}\left[2N_0|\psi_0(\mathbf{r})|^2\hat{\Psi}_0^\dagger(\mathbf{r})\hat{\Psi}_0(\mathbf{r}) - N_0^2|\psi_0(\mathbf{r})|^4\right], \tag{A.3}$$

which neglects density fluctuations and gives the same thermodynamical equilibrium mean values as the real interaction term. The second term on the right hand side of Eq.A.3 doesn't contribute to any thermodynamical measurable quantity, corresponding to a simple shift in the energy. Equation A.1, in this mean field approximation is then equal to

$$\hat{H} = \int d^3\mathbf{r}\ \hat{\Psi}_0^\dagger(\mathbf{r})\left[\hat{H}_0 - \mu + g|\Psi_0(\mathbf{r})|^2\right]\hat{\Psi}_0(\mathbf{r}). \tag{A.4}$$

If we replace the field operators by the corresponding single particle wave function, this equation takes the form of a non linear Schrodinger equation

$$\left[-\frac{\hbar^2}{2M}\nabla^2 + U(\mathbf{r}) + g|\Psi_0(\mathbf{r})|^2\right]\Psi_0(\mathbf{r}) = \mu\Psi_0(\mathbf{r}). \tag{A.5}$$

known as the Gross-Pitaevskii equation.

A.2 Thomas-Fermi approximation.

In the limit where the number of atoms in the condensate is large, the interatomic interactions will inflate the cloud up to the maximum available volume in the trap. Thus, the shape of the cloud and its density are determined mainly by the compensation of the interactions forces by the trapping potential. In this regime, the kinetic energy term is negligible and the Gross-Pitaevskii equation reduces to

$$U(\mathbf{r}) + g|\Psi_0(\mathbf{r})|^2 \simeq \mu,$$

and the amplitude of the BEC wave function is

$$|\Psi_0(\mathbf{r})| = \left\| \frac{\mu - U(\mathbf{r})}{g} \right\|^{1/2}, \tag{A.6}$$

where $\|\ldots\|$ replaces the argument if positive and is zero otherwise. This approximation of neglecting the kinetic energy term is referred to as the *Thomas-Fermi approximation*, originally used in the theory describing electronic densities in atoms. The boundary of the *BEC*, in this approximation, is the surface where the trapping energy equals the chemical potential, determined by the equation

$$\mu = U(\mathbf{r}) = \tfrac{1}{2} M \sum_\alpha \omega_\alpha^2 \alpha^2.$$

The condensate number of atoms is given by $N_0 = \int_{R^3} d\mathbf{r}\, |\psi_0(\mathbf{r})|^2$ and its density takes then the form of an ellipsoid where the density decreases parabolically from the center

$$\begin{aligned} n_0(\mathbf{r}) &= \frac{15}{8\pi} \frac{N_0}{{R_{BEC}}^3} \left\| 1 - \sum_\alpha \frac{r_\alpha^2}{R_\alpha^2} \right\| \\ &\equiv \frac{\mu}{g} \left\| 1 - \sum_\alpha \frac{r_\alpha^2}{R_\alpha^2} \right\| \end{aligned} \tag{A.7}$$

with $R_\alpha = \sqrt{2\mu/M\omega_\alpha^2}$ the BEC *radius* in the α spatial direction, R_{BEC} the corresponding geometric mean value and the chemical potential is

$$\mu = \tfrac{1}{2}\hbar\overline{\omega} \left[15 \frac{N_0 a}{\overline{\sigma}} \right]^{2/5}, \tag{A.8}$$

with the usual definition $\overline{\sigma} = \sqrt{\hbar/M\overline{\omega}}$. The *BEC* number of atoms and its peak density follows from the above expressions and are given, respectively, by

$$n_0 \equiv n_0(\mathbf{0}) = \frac{\mu}{g} \quad \text{and} \quad N_0 = \frac{5}{2}\frac{\mu}{g} {R_{BEC}}^3. \tag{A.9}$$

We end here the density characterization of the atomic sample in thermal equilibrium inside the trap. In the next Section we will derive expressions for the associated atomic flux when we switch off the trap and let the cloud expand and fall under the influence of gravity.

A.3 The *TOF* of the *BEC*.

A.3.1 The time dependent *Gross-Pitaevskii* equation. The hydrodynamical equivalent.

From Eq.A.4 we can write directly the time dependent Schrodinger equation for the condensate wave function, $\Psi_0(\mathbf{r},t)$

$$i\hbar\partial_t\Psi_0(\mathbf{r},t) = \left[-\frac{\hbar^2}{2M}\Delta + U(\mathbf{r},t) + g|\Psi_0(\mathbf{r},t)|^2\right]\Psi_0(\mathbf{r},t), \tag{A.10}$$

where, now, the trapping potential is also time dependent.

The last equation can be re-casted in a couple of other differential equations by writing the wave function in terms of a modulus and a phase[3], like

$$\Psi_0(\mathbf{r},t) = \sqrt{n_0(\mathbf{r},t)}e^{i\Phi(\mathbf{r},t)}. \tag{A.11}$$

Furthermore, the phase $\Phi(\mathbf{r},t)$ can be reported to a velocity field $\mathbf{v}(\mathbf{r},t)$ through

$$\mathbf{v}(\mathbf{r},t) = \frac{\hbar}{M}\nabla\Phi(\mathbf{r},t). \tag{A.12}$$

In the Thomas-Fermi approximation, neglecting the kinetic energy term compared to the interaction one, Eq.A.10 can then be transformed to the expressions

$$\begin{cases} \partial_t n_0(\mathbf{r},t) + \nabla\cdot[\mathbf{v}(\mathbf{r},t)n_0(\mathbf{r},t)] = 0 \\ \\ M\partial_t\mathbf{v}(\mathbf{r},t) + \nabla\left[U(\mathbf{r},t) + g\rho(\mathbf{r},t) + \frac{1}{2}Mv^2(\mathbf{r},t)\right] = 0 \end{cases}. \tag{A.13}$$

The first of these equations is simply the equation of continuity

$$\partial_t n_0(\mathbf{r},t) + \nabla\mathbf{J}(\mathbf{r},t) = 0,$$

with

$$\mathbf{J}(\mathbf{r},t) = (\hbar/2iM)\{\Psi_0^*\nabla\Psi_0 - \Psi_0\nabla\Psi_0^*\}$$

the *current density*. The second equation is the Euler equation for the velocity field. The two equations in Eqs.A.13 describes the nonviscous flow of hydrodynamical fluid [4]. These equations are derivable from the Boltzmann kinetic equation if we assumes a mean free path much smaller than any other characteristic lengths. The large collisional rate takes the fluid into a very fast relaxation to a local equilibrium and, in first order, collision integral in the Boltzmann equation can be approximately equal to zero. What we have

just described is the picture of the flow of classical fluid in a very strong collisional regime. However, the starting point was an equation of motion of a single coherent quantum state at zero temperature. This similarity found in these two very different physical situations motivated the designation of *hydrodynamical superfluid* to the BEC.

The stationary solution of Euler equation in the second line of Eqs.A.13, with a overall BEC constant phase, is just the Thomas-Fermi profile found in §A.2. Here we are interested in deriving the evolution of this profile after releasing from the trap. This can be done by using the same coordinates re-scaling used before for the thermal cloud, in Eqs.4.57 [1]. Eq.A.11 takes the form [146]

$$\Psi_0(\mathbf{r},t) = \mathcal{V}^{-1/2}\chi_0\left[\boldsymbol{\rho}(\mathbf{r},t),\tau(t)\right]\ \exp\left[i\Phi(\mathbf{r},t)\right], \tag{A.14}$$

where $\chi_0(\boldsymbol{\rho},\tau) = \sqrt{n_0(\boldsymbol{\rho},\tau)}$ and $\tau(t) = \int^t dt'\mathcal{V}^{-1}(t')$, a re-scaled time coordinate. Eq.A.12 suggests the phase $\Phi(\mathbf{r},t)$ is given by

$$\Phi(\mathbf{r},t) = M\sum_\alpha \frac{r_\alpha^2}{2\hbar}\frac{\dot{b}_\alpha(t)}{b_\alpha(t)}. \tag{A.15}$$

The trapping potential in Eq.A.10 is given by $U(\mathbf{r},t) = \frac{1}{2}M\sum_\alpha \omega_\alpha^2(t)r_\alpha^2$. Using the ansatz of Eq.A.14 and replacing $\omega_\xi(t)$ according to the equation

$$\ddot{b_\alpha}(t) + \omega_\alpha^2(t)b(t) = \frac{{\omega_{0\alpha}}^2}{b_\alpha(t)\mathcal{V}(t)}, \tag{A.16}$$

one arrives to the equation of motion for $\chi_0(\boldsymbol{\rho},\tau)$[146]

$$i\frac{\hbar}{\mathcal{V}(t)}\frac{\partial\chi_0}{\partial\tau} = -\frac{\hbar^2}{2M}\sum_\alpha \frac{1}{b_\alpha^2(t)}\frac{\partial^2\chi_0}{\partial\rho_\alpha^2} + \frac{M}{2\mathcal{V}(t)}\sum_\alpha {\omega_{0\alpha}}^2\rho_\alpha^2\chi_0 + \frac{g}{\mathcal{V}(t)}|\chi_0|^2\chi_0. \tag{A.17}$$

Quite remarkably the choice done in Eq.A.15 for the phase cancels out all terms $\nabla_{\boldsymbol{\rho}}\chi_0$. In the Thomas-Fermi approximation, the first terms in the right hand side of the last equation is neglected,

$$i\hbar\frac{\partial\chi_0}{\partial\tau} = +\frac{M}{2}\sum_\alpha {\omega_{0\alpha}}^2\rho_\alpha^2\chi_0 + g|\chi_0|^2\chi_0. \tag{A.18}$$

The solution of this last equation follows from the usual time-independent problem,

$$\chi_0(\boldsymbol{\rho},\tau) = \left(\frac{\mu}{g}\right)^{1/2}\ \left\|\sqrt{1-\frac{M}{2\mu}\sum_\alpha {\omega_{0\alpha}}^2\rho_\alpha^2}\right\|\ \exp\Big[-i\frac{\mu}{\hbar}\tau\Big], \tag{A.19}$$

[1] In this case the *effective* temperature $\theta(t)$ is constant and equal to one and the thermal velocity, v_α, is null. To keep the same notations as in references [148], [146], in here, instead of $\mathbf{R}(\mathbf{r},t)$ we will use $\boldsymbol{\rho}(\mathbf{r},t)$ with $\rho_\alpha = r_\alpha/b_\alpha$ and, replace as well $1/\Gamma$ by $\mathcal{V}(t) = \prod_\alpha b_\alpha(t)$

In this expression μ is the initial chemical potential and the coordinates $\boldsymbol{\rho}$ are re-casted to the laboratory frame coordinates r_α through the knowledge of the time evolution of the parameters $b_\alpha(t)$. The Eqs.A.16 determine the time evolution of the BEC. These equations, of entirely classical character, depends only in the initial trapping frequencies, $\omega_{0\alpha}$ and their subsequent time evolution.

Abrupt trap switch-off.
We will consider now the most usual case of sudden trap switch-off. Here, $\omega_\alpha(t)$ goes instantaneously to zero, and for our cigar shaped trap, we can re-write Eqs.A.16 as,

$$\frac{d^2}{d\theta^2}b_\perp = \frac{1}{b_\perp^3 b_\parallel} \quad \text{and} \quad \frac{d^2}{d\theta^2}b_\parallel = \frac{\lambda^2}{b_\perp^2 b_\parallel^2}, \tag{A.20}$$

where $\theta = \omega_{0\perp}t$ and λ is the aspect ratio $\lambda = \omega_{0\parallel}/\omega_{0\perp}$. In our case, $\lambda \ll 1$ and the solution for the above equations can be workout in a series expansion in powers of this parameter[68]. For $\lambda = 0$, $b_\parallel = 1$, as initially. First and second orders in λ gives the expressions

$$b_\parallel = 1 + \lambda^2\left[\theta\arctan(\theta) - \ln\left(\sqrt{1+\theta^2}\right)\right] \quad \text{and} \quad b_\perp = \sqrt{1+\theta^2}. \tag{A.21}$$

This result expresses what is known as the geometry inversion: in the less confined axis, the BEC almost keeps its size during the fall while in the other two, there is an expansion, which for $\theta \gg 1$, turns out to be approximatively linear in time. Some time after released from the trap the *BEC* changes from a cigar to a disk-shaped cloud.

The density of the expanding *BEC* is then (cf. Eqs.A.11, A.14 and A.19)

$$\begin{aligned} n_0(\mathbf{r},t) &= |\Psi_0(\mathbf{r},t)|^2 \equiv \frac{\chi_0\left[\boldsymbol{\rho}(\mathbf{r},t),\tau(t)\right]}{\mathcal{V}} \\ &= \frac{1}{\prod_\alpha b_\alpha(t)}\frac{\mu}{g}\left\|1 - \sum_\alpha \frac{r_\alpha^2}{R_\alpha^2(t)}\right\| \end{aligned} \tag{A.22}$$

with $R_\alpha(t) = b_\alpha(t)R_\alpha$.

A.3.2 The condensate detected atomic flux.

We want to derive an expression for the atomic flux crossing the plane xOy, located at $-\eta = -H + \frac{1}{2}gt^2$ below the center of the expanding cloud. We consider two approximations:

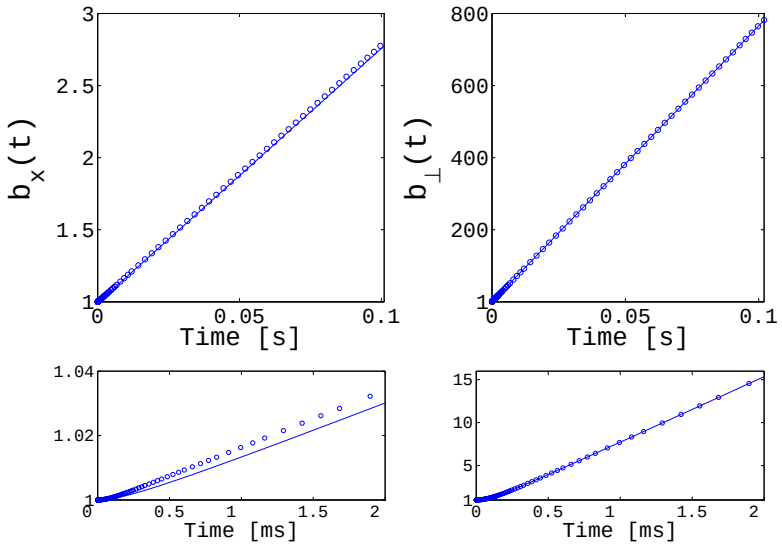

Figure A.1: Top graphs: the exact (symbols) and the approximated analytical (line) evolution of the scaling factors for our *BEC* with $\lambda \approx 1/25$ in the bias field (left) and transverse (right) axes. Bottom graph: zoom on the top graphs for the initial 2 milliseconds.

- the height of fall $\frac{1}{2}gt_0^2$ is much bigger than the *BEC* expansion, $t_0 \gg R_\perp\omega_\perp/g = \sqrt{2\mu/M}/g$ and, in a good approximation, we can disregard the cloud's expansion during its detection.
- the detector radius is larger than the expanded *BEC* and we can integrate the atomic flux over the entire xOy plane.

The condensate's *TOF* signal is then

$$\begin{aligned} I_{BEC} &= \frac{\Delta N(t_0)}{\Delta z}\frac{\Delta z}{\Delta t}\Big|_{z=H-\frac{1}{2}gt^2} \\ &\approx v_G \times n(H-\tfrac{1}{2}gt^2, t_0) \end{aligned} \tag{A.23}$$

where, using Eq.A.22,

$$n_0(z,t) = \iint dx\,dy\,n_0(\mathbf{r},t) = \frac{16}{15}\frac{N_0}{R_z(t)}\left\|1-\frac{z^2}{R_z(t)^2}\right\|^2.$$

As $\theta = \omega_\perp t \gg 1$ the second expression in Eq.A.21 may be simplified to $b_\perp(t) \simeq \omega_\perp t$ and thus $R_z(t_0) = R_z\omega_\perp t_0$. With $\delta_t = t - t_0 \ll t_0$, we get

$$I_{BEC}(\delta t) \approx \frac{15}{16}\frac{N_0}{t_{TF}}\left\|1-\left(\frac{\delta t}{t_{TF}}\right)^2\right\|^2 \tag{A.24}$$

where

$$t_{TF} = \frac{1}{g}\sqrt{\frac{2\mu}{M}}, \tag{A.25}$$

the *Thomas-Fermi time radius.*

A.3.3 The ion flux from a condensate.

The ion flux for a *pure* condensate is given by

$$\Phi = \frac{1}{\tau_i}N_0 + \tfrac{1}{2}\beta\kappa_2\langle n_0^2(\mathbf{r})\rangle + \tfrac{1}{3}L\kappa_3\langle n_0^3(\mathbf{r})\rangle, \tag{A.26}$$

where β and L are the ionizing rate constants defined for a thermal cloud and $\kappa_2 = 1/2!$ and $\kappa_3 = 1/3!$ the quantum reduction factors discussed in §4.2.2.2.

Using Eq.A.7, we have

$$\langle n_0^{q+1}\rangle = \langle n_0\rangle \times n_0^q \ \frac{I_{q+1}}{I_1},$$

with $n_0 = \mu/g$ the condensate peak density. The factor $I_{q+1}/I_1 = \frac{15\sqrt{\pi}}{8}\Gamma(q+2)/\Gamma(q+7/2)$ is equal to 4/7 and 8/21 for respectively $q = 1$ and $q = 2$. Eq.A.26 may now be written as

$$\Phi = \frac{1}{\tau_i}N_0 + \frac{2}{7}\kappa_2\beta\, N_0\, n_0 + \frac{8}{63}\kappa_3 L\, N_0\, n_0^2. \tag{A.27}$$

Finally, it is useful to derive the quantity *ion flux per atom*, defined as $\Gamma = \Phi/N_0$ (this quantity was used in Ref.[45] and is used in Appendix §B) and then equal to

$$\Gamma = \frac{\Phi}{N_0} = \frac{1}{\tau_i} + \frac{2}{7}\kappa_2\beta n_0 + \frac{8}{63}\kappa_3 L n_0^2. \tag{A.28}$$

APPENDIX B

The condensate and the determination of the ionizing rate constants.

To describe correctly the ion signal, we need to know the rate constants β and L. The inverse is also true and, for a certain ion flux signal, if we know the density of the atomic cloud we can derive these rate constants (see the argument in the beginning of §4.2.2.1). For making work this idea we need to use data of many cloud with different densities to well explore the dependence of the ion signal on the second and third power of the density. To actually get to *see* the third order process we need to use clouds as much dense as possible. Thus, condensates are very good candidates for the task. Moreover, their mean densities can be, in principle, very well determined.

This Appendix summarizes the experimental description and data analysis of the experiment we did for measuring β and L. This work was reported in Ref.[45] and a very detailed description of it may be found in the Ph.D. thesis of Olivier Sirjean[70]. In here it is described all the theoretical details in the data analysis, stressing in special the calculation of the ionizing rate constants within the Bogoliubov approximation, taking into account the quantum and thermal depletions of the atomic cloud.

We include the description of this experiment since it has a special importance in the interpretation of the data of the experiment on the measure of the scattering length, a, discussed in Chapter 5. Moreover, as it is explained in §5.4, we think that the error we have committed in the determination of a should report to a bad measurement of β and L, making relevant the description of the measurement of these constants.

B.1 The condensate.

B.1.1 The *pure BEC*.

In the *Thomas-Fermi* approximation, the *BEC* atomic flux integrated over the detector has the shape of an inverted parabola, described by Eq.A.24 of

Appendix A. In the following, we will compare this simple result with what is observed experimentally. We will also discuss the criteria we used to classify a given *TOF* as corresponding to a *pure BEC* at zero temperature.

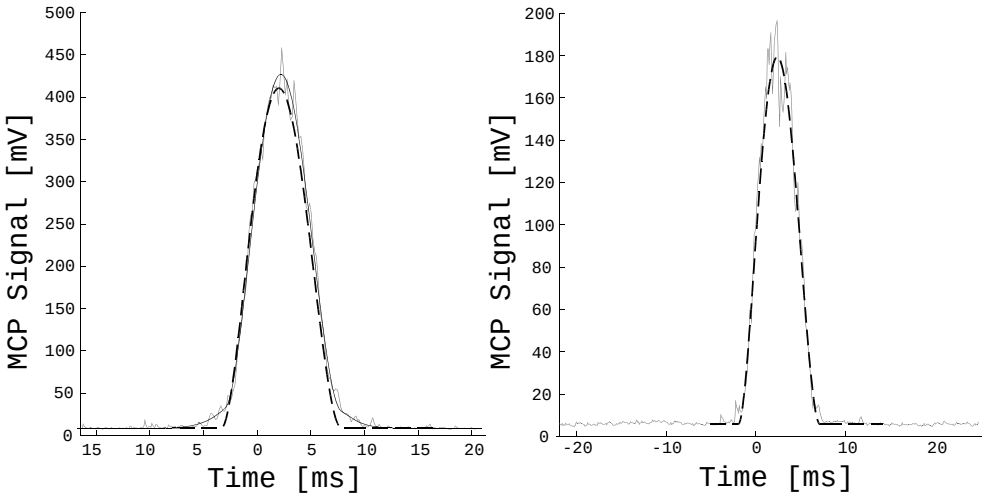

Figure B.1: The *pure BEC*. This Figure shows MCP signals for two condensates taken in the *analog mode*. The time scale is shifted 100 ms from the trap switch-off. In both graphs, the *TOF* is fitted by an expression composed by an inverted parabola truncated at zero (the *BEC* part) plus a gaussian (the thermal cloud). In the left hand side graph we compare the result of that fit (solid line) with a fit to just a *BEC* expression(dashed line). In the bottom of the graph there is still some visible thermal cloud component, where the two fitted functions differ slightly. Using this simple model, we estimated a thermal component about 25%. We know, however, that this value is overestimated since we are not accounting for the thermal cloud repulsion due to the *BEC* mean field.
In the right hand side graph, the inverted parabola fits very well the data. There is no visible thermal wings in this graph and we say that the BEC is *pure*. Actually, this is not completely true since the TOF signal corresponds to a two-dimensional integrated density and if a small thermal cloud persists around the condensate it may be washed out from the *TOF* signal. The fit of this graph to a composed *TOF* function is still compatible with the existence of a maximum of 15% of thermal cloud component. For this case, the error committed in the chemical potential is as big as 5%.

Fig. B.1 shows two typical *TOF* for cloud near $T = 0$. This two *TOF* curves were taken after a evaporative cooling where the *rf*-ramp was ramped down to just above the bias. This is done in order to get, as much as possible, a *pure* condensed cloud with no thermal component. Nonetheless, it is obvious from simple observation that we were more successful in the *TOF* of the right hand side, where the fit to an inverted parabola works

much better than in the other one. We call *pure* BEC for referring to clouds where this thermal component is not visible in the corresponding *TOF*s.

Even for *pure BEC*s, we expect always the presence of a small thermal cloud. This is ultimately due to the *thermal depletion* of the condensate, which can be modeled in the *Bogoliubov* approximation for $T \neq 0$. Thus, despite not appearing in the *TOF* a remaining thermal cloud may always exist: its presence may be washed out by the two dimensional integration of the atomic flux. Analyzing the signal to noise of a fit to an expression that accounts for both the *BEC* and the thermal cloud, we have estimated [70] that the thermal component may never be grater than 15% of the atoms in a *pure BEC*. This would correspond to an error of 5% in the estimative of the *BEC* chemical potential μ [1].

B.1.2 Chemical potential and cloud's number of atoms.

The number of condensed atoms, N_0, and the chemical potential, μ, are related through Eq.A.8. If we could calibrate our detection system to measure the absolute number of atoms in a *BEC* we could use this expression to derive a. Unfortunately, this is not the case since we detect only a percentage of the total cloud atoms. Nevertheless, if the ratio of the detected to the total number of atoms is constant, the validity of the power law expressed in Eq.A.8 can still be tested. In Fig.B.2, we represent the chemical potential of several *pure* condensates in function of the 2/5 power of the detected number of atoms. This graph shows that for condensates with number of atoms ranging from 10^3 to 2×10^4, the power law of Eq.A.8 is well respected.

The data in the graph of Figure B.2 suggests that the number of detected atoms is, in fact, proportional to the total number of atoms in the cloud.

B.2 The measure of β and L experiment.

B.2.1 The experimental procedure.

We can easily measure the cloud's ions rate production observing the corresponding detected ions flux. In the ion detection, we don't have the same calibration problem as for the atoms: the ion detection efficiency in our experiment is known. Moreover, the ion flux is an almost instantaneous measurement of the rate production since the transit time to the `MCP` is very small. Thus, the flux we measure just after triggering the trap switch-off is directly reportable to the atom's *TOF* we detect after the fall. By measuring

[1] The small thermal cloud that remains even in a *pure BEC* will produce an extra amount of ions due to collisions between these atoms and atoms from the *BEC*. This leads to a correction of the ion expressions due to the *thermal depletion*.

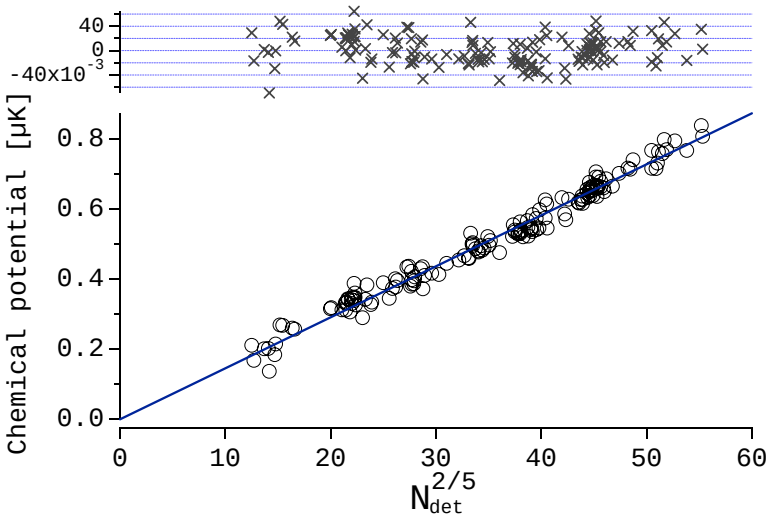

Figure B.2: Chemical potential for the *pure* condensates (see text) plotted in function of the number of detected atoms to the power of 2/5. The curve is very well fitted by a straight line, which passes at zero even if no constraints are imposed in the fit. In the upper part of graph we also present the residuals of the fit: there is no tendency for the data to deviate from the linear fit. This result is compatible with a ballistic free expansion of the condensate. This could not be the case if it existed a *lens effect* due to the cloud of polarized atoms in the magnetic sub-level $m_J = 1$ (see also the text).

this ion flux and the corresponding *TOF* for many condensates, with many different densities, we get the data we need to measure the ionization rate constants.

The ion flux may be written in terms of the ionizations rate constants and, the number of atoms in the *BEC*, N_0, and its peak density, n_0 (cf. Eq.A.27 of Appendix A),

$$\Phi = \frac{1}{\tau_i} N_0 + \frac{2}{7}\kappa_2 \beta\, N_0\, n_0 + \frac{8}{63}\kappa_3 L\, N_0\, n_0^2.$$

In the data treatment of this experiment we have used instead the *ion flux per atom*, defined as (cf. Eq.A.28)

$$\Gamma = \frac{\Phi}{N_0} = \frac{1}{\tau_i} + \frac{2}{7}\kappa_2 \beta n_0 + \frac{8}{63}\kappa_3 L n_0^2. \tag{B.1}$$

This is the quantity we fit in function of n_0 to infer the values of β and L (see Fig.B.4).

Varying the number of atoms in the *BEC*.

Varying the *BEC* density from one experimental run to another can be as

easy as involuntary. A small fluctuation in the bias field can easily change significatively the number of atoms at the end of the evaporative cooling. If the bias field increases to a value bigger than the last frequency of the $rf-$ramp, all the atoms are removed from the trap The main reason, however, that makes the number of atoms in the *BEC* to fluctuate is related with the variation in the number of atoms that are loaded into the magnetic trap, at the beginning of the evaporative cooling. A small fluctuation of this number makes, in the end, a quite large difference in condensate's number of atoms.

Along with these *uncontrolled* variations of condensate number of atoms, some experimental parameters can be manipulated to get in the end smaller or bigger *BEC*s. One way of doing that is to keep the *rf*-field on in the end of evaporation, at its last frequency, for some time before opening the trap. The *BEC*, if left in the trap without the *rf*-field would start to heat up and rapidly would become a thermal cloud. This may have several causes: elastic collisions of condensed atoms with hot He^*atoms produced in *Penning* inelastic collisions, trap anharmonicity or instabilities, etc. However, if we keep the *rf*-field on, at its last frequency, it behaves as a *rf-knife* removing out any heated atom, keeping this way the *purity* of the condensate. In this process the cloud looses continuously some atoms and the longer we keep the *rf-knife* on, the smaller gets *BEC* at the end, with also a smaller density. This is shown in Fig.B.3 where we also compare the cases where the *rf-knife* is on and turned off.

Another way for varying the final number of atoms in the *BEC* is by speeding up or slowing down the last *rf*-ramp. If we want to obtain the largest possible *BEC* the efficiency of the evaporative cooling must be optimized for a certain ramp velocity. Slower ramps takes more time to complete the evaporation and leaves more time to the atoms to heat up, faster ones will prevent thermalization to take place extracting atoms that could eventually thermalized at colder temperatures.

B.2.2 Obtained results and their analysis.

The data analysis we present here will start by assuming a *scattering length* of $a = 12$ nm. This value corresponds to the latest theoretical estimate of a[131] and, at time we made the data analysis, it was the most probable value for this constant [2]

[2]As explained in Chapter 5, by the time we write this manuscript it is known that the scattering length is much smaller, around $a = 7.5$ nm. In here, we will keep using $a = 12nm$ since it is what we have done in the original data analysis. To into account a possible mismatch of the real value of a with the one we used, we decided to present the final result for β and L parameterized by a. This would *cure* the values found for β and L for a known value of a.

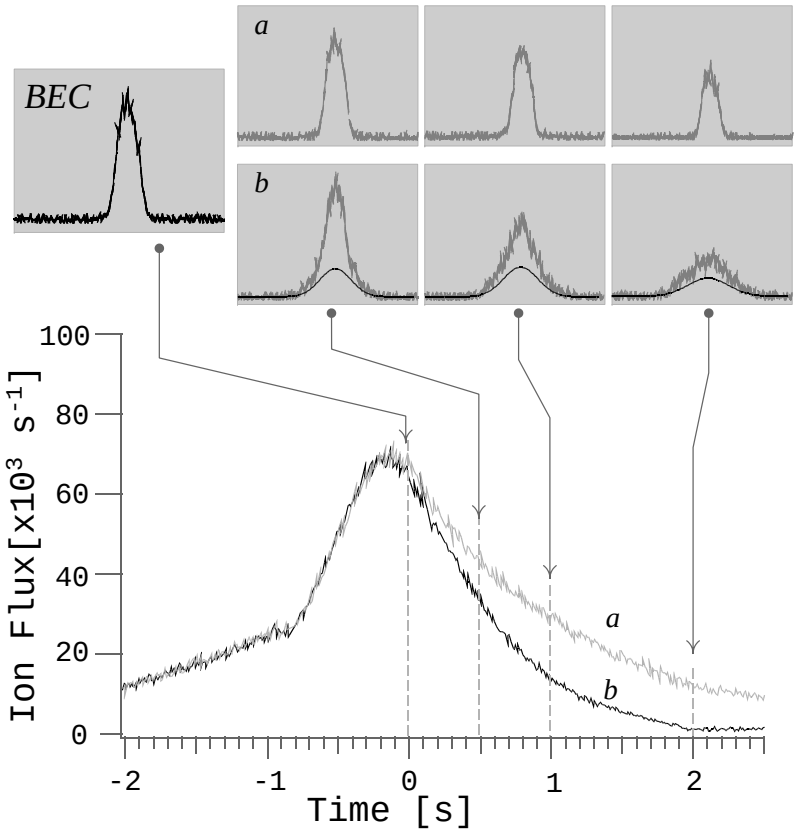

Figure B.3: The graphs in this Figure were obtained in experimental runs that had similar ion signals before $t = 0$, the time were a *pure BEC* was formed (as in Figure4.1). For times posterior to $t = 0$, the Figure shows typical behavior of the ions signal for the case were a *rf-knife* (see text) were present *a*); or in the case were it was not *b*). For these two curves the Figure shows the *TOF*signals in three different times. When the *rf-knife* is kept on, it is seen that the cloud remains condensed, with less and less atoms for longer periods before the trap switch-off. In the absence of the *rf-knife*, the cloud rapidly becomes a thermal cloud.

B.2.2.1 Analysis and results with $a = 12nm$

• Γ ***versus*** **the** ***peak density.***

If we assume a certain value for a, we can derive the *BEC* chemical potential μ from the analysis of its *TOF* signal (cf. Eq2.A.25),

$$\mu = \tfrac{1}{2} M (g\, t_{TF})^2.$$

where t_{TF} is the *Thomas-Fermi time radius*, half of the time extension of the condensate. Knowing μ, we can also get the condensate number of atoms (cf Eq. A.8),

$$N_0 = \left(\frac{2\mu}{\hbar\overline{\omega}}\right)^{5/2} \frac{\overline{\sigma}}{15a}.$$

and the corresponding peak density

$$n_0(\mathbf{0}) = \frac{\mu}{g} = \frac{\mu M}{4\pi\hbar^2 a}.$$

Selecting only data from *pure BECs* and correcting the ion flux signal by the detection system ion efficiency, we obtain an ensemble of data points for Γ and the corresponding peak density. This data is plotted in the graph of Fig.B.4. In this graph, we present data obtained for two different trap configurations, with different transverse frequencies: $\omega_\perp/2\pi = 1800 \pm 50\ Hz$ (filled circles) and $\omega_\perp/2\pi = 1200 \pm 50\ Hz$ (open circles) [3]. The two different sets of data appears to coincide in the graphical representation.

Also in the graph of Fig.B.4 are represented two fitted curves. One is an almost straight line and the other almost a parabola [4]. Both curves were obtained in fits that were constrained to give $\Gamma = 1/\tau_i \simeq 10^{-3}$ for $n_0 = 0$: the contribution corresponding to collisions between one He*atom and a molecule from the *background gas*. The *almost straight line* would be the good fitting expression in case were only *two-body* collisional processes were present. The *almost parabola* follows the law in Eq.A.28, expressing both the *two-body* and *three-body* processes. It's clear from the Figure that the *straight line* doesn't fit well the data, especially for large peak densities, and that *three-body* process has to be taken into account.

We can also fit the data to an expression where only the *background gas* and the *three-body* contributions are included. Again, for this case, the fit gets worse than the one with all the collisional process included (for clarity, the result of this fit is not shown in the graph Fig.B.4).

[3] The transverse frequency can be easy changed by adjusting the trap bias field B_0 (see §1.2.1.2). This has no influence in the slow axis oscillation frequency, which remains equal to $\omega_\parallel/2\pi = 47 \pm 3\ Hz$.

[4] These curves are not exactly a straight line and a parabola because they include the correction factor for the *quantum* and *thermal depletion* of the *BEC*.

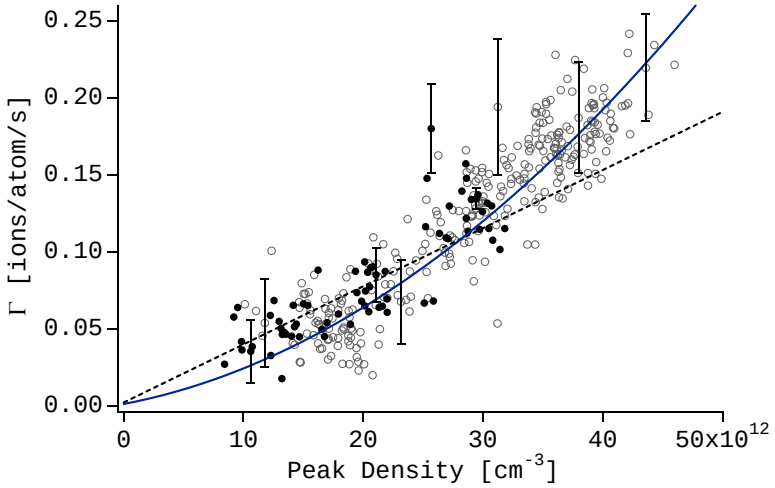

Figure B.4: The *ion flux per atom*, Γ, in function of the peak density for several *BEC* clouds. The data comes from two different sets obtained with different trap confinement in the transverse direction. The filed circles correspond to a transverse trapping frequency equal to $\omega_\perp/2\pi = 1800 \pm 50\ Hz$ and the open ones to $\omega_\perp/2\pi = 1200 \pm 50\ Hz$. The shown error bars are only indicative, being typical in their respective regions of the graph. The two curves corresponds to fits to a theoretical curves, constrained to pass in the ordinate τ_i^{-1} for a null density. The solid line includes all the collisional processes and correspond to our final fit to the data. In the fit of the dashed line, L was set to zero to put in evidence the influence of the *three-body* processes, unquestionably present. Not all the error bars justifies the data fluctuations. Note, however, that the data doesn't show any tendencies out of the fitted curve. The fluctuations are of random character and by binning together adjacent data points we would get error bars consistent with the fitted curve. In this graph we preferred to show all the data we used.

Data uncertainties and the fit *chi square* value.
The fit, present in Fig.B.4, is weighted by the uncertainty in the determination of Γ. Comparing to this one, the error we make deriving t_{TF} from the *TOF* signal is negligible. The error of Γ is therefore only related to the error we make measuring the ion flux, Φ. This latter one is obtained by averaging the ion signal for a very short period of time before the trap switch-off. Doing this, we avoid the inclusion of spurious noise fluctuations of the ion signal into the data analysis and also an estimating of the error in the determination of Γ, which is related with the standard deviation of the mean of Φ (see FigureB.4 for typical error bars).

Knowing the *noise* in Γ we can also compute a χ^2 for the several fits we have referred to. Fitting the data to the full expression for Γ, with all collisional processes included, we get $\chi^2/\nu = 0.9$ [5]. For the other two considered fits, we have obtained $\chi^2/N = 1.2$ and $\chi^2/N = 1.4$, in the cases where we have disregarded the *two-body* and the *three-body* collisions, respectively.

• Corrections due to the *quantum* and *thermal depletion*.
Due to the existence of the interatomic interactions and even for $T = 0$, some of the atoms of condensed gas populates the excited states, a phenomena known as the *quantum depletion* of the condensate. If $T \neq 0$, the number of atoms being excited out of the *BEC* increases further according to a *thermal depletion* factor.

The fits in the graphs of Fig.B.4 were done considering also the corrections due to these *quantum* and *thermal depletions* of the condensate. We consider very briefly these two effects.

The number of excited atoms, N_{ex}, can be calculated within the Bogoliubov approximation[70, 102, 149]. For $T = 0$, it is given by

$$N_{ex} = N - N_0 = \frac{8}{3\sqrt{\pi}}\sqrt{n\,a^3}N, \tag{B.2}$$

with n and N the density of the gas and its total number of atoms and, N_0 the number of those in the condensate.

The quantum depletion decreases the density of the gas and, therefore, also the rate of production of ions within the cloud. These reduction can be accounted in the definition of the collisional rate constants for the *BEC* given in Eq.4.5 of Chapter 4,

$$\beta' = \kappa_2 \times \beta \quad \text{and} \quad L' = \kappa_3 \times L,$$

where β and L are the usual rate constants defined for a thermal cloud and, non considering quantum depletion, $\kappa_2 = 1/2!$ and $\kappa_2 = 1/6!$ are the usual

[5] ν is the number of degrees of freedom in the fit which is, approximatively, the number of data points, around 370.

quantum reduction factors of Eq.A.26 (cf. §4.2.2.2. With quantum depletion, these constants becomes

$$\kappa_2 = \frac{1}{2!}(1+\epsilon_2) \quad \text{and} \quad \kappa_3 = \frac{1}{3!}(1+\epsilon_3),$$

where $\epsilon_2 = \frac{64}{3\pi}\sqrt{n_0 a^3}$ and $\epsilon_3 = \frac{64}{\pi}\sqrt{n_0 a^3}$ with $n_0 \simeq n$ the *BEC* density. These two expression, as the one in Eq.B.2, were derived and are only valid for a homogeneous gas. Nevertheless, they can be generalized for the case of interest in here of a harmonically trapped gas using a local density approximation. This results in the corrections[70]

$$\epsilon_2 \to 0.515\epsilon_2 \quad \text{and} \quad \epsilon_3 \to 0.644\epsilon_3.$$

For our largest condensates, $\epsilon_3 \sim 0.2$ and ϵ_2 is about three times smaller, corresponding to a 20% correction in L and less than 10% in β.

If $T \neq 0$, there is an extra corrective factor that depends on the temperature[70, 125]. This *thermal depletion* correction follows the same power law in the factor $n_0 a^3$ as the *quantum depletion* but with a different numerical factor and is only non negligible in the *three-body* collisional process. It can be included, as in the above definition of ϵ_3, like

$$\epsilon_3 =\to \epsilon_3 \times (0.644 + \Delta_3^{th}),$$

with Δ_3^{th} accounting for the *thermal depletion*. If we admit that not more than 10% of the atoms are in the excited states, this *thermal* correcting factor is $\Delta_3^{th} \sim 0.21$, about one third of the *three-body quantum depletion* correction.

• Final results and incertitude intervals for β and L.

We present now final results for this experiment with incertitude intervals. The results obtained for β and L were found through the data fit and by fixing $\tau_i = 1000$ s and $a = 12$ nm. Imposing a large *confidence interval*[145] of 99.99% (at the expense of also large error bars for the parameters), the final results are

$$\beta = 1.1(\pm 0.5) \times 10^{-14}\text{cm}^3\text{s}^{-1} \quad \text{and} \quad L = 2.9(\pm 0.9) \times 10^{-27}\text{cm}^6\text{s}^{-1}.$$

From the fitting *covariance matrix* we can also estimate the statistical *correlation factor* among the parameters, which is of about -0.96. This high *negative* correlation among β and L was expected since, for the same ion flux, the augmentation of one of them can be compensated by diminishing the other.

The error intervals presented above are the fit confidence regions for the parameters, which were derived through the *covariance matrix* and, therefore, symmetric around the value found by the fit for each parameter. In

	min	fit	max
$\beta_{12}/10^{-20}\mathrm{m}^3\mathrm{s}^{-1}$	0.2	1.1	2.0
$L_{12}/10^{-39}\mathrm{m}^6\mathrm{s}^{-1}$	1.2	2.9	4.7

Table B.1: Rate constants obtained in the fit shown in Figure B.4, for $a = 12$ nm. The central values correspond to the best possible fit, with $\chi^2_{min}/\nu \approx 0.9$. The values for β and L indicated by *min* and *max* correspond to the projections of the confidence region corresponding to $\chi^2/\nu = 1.1$, in the respectively smaller and bigger values of those parameters.

reality, these error interval may not be symmetric and to better estimate them we have proceeded differently. First, we adopted a maximum *chi-square* value to consider the fit acceptable: we have chosen $\chi^2/\nu = 1.1$. Then, by fitting one of the rate constants freely, we searched for the two values of the other one that still respected the χ^2 maximum value. With $\chi^2_\nu = 1.1$, the fitting *confidence interval* is almost 100.0% and corresponds to a variation of χ^2, in respect of its minimum, of about $\Delta\chi^2 \approx 60$. This large *confidence interval* along with the high *correlation factor* among the parameters results in a very conservative estimation of the uncertainties intervals of β and L. Table B.1 summarizes the obtained results.

B.2.3 Dependence of the fitting result in the scattering length.

We will finally present the early announced outcome of this experiment: the value of β and L parameterized by the scattering length, a. We obtain it by fitting the data, as explained above, but for different values of a, from 8 nm to 16 nm. The obtained values for β and L varies smoothly with a and we can represent them through the simple algebraic expressions[51]

$$\beta_a \simeq \beta_{12} \times \left(\frac{a}{12}\right)^2 \times \left[1 + 0.13\left(\frac{a-12}{12}\right)\right] \quad \text{and}$$
$$L_a \simeq L_{12} \times \left(\frac{a}{12}\right)^3 \times \left[1 - 0.28\left(\frac{a-12}{12}\right)\right], \tag{B.3}$$

where a should be input in nanometers and, β_{12} and L_{12} are the values found for $a = 12nm$. If we plot now these two expression against a, use also the above derived error intervals, we obtain the graphs of Fig.B.5. There, the shadowed regions correspond to the *full confidence regions* we may obtain for β and L. Also in the graphs we represent the algebraic expressions of Eqs.B.3 (solid line) and the theoretical predictions found by Leo *et al.*[130] (dashed line).

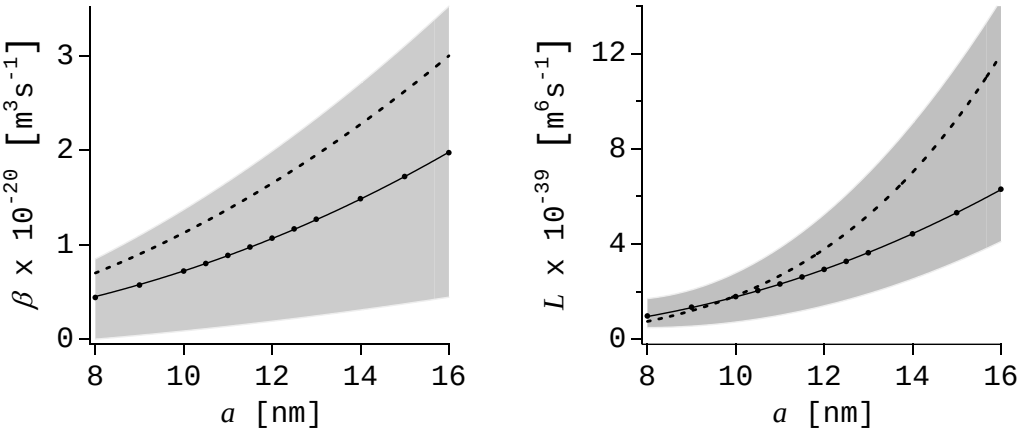

Figure B.5: Graphical representation of our final results for the rate constants, β and L. The gray regions are those where we expect to find *good values* of the rate constant for a given scattering length, a. The dots and the solid line correspond to values we found by the best fit to our data. The dashed line corresponds to theoretical predictions[130].

A P P E N D I X C

Mean Field Approximation

We use now a variational technic to derive the expression in the right hand side of Eq.4.26 in §4.3.1. We start with the second quantization many-body Hamiltonian of Eq.4.25,

$$\hat{H} = \int d^3\mathbf{r}\ \hat{\Psi}^\dagger(\mathbf{r}) \left[\hat{H}^{ho} - \mu + \frac{g}{2}\hat{\Psi}^\dagger(\mathbf{r})\hat{\Psi}(\mathbf{r})\right] \hat{\Psi}(\mathbf{r}). \tag{C.1}$$

where $\hat{H}^{ho}$ is the interactions free Hamiltonian, which in our case is just the harmonic oscillator Hamiltonian. Since the Hamiltonian of Eq.C.1 is not quadratic in the field operators we can not write the corresponding thermal equilibrium density matrix. A way to overcome this is to propose an approximated Hamiltonian H^0, quadratic in the field and that describes in the best way possible the physics of the problem. It should observe two main conditions: *i)* minimize the (*grand canonical*) free energy and, *ii)* have the same thermal average as the *true* Hamiltonian. We will start with the first of these conditions and come to the second at the end of the derivation.

Minimization of the free energy.
In the thermal equilibrium, the *true* free energy, F, derived from the *true* Hamiltonian $\hat{H}$ is, by definition, a minimum. Therefore, for any other given Hamiltonian, as H^0, the respective free energy, F^0 will always exceeds F. This is formally stated by the the Gibbs-Bogoliubov-Feynman inequality[86]

$$F \leqslant F^0 + \langle \hat{H} - \hat{H}^0 \rangle_0, \tag{C.2}$$

where, in the right hand side of this equation, the thermal average is done in the thermal equilibrium determined by H^0. By choosing an appropriate Hamiltonian H^0, which will depend on a certain variational parameter, we ought to minimize the right hand side of Eq.C.2. This procedure determines the free energy $F^0 + \langle \hat{H} - \hat{H}^0 \rangle_0$ which is, if not the *exact* free energy of the system, at least, the most approximated one for the particular choice of $\hat{H}^0$.

Here, since we want to simplify the Hamiltonian to one with only bilinear combinations of the field operators we choose

$$\hat{H^0} = \int d^3\mathbf{r}\ \hat{\Psi}^\dagger(\mathbf{r}) \left[\hat{H}^{ho} - \mu + h(\mathbf{r})\right] \hat{\Psi}(\mathbf{r}), \tag{C.3}$$

where $h(\mathbf{r})$, the variational field we need to find out, is a *c-number* that depends only on the spatial coordinates and has a clear physical interpretation: it is a *mean field potential* that describes the interatomic interaction and should, therefore, be somehow proportional to the cloud's atomic density. To find it, we need to solve the variational equation

$$\frac{\delta}{\delta h(\mathbf{r}')}\left\{F^0[h(\mathbf{r})] + \left\langle \hat{H} - \hat{H}^0[h(\mathbf{r})]\right\rangle_0\right\} = 0. \tag{C.4}$$

In the following we will deal with the derivatives of the functionals $F^0[h(\mathbf{r})]$ and $\left\langle \hat{H} - \hat{H}^0[h(\mathbf{r})]\right\rangle_0$ separately.

The functional derivative of $F^0[h(\mathbf{r})]$
$F^0[h(\mathbf{r})]$ is given by

$$F^0[h(\mathbf{r})] = -\frac{1}{\beta}\ln\left(Q^0[h(\mathbf{r})]\right).$$

where $Q^0[h(\mathbf{r})]$ is the *mean field* partition function $Q^0[h(\mathbf{r})]$ (also a functional of $h(\mathbf{r})$) which is, by definition, equal to

$$Q^0[h(\mathbf{r})] = \mathrm{Tr}\left\{\exp\left(-\beta\hat{H}^0[h(\mathbf{r})]\right)\right\}.$$

Using the two last expressions we obtain

$$\begin{aligned}\frac{\delta F^0[h(\mathbf{r})]}{\delta h(\mathbf{r}')} &= -\frac{1}{\beta}\frac{1}{Q^0}\frac{\delta Q^0[h(\mathbf{r})]}{\delta h(\mathbf{r}')} \\ &= -\frac{1}{\beta}\frac{1}{Q^0}\frac{\delta}{\delta h(\mathbf{r}')}\mathrm{Tr}\left\{e^{-\beta\hat{H}^0[h(\mathbf{r})]}\right\}.\end{aligned} \tag{C.5}$$

Exchanging now the order of the *trace* with the derivative we get

$$\begin{aligned}\frac{\delta F^0[h(\mathbf{r})]}{\delta h(\mathbf{r}')} &= \frac{1}{Q^0}\mathrm{Tr}\left\{\hat{\Psi}^\dagger(\mathbf{r})\hat{\Psi}(\mathbf{r})e^{-\beta\hat{H}^0}\right\} \\ &= \left\langle\hat{\Psi}^\dagger(\mathbf{r})\hat{\Psi}(\mathbf{r})\right\rangle_0 \\ &= n^0(\mathbf{r}),\end{aligned} \tag{C.6}$$

with $n^0(\mathbf{r})$ is the thermal equilibrium atomic density derived from the *mean field* Hamiltonian $\hat{H}^0$.

The functional derivative of $\langle \hat{H} - \hat{H}^0 \rangle_0$.
Making use of the definitions of Eqs.C.1 and C.3 it can write

$$\left\langle \hat{H} - \hat{H}^0[h(\mathbf{r})] \right\rangle_0 = \left\langle \frac{g}{2} \int_{R^3} d\mathbf{r}\ \hat{\Psi}^\dagger(\mathbf{r})\hat{\Psi}^\dagger(\mathbf{r})\hat{\Psi}(\mathbf{r})\hat{\Psi}(\mathbf{r}) - \int_{R^3} d\mathbf{r}\ h(\mathbf{r})\hat{\Psi}^\dagger(\mathbf{r})\hat{\Psi}(\mathbf{r}) \right\rangle_0 .$$

Interchanging the integrals with the average operation and using Wick's theorem, we get

$$\left\langle \hat{H} - \hat{H}_{MF}[h(\mathbf{r})] \right\rangle_{MF} = \left\{ \frac{g}{2} \times 2 \int_{R^3} d\mathbf{r}\ n^2_{MF}(\mathbf{r}) - \int_{R^3} d\mathbf{r}\ h(\mathbf{r}) n_{MF}(\mathbf{r}) \right\}.$$

We ought to compute the functional derivative of the left hand side of the last equation with respect to $h(\mathbf{r})$. It is given by

$$\begin{aligned}
&\frac{\delta}{\delta h(\mathbf{r}')} \left\langle \hat{H} - \hat{H}^0[h(\mathbf{r})] \right\rangle_0 = \\
&\quad = \int_{R^3} d\mathbf{r}\ \left\{ g \times \frac{\delta \left[n^0(\mathbf{r})\right]^2}{\delta h(\mathbf{r}')} - \frac{\delta[h(\mathbf{r}) n^0(\mathbf{r})]}{\delta h(\mathbf{r}')} \right\} = \\
&\quad = \int_{R^3} d\mathbf{r}\ 2g n^0(\mathbf{r}) \frac{\delta n^0(\mathbf{r})}{\delta h(\mathbf{r}')} - n^0(\mathbf{r})\delta(\mathbf{r} - \mathbf{r}') - h(\mathbf{r}) \frac{\delta n^0(\mathbf{r})}{\delta h(\mathbf{r}')} = \\
&\quad = -n^0(\mathbf{r}) + \int_{R^3} d\mathbf{r}\ \left[2g n^0(\mathbf{r}) - h(\mathbf{r})\right] \frac{\delta n^0(\mathbf{r})}{\delta h(\mathbf{r}')}.
\end{aligned}$$

This result along with the one of Eq.C.6 may be combined to recast Eq.C.4 to

$$\int_{R^3} d\mathbf{r}\ \left[2g n^0(\mathbf{r}) - h(\mathbf{r})\right] \frac{\delta n^0(\mathbf{r})}{\delta h(\mathbf{r}')} = 0,$$

from where we deduce

$$h(\mathbf{r}) = 2g n^0(\mathbf{r}), \tag{C.7}$$

which is the wanted result.

Eq.C.3 may now be written as

$$\hat{H}^0 = \int d^3\mathbf{r}\ \hat{\Psi}^\dagger(\mathbf{r}) \left[\hat{H}^{ho} - \mu + 2g n^0(\mathbf{r})\right] \hat{\Psi}(\mathbf{r}) + \varepsilon.$$

The constant ε was included *by hand* in this last expression to ensure that the thermal averages of the *true* and the *mean field* Hamiltonians are equal, *i.e.*

$$\left\langle \hat{H} \right\rangle_0 = \left\langle \hat{H}^0 \right\rangle_0 .$$

ε is equal to

$$\varepsilon = g \int_{R^3} d\mathbf{r} \ \left[n^0(\mathbf{r})\right]^2 , \tag{C.8}$$

and makes a constat shift on the energy spectrum. It is unimportant within the calculation of physical quantities in the thermodynamical equilibrium and can therefore be disregarded.

APPENDIX D

Fugacity determination with the χ^2 maps

D.1 Introduction

This Appendix deals with the problem of finding the fugacity of an atomic cloud by fitting its *TOF*.

The model we use for this analysis is presented in §4.3 and the explicit expression for the fitting function is derived in §4.3.3 (cf. Eq.4.50). This model describes the ballistic expansion and fall under gravity of a non-degenerate atomic cloud with mean field interactions at the thermal equilibrium [1]. As explained in §5.3.2, this expression is valid only for clouds with a fugacity strictly equal or smaller than one [2]. and is formally divergent for $Z > 1$. The analysis of *TOF*s of clouds at temperatures clearly above the critical one can be carried out with a standard *Levenberg-Marquardt* (*LM*) routine. However, the fit of *TOF*s corresponding to clouds with $Z \geq 1$ makes the *LM* routine to halt. This happens even for clouds at exactly $Z = 1$ since the routine is unable to compute the *chi-square* variation for values of the fugacity at the vicinity but bigger than $Z = 1$.

A way to prevent the routine to abort is to constrain it to search fugacities only within the domain $Z \leqslant 1$. However, with such a *fitting constraint* the routine will return $Z = 1$ for clouds that are at the critical points but also for those with $Z > 1$, rending impossible the task of sorting data at $T = T_c$.

Moreover, as we will see further, due to a non quadratic dependence of the *chi-square* on the fugacity at values close to $Z = 1$, the *LM* routine finds a value for Z that is slightly deviated from the value that, in fact, minimizes the *chi-square*.

Here, we describe a method that circumscribes these difficulties and that is able to properly sort data at $Z = 1$. Instead of using a fit to find the

[1] Interatomic interactions are not included during the fall. These are included in the *TOF* analysis in §4.3.4, where the cloud's expansion is treated in hydrodynamical regime. This leads to corrections to the temperature found in the *TOF* fit.

[2] This fugacity is defined within the re-normalization of the chemical potential according to Eq.4.28.

temperature and fugacity, we will study the variation of the *chi-square*, calculating it for a set of values of (T, Z). This will give us extra information that enables us to measure fugacities close to $Z = 1$. We call χ^2-*map* to the graphical representation of the *chi-square* in function of T and Z.

D.2 The $Z - T$ $\chi^2 - maps$.

The main graph of Fig.D.1 shows an example of a χ^2-*map*. This is a *contour* type of graph with each line representing locations with equal $\Delta\chi^2$, a quantity defined as the variation of the χ^2 relatively to its minimum value χ^2_0,

$$\Delta\chi^2 = \chi^2 - \chi^2_0.$$

The χ^2 value is computed for all locations in a grid with 20 equally spaced values for the fugacity between $Z = 0.75$ and $Z = 1.0$ and 30 values for the thermal velocity, also equally spaced, in an interval centered around an approximate value for $\sqrt{k_B T_c/M}$ and spanning a region equal to $\pm 5\%$ of this critical value ($\pm 10\%$ in temperature variation) [3].

The explicit expression defining *chi-square* is

$$\chi^2 = \sum_{i=1}^{N} \left[\frac{y_i - I_D(\delta t_i; t_0, amp, v_T, Z)}{\sigma_i} \right]^2, \tag{D.1}$$

where y_i is the value of the *TOF* signal (left hand side graph in Fig.D.1) at its i^{th} point and $I_D(\delta t_i; t_0, amp, v_T, Z)$ is the theoretical predicted value for the atomic flux at the instant of time $t_0 + \delta t_i$ (cf. Eq.4.50), with also $t_0 = \sqrt{2H/g}$ the *classical* cloud's time of fall.

The fitting function in Eq.D.1 also depends on *Amp*, which accounts for the *TOF amplitude*, closely related with the total number of atoms in the cloud. This function also depends, obviously, on the cloud's temperature and fugacity, the former rather expressed through the cloud's thermal velocity v_T. The χ^2-*map*s consider only the variation of v_T and Z, as these are the pertinent quantities within the cloud's thermometry. The actual value of $\Delta\chi^2$ plotted in a χ^2-*map* is computed by fitting the parameters *Amp* and t_0 with a *LM* routine, but using as fixed parameter the corresponding values of v_T and Z.

[3] The propose of the the procedure we describe here is to find the proper value of $\sqrt{k_B T_c/M}$, which is obviously not known initially. However, here we just need to estimate approximatively this quantity in a way that the minimum of the $\Delta\chi^2$ is still inside the χ^2-*map*. An estimation based on the result of a standard *LM* fit, constrained in the fugacity as $Z < 0.999$, gives normally a good enough result.

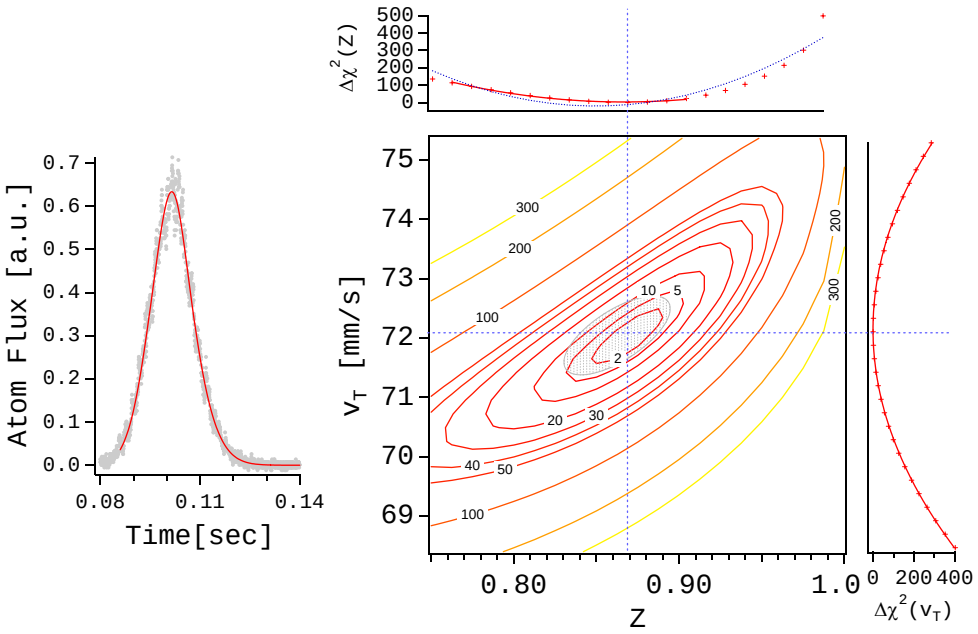

Figure D.1: The main graph shows an example of a χ^2-*map*. It represents the $\Delta\chi^2(v_t, Z) = \chi^2(v_T, Z) - \chi^2_0$ (weighed by the characteristic data noise) for the *TOF* signal, shown in the left hand side of the Figure), when the fugacity Z and the thermal velocity v_T are varied around their *good* values where $\Delta\chi^2 = 0$ (represented by the crossed dashed lines). The χ^2-*map* is a contour graph with each closed line corresponding to the same $\Delta\chi^2$. This lines delimits confidence regions on the parameters and, in particular, the 68% confidence region is given by the region inside the $\Delta\chi^2 \sim 5$ line. Superimposed in the χ^2-*map*, the shadowed ellipse corresponds to this same confidence region but computed by a conventional *Levenberg-Marquardt* routine. This graph shows that a quadratic approximation for $\Delta\chi^2$ works only close enough to $\{v_{T0}, Z_0\}$ (characterized by perfect elliptical level lines) failing for fugacities closed to one. This leads to a small deformation of the $\Delta\chi^2$ structure in the Z direction and also to slight mismatch the *LM* result and the location of χ^2_0 (see text for further comments). This deformation of the χ^2-*map* is also seen in the top inset graph, where we plot $\Delta\chi^2(v_{T0}, Z)$. This graph does not fit well to a parabola in all the Z domain (dotted line). This fit works properly only if the fit is restricted to a smaller region in the fugacity (solid line). In the v_T domain, the χ^2-*map* presents no deviations from the quadratic form. This is observed in the right hand side inset graph where $\Delta\chi^2(vT, Z_0)$ fits well to the parabola. This reflects the fact of existing no upper bound to the temperature (as is the case of the fugacity at $Z = 1$) and, also, that the domain of variation of v_T in the χ^2-*map* is small comparatively to its central value.

The *chi-square* in the expression of Eq.D.1 is weighted by a standard deviation σ_i [4] that estimates the experimental noise. It is of *shot noise* nature, given by

$$\sigma_i = \sqrt{\sigma_0^2 + k^2 y_i},$$

with also a constant residual component σ_0 [5]. This *shot-noise* character of the noise in the *TOF* is connected, ultimately, with the detection system we used based on a `MCP`, which is a discrete events detector. The good characterization of this noise is crucial for the good computation of the *chi-square* value, either in a standard *LM* routine or in the method described here.

• Location of the $\Delta\chi^2 = 0$ and the *one-sigma* confidence region.
In the χ^2-*map* of Fig.D.1, the location of χ_0^2 (the actual minimum of χ^2) is found at the location $\{v_{T0}, Z_0\}$ [6], represented in the graph of fig.D.1 by two crossed dashed line. This set of values correspond to the fugacity and the thermal velocity that better fit the *TOF* signal.

For clouds with a temperature well above T_c, as we said earlier, a *LM* routine converges to a value for the thermal velocity $v_{TLM} \approx v_{T0}$. However, as referred earlier, the value found for the fugacity Z_{LM} can be slightly smaller than Z_0. We will explain this in more detail, latter in this Appendix.

A *LM* routine also outputs confidences region for the parameters and the one corresponding to 68.3% confidence (the *one-sigma* confidence region) is represented in the χ^2-*map* of Fig.D.1 by a shadowed ellipse. This ellipse may be derived through the covariance matrix computed by the *LM* fit after having converged to its final result.

This same confidence region is also seen in the χ^2-*map* level lines: it corresponds to the region inclosed by the curve $\Delta\chi^2 = 4.72$, centered in $\{v_{T0}, Z_0\}$ [7].

---

[4] Not to be confused with the σ defined in Chapter 2 for the size of the harmonic oscillator.

[5] The noise in a particular signal was computed as the difference between the corresponding *TOF* and this same *TOF* but after be processed digitally in a low-pass routine (the cut-off was determined by the bandpass of the slow amplifier used in our *analog mode* of our detection circuit (see §1.3.3). By studying the noise in function of the amplitude of the signal in many different *TOF* signal, we have obtained the values for the parameters σ_0 and k_{ShN} (see Ref.[51]) for further details.

[6] In the following we will also use the notation χ^2_{map} for referring the minimum obtained with the χ^2-*map* strategy and χ^2_{LM} for the one found by the *LM* routine. To these values of *chi-square* corresponds the locations $\{v_{Tmap}, Z_{map}\}$ and $\{v_{TLM}, Z_{LM}\}$, respectively.

[7] This value is obtained by considering the four independent fitting parameters of Eq.D.1 [145].

• Parabolic shape of the χ^2-*map*s.

The covariance matrix computed within a *LM* routine relies in a quadratic approximation of the χ^2. The *good* values for the parameters corresponds to the location of the minima of the resulting paraboloid (in the hyperspace of all parameters) and the confidence region for each parameter may be related with its curvature in the corresponding axis.

Expanding the $\Delta\chi^2$ in series up to second order on Z and v_T, we get

$$\Delta\chi^2 \approx \tfrac{1}{2}\left[\frac{\partial^2\chi^2}{\partial v_T^2}(\Delta v_T)^2 + \frac{\partial^2\chi^2}{\partial Z^2}(\Delta Z)^2 + \right] + \frac{\partial^2\chi^2}{\partial v_T \partial Z}(\Delta v_T)(\Delta Z), \qquad \text{(D.2)}$$

The independent variation of $\Delta\chi^2$ with the parameters is shown in the top and right hand side inset graphs of the Fig.D.1, where only one parameter is varied whereas the other is kept at the value that minimizes the χ^2, v_{T0} or Z_0 depending on the case. The $\Delta\chi^2(v_T, Z_0)$ curve is quite well fitted by a parabola, confirming the validity of the second-order approximation used in the Eq.D.2 for a variation on the temperature.

This parabolic dependence is however not observed for the curve $\Delta\chi^2(v_{T0}, Z)$, along the Z axis. There are two reasons to explain this. First, the fugacity has a maximum allowed value at $Z = 1$ where all the *Bose functions* involved in the definition of the atomic flux grows very rapidly. The second reason, related to this first one, is that the interval of variation of Z-parameter is, in physical terms, very large. If we take all the χ^2-*map* domain in Z, the second order approximation of Eq.D.2 is insufficient.

Note that a small change in the fugacity δZ corresponds to a large change in the chemical potential, which is the physically meaningful quantity, related with the system's energy. If we look how the energy varies with the thermal velocity and fugacity we obtain

$$\frac{\delta E}{E} = 2\frac{\delta v_T}{v_T} \quad \text{and} \quad \frac{\delta\mu}{\mu} = \frac{k_B T}{\mu}\frac{\delta Z}{Z}.$$

Since $k_B T \gg \mu$ (even for the degenerate case), small changes on the fugacity makes much bigger effects in the scale of energy when compared with equivalent changes in the thermal velocity.

This may also be checked directly in the expression for the cloud's density and its behavior with respect to small variations of Z and v_T. In the *semi-classical* expressions, the shape of the density depends on the *Bose functions* $g_u(W)$, where $W = Z\exp\left(-\frac{1}{2}\frac{\omega^2 r^2}{v_T^2}\right)$. Differentiating W, one obtains

$$\frac{\delta W}{W} = \frac{\delta Z}{Z} + \left(\frac{\omega r}{v_T}\right)^2 \frac{\delta v_T}{v_T}.$$

This expression shows that the two parameters has an equivalent *relative* importance only nearby the cloud border, where $r \sim v_T\omega$. Thus, in the fit

procedure, the relative importance of v_T gets smaller at inner locations in the cloud. At the cloud's center it becomes null and the fugacity becomes the single relevant fitting parameter. As already noted, the $g_u(W)$ functions vary very rapidly when W approaches one. At the cloud's center, since $g_\alpha(W) \equiv g_\alpha(Z)$, the density will grow also very rapidly with Z. This fast variation of the fitting function with Z produces a deviation of the *chi-square* from the quadratic behavior of Eq.D.2, slightly deforming the χ^2-*maps* on this direction.

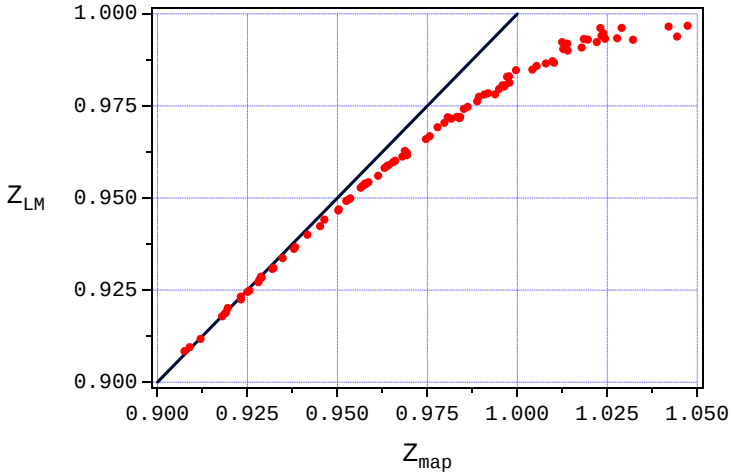

Figure D.2: Comparison between the values found by a *LM* routine and the χ^2-*map*'s method for the fugacity of several *TOF*s of clouds close to the critical phase transition. This graphs shows a tendency to the *LM* routine to return a value for Z slightly smaller than the one obtained with the χ^2-*map*s.

Is this *deformation* of the χ^2-*map* in the Z direction (*i.e.*, the deviation from a quadratic dependence on Z), that makes the parabolic fit on the top inset graph of Fig.D.1 to be not centered at Z_0 but slightly displaced for a smaller fugacity. This comes out to be the value found by the *LM* routine, which relies on the validity of the second order approximation of the *chi-square* and, in special, on the symmetry of the *chi-square* in both sides of its minimum. Within the χ^2-*map* strategy we describe here, the determination of Z_{map} takes into account only the points of $\Delta\chi^2(v_{T0}, Z)$ at the left hand side of Z_0 where the *chi-square* still follows a quadratic dependence with Z. It finds a value which is approximatively equal to Z_0.

The mismatch between the values Z_{map} and Z_{LM} gets bigger for fugacities closer to one since the *chi-square deformation* is also bigger. This can be seen in Fig.D.2, where we plot the values for the fugacity found on a *LM* fit in function of the values obtained with the χ^2-*map*'s strategy.

D.3 Getting the fugacity from a $\chi^2 - map$.

The simple observation of the $\chi^2 - map$ of a given *TOF* is, in general, enough to get an idea about the cloud's fugacity and, more importantly, if it corresponds to a degenerate cloud or not. In Fig.D.3 we picture two extreme cases where it is easy to guess that in either cases the clouds' fugacity is not in the interval $0.75 < Z < 1$: the graph *a*) corresponds to a cloud with a temperature far above the T_c whereas the graph *b*) shows the typical χ^2-*map* of a *TOF* of a degenerate cloud. In this latter, the χ^2_0 takes a value much bigger than one and the map contour lines are continuously deformed when Z increases till one.

The behavior of the χ^2-*map*s of *TOF*s with $Z \gg 1$ makes their classification as corresponding to degenerate clouds rather simple. However, for clouds where the fugacity is very close to one (either larger or smaller), this task may become considerably more difficult. To illustrate this we plot, in Fig.D.4, a χ^2-*map* of one of these *TOF* that seams to correspond to a cloud that is very close to degeneracy.

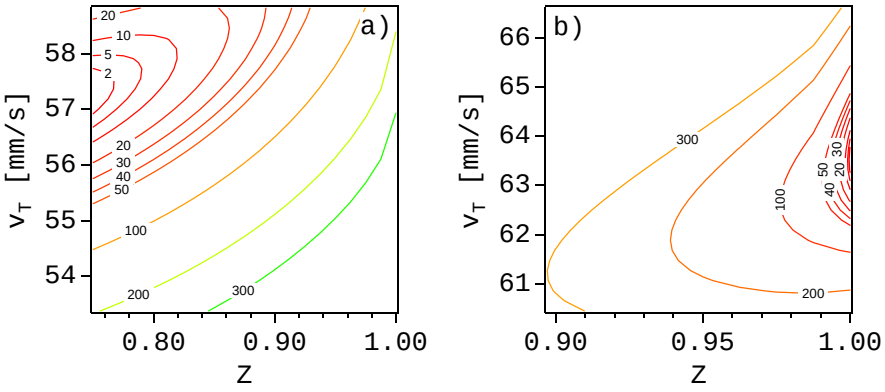

Figure D.3: Two χ^2-*map*s for *TOF*s of clouds with fugacities, *a*) much smaller and, *b*) much bigger than one. Clearly, in both graph, the *real* χ^2 minima falls out of the shown *maps*. For the first case, however, this is just because the *map* was computed for values bigger than $Z = 0.75$. An eye guided extrapolation of the ellipses for the region $Z < 0.75$ makes us almost guess what should be the fugacity. This is not case in the right hand side where the ellipses are too much deformed close to $Z = 1$.

In this particular case, the location of the χ^2_0 in the χ^2-*map* suggests that the cloud's temperature is very close but still smaller than T_c. However, due to the χ^2-*map* deformation close to $Z = 1$, it may also correspond to a cloud exactly at the critical transition point. To avoid relying on a subjective case to case analysis and for establishing well defined criteria for sorting data at $Z = 1$, we devised the χ^2-*map* strategy which we described in the following.

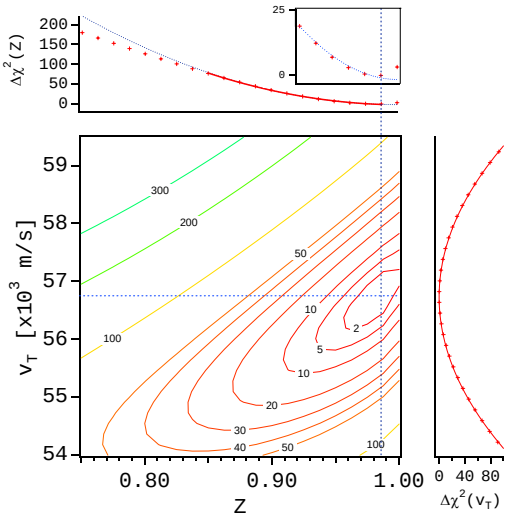

Figure D.4: A χ^2-*map* for the case of a *TOF* signal at $T \sim T_c$. The slight deformation of the *map* close to $Z = 1$ doesn't affect the almost perfect parabolic behavior of $\Delta\chi^2$ in the vT axis, where the location of the minimum of the fitted parabola gives the cloud's thermal velocity v_T. The variation of $\Delta\chi^2$ in the $Z-$axis is typical in similar situations where Z is very close but still smaller than one. To be able to well fit a parabola (solid line in the top graph), we need to constrain the fit to a smaller number of points and also to exclude the last point at $Z = 1$ (see also text).

D.3.1 χ^2-*map* strategy for finding Z_{map}.

We start by finding the location of v_{T0} with a standard *LM* routine [8], which allows computing a $\Delta\chi^2(v_{T0}, Z)$ data row. To the smallest value in this row corresponds a value of fugacity we will call Z_0' [9] We then fit $\Delta\chi^2(v_{T0}, Z)$ to a parabola restricting the fitting interval to a region where the second order is still valid, defined as $Z_0' - 0.15 < Z < Z_0'$ to $Z = 0.9875$. From this fit we obtain Z_{map} and also $\Delta\chi^2_{min} = \Delta\chi^2(v_{T0}, Z_{map})$. Now, there are three different possibilities.

- For a *TOF* corresponding to a cloud at the critical point, $\Delta\chi^2_{min}$ should be zero and $Z_{map} = 1$.
- If $\Delta\chi^2_{min}$ is still zero and $Z_{map} < 1$, then the *TOF* should correspond to a thermal cloud with a fugacity given by Z_{map}.

[8] As referred previously, the value found for the thermal velocity by a *LM* routine is approximatively equal to Z_0. Using a *LM* routine for determining v_{T0} avoids computing all the χ^2-*map*, which is a long process.

[9] This value is approximatively equal to Z_0 when this latter one is smaller than one. In this case, Z_0' approaches Z_0, by augmenting the number of points of the $\Delta\chi^2(v_{T0}, Z)$ data row. Alternatively, Z_0 can be found, as it is in the χ^2-*map* method, fitting the left hand side of this data row (built with a small number of points) to a parabola. If $Z_0 \geq 1$, Z_0' *saturates* at one.

- Finally, if $\Delta\chi^2_{min} < 0$, the actual location of the global minima of the $\Delta\chi^2$ structure should be somewhere in the region where $Z > 1$ and the TOF should correspond to a degenerate cloud (note that in here the $\Delta\chi^2 = 0$ is only artificially located at $Z = 1$).

An illustration of the latter case is shown in Fig.D.5. In the bottom graph of this Figure, we see that the fitted parabola has a minimum which is much further $Z = 1$, with an approximate *chi-square* given by $\Delta\chi^2 = -40$.

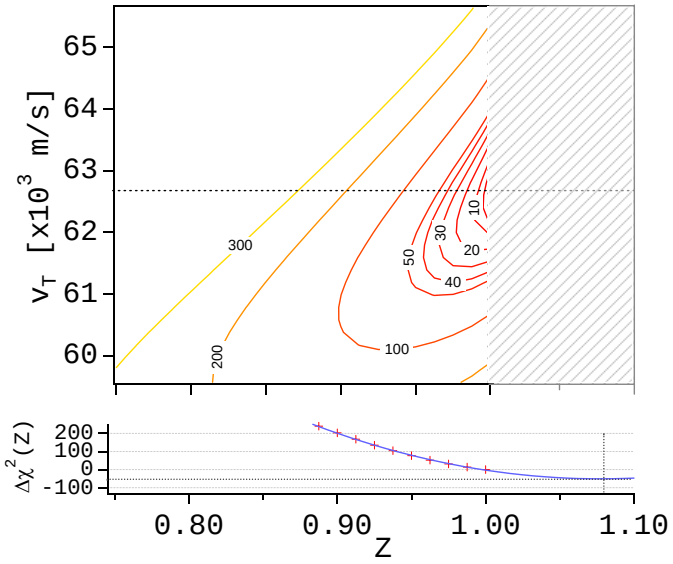

Figure D.5: This Figure sketches the procedure we used to determine if a cloud is or not at the critical transition temperature. The top graph shows the χ^2-*map* of a degenerated cloud. The bottom graph shows, as before, the parabola fitted to the $\Delta\chi^2$ row that goes through the point $\Delta\chi^2 = 0$ in the $Z-$direction. Here, the found $\Delta\chi^2_{min}$ is around -40 indicating that the cloud is indeed far from the critical transition. The found Z_{map}, much bigger than one, has no physical significance.

D.3.2 Definition of the χ^2-*map* criteria for sorting data at $T = T_c$.

The set of values $\{Z_{map}, \Delta\chi^2_{min}\}$ may define a *figure of merit* to sort clouds at $T = T_c$. Following the above referred considerations, the criteria we used to classify a given TOF as corresponding to thermal cloud above the critical temperature was

$$Z_{map} < 1 \qquad \text{and} \qquad \Delta\chi^2_{min} \simeq 0.$$

In this case, the cloud's fugacity and thermal velocity are assumed to be equal to Z_{map} and v_{Tmap} respectively. These values, and most specially the one for the thermal velocity, are comparable to the results of a standard LM routine.

A cloud is considered to be at the critical phase transition if

$$i)\ 0.9875 < Z_{map} < 1.0125 \quad \text{and} \quad ii)\ |\Delta\chi^2_{min}| < 15.$$

In here, as in the previous case, the cloud's fugacity and thermal velocity are given respectively by Z_{map} and v_{Tmap}. This latter value is approximatively equal to the one obtained fitting the data to a model where the fugacity is fixed to $Z = 1$, using a *LM* routine. This sorting criteria admits a maximum deviation of the fugacity of 0.0125 which is, approximatively, the uncertainty in Z corresponding to one standard deviation in a fit to a *TOF*.

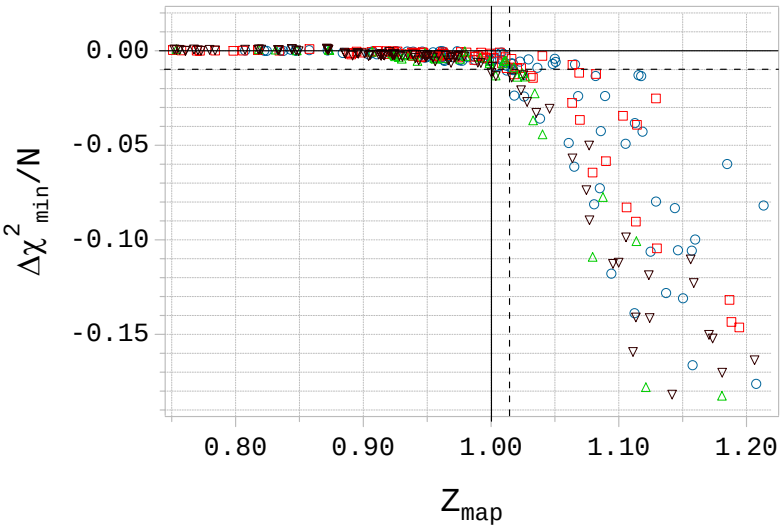

Figure D.6: The Z_{map} values found for our data. Here, the *map fugacities* are plotted against $\Delta\chi^2_{min}$, the minimum of the parabola fitted to the $\Delta\chi^2(v_{T0}, Z)$ data row. For $Z_{map} \lesssim 1$ the points have an unexpected tendency to be always slightly smaller than zero. For the points with $Z_{map} > 1$, $\Delta\chi^2_{min}$ is negative since the $\Delta\chi^2 = 0$ found inside the χ^2-*map* is not the global minimum, this one laying down outside the *map*. In theses cases, the parabola fitted to the $\Delta\chi^2(v_{T0}, Z)$ data row gives always a negative value for $\Delta\chi^2_{min}$ (and, also, a $Z_{map} > 1$). The data sorted as having $Z \geq 1$ correspond to the points in the region above and at the left hand side of the dashed lines. These are defined for $Z_{map} = 1.0125$ (vertical) and $\Delta\chi^2_{min} = 0.01N$ (horizontal), with N the number of the *TOF*points (~ 1500). The first condition agrees with the estimated error for the determination of Z_{map}, about 0.0125 (see next paragraph), the second taken arbitrarily. This latter condition works as a supplementary *check point* since the condition $Z_{map} \leqslant 1.0125$ is, almost always, sufficient for sorting the data. The different symbols represent data taken in four different days.

The maximum allowed variation of $\Delta\chi^2_{min}$, 15, was taken arbitrarily and corresponds to a variation of the *reduced chi-square* of about 0.01. In the

graph of Fig.D.6 we plot the values of $\Delta\chi^2_{min}$ in function of the corresponding values for Z_{map}, obtained in the analysis of our *TOF* data. The above criteria sorts all the data in the left hand side and above the dashed lines as *non degenerate*. This graph also shows that the constraint established for Z_{map} is almost sufficient for sorting out the data. The criteria established on $\Delta\chi^2_{min}$ is, nevertheless, a good *check point* to verify if the procedure is working properly.

D.4 Using the *semi-ideal* model for testing the χ^2-*map* method.

In the previous paragraph we have described a procedure to sort *TOF* data at $T = T_c$. The necessity of such a procedure comes, as we have pointed out before, from the fact that we don't know how to describe the *TOF* of a *slightly* degenerate cloud. We could try to extend our model for the non-degenerate case to $Z \gtrsim 1$, finding a reasonable way of extrapolating the fitting expression over that region. Instead of this, what we proposed to do was to extrapolate the structure of the χ^2-*map* for $Z \gtrsim 1$. Note that this method should not be used for deriving the chemical potential of degenerated clouds but only to determine how likely a given *TOF* corresponds to a cloud at $T = T_c$.

We may rise the question now on how valid this method should be, regarding the fact that we admit a smooth and continuous variation of the χ^2-*map* structure at the critical transition where we know that there is a brusk variation of the cloud's density.

This question may be addressed analytically if the atomic cloud is described by the simple *semi-ideal/Thomas-Fermi* model (cf. §4.2.2.2 and Ref.[47]). This model is a very simplified version of what happens in reality but has the advantage of proposing analytical expressions for the thermal cloud's density in both non-degenerate and degenerate samples. To this latter we should also add the contribution of the *BEC*, described by the Thomas-Fermi approximation (cf. §A.2 of Appendix A).

D.4.1 The analysis of synthesized data at $Z = 1$.

We start be synthesizing numerically a *TOF* signal based on the *semi-ideal/Thomas-Fermi* model with $Z = 1$ (which reduces to the simple ideal gas model of Eq.2.23) with also random gaussian *shot-noise* with the same amplitude as the one found in our signals.

For computing the χ^2-*map* of this synthesized *TOF*, we use as fitting function the same expression of *semi-ideal/Thomas-Fermi*. This expression

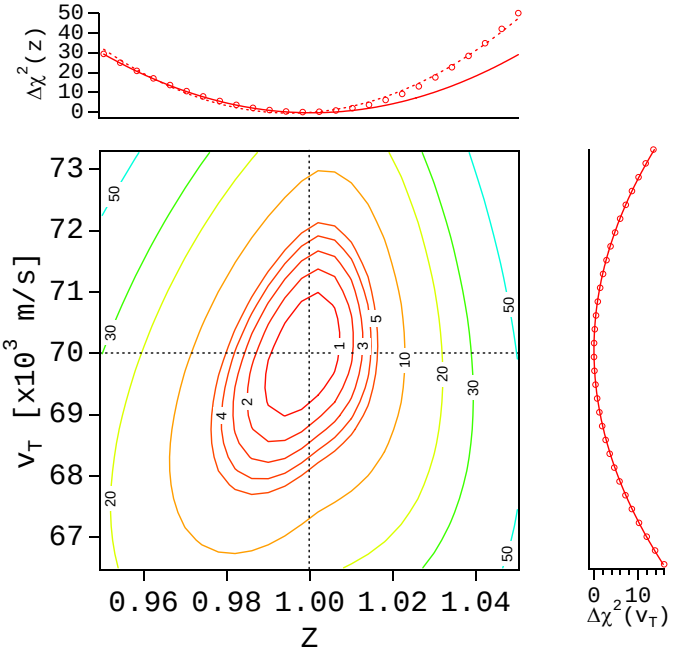

Figure D.7: χ^2-*map* of a numerically synthesized *TOF* signal, computed within the *semi-ideal* model (cf. §4.2.2.2) for $Z = 1$, $v_T = 0.07$ m/s and with added random shot noise with the same characteristics as the one found in real data. The fitting function is a piecewise function, defined according to the *semi-ideal* model alone for $Z \leqslant 1$ and accounting also for the *BEC* contribution for $Z > 1$ within the Thomas-Fermi approximation (cf. §A.2). As in the χ^2-*map* presented in Fig.D.1, the data points along the row $\Delta\chi^2(v_T, 1)$ are well fitted by a parabola. The same doesn't happen with the data row $\Delta\chi^2(0.07, Z)$. The inset graph in the top shows the parabolic fit to all the points of this data row (dashed line) and, also, only on those with $Z \leqslant 1$ (solid line). The minimum of the parabola in this latter case is located almost at $Z = 1$ whereas in the former one being shifted towards a smaller fugacity. As before, this happens due to the χ^2-*map* deformation at $Z = 1$ and the different $\Delta\chi^2$ curvatures in the regions with Z small and bigger than one. The graphs shows a similar behavior in both sides of $Z = 1$, but with different correlation factors between the two parameters: in the $Z > 1$ region the correlation gets smaller.At the transition (*i.e.* at $Z = 1$) we see no discontinuity in the contour lines of the χ^2 structure.

is

$$I(\delta t;T,\mu) = \frac{(2\pi)^{-1/2}}{\overline{\tau}^3}\frac{g}{v_T}\times \\ \times\begin{cases} g_{5/2}\left[e^{+\beta\mu}\,\mathcal{W}(\delta t)\right] - g_{5/2}\left[e^{+\beta\mu}\,\mathcal{W}(\delta t)\mathcal{W}_D\right] & \text{if } \mu \leqslant \frac{1}{2}M(g\delta t)^2 \\ 2\zeta(5/2) - g_{5/2}\left[e^{-\beta\mu}\,\mathcal{W}^{-1}(\delta t)\right] + g_{5/2}\left[e^{-\beta\mu}\,\mathcal{W}^{-1}(\delta t)\mathcal{W}_D\right] + & \\ \quad + (\beta\mu)^2\,\frac{\lambda_T}{4a}\left[1-\left(\sqrt{\frac{M}{2\mu}}g\delta t\right)^2\right]^2 & \text{, otherwise.} \end{cases}$$

where we have used the definitions of §4.3.3,

$$\mathcal{W}(\delta t) \simeq \tfrac{1}{2}\beta M g^2 \delta t^2$$

and

$$\mathcal{W}_D = \exp\left[-\tfrac{1}{2}R_D^2/(v_T t_0)^2\right]$$

with R_D the detector radius.

A typical result obtained with this procedure, with $v_T = 0.07$ m/s, is the χ^2-*map* shown in Fig.D.7, that shows different structure in either sides of $Z = 1$. As before, the inset graphs fit parabolas to the synthesized data row crossing at $Z = 1$ and $v_T = 0.07$ m/s, the location of the χ^2_0. Unlike $\Delta\chi^2(v_T, 1.0)$, which is still well fitted by a parabola, the data row corresponding to $\Delta\chi^2(0.07, Z)$ (top graph) shows a different curvature on the left and right hand sides of $Z = 1$.

However, since the *TOF* was synthesized for $Z = 1$, we should expect that the left hand side part of the $\Delta\chi^2$ fits well to a parabola centered at $Z_{map} = 1$ and with also $\Delta\chi^2_{min} = 0$. This is actually what happens with just a slight mismatch due to the random noise included in the synthesization of the *TOF*.

This noise is responsible for the uncertainty in the determination of the fugacity. To test the χ^2-*map* strategy and also estimate the influence of the *TOF* noise in the dispersion of Z_{map} we have repeated the above procedure, in a *Monte Carlo* scheme, synthesizing many different *TOF*s always for the same temperature and constants fugacities of $Z = 1$ and also $Z = 0.9875$. To keep the analogy with what we do in the analysis of real data, we build then the corresponding χ^2-*map*s using as fitting function only the non-degenerate part of Eq.D.3, valid for $Z \leqslant 1$ (or else $\mu \leqslant 0$). In end we have also computed, for each χ^2-*map*, the values Z_{map} and $\Delta\chi^2_{min}$.

Unlike the function we use for analyzing real data, in here we have a fitting model, Eq.D.3 that works properly for non-degenerate and also degenerate clouds. We can therefore compare the results we obtain for each synthesized curve with the χ^2-*map* strategy with those obtained with a standard *LM* fit using Eq.D.3 as fitting function.

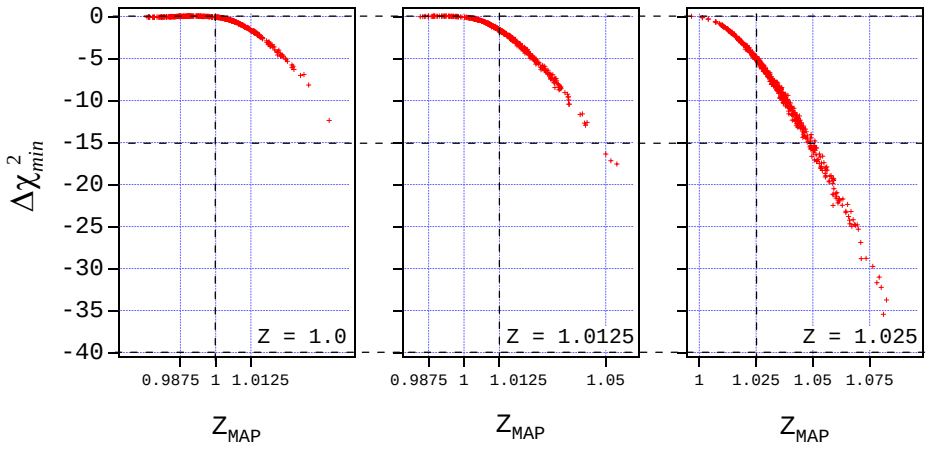

Figure D.8: $\Delta\chi^2_{min}$ values in function of the Z_{map} for 500 synthesized *TOF* using the *semi-ideal/Thomas-Fermi* model (cf. Eq.D.3) with $v_T = 0.07$ m/s and *fugacities* equal to 1.0, 1.0125 and 1.025, respectively for the left hand side, central and right hand side graphs. The χ^2-*map* routine uses a *ideal-gas* model (the first line of Eq.D.3). In the $Z = 1.0$ case, only 20% of the points have a $Z_{map} > 1.0125$. The criteria given in §D.3.2 excludes 95% of the points for the $Z = 1.025$ case from being considered to be at the critical transition point (see also text).

The result of this procedure for clouds with *fugacities* [10] equal to 1.0, 1.0125 and 1.025 is shown in the graphs of Fig.D.8. These graphs are similar to the one of Fig.D.6, with $\Delta\chi^2_{min}$ in function of Z_{map}. For the synthesized data with $Z = 1.0$, all points verifies $\Delta\chi^2_{min} < 15$ and about 70% corresponds to $0.9875 < Z_{map} < 1.0125$. All of these would be sorted as clouds at the critical point by the criteria given above in §D.3.2.

In the graph corresponding to $Z = 1.025$ case, most ($\sim 95\%$) of the shown synthesized data would be discarded from being at $T = T_c$. Finally, in the set of data synthesized with $Z = 1.0125$, we would sort only half of the points. This value should be seen as the uncertainty on the fugacity on the sorting procedure.

D.4.2 Conclusion.

The χ^2-*map* method is capable of finding the fugacity for *TOF*s at the critical point, where a standard *LM* routine fails achieving that. This allows sorting data at the critical point. Moreover, even for fugacities smaller than one, the *LM* routine returns a value for Z that is slightly smaller than the value that

[10] Here, for simplicity, we use the term "fugacity" also for degenerate clouds. In this case $Z = \exp(\mu/k_B T)$ where $\mu > 0$ is the *BEC* chemical potential and T the thermal cloud temperature.

minimizes the *chi-square* which is, supposedly, the actual cloud's fugacity. However, if $Z < 0.95$, the values obtained with the χ^2-*map* method and with a *LM* routine are very similar, being this latter much easier to implement. Concerning the values obtained for the cloud's temperature, we observed no large differences between the two methods.

Within the validity of the *semi-ideal/Thomas-Fermi* model and using the criteria $\{Z_{map} < 1.0125, \Delta\chi^2_{min} < 15\}$, we see that:

- around 70% of data synthesized with $Z = 1$ is sorted by the procedure as being at the critical point;
- 95% of the data synthesized with a *fugacity* equal to 1.025 is discarded.
- The higher bound used as sorting criteria for the fugacity, $Z = 1.0125$, corresponds to the uncertainty of the method on the determination of Z, at the critical point: 50% of the data synthesized with this value of *fugacity* was discarded.

The *semi-ideal/Thomas-Fermi* model can hardly be considered as a good one for dealing with real data. Even so, we believe that the results we obtain with it mimics the essential behavior of the χ^2-*map*s computed for real *TOF*s and analyzed within the framework of the full model describing the atomic flux with finite size effects and mean field interatomic interactions. Actually, the most important ingredients to explain the χ^2-*map*s deformation at $Z = 1$ is the presence of a phase transition which is also present in the *semi-ideal/Thomas-Fermi* model.

APPENDIX E

Published Articles

Ionization rates in a Bose-Einstein Condensate of Metastable Helium

O. Sirjean, S. Seidelin, J. V. Gomes, D. Boiron, C. I. Westbrook, A. Aspect, and G. V. Shlyapnikov, *Phys. Rev. Lett.* **89**, 220406 (2002).

⋆ ⋆ ⋆

Using ion production to monitor the birth and death of a metastable helium Bose-Einstein condensate

S. Seidelin, O. Sirjean, J. V. Gomes, D. Boiron, C. I. Westbrook, and A. Aspect, *J. Opt. B: Quantum Semiclass. Opt.* **5**(5), S112, (2003).

⋆ ⋆ ⋆

Getting the elastic scattering length by observing inelastic collisions in ultracold metastable helium atoms

S. Seidelin, J. V. Gomes, R. Hoppeler, O. Sirjean, D. Boiron, A. Aspect, and C. I. Westbrook, *Phys. Rev. Lett* **93**, 090409 (2004).

⋆ ⋆ ⋆

Hanbury Brown Twiss effect for ultracold quantum gases

M. Schellekens, R. Hoppeler, A. Perrin, J. V. Gomes, D. Boiron, A. Aspect, and C. I. Westbrook, *Science* **310**, 648 (2005).

⋆ ⋆ ⋆

Atomic density of a harmonically trapped ideal gas near Bose-Einstein transition temperature

R. Hoppeler, J. Viana Gomes, and D. Boiron, *Eur. Phys. J. D* **41**, 157 (2006).

⋆ ⋆ ⋆

Theory for a Hanbury Brown Twiss experiment with a ballistically expanding cloud of cold atoms

J. V. Gomes, A. Perrin, M. Schellekens, D. Boiron, C. I. Westbrook, and M. Belsley, *Phys. Rev. A* **74**, 053607 (2006).

Ionization Rates in a Bose-Einstein Condensate of Metastable Helium

O. Sirjean, S. Seidelin, J. Viana Gomes,* D. Boiron, C. I. Westbrook, and A. Aspect
Laboratoire Charles Fabry de l'Institut d'Optique, UMR 8501 du CNRS, F-91403 Orsay Cedex, France

G. V. Shlyapnikov
FOM Institute for Atomic and Molecular Physics, Kruislaan 407, 1098 SJ Amsterdam, The Netherlands and Russian Research Center Kurchatov Institute, Kurchatov Square, 123182 Moscow, Russia
(Received 5 August 2002; published 12 November 2002)

We have studied ionizing collisions in a BEC of metastable He. Measurements of the ion production rate combined with measurements of the density and number of atoms for the same sample allow us to estimate both the two- and three-body contributions to this rate. A comparison with the decay of the atom number indicates that ionizing collisions are largely or wholly responsible for the loss. Quantum depletion makes a substantial correction to the three-body rate constant.

DOI: 10.1103/PhysRevLett.89.220406 PACS numbers: 34.50.–s, 05.30.–d, 67.65.+z, 82.20.Pm

The observation of Bose-Einstein condensation (BEC) of metastable helium (He in the 2^3S_1 state, denoted He*) [1,2] constituted a pleasant surprise for experimentalists although the possibility had been predicted theoretically [3]. Success hinged, among other things, on a strong suppression of Penning ionization in the spin-polarized, magnetically trapped gas. Too high a rate of ionization would have prevented the accumulation of sufficient density to achieve evaporative cooling. The ionization rate is not completely suppressed however, and when the atomic density gets high enough, a magnetically trapped sample of He* does produce a detectable flux of ions. As shown in [1], this signal can even be used as a signature of BEC. The observation of ions from the condensate opens the possibility of monitoring in real time the growth kinetics of a condensate [4]. This is an exciting prospect, but to quantitatively interpret the ion rate, one needs the contributions of two- and three-body collisions.

In this paper we use the unique features of metastable atoms to detect, in a single realization, the ionization rate, the density, and the atom number. This allows us to extract two- and three-body rate constants without relying on fits to nonexponential decay of the atom number, which require good experimental reproducibility [5–7] and are difficult to interpret quantitatively [5]. After estimating the ionization rate constants, a comparison with the decay of the atom number reveals no evidence for collisional avalanche processes. Thus, by contrast with ^{87}Rb [8], He* seems to be a good candidate for studying the "hydrodynamic" regime [9], as well as the effects of quantum depletion, i.e., a departure from the Gross-Pitaevskii wave function in the Bogoliubov theory, due to atomic interactions [10]. Indeed in our analysis of the three-body ionization process, quantum depletion makes a substantial correction [11].

Much theoretical [3,12] and experimental [1,2,13,14] work has already been devoted to estimating inelastic decay rates in He*. The dominant two-body decay mechanisms, called Penning ionization,

$$\mathrm{He}^* + \mathrm{He}^* \rightarrow \begin{cases} \mathrm{He}^+ + \mathrm{He}(1S) + e^- \\ \mathrm{He}_2^+ + e^- \end{cases} \quad (1)$$

are known to be suppressed by at least 3 orders of magnitude in a spin-polarized sample, but the total rate constant has not yet been measured. The three-body reaction,

$$\begin{aligned} \mathrm{He}^* + \mathrm{He}^* + \mathrm{He}^* &\rightarrow \mathrm{He}_2^* + \mathrm{He}^*(\sim 1\ \mathrm{mK}) \\ &\hookrightarrow \mathrm{He}^+ + \mathrm{He}(1S) + e^- \end{aligned} \quad (2)$$

proceeds via three-body recombination followed by autoionization of the excited molecule. Both reactions yield one positive ion which is easily detected. We define collision rate constants according to the density loss in a thermal cloud: $\frac{dn}{dt} = -\frac{n}{\tau} - \beta n^2 - L n^3$ with n the local density, τ the (background gas limited) lifetime of the sample, and β and L the two-body and three-body ionization rate constants defined for a thermal cloud [15]. The theoretical estimates of the rate constants at 1 μK are $\beta \sim 2 \times 10^{-14}\ \mathrm{cm^3\,s^{-1}}$ [3,12] and $L \sim 10^{-26}\ \mathrm{cm^6\,s^{-1}}$ [16], and the experimental upper limits were [1,2] $\beta \leq 8.4 \times 10^{-14}\ \mathrm{cm^3\,s^{-1}}$ and $L \leq 1.7 \times 10^{-26}\ \mathrm{cm^6\,s^{-1}}$.

For a pure BEC, in the Thomas-Fermi regime with a number of atoms N_0, and a peak density n_0, one can calculate the expected ionization rate per trapped atom:

$$\Gamma = \frac{\text{ion rate}}{N_0} = \frac{1}{\tau'} + \frac{2}{7}\kappa_2 \beta n_0 + \frac{8}{63}\kappa_3 L n_0^2. \quad (3)$$

The numerical factors come from the integration over the parabolic spatial profile and the fact that although two or three atoms are lost in each type of collision, only one ion is produced. The effective lifetime $\tau' \geq \tau$ is due to *ionizing* collisions with the background gas. The factors κ_i take into account the fact that the two- and three-particle local correlation functions are smaller than those of a

 © 2002 The American Physical Society

thermal cloud. For a dilute BEC $\kappa_2 = 1/2!$ and $\kappa_3 = 1/3!$ [7,11]. Because the He* scattering length (a) is so large, quantum depletion ($\sim \sqrt{n_0 a^3}$) leads to significant corrections [11] to the κ's as we discuss below.

Much of our setup has been described previously [1,17,18]. Briefly, we trap up to 2×10^8 atoms at 1 mK in a Ioffe-Pritchard trap with a lifetime (τ) of 90 s. We use a "cloverleaf" configuration [19] with a bias field $B_0 =$ 150 mG. The axial and radial oscillation frequencies in the harmonic trapping potential are $\nu_\parallel = 47 \pm 3$ Hz and $\nu_\perp = 1800 \pm 50$ Hz, respectively [$\overline{\omega}/2\pi = (\nu_\parallel \nu_\perp^2)^{1/3} =$ 534 Hz]. A crucial feature of our setup is the detection scheme, based on a two stage, single anode microchannel plate detector (MCP) placed below the trapping region. Two grids above the MCP allow us either to repel positive ions and detect only the He* atoms, or to attract and detect positive ions produced in the trapped cloud.

To detect the ion flux, the MCP is used in counting mode: the anode pulses from each ion are amplified, discriminated with a 600 ns dead time and processed by a counter which records the time delay between successive events. Typical count rates around BEC transition are between 10^2 and 10^5 s^{-1}. We have checked that the correlation function of the count rate is flat, indicating that there is no double counting nor any significant time correlation in the ion production. The dark count rate is of order 1 s^{-1}. By changing the sign of the grid voltage, we have checked that while counting ions, the neutral He* detection rate is negligible compared to the ion rate (less than 5%) even when the radio frequency (rf) shield is on. The intrinsic ion detection efficiency of the MCP for 2 keV He^+ ions is close to the open area ratio (60%) [20]. To estimate the total ion detection efficiency, we then multiply by the geometric transmission of the two grids $(0.84)^2$. Based on Refs. [20,21], we assume this (0.42) is an upper limit on our detection efficiency.

To find the values of N_0 and n_0 corresponding to the measured ion rate, we use the MCP to observe the time-of-flight (TOF) signal of the He* atoms released from the rapidly switched off trap. The instantaneous count rate can be as high as 10^6 s^{-1}, and the MCP saturates when used in counting mode. To avoid this problem, we lower the MCP gain, and record the TOF signal in analog mode with a time constant of 400 μs. Several tests were performed to verify the linearity of the detector.

In a typical run, evaporative cooling takes place for 40 s, down to an rf-knife frequency about 50 kHz above the minimum of the trapping potential. Near the end of the ramp, the ion rate increases sharply, signaling the appearance of a BEC (Fig. 4 in [1]). After reaching the final value, the rf knife is held on at that frequency. This constitutes an rf shield which eliminates hot atoms and maintains a quasipure BEC for up to 15 s (see Fig. 3). By quasipure we mean that we see no thermal wings in signals such as shown in the inset of Fig. 1. From tests of our fitting procedure, we estimate that the smallest thermal fraction we can distinguish is about 20%, with a temperature on the order of the chemical potential. Runs with visible thermal wings were discarded.

To acquire the TOF signals corresponding to a given ion rate, we turn off the rf shield, wait 50 ms, and then turn off the magnetic trap and switch the MCP to analog mode. To be sure that the rf has no influence on the ion rate, we use only the number of ions observed during the 50 ms delay to get the rate. We fit the TOF signals to an inverted parabola squared as expected for a pure BEC in the Thomas-Fermi regime and for a TOF width ($\sim$ 5 ms) narrow compared to the mean arrival time (100 ms) [1]. Under these assumptions, the chemical potential μ depends only on the TOF width, the atomic mass, and the acceleration of gravity [22], and thus can be measured quite accurately. Figure 1 shows that μ varies as expected as $N_d^{2/5}$ with N_d the number of detected atoms in the quasipure BEC. A fit on a log-log plot gives a slope of 0.39. Residuals from the linear fit do not show any systematic variation which is a good indication of the detection linearity and of the proportionality between N_d and N_0.

To determine the collision rate constants β and L, we need an absolute calibration of the number of atoms and the density. As discussed in Ref. [1], all the atoms are not detected, and the direct calibration has a 50% uncertainty which is responsible for the large uncertainty in the scattering length a. In fact the measurement of the chemical potential gives an accurate value for the product $n_0 a = \mu m/4\pi\hbar^2$, and with the value of $\overline{\omega}$ gives the product $N_0 a = (1/15)(\hbar/m\overline{\omega})^{1/2}(2\mu/\hbar\overline{\omega})^{5/2}$ as well. Therefore, in the hopes that the He* scattering length will be measured more accurately in the future, we shall express N_0 and n_0 in terms of a. In this paper, unless stated otherwise, we suppose that $a = 20$ nm, and in our conclusions we shall discuss how our results depend on a.

Figure 2 shows the ion rate per atom Γ versus the peak density. The densest sample corresponds to $N_0 = 2 \times 10^5$

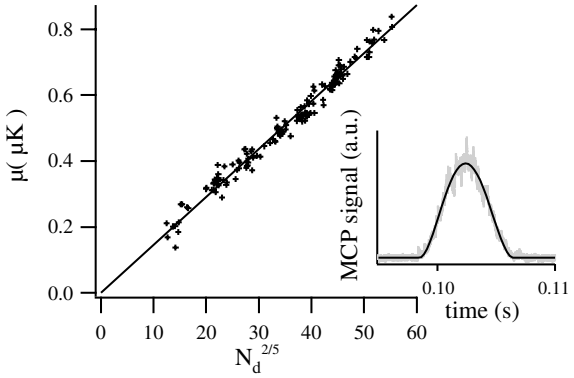

FIG. 1. Chemical potential versus number of detected atoms to the power $\frac{2}{5}$ and its linear fit. Data are for quasipure BEC. The inset shows a typical TOF signal and its inverted parabola squared fit.

atoms and $n_0 = 2.5 \times 10^{13}$ cm^{-3}. The corresponding Thomas-Fermi radii are $r_\perp \simeq 5$ μm and $r_\parallel \simeq 200$ μm. The vertical intercept in Fig. 2 corresponds to ionizing collisions with the background gas ($1/\tau'$). We have independently estimated this rate using trapped thermal clouds at 1 mK and 5 μK and found $1/\tau' \lesssim 5 \times 10^{-3}$ s^{-1}. This value is negligible at the scale of the figure.

The curvature in Fig. 2 shows that three-body ionizing collisions are significant. Before fitting the data to get β and L, we must take into account several effects. First, for three-body collisions, quantum depletion is important. For $T = 0$, on the basis of Ref. [11], we obtain a multiplicative correction to the factor κ_3 of $(1 + \epsilon) = (1 + 23.2 \times \sqrt{n_0 a^3})$ [23]. At our highest density $\epsilon \simeq 0.35$. Two-body collisions are subject to an analogous correction but approximately 3 times smaller. The fits in Fig. 2 include the density dependence of $\kappa_{2,3}$, associated with quantum depletion. The $n_0^{3/2}$ dependence introduced for two-body collisions is far too small to explain the curvature in the data. The density dependence of $\kappa_{2,3}$ does not improve the quality of the fit, but it significantly reduces the value of the fitted value of L (by 30%).

In addition, the fact that the sample probably contains a small thermal component means that collisions between the condensed and the thermal parts must be taken into account [6,11]. Assuming a 10% thermal population ($\frac{\mu}{k_B T} \simeq 1.5$), we find $\kappa_3 = \frac{1}{6}(1 + \epsilon + \epsilon')$, with an additional correction $\epsilon' \simeq 0.11$ for the densest sample [24].

Taking into account all these corrections, and assuming an ion detection efficiency of 0.42, the fitted values of the collision rate constants [15] are $\beta_{20} = 2.9(\pm 2.0) \times 10^{-14}$ cm^3 sec^{-1} and $L_{20} = 1.2(\pm 0.7) \times 10^{-26}$ cm^6 sec^{-1}, where the subscripts refer to the assumed value of a. These values are in good agreement with the theoretical estimates. The error bars are estimated as follows. We fix either β or L and use the other as a fit parameter. We repeat this procedure for different values of the fixed parameter and take the range over which we can get a converging and physically reasonable fit (i.e., no negative rate constants) as the uncertainty in the fixed parameter. These error bars are highly correlated since if β is increased, L must be decreased and vice versa. The error bars do not include the uncertainty in the absolute ion detection efficiency (see below).

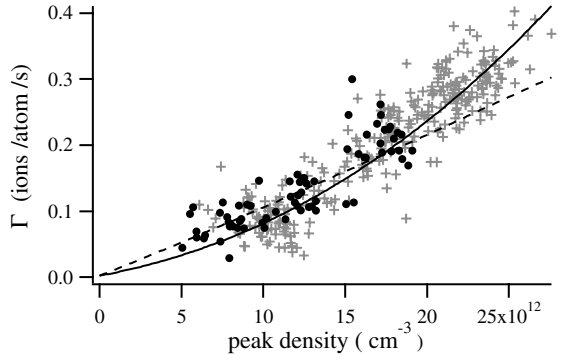

FIG. 2. Ion rate per trapped atom versus peak density for 350 different quasipure BEC's. Atom number and density are deduced from μ, $\overline{\omega}$, and a (here 20 nm). Data were taken for two different bias fields corresponding to $\nu_\perp = 1800$ Hz (crosses) and $\nu_\perp = 1200$ Hz (circles). The dashed line corresponds to the best fit involving only two-body collisions. The solid line is a fit to two- and three-body processes.

Until now we have assumed $a = 20$ nm, but current experiments give a range from 8 to 30 nm [1,2]. Using Eq. (3) and our parametrization of n_0 and N_0 in terms of a, one can see that, in the absence of quantum depletion, the values of β and L extracted from our analysis would be proportional to a^2 and a^3, respectively. Taking quantum depletion into account, no simple analytical dependence exists, but one can numerically evaluate β and L vs a and fit the results to expansions with leading terms in a^2 and a^3, respectively. The effect of quantum depletion is negligible for β [$\beta_a \approx \beta_{20}(\frac{a}{20})^2$]. For L, we find $L_a \approx L_{20}(\frac{a}{20})^3[1 - 0.21\frac{a-20}{20}]$ with a in nm.

To test the consistency of our measurements, we plot the decay of the atom number (Fig. 3). To acquire these data, we held the BEC in the trap in the presence of the rf shield for varying times. This study involves multiple BEC realizations, which typically exhibit large fluctuations in the initial atom number. We have been able to reduce this noise by using the ion signal to select only data corresponding to the same ion rate 500 ms after the end of the ramp. This time corresponds to $t = 0$ in the figure. We also plot the predicted decay curve (solid line) corresponding to ionization only. This curve results from a numerical integration of the atom loss due to ionization processes, calculated from the fitted values β_{20} and L_{20}. The fact that the error bars on β and L are correlated

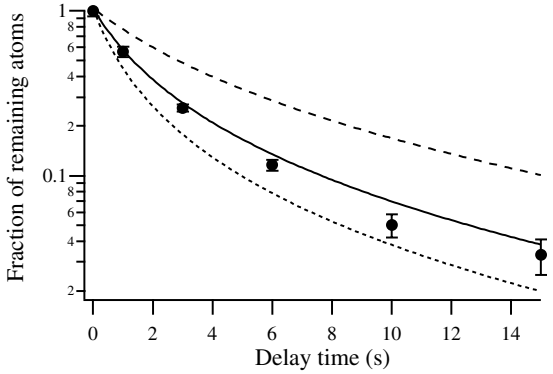

FIG. 3. Fraction of remaining atoms measured by TOF as a function of time. The rf shield is on and the cloud remains a quasipure condensate during the decay. The lines correspond to the predicted atom decay according to Eq. (3) with the fitted value of the two- and three-body rate constants for $a = 10$ nm (dashed line), $a = 20$ nm (solid line), and $a = 30$ nm (dotted line). The case of $a = 10$ nm is not necessarily excluded because other, nonionizing losses could be present.

leads to a small uncertainty on the solid curve that happens to be of the same order of magnitude as the typical error bars on the data. The observed decay agrees fairly well with the solid curve, and ionization apparently accounts for most of the loss. If the ion detection efficiency were actually lower than we assume, the predicted decay would be faster than the observed decay which is unphysical (assuming $a = 20$ nm). We conclude that our estimate of the ion detection efficiency is reasonable and does not lead to an additional uncertainty in β and L.

We also plot the curves obtained from the same analysis but with scattering lengths of 10 and 30 nm, assuming a detection efficiency of 0.42. The curve corresponding to $a = 30$ nm lies below the data points. Based on our analysis, this means that $a = 30$ nm is excluded. A scattering length of 25 nm is the largest one consistent with our data. In contrast, the decay predicted for an analysis with $a = 10$ nm is slower than the observed decay. This would mean that there are additional nonionizing losses (contributing up to half of the total loss), and/or that we have overestimated the ion detection efficiency by a factor as large as 2. In the latter case, β and L should be multiplied by the same factor. This results for $a = 10$ nm in a supplementary systematic uncertainty on β and L of a factor as large as 2.

In the event that our upper limit on the ion detection efficiency is too low, the rate constants β and L should be reduced by a factor as large as 2.4 ($= 0.42^{-1}$). In that case, our data would not exclude $a = 30$ nm and nonionizing losses could significantly contribute to the total loss.

Even though the peak densities of our BEC are small compared to those in alkalis, the elastic collision rate is high because of the large scattering length, and one must consider the possibility of collisional avalanches. For $a = 20$ nm our densest cloud has a mean free path of 7 μm and using the definition of [8] the collisional opacity is 0.8. With Rb atoms this would result in much increased loss due to avalanches [8]. Here we have to consider secondary collisions leading to both ion production and atom loss. However, for secondary ionization, mean free paths are at least 2 orders of magnitude larger than $r_{\|}$. Hence secondary ionization is unimportant. This conclusion is supported by our observation of no correlation in the time distribution of detected ions.

The good agreement between the data and the curve in Fig. 3 indicates that losses due to nonionizing collisional avalanches are not taking place either. This is in agreement with data on elastic collisions with He^+, He_2^+, and He($1S$), which have small cross sections [25]. Collisions with hot He* atoms from the reaction of Eq. (2) are more likely to play a role, but due to the higher velocity, the elastic cross section for these atoms is smaller. In Rb the situation is different because a d-wave resonance increases the total cross section [8].

The theoretical analysis shows that quantum depletion strongly affects the measured three-body rate constant. One way to experimentally demonstrate this effect would be to compare with similar measurements with thermal clouds. Absolute calibration of ion and atom detection efficiency should play no role in this comparison, if one could prove that they are the same for both situations.

We thank F. Gerbier for stimulating discussions. This work was supported by the European Union under Grants No. IST-1999-11055 and No. HPRN-CT-2000-00125, and by the DGA Grant No. 00.34.025.

*Permanent address: Departamento de Fisica, Universidade do Minho, Campus de Gualtar, 4710-057 Braga, Portugal.

[1] A. Robert *et al.*, Science **292**, 461 (2001).
[2] F. Pereira Dos Santos *et al.*, Phys. Rev. Lett. **86**, 3459 (2001); F. Pereira Dos Santos *et al.*, Eur. Phys. J. D **19**, 103 (2002).
[3] G.V. Shlyapnikov *et al.*, Phys. Rev. Lett. **73**, 3247 (1994); P.O. Fedichev *et al.*, Phys. Rev. A **53**, 1447 (1996).
[4] H.J. Miesner *et al.*, Science **270**, 1005 (1998); M. Köhl *et al.*, Phys. Rev. Lett. **88**, 080402 (2002).
[5] J.L. Roberts *et al.*, Phys. Rev. Lett. **85**, 728 (2000).
[6] J. Söding *et al.*, Appl. Phys. B **69**, 257 (1999).
[7] E.A. Burt *et al.*, Phys. Rev. Lett. **79**, 337 (1997).
[8] J. Schuster *et al.*, Phys. Rev. Lett. **87**, 170404 (2001).
[9] M. Leduc *et al.*, Acta Phys. Pol. B **33**, 2213 (2002).
[10] F. Dalfovo *et al.*, Rev. Mod. Phys. **71**, 463 (1999).
[11] Y. Kagan, B.V. Svistunov, and G.V. Shlyapnikov, JETP Lett. **42**, 209 (1985).
[12] V. Venturi *et al.*, Phys. Rev. A **60**, 4635 (1999); V. Venturi and I.B. Whittingham, Phys. Rev. A **61**, 060703(R) (2000).
[13] J.C. Hill *et al.*, Phys. Rev. A **5**, 189 (1972).
[14] N. Herschbach *et al.*, Phys. Rev. A **61**, 50 702 (2000).
[15] Collision rate constants are sometimes defined directly for a BEC ($\beta' = \beta/2$ and $L' = L/6$).
[16] P.O. Fedichev, M.W. Reynolds, and G.V. Shlyapnikov, Phys. Rev. Lett. **77**, 2921 (1996); P.F. Bedaque, E. Braaten, and H.W. Hammer, Phys. Rev. Lett. **85**, 908 (2000).
[17] A. Browaeys *et al.*, Phys. Rev. A **64**, 034703 (2001).
[18] S. Nowak *et al.*, Appl. Phys. B **70**, 455 (2000).
[19] M.O. Mewes *et al.*, Phys. Rev. Lett. **77**, 416 (1996).
[20] R.S. Gao *et al.*, Rev. Sci. Instrum. **55**, 1756 (1984).
[21] B. Deconihout *et al.*, Appl. Surf. Sci. **94/95**, 422 (1996).
[22] Y. Castin and R. Dum, Phys. Rev. Lett. **77**, 5315 (1996); Y. Kagan, E.L. Surkov, and G.V. Shlyapnikov, Phys. Rev. A **54**, R1753 (1996).
[23] The numerical factor $64/\sqrt{\pi}$ of [11] changes to 23.2 for a trapped bose gas.
[24] We have $\epsilon' = (\langle\langle 3n_0^2(n' + \alpha)\rangle\rangle + \langle 3n_0^2\langle n' + \alpha\rangle\rangle) \times \langle\langle n_0^3\rangle\rangle^{-1}$. The symbol $\langle\cdots\rangle$ denotes the integration over the condensate spatial region. The thermal part of the noncondensed density, n', and that of the anomalous average, α, are obtained in the local density approximation. This gives $\epsilon' = 7.7 \times \sqrt{n_0 a^3}$ for $(\mu/k_B T) = 1.5$.
[25] H.C.W. Beijerinck *et al.*, Phys. Rev. A **61**, 23 607 (2000).

INSTITUTE OF PHYSICS PUBLISHING JOURNAL OF OPTICS B: QUANTUM AND SEMICLASSICAL OPTICS

J. Opt. B: Quantum Semiclass. Opt. **5** (2003) S112–S118 PII: S1464-4266(03)55547-1

Using ion production to monitor the birth and death of a metastable helium Bose–Einstein condensate

S Seidelin[1], O Sirjean, J Viana Gomes[2], D Boiron, C I Westbrook and A Aspect

Laboratoire Charles Fabry de l'Institut d'Optique, UMR 8501 du CNRS, F-91403 Orsay Cedex, France

E-mail: signe.seidelin@iota.u-psud.fr

Received 29 October 2002
Published 2 April 2003
Online at stacks.iop.org/JOptB/5/S112

Abstract

We discuss observations of the ion flux from a cloud of trapped 2 $^3S_1$ metastable helium atoms. Both Bose–Einstein condensates (BEC) and thermal clouds were investigated. The ion flux is compared with time-of-flight observations of the expanded cloud. We show data concerning BEC formation and decay, as well as measurements of two- and three-body ionization rate constants. We also discuss possible improvements and extensions of our results.

Keywords: Cold atoms, Bose–Einstein condensate, metastable helium, condensate formation, Penning collisions

1. Introduction

Metastable helium (He^*) has recently joined the list of atomic species for which Bose–Einstein condensates (BEC) have been realized [1, 2]. Its major feature is the 20 eV internal energy of the metastable state. Although this metastability leads to additional possible loss channels, it has been shown that these are not a serious problem. Indeed, ionizing collisions are a benefit because their low rate is nevertheless easily detectable. Ion detection is thus a new, 'non-destructive' and real-time observation tool for studies of the phenomenon of BEC formation kinetics [3–7]. In this paper we will describe our progress toward rendering the ion signal quantitative.

Several loss mechanisms are specific to the metastable state. First, collisions with the background gas lead to Penning ionization of the background gas:

$$X + He^* \rightarrow X^+ + He + e^-.$$

The positive ion X^+ thus produced can be easily detected and if this is the dominant ion production mechanism, as it is for a dilute sample (for a density $n \lesssim 10^{10}\,\mathrm{cm}^{-3}$), the corresponding flux is proportional to the number of trapped He^* atoms. So for example we can easily measure the lifetime of a dilute, trapped sample. This linearity no longer holds when the density of the trapped cloud becomes high. Collisions between atoms in the cloud must be taken into account. The relevant ionization mechanisms involve both two-body processes:

$$He^* + He^* \rightarrow \begin{cases} He^+ + He(1S) + e^- \\ He_2^+ + e^- \end{cases} \quad (1)$$

and a three-body process:

$$\begin{aligned} He^* + He^* + He^* \quad &\rightarrow \quad He_2^* \quad +He^*(\sim 1\,\mathrm{mK}) \\ &\hookrightarrow \quad He^+ + He(1S) + e^-. \end{aligned} \quad (2)$$

When these processes are present, the ion flux is related to the spatial integral of n^2 and n^3. At BEC densities, the two- and three-body processes dominate the background gas ionization, and so detecting the ion flux in this case amounts to monitoring the atomic density.

In this paper, after a brief description of our experimental set-up, we present observations, via the ion flux, of the formation and the decay of a He* BEC. The observations are mainly qualitative, but we discuss some of the requirements for making them quantitative. We then discuss our measurements of the two- and three-body ionization rate constants both in a BEC [8] and in a thermal cloud. We discuss some of the systematic errors in these measurements and conclude with some ideas for avoiding these errors.

[1] Author to whom any correspondence should be addressed.
[2] Permanent address: Departamento de Fisica, Universidade do Minho, Campus de Gualtar, 4710-057 Braga, Portugal.

 © 2003 IOP Publishing Ltd Printed in the UK

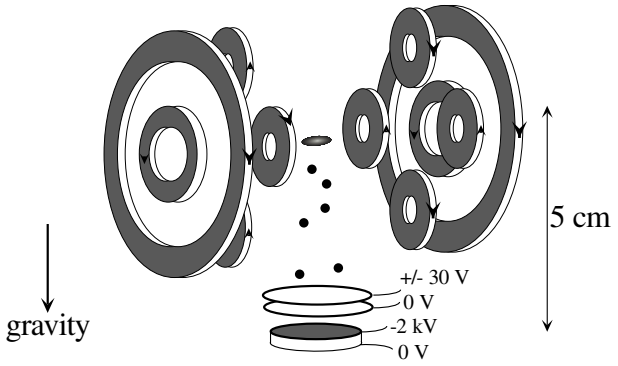

Figure 1. Experimental set-up. The cold atoms are trapped in a cloverleaf type magnetic trap. A special feature of our set-up is the MCP placed below the trapping region. Two grids above the MCP allow us either to repel positive ions and detect only the He* atoms suddenly released from the trap (TOF measurements), or to attract and detect the positive ions produced in the trapped cloud (ion rate measurements).

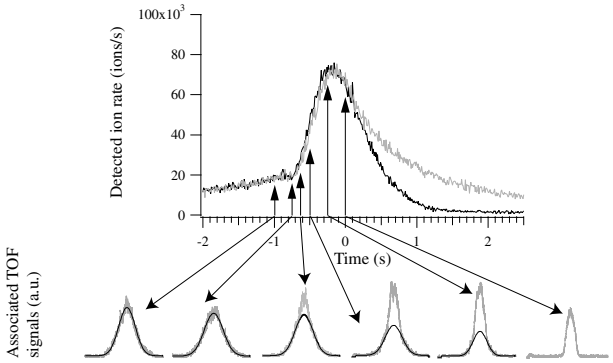

Figure 2. Single-shot measurements of the ion rate versus time and the corresponding TOF signals. Forced evaporative cooling takes place until $t = 0$ (only the last 2 s of the rf ramp are shown: from 1400 to 1000 kHz). The upper, lighter, ion curve corresponds to the case where we keep an rf shield on during the decay, while the lower, darker, decay curve is recorded without. The arrows indicate the time the trap was switched off to record the TOF. The dark curves superimposed on the TOF signals are Gaussian fits to the wings of the TOF.

2. Set-up and experimental procedure

Our set-up has been described previously [1, 8, 9]. Briefly, we trap up to 2×10^8 atoms at 1 mK in a Ioffe–Pritchard trap with a lifetime (τ) of 90 s. We use a 'cloverleaf' configuration (figure 1) [10] with a bias field $B_0 = 300$ mG. The axial and radial oscillation frequencies in the harmonic trapping potential are typically $\nu_\parallel = 47 \pm 3$ Hz and $\nu_\perp = 1200 \pm 50$ Hz respectively ($\overline{\omega}/2\pi = (\nu_\parallel \nu_\perp^2)^{1/3} = 408$ Hz). In a typical run, forced evaporative cooling takes place for 40 s and is divided into four linear ramps. The last ramp lasts for 5 s and the frequency decreases from 2000 kHz to a value between 1500 and 1000 kHz, depending on the condensed fraction wanted. A frequency of 1000 kHz (which is about 50 kHz above the minimum of the trapping potential) corresponds to the formation of a pure condensate.

A special feature of our set-up is the detection scheme, based on a two-stage, single-anode microchannel plate detector (MCP) placed 5 cm below the trapping region (figure 1). Two grids above the MCP allow us either to repel positive ions and detect only the He* atoms, or to attract and detect positive ions produced in the trapped cloud. To detect the ion flux, the MCP is used in counting mode [8]: the anode pulses from each ion are amplified, and processed by a counter which records the time delay between successive events. We can also use the MCP to record a time-of-flight (TOF) signal of the atoms released from the trap. Because the width of the TOF distribution is small (about 5 ms for a BEC) compared with the mean arrival time (100 ms), all of the atoms hit the detector with nearly the same final velocity of 1 m s^{-1}. The TOF spectra are then proportional to the spatial distribution along the vertical direction, integrated over the two horizontal directions. To record the TOF we use the MCP in analogue mode to avoid saturation due to the very high instantaneous flux [8].

3. Monitoring the evolution of a He* cloud

To monitor the evolution of an atomic cloud, one usually releases the cloud and measures the TOF signal. Such a technique is destructive, and one must repeat the cooling sequence for each measurement. The TOF signals are thus subject to fluctuations in the initial number of atoms. In our case, we have a supplementary signal: the ion rate. We can thus minimize these fluctuations, by selecting runs having identical ion rates from the time between the beginning of the last rf ramp until release.

Another type of observation is possible, however. We can use the evolution of the *value* of the ion rate, which is obtained in a single run, independent of any initial fluctuations. When the density is close to the density for BEC formation (i.e. $n \gtrsim 10^{12}$ cm^{-3}), two- and three-body collisions within the cloud dominate the ion production. Thus the ion rate is related to the density of the cloud via the two- and three-body rate constants. Under some conditions (see appendix A) a record of the ion rate followed by a TOF measurement at the end of the formation of the BEC allows one to monitor the evolution of all the parameters of the cloud. In such an observation, knowledge of the two- and three-body rate constants is essential. This is the aim of the experiments described in section 4.

3.1. Observation of condensate formation during the evaporation ramp

Before trying to do a quantitative experiment on BEC formation from of a non-equilibrium uncondensed cloud [3, 4], we can explore qualitatively what happens during our standard evaporation ramp. We show in figure 2 the evolution of the ion rate from 2 s before the end of the rf ramp to 2.5 s after it. In addition we show the TOF signals corresponding to various times before the end of the ramp, selected using their initial ion rate. Between times $t = -2$ and 0 s, the rf was ramped down linearly from 1.4 to 1 MHz. At $t = 0$ a pure condensate is formed. The comparison of the TOF and ion data first shows that the appearance of a narrow structure in the TOF spectrum corresponds, as closely as we can observe it, to an abrupt change in the slope of the ion signal. Thus, not only is the ion signal a reliable indicator of the presence of a BEC, but also a precise measure of the time of its appearance.

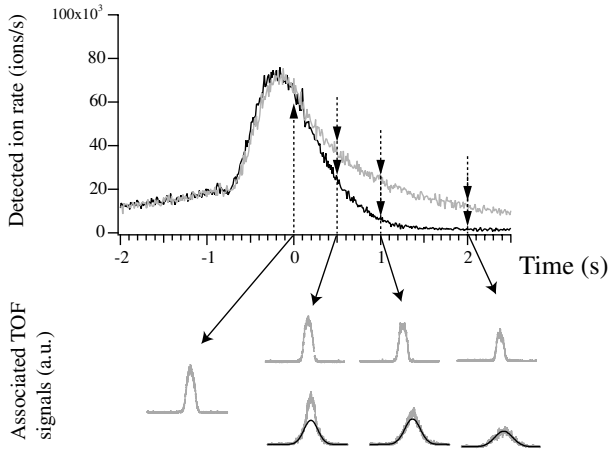

Figure 3. Same as in figure 2 except that we examine the decay of the ion signal after $t = 0$. The upper TOF curves correspond to the upper (lighter) ion decay curve (rf shield present). The lower TOF curves correspond to the lower (darker) ion curve (without rf shield). This shows that the rf shield is maintaining a quasi-pure BEC during the decay, and that in the absence of an rf shield the condensate rapidly heats up, causing the ion rate to drop even faster.

One's first reaction in looking at the ion rate signal is to assume that the higher the ion signal, the larger the BEC and the smaller the thermal cloud. Figure 2 shows, however, that this is not quite the case: the maximum in the ion signal arrives before the achievement of a pure BEC. In fact, computing the value of the ion signal is rather complex. First, as was discussed in [11, 12], as well as below, the indistinguishability of the atoms in the BEC renders the effective two- and three-body collision rate constants smaller than in the thermal cloud by factors of $1/2!$ and $1/3!$ respectively. Collisions between condensed and non-condensed atoms must also be taken into account [11] and the degree of overlap between the two clouds must be calculated. Thus it might be conceivable that the ion rate goes down when a BEC is formed. We show, however, in appendix A that for a fixed total number of atoms, the ion rate increases monotonically as a BEC becomes more and more pure. The observation in figure 2 is explained by the fact that, up until $t = 0$ in figure 2, the atoms are being evaporatively cooled as well as undergoing ionizing collisions and thus the total number of atoms must be decreasing. An explicit calculation including the atom loss is given in appendix A and agrees qualitatively with our observations.

3.2. Observing the decay of the condensate

Figure 3 shows a series of TOF spectra taken after the end of the rf ramp. Two situations are shown. In one case (upper, lighter ion curve) the rf knife was held on at the frequency corresponding to the end of the ramp. In the other case (lower, darker ion curve) the rf power was turned off completely at the end of the ramp. The data show that the condensate remains pure with the rf knife kept on. In the absence of the rf knife, the ion rate decays much faster and one sees that the sample rapidly acquires a thermal component. Since the total number of trapped atoms in the presence of a knife must be smaller than or equal to that in the absence of rf knife, we conclude that the rapid decline in ion rate is due to a loss of sample density and not of the total number of atoms. This conclusion is confirmed by a fit to the thermal wings, which reveals a heating as shown in figure 4.

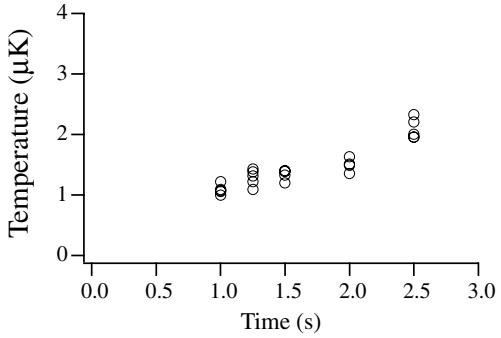

Figure 4. Heating of the condensate in the absence of an rf shield. The temperature increases from 1.1 to 2.2 μK in 1.5 s. The time $t = 0$ is the same as in figures 2 and 3. For each different time, four different TOFs have been acquired and fitted.

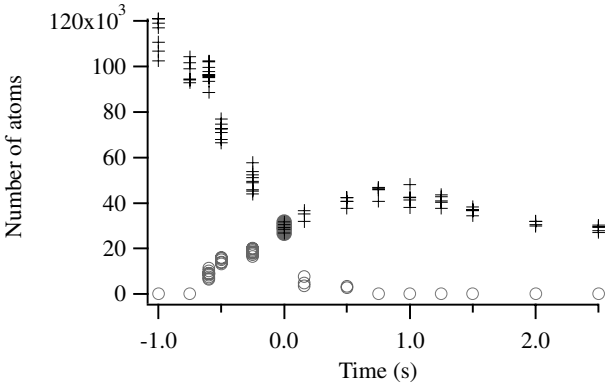

Figure 5. The measured number of atoms as a function of time. Crosses represent the total atom number, circles represent the number of atoms in the condensed part. The data come from the fits of the TOFs presented in figures 2 and 3 and correspond to the case where the rf knife is absent. The time scale indicated is the same as in figures 2 and 3. The increase in the total number after $t = 0$ is spurious (see text).

3.3. Measuring the total number of atoms

An attempt to measure the total number of atoms as a function of time is shown in figure 5. Both the total number and the condensed number as derived from fits to the TOF signals of figures 2 and 3 are plotted. Surprisingly the total number of atoms appears to increase between $t = 0$ and 1 s. There must be a systematic error, which we can account for by recalling that in our apparatus we only detect atoms which make non-adiabatic transitions to the (field insensitive) $m = 0$ state during the turn-off of the magnetic trap [1]. The fraction we observe is of the order of 10%. It is quite possible that this non-adiabatic transition does not occur with equal probability at every point in the trap. Thus clouds with different spatial distributions may be converted to the $m = 0$ state with different efficiencies. This could explain why atoms in the thermal cloud are observed with a higher efficiency than condensed atoms, as indicated in figure 5.

We conclude that our measurements of the absolute number of atoms contain uncontrolled systematic errors of the

order of a factor of two. So, even if we know the ionization rate constants, we cannot use the ion rate to study condensate growth kinetics because we need the absolute value of the initial number of atoms. It would also be useful to measure the variation in the number of atoms during formation. Such a study will have to wait for a more reliable method of releasing the atoms from the trap (see conclusion). However, the measurement of the ionization rate constants is a first step. For a BEC, we can circumvent the systematic error on the detection efficiency of the atoms to make a measurement of the ionization rate constants. This has been described in [8] and will be summarized in the following section. Afterwards, we will investigate the effect of this systematic error on the measurement for a thermal cloud.

4. Rate constants of ionizing collisions

The usual method of measuring the inelastic rate constants relies on fits to a non-exponential decay of the number of atoms. This method has some practical problems if the sample heats during the measurement: the density changes which complicates the fitting procedure. A way to avoid this heating is to apply an rf shield, but this causes atom losses, which are not due to collisions. What is even more inconvenient in our case is that what is measured in this kind of experiment is a decreasing atom number due to losses, which can be due to ionizing as well as non-ionizing collisions. We want to relate the ion rate to the density of the cloud, so what we need is the rate constants for *ionizing* two- and three-body collisions. We therefore use another method which consists of directly observing the products of the collisions, namely the number of ions, as a function of the density of the cloud.

As we have seen in section 3, there is a systematic error on the measurement of the number of atoms and thus of the density of the cloud. But we will see that we can circumvent it in the case of the BEC. Let us then assume first that we are able to measure the number of atoms accurately.

We use the MCP to detect both the ions and the TOF signal. In a single run we record the ion rate during the last seconds of the ramp until we switch off the magnetic trap and record the TOF signal (to obtain the atom number N and the density). The very last value of the ion rate recorded corresponds to ions produced by the cloud observed with the TOF signal. We repeat this sequence many times with different numbers of atoms in the cloud. The way to vary this number is to keep the atoms in the trap with an rf shield kept on. In this way we reduce the atom number and keep the temperature of the cloud constant. As explained in appendix A, the relation between ion rate and density is quite complex in the case of the presence of collisions between atoms in the condensed part and atoms in the thermal part. We therefore only examine the case of a pure BEC *or* a pure thermal cloud. In that case we can write the ion rate per atom Γ as follows:

$$\frac{\text{ion rate}}{N} = \Gamma = \frac{1}{\tau'} + \frac{1}{2}\kappa_2\beta\langle n\rangle + \frac{1}{3}\kappa_3 L\langle n^2\rangle \qquad (3)$$

where $\langle n\rangle = \frac{1}{N}\int n^2\,\mathrm{d}\boldsymbol{r}$ and $\langle n^2\rangle = \frac{1}{N}\int n^3\,\mathrm{d}\boldsymbol{r}$, n being the local density. We have also introduced the two- and three-body ionizing collision rate constants, β and L respectively, defined according to their effect on the density loss in a thermal gas[3]: $(\frac{\mathrm{d}n}{\mathrm{d}t})_{ionization} = -\frac{n}{\tau'} - \beta n^2 - Ln^3$. The effective lifetime $\tau' \geqslant \tau$ is due to *ionizing* collisions with the background gas. The numerical factors come from the fact that although two or three atoms are lost in each type of collision, only one ion is produced. The factors κ_2 and κ_3 take into account the fact that the two-and three-particle local correlation functions are different depending on whether it is a BEC or a thermal cloud. For the thermal cloud $\kappa_2 = \kappa_3 = 1$, while for a dilute BEC, one has $\kappa_2 = 1/2!$ and $\kappa_3 = 1/3!$ [11, 12]. When the sample is very dense, quantum depletion must be taken into account, which modifies these factors [11]. A measurement of β and L would allow us to test experimentally the theoretical values of κ_2 and κ_3 [8].

4.1. Rate constants for a BEC

To determine the ionizing collision rate constants β and L, we need an absolute calibration of the number of atoms in the condensate, N_0, and the peak density, n_0, in order to calculate $\langle n\rangle$ and $\langle n^2\rangle$. As discussed above, we do not have a good calibration of these quantities. In the case of a BEC, however, the measurement of the chemical potential μ obtained by a fit of the TOF signal gives an accurate value for the product $n_0 a = \mu \mathrm{m}/4\pi\hbar^2$, a being the scattering length. With the value of $\overline{\omega}$ we also obtain the product $N_0 a = (1/15)(\hbar/m\overline{\omega})^{1/2}\,(2\mu/\hbar\overline{\omega})^{5/2}$. Experimentally we confirm that $\mu \propto N_d^{2/5}$ where N_d is the number of detected atoms [8]. This is a good indication that our detector is linear and that the detection efficiency for a BEC is indeed independent of μ. Assuming a value of the scattering length ($a = 20$ nm), we therefore have an accurate measurement of n_0 and N_0. We have measured the rate constants β and L for a condensate [8]. We obtain by a fit to equation (3) (having corrected for the effect of quantum depletion and the fact that the BEC also contains a small thermal fraction) $\beta = 2.9(\pm 2.0) \times 10^{-14}$ cm^3 s^{-1} and $L = 1.2(\pm 0.7) \times 10^{-26}$ cm^6 s^{-1}. These values agree with the theoretical estimates [13, 14]. The scattering length is not well known [1, 2], so we have also given β and L for different values of a [8].

4.2. Rate constants for a thermal cloud

To determine the rate constants for a thermal cloud we need, as before, to determine the atom number and density. We cannot use the same trick as in section 4.1 to avoid systematic errors in the detection efficiency. If we want to use the above experimental method for a thermal cloud we must rely on a fit of the TOF to find the atom number and the temperature T. In appendix B, we propose a method to determine the rate constants which is independent of an absolute detection efficiency, but at this stage we will concentrate on the same technique as used for a BEC.

As we have shown above, the detection efficiency is expected to be different for a thermal cloud and we can investigate the effect of this systematic error on these measurements. We repeat the above described experiment, this time with a pure thermal cloud. To begin with, we assume that the detection efficiency is the same for a BEC and a thermal cloud. We

[3] Collision rate constants are sometimes defined directly for a BEC ($\beta' = \beta/2$ and $L' = L/6$).

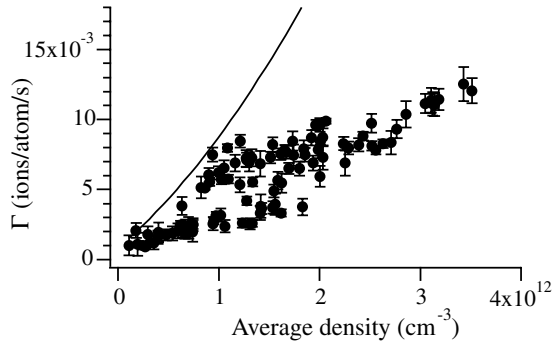

Figure 6. Ion rate per trapped atom (Γ) in a thermal cloud versus average density. The full curve corresponds to the value of β and L deduced from the condensate measurements.

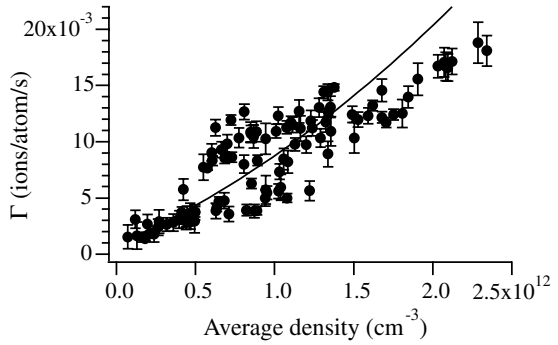

Figure 7. Same as figure 6 but assuming a detection efficiency of the thermal cloud a factor of 1.5 higher relative to the BEC. The data have simply been rescaled along both axes; the full curve is the same as in figure 6.

plot the ion rate per atom as a function of $\langle n \rangle$ in figure 6. We can extrapolate the data to obtain the vertical intercept, which corresponds to $1/\tau'$. For densities corresponding to the moment of formation of BEC, the corresponding ion rate N/τ' is negligible compared with the total ionization rate, meaning that we are dominated by two- and three-body processes (see figures 2 and 5). To compare with the results obtained for the BEC, we have also plotted the curve we would expect using the above values of β and L. It is clear that the data do not agree with this curve. Moreover, no possible pair of β and L taken within their error bars (see [8]) can transform the curve so that it agrees with the data. Nor can assuming a different scattering length. What *can* make the curve agree with the data is assuming a different detection efficiency for atoms in the thermal cloud. If we assume for example that the detection efficiency is a factor of 1.5 higher for a thermal cloud relative to a BEC (which is consistent with figure 5), the curve agrees better with the data as shown in figure 7.

The dispersion of the data points is quite large. This dispersion can be understood by examining figure 8 in which we have plotted the same data as in figure 6, but now indicating the temperature corresponding to each different point on the graph. There is a clear systematic variation with temperature. One possible explanation is that the detection efficiency is temperature dependent. This agrees with the above idea that the efficiency depends on the spatial extent of the cloud which is indeed related to the temperature. We do not know the form of the detection efficiency as a function of temperature, but comparing these data (indicating that cold atoms are better

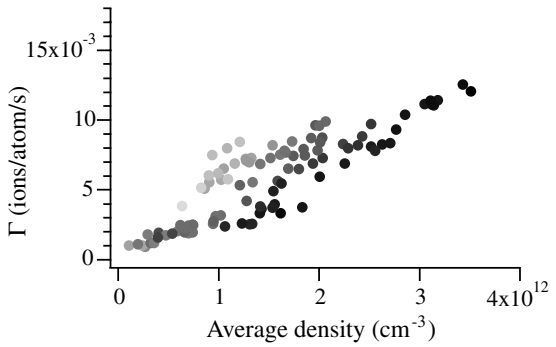

Figure 8. Same data as in figure 6 but with the different temperatures indicated. The lighter circles correspond to the point with higher temperatures (the maximum temperature is 5.5 μK), the darker circles with lower temperatures (minimum temperature 1.8 μK).

detected) with the fact that a thermal cloud is better detected than a BEC, leads us to conclude that there exists a certain temperature giving a maximal detection efficiency. Therefore the correction to the detection efficiency for thermal atoms is not just a simple factor, but rather a function of temperature. Without knowing this correction, we cannot use this method to determine the collision constants for a thermal cloud. Still, these results are a consistency check on the rate constants measured using a BEC.

5. Conclusion

We have seen that the benefits of ion detection are twofold. First, the ion rate can be used to select BECs with very similar parameters out of a sample with large fluctuations. Second, the ion rate itself can give information on the condensate on a single-shot basis. Quantitatively, we still have some difficulties interpreting the data due to systematic errors in the detection calibration.

One way to overcome this problem is to release the atoms from the trap by the mean of Raman transitions. It should be possible to transfer close to 100% of the atoms into the $m = 0$ state. This will eliminate the temperature dependence of the detection efficiency and allow us to obtain more precise measurements of β and L, both for the BEC by improving the value of the scattering length and for the thermal cloud by making the detection efficiency temperature independent.

Acknowledgments

We thank A Villing and F Moron for their assistance with the electronics. This work is supported by the European Union under grants IST-1999-11055 and HPRN-CT-2000-00125, and by the DGA grant 00.34.025. JVG thanks Fundação para a Ciência e a Tecnologia and SS acknowledges Danish Research Training Council and Danish Research Agency for financial support.

Appendix A. Predictions of the ion rate during the formation of the BEC

The two- and three-body ion rates (I_{2b} and I_{3b} respectively) in a sample containing both a BEC and a thermal cloud are given by [11]:

$$I_{2b} = \frac{1}{2}\frac{\beta}{2!}\int \mathrm{d}\boldsymbol{r}\,[n_0^2(\boldsymbol{r}) + 4n_0(\boldsymbol{r})n_{th}(\boldsymbol{r}) + 2n_{th}^2(\boldsymbol{r})] \quad (A.1)$$

$$I_{3b} = \frac{1}{3}\frac{L}{3!}\int \mathrm{d}\boldsymbol{r}\,[n_0^3(\boldsymbol{r}) + 9n_0^2(\boldsymbol{r})n_{th}(\boldsymbol{r}) + 18n_0(\boldsymbol{r})n_{th}^2(\boldsymbol{r}) + 6n_{th}^3(\boldsymbol{r})] \quad (A.2)$$

where $n_0(\boldsymbol{r})$ is the local density of the BEC and $n_{th}(\boldsymbol{r})$ is the local density of the thermal cloud. Here we have taken into account the symmetrization factors, but neglected quantum depletion.

Four parameters are needed to determine the densities of the two clouds: N_0, μ, N_{th} and T_{th}. In the Thomas–Fermi approximation, however, the BEC density depends only on μ:

$$n_0(\boldsymbol{r}) = \max\left[0, \frac{\mu - U(\boldsymbol{r})}{g}\right] \quad (A.3)$$

with $U(\boldsymbol{r})$ the harmonic trapping potential and $g = 4\pi\hbar^2 a/m$ the interaction strength. The density of the thermal cloud depends on two parameters. But, if thermodynamic equilibrium is reached, taking into account the interactions between the BEC and the thermal cloud (and neglecting the interaction energy of the thermal cloud), we can write:

$$n_{th}(\boldsymbol{r}) = \frac{1}{\lambda_{dB}^3} g_{3/2}\left(\exp\left(-\frac{1}{k_B T}(U(\boldsymbol{r}) + 2gn_0(\boldsymbol{r}) - \mu)\right)\right) \quad (A.4)$$

where λ_{dB} is the thermal de Broglie wavelength and $g_{3/2}(x) = \sum_{n=1}^{+\infty} \frac{x^n}{n^{3/2}}$. In that case, given μ, n_{th} only depends on one additional parameter.

A.1. Comparison between the ion rates created by a thermal cloud at $T = T_C$ and a pure BEC

Before trying to calculate the ion rate for any T, which requires numerical calculation, let us first examine the ion rate created by a thermal cloud at $T = T_C$ with a number of atoms N and that created by a pure BEC ($T = 0$) with a number of atoms ηN ($\eta < 1$).

In the case of two-body collisions, the ratio R_{2b} of the ion rates created by a pure BEC (I^{BEC}) and by a thermal cloud (I^{th}) is related to the ratio of the peak densities. For three-body collisions the ratio (R_{3b}) is related to the square of that ratio. Using the above equations we find:

$$\left(\frac{n_0}{n_{th}}\right) = C_0 \eta^{2/5} N^{-1/10}\left(\frac{\overline{\sigma}}{a}\right)^{3/5} \quad (A.5)$$

$$R_{2b} = \frac{I_{2b}^{BEC}}{I_{2b}^{th}} = C_2 \eta^{7/5} N^{-1/10}\left(\frac{\overline{\sigma}}{a}\right)^{3/5} \quad (A.6)$$

$$R_{3b} = \frac{I_{3b}^{BEC}}{I_{3b}^{th}} = C_3 \eta^{9/5} N^{-2/10}\left(\frac{\overline{\sigma}}{a}\right)^{6/5} \quad (A.7)$$

where $\overline{\sigma} = \sqrt{\frac{\hbar}{m\overline{\omega}}}$. The numerical factors $C_0 \simeq 0.78$, $C_2 \simeq 1.05$ and $C_3 \simeq 0.49$ are independent of the atom considered and only assume that the cloud is trapped in a 3D harmonic trap. The maximum ratios are reached in the case of no loss ($\eta = 1$). Using the typical values of our experiment ($a \simeq 20$ nm, $N \simeq 4 \times 10^5$ and $\overline{\omega} \simeq 2\pi \times 408$ Hz), we find $(\frac{n_0}{n_{th}})_{max} \simeq 4$, $(R_{2b})_{max} \simeq 5$ and $(R_{3b})_{max} \simeq 12$.

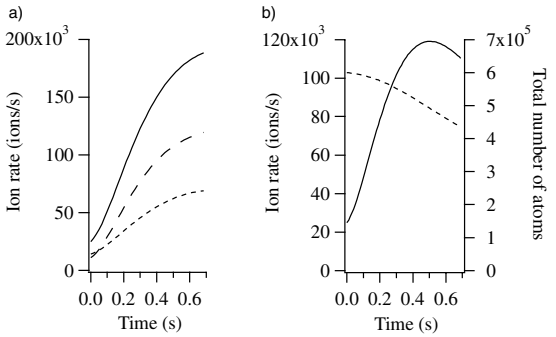

Figure A.1. Evolution of the ion rate with time. In (a) the total number of atoms is constant. We show the different contributions to the total ion rate (continuous curve) of the ion rate created by two-body collisions (short dashed curve) and three-body collisions (long dashed curve). In (b) the total number of atoms (dashed curve) decreases due to ionizing collisions. Here the ion rate exhibits a maximum before the formation of a pure BEC. For both graphs, the initial number of atoms is 6×10^5 and a linear evolution of the temperature between T_C and 0 is imposed. The rates have been calculated with the values of rate constants measured in [8].

If the total number of atoms decreases during the formation of the BEC, these ratios rapidly fall. For instance, if the number of atoms decreases by a factor of 3.5 during the last 750 ms of evaporation as shown in figure 5, we would not have seen an increase of ionization rate but roughly the same ion rate at $t = -750$ and 0 ms! This is an additional evidence of the difference of neutral atom detection efficiency for a thermal cloud and BEC (i.e. the total number of atoms decreased by less than 3.5).

A.2. Evolution of the ion rate between $T = T_C$ and $T = 0$

Using equations (A.1) and (A.2), we have numerically calculated the ion rates for all temperatures. If the cloud is at thermodynamic equilibrium all the parameters of the cloud are deduced from two parameters, for example the total number of atoms and the temperature. To simulate a time evolution of the ion rate we thus need a model for the variation of these parameters. In this appendix we will assume a linear evolution of the temperature between $T = T_C$ and 0 in 0.7 s. This is of course a simplification, but given the linearity of the evaporative cooling ramp, it is quite a good approximation.

In figure A.1(a) we show the evolution of the ion rates assuming a constant total number of atoms. The ion rate increases monotonically. We also see that the number of ions produced and thus also the number of lost atoms is not necessarily negligible compared with the total.

We can attempt to take into account these losses in our model. In the experiments described in the text, the losses are not only due to the ionizing collisions but also to the rf knife. In addition, losses not only lead to a decrease in the total number of atoms but also to a change in the temperature because these collisions change the condensed fraction. Thus, modelling the ion rate can be quite complicated. Here we wish simply to illustrate the effect of loss, so we assume that losses are only due to ionizing collisions, and we will neglect losses due to the rf knife. Figure A.1(b) shows the results. The atom number decreases by only 30% and the ion rate reaches a local

maximum before the formation of the pure BEC, as in our experiment. Extensions of our model to include losses due to the rf knife would allow one to monitor all the parameters of the cloud using the ion signal.

Appendix B. Proposed measurement of rate constants independent of absolute neutral atom detection efficiency

We will assume in this section that the absolute ion detection efficiency is known, and that two- and three-body losses are ionizing collisions [13]. The idea behind this method is that two TOF signals separated by a given time can measure the relative atom loss during this time, while the ion rate can measure the absolute atom loss. These data allow one to extract the rate constants without relying on an absolute calibration of the neutral atom detection efficiency. The method works if the neutral detection efficiency is unknown but independent of temperature. Otherwise, we must also assume that the cloud does not heat during the measurement or that we know the variation of detection efficiency with temperature.

To simplify the discussion we will neglect three-body reactions and assume that the sample does not heat during the measurement. This will allow us to derive analytical expressions, but the results are easily generalized to include heating as well as three-body reactions. We can then write the ion rate $I(t)$ as:

$$I(t) = \frac{\epsilon N(t)}{\tau'} + \frac{\beta\epsilon}{2V_{eff}} N(t)^2 \tag{B.1}$$

with τ' the lifetime due to ionizing collisions, $N(t)$ the absolute atom number, V_{eff} defined by $\langle n\rangle = N/V_{eff}$ and ϵ the ion detection efficiency. We write $N_d(t) = \alpha N(t)$ where $N_d(t)$ is the number of atoms detected and α is the neutral atom detection efficiency. Then

$$I(t) = \frac{\epsilon N_d(t)}{\alpha\tau'} + \frac{\epsilon\beta}{\alpha^2 2V_{eff}} N_d(t)^2. \tag{B.2}$$

We can also write an equation for the atom number

$$\frac{\mathrm{d}N(t)}{\mathrm{d}t} = -\frac{N(t)}{\tau} - \frac{\beta}{V_{eff}} N(t)^2 \tag{B.3}$$

with τ the total lifetime of the sample that we can measure independently at lowest density. The solution is:

$$\frac{N(t)}{N(t_0)} = \frac{1}{\left(1 + \frac{\beta}{V_{eff}} N(t_0)\tau\right)\mathrm{e}^{(t-t_0)/\tau} - \frac{\beta}{V_{eff}} N(t_0)\tau}. \tag{B.4}$$

Substituting again $N_d(t) = \alpha N(t)$ we have:

$$\frac{N_d(t)}{N_d(t_0)} = \frac{1}{\left(1 + \frac{\beta}{\alpha V_{eff}} N_d(t_0)\tau\right)\mathrm{e}^{(t-t_0)/\tau} - \frac{\beta}{\alpha V_{eff}} N_d(t_0)\tau}. \tag{B.5}$$

Thus we can measure an initial ion rate and the corresponding detected atom number $N_d(t_0)$ by a TOF signal, let the system evolve for a certain time and then again measure the ion rate and the atom number $N_d(t)$. With the evolution of the ion rate, we can deduce $\epsilon/\alpha\tau'$ and $\epsilon\beta/\alpha^2 V_{eff}$ from equation (B.1), and from the evolution of the atom number we can deduce $\beta/\alpha V_{eff}$ using equation (B.5). With the value of V_{eff} and ϵ, we can obtain the value β. We can also obtain the detection efficiency α.

If we allow for three-body reactions, the method can still be used but (B.4) is no longer analytical and must be integrated numerically. If the sample heats during the measurement, we only have to recalculate the volume V_{eff} for each TOF measurement.

The reason why we have not yet been able to apply this method is, as indicated above, that the sample is heating so that the detection efficiency changes during the measurement. As we have not been able to measure the temperature dependence of $\alpha(T)$ the above equations cannot be solved. We hope to render the detection efficiency temperature independent in the near future by using Raman transitions as mentioned in the conclusion.

References

[1] Robert A, Sirjean O, Browaeys A, Poupard J, Nowak S, Boiron D, Westbrook C I and Aspect A 2001 *Science* **292** 461

[2] Pereira D S F, Léonard J, Junmin W, Barrelet C J, Perales F, Rasel E, Unnikrishnan C S, Leduc M and Cohen-Tannoudji C 2001 *Phys. Rev. Lett.* **86** 3459

[3] Miesner H J, Stamper-Kurn D M, Andrews M R, Durfee D S, Inouye S and Ketterle W 1998 *Science* **270** 1005

[4] Köhl M, Hänsch T W and Esslinger T 2002 *Phys. Rev. Lett.* **88** 080402

[5] Kagan Yu M, Svistunov B V and Shlyapnikov G V 1992 *Sov. Phys.–JETP* **75** 387

[6] Gardiner C W, Zoller P, Ballagh R J and Davis M J 1997 *Phys. Rev. Lett.* **79** 1793

[7] Bijlsma M J, Zaremba E and Stoof H T C 2000 *Phys. Rev.* A **62** 063609-1

[8] Sirjean O, Seidelin S, Viana Gomes J, Boiron D, Westbrook C I, Aspect A and Shlyapnikov G V 2002 *Phys. Rev. Lett.* **89** 220406

[9] Browaeys A 2000 Thèse de l'Université Paris-Sud available at http://ccsd.cnrs.fr/

[10] Mewes M O, Andrews M R, van Druten N J, Kurn D M, Durfee D S and Ketterle W 1996 *Phys. Rev. Lett.* **77** 416

[11] Kagan Yu M, Svistunov B V and Shlyapnikov G V 1985 *JETP Lett.* **42** 209

[12] Burt E A, Ghrist R W, Myatt C J, Holland M J, Cornell E A and Wieman C E 1997 *Phys. Rev. Lett.* **79** 337

[13] Shlyapnikov G V, Walraven J T M, Rahmanov U M and Reynolds M W 1994 *Phys. Rev. Lett.* **73** 3247
Fedichev P O, Reynolds M W, Rahmanov U M and Shlyapnikov G V 1996 *Phys. Rev.* A **53** 1447

[14] Venturi V, Whittingham I B, Leo P J and Peach G 1999 *Phys. Rev.* A **60** 4635
Venturi V and Whittingham I B 2000 *Phys. Rev.* A **61** 060703(R)

Getting the Elastic Scattering Length by Observing Inelastic Collisions in Ultracold Metastable Helium Atoms

S. Seidelin, J. Viana Gomes,* R. Hoppeler, O. Sirjean, D. Boiron, A. Aspect, and C. I. Westbrook
Laboratoire Charles Fabry de l'Institut d'Optique, UMR 8501 du CNRS, F-91403 Orsay Cedex, France
(Received 13 January 2004; published 27 August 2004)

We report an experiment measuring simultaneously the temperature and the flux of ions produced by a cloud of triplet metastable helium atoms at the Bose-Einstein critical temperature. The onset of condensation is revealed by a sharp increase of the ion flux during evaporative cooling. Combining our measurements with previous measurements of ionization in a pure Bose-Einstein condensate, we extract an improved value of the scattering length $a = 11.3^{+2.5}_{-1.0}$ nm. The analysis includes corrections that take into account the effect of atomic interactions on the critical temperature, and thus an independent measurement of the scattering length would allow a new test of these calculations.

DOI: 10.1103/PhysRevLett.93.090409 PACS numbers: 03.75.Hh, 34.50.–s, 67.65.+z

Understanding and testing the role of interparticle interactions in dilute Bose-Einstein condensates (BEC) is an exciting area of current research. Although measurements of the interaction energy and the spectrum of excitations of a BEC have confirmed the validity of the Gross-Pitaevskii equation [1], there are still relatively few quantitative tests of other aspects, such as the effect of interactions on the value of the critical temperature (T_c) or the condensed fraction [2,3]. The success in condensing metastable helium atoms (He^*) [4,5] was greeted with interest in the community partly because the metastability offers new detection strategies unavailable with other species. To fully use these strategies, however, we are still missing an accurate value of the s-wave scattering length a, the atomic parameter which determines all elastic scattering behavior at low energies. An accurate value of a would also be useful to help clarify some puzzling results concerning measurements of He^* in the hydrodynamic regime, in which two different ways of measuring the elastic scattering rate appeared to be in contradiction [6]. Also, because He is a relatively simple atom, theoretical predictions of a are already in a rather narrow range [7,8] and these calculations should be tested.

A straightforward method to determine a is to use ballistic expansion of a BEC to measure the chemical potential for a known atom number. This was done in Refs. [4,5], but the measurements were limited by the calibration of the number of atoms. The reported values for a are 20 ± 10 and 16 ± 8 nm, respectively. A recent estimate, limited by similar effects, is $a = 10 \pm 5$ nm [9]. In this Letter, we report a new measurement of a which makes extensive use of a unique feature of He^*, spontaneous Penning ionization within the sample.

We exploit two specific situations in which the absolute atom number N is simply related to a and measured quantities: (i) for a pure BEC, the number is deduced directly from the chemical potential μ and a, and (ii) for a cloud at the BEC threshold, it is simply related to T_c. Both μ and T_c are accurately deduced from time of flight (TOF) measurements. Comparison of ion rates from a pure BEC of known chemical potential and from a cloud at T_c allows us to extract a and the ionization rate constants. The deduced value of a is independent of the absolute ion detection efficiency, assuming that this efficiency is the same in the two measurements. The ion signal is also used in another novel way: since it provides a real-time observation of the onset of BEC [10], we use it to reliably produce a cloud at threshold.

A dense cloud of He^* produces a steady flux of ions due to various ionization processes. Density losses due uniquely to *ionizing* collisions depend on the local density n according to $(dn/dt)_{\text{ionizing}} = -(n/\tau_i) - \beta n^2 - Ln^3$, with τ_i the lifetime due to ionizing collisions with the background gas and β and L the 2-body and 3-body ionization rate constants defined for a thermal cloud. The total ion rate from a thermal cloud is given by

$$\Phi = \frac{N}{\tau_i} + \frac{1}{2}\beta \int n^2 d\mathbf{r} + \frac{1}{3} L \int n^3 d\mathbf{r}. \tag{1}$$

The numerical factors reflect the fact that although two (three) atoms are lost in 2-body (3-body) collisions, only one ion is produced. Ionization measurements on a pure BEC were reported in Ref. [11], and, as a was not precisely known, β and L were given in terms of a.

For a precise measurement of a, corrections due to interactions must be taken into account. In the mean-field approach, the density is given by [1]

$$n(\mathbf{r}) = \frac{1}{\lambda^3(T)} g_{3/2}\left[\exp\left(-\frac{1}{k_B T}[V(\mathbf{r}) + 2gn(\mathbf{r}) - \mu]\right)\right], \tag{2}$$

with $\lambda(T)$ the thermal de Broglie wavelength, T the temperature k_B the Boltzmann constant, V the trapping potential $g = 4\pi\hbar^2 a/m$ the interaction constant, μ the chemical potential, and $g_\alpha(x) = \sum_{i=1}^{\infty} x^i/i^\alpha$.

The ion rate at the phase transition Φ_c can be derived from Eq. (2) by a first order perturbation theory similar to Ref. [12] but with a fixed temperature rather than a fixed atom number. We use the chemical potential of a gas in a harmonic potential at the BEC transition:

 © 2004 The American Physical Society

$$\mu_c/k_B T_c = \frac{3}{2}\frac{\tilde{\omega}}{\omega_c} + 4g_{3/2}(1)\frac{a}{\lambda_c}. \quad (3)$$

This gives

$$\Phi_c = \left(\frac{\omega_c}{\overline{\omega}}\right)^3\left[\frac{1}{\tau_i}\left(1.20 + 2.48\frac{\tilde{\omega}}{\omega_c} + 12.35\frac{a}{\lambda_c}\right) + \frac{\beta}{\lambda_c^3}\left(0.33 + 1.81\frac{\tilde{\omega}}{\omega_c} + 6.75\frac{a}{\lambda_c}\right) + \frac{L}{\lambda_c^6}\left(0.22 + 2.21\frac{\tilde{\omega}}{\omega_c} + 6.50\frac{a}{\lambda_c}\right)\right], \quad (4)$$

with $\tilde{\omega} = (2\omega_\perp + \omega_\parallel)/3$, $\overline{\omega} = (\omega_\parallel \omega_\perp^2)^{1/3}$, $\omega_c = k_B T_c/\hbar$, and $\lambda_c = \lambda(T_c)$. The numerical values come from the calculation of arithmetic series and are independent of any parameters of the cloud. The terms proportional to a/λ_c account for the atomic interactions, while the corrections proportional to $\tilde{\omega}/\omega_c$ take into account the effect of finite sample size. For the typical parameters ($T_c \sim 2\ \mu$K and $a = 12$ nm) we have $a/\lambda_c \simeq \tilde{\omega}/\omega_c \simeq 0.02$, corresponding to an interaction correction of 20%, 40%, and 60% in the three successive terms in Eq. (4). Even though the first order corrections are large, we find, using an approach similar to Ref. [13], that the second order corrections are negligible: -4%, 1.8%, and -3%, respectively. Note that finite size corrections are always smaller than those due to interactions.

Our setup has been described in Ref. [11]. Briefly, we trap up to 2×10^8 atoms at 1 mK in an Ioffe-Pritchard cloverleaf trap with τ_i estimated to be >500 s. In a typical run, forced evaporation for 30 s cools a cloud to a temperature near the phase transition. At this point, the rf-knife frequency is decreasing at a rate of 400 kHz/s. The axial and radial oscillation frequencies in the harmonic trapping potential are $\omega_\parallel/2\pi = 47 \pm 3$ Hz and $\omega_\perp/2\pi = 1225 \pm 20$ Hz, respectively. A 2-stage, single anode microchannel plate detector (MCP) is placed 5 cm below the trapping region. Two grids above the MCP allow us either to repel positive ions and detect only the He^* atoms or to attract and detect positive ions produced in the trapped cloud. As explained in Ref. [11], to detect the ion flux, the MCP is used in counting mode, whereas we record the TOF signal at low gain (analog mode) to avoid saturation. As explained in Ref. [4], the TOF signal is due to atoms in the $m = 0$ state which are insensitive to the magnetic field. However, atoms in magnetic field sensitive states are still present, and their trajectories are affected by uncontrolled residual fields. Therefore, during the time of flight, we apply a magnetic gradient in order to push these atoms away from the detector. The ratio between the detected atoms in the $m = 0$ state and the initial number of atoms in the cloud is not well known [10], so we use the TOF only to get the temperature.

The crux of the experiment is to obtain a cloud of atoms at the phase transition. To identify the BEC threshold point, we monitor the ion signal. We have shown in Ref. [10] that the onset of BEC is heralded by a sudden increase of the ion rate associated with the increased density of the condensate. More precisely, the BEC threshold corresponds to the rapid change in slope of the ion rate vs time or the maximum of the 2nd derivative [14]. Figure 1 shows a series of such ionization rates during evaporation through the BEC transition. From these curves we can determine an empirical relation between the time of the onset of condensation and the ion rate preceding it. This relation stays valid only as long as we keep the same evaporation ramp and bias field. We will refer to this as the "threshold curve." Because of fluctuations of the bias field, we observe fluctuations of the time of BEC onset from run to run. These correspond to approximately ± 60 ms in time or ± 25 kHz in frequency, a value which agrees with independent measurements of the fluctuations of the bias field.

Having established this relation, we can interrupt an evaporation sequence very close to the BEC threshold and record the instantaneous ion rate as well as the corresponding TOF signal. Only runs closer than ± 60 ms to the threshold curve are used in the analysis.

We fit the associated TOF spectrum to determine the temperature (Fig. 2). We use Eq. (2) together with μ_c given in Eq. (3) for the initial atomic density and then assume purely ballistic expansion of the cloud after the switching off of the trap. We refer to this fit as the Bose fit. The fits are weighted by an estimated uncertainty in each point of the TOF curve. To make this estimate, we chose a set of TOF spectra which appeared to show no systematic deviation from their fits and used them to estimate the amplitude of the noise. This noise varies as the square root of the amplitude of the signal, indicating that we are limited by the shot noise of the atom detection. Our procedure is only an approximate indicator of the error bars. The chi square per degree of freedom χ^2 for the fits

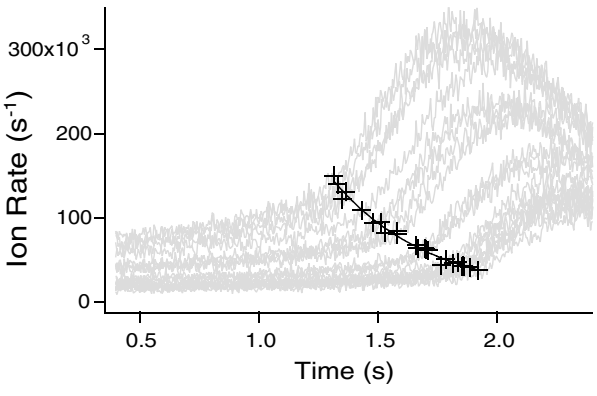

FIG. 1. Variation of the ion rate as the atomic cloud is cooled through the phase transition for various initial densities (gray curves). The rf-knife frequency at $t = 0$ is 2 MHz. The sudden increase of the ion rate (crosses) occurs at the BEC transition. The solid line passing through the transition points constitutes our empirical relation, named threshold curve.

deduced in this way ranges from 0.8 to 3. We then exclude a successively larger window (up to the rms of the TOF signal) from the fit (see Fig. 2). For all runs, we observe a variation of less than 5% and in most cases less than 3% of the temperature as the excluded window is increased.

In Fig. 2, we show an example of a typical TOF spectrum where the wings are fitted by a Gaussian and the Bose function described above. The ability of the Bose function to reproduce the center of the distribution without including it in the fit, unlike the Gaussian, confirms that the cloud is indeed close to the BEC threshold. In the following, we use the temperature given by the fit with an excluded window of half the rms width of the TOF signal in order to avoid the possibility of a small condensate component or other high density effects distorting our analysis.

Before plotting the ion rate as a function of the critical temperature, we correct the observed temperature to account for the hydrodynamic expansion of the cloud (see [2] and references therein). This is done in the spirit of Ref. [15], which uses the Boltzmann equation approach to take into account collisions during the expansion. The collision rate in Ref. [15] is calculated using a Gaussian density profile. We rather use the value calculated for an ideal Bose gas [16], which we have adapted to take interactions into account. This correction depends on the scattering length but the effect on the final value of a is only of order 0.3 nm for a ranging from 10 to 14 nm. We therefore simply assume $a = 12$ nm for this correction in the following. Due to the additional anisotropy of the expanding cloud in the horizontal (detector) plane, the fitting function should be modified; but a simulation of this effect shows that the correction to the temperature is less than 0.1%.

Finally, we correct the detected ion rate $\Phi_{c,det}$ to account for the detection efficiency α such that $\Phi_c = \Phi_{c,det}/\alpha$. It should be noted that the rate constants were

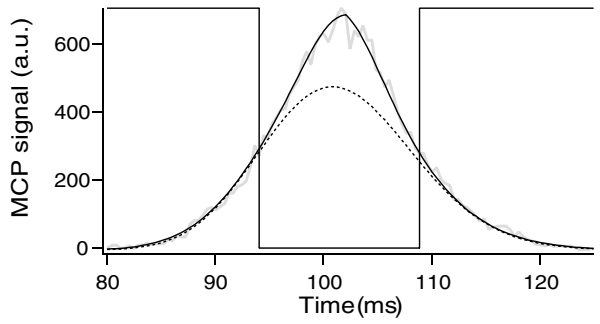

FIG. 2. Time of flight signal corresponding to a cloud released from the trap (at $t = 0$) when its ion rate is on the threshold curve. Here we have fitted the data with an excluded window indicated by the vertical lines (width equal to the rms width of the TOF signal). A Gaussian function (dotted line) does not describe the central part of the data well, while the Bose function as defined in the text (solid line) does, indicating that the cloud is close to threshold.

obtained by ion rate measurements [11]. This means that they were also corrected: $\beta = \beta_{det}/\alpha'$ and $L = L_{det}/\alpha'$. Equation (4) shows that, as long as $\alpha = \alpha'$, the detection efficiency cancels out and does not have any impact on the determination of a. We have checked experimentally that $\alpha = \alpha'$. To allow comparison with figures in earlier publications, all the figures have been corrected using the same α as earlier, namely, $\alpha = 0.42$ [10,11].

The results are plotted in Fig. 3. Curves corresponding to the expected variation for three values of the scattering length are also shown. We see that a large fraction of the data falls between $a = 10$ and 14 nm. The points at the highest temperatures, however, show a tendency to fall near the theoretical curve for $a = 10$ nm, while those at lower temperatures fall near $a = 14$ nm. To analyze this tendency further, we examine the TOF fits more closely using the χ^2 value as an indicator of the confidence level of each measurement. A large χ^2 could mean that the Bose function with μ imposed to μ_c is not the right fit function and, therefore, that the cloud is not sufficiently close to T_c. As shown in Fig. 3, outliers tend to be correlated with a large χ^2. Note, however, that the remaining scatter in the data is too large to be accounted for by our *a priori* estimates of the uncertainties in our ion rate or temperature measurements. We presume that it is due to fluctuations in the determination of the BEC threshold.

To determine the scattering length, we fit the black points in Fig. 3 with a as a free parameter and using β and L parametrized by a as in Ref. [11]. The fit gives (all points are given equal weight) $a = 11.3$ nm. Our chief estimated uncertainty stems from the fact that our data show a systematic tendency to fall above the best fit at low temperature and below it at high temperature. To estimate this uncertainty, we fit the data (including gray points) separately for T_c below and above 2 μK. We find $a = 13.8$ nm for the low temperature data and $a = 10.4$ nm for the high temperature data. The uncertainties in the measurements of β and L also contribute to the uncertainty in Eq. (4) used for fitting. In fact, the uncertainties in β and L are highly correlated [11] and their contribution to the uncertainty is less than 0.5 nm.

The error bars are obtained by summing quadratically the sources of uncertainties. Our final result for the scattering length is thus $a = 11.3^{+2.5}_{-1.0}$ nm. This result may be compared with the calculation in Ref. [8]. This work leads to $a = 8$ nm using the potential curves of Ref. [17]. From Ref. [8] one also finds that a 0.5% shift of the repulsive part of that potential would bring the theoretical value into agreement with our result. This 0.5% shift corresponds to the estimated uncertainty in the potential of Ref. [17]. Another theoretical treatment [7] gives a scattering length between 8 and 12 nm, also consistent with our results.

Our result also allows one to give values for the 2- and 3-body ionization rate constants. The error bars of Ref. [11] are modified to take into account the uncertainty

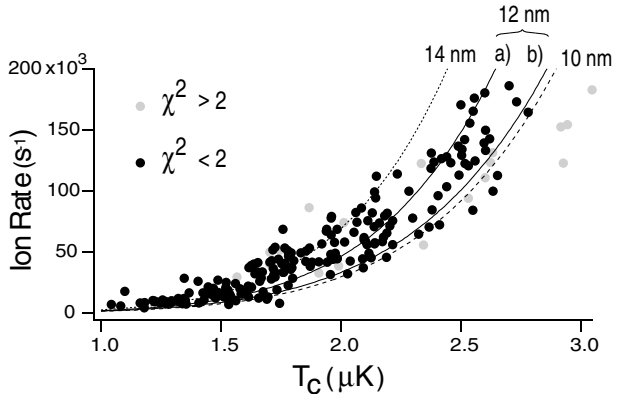

FIG. 3. Ion rate versus critical temperature. The points correspond to the results of 280 runs for which the ion rate was deemed sufficiently close to the condensation threshold. Gray indicates runs for which χ^2 in the TOF fits was above 2. The dashed line is the theoretical estimate for $a = 10$ nm, the dotted line for $a = 14$ nm [both including interaction corrections of Eq. (4)]. The two solid lines correspond to $a = 12$ nm, (*a*) with interactions and (*b*) without interactions, and illustrate the size of their effect.

of a. The uncertainty in the ion detection efficiency also contributes to the uncertainty in the rate constants. As discussed in Ref. [11], we will assume $\alpha = 0.42$ to get the central values of the rate constants. We will include a one-sided contribution to the error bars to account for the possibility, also discussed in [11], that α could be a factor of 2 smaller. We finally get $\beta = 0.9^{+1.7}_{-0.8} \times 10^{-14}$ cm^3/s and $L = 2.5^{+4.5}_{-1.7} \times 10^{-27}$ cm^6/s. The rate constants are in good agreement with theoretical predictions [8,18].

As shown in Fig. 3, curves *a* and *b*, our value of a is significantly shifted by the nonideal gas corrections of Eq. (4). Thus, when an independent measurement of the scattering length becomes available, our results can be used as a test of these corrections [19]. Note, however, that corrections to the critical temperature beyond mean-field theory [20] are small when one parametrizes the critical point in terms of an average density [13]. But an examination of the critical density measured in a local way, by imaging the ions from a cloud, for example, is sensitive to critical fluctuation phenomena which go beyond mean-field theory similar to the homogenous case [20]. Thus, refinements of the ionization measurements described here promise to continue to provide new tests of BEC physics.

This work is supported by EU Grants No. IST-2001-38863 and No. HPRN-CT-2000-00125 and by the INTAS Project No. 01-0855. S. S. is supported by the Danish Research Agency and J. V. G. by the Portuguese Foundation for Science and Technology.

*Permanent address: Departamento de Fisica, Universidade do Minho, Campus de Gualtar, 4710-057 Braga, Portugal.

[1] F. Dalfovo, S. Giorgini, L. P. Pitaevskii, and S. Stringari, Rev. Mod. Phys. **71**, 463 (1999).
[2] F. Gerbier, J. H. Thywissen, S. Richard, M. Hugbart, P. Bouyer, and A. Aspect, Phys. Rev. Lett. **92**, 030405 (2004).
[3] J. R. Ensher, D. S. Jin, M. R. Matthews, C. E. Wiemann, and E. A. Cornell, Phys. Rev. Lett. **77**, 4984 (1996).
[4] A. Robert, O. Sirjean, A. Browaeys, J. Poupard, S. Nowak, D. Boiron, C. I. Westbrook, and A. Aspect, Science **292**, 461 (2001).
[5] F. Pereira Dos Santos, J. Léonard, Junmin Wang, C. J. Barrelet, F. Perales, E. Rasel, C. S. Unnikrishnan, M. Leduc, and C. Cohen-Tannoudji, Phys. Rev. Lett. **86**, 3459 (2001).
[6] M. Leduc, J. Léonard, F. P. Dos Santos, E. Jahier, S. Schwarz, and C. Cohen-Tannoudji, Acta Phys. Pol. B **33**, 2213 (2002).
[7] A. S. Dickinson, F. X. Gadéa, and T. Leininger, J. Phys. B **37**, 587 (2004).
[8] P. Leo, V. Venturi, I. Whittingham, and J. Babb, Phys. Rev. A **64**, 042710 (2001).
[9] P. J. J. Tol, W. Hogervorst, and W. Vassen, Phys. Rev. A **70**, 013404 (2004).
[10] S. Seidelin, O. Sirjean, J. Viana Gomes, D. Boiron, C. I. Westbrook, and A. Aspect, J. Opt. B **5**, 112 (2003).
[11] O. Sirjean, S. Seidelin, J. Viana Gomes, D. Boiron, C. I. Westbrook, A. Aspect, and G. V. Shlyapnikov, Phys. Rev. Lett. **89**, 220406 (2002).
[12] S. Giorgini, L. P. Pitaevskii, and S. Stringari, Phys. Rev. A **54**, R4633 (1996).
[13] P. Arnold and B. Tomàšik, Phys. Rev. A **64**, 053609 (2001).
[14] O. Sirjean, Ph.D. thesis, Université Paris XI, 2003, available at http://tel.ccsd.cnrs.fr/documents/archives0/00/00/30/88
[15] P. Pedri, D. Guéry-Odelin, and S. Stringari, Phys. Rev. A **68**, 043608 (2003).
[16] G. M. Kavoulakis, C. J. Pethick, and H. Smith, Phys. Rev. A **61**, 053603 (2000).
[17] J. Stärck and W. Meyer, Chem. Phys. Lett. **225**, 229 (1994).
[18] G. V. Shlyapnikov, J. T. M. Walraven, U. M. Rahmanov, and M. W. Reynolds, Phys. Rev. Lett. **73**, 3247 (1994); P. O. Fedichev, M. W. Reynolds, and G. V. Shlyapnikov, Phys. Rev. Lett. **77**, 2921 (1996); P. F. Bedaque, E. Braaten, and H. W. Hammer, Phys. Rev. Lett. **85**, 908 (2000).
[19] A measurement using photoassociation spectroscopy is in progress at the Ecole Normale Supérieure in Paris [M. Leduc (private communication)].
[20] M. Holzmann, J. N. Fuchs, G. Baym, J. P. Blaizot, and F. Laloë, C. R. Phys. **5**, 21 (2004); N. Prokof'ev, O. Ruebenacker, and B. Svistunov, Phys. Rev. A **69**, 053625 (2004), and references therein.

overexpressed oncogene by QPCR in prostate cancer, with 72.0% of cases overexpressing *ERG* (*21*). By using a combination of assays, we found evidence of fusion with *TMPRSS2* in 20 of 22 (>90%) cases that overexpressed *ERG* or *ETV1*, suggesting that the fusion is the most likely cause for the overexpression. FISH analysis on a set of 29 prostate cancer cases selected independently of any knowledge of *ERG* or *ETV1* expression indicates that 23 of 29 (79%) had *TMPRSS2:ETV1* fusions or *ERG* rearrangement. It is possible that this cohort is not representative of all prostate cancer samples and that this may be an overestimate of the prevalence of *TMPRSS2* fusions with ETS family members, because our split-signal approach can detect additional rearrangements involving *ERG*. However, the reported frequencies of *ERG* or *ETV1* overexpression in prostate cancer with our fusion transcript and FISH results suggest that *TMPRSS2* fusions with *ETV1* or *ERG* occur in the majority of prostate cancer cases. Coupled with the high incidence of prostate cancer [an estimated 232,090 new cases will be diagnosed in the United States in 2005 (*22*)], the *TMPRSS2* fusion with ETS family members is likely to be the most common rearrangement yet identified in human malignancies and the only rearrangement present in the majority of one of the most prevalent carcinomas.

Future efforts will be directed at characterizing the expressed protein products, including the effects of N-terminal truncation of ERG and ETV1, and identifying downstream targets and the functional role of the fusions in prostate cancer development. Importantly, the existence of *TMPRSS2* fusions with ETS family members in prostate cancer suggests that causal gene rearrangements may exist in common epithelial cancers but may be masked by the multiple nonspecific chromosomal rearrangements that occur during tumor progression.

References and Notes

1. J. D. Rowley, *Nat. Rev. Cancer* **1**, 245 (2001).
2. T. H. Rabbitts, *Nature* **372**, 143 (1994).
3. J. D. Rowley, *Nature* **243**, 290 (1973).
4. A. de Klein *et al.*, *Nature* **300**, 765 (1982).
5. M. Deininger, E. Buchdunger, B. J. Druker, *Blood* **105**, 2640 (2005).
6. F. Mitelman, *Mutat. Res.* **462**, 247 (2000).
7. Materials and methods are available as supporting material on *Science* Online.
8. D. R. Rhodes *et al.*, *Neoplasia* **6**, 1 (2004).
9. P. A. Futreal *et al.*, *Nat. Rev. Cancer* **4**, 177 (2004).
10. Detailed results from the application of COPA to Oncomine data sets can be explored at www.oncomine.org.
11. T. Oikawa, T. Yamada, *Gene* **303**, 11 (2003).
12. T. Hsu, M. Trojanowska, D. K. Watson, *J. Cell. Biochem.* **91**, 896 (2004).
13. I. S. Jeon *et al.*, *Oncogene* **10**, 1229 (1995).
14. P. H. Sorensen *et al.*, *Nat. Genet.* **6**, 146 (1994).
15. J. Lapointe *et al.*, *Proc. Natl. Acad. Sci. U.S.A.* **101**, 811 (2004).
16. G. V. Glinsky, A. B. Glinskii, A. J. Stephenson, R. M. Hoffman, W. L. Gerald, *J. Clin. Invest.* **113**, 913 (2004).
17. R. Fonseca *et al.*, *Cancer Res.* **64**, 1546 (2004).
18. B. Lin *et al.*, *Cancer Res.* **59**, 4180 (1999).
19. D. E. Afar *et al.*, *Cancer Res.* **61**, 1686 (2001).
20. E. Jacquinet *et al.*, *Eur. J. Biochem.* **268**, 2687 (2001).
21. G. Petrovics *et al.*, *Oncogene* **24**, 3847 (2005).
22. A. Jemal *et al.*, *CA Cancer J. Clin.* **55**, 10 (2005).
23. P. J. Valk *et al.*, *N. Engl. J. Med.* **350**, 1617 (2004).
24. J. R. Vasselli *et al.*, *Proc. Natl. Acad. Sci. U.S.A.* **100**, 6958 (2003).
25. M. E. Ross *et al.*, *Blood* **102**, 2951 (2003).
26. E. Tian *et al.*, *N. Engl. J. Med.* **349**, 2483 (2003).
27. S. M. Dhanasekaran *et al.*, *FASEB J.* **19**, 243 (2005).
28. J. B. Welsh *et al.*, *Cancer Res.* **61**, 5974 (2001).
29. F. Zhan *et al.*, *Blood* **99**, 1745 (2002).
30. S. M. Dhanasekaran *et al.*, *Nature* **412**, 822 (2001).
31. E. Huang *et al.*, *Lancet* **361**, 1590 (2003).
32. C. Sotiriou *et al.*, *Proc. Natl. Acad. Sci. U.S.A.* **100**, 10393 (2003).
33. T. O. Nielsen *et al.*, *Lancet* **359**, 1301 (2002).
34. Y. P. Yu *et al.*, *J. Clin. Oncol.* **22**, 2790 (2004).

35. We thank D. Roulston and E. Fearon for helpful discussions, D. Robins and K. Burnstein for the PC3+AR cells, and R. Desphande and C. Creighton for technical assistance. Supported by the Early Detection Research Network Biomarker Developmental Lab UO1 CA111275-01 (to A.M.C.); NIH Prostate specialized program of research excellence (SPORE) P50CA69568 (to K.J.P), RO1 CA97063 (to A.M.C.), and R01AG21404 (to M.A.R.); American Cancer Society RSG-02-179-MGO (to A.M.C.); Department of Defense (PC040517 to R.M. and PC020322 to A.M.C.); and the Cancer Center Bioinformatics Core (support grant 5P30 CA46592). D.R.R. is supported by the Cancer Biology Training Program. K.J.P. is an American Cancer Society Clinical Research Professor. A.M.C. is a Pew Biomedical Scholar, and S.A.T. and D.R.R. are Fellows of the Medical Scientist Training Program. Nucleotide sequences for the *TMPRSS2:ETS* fusions have been deposited at GenBank with accession numbers DQ204770 to DQ04773.

Supporting Online Material

www.sciencemag.org/cgi/content/full/310/5748/644/DC1
Materials and Methods
Figs. S1 to S8
Tables S1 and S2

20 July 2005; accepted 22 September 2005
10.1126/science.1117679

REPORTS

Hanbury Brown Twiss Effect for Ultracold Quantum Gases

M. Schellekens,[1] R. Hoppeler,[1] A. Perrin,[1] J. Viana Gomes,[1,2] D. Boiron,[1] A. Aspect,[1] C. I. Westbrook[1]*

We have studied two-body correlations of atoms in an expanding cloud above and below the Bose-Einstein condensation threshold. The observed correlation function for a thermal cloud shows a bunching behavior, whereas the correlation is flat for a coherent sample. These quantum correlations are the atomic analog of the Hanbury Brown Twiss effect. We observed the effect in three dimensions and studied its dependence on cloud size.

Nearly half a century ago, Hanbury Brown and Twiss (HBT) performed a landmark experiment on light from a gaseous discharge (*1*). The experiment demonstrated strong correlations in the intensity fluctuations at two nearby points in space despite the random or chaotic nature of the source. Although the effect was easily understood in the context of classical statistical wave optics, the result was surprising when viewed in terms of the quantum theory. It implied that photons coming from widely separated points in a source such as a star were "bunched." On the other hand, photons in a laser were not bunched (*2*, *3*). The quest to understand the observations stimulated the birth of modern quantum optics (*4*). The HBT effect has since found applications in many other fields from particle physics (*5*) to fluid dynamics (*6*).

Atom or photon bunching can be understood as a two-particle interference effect (*7*). Experimentally, one measures the joint probability for two particles emitted from two separated source points, A and B, to be detected at two detection points, C and D. One must consider the quantum mechanical amplitude for the process $A \rightarrow C$ and $B \rightarrow D$ as well as that for $A \rightarrow D$ and $B \rightarrow C$. If the two processes are indistinguishable, the amplitudes interfere. For bosons, the interference is constructive, resulting in a joint detection probability that is enhanced compared with that of two statistically independent detection events, whereas for fermions the joint probability is lowered. As the detector separation is increased, the phase difference between the two amplitudes grows large enough that an average over all possible source points A and B washes out the interference, and one recovers the sit-

[1]Laboratoire Charles Fabry de l'Institut d'Optique, UMR 8501 du CNRS, Centre Scientifique d'Orsay, Bâtiment 503, 91403 Orsay CEDEX, France. [2]Departimento de Fisica, Universidade do Minho, 4710-057 Braga, Portugal.

*To whom correspondence should be addressed. E-mail: christoph.westbrook@iota.u-psud.fr

uation for uncorrelated detection events. This fact was used by HBT to measure the angular size of a star (*8*), but another major consequence of the observation was to draw attention to the importance of two-photon amplitudes and how their interference can lead to surprising effects. These quantum amplitudes must not be confused with classical electromagnetic field amplitudes (*3*). Two-photon states subsequently led to many other striking examples of "quantum weirdness" (*9*). In contrast to a chaotic source, all photons in a single mode laser are in the same quantum state. Hence, there is only one physical process and no bunching effect. A similar effect is expected for atoms in a Bose-Einstein condensate (BEC).

Two-particle correlations have been observed both for cold neutral atoms (*10–12*) and for electrons (*13–15*), and three-particle correlations (*16–18*) at zero distance have also been used to study atomic gases. But the full three-dimensional effect and its dependence on the size and degeneracy of a sample has yet to be demonstrated for massive particles. Here, we demonstrate the effect for a trapped cloud of atoms close to the BEC transition temperature released onto a detector capable of individual particle detection. We extract, for varying cloud sizes, a three-dimensional picture of the correlations between identical particles produced by quantum interference. We also show that a BEC shows no such correlations. The results are in agreement with an ideal gas model and show the power of single particle detection techniques applied to the study of degenerate quantum gases.

The calculation of the phase difference of the possible two-particle detection amplitudes given in (*7*) can be adapted to the case of particles of mass m traveling to a detector in a time t. One can show that the correlation length observed at the detectors, that is, the typical detector separation for which interference survives, is $l_i = \frac{\hbar t}{m s_i}$, where s_i is the source size along the direction i, $\hbar$ is the reduced Planck's constant, and we have assumed that the size of the cloud at the detector is much larger than the initial size. The optical analog of this expression, for a source of size s and wavelength λ at a distance L from the observation plane, is $l = L\lambda/2\pi s$. This is the length scale of the associated speckle pattern. The formula can be recovered for the case of atoms traveling at constant velocity v toward a detector at distance L if one identifies h/mv with the deBroglie wavelength corresponding to velocity v. The formula we give is also valid for atoms accelerated by gravity, and the interpretation of l as the atomic speckle size remains valid. A pioneering experiment on atom correlations used a continuous beam of atoms (*10*). For a continuous beam, the correlation time, or equivalently, the longitudinal correlation length, depends on the velocity width of the source and not on the source size. Thus, the longitudinal and transverse directions are qualitatively different. By contrast, our measurements are performed on a cloud of atoms released suddenly from a magnetic trap. In this case, the three dimensions can all be treated equivalently, and the relation above applies in all three. Because the trap is anisotropic, the correlation function is as well, with an inverted ellipticity. Our sample is a magnetically trapped cloud of metastable helium atoms evaporatively cooled close to the BEC transition temperature (*19*) (about 0.5 μK for our conditions). Our source is thus very small, and together with a long time of flight (308 ms) and helium's small mass, we achieve a large speckle size or correlation volume (30 μm by 800 μm by 800 μm), which simplifies the detection problem. For example, the observations are much less sensitive to the tilt of the detector than in (*10*).

To detect the atoms, we use an 8-cm-diameter microchannel plate detector (MCP). It is placed 47 cm below the center of the magnetic trap. A delay line anode permits position-sensitive detection of individual particles in the plane of the detector (*20*) (Fig. 1). Atoms are released from the trap by suddenly turning off the magnetic field. About 10% of these atoms are transferred to the magnetic field–insensitive $m = 0$ state by nonadiabatic transitions (*19*) and fall freely to the detector. The remaining atoms are removed by applying additional magnetic field gradients during the time of flight. For each detected atom, we record the in-plane coordinates x and y and the time of detection t. The atoms hit the detector at 3 m/s with a velocity spread below 1%, and so we convert t into a vertical position z. The observed root mean square (rms) resolution is $d \sim 250$ μm in x and y and 2 nm in z. These data allow us to construct a three-dimensional histogram of pair separations (Δx, Δy, and Δz) for all particles detected in a single cloud. The histograms are summed over the entire atomic distribution and over many shots, typically 1000 (*21*).

Because of our good resolution along z, we begin by concentrating on the correlation function along this axis. Normalized correlation functions for various experimental conditions are shown in Fig. 2A. To compute the normalized correlation function, we divide the pair separation histogram by the autoconvolution of the average single particle distribution along z. We also normalize the correlation function to unity for large separations. This amounts to dividing, for each elementary pixel of our detector, the joint detection probability by the product of the individual detection probabilities at the two pixels. This gives us the usual normalized correlation function $g^{(2)}(\Delta x = 0, \Delta y = 0, \Delta z)$. The HBT bunching effect corresponds to the bump in the top three graphs of Fig. 2A. The fourth graph shows the result for a BEC. No correlation is observed. [A detector saturation effect in the BEC data required a modified analysis procedure (*21*).] We have also recorded data for a cloud with a 2-mm radius and 1-mK temperature for which the correlation length is so small that the bunching effect is washed out by the in-plane detector resolution. Experimentally, the normalized correlation function in this case is indeed flat to within less than 1%.

We plot (Fig. 2B) the normalized correlation functions in the $\Delta x - \Delta y$ plane and for $\Delta z = 0$ for the same three data sets. The data in Fig. 2B show the asymmetry in the correlation function arising from the difference in the two transverse dimensions of the trapped cloud. The long axis of the correlation function is orthogonal to that of the magnetic trap.

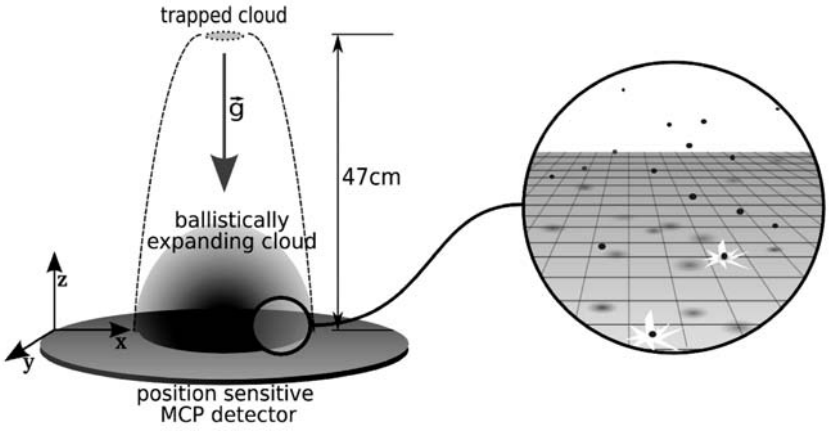

Fig. 1. Schematic of the apparatus. The trapped cloud has a cylindrical symmetry with oscillation frequencies of $\omega_x/2\pi = 47$ Hz and $\omega_y/2\pi = \omega_z/2\pi = 1150$ Hz. During its free fall toward the detector, a thermal cloud acquires a spherical shape. A 1-μK temperature yields a cloud with an rms radius of about 3 cm at the detector. Single particle detection of the neutral atoms is possible because of each atom's 20-eV internal energy that is released at contact with the MCP. Position sensitivity is obtained through a delay-line anode at the rear side of the MCP.

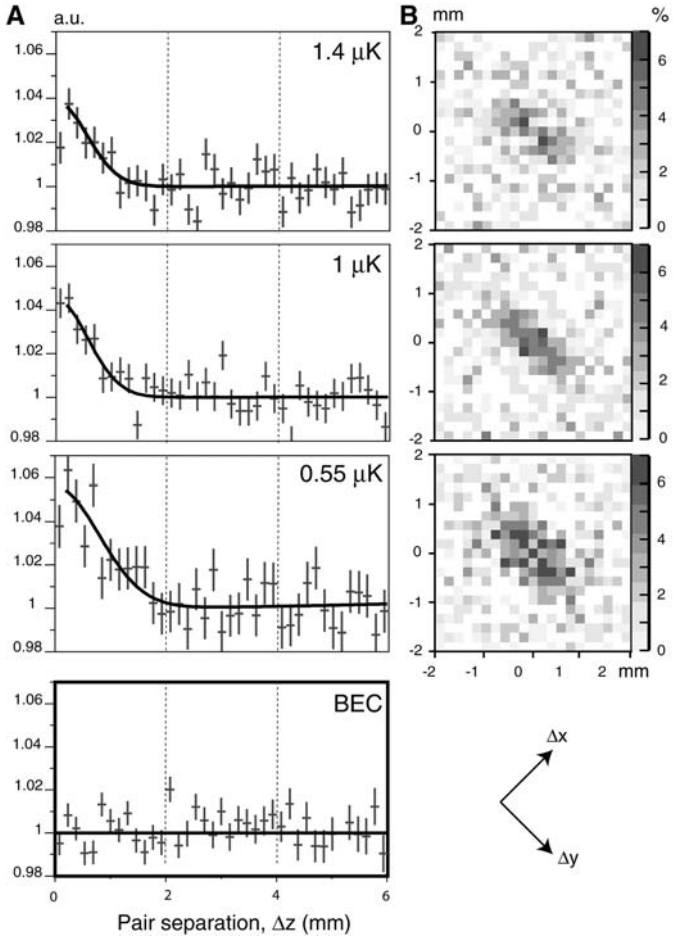

Fig. 2. (**A**) Normalized correlation functions along the vertical (*z*) axis for thermal gases at three different temperatures and for a BEC. For the thermal clouds, each plot corresponds to the average of a large number of clouds at the same temperature. Error bars correspond to the square root of the number of pairs. a.u., arbitrary units. (**B**) Normalized correlation functions in the $\Delta x - \Delta y$ plane for the three thermal gas runs. The arrows at the bottom show the 45° rotation of our coordinate system with respect to the axes of the detector. The inverted ellipticity of the correlation function relative to the trapped cloud is visible.

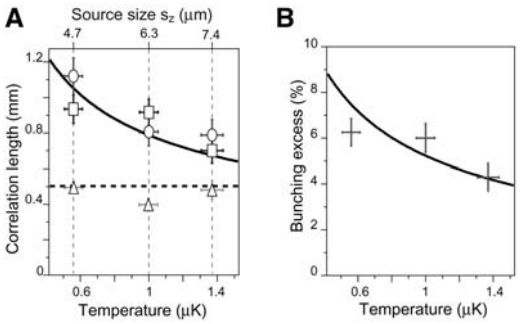

Fig. 3. Results of fits to the data in Fig. 2, A and B. (**A**) Fitted correlation lengths l_x, l_y, and l_z along the three axes (triangles, squares, and circles) as a function of temperature. The upper axis shows the corresponding source size s_z. Vertical error bars are from the fits. Horizontal error bars correspond to the standard deviation of the measured temperature. Along the *x* axis, the measurement is entirely limited by the detector resolution. The dotted horizontal line is the result of an independent estimate of the resolution. The result for the *y* axis has been corrected for the finite detector resolution as characterized by the fitted value of l_x. The *z* axis suffers from no such resolution limit. The solid curve corresponds to $\hbar t/ms_z$. (**B**) Fitted contrast η of the correlation function for the three temperatures used. The solid line corresponds to the same noninteracting gas model as the line in (A) (*21*) and includes the finite detector resolution.

We expect the experimental normalized correlation function for a thermal bosonic gas to be described by

$$g^{(2)}_{\mathrm{th}}(\Delta x, \Delta y, \Delta z) = 1 + \eta \exp\left(-\left[\left(\frac{\Delta x}{l_x}\right)^2 + \left(\frac{\Delta y}{l_y}\right)^2 + \left(\frac{\Delta z}{l_z}\right)^2\right]\right) \quad (1)$$

We have assumed here that the gas is noninteracting and that the velocity and density distribution remain roughly Gaussian even close to the BEC transition temperature. Numerical simulations indicate that this is a good approximation when the correlation function is averaged over the entire cloud (*22*). As discussed above, the correlation lengths should be inversely proportional to the sizes, s_i, of the sample. In a harmonic trap with trapping frequency ω_i along the *i* direction, one has $s_i = \sqrt{\frac{k_B T}{m\omega_i^2}}$, where k_B is Boltzmann's constant and *T* is the temperature of the atoms. Because *T* is derived directly from the time of flight spectrum, we shall plot our data as a function of *T* rather than of *s*. The parameter η would be unity for a detector whose resolution width *d* is small compared with the correlation length. Our *d* is smaller than l_y but larger than l_x, and in this case the convolution by the detector resolution results in an η given roughly by $l_x/2d \sim 5\%$. We use Eq. 1 to fit the data by using η and the l_i as fit parameters and compare the results to the ideal gas model (*21*).

The results for l_x, l_y, and l_z for our three temperatures are plotted in Fig. 3A. The fitted values of l_x are ~450 μm and are determined by the detector resolution rather than the true coherence length along *x*. The value of l_y has been corrected for the finite spatial resolution of the detector. The fitted value of l_z requires no correction, because in the vertical direction the resolution of the detector is much better. l_y and l_z are consistent and agree with the prediction using the known trap frequencies and temperatures. Figure 3B shows the fitted value of η versus temperature, along with the prediction of the same ideal gas model as in Fig. 3A, using the measured detector resolution. The data are in reasonable agreement with the model, although we may be seeing too little contrast at the lowest temperature. The run at 0.55 μK was above, but very close to, the BEC transition temperature. (We know this because, when taking data at 0.55 μK, about one-third of the shots contained small BECs; these runs were eliminated before plotting Fig. 2.) Future work will include examining whether the effect of the repulsive interactions between atoms or finite atom number must be taken into account.

The results reported here show the power of single particle detection in the study of quantum gases. The correlations we have observed are among the simplest that should be present. Two recent experiments have shown correlations in a Mott insulator (*11*) as well as in atoms produced from the breakup of molecules near a Feshbach resonance (*12*). Improved observations of these effects may be possible with individual particle detection. Other atom pair production mechanisms, such as four-wave mixing (*23*, *24*), can be investigated. A fermionic analog to this experiment using ^{3}He would also be (*25*) of great interest.

References and Notes

1. R. Hanbury Brown, R. Q. Twiss, *Nature* **177**, 27 (1956).
2. F. T. Arecchi, E. Gatti, A. Sona, *Phys. Lett.* **20**, 27 (1966).
3. R. J. Glauber, *Phys. Rev. Lett.* **10**, 84 (1963).
4. R. J. Glauber, *Quantum Optics and Electronics*, C. DeWitt, A. Blandin, C. Cohen-Tannoudji, Eds. (Gordon and Breach, New York, 1965), p. 63.
5. G. Baym, *Acta Phys. Pol. B* **29**, 1839 (1998).
6. B. Berne, R. Pecora, *Dynamic Light Scattering* (Dover, New York, 2000).
7. U. Fano, *Am. J. Phys.* **29**, 539 (1961).
8. R. Hanbury Brown, R. Twiss, *Nature* **178**, 1046 (1956).
9. J. S. Bell, *Speakable and Unspeakable in Quantum Mechanics* (Cambridge Univ. Press, Cambridge, ed. 2, 2004).
10. M. Yasuda, F. Shimizu, *Phys. Rev. Lett.* **77**, 3090 (1996).
11. S. Fölling *et al.*, *Nature* **434**, 481 (2005).

12. M. Greiner, C. A. Regal, J. T. Stewart, D. S. Jin, *Phys. Rev. Lett.* **94**, 110401 (2005).
13. M. Henny *et al.*, *Science* **284**, 296 (1999).
14. W. D. Oliver, J. Kim, R. C. Liu, Y. Yamamoto, *Science* **284**, 299 (1999).
15. H. Kiesel, A. Renz, F. Hasselbach, *Nature* **418**, 392 (2002).
16. Y. Kagan, B. V. Svistunov, G. V. Shlyapnikov, *Sov. Phys. JETP* **42**, 209 (1985).
17. E. A. Burt *et al.*, *Phys. Rev. Lett.* **79**, 337 (1997).
18. B. Laburthe Tolra *et al.*, *Phys. Rev. Lett.* **92**, 190401 (2004).
19. A. Robert *et al.*, *Science* **292**, 461 (2001); published online 22 March 2001 (10.1126/science.1060622).
20. O. Jagutzki *et al.*, *Nucl. Instrum. Methods Phys. Res. A* **477**, 244 (2004).
21. See supporting online materials on *Science* Online for details.
22. M. Naraschewski, R. Glauber, *Phys. Rev. A* **59**, 4595 (1999).
23. L. Deng *et al.*, *Nature* **398**, 218 (1999).
24. J. Vogels, K. Xu, W. Ketterle, *Phys. Rev. Lett.* **89**, 020401 (2002).
25. R. Stas, J. McNamara, W. Hogervorst, W. Vassen, *Phys. Rev. Lett.* **93**, 053001 (2004).
26. A. Öttl, S. Ritter, M. Köhl, T. Esslinger, *Phys. Rev. Lett.* **95**, 090404 (2005).
27. After submission of this manuscript, we became aware of a related experiment concerning atom correlations in an atom laser (*26*). We thank R. Sellem of the Détection Temps, Position Image Technology Division (supported by the Mission Ressources et Compétences Technologiques–CNRS Federation FR2764 and by the Université Paris-Sud) for a decisive role in the development of the time-to-digital converter, and O. Jagutzki for advice on delay lines.

Supporting Online Material
www.sciencemag.org/cgi/content/full/1118024/DC1
SOM Text

27 July 2005; accepted 5 September 2005
Published online 15 September 2005;
10.1126/science.1118024
Include this information when citing this paper.

Quantum Coherence in an Optical Modulator

S. G. Carter,[1]* V. Birkedal,[1]† C. S. Wang,[2] L. A. Coldren,[2] A. V. Maslov,[3] D. S. Citrin,[4,5] M. S. Sherwin[1]‡

Semiconductor quantum well electroabsorption modulators are widely used to modulate near-infrared (NIR) radiation at frequencies below 0.1 terahertz (THz). Here, the NIR absorption of undoped quantum wells was modulated by strong electric fields with frequencies between 1.5 and 3.9 THz. The THz field coupled two excited states (excitons) of the quantum wells, as manifested by a new THz frequency- and power-dependent NIR absorption line. Nonperturbative theory and experiment indicate that the THz field generated a coherent quantum superposition of an absorbing and a nonabsorbing exciton. This quantum coherence may yield new applications for quantum well modulators in optical communications.

Quantum three-state systems in which two of the states are strongly coupled by an intense laser field have been widely studied in atomic and molecular systems (*1*). The energies of the quantum states are altered as they are "dressed" by the strong light-matter interaction. Such dressed states were first observed by Autler and Townes (AT) in a molecular system driven by a strong radio-frequency field and probed by weak microwaves (*2*). When a radio-frequency resonance occurred, the microwave absorption line split in two. In three-state systems with weak coupling to the environment, AT splitting can evolve into electromagnetically induced transparency (EIT), in which a strong coupling beam induces transparency at a resonance at which the undriven system is opaque (*3*). This transparency is due to quantum interference between the dressed states. EIT is the basis for slow (*4*) and stopped light (*5*, *6*) in atomic systems.

A variety of quantum systems similar to atomic three-state systems can be engineered in semiconductor quantum wells (QWs). A QW is a layer of one semiconductor grown between semiconductors with larger band gaps (*7*). The layer with the smaller gap is sufficiently thin that well-defined sets of quantized states, or subbands, are associated with electron motion parallel to the growth direction. Within each subband, there is a continuum of states associated with different momenta parallel to the plane of the QW (perpendicular to the growth direction). AT-like splitting (*8*), quantum interference (*9*, *10*), and EIT (*11*, *12*) have been reported in QWs, but their observation has been more difficult than in atoms and molecules. This is in part because of much larger absorption linewidths, which result from disorder, from stronger coupling to the environment, or from scattering between subbands.

We have fabricated a particularly simple three-level system in undoped QWs (Fig. 1). The excitation with the lowest frequency occurs at about 350 THz (wavelength 857 nm or energy 1.46 eV) when an electron is promoted from the filled valence subband of highest energy (labeled h1) to the empty conduction subband of lowest energy (labeled e1). The excited electron binds with the hole it left behind to form an exciton with a hydrogen-like wave function in the QW plane. Transitions between different in-plane states (e.g., the 1s and 2p states) are allowed only for in-plane THz polarizations (*13*, *14*), which are not present in the experiments discussed here. The lowest exciton state is labeled h1X. The next exciton state, h2X, consists of an electron from e1 and a hole from the second highest valence subband, h2. NIR transitions between the crystal ground state and h2X are not allowed because of quantum mechanical selection rules. However, intersubband transitions from h1X to h2X are allowed for THz radiation polarized in the growth direction. The three states analogous to those in an AT picture are the crystal ground state, the lowest exciton h1X, and the second exciton h2X (*15*).

This report explores the NIR absorption of undoped QWs at low temperatures (~10 K) when they are driven by strong electric fields polarized in the growth direction with frequencies between 1.5 and 3.9 THz. Because the frequency of the THz laser is about 1% of that required to create an exciton, the strong laser field does not alter the populations of the quantum states of the system. Near 3.4 THz, the drive frequency is resonant with the transition between the two lowest exciton states. The AT splitting of excitons driven by strong intersubband radiation is experimentally observed, and theoretical predictions (*16*, *17*) are confirmed.

The sample consists of 10 $In_{0.06}Ga_{0.94}As$ QWs (each 143 Å) separated by $Al_{0.3}Ga_{0.7}As$ barriers (300 Å). InGaAs QWs were used instead of GaAs QWs so that the GaAs substrate was transparent for NIR light near the exciton energies. A 100-nm layer of aluminum was deposited on the surface of the sample on which the QWs were grown. The metallic boundary condition improved THz coupling and ensured that the THz field at the QWs was polarized almost perfectly in the growth direction (*18*). The interband absorption was probed using broadband, incoherent, NIR light from an 850-nm light-emitting diode focused onto the sample backside to a spot size ~250 μm in diameter. The NIR intensity was less than 0.3 W/cm^2. As illustrated in Fig. 1, the NIR beam was transmitted through the transparent substrate, interacted with the QWs, was reflected off of the Al layer, and was then collected and sent to a monochromator with an intensified charge-coupled device detector. The reflected NIR beam was measured during the 1 to 1.5 μs at the peak of the THz

[1]Physics Department and Institute for Quantum and Complex Dynamics (iQCD), Broida Hall Building 572, Room 3410, [2]Electrical and Computer Engineering Department, University of California, Santa Barbara, CA 93106, USA. [3]Center for Nanotechnology, NASA Ames Research Center, MS 229-1, Moffett Field, CA 94035, USA. [4]Electrical and Computer Engineering, Georgia Institute of Technology, Atlanta, GA 30332, USA. [5]Georgia Tech Lorraine, Metz Technopole, 2-3 rue Marconi, 57070 Metz, France.

*Present address: JILA, University of Colorado, 440 UCB, Boulder, CO 80309, USA.
†née Ciulin. Present address: Department of Chemistry, University of Aarhus, Langelandsgade 140, DK-8000 Århus C, Denmark.
‡To whom correspondence should be addressed. E-mail: sherwin@physics.ucsb.edu

EPJ D proofs
(will be inserted by the editor)

Atomic density of a harmonically trapped ideal gas near Bose-Einstein transition temperature

R. Hoppeler[1], J. Viana Gomes[1,a], and D. Boiron[1,b]

Laboratoire Charles Fabry de l'Institut d'Optique, UMR 8501 du CNRS, 91403 Orsay Cedex, France

Received 19 August 2005 / Received in final form 20 May 2006
Published online (Inserted Later) – © EDP Sciences, Società Italiana di Fisica, Springer-Verlag 2006

Abstract. We have studied the atomic density of a cloud confined in an isotropic harmonic trap at the vicinity of the Bose-Einstein transition temperature. We show that, for a non-interacting gas and near this temperature, the ground-state density has the same order of magnitude as the excited states density at the centre of the trap. This holds in a range of temperatures where the ground-state population is negligible compared to the total atom number. We compare the exact calculations, available in a harmonic trap, to semi-classical approximations. We show that these latter should include the ground-state contribution to be accurate.

PACS. 03.75.Hh Static properties of condensates; thermodynamical, statistical, and structural properties – 03.65.Sq Semiclassical theories and applications – 05.30.Jp Boson systems

The phenomenon of Bose-Einstein condensation (BEC) is a phase transition. Below the critical temperature T_c, the ground-state population, which is the order parameter, becomes macroscopic. This phenomenon, that happens strictly speaking only at the thermodynamic limit, is usually illustrated in textbooks with a homogeneous gas. Experimentally, the Bose-Einstein condensation of dilute gases has been observed since 1995 with atoms confined in a harmonic trap [1]. These stimulating experimental data have quickly pointed out that two effects had to be taken into account: the interatomic interactions and the finite number of atoms [2]. Several papers, as the present one, have studied harmonically trapped ideal gases containing a finite number of atoms. Two quantities have been investigated in detail: the atom number [3,4,6–9] and the specific heat [5,7,9]. For a finite but large (typically 10^6) number of atoms, the properties of the atomic cloud change abruptly at a characteristic temperature we will name the transition temperature T^*. This temperature is shifted compared to T_c, but by a small amount, typically of few percent for atom numbers around 10^6. There is also a characteristic temperature for the specific heat; it is different from the previous one but still close to T_c [5,9].

Surprisingly, less attention has been paid on the atomic density of an ideal gas [10]. In a homogeneous gas it is obviously equivalent to the atom number but this is no more the case in a spatially varying potential. It becomes the good parameter of the theory, in particular to perform local density approximations. This quantity is then particularly important for the study of the shift of the critical temperature by the interatomic interactions, both within the mean-field approximation [6] and beyond this approximation [11]. We will show, in the case of an isotropic harmonic trapping and for a finite atom number, that the ground-state density at the centre of the trap increases much more sharply than its population as the temperature decreases. This leads to the fact that near the Bose-Einstein transition temperature the density is already dominated by the ground-state contribution. This holds whatever the atom number is, and is a remanence of the infinite compressibility of an ideal gas at the thermodynamic limit [12]. Usual semi-classical approximations do not take into account the ground-state contribution and then fail in the vicinity of the Bose-Einstein transition temperature. This is not a finite size effect in the sense that it is not related to the discretization of the excited states energy levels. We will compare the exact results with semi-classical approximations. The addition of the ground-state contribution on the latter ones improves their accuracy. We will finally show that the influence of the ground-state is smaller if the measured quantity is the density integrated over at least one dimension. It is still large for typical experimental parameters.

We will perform our calculations in the grand canonical ensemble (GCE). Then, the Bose-Einstein distribution gives the population N_i of a given energy level ϵ_i: $N_i = (e^{\beta(\epsilon_i-\mu)}-1)^{-1}$ with $\sum_{i=0}^{\infty} N_i = N$. Here $\beta = 1/k_BT$ with

[a] *Permanent address:* Departamento de Fisica, Universidade do Minho, Campus de Gualtar, 4710-057 Braga, Portugal.
[b] e-mail: `denis.boiron@iota.u-psud.fr`

k_B the Boltzmann's constant, μ the chemical potential and N the total atom number. The equivalence between GCE and the canonical or microcanonical ensemble, these latter being probably more appropriate descriptions, is generally not guaranteed, especially for systems that are not at the thermodynamic limit. For instance, it is well-known that the GCE predicts unphysical large fluctuations of the condensate population at low temperature [13]. However, the authors of references [10,14,15] have shown that the occupation numbers N_i in GCE are very close to the ones in the canonical ensemble. The difference is more pronounced for small atom number and anisotropic clouds. As a result and because GCE enables to give analytic expressions on contrary to the other ensembles, we will use GCE in the following.

For a fixed atom number, the chemical potential increases as the temperature decreases. As μ has to be smaller than ϵ_0, the ground-state energy, the excited states population will saturate when μ approaches ϵ_0 whereas N_0 is still increasing: $N - N_0 = \sum_{i=1}^{\infty} N_i(\mu, T) \leq \sum_{i=1}^{\infty} N_i(\epsilon_0, T)$. As in references [2,16], we will define the transition temperature T^* as the temperature for which the excited states saturated population is equal to the total atom number:

$$\sum_{i=1}^{\infty} N_i(\epsilon_0, T^*) = N. \quad (1)$$

As pointed out in the introduction, there is not a unique definition of the transition temperature for a finite atom number. Other definitions use, for instance, a change in the slope for the condensate fraction in function of temperature (more explicitly $d^3(N_0/N)/dT^3 = 0$) [17], a change in the power dependence on the condensate fraction in function of the atom number [9], which are also pertinent. We have checked that these various definitions affect marginally the value of T^* and do not modify our conclusions [18]. In the following we will then use equation (1) to define T^*. Note that the chemical potential μ^* at the transition temperature is close but not equal to the ground-state energy; it is determined by the constraint

$$\sum_{i=0}^{\infty} N_i(\mu^*, T^*) = N. \quad (2)$$

There are only a few examples of trapping potentials where the eigen-energies and the eigen-functions are known exactly. Semi-classical approximations give usually accurate enough results and are suited to include interatomic interactions, at least perturbatively. We will derive various type of semi-classical approximations in the following and test their accuracy because the harmonic potential is an exactly solvable potential.

We will first examine the situation where $\hbar\omega \ll k_B T$ with ω the oscillation frequency of the isotropic harmonic trap. This corresponds to the large atom number limit and semi-classical approximations should work. Replacing the discrete energy spectrum by a continuous one and neglecting the ground-state energy ϵ_0, the density is $\rho(r) = \frac{1}{\lambda^3} g_{\frac{3}{2}}[z \exp(-\frac{\tau}{2}(r/\sigma)^2]$ with $z = e^{\beta\mu}$ the fugacity, $\tau = \hbar\omega/k_B T$ and $g_{\frac{3}{2}}(\ )$ a Bose function [19]. With the above notation, the thermal de Broglie wavelength is $\lambda = \sigma\sqrt{2\pi\tau}$ and the size of the cloud is $\sqrt{k_B T/m\omega^2} = \sigma/\sqrt{\tau}$. Similarly, the atom number is $N = g_3(z)/\tau^3$. Equation (1) leads then to $N = \zeta(3)/\tau^{*3}$, with τ^* the value of τ at $T = T^*$. The above expressions for the density and atom number are in fact approximations for the excited states and do not contain the ground-state contribution. Then μ^* defined by equation (2) is equal to 0 and $z^* = 1$. The transition temperature defined here corresponds to the critical temperature T_c. The peak density at the transition temperature is then given by $\rho(0)\lambda^3 = g_{\frac{3}{2}}(z^*) = \zeta(3/2) \approx 2.612$. For temperatures below T_c, the excited states population is given by $\zeta(3)/\tau^3$. Then, the ground-state population fraction is $N_0/N = 0$ for $T > T_c$ and $N_0/N = 1 - (T/T_c)^3$ for $T < T_c$. This fraction will be plotted in Figure 1, labelled with sc_∞.

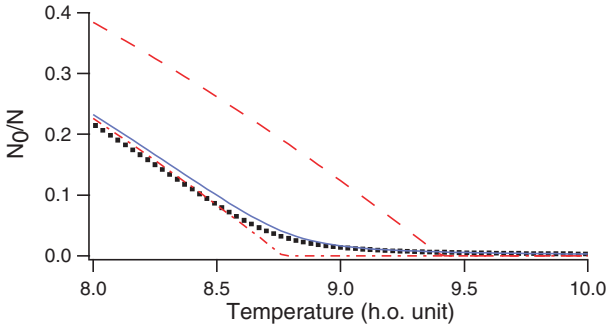

Fig. 1. Ground-state population fraction in function of the temperature in $\hbar\omega/k_B$ unit for a cloud of 10^3 atoms. The dotted curve corresponds to the exact result given by model *ex*. The solid, dot-dashed and dashed lines correspond respectively to the semi-classical models *sc*, sc_0 and sc_∞. The last two neglect the ground-state contribution above their corresponding transition temperature and the first two take into account finite size effects. The model *sc* is the closest to *ex* near Bose-Einstein transition.

These approximations are too crude and give inaccurate results for the atomic density, however. The reason is that the ground-state contribution cannot be neglected. A better expression is $\rho(r) = \frac{1}{\lambda^3} g_{\frac{3}{2}}[z e^{-\frac{\tau}{2}(r/\sigma)^2}] + \rho_0(r)$ and similarly $N = \frac{1}{\tau^3} g_3(z) + N_0$ with $\rho_0(r) = [N_0/(\sqrt{\pi}\sigma)^3] e^{-(r/\sigma)^2}$ and $N_0 = z/(1-z)$. The value of T^* is unchanged as it is defined by the excited states saturation, but z^* is now different from 1. Using $g_3(z^*) \approx \zeta(3) - \zeta(2)x^*$ with $z^* = e^{-x^*}$ ($x = \beta(\epsilon_0 - \mu) > 0$), one finds using equation (2) that $x^* \approx \tau^{*3/2}/\sqrt{\zeta(2)}$ [9]. The ground-state population is $\sim 1/x^*$ and, as expected, is vanishingly small as $\tau^* \to 0$ compared to the excited-state population $\zeta(3)/\tau^{*3}$. The ground-state peak density is $\sim 1/(\sqrt{\pi}\sigma)^3 x^*$ whereas the excited state peak density is $\zeta(3/2)/\lambda^{*3}$. As $\lambda^* = \sigma\sqrt{2\pi\tau^*}$, the two quantities have the same order of magnitude! The above high-N analysis predicts then that the degeneracy parameter at the transition temperature is $\rho(0)\lambda^3 = \zeta(3/2) + 2\sqrt{2\zeta(2)} \approx 6.24$

and not 2.612. The ground-state population is extremely small but the size of its wave-function is also extremely small compared to the atomic cloud size. For a harmonic trap both depend on the same small parameter, raised to the same power. So, even for very large atom number, the traditional criterion for BEC should be modified. This effect is linked to the pathological behaviour of the ground-state density at the thermodynamic limit, i.e. the infinite compressibility of an ideal gas [12]. This limit means $N \to \infty$ with $N\omega^3 \to$ constant. The ground-state size being $\sigma = \sqrt{\hbar/m\omega}$, the density of that state behaves as $\sqrt{N}$ below threshold and is then infinite at the thermodynamic limit whereas the density above T_c is finite.

We will now address the case of atom numbers in the accessible experimental range, 10^3–10^6. It is well-known that the transition temperature will be shifted compared to T_c [3,4,7]. A better approximation, which takes into account the ground-state energy to first order, is $\rho(r) = \frac{1}{\lambda^3}\{g_{\frac{3}{2}}[\tilde{z}(r)] + \frac{3\tau}{2} g_{\frac{1}{2}}[\tilde{z}(r)]\}$ where $\tilde{z}(r) = ze^{-\frac{\tau}{2}(r/\sigma)^2}$. Then $N = \frac{1}{\tau^3}[g_3(z) + \frac{3\tau}{2} g_2(z)]$. The corresponding transition temperature is T^*_{sc} such that $N = \frac{1}{\tau^{*3}_{sc}}[\zeta(3) + \frac{3}{2}\zeta(2)\tau^*_{sc}]$. This is the usual semi-classical approximation found in the literature. The ground-state population fraction is then $N_0/N = 0 \quad \text{for} \quad T > T^*_{sc}$ and

$$N_0/N = 1 - \left(\frac{T}{T^*_{sc}}\right)^3 \frac{\zeta(3) + \frac{3\tau}{2}\zeta(2)}{\zeta(3) + \frac{3\tau^*_{sc}}{2}\zeta(2)}$$

for $T < T^*_{sc}$. This fraction, also plotted in Figure 1, will be labelled with sc_0. Note that $g_{\frac{1}{2}}(z)$ diverges at $z = 1$ [20], meaning that this approximation is intrinsically inaccurate near the centre of the trap and near the transition temperature. This divergence is however weak, and any spatial integration would give a finite result. We can still cure this pathology by adding, as before, the ground-state contribution. We obtain then

$$\begin{cases} \rho_{sc}(r) = \dfrac{1}{\lambda^3}\{g_{\frac{3}{2}}[\tilde{z}(r)] + \dfrac{3\tau}{2} g_{\frac{1}{2}}[\tilde{z}(r)]\} + \dfrac{z}{1-z}\dfrac{e^{-(\frac{r}{\sigma})^2}}{(\sqrt{\pi}\sigma)^3} \\ N = \dfrac{1}{\tau^3}[g_3(z) + \dfrac{3}{2}\tau g_2(z)] + \dfrac{z}{1-z} \\ T^*_{sc} \text{ such that } N = \dfrac{1}{\tau^{*3}_{sc}}[\zeta(3) + \dfrac{3}{2}\zeta(2)\tau^*_{sc}] \end{cases} . \tag{3}$$

This semi-classical approximation will be labelled with sc in the following. The comparison of T^*_{sc} with the value given by the exact model (see below) can be used to check the finite size correction. Even so, this comparison is useless to check the contribution coming from the ground state since it does not depend on it (same transition temperature as sc_0).

We can now test these semi-classical approximations for a harmonically trapped gas. As we referred before, for this case, the eigen-energies and the eigen-functions are known exactly. The corresponding expressions of the atomic density and atom number [13], labelled with ex in the following, are:

$$\begin{cases} \rho_{ex}(r) = \dfrac{1}{(\sqrt{\pi}\sigma)^3}\displaystyle\sum_{l=1}^{\infty} \dfrac{z^l}{(1-e^{-2\tau l})^{3/2}}\, e^{-\tanh(\frac{\tau l}{2})(\frac{r}{\sigma})^2} \\ N = \displaystyle\sum_{l=1}^{\infty} \dfrac{z^l}{(1-e^{-\tau l})^3} \\ T^*_{ex} \text{ such that } N = \displaystyle\sum_{l=1}^{\infty}\left(\dfrac{1}{(1-e^{-\tau^*_{ex} l})^3} - 1\right) \end{cases}$$

where, here $z = e^{\beta(\mu-\epsilon_0)}$. The semi-classical model corresponds to a Taylor expansion in τ of these last expressions.

In Figure 1 we plot the ground-state population fraction in function of the temperature for the various models described above. When the number of atoms is only 10^3, finite size effects are large. The prediction of model sc_∞ is clearly wrong compared to the exact model prediction. On contrary models sc_0 and sc give a result close to the one of ex [21]. Figure 2 shows the relative deviations of T_c and T^*_{sc} from T^*_{ex} in function of the atom number. As expected the different values are similar but, as above, the model sc give a closer result to ex than sc_∞. The value T^*_{sc} deviates less than 1% for $N > 400$ and the relative shift is $\sim 10^{-4}$ for typical experimental atom numbers. This is well below actual experimental uncertainties. The thermodynamic value T_c deviates more, typically 1% but is still close to T^*_{ex} [3,4,7,9]. The discrepancy with T_c would have been more pronounced for an anisotropic trap (see below).

This two figures illustrate what is called finite size effects, the fact that the energy level spacing is not negligible compared to the temperature. What we are interested in is the role of the ground-state. For this, the transition temperature and the condensate population fraction are not the best observables. It is nevertheless already clear from Figure 1 that sc is a significant improved model to describe semi-classically a cloud near degeneracy compared to sc_0. The high-N model predicts that the ground-state influence should be much more pronounced on the peak density. We will now focus our attention on that observ-

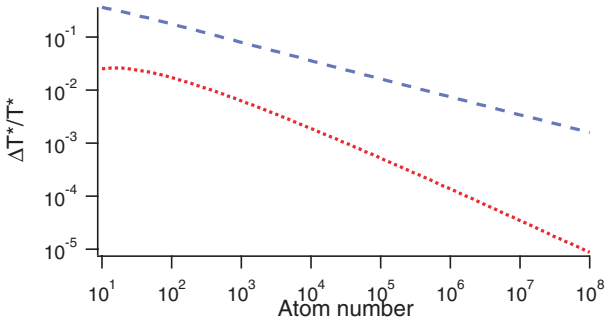

Fig. 2. Relative shift of the semi-classical transition temperatures T_c (dashed line) and T^*_{sc} (dotted line) to T^*_{ex} (see text) in function of the atom number. Both temperatures converge for high atom numbers. The critical temperature at thermodynamic limit, T_c, deviates by less than 1% for $N > 5 \times 10^5$. The semi-classical transition temperature defined for a finite atom number, T^*_{sc}, is much more accurate and deviates by less than 1% for $N > 400$.

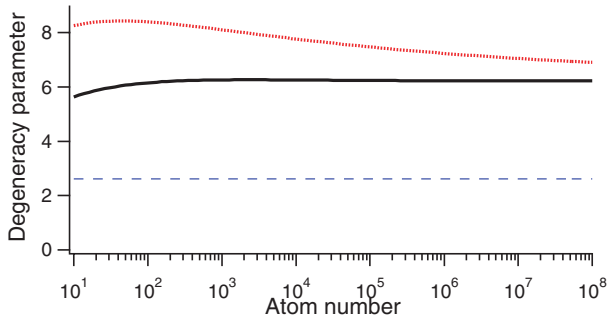

Fig. 3. Degeneracy parameter $\rho(0)\lambda^3$ in function of the atom number N for clouds at the transition temperature. The dotted line corresponds to the semi-classical model *sc* at $T = T^*_{sc}$ and the solid line to model *ex* at $T = T^*_{ex}$. Even if the degeneracy parameters are somewhat different, they both differ significantly to the usual value of 2.612 (dashed horizontal line). This deviation is due to an under-estimation of the ground-state density. The actual values are close to our high-N prediction of 6.24 (see text).

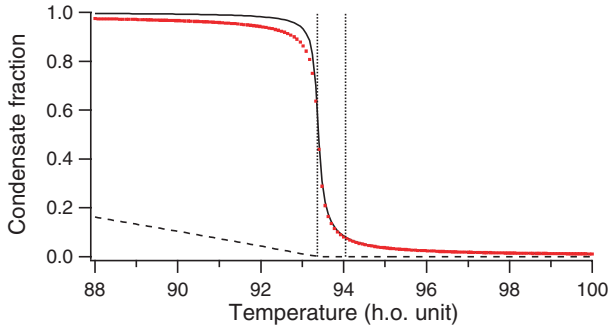

Fig. 4. Condensate atom number fraction N_0/N (dashed line) and peak density fraction $\rho_0(0)/\rho(0)$ (solid line) in function of the temperature in harmonic oscillator unit $\hbar\omega/k_B$, using model *ex*. The cloud contains 10^6 atoms. The transition temperature is $T^*_{ex} = 93.37\hbar\omega/k_B$ and the asymptotic thermodynamic temperature is $T_c = 94.05\hbar\omega/k_B$. The positions of these temperatures are shown as vertical lines in the figure. The ground-state peak density increases much more sharply than the ground-state population around the transition temperature. The former has also a significant value above T^*_{ex}. The model *sc* is indistinguishable for N_0/N, but is slightly different for $\rho_0(0)/\rho(0)$ (dotted line).

able, only in the more pertinent comparison between the models *sc* and *ex*.

This is first illustrated in Figure 3 where the degeneracy parameter $\rho(0)\lambda^3$ is plotted in function of the atom number for clouds at $T = T^*$. We plot this number for the semi-classical approximation *sc* and for the exact model, *ex*. The two curves are higher than 2.612. This highlights the inaccuracy of the standard semi-classical models (sc_0 or sc_∞) that do not take into account the ground-state contribution. It confirms also the calculation developed above. The degeneracy parameter is astonishingly constant till 10^3 atoms and does not differ much even for smaller atom numbers. Models *sc* and *ex*, which have almost the same transition temperature, have the same

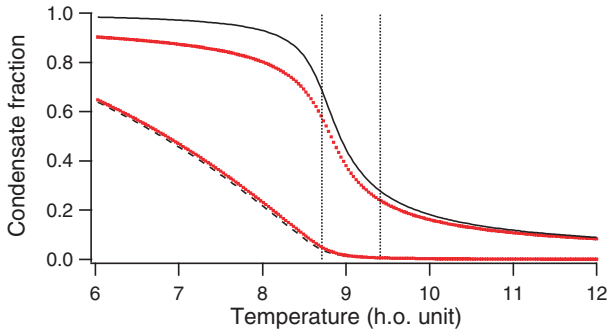

Fig. 5. Same as in Figure 4 but with 10^3 atoms. The transition temperature is $T^*_{ex} = 8.71\hbar\omega/k_B$ and the asymptotic thermodynamic temperature is $T_c = 9.41\hbar\omega/k_B$. Since the number of populated states is considerably reduced compared to Figure 4, the discrepancy between *sc* (dotted lines) and *ex* is more pronounced. This also explains why the increase of the condensate peak density is slower.

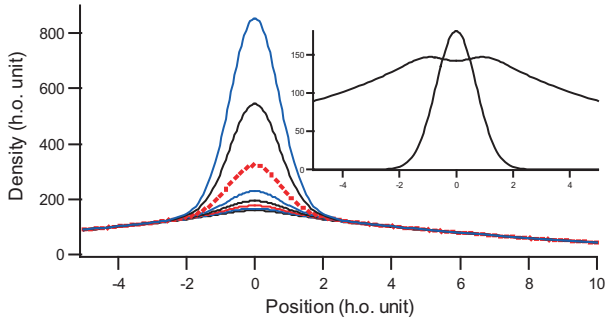

Fig. 6. Atomic density ρ_{ex} in function of r/σ where σ is the size of the harmonic oscillator ground-state. The temperature is $T = 93.37\hbar\omega/k_B$ and the atom number N spans from 0.990×10^6 to 1.004×10^6 by step of 2000 atoms. The curve at threshold is in dotted line and corresponds to 10^6 atoms. The inset shows the excited states and ground state density profile at threshold. The dip around $r = 0$ is mainly due to the first excited state population.

asymptotic value of the degeneracy parameter. This value, 6.24, is the one predicted by our high-N analysis. The model *sc* is significantly higher than this value for experimentally accessible atom numbers. This is because our first analysis does not take into account the $\frac{3}{2}\tau$ term of model *sc*. To first order [19],

$$x^*_{sc} \approx \frac{(\tau^*_{sc})^{\frac{3}{2}}}{\sqrt{\zeta(2)}}\left(1 + \frac{9}{8\zeta(2)}\tau^*_{sc}\ln\tau^*_{sc}\right)$$

and is then slightly smaller than $(\tau^*_{sc})^{3/2}/\sqrt{\zeta(2)}$. Consequently the ground-state peak density is bigger at T^*_{sc} using model *sc* than at T_c using the high-N model. The excited states peak density is also higher in model *sc* because of this $\frac{3}{2}\tau g_{\frac{1}{2}}$ term.

The next three figures deal with the cloud properties around the Bose-Einstein threshold. Figures 4 and 5 show the evolution of the condensate fraction N_0/N and the condensate peak density fraction in function of T for two different atom numbers, 10^6 and 10^3. Figure 6 shows the

density profile of clouds near degeneracy. What prevails in Figure 4 is the sharp increase of the condensate peak density compared to the condensate population. Moreover the models *sc* and *ex* give very close results validating our analysis on the ground-state contribution near degeneracy. This means that the peak density is a much better marker of the Bose-Einstein threshold than the atom number. This feature is in fact used experimentally: the appearance of a small peak over a broad distribution is the usual criterion to distinguish clouds above or below the transition temperature. This sharpness also explains why the value of the peak density is very sensitive to the value of the temperature (cf. Fig. 3). Figure 4 shows also that, above threshold, the ground-state peak density fraction decays slowly. This is even more pronounced in Figure 5 where $N = 10^3$ instead of 10^6. It comes from the fact that the number of populated states is not macroscopic anymore ($k_B T < 10\hbar\omega$) and then the transition is smoother for smaller atom number. Once again, the density is a better marker of degeneracy than the atom number. This figure shows also that the $\frac{3}{2}\tau$ term and the ground-state contribution make the model *sc* still very close to model *ex*, respecting the density and population fractions, even for 10^3 atoms.

The above analysis is focused on the peak density i. e. at the centre of the cloud. Figure 6 shows the total density profile of clouds, all at the same temperature, but containing different numbers of atoms around N_{ex}^*, the number of atoms for which $T = T_{ex}^*$ ($N = N_{ex}^*$ corresponds to the dotted line). This figure simulates somehow an experimental observation of BEC threshold. Only the central part is sensitive to the atom number; this corresponds to the condensate growing as the number of atoms is increased and to the fact that the excited states are already saturated for these atom numbers. Moreover, by looking at the graph, one would rather think that the Bose-Einstein transition occurs for a smaller atom number. This points out that the definition on the transition temperature based on an atom number criterion does not fully correspond to the one based on the atomic density which would be more connected to experiments. The inset shows the excited states and ground state density profiles at threshold. The excited states density exhibits a dip in the centre of the cloud, obviously not present in semi-classical models (monotonic functions). We check that the height of the dip is proportional to $1/\tau$ and can almost be totally attributed to the first excited state population. The aim of this paper is to show the importance of the ground-state in the study of non-interacting clouds close to threshold. The inset reveals that the first excited state density is also largely under-estimated; it represents ∼10% of the peak density whereas it contributes only to ∼0.1% of the population.

We have shown results on the atomic density at the vicinity of the transition temperature. Detection techniques consist rather on 1D-integrated density, corresponding to 2D absorption images, or 2D-integrated density [23]. One can show that, at threshold, the 1D and 2D-integrated peak density of the ground-state are vanishingly small for large atom numbers on contrary to the non-integrated case. The peak 1D-integrated density fraction behaves at threshold as $\sqrt{\tau}$ and the 2D-integrated peak density as τ. For typical atom number this is nevertheless not negligible. This is illustrated in Figure 7 where is plotted the condensate peak density fraction for 3D, 2D and 1D images of clouds at threshold. The calculations use the model *ex*. At the transition temperature T_{ex}^*, the ground-state contributes to more than 10% for $N < 2500$ atoms in 1D images and for $N < 8 \times 10^6$ atoms for 2D images. It means that, even with the conventional technique of absorption images, the effect should be experimentally observable if interactions could be switched off using, for instance, the magnetic tunability of the scattering length close to a Feshbach resonance [24].

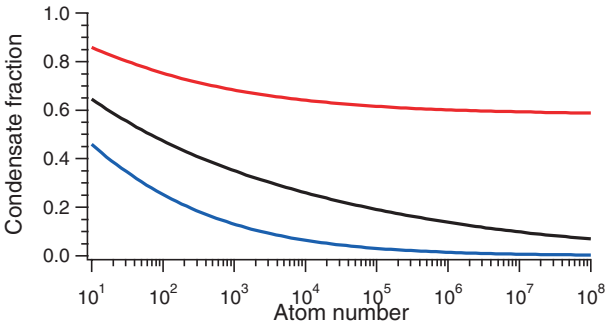

Fig. 7. Contribution of the ground-state on the peak density for, from bottom to top, 1D, 2D and 3D images in function of the number of trapped atoms. The clouds are at the transition temperature T_{ex}^* and the calculations use model *ex*. A 3D image would give the density in all three dimensions of space [25] whereas a 2D (resp. 1D) image corresponds to the density integrated over one (resp. 2) dimension. For $N = 10^4$ atoms the ground-state contributes to ∼26% in 2D images and ∼6% in 1D images. In contrast to 3D image, the ground-state contribution is very small for large atom number; it is not for typical atom numbers accessible in experiments.

Apart from the atomic density, two- and three-body inelastic loss rates will also be affected and could be 20 to 30% higher than predicted by model sc_0 around the transition temperature for typical atom numbers. Finally, in most experimental set-ups, the trapping potential is anisotropic and finite size effects are then stronger. Indeed the term $\frac{3}{2}\tau$ in equation (3) should be replaced by $\frac{3}{2}\frac{\tilde{\omega}}{\bar{\omega}}\tau$, with $\bar{\omega} = (\prod_i \omega_i)^{1/3}$ the geometric mean and $\tilde{\omega} = \frac{1}{3}\sum_i \omega_i$ the arithmetic mean [3]. Whatever the anisotropy is, $\tilde{\omega}$ is always larger than ω, making the finite size contribution stronger. To first order and if $k_B T_{ex}^* \gg \hbar\omega_i$ for $i = x, y$ and z, the ground-state contribution should be the same since our high-N analysis does not depend on any anisotropy.

In conclusion, we have shown that the density of an ideal atomic gas is dominated by the ground-state contribution near the transition temperature. The inter-atomic interactions have been neglected in our analysis and will modify our conclusions. With repulsive interactions, the clouds tends to decrease its density at the centre of the

cloud whereas it tends to increase it with attractive interactions. Previous calculations have treated separately finite size and interactions effects, both corrections being finally added [6]. Since the ground-state has a non-perturbative effect on the density, our analysis tends to prove that both effects have to be investigated together. The approach of reference [10] could in this respect provide helpful informations. Feshbach resonances, which enable to tune the interactions strength, constitute a powerful tool to check the accuracy of the different theoretical models. Moreover, a full three-dimensional density measurement would also be valuable; this type of measurement is at the edge to be available in our experiment on metastable helium in Orsay [25].

We thank S. Giorgini for stimulating discussions. The Atom Optics group of LCFIO is member of the Institut Francilien de Recherche sur les Atomes Froids (IFRAF).

References

1. *Proceedings of the International School of Physics "Enrico Fermi"*, Course CXL, edited by M. Inguscio, S. Stringari, C.E. Wieman (IOS Press, Amsterdam, 1999)
2. F. Dalfovo, S. Giorgini, L.P. Pitaeskii, S. Stringari, Rev. Mod. Phys. **71**, 463 (1999)
3. S. Grossmann, M. Holthaus, Z. Naturforsch. A **50**, 921 (1995)
4. W. Ketterle, N.J. van Druten, Phys. Rev. A **54**, 656 (1996)
5. K. Kirsten, D.J. Toms, Phys. Rev. A **54**, 4188 (1996)
6. S. Giorgini, L.P. Pitaevskii, S. Stringari, Phys. Rev. A **54**, R4633 (1996)
7. H. Haugerud, T. Haugest, F. Ravndal, Phys. Lett. A **225**, 18 (1997)
8. S. Giorgini, L.P. Pitaevskii, S. Stringari, J. Low Temp. Phys. **109**, 309 (1997)
9. R.K. Pathria, Phys. Rev. A **58**, 1490 (1998)
10. W. Krauth, Phys. Rev. Lett. **77**, 3695 (1996)
11. P. Arnold, B. Tomàšik, Phys. Rev. A **64**, 053609 (2001)
12. K. Huang, *Statistical Mechanics* (Wiley, 1987)
13. L.D. Landau, E.M. Liftshiz, *Statistical Physics* (Butterworths, 1996)
14. H.D. Politzer, Phys. Rev. A **54**, 5048 (1996)
15. C. Herzog, M. Olshanii, Phys. Rev. A **55**, 3254 (1997)
16. Y. Castin, lecture note in *"Coherent atomic matter waves"*, Les Houches, Session LXXII, edited by R. Kaiser, C.I. Westbrook, F. David (Springer, 2001)
17. T. Bergeman, D.L. Feder, N.L. Balazs, B.I. Schneider, Phys. Rev. A **61**, 063605 (2000)
18. In reference [9], the transition temperature was indeed T_{sc} (see later in the text). The transition temperature defined by the maximum of the second derivative of the condensate fraction has been calculated for atom number in the range 10^3–10^8; the relative deviation is below $\sim 10^{-3}$ on the transition temperature and $\sim 10^{-2}$ on the condensate peak density fraction
19. We use the usual definition of Bose functions $g_a(x) = \sum_{l=1}^{\infty} x^l/l^a$. We remind that $g_a(1) = \zeta(a)$ with $\zeta(\ )$ the Riemann Zeta function. Note that $g_1(x) = -\ln(1-x)$ and $dg_a/dx(x) = g_{a-1}(x)/x$
20. After submission of this article, we have been aware of a different type of semi-classical approximations which does not give rise to divergences. See V.I. Yukalov, Phys. Rev. A **72**, 033608 (2005)
21. We use the result of reference [22] for the calculation of the Bose functions near the transition temperature. For the series in model *ex*, the convergence is very slow but can easily be accelerated. For instance, it is much better to write $N = \frac{z}{1-z} + \sum_{l=1}^{\infty} z^l (\frac{1}{1-e^{-\tau l}} - 1)$ because the second term converges for large l because of the z^l part *and* because of the $(\frac{1}{1-e^{-\tau l}} - 1)$ part
22. J.E. Robinson, Phys. Rev. **83**, 678 (1951)
23. A. Robert, O. Sirjean, A. Browaeys, J. Poupard, S. Nowak, D. Boiron, C.I. Westbrook, A. Aspect, Science **292**, 461 (2001); published online 22 march 2001 (10.1126/science.1060622)
24. V. Vuletic, A.J. Kerman, C. Chin, S. Chu, Phys. Rev. Lett. **82**, 1406 (1999)
25. M. Schellekens, R. Hoppeler, A. Perrin, J. Viana Gomes, D. Boiron, A. Aspect, C.I. Westbrook, Science **310**, 648 (2005); published online 15 september 2005 (10.1126/science.1118024)

Theory for a Hanbury Brown Twiss experiment with a ballistically expanding cloud of cold atoms

J. Viana Gomes,[1,2] A. Perrin,[1] M. Schellekens,[1] D. Boiron,[1,*] C. I. Westbrook,[1] and M. Belsley[2]
[1]*Laboratoire Charles Fabry de l'Institut d'Optique, UMR 8501 du CNRS et Université Paris 11, 91403 Orsay Cedex, France*
[2]*Departamento de Fisica, Universidade do Minho, Campus de Gualtar, 4710-057 Braga, Portugal*
(Received 19 June 2006; published 7 November 2006)

We have studied one-body and two-body correlation functions in a ballistically expanding, noninteracting atomic cloud in the presence of gravity. We find that the correlation functions are equivalent to those at thermal equilibrium in the trap with an appropriate rescaling of the coordinates. We derive simple expressions for the correlation lengths and give some physical interpretations. Finally a simple model to take into account finite detector resolution is discussed.

DOI: 10.1103/PhysRevA.74.053607 PACS number(s): 03.75.Hh, 05.30.Jp

I. INTRODUCTION

Whether a source emits photons or massive particles, if it is to be used in an interferometric experiment, an essential property is its coherence. The study of coherence in optics has shown that more than one kind of coherence can be defined [1]. The most familiar type of coherence is known as first order coherence and is related to the visibility of interference fringes in an interferometer. It is proportional to the value of the correlation function of the associated field. Second order coherence is less intuitive and corresponds to the correlation function of the intensity or squared modulus of the field. From a particle point of view, second order coherence is a way of quantifying density correlations and is related to the probability of finding one particle at a certain location given that another particle is present at some other location. Particle correlations can arise simply from exchange symmetry effects and exist even when there is no interaction between the particles. This fact was clearly demonstrated in the celebrated Hanbury Brown Twiss experiment which showed a second order correlation for photons coming from widely separated points in a thermal source such as a star [2].

Analogous correlations in massive particles have also been studied, particularly in the field of nuclear physics [3–7]. Spatial correlations using low energy electrons have also been studied [8,9]. The advent of laser and evaporative cooling techniques has also made it possible to look for correlations between neutral atoms and recently a wide variety of different situations have been studied [10–16]. Correlation phenomena are generally richer when using massive particles because they can be either bosons or fermions, they often have a more complex internal structure and a large range of possible interactions with each other. In the field of ultracold atoms, the many theoretical papers to date have included treatments of bosons in a simple three-dimensional (3D) harmonic trap [17,18], a one-dimensional (1D) bosonic cloud in the Thomas-Fermi regime and Tonks-Girardeau limit [19–21], the Mott insulator or superfluid phase for atoms trapped in optical lattices [22] and the two-dimensional (2D) gas [23].

Almost all these theoretical treatments have dealt with atomic clouds at thermal equilibrium. On the other hand, all the experiments so far except Ref. [16] have measured correlations in clouds released from a trap which expand under the influence of gravity and possibly interatomic interactions. It is generally not trivial to know how the correlation properties evolve during expansion. Moreover, matter waves have different dispersion characteristics than light. All this raises interesting questions concerning the value of the correlation lengths during the atomic cloud expansion. In particular we would like to know how to use the results of Ref. [17] to analyze the experimental results of Ref. [15], a conceptually simple experiment in which second order correlations were measured in a freely expanding cloud of metastable helium atoms. The correlation length was defined as the characteristic length of the normalized second order correlation function. We will use the same definition in this paper (see Sec. II A for details).

To illustrate a more general question that comes up in thinking about the coherence of de Broglie waves, consider a beam of particles with mean velocity v hitting a detector. Two obvious length scales come immediately to mind, the de Broglie wavelength $\hbar/(m\Delta v)$ associated with the velocity spread Δv and the length associated with the inverse of the energy spread of the source $\hbar v/m(\Delta v)^2$. These two scales are obviously very different if v is large compared to the velocity spread. In this paper, we will show that in an experiment such as Ref. [15], the correlation length corresponds to neither of the above length scales, although they can be relevant in other situations. We find that the correlation length after an expansion time t of a cloud of initial size s is $\hbar t/ms$. This result is the atom optical analog of the van Cittert-Zernike theorem [24]. It has also been stated in a different form in Ref. [25]. For the special case of an ideal gas in a harmonic trap of oscillation frequency ω, the correlation length can be recast as $\lambda\omega t$ where λ is the thermal de Broglie wavelength. Hence the correlation length after expansion is simply dilated compared to that at equilibrium with the same scaling factor as the spatial extent of the cloud itself.

We will confine ourselves here to the case of a cloud of noninteracting atoms released suddenly from a harmonic

*Electronic address: denis.boiron@institutoptique.fr; http://www.atomoptic.fr

 ©2006 The American Physical Society

trap. The paper is organized as follows. We will begin in Sec. II with some simple definitions and general results about the correlation properties of a noninteracting cloud both at thermal equilibrium in a trapping potential and after a ballistic expansion. Without making any assumptions about the form of the trapping potential, we can only find simple analytical results in the limit of a nondegenerate gas. Next we will make a more exact and careful treatment by specializing to the very important case of a harmonic potential. We introduce the flux operator [26] involved in the experimental electronic detection with metastable helium and then calculate the correlation function of the flux. We will summarize the results and give a physical interpretation in Sec. IV. This interpretation will allow us to comment on the rather different case of a continuous beam as in the experiments of Refs. [7,10,14]. In Sec. V we will use our results to analyze the experimentally important problem of finite detector resolution. Finally, the Appendix adds some detailed calculations concerning the expressions found in Sec. III B.

II. GENERAL RESULTS ON CORRELATION FUNCTIONS OF NONINTERACTING GASES

Here we recall some basic results concerning the density and first and second order correlation functions for a cloud of noninteracting bosons at thermal equilibrium. A more detailed analysis can be found in Ref. [17]. Theoretical treatments that take into account interatomic interactions can be found in Refs. [17,18,27]. We also give some approximate results for a noninteracting gas after it has expanded from a trap.

A. Definitions

Consider a cloud of N atoms at thermal equilibrium at a temperature T, confined in a trapping potential. This potential is characterized by $\{\epsilon_{\mathbf{j}}, \psi^0_{\mathbf{j}}(\mathbf{r})\}$ the energy and wave function of level $\mathbf{j}$ (here supposed nondegenerate for simplicity). In second quantization, one defines the field operators

$$\hat{\Psi}^\dagger(\mathbf{r}) = \sum_{\mathbf{j}} \psi^*_{\mathbf{j}}(\mathbf{r})\hat{a}^\dagger_{\mathbf{j}}, \quad \hat{\Psi}(\mathbf{r}) = \sum_{\mathbf{j}} \psi_{\mathbf{j}}(\mathbf{r})\hat{a}_{\mathbf{j}}.$$

The operator $\hat{a}^\dagger_{\mathbf{j}}$ creates and $\hat{a}_{\mathbf{j}}$ annihilates one particle in state $|\psi_{\mathbf{j}}\rangle$ whereas $\hat{\Psi}^\dagger(\mathbf{r})$ creates and $\hat{\Psi}(\mathbf{r})$ annihilates a particle at position $\mathbf{r}$.

Correlation functions and the atomic density are statistical averages of such field operators. We use the Bose-Einstein distribution, $\langle \hat{a}^\dagger_{\mathbf{j}}\hat{a}_{\mathbf{k}}\rangle = \delta_{\mathbf{jk}}(e^{\beta(\epsilon_{\mathbf{j}}-\mu)}-1)^{-1}$ where $\beta = 1/(k_B T)$, k_B is the Boltzmann constant and μ is the chemical potential. The value of μ ensures the normalization $\Sigma_{\mathbf{j}}\langle \hat{a}^\dagger_{\mathbf{j}}\hat{a}_{\mathbf{j}}\rangle = N$. We can then define

(a) the first order correlation function $G^{(1)}(\mathbf{r},\mathbf{r}') = \langle \hat{\Psi}^\dagger(\mathbf{r})\hat{\Psi}(\mathbf{r}')\rangle$,

(b) the second order correlation function $G^{(2)}(\mathbf{r},\mathbf{r}') = \langle \hat{\Psi}^\dagger(\mathbf{r})\hat{\Psi}(\mathbf{r})\hat{\Psi}^\dagger(\mathbf{r}')\hat{\Psi}(\mathbf{r}')\rangle$,

(c) and the density $\rho_{\mathrm{eq}}(\mathbf{r}) = \langle \hat{\Psi}^\dagger(\mathbf{r})\hat{\Psi}(\mathbf{r})\rangle = G^{(1)}(\mathbf{r},\mathbf{r})$.

Several other first and second order correlation functions can be defined (see below) but these are the most common ones. The first order correlation function appears in interference experiments whereas second order correlation functions are related to intensity interference or density fluctuation. First and second order correlation functions are connected for thermal noninteracting atomic clouds. The $G^{(2)}$ function contains a statistical average of the type $\langle \hat{a}^\dagger_{\mathbf{j}}\hat{a}_{\mathbf{k}}\hat{a}^\dagger_{\mathbf{l}}\hat{a}_{\mathbf{n}}\rangle$ which can be calculated through the thermal averaging procedure (Wick theorem [28]). One finds $\langle \hat{a}^\dagger_{\mathbf{j}}\hat{a}_{\mathbf{k}}\hat{a}^\dagger_{\mathbf{l}}\hat{a}_{\mathbf{n}}\rangle = \langle \hat{a}^\dagger_{\mathbf{j}}\hat{a}_{\mathbf{j}}\rangle\langle \hat{a}^\dagger_{\mathbf{k}}\hat{a}_{\mathbf{k}}\rangle \times(\delta_{\mathbf{jl}}\delta_{\mathbf{kn}} + \delta_{\mathbf{jn}}\delta_{\mathbf{kl}}) + \langle \hat{a}^\dagger_{\mathbf{j}}\hat{a}_{\mathbf{j}}\rangle\delta_{\mathbf{kl}}\delta_{\mathbf{jn}}$, which leads to

$$G^{(2)}(\mathbf{r},\mathbf{r}') = \rho_{\mathrm{eq}}(\mathbf{r})\rho_{\mathrm{eq}}(\mathbf{r}') + |G^{(1)}(\mathbf{r},\mathbf{r}')|^2 + \rho_{\mathrm{eq}}(\mathbf{r})\delta(\mathbf{r}-\mathbf{r}').$$

The last term is the so-called shot-noise term. It will be neglected in the following because it is proportional to N whereas the others are proportional to N^2.

It is convenient to define a normalized second order correlation function

$$g^{(2)}(\mathbf{r},\mathbf{r}') = \frac{G^{(2)}(\mathbf{r},\mathbf{r}')}{\rho_{\mathrm{eq}}(\mathbf{r})\rho_{\mathrm{eq}}(\mathbf{r}')}.$$

If the cloud has a finite correlation length, then for distances larger than this length the first order correlation function vanishes. Then $g^{(2)}(\mathbf{r},\mathbf{r}) = 2$ and $g^{(2)}(\mathbf{r},\mathbf{r}') \to 1$ when $|\mathbf{r}-\mathbf{r}'| \to \infty$. This means that the probability of finding two particles close to each other is enhanced by a factor of 2, compared to the situation where they are far apart. This is the famous bunching effect first observed by Hanbury Brown and Twiss with light [2].

The above expression of the $G^{(2)}$ function cannot be applied in the vicinity and below the Bose-Einstein transition temperature. The calculation of $\langle \hat{a}^\dagger_{\mathbf{j}}\hat{a}_{\mathbf{k}}\hat{a}^\dagger_{\mathbf{l}}\hat{a}_{\mathbf{n}}\rangle$ is performed in the grand canonical ensemble which assumes the existence of a particle reservoir that does not exist for the condensate. It is well known [29] that this gives unphysically large fluctuations of the condensate at low enough temperature. This pathology disappears at the thermodynamic limit if there is an interatomic interaction [29]. It has also been shown that it cancels for a finite number of noninteracting particles if one uses the more realistic canonical ensemble [30]. One way to keep using the grand canonical ensemble is to add the canonical result for the ground state [17]. This approach is validated by the results in Ref. [30] and will be used in the following. The largest deviation is expected to occur near the transition temperature [30]. The contribution of the ground state is $-\langle \hat{a}^\dagger_{\mathbf{0}}\hat{a}_{\mathbf{0}}\rangle^2\delta_{\mathbf{j0}}\delta_{\mathbf{k0}}\delta_{\mathbf{l0}}\delta_{\mathbf{n0}}$. Then, with ρ_0 the ground-state density, it follows that,

$$G^{(2)}(\mathbf{r},\mathbf{r}') = \rho_{\mathrm{eq}}(\mathbf{r})\rho_{\mathrm{eq}}(\mathbf{r}') + |G^{(1)}(\mathbf{r},\mathbf{r}')|^2 - \rho_0(\mathbf{r})\rho_0(\mathbf{r}'). \tag{1}$$

The normalized second-order then becomes

$$g^{(2)}(\mathbf{r},\mathbf{r}') = 1 + \frac{|G^{(1)}(\mathbf{r},\mathbf{r}')|^2}{\rho_{\mathrm{eq}}(\mathbf{r})\rho_{\mathrm{eq}}(\mathbf{r}')} - \frac{\rho_0(\mathbf{r})\rho_0(\mathbf{r}')}{\rho_{\mathrm{eq}}(\mathbf{r})\rho_{\mathrm{eq}}(\mathbf{r}')}.$$

Because the ground state density is negligible for a thermal cloud, the normalized correlation function $g^{(2)}(\mathbf{r},\mathbf{r}')$ still goes from 2 to 1 as the separation of $\mathbf{r}$ and $\mathbf{r}'$ increases. On the other hand, for a BEC at $T=0$, only the ground state is occupied. Then $|G^{(1)}(\mathbf{r},\mathbf{r}')|2 = \rho_{\mathrm{eq}}(\mathbf{r})\rho_{\mathrm{eq}}(\mathbf{r}') = \rho_0(\mathbf{r})\rho_0(\mathbf{r}')$ and

$g^{(2)}(\mathbf{r},\mathbf{r}')=1$. The amount of particle bunching present in the second order correlation function can be quantified as $g^{(2)}(\mathbf{r},\mathbf{r}')-1$ and this typically decays exponentially as the modulus squared of the separation between the two points increases. We define the correlation length to be the characteristic length over which the amount of particle bunching decays, that is the distance over which $g^{(2)}(\mathbf{r},\mathbf{r}')-1$ decays to $1/e$ of its maximum value. The correlation length of a BEC is infinite. Such a system is said to exhibit bunching at high temperature over the correlation length and no bunching in the condensed phase.

B. Correlations in an expanding cloud

In most experiments, particle correlations and other characteristics are not directly measured in the atom cloud, (Ref. [16] is an exception). Rather, the cloud is released from a trap and allowed to expand during a "time of flight" before detection. For a sufficiently long time of flight, and neglecting interactions between the atoms, the positions one measures at a detector reflect the initial momenta of the particles. The results of Sec. II A concerning the correlation functions in position space all have analogs in momentum space. In fact the correlation functions in the two reciprocal spaces are closely related. At equilibrium, i.e., inside the trap, the following relationships can be easily derived:

$$\int d\mathbf{p} G^{(1)}(\mathbf{p},\mathbf{p}) e^{-i\mathbf{p}\cdot\mathbf{r}/\hbar} = \int d\mathbf{R} G^{(1)}(\mathbf{R}-\mathbf{r}/2,\mathbf{R}+\mathbf{r}/2),$$

$$\int d\mathbf{r} G^{(1)}(\mathbf{r},\mathbf{r}) e^{i\mathbf{q}\cdot\mathbf{r}/\hbar} = \int d\mathbf{P} G^{(1)}(\mathbf{P}-\mathbf{q}/2,\mathbf{P}+\mathbf{q}/2).$$

In other words, the spatial correlation length is related to the width of the momentum distribution and the momentum correlation length is related to the width of the spatial distribution, i.e., the size of the cloud. No equally simple and general relationship holds for the second order correlation functions. This is because, close to the BEC transition temperature, and at points where the ground state wave function is not negligible, the special contribution of the ground state, the last term in Eq. (1) must be included, and this contribution depends on the details of the confining potential. On the other hand, for an ideal gas far from the transition temperature one can neglect the ground state density, make the approximation that the correlation length is very short, neglect commutators such as $[\hat{\mathbf{r}},\hat{\mathbf{p}}]$, and then write the thermal density operator as $\hat{\sigma}=e^{-\beta(\hat{\mathbf{P}}^2/2m)}e^{-\beta V(\hat{\mathbf{r}})}$. These approximations lead to

$$G^{(2)}(\mathbf{p},\mathbf{p}') = \rho_{\mathrm{eq}}(\mathbf{p})\rho_{\mathrm{eq}}(\mathbf{p}') + |G^{(1)}(\mathbf{p},\mathbf{p}')|^2$$

and

$$G^{(1)}(\mathbf{P}-\mathbf{q}/2,\mathbf{P}+\mathbf{q}/2) \sim e^{-\beta(\mathbf{P}^2/2m)} \int d\mathbf{r} e^{-\beta V(\mathbf{r})} e^{i\mathbf{q}\cdot\mathbf{r}/\hbar}.$$

One sees that in this limit, the interesting part of $G^{(2)}$ in momentum space is proportional to the square of the Fourier transform of the density distribution and independent of the mean momentum $\mathbf{P}$. This result is the analog of the van Cittert-Zernike theorem [24]. For a trapped cloud of size s_α in the α direction, one has a momentum correlation "length" given by

$$p_\alpha^{(\mathrm{coh})} = \frac{\hbar}{s_\alpha}. \tag{2}$$

If atoms are suddenly released from a trap and allowed to freely evolve for a sufficiently long time t, the positions of the particles reflect their initial momenta and the spatial correlation length at a detector is given by

$$l_\alpha^{(d)} = \frac{p_\alpha^{(\mathrm{coh})}}{m} t = \frac{\hbar t}{m s_\alpha}. \tag{3}$$

The normalized second order correlation function is then a Gaussian of rms width $l^{(d)}/\sqrt{2}$. This result was experimentally confirmed in Ref. [15]. One wonders however, to what extent the approximations we have made are valid. The clouds used in Ref. [15] were in fact very close to the transition temperature so that effects due to the Bose nature of the density matrix may be important. Although the time of flight was very long, it is useful to quantify the extent to which identifying the momentum correlation length in the trap with the spatial correlation length at the detector is accurate. Finally, the effect of gravity on the falling atoms never appears in the above approximate treatment, and we would like to clarify the role it plays. In order to answer these questions we undertake a more careful calculation. We will confine ourselves to atoms initially confined in a harmonic trap, a good approximation to the potential used in most experiments, and happily, one for which the eigenstates and energies are known exactly.

III. DENSITY AND CORRELATION FUNCTIONS FOR A HARMONIC TRAP

A. At equilibrium in the trap

The eigenfunctions for a three-dimensional harmonic potential of oscillation frequency ω_α in the α direction, are given by

$$\psi_{\mathbf{j}}^0(\mathbf{r}) = \prod_{\alpha=x,y,z} A_{j_\alpha} e^{-r_\alpha^2/2\sigma_\alpha^2} H_{j_\alpha}(r_\alpha/\sigma_\alpha).$$

Here $\sigma_\alpha=\sqrt{\hbar/m\omega_\alpha}$ is the harmonic oscillator ground-state size, H_{j_α} is the Hermite polynomial of order j_α and $A_{j_\alpha}=[\sqrt{\pi}\sigma_\alpha 2^{j_\alpha}(j_\alpha)!]^{-1/2}$. The eigenenergies are given by $\epsilon_{\mathbf{j}}=\Sigma_{\alpha=x,y,z}\hbar\omega_\alpha(j_\alpha+1/2)$. Then [17,29], with $\tau_\alpha=\beta\hbar\omega_\alpha$ and $\tilde{\mu}=\mu-\hbar\Sigma\omega_\alpha/2$, one finds

$$\rho_{\mathrm{eq}}(\mathbf{r}) = \frac{1}{\pi^{3/2}} \sum_{l=1}^{\infty} e^{\beta l\tilde{\mu}} \prod_\alpha \frac{1}{\sigma_\alpha\sqrt{1-e^{-2\tau_\alpha l}}} e^{-\tanh(\tau_\alpha l/2)(r_\alpha^2/\sigma_\alpha^2)}$$

and

$$G^{(1)}(\mathbf{r},\mathbf{r}') = \frac{1}{\pi^{3/2}}\sum_{l=1}^{\infty} e^{\beta l\tilde{\mu}}\prod_{\alpha}\frac{1}{\sigma_\alpha\sqrt{1-e^{-2\tau_\alpha l}}}\exp\left[-\tanh\left(\frac{\tau_\alpha l}{2}\right)\right.$$
$$\left.\times\left(\frac{r_\alpha + r'_\alpha}{2\sigma_\alpha}\right)^2 - \coth\left(\frac{\tau_\alpha l}{2}\right)\left(\frac{r_\alpha - r'_\alpha}{2\sigma_\alpha}\right)^2\right].$$

The above expressions can be transformed into more familiar forms in limiting cases:

(i) For high temperature, $\mu\to-\infty$ and one recovers the Maxwell-Boltzmann distribution. The density is $\rho_{\mathrm{eq}}(\mathbf{r}) = \frac{N}{\lambda^3}\Pi_\alpha\tau_\alpha e^{-(\tau_\alpha/2)(r_\alpha^2/\sigma_\alpha^2)}$ with $\lambda=\hbar\sqrt{2\pi}/\sqrt{mk_BT}$ the thermal de Broglie wavelength. The size of the cloud is $s_\alpha=\sigma_\alpha/\sqrt{\tau_\alpha} = \sqrt{k_BT/m\omega_\alpha^2}$. The first order correlation function is

$$G^{(1)}(\mathbf{r},\mathbf{r}') = \frac{N}{\lambda^3}\prod_{\alpha}\tau_\alpha e^{-(\tau_\alpha/2)((\mathbf{r}_\alpha+\mathbf{r}'_\alpha)/2\sigma_\alpha)^2}e^{-\pi((\mathbf{r}_\alpha-\mathbf{r}'_\alpha)/\lambda)^2}. \tag{4}$$

Using our definition, the correlation length is $l^{(t)}=\lambda/\sqrt{2\pi}$.

(ii) For a temperature close to but above the Bose-Einstein transition temperature, one must keep the summation over the index l. The density is $\rho_{\mathrm{eq}}(\mathbf{r}) = \frac{1}{\lambda^3}g_{3/2}(e^{\beta\tilde{\mu}}\Pi_\alpha e^{-(\tau_\alpha/2)(r_\alpha^2/\sigma_\alpha^2)})$, where $g_a(x)=\Sigma_{l=1}^{\infty}x^l/l^a$ is a Bose function. The first order correlation function is

$$G^{(1)}(\mathbf{r},\mathbf{r}') = \frac{1}{\lambda^3}\sum_{l=1}^{\infty}\frac{e^{l\beta\tilde{\mu}}}{l^{3/2}} \times\prod_{\alpha} e^{-(\tau_\alpha l/2)((\mathbf{r}_\alpha+\mathbf{r}'_\alpha)/2\sigma_\alpha)^2}e^{-(\pi/l)((\mathbf{r}_\alpha-\mathbf{r}'_\alpha)/\lambda)^2}.$$

As the temperature decreases, the number of values of l that contribute significantly to the sum increases. It is then clear from the above expression for $G^{(1)}$ that the correlation length near the center of the trap will increase and that the normalized correlation function is no longer Gaussian. Far from the center, only the $l=1$ term is important and the correlation function remains Gaussian. Thus close to degeneracy the correlation length is position dependent (for an explicit example see Sec. III B 5).

(iii) Near and below the transition temperature, the second order correlation function is given by Eq. (1) with $\rho_0(\mathbf{r}) = \frac{e^{\beta\tilde{\mu}}}{1-e^{\beta\tilde{\mu}}}\Pi_\alpha\frac{e^{-r_\alpha^2/\sigma_\alpha^2}}{(\sqrt{\pi}\sigma_\alpha)^3}$. As the temperature decreases, the correlation at zero distance, $g^{(2)}(0,0)$ decreases from 2 to 1 and the correlation length increases. Around the transition temperature, $g^{(2)}(0,0)$ is already significantly different from 2 since the condensate peak density is already very large for a noninteracting harmonically trapped cloud [31]. At $T=0$, the correlation length is infinite and $g^{(2)}(\mathbf{r},\mathbf{r}')=1$.

B. Correlations in a harmonically trapped cloud after expansion

Here we consider the cloud after expansion. First we discuss two classes of detection methods which must be distinguished before calculating correlation functions.

1. Detection

We assume that the trapping potential is switched off instantaneously at $t=0$. The cloud expands and falls due to gravity. Two types of detection can be performed:

(a) *Snap shot*. An image is taken of the entire cloud at $t=t_0$. We have then access to

$$G^{(2)}_{im}(\mathbf{r},t_0;\mathbf{r}',t_0) = \langle\hat{\Psi}^\dagger(\mathbf{r},t_0)\hat{\Psi}(\mathbf{r},t_0)\hat{\Psi}^\dagger(\mathbf{r}',t_0)\hat{\Psi}(\mathbf{r}',t_0)\rangle.$$

The usual imaging technique is absorption, and so one has access to the above correlation functions integrated along the imaging beam axis. This was used for the experiments of Refs. [12,13].

(b) *Flux measurement*. The atoms are detected when they cross a given plane. We will only consider the situation in which this plane is horizontal at $z=H$. One has access to

$$G^{(2)}_{fl}(\mathbf{r}=\{x,y,z=H\},t;\mathbf{r}'=\{x',y',z'=H\},t') = \langle\hat{I}(\mathbf{r},t)\hat{I}(\mathbf{r}',t')\rangle,$$

where $\hat{I}$ is the flux operator defined below. The detection systems required for such experiments correspond most closely to those of Refs. [10,15], in which a microchannel plate, situated below the trapped cloud, recorded the arrival times and in one case the positions of the atoms. It also corresponds closely to imaging a cloud that crosses a thin sheet of light [32], or to the experiment of Ref. [14], in which the transmission of a high finesse optical cavity records atoms as they cross the beam.

These two correlation functions are different, but if the detection is performed after a long time of flight, they are in fact nearly equivalent. This equivalence will be discussed in the following.

The flux operator is defined quantum mechanically by

$$\hat{I}(\mathbf{r},t) = \frac{\hbar}{m}\,\mathrm{Im}[\hat{\Psi}^\dagger(\mathbf{r},t)\partial_z\hat{\Psi}(\mathbf{r},t)] = \frac{\hbar}{2mi}[\hat{\Psi}^\dagger(\mathbf{r},t)\partial_z\hat{\Psi}(\mathbf{r},t) - \partial_z\hat{\Psi}^\dagger(\mathbf{r},t)\hat{\Psi}(\mathbf{r},t)].$$

The flux has thus the dimensions of a density times a velocity. We will give the explicit expression of this velocity in the Sec. III B 4. Here, the atomic field operators $\hat{\Psi}(\mathbf{r},t)$ depend on space coordinates as well as on time. They represent the time evolution of the atomic field during the flight of the atoms, falling from the trap. The field operators for the falling cloud can be easily derived if we assume that there are no interactions between the atoms and that the occupation number in each mode is constant (as in free expansion). In this case, these operators can be defined as

$$\hat{\Psi}^\dagger(\mathbf{r},t) = \sum_{\mathbf{j}}\psi^*_{\mathbf{j}}(\mathbf{r},t)\hat{a}^\dagger_{\mathbf{j}}, \quad \hat{\Psi}(\mathbf{r},t) = \sum_{\mathbf{j}}\psi_{\mathbf{j}}(\mathbf{r},t)\hat{a}_{\mathbf{j}},$$

where the spatiotemporal dependence is carried by the wave function and the statistical occupation by the creation and annihilation operators.

2. Ballistic expansion of a harmonic oscillator stationary state

After switching off the trap, the harmonic oscillator wave functions noted $\psi^0_{\mathbf{j}}$ are no longer stationary states. There are

two ways to calculate the correlation after expansion: propagation of wave functions or propagation of the density matrix (the Schrödinger or the Heisenberg picture). In the following we will use the first approach which is physically more transparent (see Ref. [33] for the Heisenberg picture).

The ballistic expansion of a cloud is easy to calculate with the appropriate Green function. The Green function K is defined as

$$\psi_{\mathbf{j}}(\mathbf{r},t)=\int_{-\infty}^{\infty}\mathbf{d}r_0K(\mathbf{r},t;\mathbf{r}_0,t_0)\psi_{\mathbf{j}}^0(\mathbf{r}_0,t_0).$$

As the $\psi_{\mathbf{j}}^0$ functions are stationary states for $t<0$, we can take $t_0=0$ in the following. The Green function for particles in an arbitrarily time-varying quadratic potential is known [34]. After expansion, the potential is only due to gravity and the Green function is then

$$K(\mathbf{r},t;\mathbf{r}_0)=\left(\frac{m}{2i\pi\hbar t}\right)^{3/2}e^{ia(\mathbf{r}-\mathbf{r}_0)^2}e^{ib(z+z_0)}e^{-ic}$$

with $a=\frac{m}{2\hbar t}$, $b=\frac{mgt}{2\hbar}$, and $c=\frac{mg^2t^3}{24\hbar}$.

One can then derive an analytical expression of $\psi_{\mathbf{j}}(\mathbf{r},t)$ [35,36],

$$\psi_{\mathbf{j}}(\mathbf{r},t)=e^{i\phi(\mathbf{r},t)}\prod_{\alpha}\frac{e^{ij_\alpha(\delta_\alpha+3\pi/2)}}{\sqrt{\omega_\alpha t-i}}\psi_{\mathbf{j}}^0(\tilde{\mathbf{r}}),\tag{5}$$

where $\delta_\alpha=\tan^{-1}\left(\frac{1}{\omega_\alpha t}\right)$,

$$\phi(\mathbf{r},t)=\frac{m}{2\hbar t}\left[(\tilde{x}\omega_x t)^2+(\tilde{y}\omega_y t)^2+(\tilde{z}\omega_z t)^2+2gt^2\left(z-\frac{1}{8}gt^2\right)\right]-c-\frac{3\pi}{4}\tag{6}$$

and, with $\tilde{\mathbf{r}}=\{\tilde{x},\tilde{y},\tilde{z}\}$,

$$\tilde{x}=\frac{x}{\sqrt{1+\omega_x^2t^2}},\quad \tilde{y}=\frac{y}{\sqrt{1+\omega_y^2t^2}},\quad \tilde{z}=\frac{H-\frac{1}{2}gt^2}{\sqrt{1+\omega_z^2t^2}}.\tag{7}$$

In the case of flux measurement, the position of the detector is fixed at $z=H$. The phase $\phi(\tilde{x},\tilde{y},t)$ is global as it does not depend on the index $\mathbf{j}$; it will cancel in second order correlation measurements. This is in contrast to interferometric measurements where it is this phase that gives rise to fringes. The above results show that after release, the wave function is identical to that in the trap except for a phase factor and a scaling factor in the positions [37]. This scaling is obviously a property of a harmonic potential, and it considerably simplifies the expression of the correlation functions as we will see below.

3. Flux operator

Using $\partial_z H_n(z)=2nH_{n-1}(z)$, the spatial derivative of the wave function can be written

$$\partial_z\psi_{\mathbf{j}}(\mathbf{r},t)=\frac{m}{\hbar}[(iv_2-v_1)\psi_{j_z}(z,t)-iv_3\sqrt{j_z}\psi_{j_z-1}(z,t)]\psi_{j_x}(x,t)\psi_{j_y}(y,t),$$

where the velocities v_1, v_2, and v_3 are time dependent and are given by

$$v_1(t)=\omega_z\frac{H-\frac{1}{2}gt^2}{1+\omega_z^2t^2},\tag{8}$$

$$v_2(t)=\frac{1}{t}\left(H+\frac{1}{2}gt^2-\frac{H-\frac{1}{2}gt^2}{1+\omega_z^2t^2}\right),\tag{9}$$

$$v_3(t)=\frac{\sqrt{2}\omega_z\sigma_z}{\sqrt{1+\omega_z^2t^2}}e^{i\delta_z}.\tag{10}$$

The velocity v_2 is usually much larger than the other two and will give the dominant contribution for the mean flux and the second order correlation function. An atom with zero initial velocity will acquire after a time t a velocity gt which is close to $v_2(t)$. The flux operator is

$$\hat{I}(\mathbf{r},t)=\sum_{\mathbf{j},\mathbf{k}}\left(v_2\psi_{\mathbf{j}}^*\psi_{\mathbf{k}}-\frac{1}{2}(v_3\sqrt{k}\psi_{\mathbf{j}}^*\psi_{\mathbf{k}-1_\mathbf{z}}+v_3^*\sqrt{j}\psi_{\mathbf{j}-1_\mathbf{z}}^*\psi_{\mathbf{k}})\right)\hat{a}_{\mathbf{j}}^\dagger\hat{a}_{\mathbf{k}},\tag{11}$$

where $\mathbf{j}-\mathbf{1_z}$ is the vector (j_x,j_y,j_z-1) and where we write $\psi=\psi(\mathbf{r},t)$.

4. Mean density and mean flux

We will first calculate the mean density $\rho(\mathbf{r},t)=\langle\hat{\Psi}^\dagger(\mathbf{r},t)\hat{\Psi}(\mathbf{r},t)\rangle$. Using Eq. (5), one finds easily that $\rho(\mathbf{r},t)=\frac{1}{\Pi_\alpha\sqrt{1+\omega_\alpha^2t^2}}\rho_{\mathrm{eq}}(\tilde{\mathbf{r}})$. This means that the density has the same form during expansion up to an anisotropic scale factor given by Eq. (7) [37,38]. The statistical average of Eq. (11) leads to

$$\langle\hat{I}(\mathbf{r},t)\rangle=\sum_{\mathbf{j}}\left(v_2|\psi_{\mathbf{j}}|^2-\frac{\sqrt{j_z}}{2}(v_3\psi_{j_z}^*\psi_{j_z-1}+v_3^*\psi_{j_z}\psi_{j_z-1}^*)|\psi_{j_x}\psi_{j_y}|^2\right)\times\langle\hat{a}_{\mathbf{j}}^\dagger\hat{a}_{\mathbf{j}}\rangle.$$

Because $v_3\psi_{j_z}^*\psi_{j_z-1}=i\frac{|v_3|}{\sqrt{1+\omega_z^2t^2}}\psi_{j_z}^0(\tilde{z})\psi_{j_z-1}^0(\tilde{z})=-v_3^*\psi_{j_z}\psi_{j_z-1}^*$, the second term cancels out. Then, without any approximation,

$$\langle\hat{I}(\mathbf{r},t)\rangle=\frac{v_2(t)}{\prod_\alpha\sqrt{1+\omega_\alpha^2t^2}}\rho_{\mathrm{eq}}(\tilde{\mathbf{r}})=v_2(t)\rho(\mathbf{r},t).$$

The flux is proportional to the density of a cloud at thermal equilibrium with rescaled coordinates. This means that the mean flux of an expanding noninteracting cloud is proportional to the atomic density without any approximation. This result holds with and without gravity taken into account.

5. Second order correlation

Here we calculate the correlation functions. A discussion is given in the next section. The snap-shot correlation function is

$$G^{(2)}_{im}(\mathbf{r},t;\mathbf{r}',t) = \sum_{\mathbf{j},\mathbf{k},\mathbf{l},\mathbf{n}} \psi^*_{\mathbf{j}}\psi_{\mathbf{k}}\psi'^*_{\mathbf{l}}\psi'_{\mathbf{n}}\langle \hat{a}^\dagger_{\mathbf{j}}\hat{a}_{\mathbf{k}}\hat{a}^\dagger_{\mathbf{l}}\hat{a}_{\mathbf{n}}\rangle.$$

Using Eq. (5), one finds, without any approximation (except the neglect of the shot-noise term):

$$G^{(2)}_{im}(\mathbf{r},t;\mathbf{r}',t) = \frac{1}{\prod_\alpha (1+\omega_\alpha^2 t^2)} \times[\rho_{\rm eq}(\tilde{\mathbf{r}})\rho_{\rm eq}(\tilde{\mathbf{r}}') + |G^{(1)}(\tilde{\mathbf{r}},\tilde{\mathbf{r}}')|^2 - \rho_0(\tilde{\mathbf{r}})\rho_0(\tilde{\mathbf{r}}')].$$

As in the case of the mean density, the snap-shot correlation function has the same form as in the trap except for an anisotropic scale factor.

The calculation of $G^{(2)}_{fl}$ is similar,

$$\langle \hat{I}(\mathbf{r},t)\hat{I}(\mathbf{r}',t')\rangle = -\left(\frac{\hbar}{2m}\right)^2 \sum_{\mathbf{j},\mathbf{k},\mathbf{l},\mathbf{n}} [\psi^*_{\mathbf{j}}(\partial_z\psi_{\mathbf{k}}) - (\partial_z\psi^*_{\mathbf{j}})\psi_{\mathbf{k}}] \times[\psi'^*_{\mathbf{l}}(\partial_z\psi'_{\mathbf{n}}) - (\partial_z\psi'^*_{\mathbf{l}})\psi'_{\mathbf{n}}]\langle \hat{a}^\dagger_{\mathbf{j}}\hat{a}_{\mathbf{k}}\hat{a}^\dagger_{\mathbf{l}}\hat{a}_{\mathbf{n}}\rangle.$$

Two major differences appear compared to the mean flux calculation: the terms in v_3 and the phase factor $\delta_\alpha + 3\pi/2$ in Eq. (5) do not cancel. This makes the exact calculation very tedious. It is postponed to the Appendix.

Experiments are usually performed in situations satisfying two conditions: (1) the width of the cloud after expansion is much larger than that of the trapped cloud, and (2) the mean velocity acquired during free fall is much larger than the velocity spread of the trapped cloud. The first condition means that $\omega_\alpha t \gg 1$ and the second one that $gt \gg \sqrt{k_B T/m}$. The latter condition also means that the mean arrival time, $t_0 = \sqrt{2H/g}$, is much larger than the time width $\sqrt{k_B T/mg^2}$ of the expanding cloud. With these approximations the scale factors become quite simple. $\tilde{x} \sim \frac{x}{\omega_x t_0}$, $\tilde{y} \sim \frac{y}{\omega_y t_0}$ and $\tilde{z} \sim \frac{H-(1/2)gt^2}{\omega_z t_0} \sim \frac{g(t_0-t)}{\omega_z}$. In particular, the coordinate $\tilde{z}$ is proportional to the arrival time t. This means that in experiments that measure arrival times, the results have the same form when expressed as a function of vertical position.

In the correlation function of the flux, the above approximations also lead to $v_2 \approx \sqrt{2gH}$ and $|\sqrt{j_z}v_3/v_2| \approx \sqrt{\frac{k_B T}{\hbar\omega_z}}\frac{\sigma_z}{\sqrt{2H}} = \frac{s_z}{\sqrt{2H}}$ where s_z is the width of the cloud inside the trap and where the typical value of the occupied trap level, j_z, is $\sim \frac{k_B T}{\hbar\omega_z}$. The term containing v_3 is then very small compared to the one proportional v_2. In Ref. [15] for instance the above ratio is $\sim 10^{-5}$. We will neglect terms containing v_3 in the following. The phase factors δ_α in Eq. (5) are also very small since $\omega_\alpha t \gg 1$ and can be neglected (see the Appendix).

Under all these approximations, one finds

$$G^{(2)}_{fl}(\mathbf{r},t;\mathbf{r}',t') = \frac{v_2 v_2'}{\prod_\alpha \sqrt{(1+\omega_\alpha^2 t^2)(1+\omega_\alpha^2 t'^2)}}[\rho_{\rm eq}(\tilde{\mathbf{r}})\rho_{\rm eq}(\tilde{\mathbf{r}}') + |G^{(1)}(\tilde{\mathbf{r}},\tilde{\mathbf{r}}')|^2 - \rho_0(\tilde{\mathbf{r}})\rho_0(\tilde{\mathbf{r}}')].$$

We again find the same correlation function as in the trap, rescaled by a slightly different factor compared to $G^{(2)}_{im}$. This factor simply reflects the expansion of the cloud between the times t and t'.

The scaling laws for the harmonic potential result in a very simple expression for the correlation lengths at the detector,

$$l^{(d)}_\alpha = l^{(t)}\sqrt{1+(\omega_\alpha t)^2}. \tag{12}$$

Where $l^{(d)}_\alpha$ is the correlation length along the α direction at the detector and $l^{(t)}_\alpha$ is the correlation length in the trap. If the gas is far from degeneracy $l^{(t)} = \frac{\lambda}{\sqrt{2\pi}}$, and we recover the result of Eq. (3). Close to degeneracy the correlation length is position dependent. In the case of a pulse of atoms as in Ref. [15], this formula applies along all three space axes. In addition, when making a flux measurement, one often expresses the longitudinal correlation length as a correlation time. For a pulse of atoms from a harmonic trap, with a mean velocity v at the detector, the correlation time is

$$t^{(\rm coh)} = \frac{l^{(d)}_z}{v} = l^{(t)}\frac{\omega_z}{g}. \tag{13}$$

It is independent of the propagation time as long as $\omega_z t \gg 1$.

These calculations are illustrated in the following figures. For simplicity we have used an isotropic trapping potential. As pointed out above, the normalized second-order correlation functions $g^{(2)}_{im}$ and $g^{(2)}_{fl}$ are virtually identical with typical parameters (see the Appendix) and we will use the shorter notation $g^{(2)}$. In Fig. 1 we show the normalized correlation function $g^{(2)}(\tilde{r},0)$ as a function of $\tilde{r} \sim r/\omega t$ for various temperatures in the vicinity the Bose-Einstein phase transition T^*. We use the saturation of the excited state population to define T^* [31]. This is the correlation function *at the center of the cloud*. One sees that at $T = T^*$ (the thick dashed line in the figure), the correlation function at zero distance is already significantly diminished compared to higher temperatures. The correlation length, on the other hand, is larger than $\lambda\omega t/\sqrt{2\pi}$. Also, one sees that the correlation function is almost flat for temperatures a few percent below T^*.

In many experiments of course, one does not measure the local correlation function, but the correlation function averaged over all points in the sample [15]. The effect of this averaging is shown in Fig. 2. We plot $g^{(2)}_m(\tilde{r}) = \frac{\int d\mathbf{R} G^{(2)}(\mathbf{R}+\tilde{r}\mathbf{e},\mathbf{R})}{\int d\mathbf{R} G^{(1)}(\mathbf{R}+\tilde{r}\mathbf{e},\mathbf{R}+\tilde{r}\mathbf{e})G^{(1)}(\mathbf{R},\mathbf{R})}$, where the vector $\mathbf{e}$ is a unit vector in some direction. One sees that the amplitude of the correlation function decreases more slowly, and that after averaging, the correlation length hardly varies as one passes T^*.

To illustrate how local the effects which distinguish Figs. 1 and 2 are, we also plot in Fig. 3 the value of $g^{(2)}(\tilde{r},\tilde{r})$, the zero distance correlation function as a function of $\tilde{r}$ in the vicinity of the cloud center. One sees that even below T^*, the

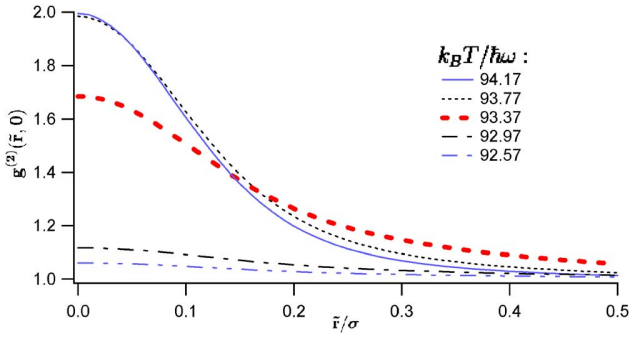

FIG. 1. (Color online) Two-body normalized correlation function at the trap center, $g^{(2)}(\tilde{r},0)$ for 10^6 atoms as a function of the position $\tilde{r}=r/\omega t$ for various temperatures around transition temperature. The horizontal axis is labelled in units of the size of the harmonic oscillator wave function σ. The thick dashed line corresponds to the transition temperature T^* defined in Ref. [31] and is $93.37\hbar\omega/k_B$ for 10^6 atoms. The temperature step is $0.4\hbar\omega/k_B$. The thermal de Broglie wavelength is $\sim 0.26\sigma$. The effect of the ground state population is clearly visible in the reduction of $g^{(2)}(0,0)$, and in the rapid flattening out of the correlation function slightly below T^*.

correlator is close to 2 at a rescaled distance of a few times the harmonic oscillator length scale. We can simply interpret this effect by observing that at $\tilde{r}$ the effective chemical potential is $\mu - V(\tilde{r})$. Away from the center, the effective chemical potential is small and this part of the cloud can be described as a Boltzmann cloud.

Before interpreting these results further, we recall some of our assumptions and their possible violation. First, we obtain Eq. (12) if we make a semiclassical approximation assuming that k_BT greatly exceeds the energy spacing in the trap in each dimension of space. In an anisotropic trap, this condition can be violated in one or two dimensions and then correlation length along these directions will be larger and can become infinite for a small enough temperature. Second, we have assumed a noninteracting gas throughout.

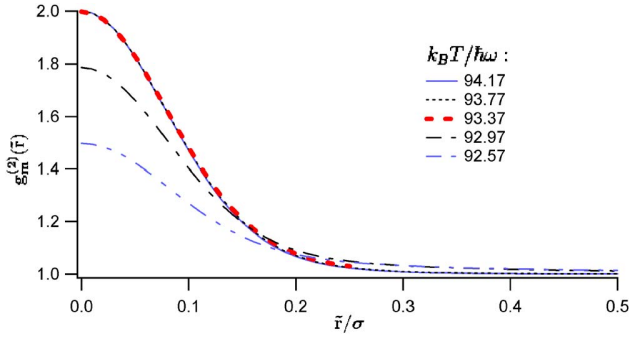

FIG. 2. (Color online) Two-body normalized correlation function $g_m^{(2)}(\tilde{r})$ for 10^6 atoms as a function of $\tilde{r}$. This function is an average of the two-body correlation function over the cloud. The conditions are the same conditions as for Fig. 1. Unlike Fig. 1, the shape is always almost Gaussian and converges more slowly to a flat correlation for low temperatures. This is because only a small region around $\tilde{r}=0$ is fully sensitive to the quantum atomic distribution.

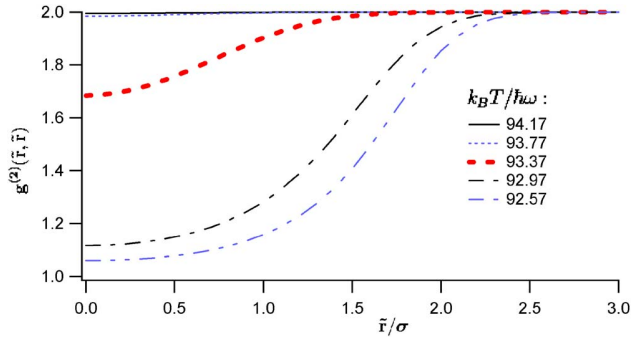

FIG. 3. (Color online) Two-body normalized correlation function $g^{(2)}(\tilde{r},\tilde{r})$ for 10^6 atoms as a function of $\tilde{r}$. The conditions are the same as for Fig. 1. Even for $T<T^*$ the correlation goes to 2 far from the center. This is due to the finite spatial extent of the condensate. It can also be understood in terms of the chemical potential $\mu(\tilde{r})$ which, in a local density approximation, decreases as $\tilde{r}$ increases and thus the correlation is equivalent to that of a hotter cloud.

Repulsive interactions inflate the trapped cloud, and thus reduce the length $l^{(d)}$ at the detector. We expect this to be the main effect for atomic clouds above the Bose-Einstein transition threshold, where the effects of atomic interactions are typically small. The reduction is typically a few percent. Even slightly below T^*, the condensate density is quite high, expelling the thermal atoms from the center of the trap. The effects of interactions inside the trap and during the cloud's expansion cannot be neglected. Taking them into account is then complex and beyond the scope of this paper.

IV. PHYSICAL INTERPRETATIONS

The main result of this paper is that in an experiment which averages over a detector in the sense of Fig. 2, even at $T=T^*$, the correlation lengths at the detector are well approximated by

$$l_\alpha^{(d)} = l^{(t)}\omega_\alpha t.$$

The correlation length increases linearly with the time of flight. A simple way to understand this result is to consider the analogy with optical speckle. Increasing the time of flight corresponds to increasing the propagation distance to the observation plane in the optical analog. The speckle size, i.e., the correlation length, obviously increases linearly with the propagation distance. Another way to understand the time dependence is to remark that after release, the atomic cloud is free and the phase space density should be constant. Since the density decreases with time as $\Pi_\alpha(\omega_\alpha t)$ and the spread of the velocity distribution is constant, the correlation volume must increase by the same factor [25].

Yet another way to look at the correlation length is to observe that, far from degeneracy, the correlation length inside the trap is the thermal de Broglie wavelength, that is, $\frac{\lambda}{\sqrt{2\pi}} = \hbar/\Delta p$ where $\Delta p = m\Delta v$ is the momentum width of the cloud. By analogy, after expansion, the correlation length is $\hbar/(\Delta p)_{\mathrm{loc}}$, where $(\Delta p)_{\mathrm{loc}}$ is the "local" width of the momen-

tum distribution. As the pulse of atoms propagates, fast and slow atoms separate, so that at a given point in space the width in momentum is reduced by a factor $\frac{s_\alpha}{\Delta v t}$.

For a continuous beam, the formula (12) only applies in the transverse directions. In the longitudinal direction, an argument in terms of a local thermal de Broglie wavelength can be used to find the coherence length or time. If the atoms travel at velocity v without acceleration, the momentum spread and correlation length remain constant. Defining the energy width of the beam as $\Delta E = mv\Delta v$, one finds a correlation time $\lambda/v = \hbar/\Delta E$ [7]. In the presence of an acceleration such as gravity, the momentum spread of the beam decreases (the energy spread at any point ΔE is constant), which increases the correlation length. The correlation time, however, remains $\hbar/\Delta E$ [10].

The result that the coherence length of a cloud of atoms can vary with the distance of propagation, is in apparent contradiction with the results of Refs. [39,40]. Those papers give convincing reasons, both experimental and theoretical, for why the dispersion associated with the propagation of massive particles should *not* result in an increase of the coherence length. The contradiction is resolved by noting that the Mach-Zender interferometer considered in that work is sensitive to the function $f(\mathbf{r},t) = \int d\mathbf{R} G^{(1)}(\mathbf{R},t;\mathbf{R}+\mathbf{r},t)$. If the Hamiltonian commutes with the momentum operator, i.e., if plane waves are stationary states, one can easily demonstrate that the function f and hence its width are independent of the time t. The experiments we analyze are sensitive to the *modulus of* $G^{(1)}$ whose width will always increase with time. Thus the coherence length can depend on the interferometer as well as the source.

The role of the acceleration of gravity in these experiments is minor. It governs the propagation time and the speed of the particles when they reach the detector. In a pulsed beam, gravity has no effect on the correlation length, although it does affect the correlation time. It also renders the rescaling of the z coordinate linear for large times so that the correlation function in position z and time have the same form. Without gravity (cancellation with a magnetic field gradient for example), a pulse of atoms would take longer to reach the detector, thereby giving the correlation length more time to dilate, and in addition they would hit the detector at a lower velocity. The correlation time would then increase with time and its order of magnitude would be $\frac{\lambda \omega t_0}{v_T} = \frac{\hbar\omega}{k_B T} t_0$ where $v_T = \sqrt{k_B T/m}$ is the thermal velocity and $t_0 = v_T/H$ is the time of flight to the detector.

V. EFFECT OF FINITE DETECTOR RESOLUTION

In the preceding sections, the detector was considered ideal, i.e., with arbitrarily good spatial and temporal resolution. Here we will consider a model of a more realistic detector, in which we suppose that the spatial resolution in the x-y plane is Gaussian. This is often the case due to smearing in pixels [13,16] and is also approximately true in Ref. [15]. To simplify the discussion we will restrict our analysis to the case $T \gg T^*$ and use a Maxwell-Boltzmann distribution rather than Bose-Einstein distribution. In this case, each direction of space is independent and we will only consider one direction at a time in the following.

There are three different scales in the problem: the size of the cloud at the detector $s(t) \approx \sqrt{\frac{k_B T}{m}} t$, the correlation length at the detector $l^{(d)}$ and the rms width of the detector resolution function d. The definition of the resolution function is that for a density $\rho(x) = A e^{-x^2/2s(t)^2}$, the observed density is given by a convolution

$$\rho_{\rm obs}(x) = \int dx_0 \rho(x_0) \frac{e^{-(1/2)[(x-x_0)/d]^2}}{\sqrt{2\pi} d} = \frac{A}{\sqrt{1 + d^2/s(t)^2}} e^{-\{x^2/2[s(t)^2+d^2]\}}.$$

Similarly if $G^{(1)}(x,x') = A e^{i\phi} e^{-(x+x')^2/2(2s)^2} e^{-(x-x')^2/2(l^{(d)})^2}$ is the first order correlation function and $G^{(1)}_{\rm obs}(x,x')$ the observed one, we have

$$|G^{(1)}_{\rm obs}(x,x')|^2 = \int dx_0 dx_0' |G^{(1)}(x_0,x_0')|^2 \times \frac{e^{-(1/2)[(x-x_0)/d]^2}}{\sqrt{2\pi} d} \frac{e^{-(1/2)[(x'-x_0')/d]^2}}{\sqrt{2\pi} d} \quad (14)$$

$$= \frac{|A|^2}{\sqrt{[1 + d^2/s^2(t)][1 + 4d^2/(l^{(d)})^2]}} \times e^{-\{(x+x')^2/4[s(t)^2+d^2]\}} e^{-\{(x-x')^2/[l^{(d)}]^2+4d^2\}} \quad (15)$$

Consequently, with $\alpha = x, y$ and z:

(i) The amplitude of the normalized correlation function becomes

$$g^{(2)}_{\rm obs}(\mathbf{0},\mathbf{0}) = \left(\frac{G^{(1)}_{\rm obs}(\mathbf{0},\mathbf{0})}{\rho_{\rm obs}(\mathbf{0})} \right)^2 = 1 + \prod_\alpha \sqrt{\frac{1 + d_\alpha^2/s_\alpha^2(t)}{1 + 4d_\alpha^2/(l_\alpha^{(d)})^2}}.$$

(ii) The observed widths of the cloud are $s_\alpha(t) \to \sqrt{s_\alpha^2(t) + d_\alpha^2}$.

(iii) The observed correlation lengths are $l_\alpha^{(d)} \to \sqrt{(l_\alpha^{(d)})^2 + (2d_\alpha)^2}$. The factor 2 can be understood as $\sqrt{2} \times \sqrt{2}$ where the first term comes from the fact that d_α is defined for one particle and not for a pair of particles and the second one comes from the fact that the correlation length is not defined as an rms width.

In the experiment of Ref. [15] the trapped cloud had a cigar shape. At the detector the cloud was spherical but the correlation volume was anisotropic with $l_x^{(d)} \ll d \approx l_y^{(d)}/4$. In the third (vertical) direction, the resolution width was much smaller than any other length scale. The observed contrast of the correlation function was therefore approximately, $\frac{l_x^{(d)}}{2d}$.

VI. CONCLUSION

The most important conclusion of this paper is that the expansion of a noninteracting cloud from a harmonic trap in

thermal equilibrium, admits a rather simple, analytical treatment of the time variation of the density and the correlation functions. In such a pulse of atoms, correlation lengths scale in the same way as the size of the density profile. The agreement with experiment indicates that the neglect of interactions is a good approximation above the BEC transition temperature. An important next step however, is to examine interaction effects so that the next generation of experiments, which will be more precise and better resolved, can be fully interpreted.

ACKNOWLEDGMENTS

The Atom Optics group of LCFIO is member of the Institut Francilien de Recherche sur les Atomes Froids (IFRAF) and of the Fédération LUMAT of the CNRS (FR2764). This work is supported by the PESSOA Program 07988NJ, by the Atom Chips network MCRTN-CT-2003-505032, and the ANR under Contract No. 05-NANO-008-01.

APPENDIX

Explicit expression of the flux correlation function

We found in Sec. III B, the following expression for the flux operator:

$$\hat{I}(\mathbf{r},t)=\sum_{\mathbf{j},\mathbf{k}}\left(v_2\psi_{\mathbf{j}}^*\psi_{\mathbf{k}}-\frac{1}{2}(v_3\sqrt{k}\psi_{\mathbf{j}}^*\psi_{\mathbf{k}-1_z}+v_3^*\sqrt{j}\psi_{\mathbf{j}-1_z}^*\psi_{\mathbf{k}})\right)\hat{a}_{\mathbf{j}}^\dagger\hat{a}_{\mathbf{k}},$$

where $\mathbf{j}-1_\mathbf{z}$ is the vector (j_x,j_y,j_z-1) and where we write $\psi=\psi(\mathbf{r},t)$.

The second order correlation function for the flux is then,

$$\begin{aligned}\langle\hat{I}(\mathbf{r},t)\hat{I}(\mathbf{r}',t')\rangle=&\sum_{\mathbf{j},\mathbf{k},\mathbf{l},\mathbf{n}}\left(v_2\psi_{\mathbf{j}}^*\psi_{\mathbf{k}}-\frac{1}{2}(v_3\sqrt{k_z}\psi_{\mathbf{j}}^*\psi_{\mathbf{k}-1_z}\right.\\&\left.+v_3^*\sqrt{j_z}\psi_{\mathbf{j}-1_z}^*\psi_{\mathbf{k}})\right)\\&\times\left(v_2'\psi'^*_{\mathbf{l}}\psi'_{\mathbf{n}}-\frac{1}{2}(v_3'\sqrt{n_z}\psi'^*_{\mathbf{l}}\psi'_{\mathbf{n}-1_z}\right.\\&\left.+v'^*_3\sqrt{l_z}\psi'^*_{\mathbf{l}-1_z}\psi'_{\mathbf{n}})\right)\\&\times\langle\hat{a}_{\mathbf{j}}^\dagger\hat{a}_{\mathbf{k}}\hat{a}_{\mathbf{l}}^\dagger\hat{a}_{\mathbf{n}}\rangle.\end{aligned}$$

Neglecting the shot-noise and ground-state contributions, this leads to

$$\langle\hat{I}(\mathbf{r},t)\hat{I}(\mathbf{r}',t')\rangle=\langle\hat{I}(\mathbf{r},t)\rangle\langle\hat{I}(\mathbf{r}',t')\rangle+\mathrm{Re}(A)$$

with

$$\begin{aligned}A=\sum_{\mathbf{j},\mathbf{l}}\left(\right.&v_2v_2'\psi_{\mathbf{j}}^*\psi_{\mathbf{j}}'\psi_{\mathbf{l}}\psi'^*_{\mathbf{l}}+\frac{1}{2}v_3v_3'\sqrt{j_zl_z}\psi_{\mathbf{j}}^*\psi'^*_{\mathbf{j}-1_z}\psi_{\mathbf{l}-1_z}\psi'^*_{\mathbf{l}}\\&+\frac{1}{2}v_3v'^*_3l_z\psi_{\mathbf{j}}^*\psi_{\mathbf{j}}'\psi_{\mathbf{l}-1_z}\psi'^*_{\mathbf{l}-1_z}-v_2v_3'\sqrt{j_z}\psi_{\mathbf{j}}^*\psi'^*_{\mathbf{j}-1_z}\psi_{\mathbf{l}}\psi'^*_{\mathbf{l}}\\&\left.-v_2'v_3\sqrt{l_z}\psi_{\mathbf{j}}^*\psi_{\mathbf{j}}'\psi_{\mathbf{l}-1_z}\psi'^*_{\mathbf{l}}\right)\langle\hat{a}_{\mathbf{j}}^\dagger\hat{a}_{\mathbf{j}}\rangle\langle\hat{a}_{\mathbf{l}}^\dagger\hat{a}_{\mathbf{l}}\rangle.\end{aligned}$$

We write $A=\Sigma_{i=1}^5T_i$ where the T_i terms can be recast, using $\tan\delta_\alpha=1/\omega_\alpha t$, $\tan\delta'_\alpha=1/\omega_\alpha t'$, $\Delta_\alpha=\delta'_\alpha-\delta_\alpha$, $\Sigma_\alpha j_\alpha(\delta'_\alpha-\delta_\alpha)=\mathbf{j}\cdot\mathbf{\Delta}$, $\psi_{\mathbf{l}}^0=\psi_{\mathbf{l}}^0(\tilde{\mathbf{r}})$, and $\psi'^0_{\mathbf{l}}=\psi_{\mathbf{l}}^0(\tilde{\mathbf{r}}')$,

$$T_1=v_2v_2'\sum_{\mathbf{j},\mathbf{l}}\psi_{\mathbf{j}}^*\psi_{\mathbf{j}}'\psi_{\mathbf{l}}\psi'^*_{\mathbf{l}}\langle\hat{a}_{\mathbf{j}}^\dagger\hat{a}_{\mathbf{j}}\rangle\langle\hat{a}_{\mathbf{l}}^\dagger\hat{a}_{\mathbf{l}}\rangle=\frac{v_2v_2'}{\prod_\alpha\sqrt{(1+\omega_\alpha^2t^2)(1+\omega_\alpha^2t'^2)}}\sum_{\mathbf{j},\mathbf{l}}\psi_{\mathbf{j}}^0\psi'^0_{\mathbf{j}}\psi_{\mathbf{l}}^0\psi'^0_{\mathbf{l}}e^{i\Sigma_\alpha(j_\alpha-l_\alpha)(\delta'_\alpha-\delta_\alpha)}\langle\hat{a}_{\mathbf{j}}^\dagger\hat{a}_{\mathbf{j}}\rangle\langle\hat{a}_{\mathbf{l}}^\dagger\hat{a}_{\mathbf{l}}\rangle$$

$$=\frac{v_2v_2'}{\prod_\alpha\sqrt{(1+\omega_\alpha^2t^2)(1+\omega_\alpha^2t'^2)}}\left|\sum_{\mathbf{j}}\psi_{\mathbf{j}}^0\psi'^0_{\mathbf{j}}e^{i\mathbf{j}\cdot\mathbf{\Delta}}\langle\hat{a}_{\mathbf{j}}^\dagger\hat{a}_{\mathbf{j}}\rangle\right|^2,$$

$$T_2=\frac{1}{2}v_3v_3'\sum_{\mathbf{j},\mathbf{l}}\sqrt{j_zl_z}\psi_{\mathbf{j}}^*\psi'_{\mathbf{j}-1_z}\psi_{\mathbf{l}-1_z}\psi'^*_{\mathbf{l}}\langle\hat{a}_{\mathbf{j}}^\dagger\hat{a}_{\mathbf{j}}\rangle\langle\hat{a}_{\mathbf{l}}^\dagger\hat{a}_{\mathbf{l}}\rangle=$$

$$-\frac{1}{2}\frac{|v_3v_3'|}{\prod_\alpha\sqrt{(1+\omega_\alpha^2t^2)(1+\omega_\alpha^2t'^2)}}\left(\sum_{\mathbf{j}}\sqrt{j_z}\psi_{\mathbf{j}}^0\psi'^0_{\mathbf{j}-1_z}e^{i\mathbf{j}\cdot\mathbf{\Delta}}\langle\hat{a}_{\mathbf{j}}^\dagger\hat{a}_{\mathbf{j}}\rangle\right)\left(\sum_{\mathbf{l}}\sqrt{l_z}\psi_{\mathbf{l}-1_z}^0\psi'^0_{\mathbf{l}}e^{-i\mathbf{l}\cdot\mathbf{\Delta}}\langle\hat{a}_{\mathbf{l}}^\dagger\hat{a}_{\mathbf{l}}\rangle\right),$$

$$T_3=\frac{1}{2}v_3v'^*_3\sum_{\mathbf{j},\mathbf{l}}l_z\psi_{\mathbf{j}}^*\psi_{\mathbf{j}}'\psi_{\mathbf{l}-1_z}\psi'^*_{\mathbf{l}-1_z}\langle\hat{a}_{\mathbf{j}}^\dagger\hat{a}_{\mathbf{j}}\rangle\langle\hat{a}_{\mathbf{l}}^\dagger\hat{a}_{\mathbf{l}}\rangle=\frac{1}{2}\frac{|v_3v_3'|}{\prod_\alpha\sqrt{(1+\omega_\alpha^2t^2)(1+\omega_\alpha^2t'^2)}}\left(\sum_{\mathbf{j}}\psi_{\mathbf{j}}^0\psi'^0_{\mathbf{j}}e^{i\mathbf{j}\cdot\mathbf{\Delta}}\langle\hat{a}_{\mathbf{j}}^\dagger\hat{a}_{\mathbf{j}}\rangle\right)\left(\sum_{\mathbf{l}}l_z\psi_{\mathbf{l}-1_z}^0\psi'^0_{\mathbf{l}-1_z}e^{-i\mathbf{l}\cdot\mathbf{\Delta}}\langle\hat{a}_{\mathbf{l}}^\dagger\hat{a}_{\mathbf{l}}\rangle\right),$$

$$T_4=-v_2v_2'\sum_{\mathbf{j},\mathbf{l}}\sqrt{j_z}\psi_{\mathbf{j}}^*\psi'_{\mathbf{j}-1_z}\psi_{\mathbf{l}}\psi'^*_{\mathbf{l}}\langle\hat{a}_{\mathbf{j}}^\dagger\hat{a}_{\mathbf{j}}\rangle\langle\hat{a}_{\mathbf{l}}^\dagger\hat{a}_{\mathbf{l}}\rangle=-i\frac{v_2|v_3'|}{\prod_\alpha\sqrt{(1+\omega_\alpha^2t^2)(1+\omega_\alpha^2t'^2)}}\left(\sum_{\mathbf{j}}\sqrt{j_z}\psi_{\mathbf{j}}^0\psi'^0_{\mathbf{j}-1_z}e^{i\mathbf{j}\cdot\mathbf{\Delta}}\langle\hat{a}_{\mathbf{j}}^\dagger\hat{a}_{\mathbf{j}}\rangle\right)\left(\sum_{\mathbf{l}}\psi_{\mathbf{l}}^0\psi'^0_{\mathbf{l}}e^{-i\mathbf{l}\cdot\mathbf{\Delta}}\langle\hat{a}_{\mathbf{l}}^\dagger\hat{a}_{\mathbf{l}}\rangle\right),$$

$$T_5 = -v_2' v_3 \sum_{\mathbf{j},\mathbf{l}} \sqrt{l_z}\psi_{\mathbf{j}}^{*}\psi_{\mathbf{j}}'\psi_{\mathbf{l}-1_{\mathbf{z}}}\psi'^{*}_{\mathbf{l}}\langle \hat{a}_{\mathbf{j}}^{\dagger}\hat{a}_{\mathbf{j}}\rangle\langle \hat{a}_{\mathbf{l}}^{\dagger}\hat{a}_{\mathbf{l}}\rangle = -i\frac{v_2'|v_3|}{\prod_{\alpha}\sqrt{(1+\omega_\alpha^2 t^2)(1+\omega_\alpha^2 t'^2)}}\left(\sum_{\mathbf{j}}\psi_{\mathbf{j}}^0\psi'^0_{\mathbf{j}}e^{i\mathbf{j}\cdot\boldsymbol{\Delta}}\langle \hat{a}_{\mathbf{j}}^{\dagger}\hat{a}_{\mathbf{j}}\rangle\right)\left(\sum_{\mathbf{l}}\sqrt{l_z}\psi_{\mathbf{l}-1_{\mathbf{z}}}^0\psi'^0_{\mathbf{l}}e^{-i\mathbf{l}\cdot\boldsymbol{\Delta}}\langle \hat{a}_{\mathbf{l}}^{\dagger}\hat{a}_{\mathbf{l}}\rangle\right).$$

The term T_1 is a real number which is not the case for T_2, T_3, T_4, and T_5.

Calculation for harmonic oscillator stationary states

All the above terms can be calculated analytically. All the series are identical in the direction x and y. We are then left with the calculation of three series in only one direction,

$$\sum_{n=0}^{\infty}\sqrt{n}\psi_{n-1}^0(\tilde{z})\psi_n^0(\tilde{z}')e^{-nu},$$

$$\sum_{n=0}^{\infty}\sqrt{n}\psi_n^0(\tilde{z})\psi_{n-1}^0(\tilde{z}')e^{-nu},$$

$$\sum_{n=0}^{\infty}n\psi_{n-1}^0(\tilde{z})\psi_{n-1}^0(\tilde{z}')e^{-nu}.$$

The function $g_u(\tilde{z},\tilde{z}')=\Sigma_{n=0}^{\infty}\psi_n^0(\tilde{z})\psi_n^0(\tilde{z}')e^{-nu}$ is known [17,29] and its expression is

$$g_u(\tilde{z},\tilde{z}') = \frac{1}{\sigma\sqrt{\pi(1-e^{-2u})}}\exp\left[-\tanh\left(\frac{u}{2}\right)\left(\frac{\tilde{z}+\tilde{z}'}{2\sigma}\right)^2 - \coth\left(\frac{u}{2}\right)\left(\frac{\tilde{z}-\tilde{z}'}{2\sigma}\right)^2\right].$$

Using

$$\tilde{z}\psi_n^0(\tilde{z}) = \frac{\sigma}{\sqrt{2}}\langle\tilde{z}|\hat{a}+\hat{a}^{\dagger}|\psi_n^0\rangle = \frac{\sigma}{\sqrt{2}}[\sqrt{n}\psi_{n-1}^0(\tilde{z})+\sqrt{n+1}\psi_{n+1}^0(\tilde{z})],$$

one finds

$$\tilde{z}g_u(\tilde{z},\tilde{z}') = \frac{\sigma}{\sqrt{2}}\left(\sum\sqrt{n}\psi_{n-1}^0(\tilde{z})\psi_n^0(\tilde{z}')e^{-nu} + e^{u}\sum\sqrt{n}\psi_n^0(\tilde{z})\psi_{n-1}^0(\tilde{z}')e^{-nu}\right).$$

It follows easily that

$$\sum_{n=0}^{\infty}\sqrt{n}\psi_{n-1}^0(\tilde{z})\psi_n^0(\tilde{z}')e^{-nu} = \frac{\sqrt{2}}{\sigma}\frac{\tilde{z}-e^{u}\tilde{z}'}{1-e^{2u}}g_u(\tilde{z},\tilde{z}'),$$

$$\sum_{n=0}^{\infty}\sqrt{n}\psi_n^0(\tilde{z})\psi_{n-1}^0(\tilde{z}')e^{-nu} = \frac{\sqrt{2}}{\sigma}\frac{\tilde{z}'-e^{u}\tilde{z}}{1-e^{2u}}g_u(\tilde{z},\tilde{z}').$$

Moreover,

$$\sum_{n=0}^{\infty}n\psi_{n-1}^0(\tilde{z})\psi_{n-1}^0(\tilde{z}')e^{-nu} = e^{-u}[g_u(\tilde{z},\tilde{z}')-\partial_u g_u(\tilde{z},\tilde{z}')].$$

Then,

$$\sum_{n=0}^{\infty}n\psi_{n-1}^0(\tilde{z})\psi_{n-1}^0(\tilde{z}')e^{-nu} = \left[\frac{1}{1-e^{-2u}}+\frac{1}{2}\left(\frac{\tilde{z}+\tilde{z}'}{2\sigma\cosh\frac{u}{2}}\right)^2 - \frac{1}{2}\left(\frac{\tilde{z}-\tilde{z}'}{2\sigma\sinh\frac{u}{2}}\right)^2\right]e^{-u}g_u(\tilde{z},\tilde{z}').$$

Explicit expression of the flux correlation function—Part II

We define $G_B^{(1)}(\mathbf{r},\mathbf{r}',\mathbf{u})=\Sigma_{\mathbf{n}}^{\infty}\psi_{\mathbf{n}}^0(\mathbf{r})\psi_{\mathbf{n}}^0(\mathbf{r}')e^{-\mathbf{nu}}$. This function, the 3D equivalent of the function g_u, is connected to the one-body correlation function by $G^{(1)}(\mathbf{r},\mathbf{r}')=\Sigma_{l=1}^{\infty}e^{\beta l\tilde{\mu}}G_B^{(1)}(\mathbf{r},\mathbf{r}',l\boldsymbol{\tau})$ with $\tau_\alpha=\beta\hbar\omega_\alpha$.

Then,

$$T_1 = \frac{v_2 v_2'}{\prod_{\alpha}\sqrt{(1+\omega_\alpha^2 t^2)(1+\omega_\alpha^2 t'^2)}}\left|\sum_l e^{\beta l\tilde{\mu}}G_B^{(1)}(\tilde{\mathbf{r}},\tilde{\mathbf{r}}',l\boldsymbol{\tau}-i\boldsymbol{\Delta})\right|^2,$$

$$T_2 = -\frac{1}{2}\frac{|v_3 v_3'|}{\prod_{\alpha}\sqrt{(1+\omega_\alpha^2 t^2)(1+\omega_\alpha^2 t'^2)}}\left(\sum_l e^{\beta l\tilde{\mu}}\frac{\sqrt{2}}{\sigma}\frac{\tilde{z}-e^{l\tau_z-i\Delta_z}\tilde{z}'}{1-e^{2(l\tau_z-i\Delta_z)}}G_B^{(1)}(\tilde{\mathbf{r}},\tilde{\mathbf{r}}',l\boldsymbol{\tau}-i\boldsymbol{\Delta})\right) \times\left(\sum_k e^{\beta k\tilde{\mu}}\frac{\sqrt{2}}{\sigma}\frac{\tilde{z}'-e^{k\tau_z+i\Delta_z}\tilde{z}}{1-e^{2(k\tau_z+i\Delta_z)}}G_B^{(1)}(\tilde{\mathbf{r}},\tilde{\mathbf{r}}',k\boldsymbol{\tau}+i\boldsymbol{\Delta})\right),$$

$$T_3 = \frac{1}{2}\frac{|v_3 v_3'|}{\prod_\alpha \sqrt{(1+\omega_\alpha^2 t^2)(1+\omega_\alpha^2 t'^2)}}\left(\sum_l e^{\beta l\tilde{\mu}} G_B^{(1)}(\tilde{\mathbf{r}},\tilde{\mathbf{r}}',l\boldsymbol{\tau}-i\boldsymbol{\Delta})\right)\times\left\{\sum_k e^{\beta k\tilde{\mu}}\left[\frac{1}{1-e^{-2(k\tau_z+i\Delta_z)}}+\frac{1}{2}\left(\frac{\tilde{z}+\tilde{z}'}{2\sigma\cosh\dfrac{k\tau_z+i\Delta_z}{2}}\right)^2\right.\right.$$
$$\left.\left.-\frac{1}{2}\left(\frac{\tilde{z}-\tilde{z}'}{2\sigma\sinh\dfrac{k\tau_z+i\Delta_z}{2}}\right)^2\right]e^{-(k\tau_z+i\Delta_z)}G_B^{(1)}(\tilde{\mathbf{r}},\tilde{\mathbf{r}}',k\boldsymbol{\tau}+i\boldsymbol{\Delta})\right\},$$

$$T_4 = -i\frac{v_2|v_3'|}{\prod_\alpha \sqrt{(1+\omega_\alpha^2 t^2)(1+\omega_\alpha^2 t'^2)}}\left(\sum_l e^{\beta l\tilde{\mu}}\frac{\sqrt{2}}{\sigma}\frac{\tilde{z}-e^{l\tau_z-i\Delta_z}\tilde{z}'}{1-e^{2(l\tau_z-i\Delta_z)}}G_B^{(1)}(\tilde{\mathbf{r}},\tilde{\mathbf{r}}',l\boldsymbol{\tau}-i\boldsymbol{\Delta})\right)\times\left(\sum_k e^{\beta k\tilde{\mu}}G_B^{(1)}(\tilde{\mathbf{r}},\tilde{\mathbf{r}}',k\boldsymbol{\tau}+i\boldsymbol{\Delta})\right),$$

$$T_5 = -i\frac{|v_3|v_2'}{\prod_\alpha \sqrt{(1+\omega_\alpha^2 t^2)(1+\omega_\alpha^2 t'^2)}}\left(\sum_l e^{\beta l\tilde{\mu}}G_B^{(1)}(\tilde{\mathbf{r}},\tilde{\mathbf{r}}',l\tau-i\boldsymbol{\Delta})\right)\times\left(\sum_k e^{\beta k\tilde{\mu}}\frac{\sqrt{2}}{\sigma}\frac{\tilde{z}'-e^{k\tau_z+i\Delta_z}\tilde{z}}{1-e^{2(k\tau_z+i\Delta_z)}}G_B^{(1)}(\tilde{\mathbf{r}},\tilde{\mathbf{r}}',k\tau+i\boldsymbol{\Delta})\right).$$

The dominant term is T_1 and is the one used in Sec. III B 5.

Contribution of neglected terms in the correlation of the flux

Here we evaluate the neglected terms T_2 to T_5 and the shot-noise contribution. They will be evaluated in the case of clouds far above BEC threshold. Under this assumption, all the functions are separable in the variables x, y, and t and the summation over the index l in the preceding equations reduces to the single term $l=1$.

Shot-noise contribution

Using the above analysis one can show that the main term is still proportional to $v_2 v_2'$. The additional term is then,

$$\frac{v_2 v_2'}{\prod_\alpha \sqrt{(1+\omega_\alpha^2 t^2)(1+\omega_\alpha^2 t'^2)}}e^{\beta\tilde{\mu}}G_B^{(1)}(\tilde{\mathbf{r}},\tilde{\mathbf{r}}',\boldsymbol{\tau}-i\boldsymbol{\Delta})G_B^{(1)}(\tilde{\mathbf{r}},\tilde{\mathbf{r}}',i\boldsymbol{\Delta}).$$

For $t=t'$, $\boldsymbol{\Delta}=\mathbf{0}$ and $G_B^{(1)}(\tilde{\mathbf{r}},\tilde{\mathbf{r}}',\mathbf{0})=\delta(\tilde{\mathbf{r}}-\tilde{\mathbf{r}}')$. The shot-noise term is then

$$\frac{v_2^2}{\prod_\alpha (1+\omega_\alpha^2 t^2)}\rho_{\mathrm{eq}}(\tilde{\mathbf{r}})\delta(\tilde{\mathbf{r}}-\tilde{\mathbf{r}}').$$

As expected, this term corresponds also to the one at equilibrium with rescaled coordinates.

T_2–T_5 contribution

We have $G_{fl.}^{(2)}(\mathbf{r},t;\mathbf{r}',t')=\langle\hat{I}(\mathbf{r},t)\hat{I}(\mathbf{r}',t')\rangle=\langle\hat{I}(\mathbf{r},t)\rangle\times\langle\hat{I}(\mathbf{r}',t')\rangle+\mathrm{Re}(A)$ where $A=\Sigma_{i=1}^5 T_i$.

Case $t=t'$:

(a) $\boldsymbol{\Delta}=\mathbf{0}$, then $T_1=\frac{v_2 v_2'}{\prod_\alpha\sqrt{(1+\omega_\alpha^2 t^2)(1+\omega_\alpha^2 t'^2)}}|G^{(1)}(\tilde{\mathbf{r}},\tilde{\mathbf{r}}')|^2$, T_2 and T_3 are real number and $\mathrm{Re}(T_4)=\mathrm{Re}(T_5)=0$.

(b) One finds, to leading orders, $g^{(2)}(0,0,t;0,0,t)-2\approx\frac{1}{8}\left(\frac{s_z}{H}\right)^2\left(1-2\frac{t-t_0}{t_0}\right)\left(1-\frac{\tau_z^2}{6}\right)$ where s_z is the initial size of the cloud in the vertical direction and $t_0=\sqrt{2H/g}$.

(c) The deviation from 2 is extremely small in the experimental conditions of Ref. [15] ($\sim 10^{-11}$) but shows that the bunching is strictly speaking not 2 at the center. This behavior is expected for any flux correlation function of dispersive waves [41].

(d) The correlation lengths at the detector are not modified by the additional terms.

Case $t\neq t'$:

(a) The correlation function can be written as

$$g^{(2)}(0,0,t;0,0,t')=1+\frac{|G_B^{(1)}(\tilde{\mathbf{r}},\tilde{\mathbf{r}}',\boldsymbol{\tau}+i\boldsymbol{\Delta})|^2}{G_B^{(1)}(\tilde{\mathbf{r}},\tilde{\mathbf{r}},\boldsymbol{\tau})G_B^{(1)}(\tilde{\mathbf{r}}',\tilde{\mathbf{r}}',\boldsymbol{\tau})}(1+\epsilon).$$

(b) where

$$\frac{|G_B^{(1)}(\tilde{\mathbf{r}},\tilde{\mathbf{r}}',\boldsymbol{\tau}+i\boldsymbol{\Delta})|^2}{G_B^{(1)}(\tilde{\mathbf{r}},\tilde{\mathbf{r}},\boldsymbol{\tau})G_B^{(1)}(\tilde{\mathbf{r}}',\tilde{\mathbf{r}}',\boldsymbol{\tau})}\approx e^{-[(t-t')/t^{(\mathrm{coh})}]^2[1-(\tau_z^2)/6]1-[(t+t'-2t_0)/t_0]}$$

and

(c)

$$\epsilon\approx\frac{1}{8}\left(\frac{w_z}{H}\right)^2\left[1-\left(\frac{t+t'-2t_0}{t_0}\right)\right]\left(1-\frac{\tau_z^2}{6}\right)-\frac{3}{2(\omega_z t_0\tau_z)^2}\left(\frac{t-t'}{t_0}\right)^2\left(1+\frac{\tau_z}{3}\right).$$

We have neglected terms in $\tau_z,(t-t_0)^3,(t'-t_0)^3,(t-t_0)^2(t'-t_0),(t-t_0)(t'-t_0)^2$, and higher orders.

(d) The value of ϵ is extremely small ($\sim 10^{-10}$) using Ref. [15]. The deviation from $e^{-[(t-t')/t^{(\mathrm{coh})}]^2}$ is mainly due to the mean time $(t+t')/2$ contribution and changes the value of the correlation time in the wings of the time of flight by $\sim 3\%$. The effect of the phase factor $\boldsymbol{\Delta}$ is negligible.

[1] L. Mandel and E. Wolf, *Optical Coherence and Quantum Optics* (Cambridge University Press, Cambridge, 1995).
[2] R. Hanbury Brown and R. Q. Twiss, Nature (London) **177**, 27 (1956).
[3] G. Baym, Acta Phys. Pol. B **29**, 1839 (1998).
[4] D. H. Boal, C.-K. Gelbke, and B. K. Jennings, Rev. Mod. Phys. **62**, 553 (1990).
[5] U. Heinz and B. V. Jacak, Annu. Rev. Nucl. Part. Sci. **49**, 529 (1999).
[6] C.-Y. Wong, *Introduction to High-Energy Heavy-Ion Collisions* (World Scientific, Singapore, 1994).
[7] M. Iannuzzi, A. Orecchini, F. Sacchetti, P. Facchi, and S. Pascazio, Phys. Rev. Lett. **96**, 080402 (2006).
[8] M. Henny, S. Oberholzer, C. Strunk, T. Heinzel, K. Ensslin, M. Holland, and C. Schonenberger, Science **284**, 296 (1999).
[9] W. D. Oliver, J. Kim, R. C. Liu, and Y. Yamamoto, Science **284**, 299 (1999).
[10] M. Yasuda and F. Shimizu, Phys. Rev. Lett. **77**, 3090 (1996).
[11] D. Hellweg, L. Cacciapuoti, M. Kottke, T. Schulte, K. Sengstock, W. Ertmer, and J. J. Arlt, Phys. Rev. Lett. **91**, 010406 (2003).
[12] M. Greiner, C. A. Regal, J. T. Stewart, and D. S. Jin, Phys. Rev. Lett. **94**, 110401 (2005).
[13] S. Fölling, F. Gerbier, A. Widera, O. Mandel, T. Gericke, and I. Bloch, Nature (London) **434**, 481 (2005).
[14] A. Öttl, S. Ritter, M. Köhl, and T. Esslinger, Phys. Rev. Lett. **95**, 090404 (2005).
[15] M. Schellekens, R. Hoppeler, A. Perrin, J. Viana Gomes, D. Boiron, A. Aspect, and C. I. Westbrook, Science **310**, 648 (2005).
[16] J. Esteve, J.-B. Trebbia, T. Schumm, A. Aspect, C. I. Westbrook, and I. Bouchoule, Phys. Rev. Lett. **96**, 130403 (2006).
[17] M. Naraschewski and R. J. Glauber, Phys. Rev. A **59**, 4595 (1999).
[18] M. Holzmann and Y. Castin, Eur. Phys. J. D **7**, 425 (1999).
[19] K. V. Kheruntsyan, D. M. Gangardt, P. D. Drummond, and G. V. Shlyapnikov, Phys. Rev. Lett. **91**, 040403 (2003).
[20] C. Mora and Y. Castin, Phys. Rev. A **67**, 053615 (2003).
[21] M. A. Cazalilla, J. Phys. B **37**, 1 (2004).
[22] E. Altman, E. Demler, and M. D. Lukin, Phys. Rev. A **70**, 013603 (2004).
[23] C. Gies and D. A. W. Hutchinson, Phys. Rev. A **70**, 043606 (2004).
[24] M. Born and E. Wolf, *Optics*, 6th ed. (Pergamon, Oxford 1980), Chap. 10.4.
[25] D. E. Miller, J. R. Anglin, J. R. Abo-Shaeer, K. Xu, J. K. Chin, and W. Ketterle, Phys. Rev. A **71**, 043615 (2005).
[26] N. K. Whitlock, S. M. Barnett, and J. Jeffers, J. Phys. B **36**, 1273 (2003).
[27] W. Krauth, Phys. Rev. Lett. **77**, 3695 (1996).
[28] W. H. Louisell, *Quantum Statistical Properties of Radiation* (Wiley, New York, 1973).
[29] L. D. Landau and E. M. Liftshiz, *Statistical Physics* (Butterworth, London, 1996).
[30] H. D. Politzer, Phys. Rev. A **54**, 5048 (1996).
[31] R. Hoppeler, J. C. Viana Gomes, and D. Boiron, Eur. Phys. J. D (to be published).
[32] A. G. Sinclair and M. A. Kasevich, Rev. Sci. Instrum. **68**, 1657 (1997).
[33] C. Cohen-Tannoudji, lecture notes at the Collège de France (1992) available at http://www.phys.ens.fr/cours/college-de-france/1992-93/1992-93.htm
[34] R. P. Feynmann and A. R. Hibbs, *Quantum Mechanics and Path Integrals* (McGraw-Hill, New York, 1965).
[35] I. S Gradshteyn and I. M. Ryzhik, *Table of Integrals, Series, and Products* (Academic, London, 1980).
[36] M. Naraschewski, H. Wallis, A. Schenzle, J. I. Cirac, and P. Zoller, Phys. Rev. A **54**, 2185 (1996).
[37] Y. Castin and R. Dum, Phys. Rev. Lett. **77**, 5315 (1996).
[38] Y. Kagan, E. L. Surkov, and G. V. Shlyapnikov, Phys. Rev. A **54**, R1753 (1996).
[39] H. Kaiser, S. A. Werner, and E. A. George, Phys. Rev. Lett. **50**, 560 (1983).
[40] A. G. Klein, G. I. Opat, and W. A. Hamilton, Phys. Rev. Lett. **50**, 563 (1983).
[41] A. Perrin, D. Boiron, and M. Belsley (unpublished).

Bibliography

[1] A. Einstein, "Quantentheorie des einatomigen idealen Gases. Zweite Abhandlung", *Sitzungber. Preuss. Akad. Wiss.* **1925**, 3 (1925).

[2] S. Bose, "Plancks Gesetz und Lichtquantenhypothese", *Z. Phys.* **26**, 178 (1924).

[3] F. Dalfovo, S. Giorgini, L. P. Pitaevskii, and S. Stringari, "Theory of Bose-Einstein condensation in trapped gases", *Rev. Mod. Phys.* **71**, 463 (1999).

[4] K. Huang, *Statistical mechanics* (Wiley, New York, 1990).

[5] M. R. Andrews, C. Townsend, H.-J. Miesner, D. Durfee, D. Kurn, , and W. Ketterle, "Observation of interference between two Bose condensates.", *Science* **275**, 637 (1997).

[6] B. P. Anderson and M. A. Kasevich, "Macroscopic Quantum Interference from Atomic Tunnel Arrays", *Science* **282**, 1686 (1998).

[7] M.-O. Mewes, M. R. Andrews, D. M. Kurn, D. S. Durfee, C. G. Townsend, and W. Ketterle, "Output Coupler for Bose-Einstein Condensed Atoms", *Phys. Rev. Lett.* **78**, 582 (1997).

[8] E. Hagley, L. Deng, M. Kozuma, J. Wen, K. Helmerson, S. Rolston, and W. Phillips, "A Well-Collimated Quasi-Continuous Atom Laser", *Science* **283**, 1709 (1999).

[9] I. Bloch, T. W. Hänsch, and T. Esslinger, "Atom Laser with a cw Output Coupler", *Phys. Rev. Lett.* **82**, 3008 (1999).

[10] I. Bloch, T. W. Hänsch, and T. Esslinger, "Measurement of the spatial coherence of a trapped Bose gas at the phase transition", *Nature* **403**, 166 (2000).

[11] P. Meystre, *Atom Optics* (Springer Verlag, New York, 2001).

[12] S. L. Rolston and W. D. Phillips, "Nonlinear and quantum atom optics", *Nature* **416**, 219 (2002).

[13] A. Ashkin, "Acceleration and Trapping of Particles by Radiation Pressure", *Phys. Rev. Lett.* **24**, 156 (1970).

[14] J. E. Bjorkholm, R. R. Freeman, A. Ashkin, and D. B. Pearson, "Observation of Focusing of Neutral Atoms by the Dipole Forces of Resonance-Radiation Pressure", *Phys. Rev. Lett.* **41**, 1361 (1978).

[15] S. Chu, J. E. Bjorkholm, A. Ashkin, and A. Cable, "Experimental Observation of Optically Trapped Atoms", *Phys. Rev. Lett.* **57**, 314 (1986).

[16] D. J. Wineland, R. E. Drullinger, and F. L. Walls, "Radiation-Pressure Cooling of Bound Resonant Absorbers", *Phys. Rev. Lett.* **40**, 1639 (1978).

[17] A. L. Migdall, J. V. Prodan, W. D. Phillips, T. H. Bergeman, and H. J. Metcalf, "First Observation of Magnetically Trapped Neutral Atoms", *Phys. Rev. Lett.* **54**, 2596 (1985).

[18] P. D. Lett, R. N. Watts, C. I. Westbrook, W. D. Phillips, P. L. Gould, and H. J. Metcalf, "Observation of atoms laser cooled below the Doppler limit", *Phys. Rev. Lett.* **61**, 169 (1988).

[19] H. F. Hess, G. P. Kochanski, J. M. Doyle, N. Masuhara, D. Kleppner, and T. J. Greytak, "Magnetic trapping of spin-polarized atomic hydrogen", *Phys. Rev. Lett.* **59**, 672 (1987).

[20] N. Masuhara, J. M. Doyle, J. C. Sandberg, D. Kleppner, T. J. Greytak, H. F. Hess, and G. P. Kochanski, "Evaporative Cooling of Spin-Polarized Atomic Hydrogen", *Phys. Rev. Lett.* **61**, 935 (1988).

[21] M. H. Anderson, J. R. Ensher, M. R. Matthews, C. E. Wieman, and E. A. Cornell, "Observation of Bose-Einstein Condensation in a Dilute Atomic Vapor", *Science* **269**, 198 (1995).

[22] K. B. Davis, M.-O. Mewes, M. R. Andrews, N. J. van Druten, D. S. Durfee, D. M. Kurn, and W. Ketterle, "Bose-Einstein Condensation in a Gas of Sodium Atoms", *Phys. Rev. Lett.* **75**, 3969 (1995).

[23] C. C. Bradley, C. A. Sackett, J. J. Tollet, and R. G. Hulet, "Evidence of Bose-Einstein Condensation in an Atomic Gas with Attractive Interactions", *Phys. Rev. Lett.* **75**, 1687 (1995).

[24] G. Modugno, G. Ferrari, G. Roati, R. J. Brecha, A. Simoni, and M. Inguscio, "Bose-Einstein Condensation of Potassium Atoms by Sympathetic Cooling", *Science* **294**, 1320 (2001).

[25] S. L. Cornish, N. R. Claussen, J. L. Roberts, E. A. Cornell, and C. E. Wieman, "Stable ^{85}Rb Bose-Einstein Condensates with Widely Tunable Interactions", *Phys. Rev. Lett.* **85**, 1795 (2000).

[26] T. Weber, J. Herbig, M. Mark, H.-C. Nägerl, and R. Grimm, "Bose-Einstein Condensation of Cesium", *Science* **299**, 232 (2002).

[27] R. Grimm, M. Weidemuller, and Y. B. Ovchinnikov, "Optical dipole traps for neutral atoms", *Advances in Atomic, Molecular and Optical Physics* **42**, 95 (2000).

[28] Y. Takasu, K. Maki, K. Komori, T. Takano, K. Honda, M. Kumakura, T. Yabuzaki, and Y. Takahashi, "Spin-Singlet Bose-Einstein Condensation of Two-Electron Atoms", *Phys. Rev. Lett.* **91**, 040404 (2003).

[29] A. Griesmaier, J. Werner, S. Hensler, J. Stuhler, and T. Pfau, "Bose-Einstein Condensation of Chromium", *Phys. Rev. Lett.* **94**, 160401 (2005).

[30] D. G. Fried, T. C. Killian, L. Willmann, D. Landhuis, S. C. Moss, D. Kleppner, and T. J. Greytak, "Bose-Einstein Condensation of Atomic Hydrogen", *Phys. Rev. Lett.* **81**, 3811 (1998).

[31] A. Robert, O. Sirjean, A. Browaeys, J. Poupard, S. Nowak, D. Boiron, C. I. Westbrook, and A. Aspect, "A Bose-Einstein Condensate of Metastable Atoms", *Science* **292**, 461 (2001).

[32] F. P. D. Santos, J. Léonard, J. Wang, C. J. Barrelet, F. Perales, E. Rasel, C. S. Unnikrishnan, M. Leduc, and C. Cohen-Tannoudji, "Bose-Einstein Condensation of Metastable Helium", *Phys. Rev. Lett.* **86**, 3459 (2001).

[33] V. P. Mogendorff, *Cold Ne* collision dynamics*, Phd thesis, Eindhoven University of Technology, 2004, available at http://alexandria.tue.nl/extra2/200413106.pdf.

[34] M. Walhout, H. J. L. Megens, A. Witte, and S. L. Rolston, "Magneto-optical trapping of metastable xenon: Isotope-shift measurements", *Phys. Rev. A* **48**, R879 (1993).

[35] J. Poupard, *Mesure de deux caractéristiques de l'Hé métastable important pour le refroidissement radiatif.*, Thèse de doctorat, Université de Paris XI, 2000.

[36] T. W. Hänsch and A. L. Schawlow, "Cooling of gases by laser radiation", *Opt. Comm.* **13**, 68 (1975).

[37] W. D. Phillips and H. Metcalf, "Laser Deceleration of an Atomic Beam", *Phys. Rev. Lett.* **48**, 596 (1982).

[38] W. Ketterle, D. S. Durfee, and D. M. Stamper-Kurn, in *Bose-Einstein Condensation in Atomic Gases*, edited by M. Inguscio, S. Stringari, and C. Wieman (IOS, Amsterdam, 1999), also available in cond-mat/9904034.

[39] G. V. Shlyapnikov, J. T. M. Walraven, U. M. Rahmanov, and M. W. Reynolds, "Decay Kinetics and Bose Condensation in a Gas of Spin-Polarized Triplet Helium", *Phys. Rev.Lett.* **73**, 3247 (1994).

[40] A. S. Tychkov, T. Jeltes, J. M. McNamara, P. J. J. Tol, N. Herschbach, W. Hogervorst, and W. Vassen, "Metastable helium Bose-Einstein condensate with a large number of atoms", *Phys. Rev. A* **73**, 031603 (2006).

[41] J. A. Swansson, R. G. Dall, and A. G. Truscott, "Efficient loading of a He^* magneto-optic trap using a liquid He cooled source", *Rev. of Sci. Instrum.* **77**, 046103 (2006).

[42] R. J. W. Stas, J. M. McNamara, W. Hogervorst, and W. Vassen, "Simultaneous Magneto-Optical Trapping of a Boson-Fermion Mixture of Metastable Helium Atoms", *Phys. Rev. Lett.* **93**, 053001 (2004).

[43] C. J. Myatt, E. A. Burt, R. W. Ghrist, E. A. Cornell, and C. E. Wieman, "Production of Two Overlapping Bose-Einstein Condensates by Sympathetic Cooling", *Phys. Rev. Lett.* **78**, 586 (1997).

[44] J. L. Wiza, "Microchannel plate detectors", *Nucl. Instr. and Meth.* **162**, 587 (1979).

[45] O. Sirjean, S. Seidelin, J. V. Gomes, D. Boiron, C. I. Westbrook, A. Aspect, and G. V. Shlyapnikov, "Ionization Rates in a Bose-Einstein Condensate of Metastable Helium", *Phys. Rev. Lett.* **89**, 220406 (2002).

[46] S. Seidelin, J. V. Gomes, R. Hoppeler, O. Sirjean, D. Boiron, A. Aspect, and C. I. Westbrook, "Getting the elastic scattering length by observing inelastic collisions in ultracold metastable helium atoms", *Phys. Rev. Lett* **93**, 090409 (2004).

[47] M. Naraschewski and D. M. Stamper-Kurn, "Analytical description of a trapped semi-ideal Bose gas at finite temperature", *Phys. Rev. A* **58**, 2423 (1998).

[48] S. Giorgini, L. P. Pitaevskii, and S. Stringari, "Condensate fraction and critical temperature of a trapped interacting Bose gas", *Phys. Rev. A* **54**, R4633 (1996).

[49] R. Hoppeler, *De la consensation de Bose-Einstein à l'effet Hanbury Brown & Twiss atomique de l'hélium métastable*, Thèse de doctorat, Université de Paris XI, 2005, available at http://tel.ccsd.cnrs.fr.

[50] M. Schellekens, Thèse de doctorat, Université de Paris XI, still in redaction.

[51] S. Seidelin, *Collisions dans un gaz d'Hélium métastable au voisinage de la dégénérescence quantique*, Thèse de doctorat, Université de Paris XI, 2004, available at http://tel.ccsd.cnrs.fr.

[52] J. V. Gomes, A. Perrin, M. Schellekens, D. Boiron, C. I. Westbrook, and M. Belsley, "Theory for a Hanbury Brown Twiss experiment with a ballistically expanding cloud of cold atoms", *Phys. Rev. A* **74**, 053607 (2006).

[53] A. Aspect, E. Arimondo, R. Kaiser, N. Vansteenkiste, and C. Cohen-Tannoudji, "Laser Cooling below the One-Photon Recoil Energy by Velocity-Selective Coherent Population Trapping", *Phys. Rev. Lett.* **61**, 826 (1988).

[54] J. Lawall, F. Bardou, B. Saubamea, K. Shimizu, M. Leduc, A. Aspect, and C. Cohen-Tannoudji, "Two-Dimensional Subrecoil Laser Cooling", *Phys. Rev. Lett.* **73**, 1915 .

[55] M. Kasevich and S. Chu, "Laser cooling below a photon recoil with three-level atoms", *Phys. Rev. Lett.* **69**, 1741 (1992).

[56] N. Davidson, H.-J. Lee, M. Kasevich, and S. Chu, "Raman cooling of atoms in two and three dimensions", *Phys. Rev. Lett.* **72**, 3158 (1994).

[57] J. Dziarmaga and M. Lewenstein, "Laser Cooling of Fermions to the Superfluid Transition Temperature", *Physical Review Letters* **94**, 090403 (2005).

[58] K. M. O'Hara, S. L. Hemmer, M. E. Gehm, S. R. Granade, and J. E. Thomas, .

[59] Y. Castin, J. I. Cirac, and M. Lewenstein, "Reabsorption of Light by Trapped Atoms", *Phys. Rev. Lett.* **80**, 5305 (1998).

[60] J. I. Cirac, M. Lewenstein, and P. Zoller, "Collective laser cooling of trapped atoms", *E. Phys. Lett.* **35**, 647 (1996).

[61] "Theory of relativistic magnetic dipole transitions : lifetime of the metastable 23S state of the heliumlike Ions", .

[62] "Experimental determination of the single-photon transition rate between the 2^3S_1 and the 1^1S_0 states of He", .

[63] W. H. Wing, "On neutral particle trapping in quasistatic electromagnetic fileds", *Prog. Quant. Electr.* **8**, 181 (1984).

[64] M.-O. Mewes, M. R. Andrews, N. J. van Druten, D. M. Kurn, D. S. Durfee, and W. Ketterle, "Bose-Einstein Condensation in a Tightly Confining dc Magnetic Trap", *Phys. Rev. Lett.* **77**, 416 (1996).

[65] H. F. Hess, G. P. Kochanski, J. M. Doyle, N. Masuhara, D. Kleppner, and T. J. Greytak, "Magnetic trapping of spin-polarized atomic hydrogen", *Phys. Rev. Lett.* **59**, 672 (1987).

[66] D. E. Pritchard, "Cooling Neutral Atoms in a Magnetic Trap for Precision Spectroscopy", *Phys. Rev. Lett.* **51**, 1336 (1983).

[67] A. Robert, *Réalisation d'un condensat de Bose-Einstein d'Hélium métastable*, Thèse de doctorat, Université de Paris XI, 2001, available at http://tel.ccsd.cnrs.fr.

[68] Y. Castin and R. Dum, "Bose-Einstein condensates in time-dependent traps.", *Phys. Rev. Lett.* **77**, 5315 (1996).

[69] S. Stringari, "Collective excitations of a trapped Bose-Condensed gas.", *PRL* **77**, 2360 (1996).

[70] O. Sirjean, *Collisions ionisantes: un nouveau diagnostic pour les condensats d'hélium métastable*, Thèse de doctorat, Université de Paris XI, 2003, available at http://tel.ccsd.cnrs.fr.

[71] D. W. .Snoke and J. P. Wolfe, "Population dynamics of a Bose gas near saturation", *Phys. Rev. B* **39**, 4030 (1989).

[72] A. Browaeys, *Piégeage magnétique d'un gaz d'Hélium métastable : vers la condensation de Bose-Einstein*, Thèse de doctorat, Université de Paris VI, 2000, available at http://tel.ccsd.cnrs.fr.

[73] R. Kaiser, *Manipulation par laser d'hélium métastable : effect Hanle mécanique, refroidissement sous le recul d'un photon*, Thèse de doctorat, Université Paris VI, 1990, available at http://tel.ccsd.cnrs.fr.

[74] A. Gallagher and D. E. Pritchard, "Exoergic collisions of cold $Na^* - Na$", *Phys. Rev. Lett.* **63**, 957 (1989).

[75] M. Walhout, U. Sterr, C. Orzel, M. Hoogerland, and S. L. .Rolston, "Optical Control of Ultracold Collisions in Metastable Xenon", *Phys. Rev. Lett.* **74**, 506 (1995).

[76] P. S. Julienne and F. H. Mies, "Collisions of ultracold trapped atoms", *J. Opt. Soc. Am. B* **6**, 2257 (1989).

[77] P. O. Fedichev, M. W. Reynolds, and G. V. Shlyapnikov, "Three-Body Recombination of Ultracold Atoms to a Weakly Bound s Level", *Phys. Rev. Lett.* **77**, 2921 (1996).

[78] H. C. W. Beijerinck, E. J. D.Vredenbregt, R. J. W. Stas, M. R. Doery, and J. G. C. Tempelaars, "Prospects for Bose-Einstein condensation of metastable neon atoms", *Phys. Rev. A* **61**, 023607 (2000).

[79] H. C. W. Beijerinck, "Heating rates in collisionally opaque alkali-metal atom traps: Role of secondary collisions", *Phys. Rev. A* **62**, 063614 (2000).

[80] R. Gao, P. Gibner, J. Newman, K. Smith, and R. Stebbings, "Absolute and angular efficiencies of a microchanel-plate position sensitive detector", *Rev. Sci. Instrum.* **55**, 1756 (1984).

[81] R. Hoppeler, J. Viana Gomes, and D. Boiron, "Atomic density of an harmonically trapped ideal gas near Bose-Einstein transition temperature", *Eur. Phys. J. D* **41**, 157 (2006).

[82] C. Cohen-Tannoudji, (Lecture notes at the Collège de France, 1992-93), http://www.phys.ens.fr/cours/college-de-france.

[83] M. Naraschewski, H. Wallis, A. Schenzle, J. I. Cirac, and P. Zoller, "Interference of Bose condensates", *Phys. Rev. A* **54**, 2185 (1996).

[84] M. Schellekens, R. Hoppeler, A. Perrin, J. V. Gomes, D. Boiron, A. Aspect, and C. I. Westbrook, "Hanbury Brown Twiss effect for ultracold quantum gases", *Science* **310**, 648 (2005).

[85] L. D. Landau and E. M. Lifshitz, *Statistical Physics, part 1* (Butterworth-Heynemann Ltd., London, 1980).

[86] R. P. Feynman, *Statistical Mechanics: A Set of Lectures* (Perseus Books, 1972).

[87] R. P. Feynman and A. Hibbs, *Quantum mechanics and path integrals* (Mc-Graw Hill, New-York, 1965).

[88] R. K. Pathria, "Bose-Einstein condensation of a finite number of particles confined to harmonic traps", *Phys. Rev. A* **58**, 1490 (1998).

[89] S. Flügge, *Pratical Quantum Mechanics* (Springer-Verlag, 1971).

[90] I. S. Gradshteyn and I. M. Ryzhik, *Table of series, integrals and products* (7.374 − 8) (Academic Press, London, 1980).

[91] A. E. Siegman, *Lasers* (University Science Books, 1986).

[92] R. Loudon, *The quantum theory of light, 2nd Ed.* (Oxford University Press, 1983).

[93] R. Hanbury and R. Q. Twiss, "Correlation between photons in two coherent beams of light", *Nature* **177**, 27 (1956).

[94] M. Yasuda and F. Shimizu, "Observation of Two-Atom Correlation of an Ultracold Neon Atomic Beam", *Phys. Rev. Lett.* **77**, 3090 (1996).

[95] F. T. Arecchi, "Measurement of the Statistical Distribution of Gaussian and Laser Sources", *Phys. Rev. Lett.* **15**, 912 (1965).

[96] D. Meltzer and L. Mandel, "Dynamics of a Q-Switched Laser near Threshold", *Phys. Rev. A* **3**, 1763 (1971).

[97] M. Born and E. Wolf, *Optics* (Pergamon, Oxford, 1980).

[98] Goodman, *Statistical optics* (John Wiley & Sons, New York, 1985).

[99] R. Hanbury Brown and R. Q. Twiss, "A Test of a New Stellar Interferometer on Sirius", *Nature* **178**, 1046 (1956).

[100] M.Naraschewski and R. Glauber, "Spatial coherence and density correlations of trapped Bose gases", *Phys. Rev. A* **59**, 4595 (1999).

[101] W. H. Louisell, *Quantum Statistical Properties of Radiation* (Wiley, 1973).

[102] A. L. Fetter and J. D. Walecka, *Quantum Theory of Many-Particle Systems* (Dover, 1971).

[103] D. F. Walls and G. J. Milburn, *Quantum optics* (Springer-Verlag, Berlin, 1988).

[104] L. Mandel and E. Wolf, *Optical coherence and quantum optics* (Cambridge University Press, Cambridge, MA, 1990).

[105] H. D. Politzer, "Condensate fluctuations of a trapped, ideal Bose gas", *Phys. Rev. A* **54**, 5048 (1996).

[106] S. Fölling, F. Gerbier, A. Widera, O. Mandel, T. Gericke, and I. Bloch, "Spatial quantum noise interferometry in expanding ultracold atom clouds", *Nature* **434**, 481 (2005).

[107] M. Greiner, C. A. Regal, J. T. Stewart, and D. S. Jin, "Probing Pair-Correlated Fermionic Atoms through Correlations in Atom Shot Noise", *Phys. Rev. Lett.* **94**, 110401 (2005).

[108] A. Ottl, S. Ritter, M. Kohl, and T. Esslinger, "Correlations and Counting Statistics of an Atom Laser", *Phys. Rev. Lett.* **95**, 090404 (2005).

[109] A. G. Sinclair and M. A. Kasevich, "Detector for spatial and temporal imaging of single photons", *Rev. Sci. Instrum.* **68**, 1657 (1997).

[110] D. E. Miller, J. R. Anglin, J. R. Abo-Shaeer, K. Xu, J. K. Chin, and W. Ketterle, "High-contrast interference in a thermal cloud of atoms", *Phys. Rev. A* **71**, 043615 (2005).

[111] U. Heinz and B. V. Jacak, "Two-particle correlations in relativistic heavy-ion collisions", *Ann. Rev. Nucl. Part. Sci* **49**, 529 (1999).

[112] M. Iannuzzi, A. Orecchini, F. Sacchetti, P. Facchi, and S. Pascazio, "Direct Experimental Evidence of Free-Fermion Antibunching", *Phys. Rev. Lett.* **96**, 080402 (2006).

[113] G. Baym, "The physics of Hanbury Brown-Twiss intensity interferometry: from stars to nuclear collisions", *ACTA PHYS.POLON.B* **29**, 1839 (1998).

[114] D. H. Boal, C.-K. Gelbke, and B. K. Jennings, "Intensity interferometry in subatomic physics", *Rev. Mod. Phys.* **62**, 553 (1990).

[115] C. Y. Wong, *Introduction to High-Energy Heavy-Ion Collisions* (World Scientific, 1994).

[116] M. Henny, S. Oberholzer, C. Strunk, T. Heinzel, K. Ensslin, M. Holland, and C. Schonenberger, "The Fermionic Hanbury Brown and Twiss Experiment", *Science* **284**, 296 (1999).

[117] W. D. Oliver, J. Kim, R. C. Liu, and Y. Yamamoto, "Hanbury Brown and Twiss-Type Experiment with Electrons", *Science* **284**, 299 (1999).

[118] D. Hellweg, L. Cacciapuoti, M. Kottke, T. Schulte, K. Sengstock, W. Ertmer, and J. J. Arlt, "Measurement of the Spatial Correlation Function of Phase Fluctuating Bose-Einstein Condensates", *Phys. Rev. Lett.* **91**, 010406 (2003).

[119] J. Esteve, J.-B. Trebbia, T. Schumm, A. Aspect, C. I. Westbrook, and I. Bouchoule, "Observations of Density Fluctuations in an Elongated Bose Gas: Ideal Gas and Quasicondensate Regimes", *Phys. Rev. Lett.* **96**, 130403 (2006).

[120] T. Jeltes *et al.*, "Comparison of the Hanbury BrownTwiss effect for bosons and fermions.", *Nature* **445**, 402 (2007).

[121] T. Rom, T. Best, D. van Oosten, U. Schneider, S. Fölling, B. Paredes, and I. Bloch, "Free Fermion Antibunching in a Degenerate Atomic Fermi Gas Released from an Optical Lattice", *Nature* **444**, 733 (2006).

[122] RoentDek, Manual of the *MCP-Delay line* model DLD80., available on the manufacturer's web page: http://www.roentdek.com/.

[123] O. Jagutzki, V. Mergel, K. Ullmann-Pfleger, L. Spielberger, U. Spillmann, R. Dörner, and H. Schmidt-Böcking, "A Broad-Application Microchannel-Plate Detector System for Advanced Particle or Photon Detection Tasks: Large Area Imaging, Precise Multi-Hit Timing Information and High Detection Rate", *Nucl. Instr. and Meth. in Phys. Res. A* **477**, 244 (2002).

[124] S. Seidelin, O. Sirjean, J. V. Gomes, D. Boiron, C. I. Westbrook, and A. Aspect, "Using ion production to monitor the birth and death of a metastable helium Bose Eintein condensate.", *J. Opt. B: Quantum Semiclass. Opt.* **5**, S112 (2003).

[125] Y. Kagan, B. V. Studinov, and G. V. Shlyapnikov, "Effect of Bose condensation on inelastic processes", *JETP Lett.* **42**, 209 (1985).

[126] C. Cohen-Tannoudji, (Lecture notes at the Collège de France, 1996-97), http://www.phys.ens.fr/cours/college-de-france.

[127] O. J. Luiten, M. W. Reynolds, and J. T. M. Walraven, "Kinetic theory of the evaporative cooling of a trapped gas", *Phys. Rev. A* **53**, 381 (1996).

[128] M. Abramowitz and I. Stegun, *Handbook of mathematical functions* (Dover Publications, New York, 1970).

[129] F. X. Gadea, T. Leininger, and A. S. Dickinson, "Calculated scattering length for spin-polarized metastable helium", *Journal of Chemical Physics* **117**, 7122 (2002).

[130] P. J. Leo, V. Venturi, I. B. Whittingham, and J. Babb, "Ultracold collisions of metastable helium atoms", *Phys. Rev. A* **64**, 42710 (2002).

[131] A. S. Dickinson, F. X. Gadea, and T. Leininger, "Scattering length for spin-polarized metastable helium-3 and helium-4", *J. Opt. B: At. Mol. Opt. Phys.* **37**, 587 (2004).

[132] P. M. Chikin and T. C. Lubensky, *Principles of condensed matter physics* (Cambridge University Press, 1995).

[133] H.-J. Miesner, D. M. Stamper-Kurn, M. R. Andrews, D. S. Durfee, S. Inouye, and W. Ketterle, "Bosonic stimulation in the formation of a Bose-Einstein condensate", *Science* **279**, 1005 (1998).

[134] R. G. Newton, *Scattering Theory of Waves and Particles: Second Edition* (Dover, 1982).

[135] F. Gerbier, J. H. Thywissen, S. Richard, M. Hugbart, P. Bouyer, and A. Aspect, "Critical Temperature of a Trapped, Weakly Interacting Bose Gas", *Phys. Rev. Lett.* **92**, 030405 (2004).

[136] P. Arnold and B. Tomášik, "Tc for trapped dilute Bose gases: A second-order result", .

[137] H. F. Trotter, *Proc. Am. Math. Soc.* **10**, 545 (1959).

[138] M. Holzmann and Y. Castin, "Pair correlation function of an inhomogeneous interacting Bose-Einstein condensate", *Eur. Phys. J. D* **7**, 425 (1999).

[139] D. R. De Raedt, *Phys. Rev. A* **28**, 3575 .

[140] I. Shvarchuck, C. Buggle, D. S. Petrov, M. Kemmann, W. von Klitzing, G. V. Shlyapnikov, and J. T. M. Walraven, "Hydrodynamic behavior in expanding thermal clouds of ^{87}Rb", *Phys. Rev. A* **68**, 063603 (2003).

[141] P. Pedri, D. Guéry-Odelin, and S. Stringari, "Dynamics of a classical gas including dissipative and mean-field effects", *Phys. Rev. A* **68**, 043608 (2003).

[142] J. Kim, S. Moal, M. Portier, J. Dugué, M. Leduc, and C. Cohen-Tannoudji, "Frequency shifts of photoassociative spectra of ultracold metastable helium atoms: A new measurement of the s-wave scattering length.", *Europhys. Lett.* **72**, 548 (2005).

[143] S. Moal, M. Portier, J. Kim, J. Dugue, U. D. Rapol, M. Leduc, and C. Cohen-Tannoudji, "Accurate Determination of the Scattering Length of Metastable Helium Atoms Using Dark Resonances between Atoms and Exotic Molecules", *Phys. Rev. Lett.* **96**, 023203 (2006).

[144] All the *Levenberg-Marquardt* fitting analysis done throughout this thesis was done with a routine of `Igor`, a software by *WaveMetrics, Inc.*

[145] W. H. Press, B. P. Flannery, S. A. Teukolsky, and W. T. Vetterling, *Numerical Recipes in Fortran* (Cambridge University Press, 1992).

[146] Y. Kagan, E. L. Surkov, and G. V. Shlyapnikov, "Evolution of a Bose gas in anisotropic time-dependent traps", *Phys. Rev. A* **55**, R18 (1997).

[147] A. Perrin, Thèse de doctorat, Université de Paris XI, still in redaction.

[148] Y. Kagan, E. L. Surkov, and G. V. Shlyapnikov, "Evolution of a Bose-condensed gas under variations of the confining potential", *Phys. Rev. A* **54**, R1753 (1996).

[149] C. Cohen-Tannoudji, (Lecture notes at the Collège de France, 1997-98), http://www.phys.ens.fr/cours/college-de-france.

Résumé

En 2001, la condensation de Bose-Einstein (CBE) a été obtenue dans l'hélium métastable (He^*). L'état métastable a une vie de 9000 sec et une énergie interne de 20 eV. Cette énergie peut être utilisé dans la détection des atomes avec une galette de micro-canaux (MCP). L'extrêmement bonne réponse temporelle de l'MCP et ce fort gain a permis une expérience de corrélation de densité avec des particules massives, similaire à celle de R. Twiss et R. Hanbury Brown (HBT). D'autre part, les collisions non élastiques dans l'échantillon de He^* produisent un flux d'ions, petit mais discernable, proportionnel à la densité du nuage. Ceci permet de suivre l'évolution du nuage vers la CBE, passant par la transition de phase, en temps réel et d'une manière non invasive.

Dans cette dissertation nous rendons compte de trois expériences : i) la détermination des constantes d'ionisation à deux- et trois-corps pour l'He^* ; ii) la détermination de a, la longueur de diffusion de l'He^* ; iii) la mesure de la fonction de corrélation d'intensité d'une nuage de He^* en chute libre. On a vu récemment que notre mesure de a a été affectée par une grande erreur systématique : ici nous proposons une explication possible. Nus décrivons des méthodes pour déterminer la température et le fugacité d'un nuage thermique. Enfin, une partie importante de la thèse est consacré à la dérivation d'une expression analytique pour la fonction de corrélation d'intensité du flux atomique. Cette analyse a dérivé des valeurs typiques pour la longueur de cohérence atomique transversale et longitudinale que a confirmé la possibilité de réaliser HBT dans notre expérience.

Mots-clés : Condensation de Bose-Einstein – Hélium Métastable – longueur de diffusion – Hanbury Brown & Twiss – Thermometry d'Atoms Froid – Transition de Phase – Fonction de Corrélation de Densité – Flux Atomique

Abstract

In 2001 metastable Helium (He^*) attained Bose-Einstein condensation (*BEC*). The metastable state has a lifetime of 9000 sec and an internal energy of 20 eV. This energy can be to detect individual atoms using a micro-channel plate. The extremely good time response and high gain of this detector makes it possible to carry out a density correlation measurement with massive particles similar to the pioneering experiment of R. Hanbury Brown and R. Twiss in optics. In addition, inelastic collisions between He^* atoms produce a small but detectable flux of ions proportional to the cloud's density. This allows one to follow the evolution of the cloud's density toward *BEC*, passing through the phase transition, in real time and in a non invasive way.

In this dissertation we report on three different experiments: i) the determination of the two- and three-body ionizing rate constants of He^*; ii) the determination of a, the He^* scattering length; iii) the measure of the intensity correlation function of a falling He^* cloud. It has been shown lately that our measure of a was affected by a large systematic error and we propose a possible explanation. We describe methods to determine the temperature and fugacity of a thermal cloud. Finally a major portion of the thesis is devoted to the derivation of an analytical expression for the intensity correlation function of the atomic flux. This theoretical analysis has derived typical values for the transverse and longitudinal atomic coherence length that confirmed the possibility of performing a *HBT* experiment with *HBT* greatly facilitating the study of the necessary upgrades of our apparatus.

Keywords: Bose-Einstein Condensation – Metastable Helium – Scattering length – Hanbury Brown & Twiss – Cold Atoms' Thermometry – Phase Transition – Density Correlation Function – Atomic Flux